The Nonlinear Dynamics Involved in the Seismic Assessment and Retrofit of Reinforced Concrete Buildings

Patricio Ignacio Quintana Gallo

A thesis submitted in partial fulfilment of the requirements
for the Degree of
Doctor of Philosophy in Civil Engineering

Under the supervision of:

Professor Stefano Pampanin (Senior supervisor)
Emeritus Professor Athol J. Carr (Co-supervisor)
and
Professor Patricio Bonelli C. (External supervisor, USM, Chile)

Department of Civil and Natural Resources Engineering
College of Engineering
University of Canterbury
Christchurch, New Zealand.

This thesis is dedicated to my grandparents

Hugo Rebolledo Berroeta
and
Marta Perelló Nieto

ABSTRACT

Seismically vulnerable buildings constitute a major problem for the safety of human beings. In many parts of the world, reinforced concrete (RC) frame buildings designed and constructed with substandard detailing, no consideration of capacity design principles, and improper or no inclusion of the seismic actions, have been identified. Amongst those vulnerable building, one particular typology representative of the construction practice of the years previous to the 1970's, that most likely represents the worst case scenario, has been widely investigated in the past. The deficiencies of that building typology are related to non-ductile detailing in beam column joints such as the use of plain round bars, the lack of stirrups inside the joint around the longitudinal reinforcement of the column, the use of 180° end hooks in the beams, the use of lap splices in potential 'plastic hinge' regions, and substandard quality of the materials. That type of detailing and the lack of a capacity design philosophy create a very fragile fuse in the structure where brittle inelastic behaviour is expected to occur, which is the panel zone region of exterior beam column joints.

The non-ductile typology described above was extensively investigated at the University of Canterbury in the context of the project 'Retrofit Solutions for New Zealand Multi-Storey Buildings' (2004-2011), founded by the 'Foundation for Research, Science and Technology' *Tūāpapa Rangahau Pūtaiao*. The experimental campaign prior to the research carried out by the author consisted of quasi-static tests of beam column joint subassemblies subjected to lateral loading regime, with constant and varying axial load in the column. Most of those specimens were representative of a plane 2D frame (knee joint), while others represented a portion of a space 3D frame (corner joints), and only few of them had a floor slab, transverse beams, and lap splices. Using those experiments, several feasible, cost-effective, and non-invasive retrofit techniques were developed, improved, and refined. Nevertheless, the slow motion nature of those experiments did not take into account the dynamical component inherent to earthquake related problems. Amongst the set of techniques investigated, the use of FRP layers for strengthening beam column joints is of particular interest due to its versatility and the momentum that its use has gained in the current state of the practice. That particular retrofit technique was previously used to develop a strengthening scheme suitable for plane 2D and space 3D corner beam column joints, but lacking of floor slabs. In addition, a similar scheme was not developed for exterior joints of internal frames, referred here as 'cruciform'.

In this research a 2/5 scale RC frame model building comprising of two frames in parallel (external and internal) joined together by means of floor slabs and transverse beams, with non-ductile characteristics identical to those of the specimens investigated previously by others, and also including lap splices, was developed. In order to investigate the dynamic response of that building, a series of shake table tests with different ground motions were performed. After the first series of tests, the specimen was modified by connecting the spliced reinforcement in the columns in order to capture a different failure mode. Ground motions recorded during seismic events that occurred during the initial period of the experimental campaign (2010) were used in the subsequent experiments. The hierarchy of strengths and sequence of events in the panel zone region were evaluated in an extended version of the bending moment-axial load (M-N) performance domain developed by others. That extension was required due to the asymmetry in the beam cross section

introduced by the floor slab. In addition, the effect of the torsion resistance provided by the spandrel (transverse beam) was included.

In order to upgrade the brittle and unstable performance of the as-built/repaired specimen, a practical and suitable ad-hoc FRP retrofit intervention was developed, following a partial retrofit strategy that aimed to strengthen exterior beam column joints only (corner and cruciform). The ability of the new FRP scheme to revert the sequence of events in the panel zone region was evaluated using the extended version of the M-N performance domain as well as the guidelines for strengthening plane joints developed by others. Weakening of the floor slab in a novel configuration was also incorporated with the purpose of reducing the flexural capacity of the beam under negative bending moment (slab in tension), enabling the damage relocation from the joint into the beam. The efficacy of the developed retrofit intervention in upgrading the seismic performance of the as-built specimen was investigated using shake table tests with the input motions used in the experiments of the as-built/repaired specimen.

Numerical work aimed to predict the response of the model building during the most relevant shake table tests was carried out. By using a simple numerical model with concentrated plasticity elements constructed in Ruaumoko2D, the results of blind and post-experimental predictions of the response of the specimen were addressed. Differences in the predicted response of the building using the nominal and the actual recorded motions of the shake table were investigated. The dependence of the accuracy of the numerical predictions on the assumed values of the parameters that control the hysteresis rules of key structural members was reviewed.

During the execution of the experimental campaign part of this thesis, two major earthquakes affected the central part of Chile (27 of February 2010 Maule earthquake) and the Canterbury region in New Zealand (22 February 2011 Canterbury earthquake), respectively. As the author had the opportunity to experience those events and investigate their consequences in structures, the observations related to non-ductile detailing and drawbacks in the state of the practice related to reinforced concrete walls was also addressed in this research, resulting in preliminary recommendations for the refinement of current seismic code provisions and assessment guidelines. The investigations of the ground motions recorded during those and other earthquakes were used to review the procedures related to the input motions used for nonlinear dynamic analysis of buildings as required by most of the current code provisions. Inelastic displacement spectra were constructed using ground motions recorded during the earthquakes mentioned above, in order to investigate the adequacy of modification factors used to obtain reduced design spectra from elastic counterparts. Finally a simplified assessment procedure for RC walls that incorporates capacity compatible spectral demands is proposed.

ACKNOWLEDGEMENTS

I would like to thank my senior supervisor, Professor Stefano Pampanin for his support, advices and above everything for his patience. To him, my deepest gratitude for giving me the opportunity to come to the University of Canterbury where I always wanted to continue my postgraduate studies. His support and understanding during difficult periods of my life is also greatly acknowledged. Emeritus Professor Athol Carr has been for me a never-ending source of inspiration and encouragement during the development of this research, and a mould for consensus. I would like to thank him for his support during crucial moments of my PhD. It has been a great honour to work under his supervision. I would like to express my sincere gratitude to Professor Patricio Bonelli for his support on the backstage of this research; his guidance and advices were very important during the development of this work, especially during the time spent in Chile, when I had the opportunity to inspect damaged buildings after the 2010 earthquake and lecture a course at my former university in Valparaíso, Chile. My deepest gratitude towards the FRST foundation for providing my scholarship and funding for travel expenses.

I also would like to thank my former classmates Weng Yuen Kam, Sahin Taskigedik, Masoud Moghaddasi, Alejandro Amaris, Michael Newcombe, and Francesco Sarti, whose input helped to make a better contribution. In particular I would like to thank Umut Akguzel for his support during the experimental part of my studies; his assistance in developing the retrofit intervention presented in this thesis is greatly acknowledged. The support provided by the staff of the structures laboratory Stuart Toase, Gavin Keats, Peter Coursey, Tim Perigo, and Dave McPherson is greatly appreciated. Thanks to John Maley for his technical support during the shake table tests, in particular for the shake table characterization. Special thanks to Mosese Fifita, whose wisdom and generosity was of great inspiration; his input was fundamental during the design and construction of the model building. The input provided by Dr. Antonio Di Cesare, Domenico Nigro and Dr. Felice Ponzo from the University of the Basilicata in Potenza is greatly acknowledged; their advice on a suitable repairing method for the as-built specimen was fundamental to continue the research. Special thanks to Dr. Lucy Johnston for her support.

The work done by Contech New Zealand and the materials provided by SIKA are enormously appreciated. Thanks to the New Zealand Society for Earthquake Engineering (NZZEE) for inviting me to the 'Learning from Earthquakes' mission to Chile, in particular to Peter Smith, Hugh Cowan, and Claudio Oyarzo-Vera. Thanks to Civil Defence and Christchurch city council for allowing me to be part of the building inspection after the 22 February 2011 earthquake. Thanks to my friends Elizabeth Ackermann, Helekiwe Kachali, Vicente Gonzalez, Sarah Baeven, Cristian Leaman, Marcela Palomino, Sebastian Hernandez, Mauricio Cifuentes, Marcelo Lucero, and Cristian Deney for their support during the PhD process. I also would like to express my gratitude towards Dr. David Carradine and Dr. George Allan for their advices and guidance during the time I lived in Wellington.

I would like to thank the enormous support provided by my grandparents Hugo Rebolledo Berroeta and Marta Perelló Nieto, and my mother Gabriela Gallo Perelló: Their patience, love and tolerance have no limits. To my brothers Diego García Gallo, Cristóbal Quintana Lopetegui, and Álvaro Quintana Lopetegui, and my little sister Gabriela García Gallo, thanks for making my life happier during this time. Thanks to Nuria Maureira for providing me an example of sacrifice and perseverance in life.

‘When Kant said "Our intellect does not draw its laws from nature but imposes its laws upon nature", he was right. But in thinking that these laws are necessarily true, or that we necessarily succeed in imposing them upon nature, he was wrong. Nature very often resists quite successfully, forcing us to discard our laws as refuted; but if we live we may try again’

Karl Popper

TABLE OF CONTENTS

NOMENCLATURE

[AB]	Evaluation matrix for as-built beam column joints
[R]	Evaluation matrix for retrofitted beam column joint
$\|P_{exc}$	Probability of exceedance
Δ	Lateral displacement measured at the top of each floor
a	Acceleration
a	Flange to web area ratio in asymmetric walls
A_0	Gross area enclosed by shear flow path
A_0	Effective acceleration of the soil, Chilean code
AB_{ij}	Event in the sequence number i under the scenario j in the as-built specimen
A_c	Column cross sectional area
A_{cp}	Area enclosed by outside perimeter of concrete cross section
A_f	Area of the flange in asymmetric walls
A_g	Gross cross sectional area of a structural member
A_s	Area of a single rebar of the slab reinforcement
A_s	Area of longitudinal steel concentrated in the wall ends; area of the steel located in the flange for asymmetric walls
A_{sl}	Area of the corner longitudinal reinforcement bar
A_{st}	Cross sectional area of horizontal elements restraining in the length b_c
A_{st}	Area of the transverse stirrup
A_t	Area of the transverse hook rebar
B	Beam element, for the evaluation of the hierarchy of strengths and sequence of events
b_0	Effective width of the spandrel for torsion
b_0	Effective width for torsion
b_c	Length of the cross section orthogonal to the confining reinforcement direction
b_c	Width of the column cross section
b_{cX}	Length of the cross section orthogonal to the confining reinforcement direction X
b_{cY}	Length of the cross section orthogonal to the confining reinforcement direction Y
b_{eff}	Effective slab width acting in tension

b_{eff}^{es}	Portion of the slab effective in tension at each side of the column
b_j	Effective width of the joint
b_s	Width of the slab strengthened with GFRP
BS	Strengthened section of the beam, for the evaluation of the hierarchy of strengths and sequence of events
b_w	Width of the beam web
BW	Rectangular section of the beam in the weakened region of the slab, for the evaluation of the hierarchy of strengths and sequence of events
C	Column element, for the evaluation of the hierarchy of strengths and sequence of events
c_1	Empirical coefficient used to calculate $l_{b,max}$
c_2	Empirical coefficient used to calculate $l_{b,max}$
C_b^{AC}	Compression force in the beam at the intersection with the joint, AC situation
C_b^{AT}	Compression force in the beam at the intersection with the joint, AT situation
c_c	Neutral axis depth in the potential yield regions of a wall computed for ultimate limit state, New Zealand standard
c_c	Largest neutral axis depth calculated for the factored axial force and nominal moment strength consistent with the design displacement δ_u, ACI318 code
C_c^B	Compression force in the bottom column at the intersection with the joint
C_c^T	Compression force in the top column at the intersection with the joint
CFRP	Carbon Fibre Reinforced Polymer
C_h	Spectral shape factor, New Zealand standard
CQC	Complete quadratic combination, for spectral modal analysis
C_s^{AC}	Compression force in the slab as a result of negative bending moment in the beam, AC situation
c_u	Neutral axis at ultimate top displacement of a wall
d	Effective depth of the beam cross section
d	Effective height of the steel in tension
DAF	Dynamic amplification factor
d_b	Nominal diameter of a reinforcing bar
d_c	Column effective cross section height
d_{fb}	Depth of the FRP on the beam surface
d_{fc}	Depth of the FRP on the column

dM	Variation in the moment
d_m	Maximum displacement in a hysteretic cycle; determines the degrading power function in degrading hysteretic rules
dP	Axial load variation due to seismic actions
d_p	Plastic displacement reached in a hysteretic cycle when the reversal starts
dP_{2D}	Variation of the axial load, plane 2D beam column joint
$Dr_{i,max}$	Maximum inter-storey drift in the floor i
D_{rt}	Top storey drift
D_{rtd}	Top storey drift demand
D_{rtu}	Ultimate top storey drift
DR_u^{AC}	Ultimate top storey drift for asymmetric walls in the AC situation (flange in compression)
DR_u^{AT}	Ultimate top-storey drift of an asymmetric wall in the AT situation (flange in tension)
DR_y^{AC}	Yielding top-storey drift of an asymmetric wall in the AC situation (flange in compression)
DR_y^{AT}	Yielding top-storey drift of an asymmetric wall in the AT situation (flange in tension)
D_t	Top storey displacement
D_{tp}	Plastic top storey displacement
D_{ty}	Top storey yielding displacement
d_y	Yielding displacement reached in a hysteretic cycle
E	Modulus of elasticity
e	Lever arm of the equivalent forces representing the bending moment in columns (Chapter 4)
E_c	Modulus of elasticity of the concrete
E_f	Modulus of elasticity of the GFRP
EI	Flexural elastic stiffness of a frame element
E_{ij}	Element whose capacity is triggered in the sequence order number i under the demand curve j
E_r	Modulus of elasticity dimensionless ration
E_s	Modulus of elasticity of the steel
E_{sh}	Strain hardening tangent modulus for steel at ε_{sh}
e_w	Web thickness of a wall

F	Orthogonal force resisted by the corner longitudinal bars
F	Lateral force that produces the inelastic mechanism of the building
f_c	Stress in the concrete
f_c'	Specified concrete compression strength
f_{c0}'	Compression strength of the unconfined concrete
f_{cc}'	Compression strength of the confined concrete
F_{cr}^-	Cracking action in the negative direction, Revisited Takeda and Revisited SINA rules
F_{cr}^+	Cracking action in the positive direction, Revisited Takeda and Revisited SINA rules
f_{ct}	Tensile strength of the concrete
F_f	Additional resisting force provided by the GFRP for torsion
f_{le}	Equivalent lateral pressure (MPa)
f_{leX}	Effective lateral pressure acting perpendicular to the core dimension b_{cX}
f_{leY}	Effective lateral pressure acting perpendicular to the core dimension b_{cY}
f_{lX}	Equivalent lateral pressure in the X direction (MPa)
f_{lY}	Equivalent lateral pressure in the Y direction (MPa)
FRP	Fibre Reinforced Polymer
f_s	Stress in the steel
f_{st}	Stress in the steel at maximum elongation
f_{su}	Ultimate stress of the steel
f_y	Yielding stress of the steel
F_y^-	Yielding action in inelastic elements for hysteretic rules, negative direction
F_y^+	Yielding action in inelastic elements for hysteretic rules, positive direction
f_{ys}	Yielding stress of the slab steel in tension
f_{yt}	Yielding stress of the transverse reinforcement steel
f_v	Axial stress in the joint (Chapter 6)
g	Acceleration of gravity
G	Shear modulus of the concrete
GA_s	Shear stiffness of a frame element

GFRP	Glass Fibre Reinforced Polymer
GJ	Torsional elastic stiffness of a rotational spring
g_r	Acceleration of gravity dimensionless ratio
h	Inter-storey height
h_0	Effective height of the spandrel cross section for torsion
h_b	Height of the transverse beam cross section
h_c	Column cross section height
h_{cr}	Vertical extension of confinement elements in walls
h_s	Slab thickness
h_s	Clear storey height, New Zealand standard
h_w	Wall height
i	Order of occurrence of an event in the M-N performance domain
I	Importance factor, Chilean Code
j	Lever arm of the equivalent forces representing the bending moment in beams (Chapter 4)
j	Demand curve number j in the M-N performance domain
J	Joint element, for the evaluation of the hierarchy of strengths and sequence of events
jd	Effective lever arm of the resisting pair of forces in the beam (Chapter 5)
jd^{2D}	Effective lever arm in the beam in a plane 2D joint
jd^{AC}	Effective lever arm in an asymmetric beam, AC situation
jd^{AT}	Effective lever arm in an asymmetric beam, AT situation
J_E	Equivalent polar moment of inertia of a rectangular section
k	Ratio between the maximum compressive stress of the confined and unconfined concrete
k	Factor used in the calculation of the torque that produces cracking
K	Coefficient of the Saatcioglu and Razvi stress-strain model for concrete
k_0	Initial stiffness in plastic hinges of frame elements; initial stiffness in hysteretic rules
k_1	Coefficient which depends on the Poisson modulus, empirically inferred using regression analyses
k_2	Coefficient introduced for reducing the average lateral pressure of confinement hooks, related to the stiffness of the element restraining longitudinal bars

k_{2X}	Coefficient introduced for reducing the average lateral pressure of confinement hooks, related to the stiffness of the element restraining longitudinal bars, X direction
k_{2Y}	Coefficient introduced for reducing the average lateral pressure of confinement hooks, related to the stiffness of the element restraining longitudinal bars, Y direction
K_{cr}	Twist stiffness of the transverse beam under pure torsion
K_t	Torsion stiffness of the section in radians per unit of length
k_u	Unloading stiffness in hysteretic rules
k_μ	Factor that reduces the elastic acceleration spectrum, New Zealand standard
l	Length
l	Longitudinal direction of the GFRP laminates
l_b	Half of the beam span length measured from adjacent columns centerlines
$l_{b,max}$	Critical value for the length of the GFRP laminates in the transverse direction for debonding
l_{bt}	Development length of the GFRP laminates in the transverse direction
l_c	Column length, measured from the mid-height of two consecutive floors, assumed to be inflection points
l_c	Confined length of a wall measured from the extreme fibre in compression
l_c^{ACI}	Confinement length of a wall required by the ACI318 code
l_c^{EC8}	Confinement length of a wall required by the Eurocode 8
$l_c^{NZ\text{-}D}$	Confinement length of a ductile wall required by the New Zealand standard
$l_c^{NZ\text{-}LD}$	Confinement length of a limited ductility wall required by the New Zealand standard
L_{eff}	Effective orthogonal length of the transverse beam under torsion
l_{n1}	Specimen long span length
l_{n2}	Specimen short span length
l_p	Plastic hinge length
l_r	Length dimensionless ratio (scale factor)
l_s	Length of the beam span, measured between the center line of the supporting columns
l_w	Wall length
m	Number of demand scenarios considered in the M-N performance domain
m_0	Artificial mass per unit of area required to achieve similitude

M_b	Beam bending moment
$M_{b,R}^{AC}$	Bending moment strength of the retrofitted beam for the design strain limit in the FRP, AC situation
$M_{b,R}^{AT}$	Bending moment strength of the retrofitted beam for the design strain limit in the FRP, AT situation
M_b^{AC}	Bending moment in the beam, AC situation
M_b^{AT}	Bending moment in the beam, AT situation
M_{by}^{2D}	Yielding moment capacity of the section of the beam where the slab has been cut (rectangular section)
M_{by}^{2D}	Yielding moment of the rectangular 2D beam
$M_{by}^{2D(-)}$	Negative yielding moment capacity of the rectangular beam
$M_{by}^{2D(+)}$	Positive yielding moment capacity of the rectangular beam
M_{by}^{AC}	Yielding moment of the beam in the AC situation (positive moment)
M_{by}^{AT}	Yielding moment of the beam in the AT situation (positive moment)
M_c	Bending moment of the column acting at the face of the joint, conceived as the sum of half of the moment induced by top and bottom columns in the joint
$M_{c,R}$	Retrofitted column moment strength
M_c^B	Bottom column bending moment
M_{crit}	As-built column flexural capacity in the critical section
M_c^T	Top column bending moment
M_{cy}^{2D}	Yielding moment of the column in a plane 2D beam column joint
M_{cy}^{AC}	Yielding moment of the column in the AC situation (positive moment)
M_{cy}^{AT}	Yielding moment of the column in the AT situation (negative moment)
M_{cy}^B	Bottom column yielding moment
M_{cy}^T	Top column yielding moment
m_D	Dimensionless moment
M_{ij}	Moment associated to the event E_{ij}
$M_{j,AB}$	Equivalent resisting moment of the as-built joint
$M_{j,FRP}$	Equivalent resisting moment of the joint provided by the GFRP
$M_{j,R}$	Equivalent resisting moment of the retrofitted joint

$M_{j,R}^{AC}$	Equivalent moment of the retrofitted corner joint, AC situation
$M_{j,R}^{AT}$	Equivalent moment of the retrofitted corner joint, AT situation
M_j^{2D}	Equivalent cracking moment of the joint in a plane 2D beam column joint
$M_j^{2D(-)}$	Negative equivalent moment capacity of the joint (plane 2D)
$M_j^{2D(+)}$	Positive equivalent moment capacity of the joint (plane 2D)
M_j^{AC}	Cracking moment of the joint in the AC situation (positive moment)
M_j^{AT}	Cracking moment of the joint in the AT situation (negative moment)
M_m	Mass physical quantity in the model domain
m_m	Mass per unit of area, model domain
m_p	Mass per unit of area, prototype domain
M_r	Mass dimensionless ratio
m_r	Mass per unit of area dimensionless ratio
M_{slab}^{AT}	Moment induced in the slab due to compatibility of deformations
M_{TB}^{AC}	Torsion moment in the transverse beam or spandrel, AC situation
M_{TB}^{AT}	Torsion moment in the transverse beam or spandrel, AT situation
M_u	Factored bending moment in the critical section of a wall obtained from the analysis
n	Number of elements evaluated in the M-N performance domain
N	Actual number of bars inside the distance s_s
n	Number of reinforcing bars in the slab that define the effective width in tension
n	Number of storeys of a building
N	Near fault factor, New Zealand Standard
n_f	Number of GFRP layers resisting in torsion
n_{fb}	Number of GFRP sheets on the beam face
n_{fc}	Number of GFRP sheets on the column face
N_i	Axial force at the base of the column i
N_{ij}	Axial load associated to the event E_{ij}
N_v	Axial load in the joint
p	Strain hardening power coefficient

p	Parameter that modifies the acceleration design spectrum depending on the soil, Chilean code
P	Total seismic weight of the structure, Chilean code
$p(x,y,x,t)$	Stress vector field in the joint dependent of time
$p(x,y,z)$	Stress vector field in the joint independent of time
p_c	Principal compression stress in the joint
p_{cc}	Principal compression stress in the concrete
$p_{cc,max}$	Maximum compression stress in the concrete inside the joint
p_{cp}	Outside perimeter of concrete cross section
PGA	Peak ground acceleration
PGD	Peak ground displacement
p_t	Maximum tensile principal stress in the joint
p_{tc}	Principal tensile stress in the concrete
$p_{tc,0}$	Principal tensile stress in the concrete at cracking
$p_{tcD,0}$	Dimensionless principal tensile stress in the concrete at cracking
p_{tD}	Dimensionless tensile principal stress in the joint
p_{tD}^{2D}	Dimensionless tensile principal stress in a plane 2D joint
p_{tD}^{3D}	Dimensionless tensile principal stress in a space 3D joint
p_{tf}	Principal tensile stress in the joint due to the resisting action of the GFRP
p_{tt}	Principal tensile stress in the joint due to the resisting action of the concrete and the FRP
P_v	Axial load
Q_0	Base shear
Q_{max}	Maximum base shear required by the Chilean code NCh433
Q_{min}	Minimum base shear required by the Chilean code NCh433
r	Bi-linear factor for hysteresis rules
R^*	Reduction factor of the basic elastic acceleration spectrum, Chilean code
r_0	Initial position vector
R_0	Modification factor of the structural response
R_{ij}	Evaluation row vector of the retrofitted matrix

R_u	Return period factor for ultimate limit state, New Zealand standard
s	Spacing of the confinement hoops (Chapter 5)
s	Spacing between adjacent stirrups
S	Spandrel element, for the evaluation of the hierarchy of strengths and sequence of events
S	Factor that depends on the soil type for the definition of Q_{min}, Chilean code
s_0	Maximum value for the spacing of confinement elements, ACI318 code
S_a	Spectral acceleration
SBE	Special boundary elements
S_d	Spectral displacement
S_d^{avg}	Average value of the spectra obtained with the ground motions recorded during the 2011 Canterbury earthquake
S_d^{NZS}	Displacement spectrum constructed from the New Zealand code acceleration spectrum
s_l	Spacing between 'nodes' where stiff lateral restraint is imposed onto the longitudinal rebar
S_p	Structural performance factor, New Zealand standard
s_s	Distance between the face and the column and the most distant bar considered to be active in tension
s_v	Vertical spacing of confinement elements
t	Time
t	Width of the perimeter wall for torsion
T	Tension force resisted by the steel in a beam when bending
t	Transverse direction of the GFRP sheets
T^*	Period with the largest effective translational mass in the direction of analysis, Chilean code
T_0	Parameter that modifies the acceleration design spectrum depending on the soil, Chilean code
T_1	Period of the fundamental mode of vibration of a structure
T_b^{AC}	Tension force in the beam at the intersection with the joint, AC situation
T_b^{AT}	Tension force in the beam at the intersection with the joint, AT situation
T_c	Torsion resistance provided by the concrete
T_c^B	Tension force at the bottom column at the intersection with the joint when bending
T_{cr}	Torque associated to cracking in the transverse beam or spandrel

T_c^T	Tension force in the top column at the intersection with the joint
t_f	FRP laminates thickness
T_f	Tensile force developed in the FRP laminates on the top of the slab
T_n	Natural period of vibration of the mode *n*
T_p	Predominant period of the ground motion
T_{pr}	Probable torsion capacity accounting for over-strength
t_r	Time dimensionless ratio
T_s	Tension force in the slab reinforcement
T_s	Tensile force developed in the top steel of the beam
T_s	Tensile force developed in the top reinforcement of the beam and the active width of the slab
$T_{s,ret}$	Tensile force in the retrofitted slab
T_{slab}	Tensile force in the slab steel outside the gap region
T_{tb}	Torsion moment resisted by the transverse beam
$T_{tb,R}$	Torsion moment resisted by the retrofitted spandrel or transverse beam
T_y	Torque associated to the development of yielding in the transverse beam stirrups
u	Horizontal displacement in the *x-y* reference system
v	Vertical displacement in the *x-y* reference system
v_b	Shear stress in the beam
V_b	Shear force in the beam
$V_b^{2D(-)}$	Negative shear force in the rectangular beam
$V_b^{2D(+)}$	Positive shear force in the rectangular beam
V_{b3}	Shear force in the beam, third floor (Chapter 4)
V_b^{AC}	Shear force in the beam, AC situation
v_b^{AC}	Shear stress in the beam, AC situation
V_b^{AT}	Shear force in the beam, AT situation
v_b^{AT}	Shear stress in the beam, AT situation
V_c	Shear force in the columns, measured at the mid-height of two consecutive floors in beam column joint subassemblies

V_c^B	Shear force in the bottom column
v_c^B	Shear stress in the bottom column
V_c^T	Shear force in the top column
v_c^T	Shear stress in the top column
v_f	Nominal shear stress contribution of the FRP
v_{jh}	Joint nominal shear stress
v_{jh}	Joint horizontal shear stress
V_{jh}	Joint horizontal shear force, measured at the mid-height of the joint
v_{jt}	Total shear resisted by the composite section
v_s^{AC}	Shear stress in the slab, AC situation
V_{slab}^{AT}	Shear induced in the slab for compatibility of deformations
V_u	Factored shear force in the critical section of a wall obtained from the analysis
W_E	External virtual work applied to a structure
W_I	Internal virtual work done by a structure
x	Horizontal component in the reference system
x	Short dimension of the spandrel cross section (Chapter 5)
x_0	Distance measured from the centerline of the perimeter wall of width t in the short side direction
y	Vertical component in the reference system
y	Long dimension of the spandrel cross section (Chapter 5)
y_0	Distance measured from the centerline of the perimeter wall of width t in the long side direction
Z	Hazard factor, New Zealand Standard
Z	Slope of the linear approximation for the ultimate ductility sequence of beams for different slab effective widths
z_0	Width of the FRP laminate inside the gap region
$Z_{0.3}$	Z adjusted to ε_{cu} = 0.3%
$Z_{0.3D}$	Z adjusted to ε_{cu} = 0.3%, dimensionless
$Z_{0.8}$	Z adjusted to ε_{cu} = 0.8%
$Z_{0.8D}$	Z adjusted to ε_{cu} = 0.8%, dimensionless

Z_m	Slope of the descending branch in the stress-strain relationship of concrete
α	Angle between the direction of the transverse bars and the longitudinal direction of the element
α	Direction angle of concrete cracking in the outside of the beam
α	Coefficient that relates the shear force to the variation in the axial load of the column
α	Unloading power function parameter in Modified Takeda Rule
α	Reduction factor of the initial stiffness after cracking in the positive direction in Revisited Takeda and Revisited SINA rules
α	Basic elastic acceleration spectrum, Chilean code
α	Factor that relates the length of a wall and the plastic hinge length
α'	Rate of variation of the moment as a function of the axial load
β	Inverse of the parameter α'
β	Reloading degrading parameter in Modified Takeda Rule
β	Reduction factor of the initial stiffness after cracking in the negative direction in Revisited Takeda and Revisited SINA rules
β_t	Constant that depends on the slenderness ratio of the section x/y for torsion strength calculations
γ	Average angle of shear distortion in the joint
γ	Unloading power function parameter in Revisited Takeda and Revisited SINA Rules
γ_0	Angular distortion in the concrete at cracking
γ_{xy}^{AC}	Angular distortion measured from axis x in the direction of axis y, AC situation
γ_{xy}^{AT}	Angular distortion measured from axis x in the direction of axis y, AT situation
γ_{yx}	Angular distortion in Mohr's circle
γ_{yx}^{AC}	Angular distortion measured from axis y in the direction of axis x, AC situation
γ_{yx}^{AT}	Angular distortion measured from axis y in the direction of axis x, AT situation
Γ_ϕ	Modal amplification factor
δ	Reloading degrading parameter in Revisited Takeda and Revisited SINA rules
ΔM	Increment in the mass of the experimental model required to achieve similitude
ΔM_r	Dimensionless increment in the mass of the experimental model required to achieve similitude
Δ_u	Displacement induced at the outer face of the top storey column, rocking action (Chapter 4)

δ_u	Ultimate top displacement of a wall required by the analysis, ACI318 code
$\delta\varepsilon_0^{cB}$	Axial strain variation in the bottom column due to seismic actions
$\delta\varepsilon_0^{cT}$	Axial strain variation in the top column due to seismic actions
ε_0	Strain of the concrete at peak stress
ε_0^{+}	Strain in the steel at zero stress after the maximum elongation has been reached in the previous cycle
ε_{01}	Strain corresponding to peak stress for unconfined concrete with the same mechanical characteristics (same f_c')
ε_{085}	Strain at 85% of the maximum strain ε_{01} of the equivalent unconfined concrete
ε_1	Strain value corresponding to peak stress (f_{cc}')
ε_1	Maximum principal strain in the panel zone
ε_2	Minimum principal strain in the panel zone
ε_{50h}	Additional strain provided by the confinement hoops at 50% of the maximum stress in confined concrete
ε_{50u}	Strain in the unconfined concrete at 50% of the maximum stress
ε_{85}	Strain at 85% of the maximum stress ($0.85f_{cc}'$)
ε_c	Strain in the concrete
ε_{cm}	Maximum compression strain in the concrete
ε_{cm}^{b}	Maximum strain in the concrete in compression under pure bending, beam
ε_{cm}^{cB}	Maximum strain in the concrete in compression under pure bending, bottom column
ε_{cm}^{cBT}	Maximum strain in the concrete in compression under bending moment and axial load actions, bottom column
ε_{cm}^{cT}	Maximum strain in the concrete in compression under pure bending, top column
ε_{cm}^{cTT}	Maximum strain in the concrete in compression under bending moment and axial load actions, top column
ε_{cu}	Ultimate strain of the unconfined concrete
ε_{cu}	Maximum compression strain for spalling of the unconfined concrete, Eurocode 8
$\varepsilon_{cu,c}$	Maximum compression strain in the confined concrete, Eurocode 8
$\varepsilon_{cu,c}$	Ultimate strain of the confined concrete
ε_f	Strain developed in the GFRP around the spandrel
$\varepsilon_{f,deb}$	Debonding stress of the GFRP

ε_{ft}	Maximum tensile strain of the GFRP
$\varepsilon_{ft,max}$	Maximum transverse strain in the GFRP
ε_{ftD}	Design maximum tensile strain of the GFRP
ε_{fu}	Ultimate (design) tensile strain of the GFRP
ε_{l}	Average compressive longitudinal strain in the concrete
ε_{p}^{*}	Critical compression strain in the steel at the onset of buckling after elongation has occurred
ε_{s}	Strain in the steel
$\varepsilon_{s,cr}$	Strain at the onset of buckling measured from the zero strain axis
ε_{s}^{AC}	Maximum strain in the slab, AC situation
ε_{s}^{AT}	Maximum strain in the slab, AT situation
ε_{sh}	Strain in the steel when hardening begins
ε_{sm}^{b}	Maximum strain in the steel in tension under pure bending, beam
ε_{sm}^{cB}	Maximum strain in the steel in tension under pure bending, bottom column
ε_{sm}^{cBT}	Maximum strain in the steel in tension under bending moment and axial load actions, bottom column
ε_{sm}^{cT}	Maximum strain in the steel in tension under pure bending, top column
ε_{sm}^{cTT}	Maximum strain in the steel in tension under bending moment and axial load actions, top column
ε_{su}	Ultimate strain of the steel
$\varepsilon_{su,t}$	Ultimate elongation strain in the steel
ε_{t}	Average compressive transverse strain in the concrete
ε_{tb}^{AC}	Maximum strain in the transverse beam or spandrel due to twist, AC situation
ε_{tb}^{AT}	Maximum strain in the transverse beam or spandrel due to twist, AT situation
ε_{xx}	Axial strain in the direction *x* in Mohr's circle
ε_{y}	Yielding strain of the steel
ε_{yy}	Axial strain in the direction *y* in Mohr's circle
η	Confinement length ratio
η^{ACI}	Confinement length ratio of a wall required by the ACI318 code
η^{EC8}	Confinement length ratio of a wall required by the Eurocode 8

$\eta^{NZ\text{-}D}$	Confinement length ratio of a ductile wall required by the New Zealand standard
$\eta^{NZ\text{-}LD}$	Confinement length ratio of a limited ductility wall required by the New Zealand standard
θ	Lateral angle or drift in the first storey
θ	Direction of the principal maximum principal stress σ_1
θ_h	Rotation at the base of the top storey column, rocking action (Chapter 4)
θ_h^N	Rotation at the base of the top storey column, rocking action negative direction (Chapter 4)
θ_h^P	Rotation at the base of the top storey column, rocking action positive direction (Chapter 4)
θ_t	Angle of twist (Chapter 5)
θ_{t1}	Angular twist consistent with ε_{tb}^{AC}
θ_{tc}	Angular twist in the concrete
θ_{tn}	Angular twist consistent with the nominal torsion resistance of the spandrel
θ_v	Lateral rotation of the top storey column, rocking action (Chapter 4)
θ_v^N	Rotation at the base of the top storey column, rocking action negative direction (Chapter 4)
θ_v^P	Rotation at the base of the top storey column, rocking action positive direction (Chapter 4)
λ	Factor that modifies c_c depending on the ductility class of the structural wall, New Zealand standard
μ	Structural ductility factor of a building in the direction of analysis, New Zealand standard
μ_t	Top displacement ductility of a wall
μ_ϕ	Ductility of curvature
$\mu_{\phi u}$	Ultimate ductility of curvature
ν	Poisson ratio
ν	Axial load ratio
ξ	Viscous damping
ξ_{avg}	Average measured elastic viscous damping
π_j	Dimensionless product number j
ρ	Density
ρ	Reinforcement ratio (Saatcioglu and Razvi model)
ρ_{fl}	Vertical GFRP reinforcement ratio

ρ_{ft}	Horizontal GFRP reinforcement ratio
ρ_h	Confinement steel to concrete area ratio (Chapter 5)
ρ_s	Longitudinal reinforcement ratio concentrated at the end of the wall
ρ_{se}	Equivalent transverse reinforcement ratio (the transverse steel inside a slab portion b_{eff} and thickness h_s)
σ	Stress
σ_0	Initial stress
σ_1	Maximum principal stress σ_1
σ_{11}	Principal compression stress in Mohr's circle
σ_2	Minimum principal stress in the concrete
σ_{22}	Principal tension stress in Mohr's circle
ΣA_s	Sum of the transverse reinforcement contained in both orthogonal directions (b_{cX} and b_{cY})
σ_l	Average compressive longitudinal stress in the concrete
ΣM_0	Sum of the moments in the columns at the base of the structure
ΣM_T	Sum of the moments at the top of the first storey
σ_r	Dimensionless ratio, stress
σ_t	Average compressive transverse stress in the concrete
ΣV_0	Sum of the shear forces in the columns at the base of the structure (total base shear)
σ_{xx}	Axial stress in the direction x in Mohr's circle
σ_{yx}	Shear stress in Mohr's circle
σ_{yy}	Axial stress in the direction y in Mohr's circle
σ_v	Axial stress in the joint
τ	Shear flow in the width t
τ_c	Torsion stress in the concrete
τ_{cr}	Maximum shear principal stress in torsion
τ_{max}	Maximum shear stress in Mohr's circle
Φ	Factor that multiplies the initial stiffness for the negative direction in Revisited Takeda and Revisited SINA rules
φ_{ow}	Ratio of the moment of resistance at over-strength to the moment resulting from specified earthquake actions

ϕ^R	Curvature rectangular beam
ϕ_u	Ultimate curvature
ϕ_y	Yielding curvature
ϕ_y^{AC}	Yielding curvature, asymmetric beam or wall, AC situation
ϕ_y^{AT}	Yielding curvature, asymmetric beam or wall, AT situation
ϕ_{yD}	Dimensionless nominal yielding curvature
ψ	Wall slenderness ratio
ψ_t	Factor that depends on the ratio x/y for torsion calculations
ω	Geometric coefficient for the calculation of the equivalent resisting moment of the joint
ω^{AC}	Geometric coefficient for the calculation of the equivalent resisting moment of the joint, AC situation
ω^{AT}	Geometric coefficient for the calculation of the equivalent resisting moment of the joint, AT situation

1 INTRODUCTION AND SCOPE OF THE RESEARCH

1.1 INTRODUCTION

Recent experiences with damaging earthquakes near urban centres as well as research findings validating the vulnerability of non-ductile reinforced concrete (RC) frame buildings, designed according to old codes (pre 1970's), have led to the urgent need of seismic assessment and retrofit of such structures. The lack of consideration of seismic actions in some cases or their inadequacy in others, together with the lack of capacity design philosophy and the use of non-ductile detailing of the reinforcement, have been recognized as the main deficiencies in the design of such structures (Priestley 1997, Hakuto et al. 2000, Park 2002, Pampanin et al. 2002, Calvi et al. 2002, Pampanin 2005).

Traditional seismic retrofitting strategies and techniques such as concrete or steel jacketing, epoxy repair, etc., have shown to provide an adequate solution, but with the drawback of high invasiveness and time-consumption, as well as impracticability in many cases (Rodriguez and Park 1991, Bracci et al. 1995, Sugano 1996, Engindemiz et al. 2005). In order to cope with those issues, in the past five years, extensive research on feasible, non-invasive retrofit techniques has been carried out at the Civil and Natural Resources Engineering Department of the University of Canterbury, within the project 'Retrofit Solutions for New Zealand Multi-Storey Buildings', funded by the 'Foundation for Research, Science and Technology' (*Tūāpapa Rangahau Pūtaiao*). Extensive experimental work was done to develop and/or improve some of the aforementioned retrofit solutions, focusing on the low invasiveness, the cost-effectiveness and the efficacy. These are: the Metallic Haunch (Pampanin et al. 2006, Chen 2006), Glass Fibre Reinforced Polymer layers (FRP) (Akguzel 2011), and selective weakening and external post-tensioning (Kam 2010).

The experimental work done to validate those techniques, consisted in quasi-static (slow motion) cyclic experimental tests of 2/3 scale beam column joint subassemblies representative of a structural typology with the following non-ductile detailing: (1) plain round reinforcement, (2) 180° end hooks in beams, (3) no transverse reinforcement about the column longitudinal reinforcement inside the joint, and (4) lap splices in plastic hinge zones (Pampanin et al. 2002). In most of the cases though, lap splices were not included, one exception being a specimen tested by Kam (2010). Most of those specimens were plane knee beam column joints tested under uni-directional lateral loading (displacement) protocol (Chen 2006, Kam 2010, Akguzel 2011). Others, with a more realistic representation of the problem, had a transverse beam and were tested under bi-directional lateral loading (Akguzel 2010). In both cases, some of the specimens were tested using constant and varying axial load at the top of the column. A slab was added in a last stage, resulting in the experimental tests of two corner and two cruciform exterior beam column joint assemblies (Kam et al. 2010). That is particularly relevant for the development of realistic FRP scheme, not covered by the previous researchers of the project.

The experimental results have shown the efficacy of the techniques in upgrading the behaviour of the subassemblies when modifying the hierarchy of strength and the sequence of events in the subassemblies to produce the desired failure mechanism, increasing the ductility capacity, and increasing or decreasing the strength of the subassembly. However, no work was done to validate those findings in the context of

structural dynamics, which in the experimental case implies shake table tests of a building whose beam column joints are representative of the subassemblies studied by the previous researchers involved in the same project. In addition, the analytical tools for the evaluation of the hierarchy of strengths and the sequence of events in the panel zone region in the M-N performance domain (Pampanin et al. 2007) was limited to symmetrical cross sections in the beam, not true when the slab is incorporated.

In the literature, the information related to shake table tests of buildings in general is scarce. Particularly, relatively little dynamic testing of non-ductile RC frames has been carried out as well. Most of the specimens reported to date were plane 2D frames or 3D frame buildings symmetrical in plane, i.e. two internal frames or two external frames jointed together by floor slabs and transverse beams. Some of those specimens were also very small in sized (1/4 scale), and the distortion in the experiment may be excessive. The testing protocol commonly used in shake table tests is also a matter of discussion. Typically, the input motions used to simulate the earthquake ground motions are altered versions of the original records modified to suit the design spectra of a certain region. Those inputs are used in most of the cases at increasing amplitudes, normally in terms of the PGA. The drawback of that testing protocol is that the dynamical characteristics of the specimen are modified after each test, especially after critical structural members suffer important inelastic incursions, and by the time the most demanding version of the input motion is used, the initial conditions of the tests are completely different from those of initial tests at low amplitudes.

The task of predicting the response of experimental models subjected to shake table tests is a difficult one. From the 1970's advances in computer science has enabled the used of increasingly more powerful computers, and allowed for the development of very refined numerical models (Otani 1974). However, a simple finite element model can be very useful. Concentrated plasticity (or inelasticity) elements can be used to represent at a macro-scale the nonlinear behaviour of structural elements and used to construct a suitable model in a computer program like Ruaumoko (Carr 2008). If the response of the experimental model involves nonlinear behaviour in structural members, then the prediction of that response becomes more complicated, and there is strong dependence on the parameters that control the onset of the nonlinearity and the hysteretic rule used in the numerical model, the definition of chaotic behaviour (Lorenz 1963, 1993). Equally important, differences in the input motion that is intended for the test (i.e. nominal input) and the actual recorded motion of the shake table are also a problem more on the side of open dynamical systems (Bertalanffy von, L. 1950, Quintana-Gallo et al. 2013), and may lead to very different results. That raises the question about how accurate can a blind prediction be given that the input motion that one needs to use is inevitably different from the actual one, available only after the experiment takes place.

During the development of the experimental work included in this thesis, the author had the opportunity to experience two major seismic events: the 27 February 2010 Maule earthquake that affected the central part of Chile, and the 22 February 2011 Canterbury earthquake, that affected the city of Christchurch, New Zealand. After those seismic events, during the building inspection process, new problems related to the ductility of structural RC walls were revealed (EERI 2010, Cowan et al. 2011, EERI 2011, Pampanin et al. 2012a,b).

Chilean RC buildings are normally constructed with a large amount of structural walls, even though in the last years, dual systems are increasingly more common. The response of those buildings during the 2010 Maule earthquake was overall satisfactory. However, there was one collapsed some partial-collapsed and many irreparably damaged buildings. Walls developed in many cases brittle-nature damage characterized by a concentrated crushed area and buckled longitudinal reinforcement along the web. That pattern had apparently not been observed previously seismic events in the country. In most of the damaged RC walls inspected by the author, the walls lacked of horizontal elements in the boundary for confinement of the concrete and avoid buckling in the longitudinal rebar, despite many of them were constructed in the 2000's. One reason for the existence of that major deficiency in the detailing is that before amendments introduced in 2010 and 2011, in Chile the use of the 1995 version of the ACI318 (ACI Committee 318, 1995) was allowed by the Chilean loading code Nch433Of.1996 (INN 1996), and important improvements related to ductile design of walls was introduced in the 1999 version of the same document. However the relaxation in the detaining is thought to be also the reflection of a demand-based design philosophy, which makes use of evidence gathered in the past to control the required detailing in structures.

In New Zealand, RC buildings are normally constructed with much less structural walls than in Chile. Most of the times frames are preferred and walls are used in the staircase and elevator areas, as central cores. That was the case of the structure of the two RC buildings that collapsed during the 2011 Canterbury earthquake (Pampanin et al. 2012a,b). In some other RC buildings, structural walls were importantly damaged, in a brittle nature fashion, even if special transverse elements were provided at the ends of the walls as specified in the NZS3101 standard from the 1995 version onward (Standards New Zealand 1995). Nevertheless, in some cases it was observed that the spacing of the horizontal elements was very large and jeopardized the functionality of those boundary elements. In addition, the New Zealand RC Standard does not require the use of transverse hooks or crossed ties about longitudinal bars in the middle of the web, which may have played an important role in ensuring ductile behaviour in critical regions, as stated in the ENV1998:2008 Eurocode8 guidelines for the seismic design of RC walls (European Committee for Standardization 2004).

Despite the conjectures related to the causes of the non-desired behaviour of RC walls during those two earthquakes, it is a fact that ductile nature mechanisms were not ensured with the code provisions they were designed with. That suggests that there are aspects where they can be improved as preliminary discussed in Bonelli et al. (2012).

1.2 RESEARCH MOTIVATION

There is a large stock of non-ductile RC frame buildings that have the deficiencies described above. Those buildings are acknowledged to be seismically vulnerable and thus they need to be retrofitted. Amongst the different retrofit solutions available to date, the solutions investigated at the University of Canterbury in the context of the project 'Retrofit Solutions for New Zealand Multi-Storey Buildings' have been demonstrated to be effective in most of the cases. However, those techniques have only been tested in beam-column joint subassemblies under slow motion loading protocols at increasing inter-storey drift levels, and so has the behaviour of the benchmark or as-built specimen been investigated. Those tests can provide valuable information on the nonlinear

mechanics of the subassemblies, but cannot provide insight on the dynamical component of the problem, fundamental in seismic engineering. Hence, there is a need to provide information about the response of a complete building-like experimental model representative of the structural typology under investigation with the greatest degree of realism possible.

Most of the subassemblies used in the previous research lacked of realism in the representation of exterior beam column joints because they were plane 2D only (i.e. no spandrels and slab) or 3D corner, but without a floor slab. As a result some of the technics developed or improved are not suitable for real applications. Such was the case of the FRP solution developed by Akguzel (2010). As a result, there is a need for a modification of the scheme in order to account for the presence of the floor slab in corner beam column joints, and there is a need for developing a new scheme for exterior joints of internal frames (cruciform joints). The presence of the slab introduces asymmetry in the flexural strength and stiffness of the beam. As a consequence, an extension of the analytical tools for the estimation of the hierarchy of strengths and sequence of events in the panel zone is required to be developed.

A more recently identified set of non-ductile RC wall or dual system buildings in Chile, New Zealand and perhaps other parts of the world, require attention. The findings related to the undesired nature of the observed damage pattern in recently constructed RC walls need to be discussed in depth in order to generate ideas for future experimental and numerical investigations on the topic. Seismic codes appear to have some drawbacks, and some preliminary suggestions for their modification in the light of the in-situ observations.

1.3 OBJECTIVES AND SCOPE OF THE RESEARCH

The finality of this research is to provide insight about the nonlinear dynamics involved in the seismic assessment and retrofit of non-ductile RC buildings, based on experimental and numerical research as well observations during real earthquakes. The main objectives are:

(1) To provide experimental information on the dynamical response of a non-ductile model frame building with the deficiencies mentioned before, using shake table tests, with and without lap splices.

(2) To develop an extended version of the analytical procedure for the evaluation of the hierarchy of strengths and sequence of events in beam column joints in the bending moment-axial load (M-N) performance domain, to account for the asymmetry in the beam and the activated torsion resistance of the spandrel as a result of the inclusion of a floor slab.

(3) To develop a suitable and realistic retrofit intervention to upgrade the as-built building using an extension and combination of previously developed techniques, with focus on practical implementation issues;

(4) To investigate the efficiency of that retrofit intervention to impose the intended hierarchy of strengths and sequence of events in exterior beam column joint the

dynamic range and provide experimental information of the response of the retrofitted model building, using shake table tests.

(5) To construct a simple numerical model able to predict with a good degree of accuracy the dynamic response of the model building tested in the as-built and retrofitted conditions. To discuss the most relevant issues related to the dependence of those predictions on the hysteretic parameters assumed a priori in the model, with focus on practical engineering consequences.

(6) To provide information related to the likelihood of the existence of a new set of RC walls with non-ductile detailing constructed in Chile in and New Zealand.

(7) To raise concerns about the efficiency of some current code provisions related to ductile detailing of RC walls and the adequacy of the motion protocol of nonlinear dynamic methods for the analysis of structures.

1.4 OVERVIEW

Chapter 2 presents a review of experimental research done on non-ductile as-built and retrofitted exterior beam column joint subassemblies as part of the Retrofit Project. The developed and/or improved retrofit techniques are reviewed as well as others available in the literature. In that chapter a review of shake table tests experiments of plane frames and building-like experimental models. In Chapter 3 the theoretical conception, the design and the features of the as-built experimental model developed are presented. Similitude requirements are discussed.

In Chapter 4, the results of the shake table tests of the as-built specimen before and after the lap splices in the columns were removed are presented. The recorded response of the specimen during four experiments is presented in terms of inter-storey drifts and floor accelerations, and the observed damage after each test is shown. In Chapter 5 the seismic assessment of the as-built specimen without lap splices is presented. The hierarchy of strengths and the expected sequence of events of exterior beam column joints are evaluated in an extended version of the M-N performance domain that accounts for asymmetry in the beam and incorporates the torsion resistance of the spandrel.

In Chapter 6, the design of the developed retrofit intervention is presented. The intervention incorporates an extended version of the FRP scheme proposed by Akguzel (2011) for corner beam column joints without floor slabs, a new FRP scheme for exterior joints of internal frames, named cruciform joints, as well as weakening of the floor slab in a configuration conceived to ensure the relocation of the damage from the joints into the beams. The inelastic mechanism of the retrofitted specimen is reviewed in order to evaluate the adequacy of the size of the FRP layers from the boundary of the panel zone.

In Chapter 7 the results of the shake table tests of the retrofitted specimen are presented. The response of the specimen is presented in terms of the recorded inter-storey drifts and floor accelerations histories of each floor. The observed damage in the structure at the end of the experiments is presented. Differences in the nominal and recorded motions are investigated.

In Chapter 8 numerical predictions of the specimen response in the as-built, as-built/repaired, and retrofitted conditions during the most relevant experiments is presented. The predictions were obtained with a finite element model with concentrated plasticity (or inelasticity) springs, using different hysteresis rules. A discussion on the differences of the prediction obtained a priori with the nominal input and a posteriori with the recorded input is presented, together with the strong dependence of the predicted response on the parameters that define the hysteretic behaviour and especially the one that defines the onset of nonlinearity: the bi-linear factor. The modifications done to the initial model that provide the best degree of accuracy in the prediction are explained, and the stability of the solution discussed.

In Chapter 9, observations on the performance of RC walls members during the 27 February Maule Chile earthquake are presented. Pictures with the developed brittle-nature damage pattern are shown. Conjectures are made about the mechanics behind that failure mode in the light of the damage pattern observed as well as some ideal numerical work. A critique to the Chilean standard for the seismic design of buildings (NCh433of.1996) is made, and some drawbacks in the ACI318 seismic provisions are identified.

In Chapter 10, observations on the performance of RC walls members during the 22 February 2011 Canterbury New Zealand earthquake are presented. The failure mode of many RC walls is illustrated, and potential drawbacks of the New Zealand concrete standard NZS3101 are identified. In addition, the ground motions recorded during this and the Male earthquake are examined and elastic and inelastic spectra generated. Differences in the magnitude of the elastic and inelastic spectral responses are discussed, and the adequacy of reduction factors equal or greater than 1 is reviewed in the lights of those findings. Finally, a simplified assessment procedure for RC structural walls is proposed. That procedure incorporated the demand in terms of capacity-compatible inelastic spectra instead of reduced versions of elastic counterparts of any kind.

Finally, in Chapter 11, preliminary recommendations for the improvement seismic code provisions are made based on the evidence gathered during the two aforementioned seismic events.

1.5 REFERENCES

ACI Committee 318 (1995), *Building Code Requirements for Structural Concrete and Commentary* (ACI 318R-95), American Concrete Institute, Farmington Hills, Michigan, USA.

Akguzel, U. (2011), 'Seismic Performance of FRP Retrofitted Exterior RC Beam-Column Joints under Varying Axial and Bidirectional Loading', *a thesis presented for the degree of Doctor of Philosophy in Civil Engineering*, University of Canterbury, Christchurch, New Zealand.

Bertalanffy von, L. (1950), 'An Outline of General System Theory', *British Journal of the Philosophy of Science*, Vol. 1, pp. 134-164.

Bonelli, P., Restrepo, J., Quintana-Gallo, P., Pampanin, S., Carr, A.J. (2012), 'Improvements for the Seismic Design of Reinforced Concrete Walls in Chile and

Suggestions for the Refinement of Other Seismic Code Provisions' *Proceedings of the NZSEE Annual Conference*, Christchurch, New Zealand, paper 117.

Bracci, J., Reinhorn, A., and Mander, J. (1995), 'Seismic retrofit of reinforced concrete buildings designed for gravity loads: Performance of structural model', *ACI Structural Journal*, Vol.92 (6), pp. 711-723.

Calvi, G.M., Magenes, G., and Pampanin, S. (2002), 'Relevance of Beam-Column Joint Damage and Collapse in RC Frame Assessment', *Journal of Earthquake Engineering*, Vol. 6, Special Issue 1, pp.75-100.

Carr, A. J. (2008), *Ruaumoko – Program for Inelastic Dynamic Analysis*, Volume 1: Theory, Department of Civil and Natural Resources Engineering, University of Canterbury, Christchurch, New Zealand.

Chen (2006), 'Retrofit Strategy of Non-Seismically Designed Frame Systems Based on a Metallic Haunch System', *a thesis presented for the degree of Master in Civil Engineering*, University of Canterbury, Christchurch, New Zealand.

Cowan, H., Beattie, G., Hill, K., Evans, N., McGhie, C., Gibson, G., Lawrence, G., Hamilton, J., Allan, P., Bryant, M., Davis, M., Hyland, C., Oyarzo-Vera, C., Quintana-Gallo, P., and Smith, P. C. (2011), 'The M8.8 Maule Chilean Earthquake', *Bulletin of the New Zealand Society for Earthquake Engineering*, Vol.44, No.3, pp. 123-166.

EERI (2010), 'The M_W 8.8 Chile Earthquake of February 27, 2010', *Learning from Earthquakes, Special Earthquake Report*, Earthquake Engineering Research Institute, San Francisco, California, USA.

EERI (2011), 'The M_w 6.3 Christchurch, New Zealand earthquake of February 22, 2011', *EERI Special Earthquake Report*, Earthquake Engineering Research Institute, San Francisco, California, USA.

Engindeniz, M., Kahn, L., and Zureick A. (2005), 'Repair and Strengthening of Reinforced Concrete Beam-Column Joints: State of the Art', *ACI Structural Journal*, Vol. 102(2), pp. 187-197.

European Committee for Standardization (2004), *Eurocode8 – Design Provisions for Earthquake Resistance of Structures, ENV 1998-1 Specific Rules for Various Materials and Elements*, Brussels, Belgium.

Hakuto, S., Park, R., and Tanaka, H. (2000), 'Seismic Load Tests on Interior and Exterior Beam-Column Joints with Substandard Reinforcing Details', *ACI Structural Journal*, Vol. 97(1), pp. 11-25.

INN (1996), *Seismic Design of Buildings*, Norma Chilena Oficial NCh433Of.96, Instituto Nacional de Normalización, Santiago, Chile (*in Spanish*)

Kam, W.Y., Quintana-Gallo, P., Akguzel, U., Pampanin, S. (2010), 'Influence of Slab on the Seismic Response of Substandard Exterior Reinforced Concrete Beam Column

Joints', *Proceedings of the for 9th US and 10th Canadian National Conference on Earthquake Engineering*, Toronto, Canada.

Kam, W. (2010), 'Selective Weakening and Post-Tensioning for the Seismic Retrofit of Non-Ductile RC Frames', *a thesis presented for the degree of Doctor of Philosophy in Civil Engineering*, University of Canterbury, Christchurch, New Zealand.

Lorenz, E. (1963), 'Deterministic Non Periodic Flow', *MIT Press*, Massachusetts, USA.

Lorenz, E. (1993), *The Essence of Chaos*, University of Washington Press, Washington State, USA.

Otani, S. (1974), SAKE, *A computer Program for Inelastic Response or R/C Frames to Earthquakes*, University of Illinois, Urbana Champaign, Illinois, USA.

Pampanin, S., Calvi, G.M., Moratti, M. (2002), 'Seismic Behavior of RC Beam Column Joints Designed for Gravity Loads', *12th ECEE*, London, England, paper n. 726.

Pampanin, S. (2005), 'Controversial Aspects in Seismic Assessment and Retrofit of Structures in Modern Times: Understanding and Implementing Lessons from Ancient Heritage', *New Zealand Concrete Society Conference*, Auckland, New Zealand.

Pampanin, S., Christopoulos, C., Chen, T. (2006), 'Development and Validation of a Metallic Haunch Seismic Retrofit Solution for Existing Under-Designed RC Frame Buildings", *Earthquake Engineering and Structural Dynamics*, Vol. 35, pp. 1739-1766.

Pampanin, S., Bolognini D., and Pavese, A. (2007) 'Performance-Based Seismic Retrofit Strategy for Existing Reinforced Concrete Frame Systems Using Fiber-Reinforced Polymer Composites', *Journal of Composites for Construction*, ASCE, Vol. 11(2), pp. 211-226.

Pampanin, S., Kam, W. Y., Akguzel, U., Tasligedik, A. S., Quintana-Gallo, P. (2012a), *The observed earthquake damage of reinforced concrete buildings in the Christchurch CBD on the 22 February 2011 Earthquake – Part I: Overview*, Department of Civil and Natural Resources Engineering, University of Canterbury, Christchurch, New Zealand.

Pampanin, S., Kam, W. Y., Akguzel, U., Tasligedik, A. S., Quintana-Gallo, P. (2012b), *The observed earthquake damage of reinforced concrete buildings in the Christchurch CBD on the 22 February 2011 Earthquake – Part II: Damage Observation*, Department of Civil and Natural Resources Engineering, University of Canterbury, Christchurch, New Zealand.

Park, R. (2002) 'A Summary of Simulated Seismic Load Tests on Reinforced Concrete Beam-Column Joints, Beams and Columns with Substandard Reinforcing Details', *Journal of Earthquake Engineering*, Vol. 6(2), pp. 147-174.

Priestley, M.J.N. (1997), 'Displacement-based Seismic Assessment of Existing Reinforced Concrete Buildings', *Journal of Earthquake Engineering*, Vol. 29, n4, p 356-272.

Quintana-Gallo, P., Rebolledo, R., and Allan, G. (2013), 'Dealing with Uncertainty in Earthquake Engineering: a Discussion on the Application of the Theory of Open Dynamical Systems, *Obras y Proyectos*, Vol 14(2), pp. 66-77 (*in English*).

Rodriguez, M. and Park, R. (1991), 'Repair and Strengthening of Reinforced Concrete Buildings for Seismic Resistance', *Earthquake Spectra*, Vol. 7(3), pp. 439-459.

Standards New Zealand (1995), NZS3101:1995, *Concrete structures standard*, Wellington, New Zealand.

Sugano, S. (1996), 'State-of-the-Art in Techniques for Rehabilitation of Buildings', *Proceedings of the 11th WCEE*, Acapulco, Mexico

Part I: RC Frames

2 PREVIOUS RESEARCH ON SEISMIC ASSESSMENT AND RETROFIT OF NON-DUCTILE RC FRAMES

2.1 INTRODUCTION

Recent experiences with damaging earthquakes near urban centers as well as research findings have validated the seismic vulnerability of non-ductile reinforced concrete (RC) frame buildings designed according to old codes (pre-1970s). These findings have led to an urgent need for assessing and retrofitting such structures. Lack of consideration of seismic actions in some cases, and/or the use of older seismic code provisions which do not incorporate capacity design concepts and ductile detailing principles have been recognized as the main source of vulnerability in this typology. Non-ductile detailing in the worst case, corresponds to the use of plain round bars, 180° end hook in beam longitudinal reinforcement, lap splices in potential plastic hinge zones, and no transverse reinforcement in the panel zone (Priestley 1996, Hakuto et al. 2000, Calvi et al. 2002a, Pampanin et al. 2002, Park 2002).

Traditional seismic retrofit strategies and techniques such as concrete jacketing, epoxy repair, concrete replacement with structural mortar, and steel jacketing, have shown to provide an adequate solution, with the drawback of high invasiveness, and time-consumption. In the past five years, extensive research on feasible, non-invasive retrofit techniques has been carried out at the Department of Civil and Natural Resources Engineering of the University of Canterbury, within the project "Retrofit Solutions for New Zealand Multi-storey Buildings" funded by the "Foundation for Research Science and Technology" (FRST). This research, focused on RC frame buildings, has been carried out in experimental tests on beam column joint subassemblies, representing portions of one of the worse cases in non-ductile typologies. Seismic actions have been simulated using uni-axial and bi-axial lateral loading protocols as well as constant and varying axial load in the column. The case study of the corner beam column joints tested under bi-directional loading protocol with varying axial load in the column represents one of the most realistic cases tested (Pampanin et al. 2007). However, with the incorporation of a cast in situ floor slab in the corner specimen, a bigger degree of realism in the subassembly was achieved in the latest tests performed at the University of Canterbury in 2009, which confirmed the vulnerability of the typology under study (Kam et al. 2010).

In other laboratory facilities, non-ductile RC frame model buildings have been constructed using different scales and geometry and tested using different methods such as quasi-static and pseudo-dynamic lateral loading and dynamic shake table tests. Experiments reported in the literature range from plane frames tested quasi-statically, more complex 3D models tested pseudo-dynamically, to bi-directional shake table tests of small-scale specimens, including infill panels in some cases. The scope of these experiments has been to show the seismic vulnerability of a certain typology and/or test the ability of a certain retrofit intervention to upgrade the response of the as-built model, using different techniques and technologies.

In this Chapter, a review of the research previously done in beam column joint subassemblies similar to those incorporated in the model used in the shake table tests described in this thesis. The most relevant experimental research on non-ductile frame

specimens tested under quasi-static, pseudo-dynamic and dynamic (shake table) loading protocol is presented. A large spectrum of retrofit techniques involving different technologies is reviewed in order to identify their pros and cons. In particular, FRP laminates layout is reviewed with the intension of identifying similarities with the layout presented in Chapter 6. Focus is placed on identifying gaps in term of the degree of realism the experiments in terms of specimen geometry, testing method, and dynamic input motion protocol if applicable.

2.2 NON-DUCTILE RC BEAM COLUMN JOINT SUBASSEMLIES TESTED UNDER QUASI-STATIC LATERAL LOADING PROTOCOL

In the last 20 years, important experimental and analytical studies have been carried out on non-ductile beam column joint subassemblies (Aycardi et al. 1994, Sugano 1996, Beres et al. 1996, Hakuto et al. 2000, Calvi et al. 2002a, Pampanin et al. 2002, 2006, 2007, Pampanin 2005, Park 2002, Kam et al. 2010, Kam 2010, Akguzel 2011). The purpose of this research has been related to the assessment of the seismic vulnerability of RC frame buildings designed according to the engineering practice of the years previous to the introduction of capacity design and ductile detailing concepts, and the introduction of modern seismic codes (Park and Paulay 1976, Paulay and Priestley 1992).

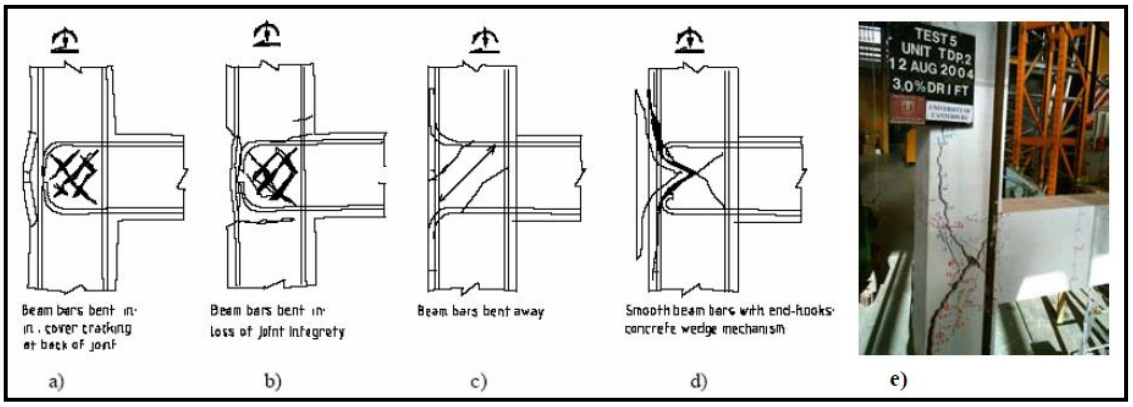

Figure 2.1: Alternative damage mechanisms for exterior Tee-joints: a,b) beam bars bent in joint region; c) beam bars bent outside the joint region; d, e) end-hook anchorage: "concrete wedge" mechanism (from Pampanin 2005).

Beam column joint subassemblies – exterior and interior – typically 2/3 to full-scale, have been tested under quasi-static lateral loading protocol, either uni-directional or bi-directional, with no axial load on the column, or using constant additional axial load. More recently varying the axial load in the column has been incorporated in order to simulate seismic effects more realistically (Pampanin et al. 2007). In Figure 2.1, the details of a 2/3 corner joint corresponding to a subassembly of the non-ductile prototype frame used in this thesis is presented. Figures indicate four different detailing layouts, with d) being the most vulnerable. The reproduction of the failure mode in the laboratory is also shown in Figure 2.1 (Pampanin 2005).

The experiment of the specimen shown in Figure 2.1 represents the simplest case in geometry, which is a plane 2D knee joint. Lateral loading in this case is uni-directional only, but the axial load can vary directly proportionally to the lateral force applied

(Pampanin et al. 2002, 2006a, Kam et al. 2010). Corner 3D beam column joint subassemblies have been tested bi-directionally also including varying axial load (Pampanin et al. 2007, Akguzel 2011). However, those specimens lacked floor slab which is an element added in a last stage of the experimental campaign. For that, two beam column joints slab specimens (one 2D and one 3D) were constructed (Kam et al. 2010). For further details on this kind of experimental research, the interested reader is referred to Kam (2010).

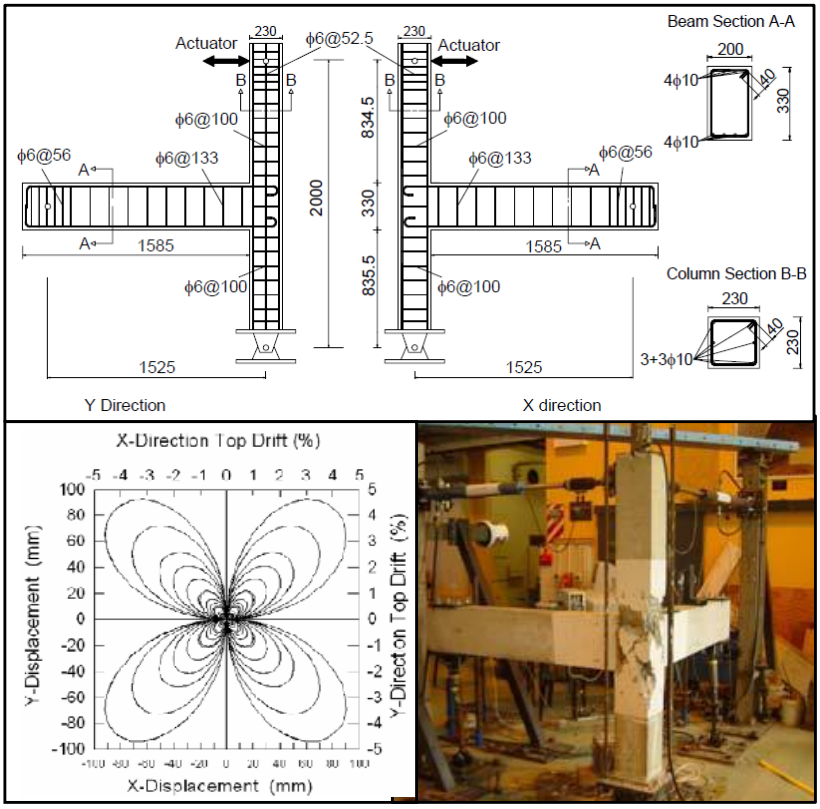

Figure 2.2: Top: 3D benchmark specimen details; bottom left: bi-directional loading protocol; bottom right: specimen after reaching 4% drift on each direction (from Pampanin et al. 2007).

Figure 2.3 Left: Collapsed RC frame building during the 1999 Kocaeli earthquake; right: corner beam-column joint slab specimen tested at the University of Canterbury (August, 2009).

2.3 RETROFIT SOLUTIONS FOR NON-DUCTILE FRAMES AVAILABLE IN THE LITERATURE

As explained previously, real experiences during earthquake and experimental work have confirmed the potential inability of some structures to withstand seismic events safely. This is understood as seismic vulnerability of a building, which introduces the *ethical* and in some cases legal need for retrofitting that structure. Retrofit is understood as the art of using available techniques and technology for upgrading a seismically vulnerable building by means of a suitable conceptual strategy and intervention. Within a traditional performance based design of structures, different limit states or performance levels can be targeted. The performance level targeted is typically defined by the technology required for achieving that goal (Pampanin 2005).

Several retrofit strategies and techniques have been suggested in the past, as reported in literature review reports and papers (Sugano 1996, FEMA-356 2000, fib 2003, Engindeniz et al. 2005, Thermou et al. 2006). Those techniques, which correspond to the state of the practice, are listed below (see Figure 2.4).

- Epoxy repair
- Removal and replacement
- Concrete jacketing
- Concrete masonry unit jacketing
- Steel jacketing and addition of external steel elements
- Strengthening with Fibre-Reinforced Polymer (FRP) composite materials

Figure 2.4: Top left: structural mortar repairing – epoxy crack injection; top middle: external RC jacketing in a central column; top right: adjacent RC element added to an existing weak column; bottom left: foundation upgrading and RC walls added to an existing frame; FRP layers CFRP layers applied to beams for shear resistance (from Thermou et al. 2006).

From these retrofit methods already being implemented in practice, strengthening with FRP laminates seems to be the most feasible solution, due to the versatility of the material for location, the lesser degree of labour-intensiveness, and the reduced loss of floor space and disruption to building occupancy (Thermou et al. 2006).

More recently, alternative non-invasive solutions have been introduced as well as high-performance solutions based on passive control systems, such as shape memory alloys, as, listed below (Dolce et al. 2000, 2005, Dolce et al. 2006a,b,c, DesRoches et al. 2004, Marriott 2009).

- Dissipating steel braces
- Shape memory alloys (SMA) braces
- Traditional (rubber) base isolation
- SMA base isolation
- CFRP laminates
- DIS-CAM system

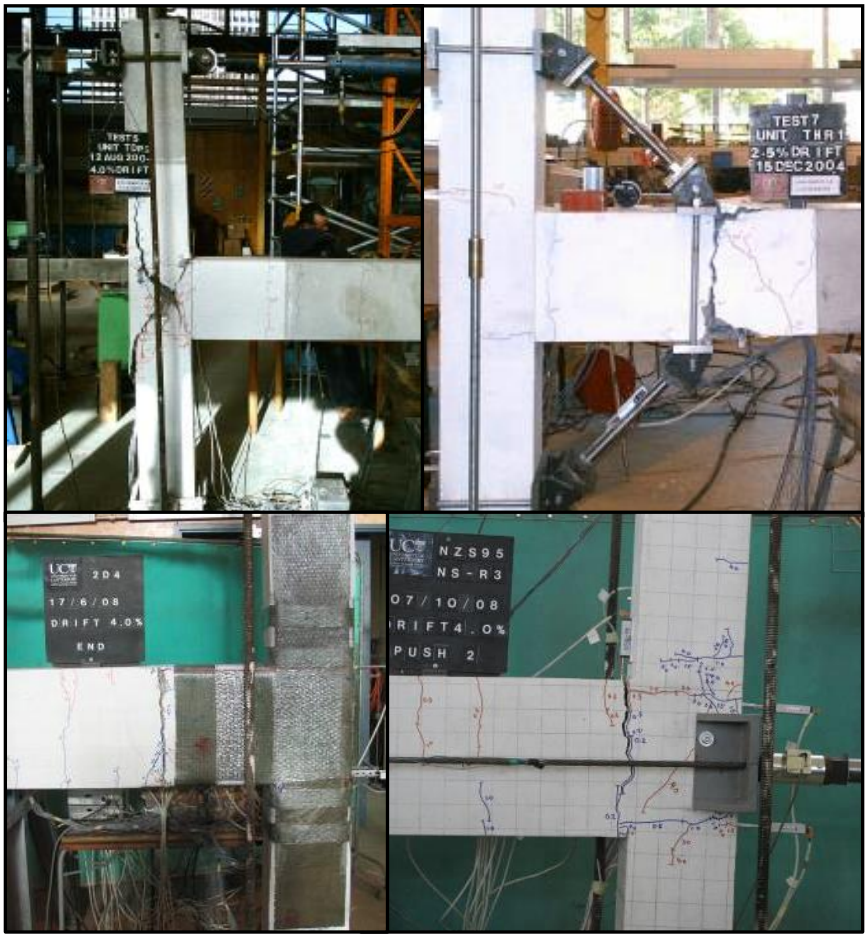

Figure 2.5: Top left: as-built specimen; top right: metallic haunch, bottom left: GFRP layers; bottom right: selective weakening and external post-tensioning.

At the University of Canterbury, extensive experimental work has been done to develop new and/or improve recently popular retrofit solutions, focusing on the low invasiveness, the cost-effectiveness and the efficacy. Solutions targeting a life safety limit state such as

the Metallic Haunch (Pampanin et al. 2006, Chen 2006), Glass Fibre Reinforced Polymer layers (GFRP) (Akguzel 2011), and selective weakening and external post-tensioning (Kam 2010) have been implemented and tested in 2/3 scale beam column joint subassemblies. In addition, external rocking walls as a high performance solution targeting a damage control performance level as been experimentally and numerically developed (Marriott 2009).

Results have shown the efficacy of these techniques of upgrading the behavior of the subassemblies by relocating brittle inelastic incursions in the joint into ductile bending rotations in the beam. This is analytically done by reversing the hierarchy of strengths in the panel zone region in order to shift the sequence of inelastic incursions (sequence of events) in the subassembly, achieving a more ductile and stable failure mechanism (see Figure 2.5). In Figure 2.5 the ability of 3 retrofit solutions for relocating the damage away from the panel zone region, mitigating the shear failure in the joint. In all cases, by different means, the flexural inelastic behavior in the beams is reached, keeping the column and joint within the elastic range, as per capacity design concepts, imposing a ductile failure mechanism. In the case of the Metallic Haunch, the strength and stiffness of the system are also increased, whereas in the weakened specimen, the strength in the positive moment direction is reduced. In the specimen retrofitted with GFRP, finally, the strength is increased, but not the stiffness so much, due to bond deterioration of the GFRP, for which an improved way of anchoring is needed.

2.4 FRAME MODELS AS BUILT AND/OR RETROFITTED TESTED UNDER QUASI-STATIC AND PSEUDO-DYNAMIC LATERAL LOADING

A reduced number of slow motion – laterally simulated seismic loading tests of non-ductile frame assemblies have been reported in the literature. In the context of experimental work done at the European Laboratory for Structural Assessment (ELSA) at the European Joint Research Centre in Ispra (Italy) a RC frame model building was tested following a pseudo-dynamic bi-directional loading protocol (Pinto 1995).

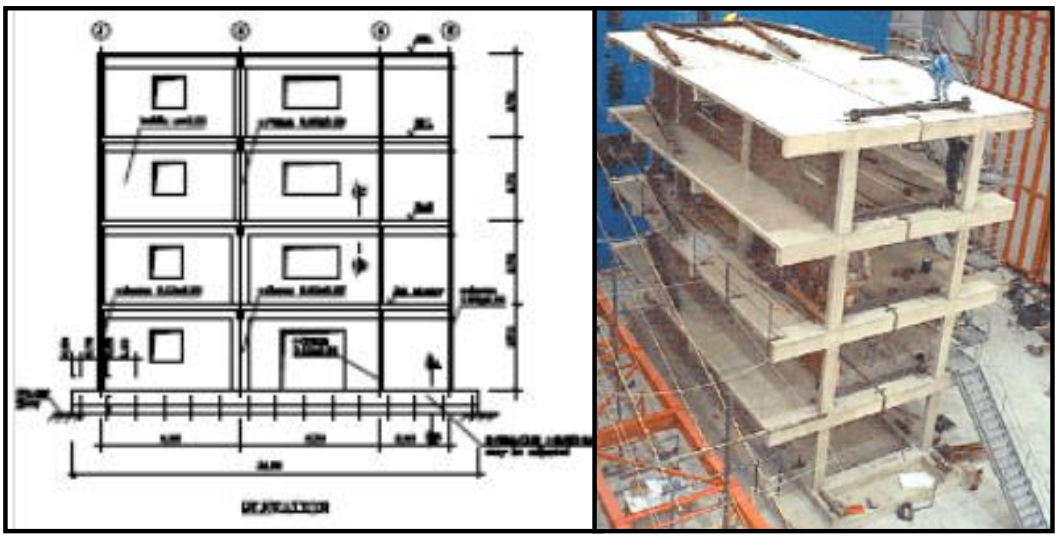

Figure 2.6: Full scale 3D 4-storey – 3 bay RC frame building tested under pseudo-dynamic loading protocol at ELSA (from Pinto 2005).

The full scale 3D specimen consisted of two 4-storey, 3-bay interior frames jointed together by casted in situ floor slabs and transverse beams. Infill panels were included in 2 of the 3 bays, as shown in Figure 2.6.

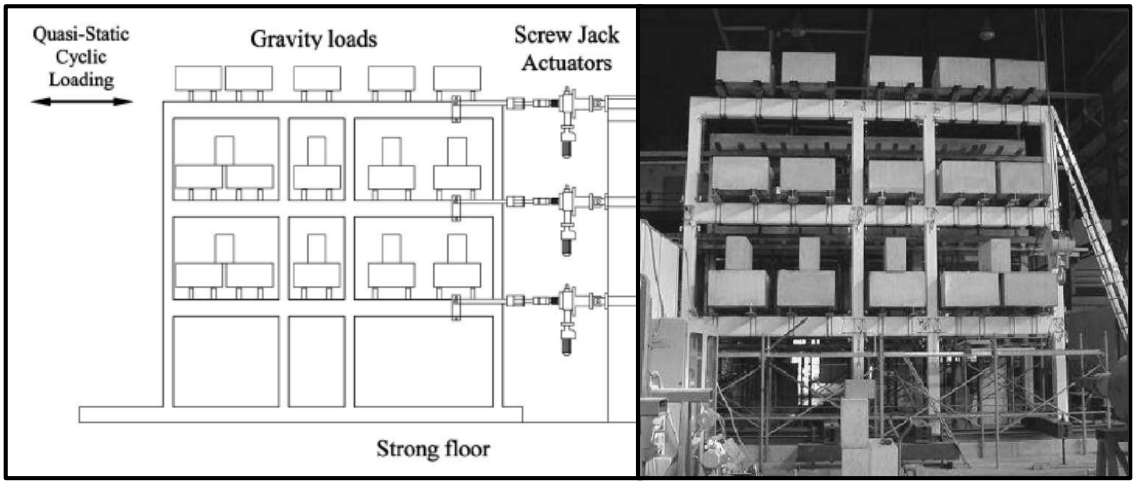

Figure 2.7: 2/3 scale, 3-storey, 3-bay plane RC frame tested under uni-directional quasi-static loading (from Calvi et al. 2002b).

More recently, at the ROSE School in Pavia (Italy), a 2/3 scale, 3-bay, 3-storey plane RC frame designed for gravity loads only was tested under quasi-static lateral loading protocol, as reported in Calvi et al. (2002a,b) (see Figure 2.7). The experiments were done in parallel with a series of equivalent beam column joint subassemblies (Pampanin et al. 2002), in order to understand the mechanics of the damage pattern of the assessed to be seismically vulnerable building (non-ductile).

Figure 2.8: 2/5 scale, 4-storey, 2-bay (symmetrical) RC frame experimental model (from Cardone et al. 2004 – courtesy of Dr. Antonio Di Cesare).

At the University of the Basilicata, in Potenza (Italy), a 2/5 scale 3D model building consisting of two 4-storey, 2-bay exterior frames jointed together by floor slabs and transverse beams was tested under uni-directional pseudo-dynamic loading regime (see

Figure 2.8). The specimen was tested with and without base isolators, as a complementary study of shake table tests of a similar 1/4 scale specimen for proving information about the efficiency these retrofit technique (Cardone et al. 2004).

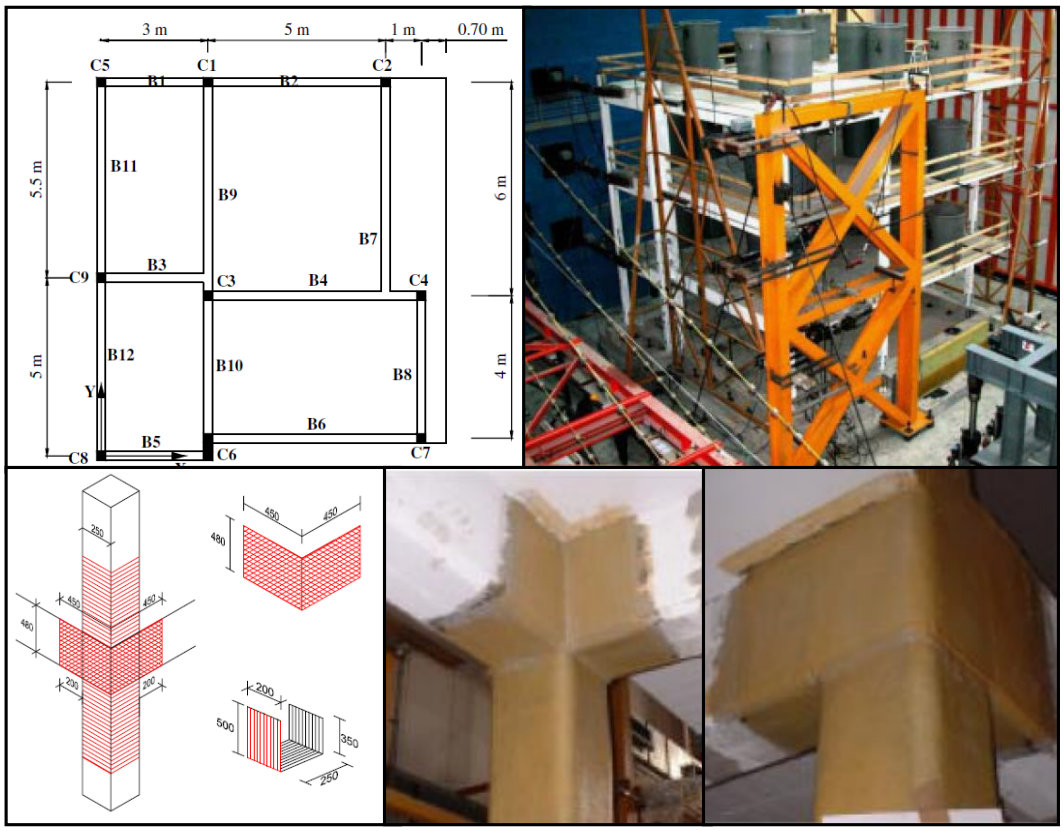

Figure 2.9: Pseudo-dynamic test of an as-built and retrofitted building performed at ENEA (Rome) (from Di Ludovico et al. 2008).

Lastly, a full scale 3D model building with clearly realistic layout was tested at the ELSA laboratory in Rome (Di Ludovico et al. 2008). The structure was designed for gravity loads only and retrofitted with FRP laminates. A bi-directional pseudo-dynamic lateral loading protocol was used for simulating seismic actions. Test series followed the use of a certain slow motion lateral loading meant to represent the response of the building under a dynamic input of different equivalent PGA levels (0.20g and 0.40g). The as-built specimen was tested till 0.20g, then retrofitted and tested till reaching a 0.40g equivalent lateral load level. In a final series, the specimen was re-tested retrofitted at 0.20g and 0.40g lateral force levels. The FRP scheme for upgrading critical elements like beam column joints was done following a force-based approach. The constructed as-built specimen and some details of the retrofit intervention are presented in Figure 2.9. The complete description of the latter can be found in Di Ludovico et al. (2008).

2.5 SHAKE TABLE TESTS OF NON-DUCTILE AS-BUILT AND/OR RETROFITTED RC FRAME EXPERIMENTAL MODELS

Shake table tests of non-ductile RC frame experimental models both as-built and retrofitted are rather scarce in the (to date) available literature. At the University of New

York at Buffalo, a 1/3 scale, 3-storey, 3-bay model structure concerning two symmetric interior frames, representing a model version of a RC structure designed for gravity loads only was tested on the shake table facilities (Bracci et al. 1995). The specimen presented in Figure 2.10, was initially tested as-built and then repaired and retrofitted with heavy concrete jacketing. Results showed firstly the vulnerability of the as-built specimen and secondly the efficacy of concrete jacketing as a retrofit technique for upgrading the performance of the specimen. However, it was highlighted that practical difficulties for executing the intervention, the cost of implementation and the time consuming characteristics of the strategy were rather high.

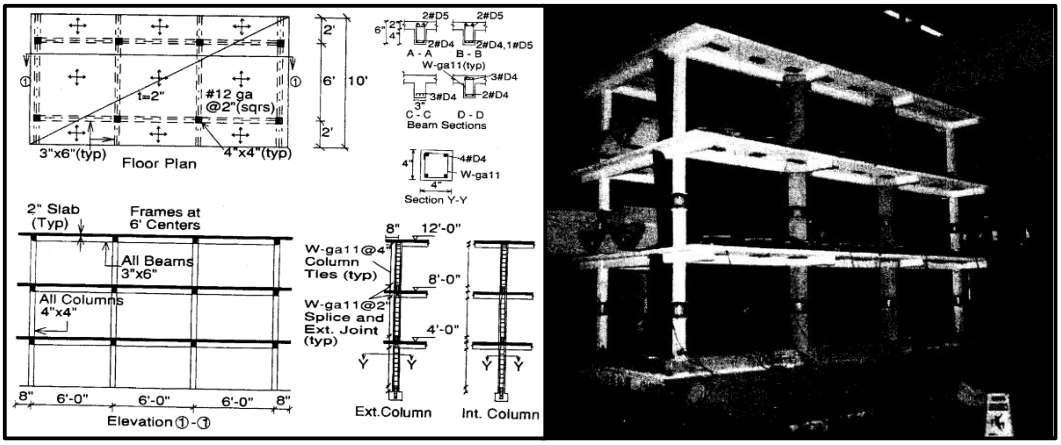

Figure 2.10: non-ductile 1/3 scale frame model tested under 2D shake table excitation at the University of New York at Buffalo, USA (from Bracci et al. 1995).

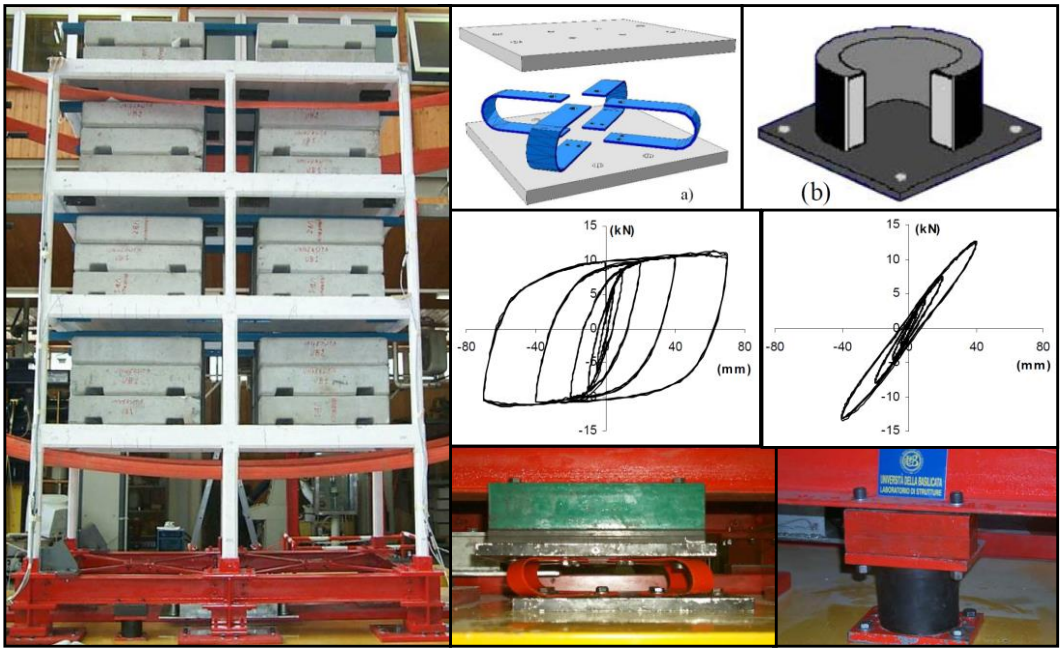

Figure 2.11: 1/4 scale 3D model – two external frames; traditional rubber base isolators and hysteretic U-shaper steel dissipaters (from Cardone et al. 2004).

More recently, as reported in Cardone et al. (2004), a 1/4 scale 3D specimen (see Figure 2.11) similar to that tested pseudo-dynamically at a larger scale (see Figure 2.8) under

uni-directional shake table excitation at the University of Basilicata in Potenza, Italy, confirming in the dynamic range the efficacy of traditional base isolation and hysteretic dissipaters as a reliable retrofit technique.

At the Technical University of Athens, shake table tests of series of 1/3.3 scale (30%), 3-storey, 2-bay (symmetrical) individual interior RC frames were performed in the context of the development of high performance retrofit techniques. The experimental campaign included testing of an as-built specimen with and without infill panels, and bare frame specimens retrofitted with dissipating steel and shape memory alloys (SMA) braces as well as SMA isolators (Dolce et al. 2000, 2005, 2007). The structural layout of the frame includes floor slabs and short transverse beams (stubs) at each floor level and on each side of the frames. The testing protocol followed the use of one unique ground motion at increasing PGA levels in subsequent tests. The specimens are illustrated in Figure 2.12.

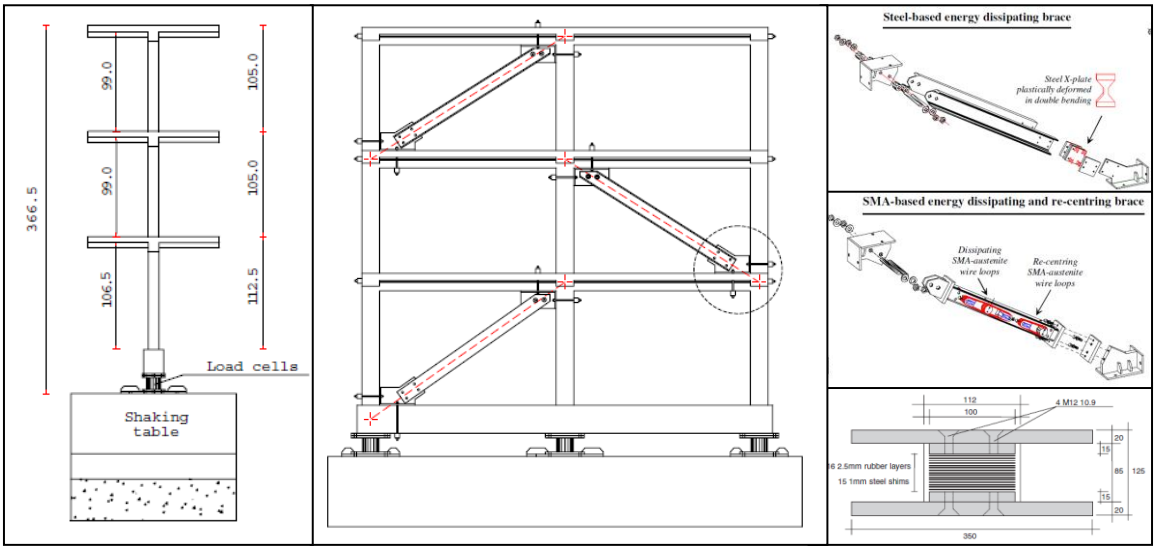

Figure 2.12: Steel and SMA braces and base isolation (from Dolce et al. 2005 and 2007).

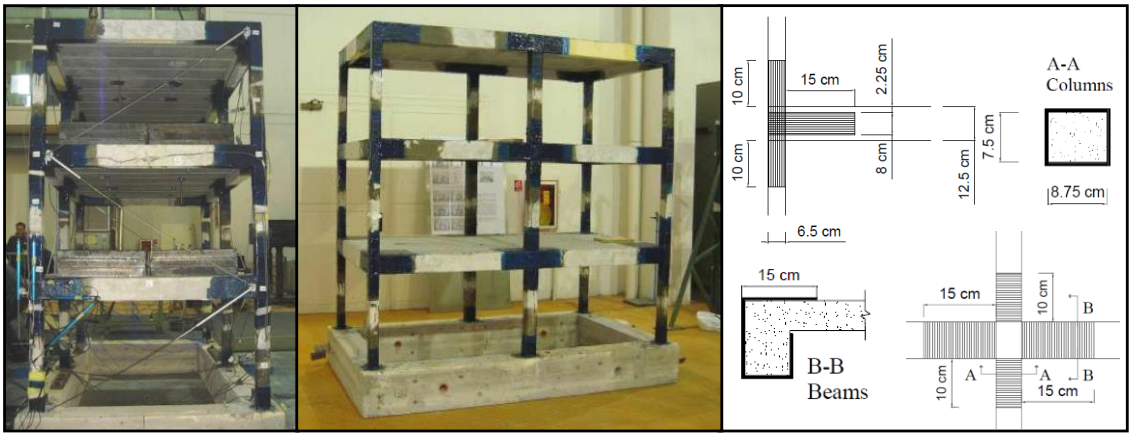

Figure 2.13: 3D model retrofitted with CFRP laminates – layout and laminates location (from Dolce et al. 2006b).

Also in Italy, the TREMA projects which involved the partnership of ENEA, the National Department of Civil Protection, and the University of Basilicata, consisted in a series of

shake table tests of non-ductile RC frame model buildings. The 3D specimens, consisted of two 1/4 scale, 3-storey, 2-bay external frames, jointed together by means of floor slabs and transverse beams represented the typical features of buildings constructed till 1971 in Italy (Dolce et al. 2006a). Undamaged (as-built) and damaged/repaired stages were investigated using bi-directional shake table tests. The TREMA project consisted in the seismic upgrading of the as-built model using Carbon Reinforced Fibre Polymer (CFRP) layers as well as an innovative technique called the DIS-CAM system, evolution of the original CAM system (Dolce et al. 2006b,c).

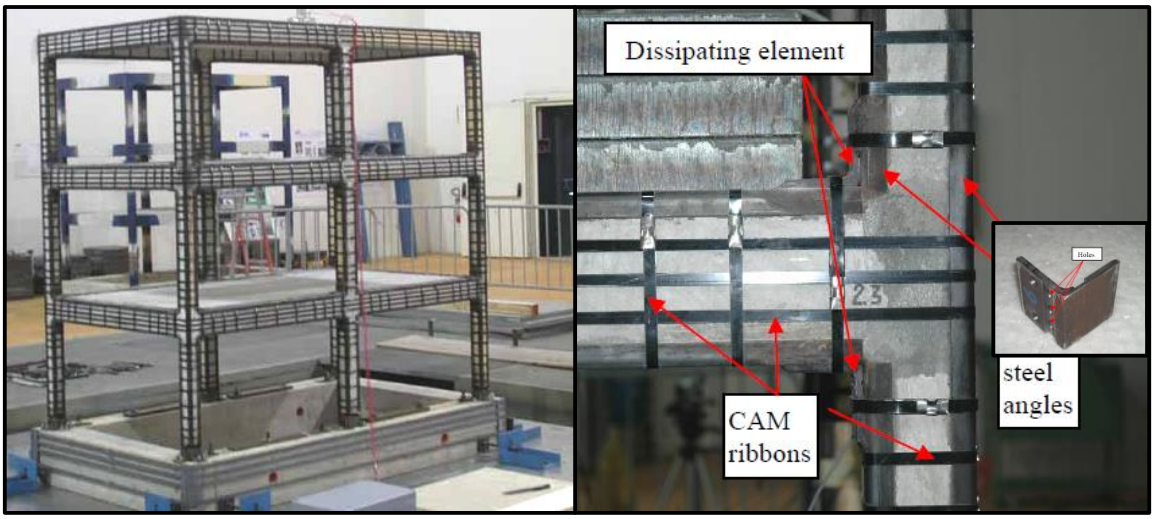

Figure 2.14: DIS-CAM system (from Dolce et al. 2006c).

The specimen retrofitted with CFRP laminates is presented in Figure 2.13. In this case the retrofit strategy was to upgrade all beam column joints in the model, which has been called a full retrofit strategy (Calvi et al. 2002a, Pampanin 2005). Since the specimen comprises of two external frames only, a retrofit strategy for upgrading exterior joints of internal frames was not investigated. In this case, the CFRP laminates layout for the interior joint represent the same geometry of an exterior joint of an internal frame, only tested in the strong direction. In addition, as presented in the drawings of Figure 2.13, the FRP laminates layout incorporated the use of external faces of beams and columns, with no counterparts on the interior side.

The DIS-CAM system consists in the CAM system with additional hysteretic dissipaters. The CAM system consists in post-tensioned steel ribbons added to elements close to the panel zone region for providing confinement and shear capacity. The dissipation system incorporated consists in the addition of dissipating steel angles in the beam-column interface as shown in Figure 2.14. Both methods showed positive results.

At the National Centre of Research on Earthquake Engineering (NCREE) in Taiwan, in collaboration with the University of British Columbia (Canada), a series of four 2/3 scale, 2 floor, 2-bays individual plane frames were tested under uni-directional shake table excitation (Elwood 2009). The non-ductile specimens were designed to fail in different critical elements, including failure in the columns, and the joints.

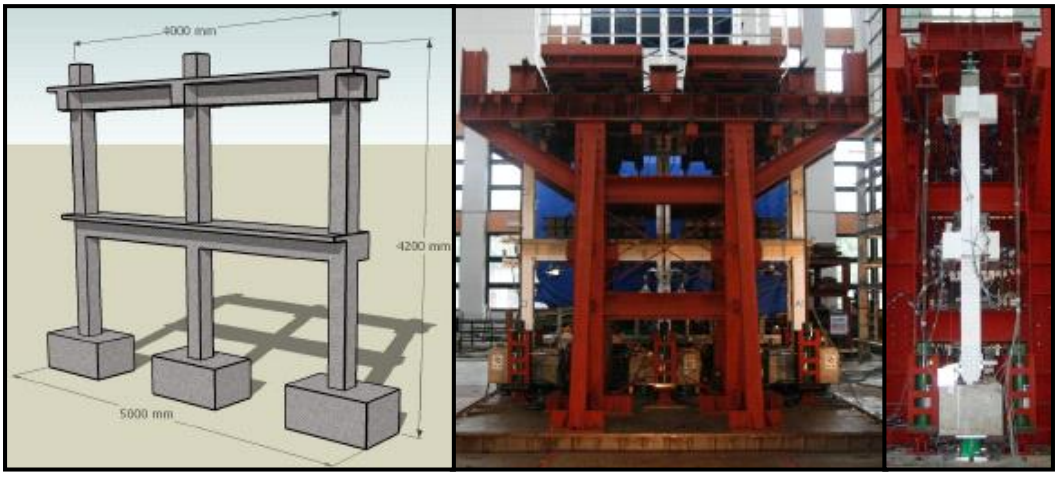

Figure 2.15: Left: 2/3 scale, 2-storey, 2-bay single frames tested at the NCREE, Taiwan (courtesy of Prof. Kenneth Elwood).

At the University of California San Diego, a series of individual 2/5 scale interior frames retrofitted with engineered cementitious composite materials (ECC) and GFRP laminates were tested on the shake table (Shing et al. 2009). The specimens included floor slabs, stubs and clay brick infill panels, revealing the undesirable effect of infill panels on the behaviour of the frames as well as the feasibility of the proposed retrofit technique/technology (Figure 2.16).

Figure 2.16: Shake table test of single frames with infill panels performed at the University of California San Diego (from Shing et al. 2009).

2.6 LIMITATIONS OF EXPERMENTAL TESTING PROCEDURES

2.6.1 Earthquake Phenomenon and Seismic Demand Simulation

All research review in this chapter has the same drawback: a low level of realism in the simulation of seismic demand, which is a 3D dynamic ground motion of the foundation soil. In seismology, the mathematical formulation for understanding the propagation of seismic energy from the nominal fault rupture through the crust corresponds to a classical wave equation used in other disciplines like acoustics or electromagnetism. This equation requires the assumption of the crust to be an infinite, homogeneous, isotropic and linear space where seismic wave propagate (Newmark and Rosenblueth 1971).

The previous comments are intended to highlight the large degree of complexity involved in the mathematical understanding of the earthquake phenomenon itself. Even though parameters as the modulus of elasticity (E), density (ρ) and Poisson ratio (v) are assumed to be constant along the path from the fault rupture to the building's footing, the problem involves high levels of complexity. When incorporating dependence of the parameters E, ρ, and v on the position or the velocity of seismic waves, the problem becomes also extremely nonlinear (Strogatz 1994). Therefore, what we can predict to be the movement of the soil under a structure may only be a refutable conjecture, and any prediction of the seismic demand to occur in the future, may just be a representation of a scenario that will hardly be repeated again.

In the experimental research reviewed in this chapter, the simulation of the seismic demand is far away from representing a real seismic demand like the one described in the previous paragraphs. So far the most realistic way of simulating seismic demands has been the dynamic simulation of one or two horizontal components in full and small scale specimens, respectively.

2.6.2 Methods for Simulating the Seismic Response of Experimental Models

In experiments performed in beam column joint subassemblies subjected to quasi-static lateral loading, as well as in frame models tested using pseudo-dynamic loading protocol, time is the main parameter neglected in the problem. Even though the response is being simulated by imposing a certain set of strains in the experimental model, the lack of consideration of the *natural dynamic response* is not being taken into consideration. The size of specimens tested quasi-statically and pseudo-dynamically has been typically larger than those used in shake table tests, due to the lower cost of the technology required for those purposes when compared to high capacity shake tables. However, the benefits of research related to experiments performed in the dynamic range can be much more beneficial than the same experiments performed using a slowly imposed response in large models, in the light of the higher degree of realism of the tests.

2.6.3 Scaling Factors and Model Distortion

It is understood that a true replica of a prototype building is almost impossible to construct in the laboratory if a scale factor for the length (l_r) smaller that 1 is being used. When incorporating gravity loads into the problem, the acceleration in the prototype and model domains must be the same. When using prototype materials in terms of stiffness

and strength, the material density needs to be increased by $1/l_r$ times. The latter restriction can be solved by artificially adding extra mass in the form of concrete blocks and/or steel plates on top of each floor. Nevertheless, this is practical up to a certain level only, when it is impossible to locate the extra mass and it starts to interfere in the structural characteristics of the experimental model.

In addition, time measurements in the model domain must be contracted when compared to the prototype domain by a factor equal to the square root of l_r. This contraction can induce important distortions due to strain rate effects. For example, if $l_r = 0.25$ is being used, then time runs two times faster in the experiment than what would be observed in the 'real world'. Since prototype materials are being used, a large difference in the strain rate may introduce important distortion on the simulation of the response.

Size effects have also been recognized as an important source of distortion in experimental modelling. It has been acknowledged that small size specimens have led to non-conservative numerical results even if replicating a certain phenomenon qualitatively with a good approximation. As has been suggested in the literature (Morcarz and Krawinckler 1981), a scale factor of 1/3 is seen as a strict limit for size effects to become important.

2.6.4 Shake Table Testing Protocol and Input Motion Selection

Most of the shake table test reviewed here have followed an experimental protocol which includes ground motions modified in their frequency content and amplitude in order to fit a given design spectrum. These input motions are used for successive shake table tests at increasing PGA levels, after which damage is inspected in the model. This is a so called 'fragility' approach, which relates the PGA of a particular ground motion to the seismic intensity. As the occurrence of a certain PGA level is typically related to probability laws, then damage is related to a certain probability of occurrence as well.

However, as it is understood that seismic intensity is a direct measurement of damage in a certain set of structures and not a measurement of seismological parameters themselves, it is believed that the procedure may be fallacious. It is argued that for the testing protocol to be realistic, then the number of specimens should be equal to the amount of tests where the elastic range is exceeded. The reasoning behind this idea is that inelastic incursions will inevitably change the initial conditions of the specimen for the next test, due to the formation of residual strains in the previous one.

Finally, by increasing the PGA level only, the response spectrum is not being changed in shape since the frequency content of the input is the same in all cases. This is the spectrum is only being shifted up by a linear factor. Therefore when the *next ground motion* comes and differs in predominant frequencies to those 'adjusted' to fit mean calibrated spectra, the fragility procedure developed for a *previous ground motion* would not be able to represent, in most of the cases, a reasonable prediction.

2.7 CONCLUDING REMARKS

All the experimental and theoretical effort has revealed the seismic vulnerability of different non-ductile RC structural typologies, as summarized above. Most of them have

led to the conclusion that one of the weakest elements in a frame structure is the panel zone region, whose severe damage, especially in corner joints, may lead to the collapse of a complete building due to a soft storey mechanism.

In order to investigate the structural dynamics behind the non-ductile frame typology studied recently at the University of Canterbury, shake table tests of a frame model specimen were understood to be the natural step forward after a series of quasi-static test on beam column joint subassemblies (Figure 2.1). The specimen, whose description is presented in Chapter 3, was designed considering all the restriction of the laboratory facilities, in terms of size, weight and velocity of the shake table, as well as considering all the relevant research previously described.

2.8 REFERENCES

Akguzel, U. (2011) 'Seismic Performance of FRP Retrofitted Exterior RC Beam-Column Joints under Varying Axial and Bidirectional Loading', *a thesis presented for the degree of Doctor of Philosophy in Civil Engineering*, University of Canterbury, Christchurch, New Zealand.

Aycardi, L.E., Mander, J.B., Reinhorn, A.M. (1994), 'Seismic Resistance of Reinforced Concrete Frame Structures Designed only for Gravity Loads - Experimental Performance of Subassemblages', *ACI Structural Journal*, Vol.91(5), pp.552-563.

Beres, A., Pessiki, S., White, R, and Gergely, P. (1996), 'Implications of Experiments on the Seismic Behaviour of Gravity Load Designed RC Beam-To-Column Connections', *Earthquake Spectra*, Vol.12(2), pp.185-198.

Bracci, J., Reinhorn, A., and Mander, J. (1995), 'Seismic Retrofit of Reinforced Concrete Buildings Designed for Gravity Loads: Performance of Structural Model', *ACI Structural Journal*, Vol.92(6), pp. 711-723.

Calvi, G.M., Magenes, G., and Pampanin, S. (2002a), 'Relevance of Beam-Column Joint Damage and Collapse in RC Frame Assessment', *Journal of Earthquake Engineering*, Vol. 6, Special Issue 1, pp.75-100.

Calvi, G.M., Magenes, G., and Pampanin, S. (2002b), 'Experimental Test on a Three Storey R.C. Frame Designed for Gravity Loads Only', *12th European Conference on Earthquake Engineering*, London, England, paper n. 727.

Cardone, D., Di Cesare, A., Dolce, M., Moroni, C., Massucaa, A., Nigro, D., Ponzo, F. (2004), 'Studio sperimentale dell'adeguamento sismico mediante isolamento alla base di strutture intelaiata esistenti di conglomerato cementizio armato Relazione finale sui risultati ottenuti nel corso delle prove', *Dipartamento di Strutture, Geotecnica, Geologia applicata all'Ingegneria*, Potenza, Italy (*in Italian*)

Cardone D, De Canio G, Dolce M, Marnetto R, Moroni C, Nicoletti M, Nigro D, Pizzari A, Ponzo FC, Renzi E, Santarsiero G, Spina D. (2003), 'Comparison of Different Passive Control Techniques through Shaking Table Tests' *Proceedings of 8th World Seminar on*

Seismic Isolation, Energy Dissipation and Active Vibration Control of Structures, Yerevan, Armenia.

Di Ludovico, M., Prota, A., Manfredi, G., Consenza, E. (2008), 'Seismic Strengthening of an Under-Designed RC Structure with FRP', *Earthquake Engineering and Structural Dynamics*, Vol. 37, pp.141-162.

Dolce, M., Cardone, D., and Marnetto R. (2000), 'Implementation and Testing of Passive Control Devices Based on Shape Memory Alloys', *Earthquake Engineering and Structural Dynamics*, Vol.29(7), pp. 945-968.

Dolce, M., Cardone, D., Ponzo, F., Valente, M. (2005), 'Shaking Table Tests of RC Frames Without and With Passive Control Systems', *Earthquake Engineering and Structural Dynamics*, Vol. 34, pp. 1687-1717.

Dolce, M., Cardone, D., Moroni, C., Nigro, D., Ponzo, F.C., Santarsiero, G., De Canio, G., Renieri, N., Renzi, E., Goretti, A., Nicoletti, M., Spina, D., Lamonarca, B. Marnetto, R. (2006a), 'SICURO and TREMA Projects: the Seismic Performance of RC Frames Seismically Upgraded with Different Systems', *Proceedings of the fib 2nd International Congress*, Naples, Italy.

Dolce, M., Moroni, C., Nigro, D., Ponzo, F.C., Goretti, A., Spina, D., Lamonarca, B., Giordano, F., De Canio, G., Rainieri, N., Marnetto, R. (2006b), 'TREMA Project: Experimental Evaluation of Seismic Performance of a RC ¼ Scaled Model Upgraded with FRP', *Proceedings of the fib 2nd International Congress*, Naples, Italy.

Dolce, M., Moroni, C., Nigro, D., Ponzo, F.C., Santarsiero, G., Di Croce, M., De Canio, G., Renieri, N., Campanero, M., Berardis, S., Goretti, A., Spina, D., Lamonarca, B. Marnetto, R. (2006c), 'TREMA Project: Experimental Evaluation of Seismic Performance of a RC ¼ Scaled Model Upgraded with the DIS-CAM System', *Proceedings of the fib 2nd International Congress*, Naples, Italy.

Dolce, M., Cardone D, Ponzo, F., (2007), 'Shaking-Table Tests on Reinforced Concrete Frames with Different Isolation Systems', *Earthquake Engineering and Structural Dynamics*, Vol.36, pp.573–596.

Durrani, A., Zerbe, H. (1987), 'Seismic Resistance of R/C Exterior Connections with Floor Slab', *ACI Structural Journal*, Vol. 113(8), pp. 1850-64.

Ehsani, M., Wight, J. (1985), 'Effect of Transverse Beams and Slab on Behaviour of Reinforced Concrete Beam-To-Column Connections', *ACI Structural Journal*, Vol. 82(2), pp. 188-195.

Elwood, K. (2009), 'Collapse Behaviour of Non-ductile Concrete Columns and Frames', *Seminar dictated at the Department of Civil and Natural Resources Engineering*, University of Canterbury, Christchurch, New Zealand.

Engindeniz, M., Kahn, L., and Zureick A. (2005), 'Repair and Strengthening of Reinforced Concrete Beam-Column Joints: State of the Art', *ACI Structural Journal*, Vol. 102(2), pp. 187-197.

FEMA-356 (2000), *Pre-Standard and Commentary for the Seismic Rehabilitation of Buildings*, Federal Emergency Management Agency, Washington D.C., USA

fib (2003), 'Seismic Assessment and Retrofit of Reinforced Concrete Buildings: State-of-the-art report', *International Federation for Structural Concrete (fib)*, Lausanne, Switzerland.

Hakuto, S., Park, R., and Tanaka, H. (2000), 'Seismic Load Tests on Interior and Exterior Beam-Column Joints with Substandard Reinforcing Details', *ACI Structural Journal*, Vol. 97(1), pp. 11-25.

Kam, W.Y. (2011), 'Selective Weakening and Post-Tensioning for the Seismic Retrofit of Non-Ductile RC Frames', *a thesis presented for the degree of Doctor of Philosophy in Civil Engineering*, University of Canterbury, Christchurch, New Zealand.

Kam, W.Y., Quintana-Gallo, P., Akguzel, U., Pampanin, S. (2010), 'Influence of Slab on the Seismic Response of Substandard Exterior Reinforced Concrete Beam Column Joints', *Proceedings of the for 9th US and 10th Canadian National Conference on Earthquake Engineering*, Toronto, Canada.

Marriott, D.J. (2009), 'The Development of High-Performance Post-Tensioned Rocking Systems for the Seismic Design of Structures', *a thesis presented for the degree of Doctor of Philosophy in Civil Engineering*, Department of Civil and Natural Resources Engineering, University of Canterbury, Christchurch, New Zealand.

Morcarz, P., Krawinkler, H., (1981), 'Theory and Application of Experimental Model Analysis in Earthquake Engineering', *Report No.50*, John Blume Earthquake Engineering Center, Department of Civil and Environmental Engineering, Stanford University, California, USA.

Newmark, N.M. and Rosenblueth, E. (1971), *Fundamentals of earthquake engineering*, Prentice Hall Inc., New Jersey, USA.

Pampanin, S., Calvi, G.M., Moratti, M. (2002), 'Seismic Behavior of RC Beam Column Joints Designed for Gravity Loads', *12th ECEE*, London, England.

Pampanin, S., Magenes, G., Carr, A. (2003), 'Modelling of Shear Hinge Mechanism in Poorly Detailed RC Beam-Column Joints', *Proceedings of the fib symposium Concrete Structures in Seismic Regions*, Athens, Greece.

Pampanin, S. (2005), 'Controversial Aspects in Seismic Assessment and Retrofit of Structures in Modern Times: Understanding and Implementing Lessons from Ancient Heritage', *Proceedings of the NZC Society Conference*, Auckland, New Zealand.

Pampanin, S., Christopoulos, C., Chen, T. (2006), 'Development and Validation of a Metallic Haunch Seismic Retrofit Solution for Existing Under-Designed RC Frame Buildings', *Earthquake Engineering and Structural Dynamics*, Vol. 35, pp. 1739-1766.

Pampanin, S., Bolognini D., and Pavese, A. (2007), 'Performance-Based Seismic Retrofit Strategy for Existing Reinforced Concrete Frame Systems Using Fibre-Reinforced

Polymer Composites', *Journal of Composites for Construction,* ASCE, Vol. 11(2), pp. 211-226.

Park, R. (2002), 'A Summary of Simulated Seismic Load Tests on Reinforced Concrete Beam-Column Joints, Beams and Columns with Substandard Reinforcing Details', *Journal of Earthquake Engineering,* Vol. 6(2), pp. 147-174.

Park, R. and Paulay, T. (1975), *Reinforced Concrete Structures*, John Wiley and Sons Inc., New York, USA.

Paulay, T. and Priestley, M.J.N. (1992), *Seismic design of reinforced concrete and masonry buildings,* John Wiley and Sons, New York, USA

Pinto, A. (1995), 'Assessment and Retrofit of Full-Scale Models of Existing RC Frames', *Seismic Assessment and Rehabilitation of Existing Buildings - International Closing Workshop*, Istanbul, Turkey.

Priestley, M.J.N. and Calvi, J.M. (1991), 'Towards a Capacity-Design Assessment Procedure for Reinforced Concrete Frames', *Earthquake Spectra*, Vol. 7(3), pp. 413-437.

Priestley, M.J.N. (1996), 'Displacement-Based Seismic Assessment of Existing Reinforced Concrete Buildings', *Bulletin of the NZSEE,* Vol. 29(4), pp. 256-267.

Sugano, S. (1996), 'State-of-the-Art in Techniques for Rehabilitation of Buildings', *Proceedings of the 11th WCEE,* Acapulco, Mexico.

3 EXPERIMENTAL MODEL DESIGN

3.1 INTRODUCTION

The experimental model was based on a prototype full scale RC structure as well as in one particular 2D frame designed by others (Marriott et al. 2007). Two of those frames were scaled down to a 2/5 scale in the linear dimension, which was the maximum value possible, considering the limitations of the Structures Laboratory facilities in space and the shake table in capacity. This plain frame was conceived by understanding it as a portion of the prototype building slightly modified. Two identical frames similar to those selected by Marriott et al. (2007) were relocated in an exterior part of the prototype as shown in Figure 3.1, creating an exterior portion composed by two parallel frames, one internal and one external (facade). Cast in-situ slabs and transverse beams were incorporated into the problem, and used for jointing the frames together. On one face of one frame an overhang or stub was used to simulate an internal frame. The resulting specimen consists in a 3D structure with 2 different frames – external and internal.

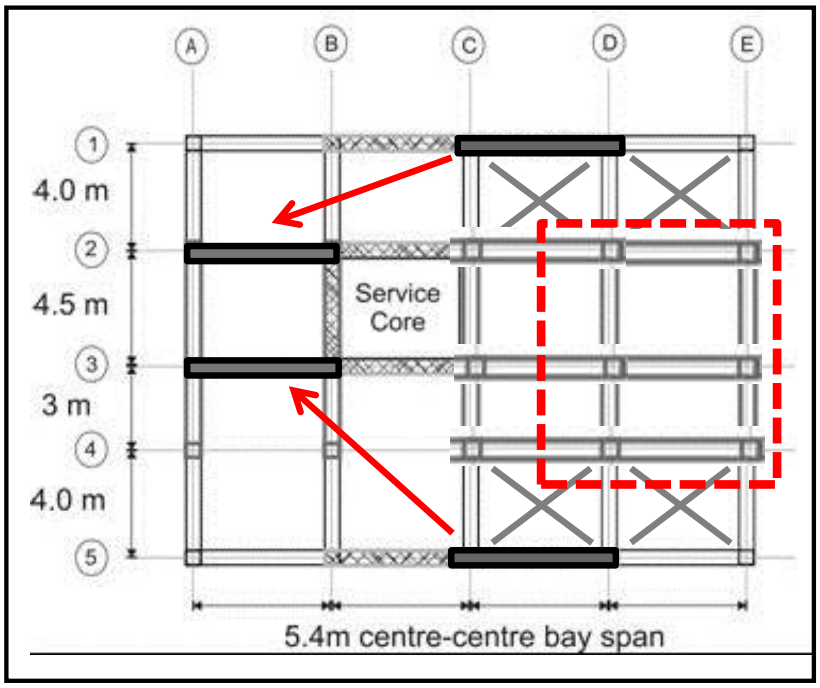

Figure 3.1: prototype plane structural elements conceptual relocation.

The main goal during the design of the as-built specimen was the development of an experimental model able to represent with the lesser degree of distortion the dynamic response of the portion of the prototype structure under a specified seismic demand, in the model domain. One fundamental issue at this stage was the acknowledgment of the fact that the construction of a 'true replica' model which satisfies all the similitude requirements needed by dimensional analysis is almost an impossible task due to material limitations (Morcarz and Krawinkler 1981). This introduces the need for the design of the most adequate distorted model. The main limitations in this case were the use of prototype materials in the concrete and steel reinforcement bars. Even though micro-concrete was used (small aggregate size concrete less than 8mm), the compressive

strength and consequently the stiffness of the concrete is the same in the model and prototype domains. The reinforcing bars were scaled down in diameter, but the modulus of elasticity (E_s) and the strength remains equal in both domains. As a result of this equality and the similitude requirements explained later, the density should be scaled up by 2.5 times, which is an impractical task. That limitation can be overcome though by artificially increasing the mass of the specimen at each floor level, evenly distributed in the floor slab.

Space limitations of the laboratory were 4.5 from the table surface to the bottom of the crane hook, and those of the shake table were 20 tons maximum in weight and 242 mm/s maximum in velocity. In order to meet those requirements, a length scale factor (l_r) equal to 2/5 was selected.

3.2 SIMILITUDE RESTRICTIONS AND SCALING FACTORS

For engineering purposes, the problem of the time history of the stresses in a body - like a building - can be described with the greatest degree of simplification as the functional of Equation 3.1 (Morcarz and Krawinkler 1981).

$$\sigma = F\left(r;t;\rho,E,a,g,l,\sigma_0,r_0\right) \tag{3.1}$$

where, σ = stress; r = position vector; t = time; ρ = density; E = modulus of elasticity; a = acceleration; g = acceleration of gravity; l = length; σ_0 = initial stress; r_0 = initial position vector.

The physical phenomenon is being measured using 10 physical quantities. In this case, it can be demonstrated that same phenomenon can be equally described with 7 products of those physical quantities, using Buckingham's PI-theorem (Buckingham 1914). For this, the selection of 3 arbitrary 'basic' quantities is required. In this case, some units of E, ρ and l can be used. Therefore, assuming that the functional presented in Equation 3.1 is complete, it can be reduced to the functional of dimensionless products shown in Equation 3.2, as the dimensionless products in the functional of Equation 3.2 must be equal in prototype and model domains. In addition, the ratio model/prototype of those numbers must be equal to one and defined by Equation 3.3.

$$\frac{\sigma}{E} = f\left(\frac{r}{l};\frac{t}{l}\sqrt{\frac{E}{\rho}};\frac{a}{g};\frac{gl\rho}{E};\frac{\sigma_0}{E};\frac{r_0}{l}\right) \tag{3.2}$$

$$\left\langle \Pi_r \right\rangle = \left\langle \left(\frac{\sigma}{E}\right)_r, \left(\frac{r}{l}\right)_r, \left(\frac{t}{l}\sqrt{\frac{E}{\rho}}\right)_r, \left(\frac{a}{g}\right)_r, \left(\frac{gl\rho}{E}\right)_r, \left(\frac{\sigma_0}{E}\right)_r, \left(\frac{r_0}{l}\right)_r \right\rangle = \langle 1 \rangle \tag{3.3}$$

The first ratio relates the stresses to the mechanical property of the material (E). If prototype materials are to be used, then $E_r = 1$, and therefore $\sigma_r = 1$ (equal stresses). The second ratio implies that if a factor of the length equal to l_r is used, then all the position in space will be reproduced with a ratio of l_r in the model structure. The third ratio introduces the time relationship in the model and prototype domains. Noting that $(E/\rho)_r$ can still be a ratio, the time ratio (t_r) is defined by Equation (3.4).

$$t_r = l_r \Big/ \sqrt{\left(\frac{E}{\rho}\right)_r} \tag{3.4}$$

Mathematically and physically, there is no reason so far to distinguish the time as an absolute dimension for the model and prototype domains (classical mechanics absolute time reference system). In this sense, the concept of a Minkowski space-time relative reference system (Minkowski 1908) can be argued as an argument for the existence of two different measurements of the time in the model and prototype domains, which depends on space coordinates.

$$\left(\frac{E}{\rho}\right)_r = l_r \tag{3.5}$$

The forth ratio - Froude's number, relates the acceleration of gravity and the absolute acceleration. When gravitational forces are not neglected, like in this case, g_r = 1, and thus a_r = 1 (equal acceleration). The fifth ratio - Cauchy's number, relates the basic fundamental properties assumed in the problem by means of g. Since in most of the cases g_r =1, then Equation 3.5 must be respected. For a more extensive version of this section, the interested reader in referred to Quintana-Gallo et al. (2010).

3.3 SPECIMEN GEOMETRY

As usual in New Zealand construction practice before the 1970's, the specimen was casted in-situ, this time on top of the shake table. In order to ensure a rigid attachment to the shake table surface, strong RC footings were anchored to the shake table surface by means of high strength threaded rods. Footings were 300 mm thick and 600 mm wide, reinforced with 10mm deformed bars. In Figure 3.3 to Figure 3.5, the main dimensions of the specimen are presented. Inter-storey heights were all equal to 1200 mm, with a total specimen height of 3900 mm, including footings. Long and short spans were 1800 mm and the short 1200 mm long, respectively. Spacing between external and internal frames was 1200 mm. The overhang on the interior side of the internal frame used for simulating boundary conditions with the rest of the ideal structure was 300 mm long from the centreline. This length is similar to the one used in Kam et al. (2010) in 2D beam column joint with slabs.

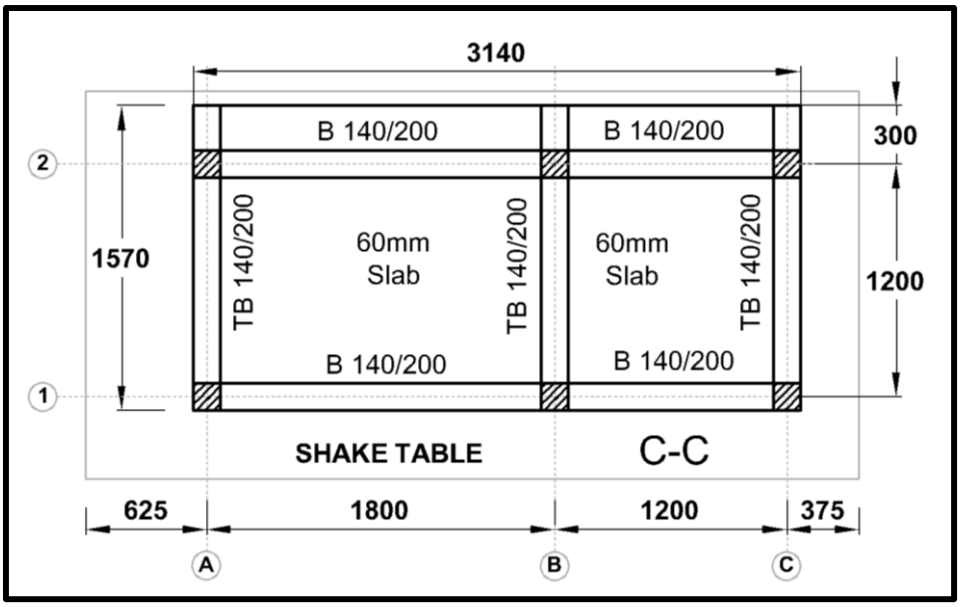

Figure 3.2: In-plane structural layout – all floors.

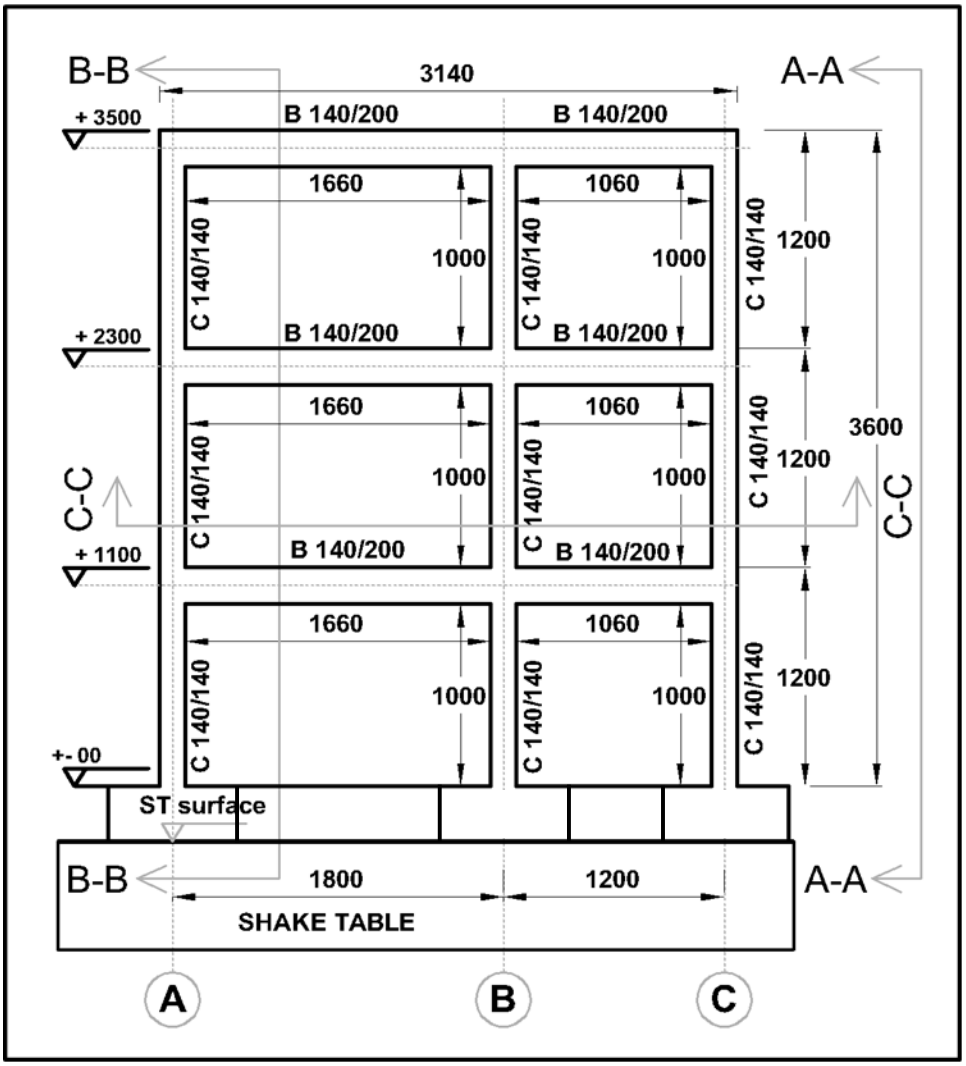

Figure 3.3: Specimen main dimensions (in millimeters) and reinforcing layout.

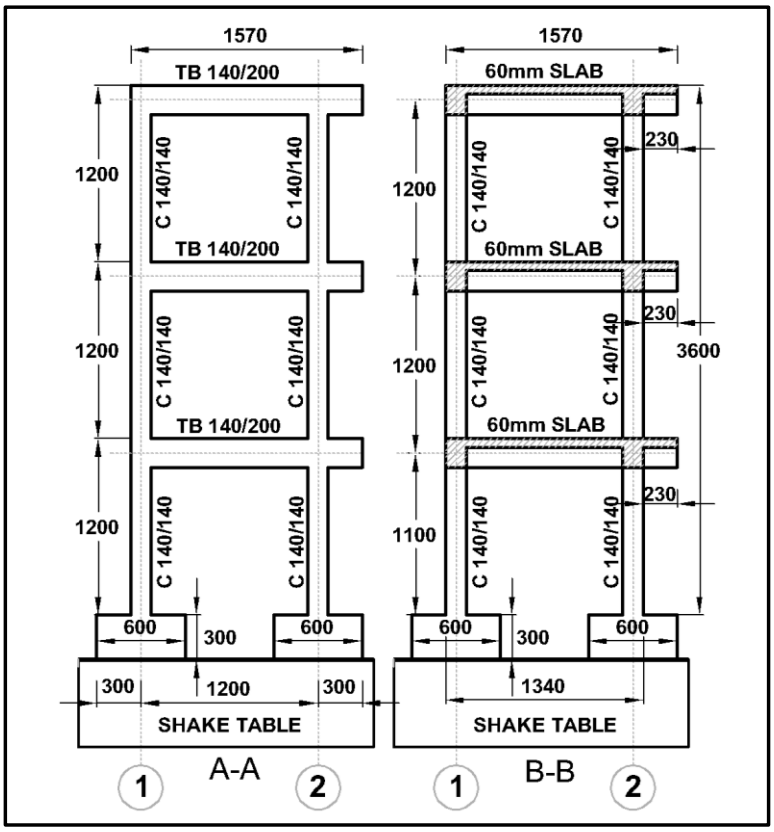

Figure 3.4: Building short direction – view A-A and B-B.

Figure 3.5: Left: As-built specimen – 3D perspective; right: linear dimension comparison: 1.75m person, crane at the highest point – including hook – 0.6m.

Columns and beam cross sections were 140x140 mm, and 140x200 mm, respectively, whereas slabs were 60 mm thick. In Figure 3.3, drawings of the longitudinal axes (1 and 2), the typical structural plane layout, and the transverse axes A, B, and C, is presented. In Figure 3.5 a picture of the specimen after removing the formwork is shown, were the 3D nature of the structure can me appreciated.

3.4 REINFORCEMENT DETAILS

Reinforcement detailing was specified according to 1955 New Zealand code (NZS95:1955, 1955). This design approach is characterized in this case by the use of plain round bars, 180° end hooks on beam bars anchorage, lack of confinement/shear resistant stirrups in the joint, lap splices in potential plastic hinge regions in columns, and no capacity design philosophy. All reinforcement consisted in plain 6mm diameter bars, with the exception of stirrups made of 4mm diameter bars. Details of reinforcement configuration in the panel zone region are shown in Figure 3.6. Slab reinforcement was anchored into perimeter the perimeter using 90° end hooks. On the external frame, hooks were anchored on the outside beam longitudinal reinforcement, whereas on the interior frame, slab bars were extended from the longitudinal beam to the overhang and anchored into the slab using smaller hook outside lengths. Other details are presented in Figure 3.7 to Figure 3.9.

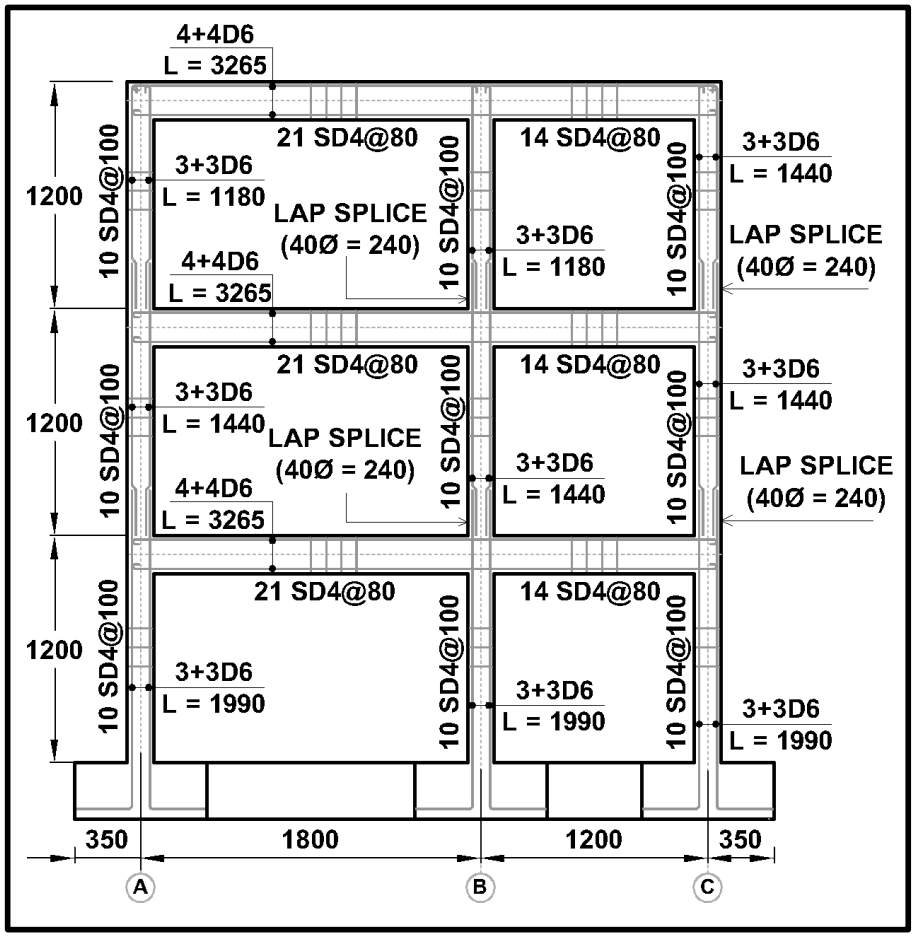

Figure 3.6: Reinforcement details, front view, axes 1 and 2.

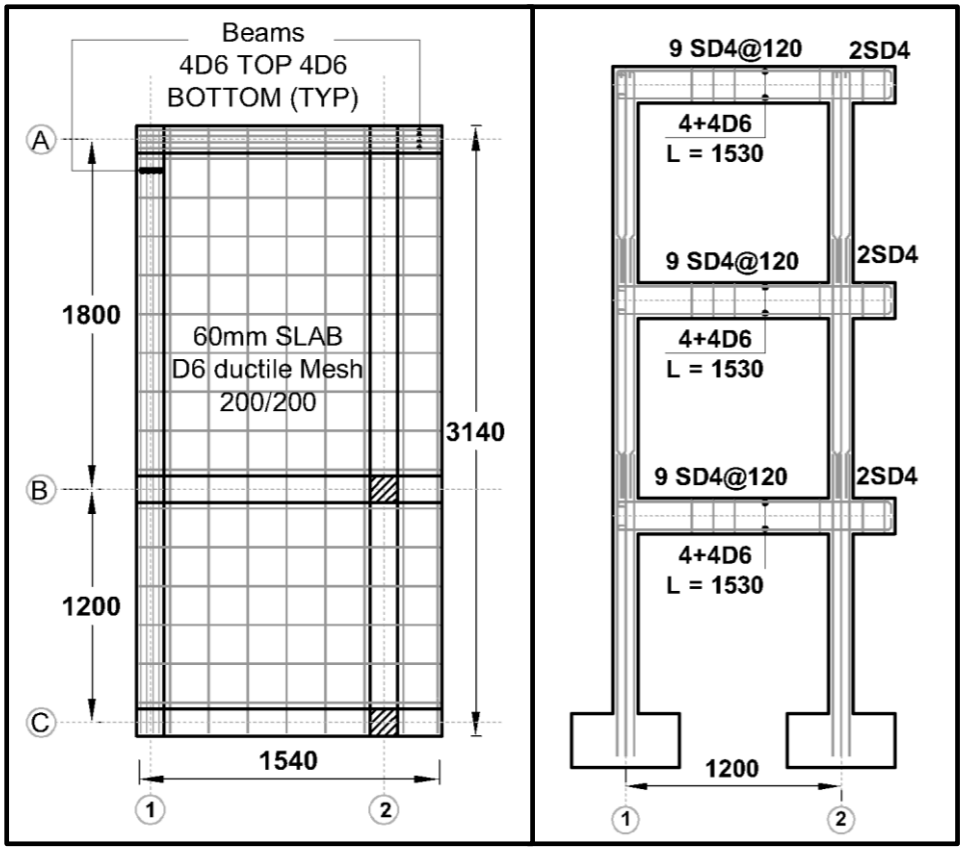

Figure 3.7: Slab and reinforcement details: axes A, B and C.

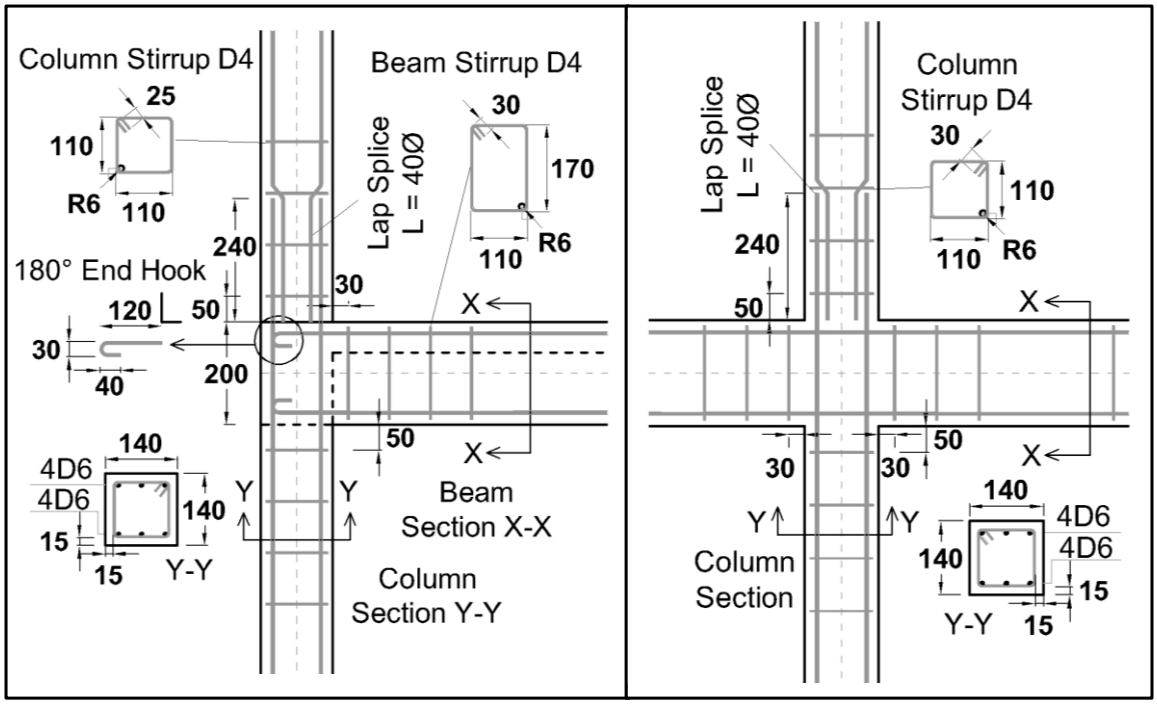

Figure 3.8: Exterior and interior beam column joint details (typical).

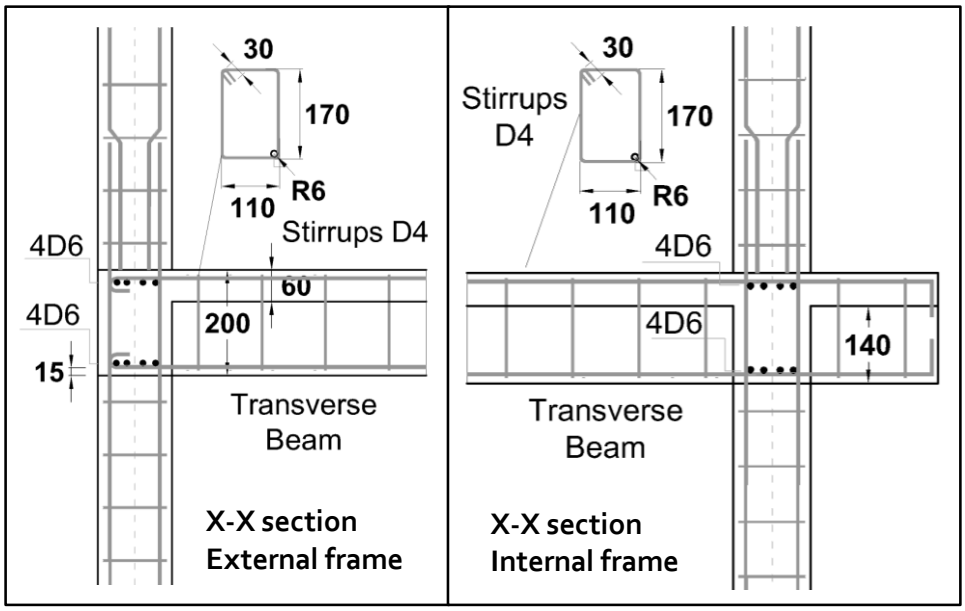

Figure 3.9: Exterior beam column joint details – transverse section – internal and external frames.

3.5 MATERIAL PROPERTIES

The specified quality for 6 mm steel used for longitudinal bars was grade 300 MPa mild steel (type 1), whereas for 4 mm bars used in stirrups a grade 500 MPa steel was specified (steel type 2). According to tensile tests performed on samples of each steel type had slightly larger yielding stresses than specified, as shown in Figure 3.10. However, that difference can be neglected for design calculations as well as numerical simulations, in light of the high uncertainty involved in the problem.

Differences in strain ductility are notorious. For Type 1, strain levels of 1% were reached without variation in the capacity (stress). Strain hardening was reached at strain levels of 10%. An average yielding stress of 385 MPa was calculated, and a mean failure stress of approximately 500 MPa. Steel type 2 on the other hand, reached 585 MPa in average for yielding stresses, without significant strain hardening. In terms of ductility, samples of this type were able to withstand in average deformations of the order of 1%.

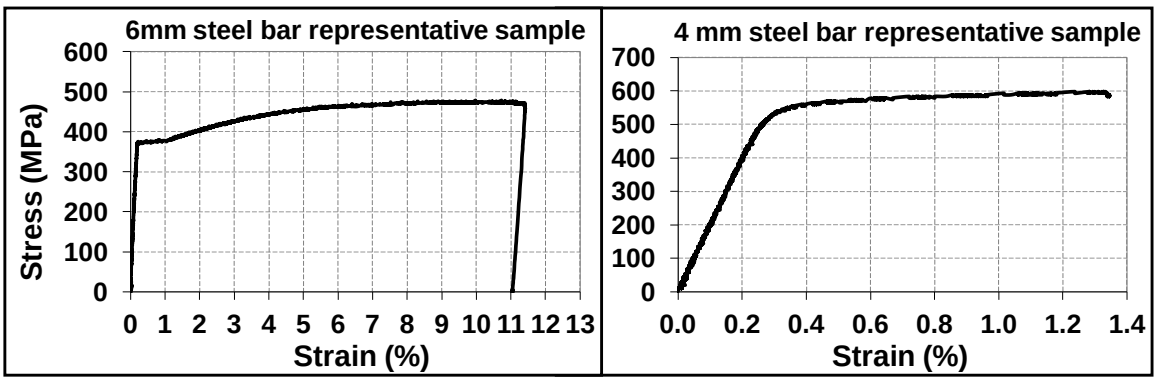

Figure 3.10: Reinforcement bars representative samples stress-strain relationship.

Concrete cylinders were tested at 28 days and during the testing days. Average values of the maximum unconfined concrete compressive stress, f_c', obtained for each case are summarized on Table 3.1, were also the results of compression test of mortar samples for the repaired specimen are presented. The substandard quality of the material was due to the addition of excessive water by the contractor. The implications of that unintended, but representative characteristic of the materials associated to the building typology under investigation, are discussed in Chapter 4.

Table 3.1: Concrete compressive strength values.

Concrete compression strength f_c' (MPa)						
Floor	Casting date	28 days	1st test		2nd and 3rd tests	
-	-	f_c'	Days from casting	f_c'	Days from casting	f_c'
1	03-Feb-10	27	184	29	273	30
2	02-Mar-10	23	157	25	246	25
3	01-Apr-10	8	127	11	216	12
Mortar	24-Sep-10	30	-	-	40	33

3.6 ARTIFICIAL MASS SIMULATION

In order to solve the restriction imposed by Equation 3.5, an artificial mass simulation approach was used (Morcarz and Krawinkler 1981). Assume that the mass of a building is lumped at each floor level and uniformly distributed in plane, as is normally done. Then, the inertial mass in the model structure (M_m) can be artificially increased by ΔM to match the mass required by Equation 3.5, in terms of the mass ratio (M_r), given by Equation 3.6.

$$M_r = l_r^2 \tag{3.6}$$

If prototype materials are used then $E_r = 1$ and $\rho_r = 1$, and the additional mass ΔM_r required to achieve M_r in the model is given by Equation 3.7, if and only if the same dimensions of the prototype structure are being used in the model. The ratio of mass per unit of area (m_r) is given by Equation 3.8 and must be equal to unity (Quintana-Gallo et al. 2010). Sometimes, additional mass is incorporated into the model when compared to the prototype. This is the mass of tributary area on one side of the interior frame, as well as live loads. In this case, an artificial mass named m_0 was added to the model in order to account for those two effects. As a consequence, the mass per unit of area in the model will be larger than in the prototype, and in order to satisfy Equation 3.6, Equation 3.9 must be respected.

$$\Delta M_r = l_r^2 \left(1 - l_r\right) \tag{3.7}$$

$$m_r = \frac{g_r M_r}{l_r^2} = 1 \tag{3.8}$$

$$(m_m - m_0)/m_p = 1 \tag{3.9}$$

where, m_m = distributed mass in the model, m_0 = artificially simulated distributed mass, m_p = distributed mass in the prototype. The total mass considered in the prototype structure, consisted in the self-weight of a subassembly plus 30% of the live load (2 kN/m^2) assumed to be present at the moment of the seismic event. Calculation of the seismic mass in the prototype structure yield typical values of mass per unit of surface (m_p) for RC frame buildings. For the first two floors m_p = 0.81 T/m^2 and for the roof m_p = 0.60 T/m^2.

Figure 3.11: Specimen with extra mass – similitude compatible with the prototype counterpart.

As in this case the mass per unit of area in the prototype structure is m_p = 0.81 and 0.60 T/m^2 for the first two floors and the third one, then in the model m_m = 1.2 and 0.9 T/m^2, respectively. Using Equation 3.9, the mass to be added externally is m_0 = 0.39, for levels 1 and 2, and 0.30 T/m^2 for level 3. Multiplying by the in plane area of the model, then 4.3 tons must be added in the first two levels, and 3.0 tons in the top one. Those masses were added to the specimen in the form of steel plates and concrete blocks evenly distributed in plane and strongly attached to the floor slab, as shown in Figure 3.11. It is obvious that the height of the block will generate some extra bending moments and shift up the centre of mass of the storey. However, this effect can be demonstrated to be negligible in this

case, just by accounting for the only distortion induced by not increasing the density of the material by 5/2 times.

As a result of the definition of the geometry and the weight of the experimental model, the axial load in the columns was very low (close to $v = P_v / A_g f_c' = 0.1$). If the specimen was scaled down in length to a smaller ratio, then the elements would have become very small and size effects would have been more important, introducing a larger amount of distortion into the problem. The time, for example, would have required further contraction, which is undesirable. On the other hand, the usable surface of the shake table (4x2 meters) did not allow for a larger separation between the external and internal frames, which would have increased the axial load ratios, but that in turn would have led to a model with a larger weight than the maximum value that the shake table could resist (20 tons = 200 kN). One could argue that the size of the cross section of the columns could have been reduced only, keeping the size of the beams constant. However, one of the objectives of the model was to replicate the beam column joints tested by previous researchers working in the same project (Pampanin et al. 2002, Pampanin et al. 2006, Kam 2010, Akguzel 2011). Thus, an alteration in those regards would have jeopardized the coherence between this and those projects.

3.7 CONCLUDING COMMENTS

Using a scale factor of $l_r = 2/5$ restrictions in height, weight and velocity were satisfied. Furthermore, this scale factor is very closely to fully exploit those restrictions. The specimen height is 3.9 m (including the footings), leaving just 600 mm from the bottom of the crane hook of the laboratory facilities for construction. The total weight, equal to 18.5 tons is very close to the maximum allowable of 20 tons, and the lateral force and overturning moment were found to be very close to the nominal capacity of the shake table (Ghee 1985). Valve saturation of the controlling system related to the maximum velocity of the input motion (240 mm/sec. nominal), would not be reached with the ground motions that were selected in a preliminary stage, even though some of them were expected to impose severe inelastic demands in the structure during the test, based on initial numerical predictions using Ruaumoko2D (Carr 2008a,b).

3.8 REFERENCES

Buckingham, E. (1914), 'On Physically Similar Systems: Illustration of the Use of Dimensional Equations', *Physical Review*, Vol. 4, pp.345–376.

Carr, A.J. (2008a), *Ruaumoko – Program for Inelastic Dynamic Analysis*, Volume 1: Theory, Department of Civil and Natural Resources Engineering, University of Canterbury, New Zealand.

Carr, A.J. (2008b), *Ruaumoko – Program for Inelastic Dynamic Analysis*, Volume 2: User Manual for the 2-Dimensional Version, Department of Civil and Natural Resources Engineering, University of Canterbury, New Zealand.

Ghee, A. B. (1985), 'Seismic Shear Strength of Circular Bridge Piers', *University of Canterbury Research Report*, University of Canterbury, Christchurch, New Zealand

Kam, W.Y., Quintana-Gallo, P., Akguzel, U., Pampanin, S. (2010), 'Influence of the Floor Slab and Transverse Beam on the Seismic Response of Under-Designed Exterior – Interior and Corner Reinforced Concrete Beam Column Joints', *Proceedings of the 9th US-Canadian National Conference on Earthquake Engineering*, Toronto, Canada.

Marriott, D., Pampanin, S., Bull, D.K., Palermo, A. (2007), 'Improving the Seismic Performance of Existing Reinforced Concrete Buildings using Advanced Rocking Wall Solutions', *Proceedings of the NZSEE Conference*, Palmerston North, paper 17.

Marriott, D. (2009), 'The Development of High-Performance Post-Tensioned Rocking Systems for the Seismic Design of Structures', *a thesis presented for the degree of Doctor of Philosophy in Civil Engineering*, University of Canterbury, Christchurch, New Zealand.

Minkowski, H. (1908), 'Space and Time', *80th Assembly of German Natural Scientists and Physicians*, Cologne, Germany.

Morcarz, P., Krawinkler, H., (1981), 'Theory and Application of Experimental Model Analysis in Earthquake Engineering', *Report No.50*, John Blume Earthquake Engineering Center, Department of Civil and Environmental Engineering, Stanford University, California, USA.

Quintana-Gallo, P., Pampanin, S., Carr, A.J., Bonelli, P. (2010), 'Shake Table Tests of Under-Designed Frames for the Seismic Retrofit of Buildings – Design and Similitude Requirements of the Benchmark Specimen, *Proceedings of the NZSEE Conference*, Wellington, paper 39.

4 SHAKE TABLE TESTS OF THE AS-BUILT AND REPAIRED SPECIMENS

4.1 INTRODUCTION

A considerable amount of research has been done recently in order to identify structural deficiencies of RC buildings. Theoretical, numerical, and experimental work has been carried out towards developing and empirically demonstrating such concepts, with focus on practical applications. The lack of knowledge of capacity design principles as well as ductile detailing have been identified as the main drawbacks in the structures designed according to the seismic code provisions official before the 1970. (Aycardi et al. 1994, Sugano 1996, Beres et al. 1996, Hakuto et al. 2000, Park 2002, Pampanin et al. 2002, 2005, 2006, 2007, Kam 2010, Akguzel 2011). Particularly, in the case of RC frame structure non-ductile detailing can be listed as:

1) the use of smooth plain round bars
2) the lack or absence of stirrups inside the joint around column longitudinal bars
3) the use of 180° end hooks for longitudinal rebar anchoring in beam ends
4) the use of lap splices in potential plastic hinge regions
5) the substandard quality of the materials used
6) poor anchorage detailing

As a complementary study of this vulnerable typology related to the dynamic response of a complete RC frame experimental model, the specimen described in Chapter 3 was tested on the shake table facilities of the Structures Laboratory of the University of Canterbury. The original as-built specimen was tested using one ground motion recorded during the Loma Prieta Earthquake (California, 1989). Three series of shake table tests were performed using the Gilroy Array #5 record (GA5). Specimen inspection and processed results indicate that the structure remained in the elastic range during Tests 1.1 and 1.2, whereas a lap splices failure mechanism developed at the bottom of the columns of the top floor during Test 1.3, being the overall response controlled by an autonomous rocking of the top floor. This is attributed to loss of bond between smooth plain round bars and low quality concrete in the upper floor, as presented in Chapter 3.

After this first test series, the specimen was excited under the actual Darfield Earthquake, which struck Christchurch on September the 10th 2010. This ground motion, corresponding to a much bigger one in terms of wave amplitude than a similitude-consistent record, corroborated the failure mode observed during Test 1.3. Right after these test series, the specimen was modified and repaired in order to capture a failure mode different from that observed in Test 1.3. For that, concrete was removed in the lap splice region and longitudinal column bars were welded to provide continuity in height. Removed concrete was then replaced with structural mortar and cracks filled with epoxy resin.

Considering valuable information gathered during the Chilean Maule 2010 and New Zealand 2010 earthquakes, ground motions recorded during those events were used in a second and third series, respectively. Firstly, the modified specimen was tested under data recorded at the Christchurch Hospital in September 2010 experiencing little damage in

the form of thin cracks in the panel zone, columns and beams (Test 2.1, PGA = 0.20g). Recorded inter-storey drifts remained below 1% in all floors, and were almost identical in the dynamical shape, indicating a fairly elastic response.

In a third series, the specimen was subjected to a ground motion recorded at Marga-Marga station, located in Viña del Mar, during the Chile Maule Earthquake (Test 2.2, PGA = 0.33g). In that case, severe damage was observed in the beam column joints of both exterior and interior frames. Diagonal cracks of considerable width were developed in both corner beam column joints on the first floor with crushing of concrete in the core, as well as crushing in the bottom of columns. In the second floor lighter damage was observed, mainly in the way of diagonal cracks in corner beam column joints. On the other hand, almost no damage was developed in the third floor. Inter-storey drift reached a maximum level very close to 4.0% in the first floor, 2.5% in the second, and remained below 1.0% in the top floor, consistent with the observed damage patter.

In this Chapter the results in terms of observed damage, the overall recorded response of the specimen in terms of inter-storey drift and floor acceleration histories, and local observations in corner beam column joints are presented for the three tests series. Results are compared and discussed.

4.2 INPUT MOTION AND TESTING PROTOCOL

Three different ground motion recorded during three different earthquakes were selected. They correspond to one horizontal component recorded at a specific station during Loma Prieta (California, 1989), Maule (Chile, 2010), and Darfield (New Zealand, 2010) earthquakes. Details of stations as well as main earthquake parameters are summarized in Table 4.1. In Figure 4.1, the scaled in time acceleration time histories used for each test series are presented, the contraction of the time and constant acceleration is consistent with similitude requirements for this case (Quintana-Gallo et al. 2010).

Table 4.1 Earthquake summary and station location.

Event	Country	M_w	Depth (km)	Station	Location	D (km)
Loma Prieta	USA	6.9	-	Gilroy Array #5	San Jose, CA	24
Darfield	New Zealand	7.1	5	ChCh Hospital	Christchurch	42
Maule	Chile	8.8	35	Marga-Marga	Viña del Mar	290

Records were obtained from international databases (University of Chile Database, GEONET – New Zealand). They were corrected in order to create a consistent series of the ground motion in terms of acceleration, velocity and displacements (Boore 2001, Boore and Bommer 2005). This correction consisted in the use of a band pass, Butterworth 4° order filter with cut-off frequencies equal to 0.10 Hz and 25.00 Hz. This removes very long period (low frequency) waves that alter the displacement history significantly, resulting in a ground motion whose spectra is not modified importantly when compared to the 'original' ground motion (Boore 2001).

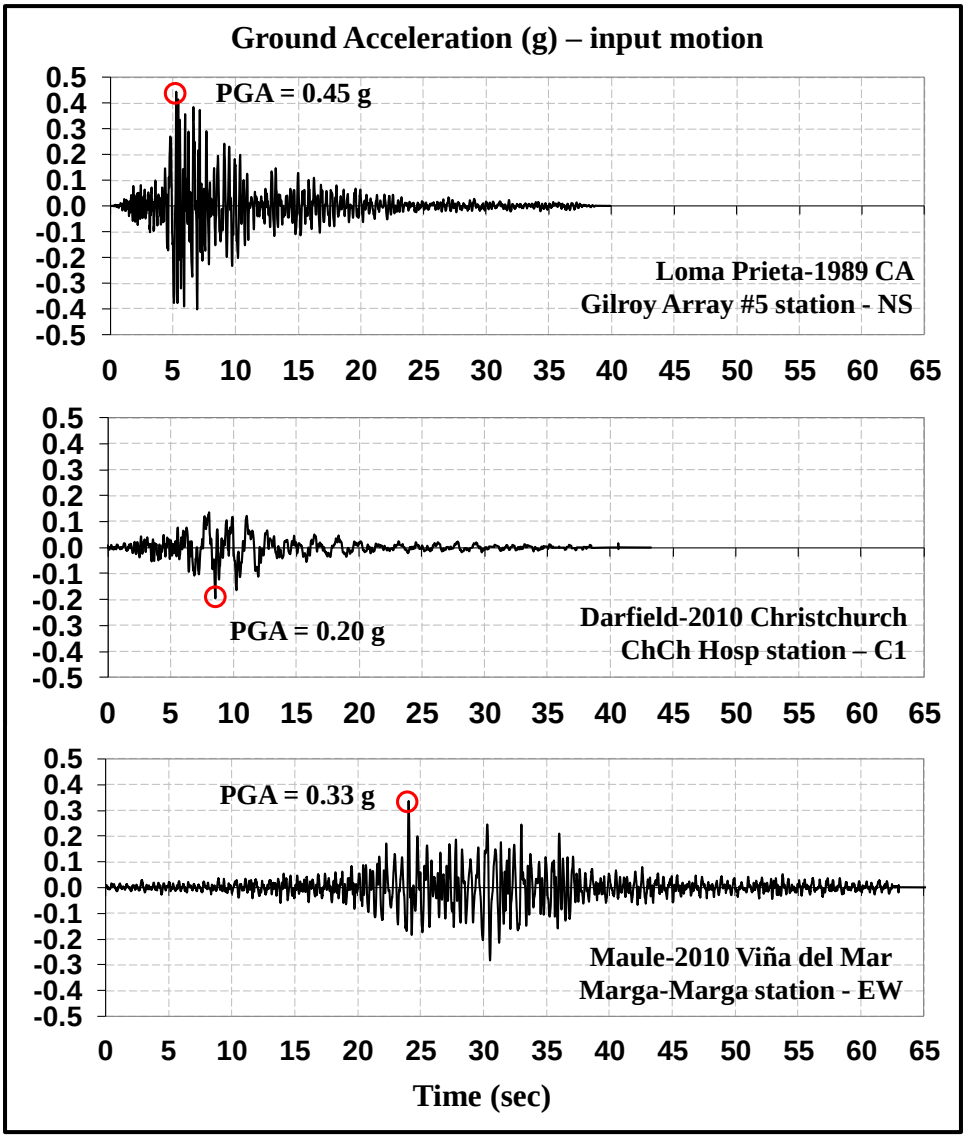

Figure 4.1: Loma Prieta 1989 (GA5), Darfield 2010 (CHH) and Maule 2010 (VMM) – Top, middle and bottom, respectively – ground motions in terms of acceleration.

In Figure 4.2 the same input motions presented in Figure 4.1 are shown in terms of ground displacements. It is the opinion of the author that this way of viewing the recorded ground motion can be much more understandable. It is also highlighted that the predominant period of the motion is can be quickly estimated using the displacement ground motion. As shown in Figure 4.3, the Fourier amplitude of each signal indicates the energy that a wave has, in the period (frequency) domain. In the model domain, the Marga-Marga record shows a high energy close to 0.6 seconds, more than twice the amplitude of the Gilroy Array #5, at about 0.3 seconds. Lastly, the Christchurch Hospital record exhibits similar amplitude with the Loma Prieta record, but with the predominant wave's period of about 1.7 sec. It can be appreciated that the biggest energy in terms of Fourier amplitudes corresponds to VMM record, being quite strong from 0.2 to 0.8 seconds.

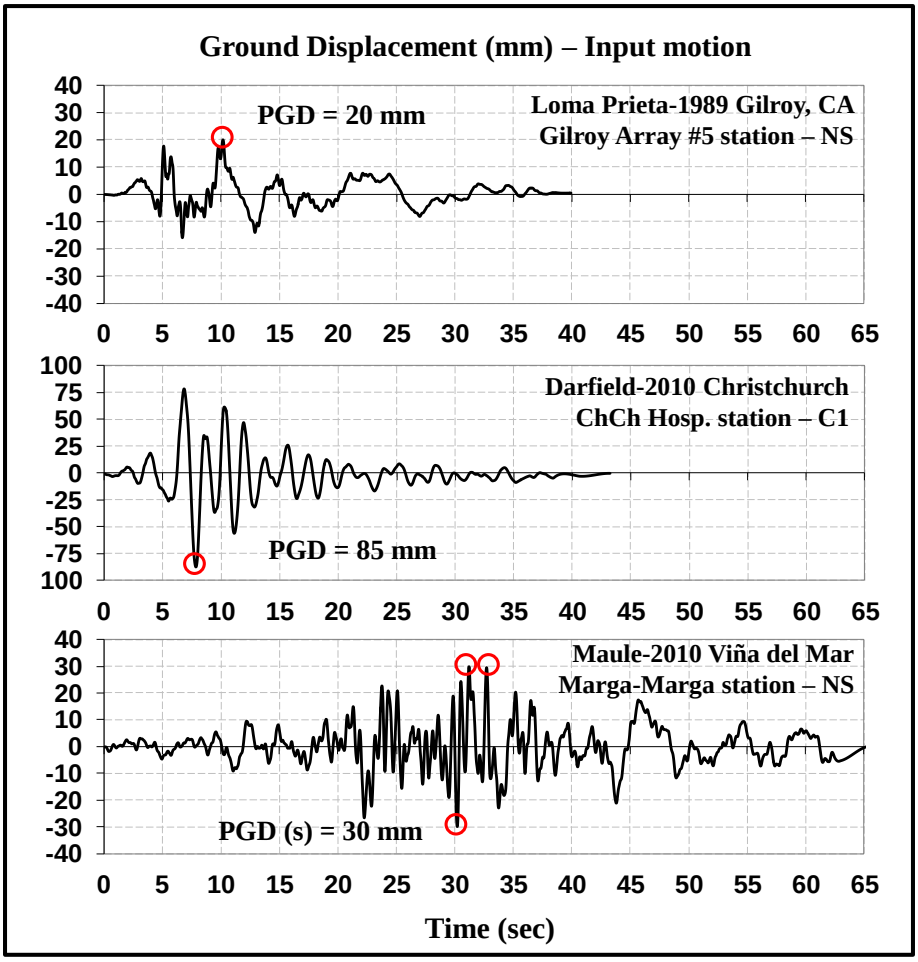

Figure 4.2: Loma Prieta 1989 (GA5), Darfield 2010 (CHH) and Maule 2010 (VMM) – Top, middle and bottom, respectively – ground motions in terms of displacement.

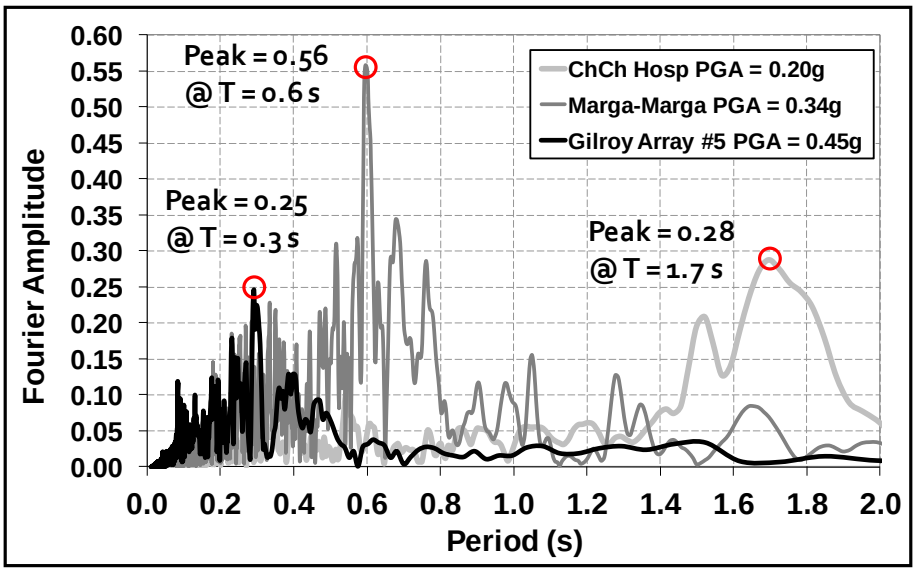

Figure 4.3: Fourier Transform function – ground motions energy in the frequency domain.

In Figure 4.4 acceleration and displacement response spectra generated with the three selected input are presented and compared with the NZS1170.5:2004 (Standards New

Zealand 2004) design counterpart. Note all the data is presented in the model domain measurement system. This implies that displacements are 2/5 times smaller and time (period) is reduced by a factor of √0.4 when compared to those measurements in the prototype domain. Spectral acceleration remains equal, since gravity forces are not being neglected. The New Zealand design spectra presented in Figure 4.4 corresponds to a place located in the city of Christchurch (Z = PGA = 0.22g; N = 1.0) on top of a soil type D, for probabilities of exceedance ($|P_{exc}$) of 1/500 and 1/2500.

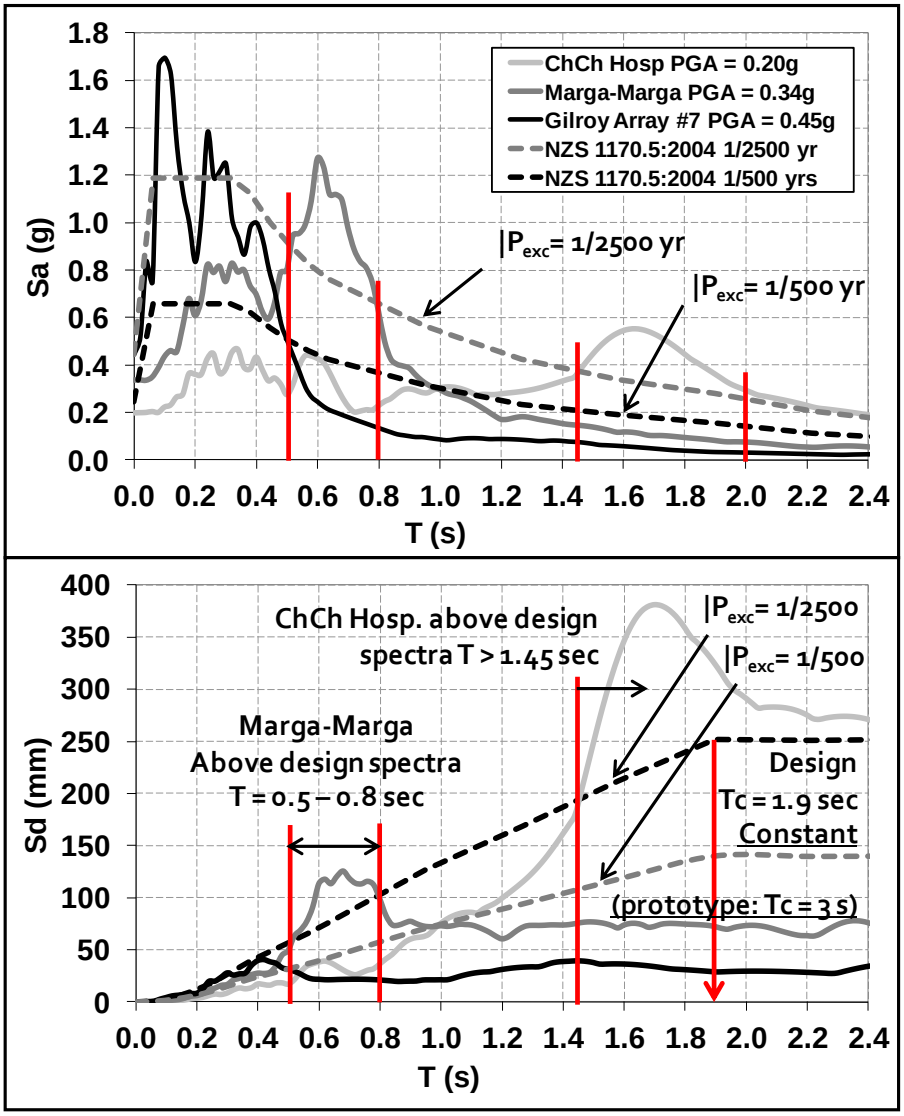

Figure 4.4: Top: acceleration and displacement spectra – comparison with NZS1705.5:2004 design spectra for a return period of 2500 years and Z = 0.22 (Christchurch).

In Table 4.2, the test belonging to each series are summarised as well as the main characteristics of the input motion for each case. In Series 1, the Gilroy Array #5 record, from the Loma Prieta-1989 earthquake was used at increased nominal PGA value, being the first one 0.45g. In Test 1.2 and 1.3, the PGA (or PGD) by 1.5 and 2.0 times, corresponding to PGA levels of 0.68g, and 0.9g, respectively.

Table 4.2 Series sequence and testing protocol.

Series	Test	Station	Record	PGA (g)	PGD (mm)	Duration (s)
1	1.1	Gilroy Array #5	GA5-1	0.45	20	40
1	1.2	Gilroy Array #5	GA5-2	0.68	30	40
1	1.3	Gilroy Array #5	GA5-3	0.90	40	40
2	2.1	Christchurch Hospital	CHH	0.20	85	40
2	2.2	Viña - Marga-Marga	VMM	0.33	30	65

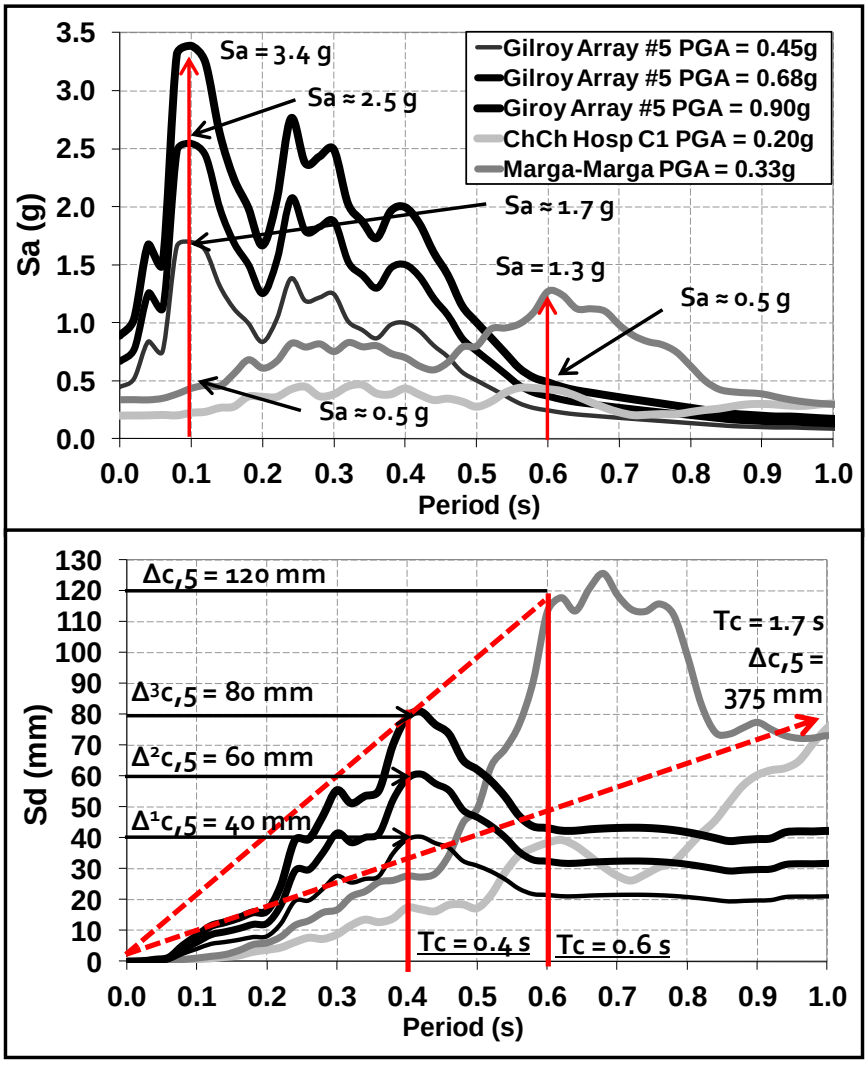

Figure 4.5: Input motion protocol in spectral ordinates.

Response spectra for each input motion are shown in Figure 4.5. It is observed that by increasing the peak value of the motion, the seismic demand reflected in the response spectra only shifts up that demand by that ratio. Therefore a variation in the frequency content of the input motion is being neglected. The latter, as shown in Figure 4.5, will be not the case for other input motions used in Series 2, described here and Series 3 presented later in this thesis. This approach is sometimes called 'fragility analyses' for estimating, erroneously in the belief of the author, since it aims to determine with a certain probability of exceedance the seismic intensity of an earthquake, which can only

be estimated after the event occurs. Moreover, intense damage observed in historical earthquakes may well be the sum of outlier events when compared to 'everyday' non-damaging earthquakes.

In the experimental series 2, the modified/repaired model building was subjected to two input motions recorded during 2010 in Chile (Viña del Mar) and 2010 New Zealand (Christchurch). In Test 2.1 a ground motion recorded in Christchurch Hospital (CHH) during Darfield-2010 earthquake at PGA = 0.20g (as recorded) was used. In Test 2.2, a ground motion recorded in Viña del Mar - Marga-Marga station (VMM) during the Maule 2010 earthquake at PGA = 0.33g was used (see Table 4.2 for details). As shown in Figure 4.5, the spectral ordinates in this case differ significantly from those corresponding to the Loma Prieta as well as the design values. These records may be considered by some as 'outliers' because they do not fit the specified design spectrum for a particular location. As a consequence the conclusion would be the same: damaging earthquakes represent in general, uncommon non-periodic events which most probably not produce ground motions whose spectra will fit the design counterpart normally calibrated with previously recorded data at a certain site. Differences in the duration and the energy of the predominant frequency of the motion as well as eventual near field effects can lead to completely different responses of structures. Two good examples of those are the differences in the characteristics of the ground motions recorded in Viña del Mar during the 1985 Valparaíso and the 2010 Maule earthquakes that affected central Chile, and the 2010 Darfield and 2011 Canterbury earthquakes that affected in much different ways in terms of damage the city of Christchurch, as discussed in Chapter 9 and 10, respectively. The tests presented here were performed in August 2010 (Series 1) and November 2010 (Series 2).

4.3 SERIES 1 MAIN RESULTS: AS-BUILT SPECIMEN TESTS

In Series 1 the as-built specimen was tested in 3 subsequent stages, referred to as Tests 1.1, 1.2 and 1.3. Tests were conducted using the same input motion used in Test 1.1 but increasing the amplitude of the signal (PGA = 0.45g) by a factor of 1.5 and 2.0 (Test 1.2 and 1.3 respectively). In this part the results of Tests 1.1 and 1.3 are presented. The results obtained during Test 1.2 are presented in Appendix A. In addition, a comparison of the nominal or intended input and the actual recorded shake table motion during the tests mentioned above are presented in Appendix B. A deeper discussion about the differences in the nominal and recorded input motions is presented in Chapter 7 and Chapter 8. The measured fundamental period of the building was estimated as T_1 = 0.24 sec. according to Fourier spectral analyses and free vibration tests (see Appendix C).

4.3.1 Global Response Measurements

The recorded response of the model in terms of inter-storey drift and floor acceleration time histories for Test 1.1 are presented in Figure 4.6 and Figure 4.7. This corresponds to the results recoded in the specimen when using GA-1 record from the Loma Prieta earthquake (PGA = 0.45g). In Figure 4.6 it can be observed a predominantly elastic response reflected in rather low inter-storey drift levels and no residual displacements. Peak values correspond to 1.0% for floors 1 and 3, and 1.2% for floor 2, being the shape of the three time-histories very similar to each other. It can also be noted in Figure 4.6 that the nominal 'peak' drift value is reached more than once in all floors (1%).

During Test 1.1, floor acceleration reached maximum values of 0.30g, 0,40g and 0,70g in storeys 1, 2 and 3, respectively. These peak values do not match, in time across the three floors, and similar values are also reached more than once in the recorded history. The third floor acceleration time history differs slightly from the other floors in shape since it reflects a more resonance-like motion. Larger accelerations as well as drifts are concentrated in between 2 and 5 seconds (model time).

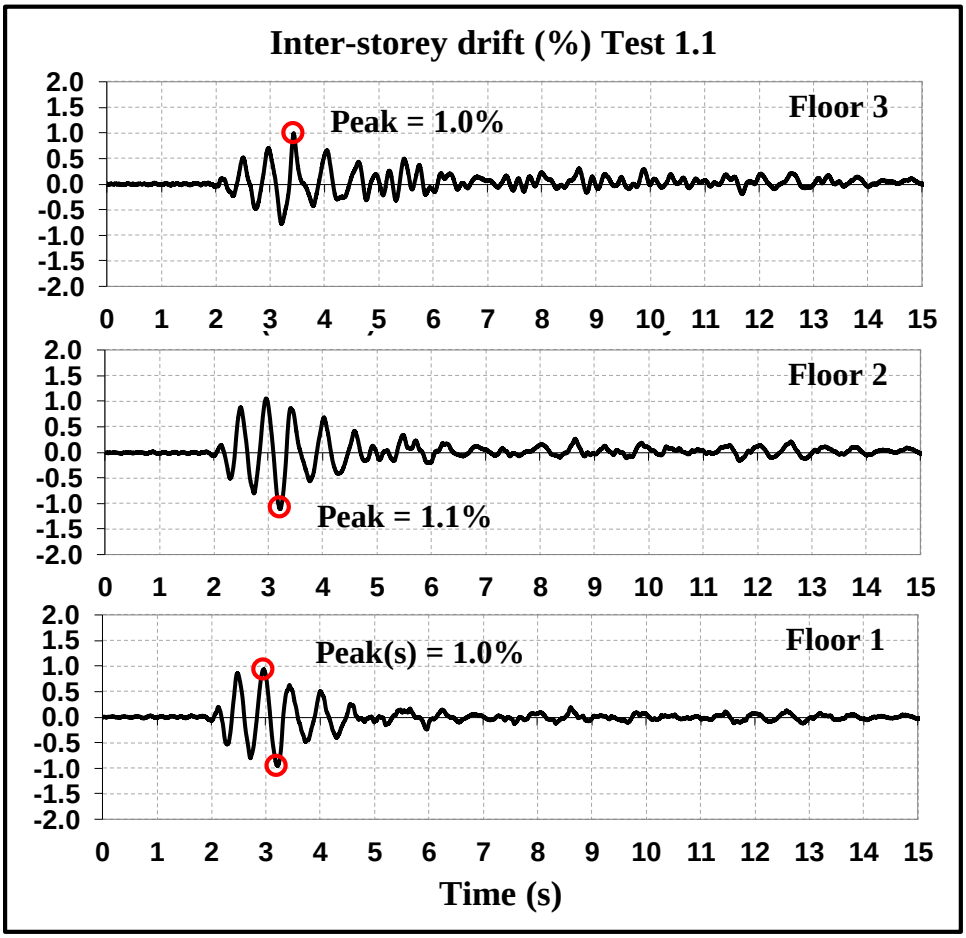

Figure 4.6: Test 1.1 recorded inter-storey drift measured at the center of mass.

The fact that the value of the maximum acceleration recorded in the first and second floors is smaller than the peak acceleration of the nominal input motion can be an indication of the development of an independent mechanism in the top floor. That is, most of the energy introduced into the system by the shake table was released in the top storey.

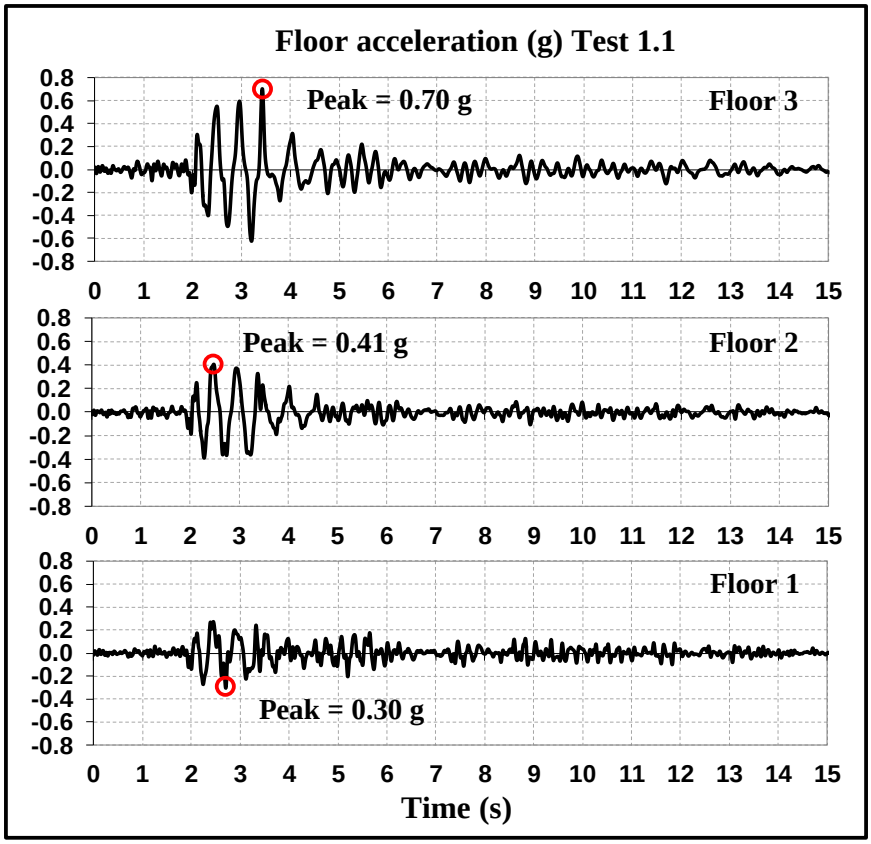

Figure 4.7: Test 1.1 recorded floor accelerations at the center of mass.

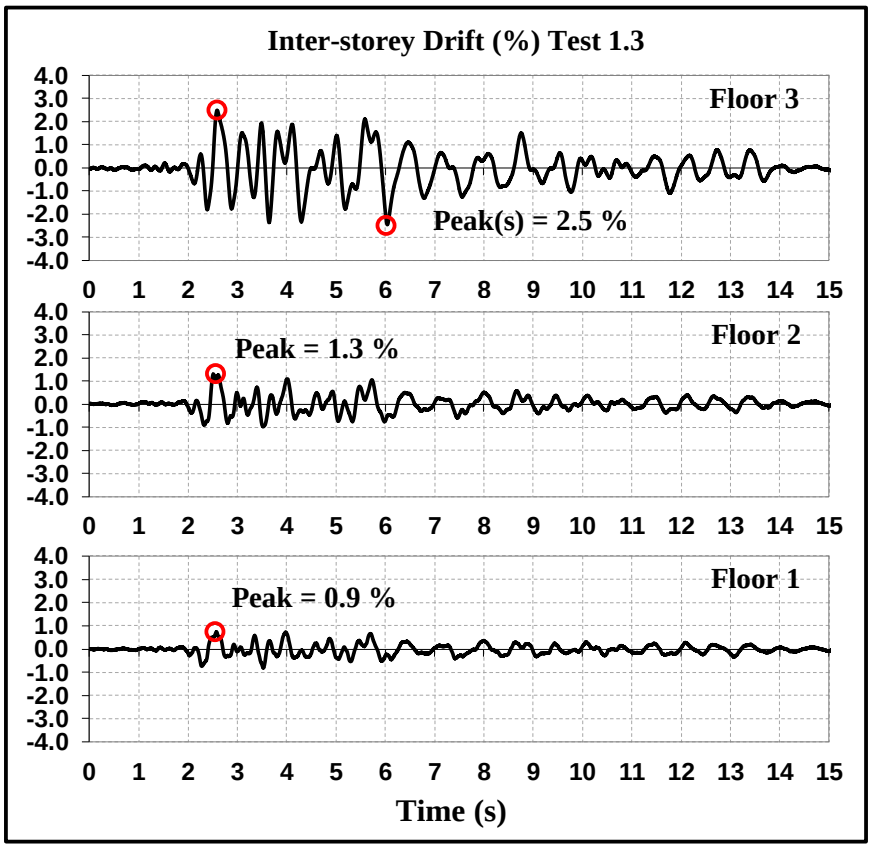

Figure 4.8: Test 1.3 measured inter-storey drift (center of mass).

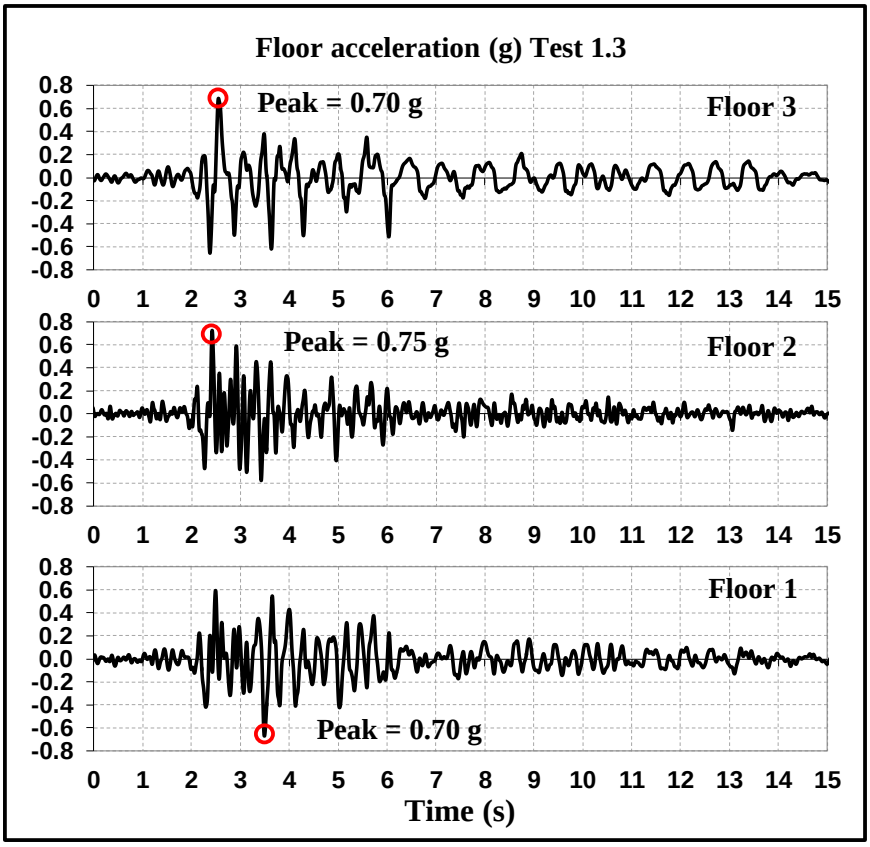

Figure 4.9: Test 1.3 recorded acceleration (center of mass).

In Figure 4.8 and Figure 4.9, global recorded results obtained from Test 1.3 are presented. They correspond to the response of the as-built specimen under GA5-3 record. In this case, as can be observed in Figure 4.8, the response was characterized by an autonomous lateral movement of the 3rd floor was observed. Top storey inter-storey drifts reached a maximum value of approximately 2.5%, whereas drift levels in floors 1 and 2 remained below 1.5%, reaching 0.9% and 1.3% for floors 1 and 2, respectively.

Recorded floor accelerations, showed in Figure 4.9, also reflect the formation of a local mechanism in the third floor, as the dominant frequency of the recorded acceleration in the third floor is much lower than the one corresponding to other floors. This increasing in the period of vibration of the third floor corresponds to a rocking storey, due to a lap splices failure as explained later. Peak values of the three recorded floor acceleration time-histories correspond to 0.70, 0.75, and 0.70 g, respectively. These peaks do not coincide in time, and close values are also reached at other times.

4.3.2 Observed Damage

After Test 1.1, no apparent damage was found. However, some indications of rocking of the third floor were found after processing the data in terms of filtered accelerations and inter-storey drifts. After Test 1.3, crack patterns indicate that most of the inelastic behaviour occurred at the base of columns and in the panel zone region. In columns of the third floor, horizontal cracks developed just above the joint or with little strain penetration, whereas on the second floor, significant horizontal cracks were found inside the panel zone. Vertical cracks and diagonal cracks developed on exterior joints, on both

faces. Crushing of concrete was observed on the bottom of third floor columns. This reflects a rocking action at the bottom of the exterior columns due to loss of bond between the concrete and the reinforcement in the column lap splices. In the top floor joints diagonal cracks were developed in the opposite direction to those of floors 1 and 2. In this case, cracks developed following the strut resulting from the beam acting with the slab in compression, whereas in the other cases, cracks tend to be oriented following the compression strut generated when the slab acts in tension.

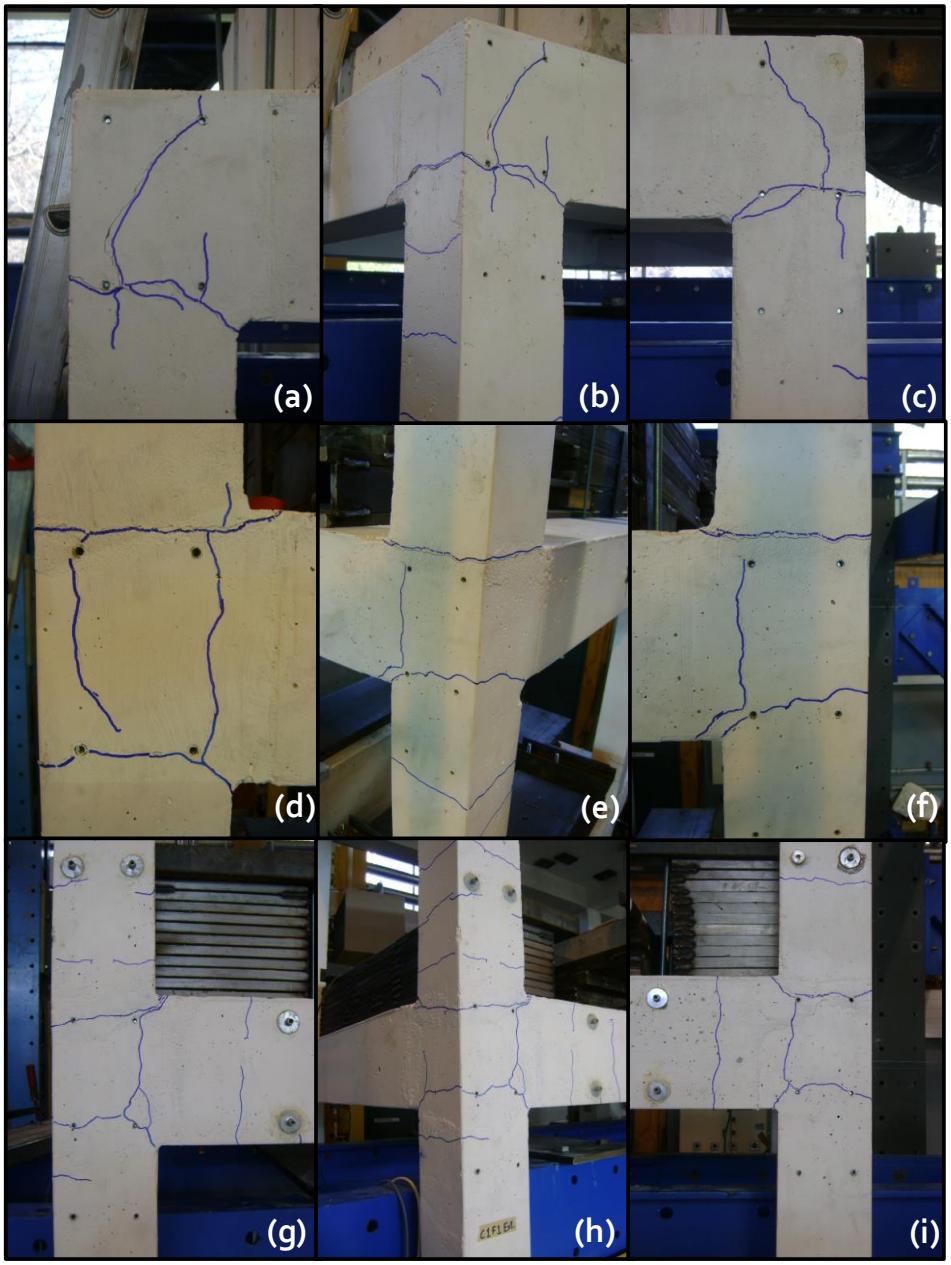

Figure 4.10: Observed damage after Test 1.3 n corner beam column joints: (a) top floor, long span joint front view, (b) top floor, long span joint 3D view, (c) top floor, short span joint front view, (d) second floor, long span joint front view, (e) second floor, long span joint 3D view, (f) second floor, short span joint front view, (g) first floor, long span joint front view, (h) first floor, long span joint 3D view, (i) first floor, short span joint front view.

The failure mode described in previous paragraphs was corroborated with the observed damage in the specimen after the Darfield Earthquake that struck the city of Christchurch on February the 4th 2011. As shown on the pictures of Figure 4.11, vertical and diagonal cracks in the same direction as observed before on the left corner joint were developed on the right corner joint. Rocking on the bottom of third floor column was clearly reflected by crushing of the concrete around the column reinforcing rebar.

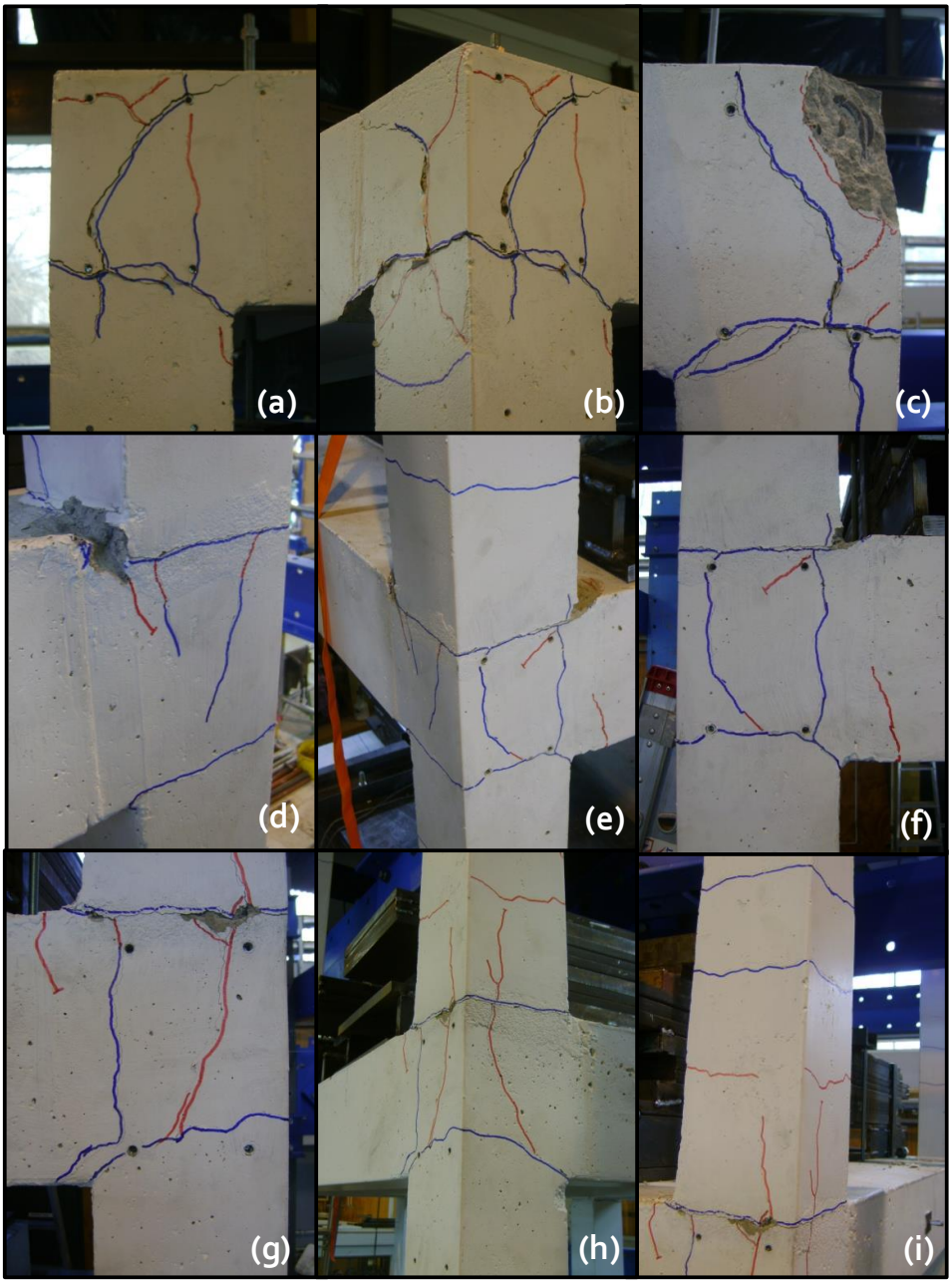

Figure 4.11: Observed damage after the *real* Darfield Earthquake which affected Christchurch on February the 4th 2010: (a) top floor, long span joint front view, (b) top floor, long span joint 3D view, (c) top floor, short span joint front view, (d) second floor, long span joint side view, (e) second floor, long span joint 3D view, (f) second floor, long span joint front view, (g) second floor, short span joint front view, (h) second floor, short span joint 3D view, (i) second floor, short span column view.

The bi-directional characteristics of the real ground motion can be appreciated in corner beam column joints, where a symmetrical damage pattern was observed. It is important to clarify that, since the ground motion affected the specimen in real time, time does not follow the similitude rules. As a consequence the maximum amplitude of the movement (PGA) that attacked the specimen is 2.5 times larger than the *similar* one in the model domain. As a consequence, displacements experienced by the model should be larger than those corresponding to a response under a similitude-compatible input motion.

4.3.3 Failure Mode Mechanics

The question as to why the lap splice failure occurred more strongly on the outer face of the columns at both ends of the specimen arises. Also, the greater compression strut which generated diagonal cracks in the joint in the opposite direction of those created in top storey joints. The proposed answer relies on the additional uplifting force that the external bars experience due to axial load variation. Consider the column on top of the 2nd floor right corner joint, shown in Figure 4.11(g, h, i). When the column bends counter clockwise, a negative pulling force is also generated by equilibrium. This pull-out force is equal to the upwards shear induced by the beam at the top of the column.

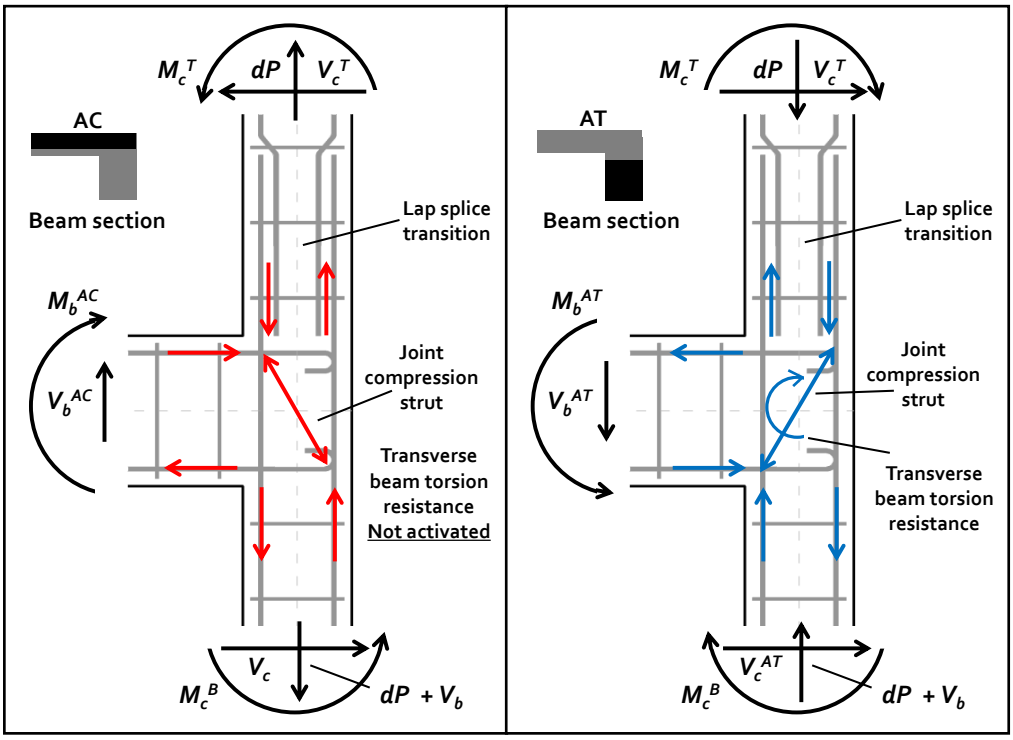

Figure 4.12: Corner beam column joints mechanics and equilibrium under seismic actions.

When the column bends clockwise on the other hand, there is an additional compression force coming from the downwards shear induced in the columns by the roof beams bending in the opposite direction. As a result, the net uplifting force that reinforcement bars located at the inner face of the exterior columns is lower than that experienced by the outer bars at when the reversed movement comes. This is anti-symmetrically reflected in the left corner joint of the 2nd floor, as shown in Figure 4.11(d, e, f). As a result, when the right exterior column experiences a seismically induced uplifting force, the left side

counterpart experiences an analogous downwards force, and vice versa. In Figure 4.12 the right side corner beam-column joint resisting mechanism and force equilibrium is presented for the beam bending in both directions. When the beam is subjected to positive bending then the top fibre of the slab (A) acts in compression, and is named AC. When the beam experiences negative bending, fibre A acts in tension, which named AT (see Figure 4.12).

In Figure 4.12: M_c^B and M_c^T are the bending moments in the bottom and top columns, respectively, V_c^B and V_c^T the shear in the bottom and top columns, respectively, M_b the bending moment in the beam, V_b the shear force in the beam, and dP the axial load variation due to seismic actions. These represent the seismic actions in the corner beam column joint. In addition in Figure 4.12 the resisting mechanism inside the panel zone is presented by means of a compression strut in the joint itself and the torsional resistance of the transverse beam, oriented in the orthogonal direction behind the joint. This mechanism is activated when the top fibre of the beam acts in tension, since it is activated by the slab bars acting in tension. When the slab acts compression (AC), torsional resistance is not activated, since there is not a 'bottom slab' to trigger this resistance mechanism. In addition, the transverse beam provides confinement on one side of the joint in the corner joints and two sides on the exterior joints of the internal frame. Axial load induced by seismic actions is directly related to the shear developed in the beam. The load denoted dP means the variation from the initial static load, which corresponds to the gravity load. As shown in Figure 4.12, the variation in the axial load from the top column to the bottom, corresponds to the shear developed in the beam which traduces in additional tension when AC, and additional compression when AT. Note also that since the bending capacity of the beam in the negative bending direction (AT) is greater than the positive counterpart, the maximum axial that the beam is able to carry into the joint will be larger for AT. In this case, for equilibrium, the additional load corresponds to a downwards compression force.

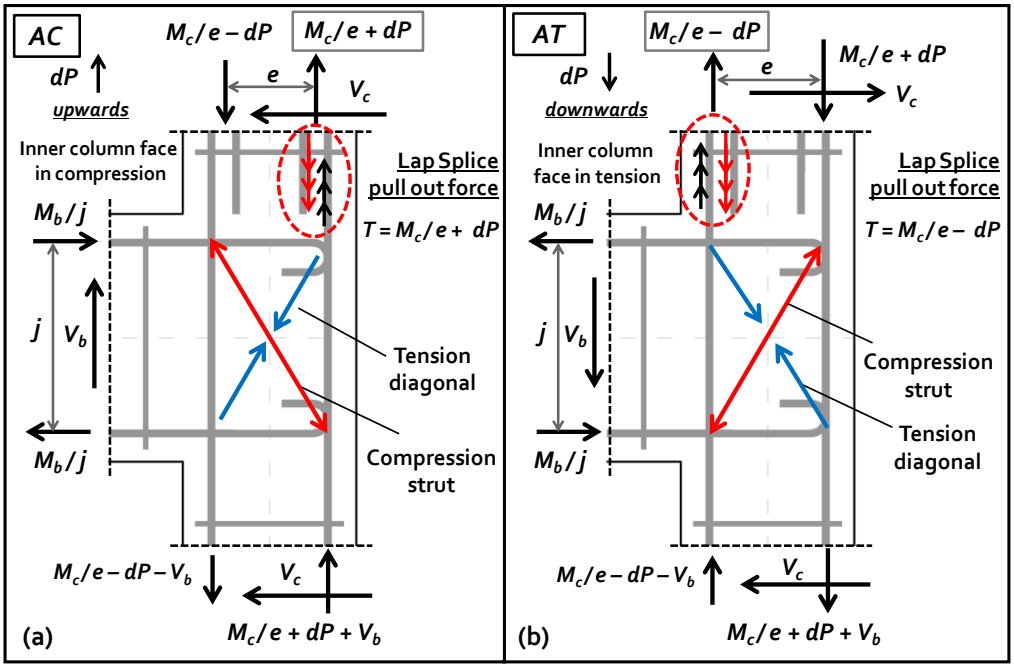

Figure 4.13: Corner beam column joint force equilibrium and critical lap splice transition under a relative top displacement (a) to the left (AC), and (b) to the right AT.

Figure 4.13 shows a closer examination into the mechanism of the corner beam column joint presented in Figure 4.12(a). In this case, the beam bends in the positive direction and the slab is compressed (AC). Moment actions are replaced with the equivalent forces developed in the concrete in compression and in the steal in tension. The forces are written in terms of the lever arm of the resulting pair of forced and the moments defined previously. As highlighted in the top right side of Figure 4.13(a), in this case, steel bars located at the outer faced of the column will be subjected to tension. This tension force comes from the column bending towards the inner face of the column and the variation in the axial (vertical) force in the column coming from the uplifting shear induced by the beam at the upper floor (top floor in this case).

The bottom of the column in the scenario of Figure 4.13(a) is presented in Figure 4.13(b). It is shown that when bond is lost between the steel bars and the concrete in the lap splice region, the top column would tend to rock on top of the joint. If it is assumed that the column pivots in compression at the inner face, then its rotation at the base (θ_h) corresponds approximately to the inter-storey drift of the top floor (θ_v). The displacement induced at the outer face of the column (Δ_u), where critical vertical bars are located, corresponds roughly to the inter-storey drift experienced by the third floor multiplied by the column effective height (d_c). Using the experimental data presented previously, as the inter-storey drift in the top floor reached a maximum value of 2.5%, then as h_c equal to 130 mm, a maximum value of $\Delta_u \approx 3$ to 4 mm. This estimation has been done because no potentiometers were located in the lap splice region in the third floor.

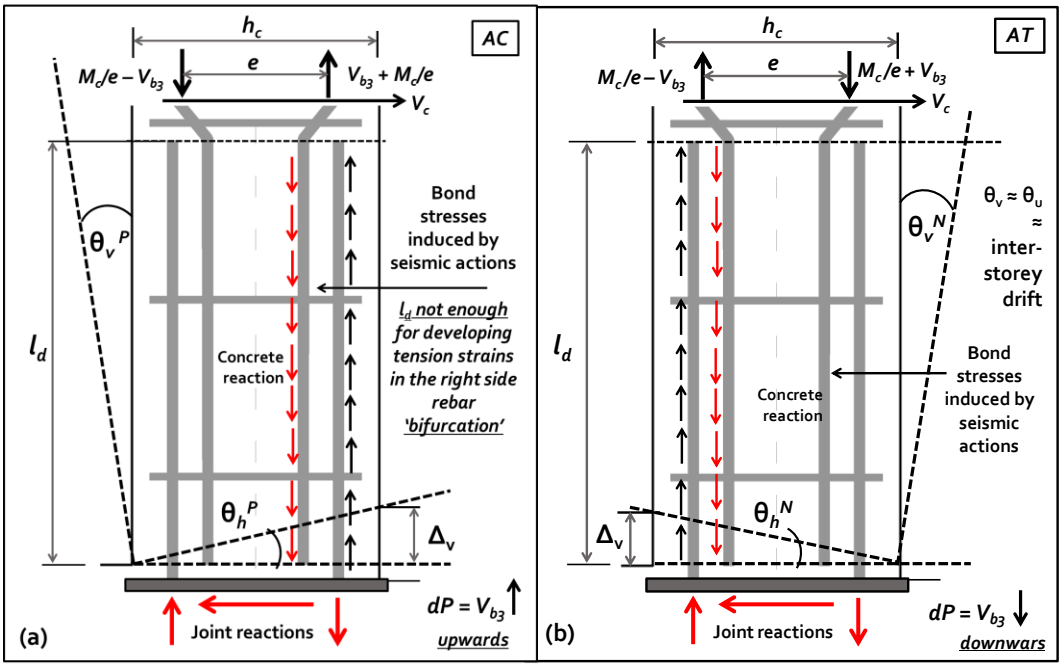

Figure 4.14: Top floor column rocking on top of second floor joints towards the left.

Assuming a maximum bond stress equal to the tensile strength of the concrete (approximated as 10% of the compression strength), for a 6 mm diameter bar with a lap splice length of 240 mm, and f_c' = 12 MPa, the maximum possible bond force corresponds to approximately 7 kN, half of the case of f_c' = 25 MPa. This implies that lap splices failure is more likely to occur with a substandard quality concrete. Assuming that

the modulus of elasticity of the concrete is the same in compression and tension, then the critical displacement at which bond is loss corresponds approximately to 2 to 3 mm, a smaller value than the indirectly estimated displacement. This explains the failure mode observed in the lap splices region, but not the severe diagonal cracking observed in top floor corner joints. The latter is the described in the following tests series results, in the light of the fact that the same failure mode occurred in corner joints of the first floor.

4.4 SPECIMEN MODIFICATION/REPAIRING PROCEDURE

After finishing the test series 1 and after the real Darfield earthquake consequences were sorted out, the specimen was repaired and structurally modified in order to simulate a new as-built specimen. Concrete around all column lap splices region was removed. Longitudinal column reinforcement was carefully welded to provide continuity in the reinforcement. Removed concrete was replaced with structural SIKA Monotop Structural Mortar, which has very similar mechanical characteristics in terms of compression strength and adherence to those of the original specimen's concrete (see Chapter 3). In Figure 4.15 the repairing/modification process sequence is presented.

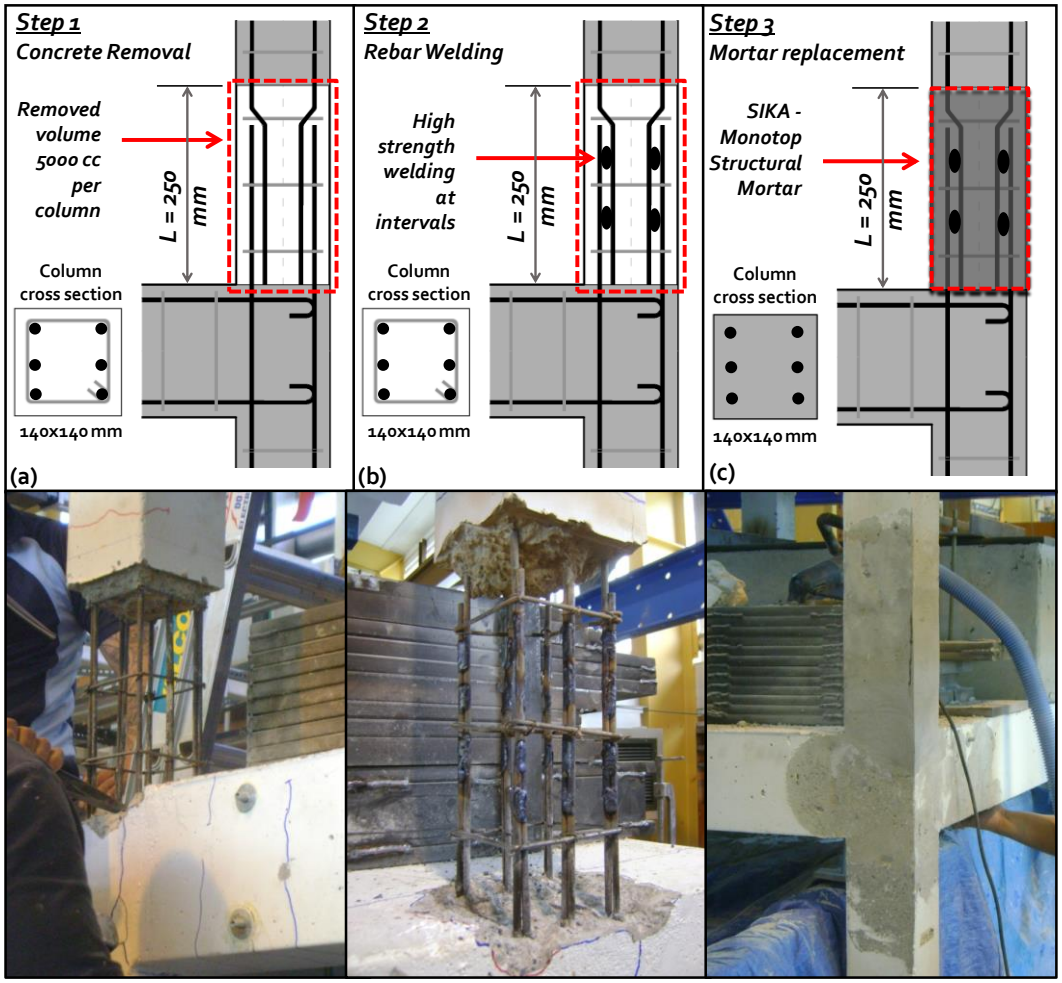

Figure 4.15: Repairing sequence: concrete removal – reinforcement welding – mortar filling.

The sequence was divided in the following steps:

1) Concrete removal
2) Column vertical rebar lap splices welding
3) Structural mortar placing
4) Crack injection with epoxy resin

All cracks were filled by injecting SIKADUR 92 string epoxy resin, with high pressure bombs. Finally, some parts were finished using SIKA 62 epoxy. The resulting specimen is then represented by the same dimensions and reinforcement showed in Chapter 3, with the exception that all longitudinal column reinforcement is now continuous in height. This modification takes away the problem that the possibility of lap splices failure to develop in the specimen, assuming that welding would fix the bars correctly. The repairing process therefore does not follow a typical 'repairing policy' which would leave the structure 'as it was before'. In the eyes of the naive observer, the specimen has been repaired and 'upgraded', since the problem the building experienced in the earlier tests was mitigated by welding the lap splices. However, this intervention is just shifting the weakest link towards another link which is just as brittle as the other. As discussed in the following paragraphs, based on the new experimental series, first floor joints are now the most vulnerable elements.

4.5 SERIES 2 – TEST 2.1 MAIN RESULTS – DARFIELD

After the specimen was repaired, it was tested twice. In the first experiment, Test 2.1, a ground motion recorded during the 2010 Darfield earthquake at Christchurch Hospital station was used, whilst in the second experiment, Test 2.2, a ground motion recorded during the 2010 Maule Chile earthquake at Viña del Mar Marga-Marga station was used as input. The fundamental period of vibration of the repaired specimen was measured as T_1 = 0.27 sec. (see Appendix C).

The main objective of Test 2.1 was to demonstrate that for this particular building, and one of the ground motions recorded during the Darfield earthquake would not experience severe if any damage, in order to replicate what was observed in RC structures after that seismic event. This implication follows the observed damage during field inspections (Pampanin et al. 2011). On the other hand, the purpose of the seconds test was to demonstrate that if another motion, from a different earthquake, such as that recorded in Viña del Mar at 450km from the hypocentre during the Maule earthquake (Cowan et al. 2011), was used as the input motion, the specimen would experience large inelastic deformations and would reveal its seismic vulnerability, which remains affecting the specimen despite the fact that it was not triggered in the previous test. The latter, represents a very adverse scenario of the building under study, as conjectured *a priori*, which is unfortunately impossible to do in real life.

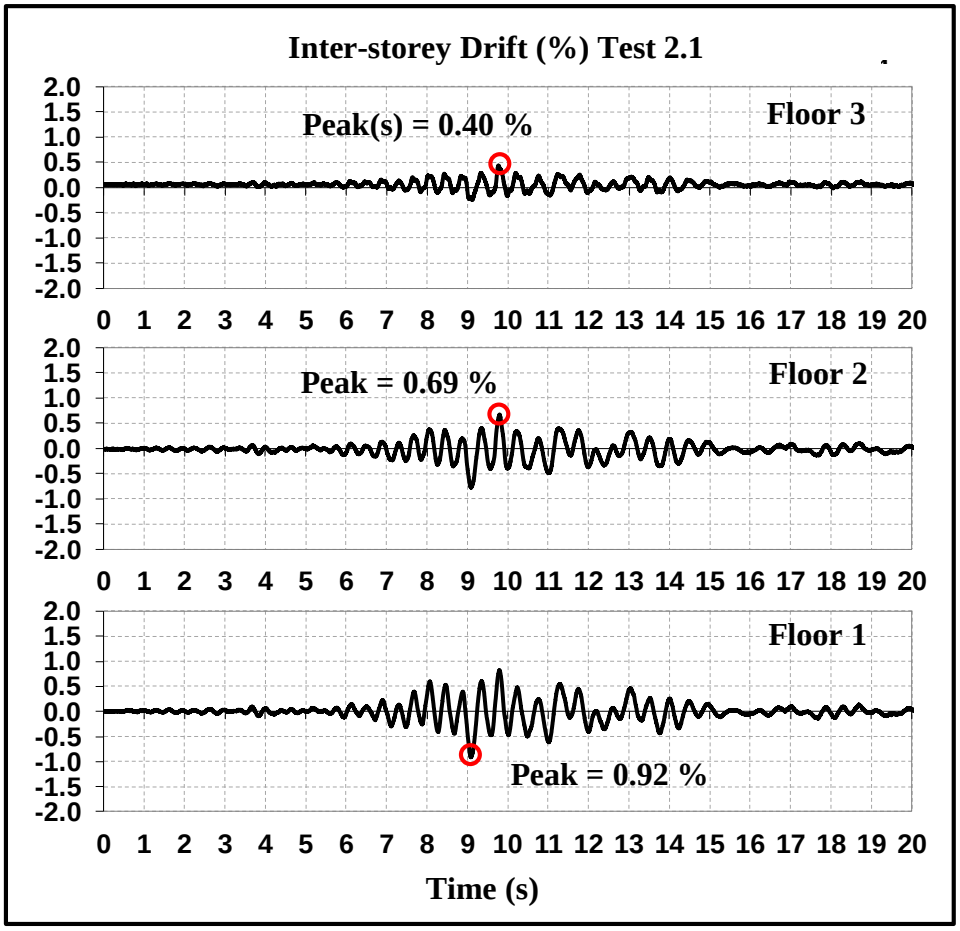

Figure 4.16: Test 2.1 measured inter-storey drift (center of mass) – Darfield ground motion.

The recorded response of the model in terms of inter-storey drift and floor acceleration time histories for Test 1.1 are presented in Figure 4.16 and Figure 4.17. This corresponds to the results recorded in the specimen when using CHCH record from the Darfield earthquake (PGA = 0.20g). In Figure 4.16 it is a predominantly elastic response is reflected at low inter-storey drift levels, and no residual displacements. Peak values of inter-storey drift reached are 0.92%, 0.69%, and 0.40% for floors 1 to 3, respectively. The plotted time-histories of different floor inter-storey drifts are very similar to each other. In this case, all peaks or similar values are repeated twice in the first and second floors. Floor accelerations remained below 0.65g in all floors, were peak values reached corresponded to 0.32g, 0.43g and 0.63g respectively. These values represent an amplification of about 2 for floors 1 and 2, and about 3 for floor 3, when compared with the peak acceleration of the motion (PGA).

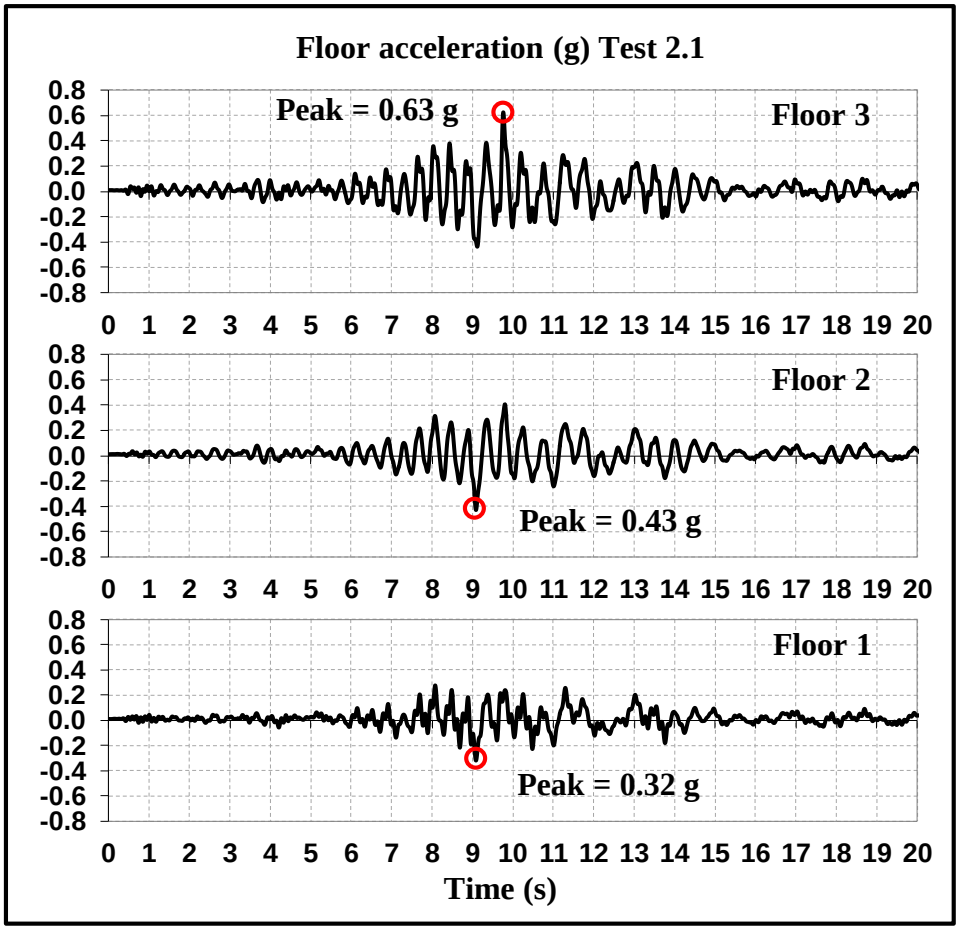

Figure 4.17: Test 2.1 recorded floor accelerations (center of mass).

As inter-storey drifts remained below 1% in floors 1 and 2, and below 0.5% in the top one, the intensity of the observed damage is in line with the light damage observed in previously reported experiments concerning quasi-static tests of non-ductile beam column joint subassemblies (Pampanin et al. 2002, 2006, 2007, Kam et al. 2010, Kam 2010, Akguzel 2011). In the test of the as-built specimens, it was observed that light diagonal cracking developed in the joints of 2D and 3D specimens at drift levels equal to 1.0%. Since the specimen used in this study was designed to match the design of the 3D beam column joints used in those studies, despite the addition of a floor slab, the obtained results in terms of damage and drift demands are coherent.

After Test 2.1 (Darfield), very thin cracks were observed in the structure. Some light cracks developed around the panel zone region and beams, but the response practically remained in the elastic range. The crack pattern after the test is shown in the pictures of Figure 4.18. It is shown that almost no damage occurred in floors 2 and 3, whereas the light cracks (shown in blue) developed in corner beam column joints in the first floor.

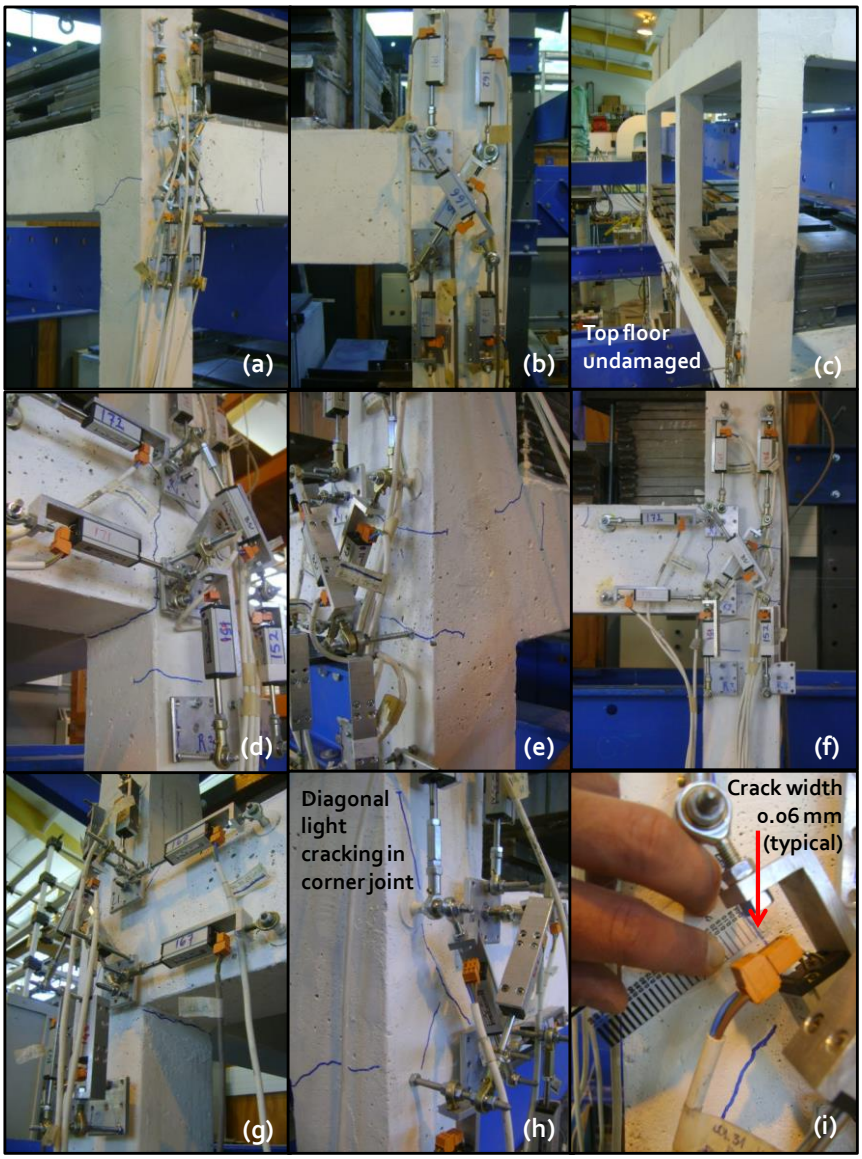

Figure 4.18: Damage in exterior beam column joints after series Test 2.1 – Darfield earthquake.

The addition of the floor slab has been preliminary studied in sub-assemblies as reported by Kam et al. (2010). The evidence found in that work, led to the preliminary conclusion that the slab did not affect much the quasi-static behaviour of the 3D specimen, but introduces an extra resistant mechanism in the panel zone, coming from the torsional resistance of the transverse beam, and the confinement of the joint in two additional faces. However, for the retrofitted 3D beam column joint, the addition of the floor slab is significantly important, since in the best case, the inelasticity will be concentrated in the beam as flexural strains. This is discussed in detail in Chapter 5.

4.6 SERIES 2 – TEST 2.2 MAIN RESULTS – MAULE

4.6.1 Global Response

After the specimen was checked, Test 2.2 was performed, this time using VMM record from the Chilean Maule earthquake. Recorded response of the model in terms of inter-

storey drift and floor acceleration time histories for Test 1.1 are presented in Figure 4.19 and Figure 4.20. Peak values reached 3.8%, 2.2%, and 1.0% in floors 1 to 3, respectively. The plotted time-histories reflect a remarked concentration of the inelasticity in the first floor. In this case, peak values are repeated several times in floors 2 and 3, and in floor 1, drift values above 2.5% were reached more than two times, apart from the peak value of 4.0%. The value of the inter-storey drifts recorded in the first floor would appear large for poorly detailed frames. However, it can be noted that due to low axial load ratio and low longitudinal reinforcement ratio, substandard columns can actually achieve a significant rotation capacity. Furthermore the fact that the inter-storey deformation demand are shared by columns, beams and joints, can further justify the achievement of those levels of drifts in this case without the collapse of the structure.

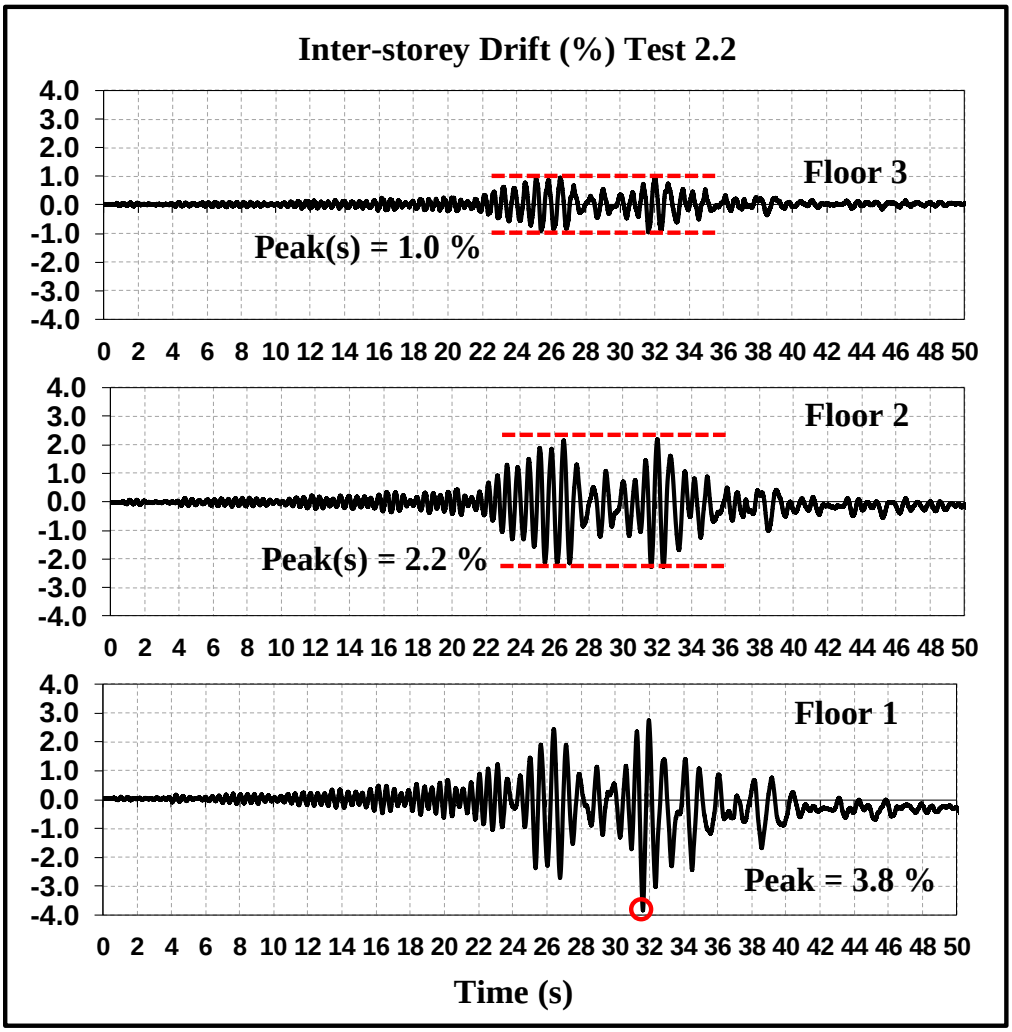

Figure 4.19: Inter-storey drift recorded time-histories, VMM record, Maule, PGA = 0.33g.

Floor accelerations reached a global maximum of 0.71g in the top floor whereas in floors 1 and 3 peak values equal to 0.60g, and 0.52, respectively, being fairly similar in shape during the duration of the response. The latter can be appreciated in the 'relevant amplitude' of the structure's motion in both tests which corresponds to only 15 sec. (*model time*; 25 sec. prototype) and a long response of the specimen during Test 2.2 of about 35 sec. (*model time*; 60 sec. prototype).

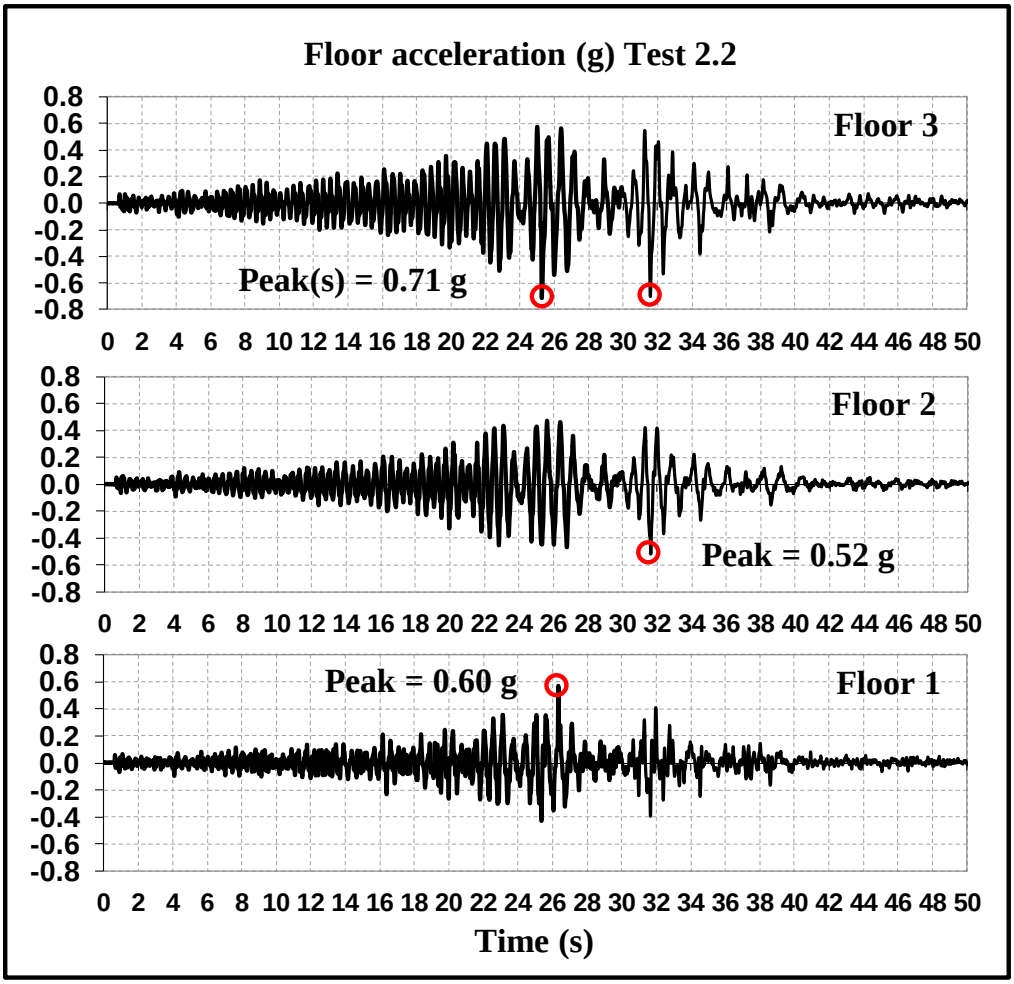

Figure 4.20: Test 3 recorded floor accelerations (center of mass).

4.1.1 Observed Damage and Failure Mode Mechanics – External Frame Corner Beam Column Joints

As shown in the images of Figure 4.21, first floor corner joints of the external frame suffered severe damage, developing a damage pattern very similar to that observed in beam column joint plane and 3D subassemblies (Pampanin et al. 2002, Pampanin et al. 2005, Pampanin et al 2007, Kam et al. 2008, Akguzel and Pampanin 2008, Kam et al. 2010, Akguzel 2011). Inelasticity in the joint developed as diagonal cracks in both directions on the joint. Crushing developed with greater intensity in the bottom-outer side of the joints, revealing that the strain demand in that region was larger than in other parts of the compression field created in the 3D geometrical body. On corner beam column joints of the second floor, diagonal also cracks were developed, with smaller widths than those measured on the first floor, and no significant crushing of concrete. This is consistent with the displacement levels reached in both floors of 2% and 4% respectively. In the top floor, no significant cracks occurred, as inter-storey drift levels remained below 0.5%. Thin cracks were also observed in columns and beams close to the panel zone region, with no evidence of crushing in the concrete.

Observations and global measurements of the response indicate that a first floor soft storey mechanism was developed, leaving the structure in a very unstable inelastic motion. The observed and measured levels of the response would fit into the category of

'near collapse' limit state in traditional performance-based design. Forensic assessment of the building revealed that all exterior beam column joints of the first floor were severely cracked inside, and the concrete was very strained in compression. However, the vertical rebar remained unbuckled.

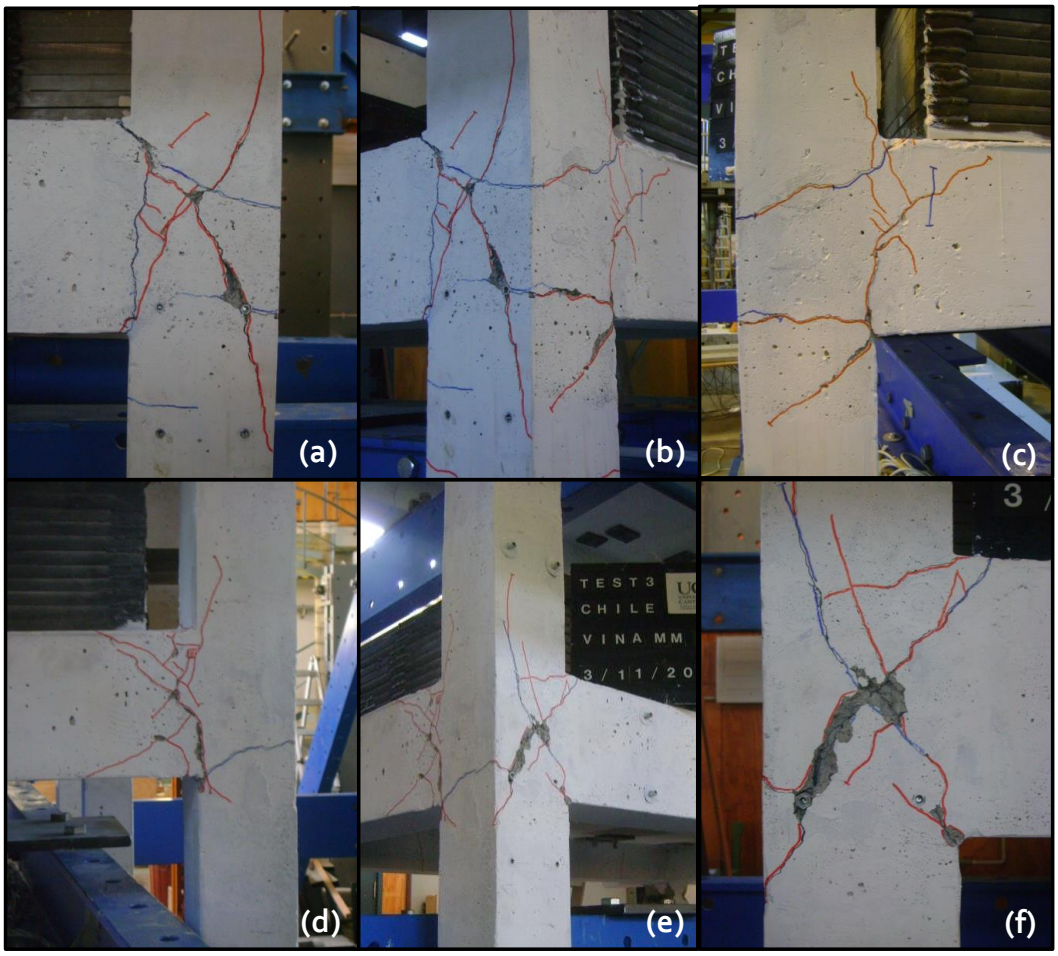

Figure 4.21: Observed damage after Test 2.2 – first floor corner beam column joints of the first floor: (a) short span joint front view, (b) short span 3D view, (c) short span side view, (d) long span joint side view, (e) long span 3D view, (f) long span front view.

In Figure 4.21 (a), (b), and (c), pictures of the right side (short span) corner joint after Test 2.2 are presented. Similarly, in Figure 4.21 (d), (e), and (f), pictures of the left side (long span) corner joint after that test. Note in Figure 4.21 (f) the development of diagonal cracks in the direction of the two diagonals of the joint. However, compression failure developed much more intensively in the bottom left side of the panel zone. This indicates an asymmetry in the damage intensity related to the mechanics involved in the beam column joint when the compression develops from in opposite directions. With reference in Figure 4.21(f), the compression strut developed in the beam column joint corresponds to a deformed state where the top of the beam and slab are subjected to positive bending. This is named an AC situation, since the top fibre 'A' is subjected to compression.

The body equilibrium of the long span beam column joint compatible with the development of a compression strut in the observed direction is presented in Figure 4.22,

where: M_c^T and V_c^T are the moment and shear actions induced by the top column, M_c^B and V_c^B are the analogue actions induced by the bottom column, M_b^{AC} and V_b^{AC} the moment and shear actions induced by the beam acting with AC, and *dP* the axial load variation induced by the top column. Note that vertical equilibrium requires that the axial force induced by the bottom column to be larger than the top one when also equilibrating the shear induced by the beam. Indeed *dP* is the sum of the shear induced in the upper floors of a given column. This makes a difference in the forces but also in the strain compatibility, by modifying the neutral axis of the columns, leading to the observed damage pattern.

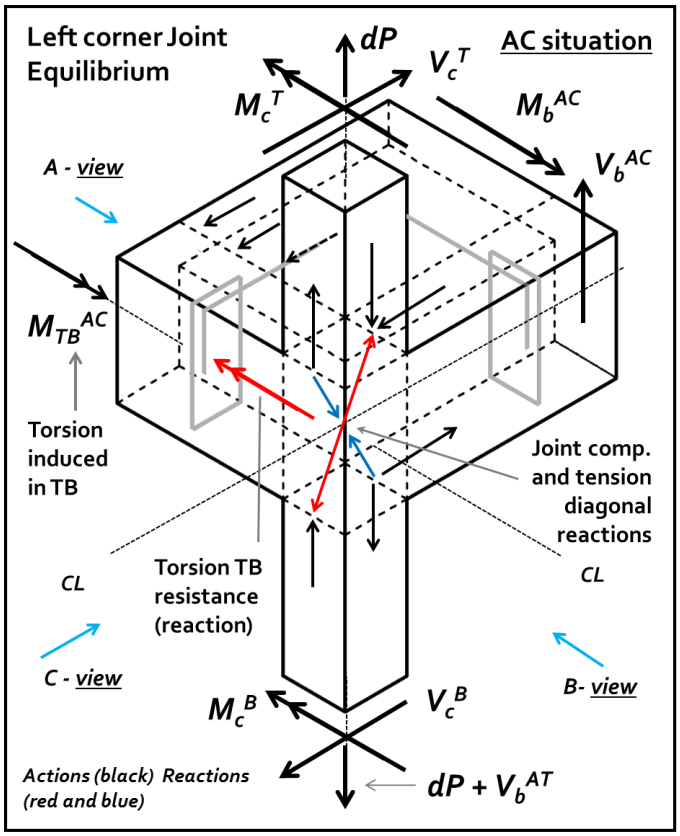

Figure 4.22: Corner beam column joint slab equilibrium and resisting mechanism.

In Figure 4.22 a movement of the top column towards the top right side of the isometric figure, a movement towards the bottom left in the bottom column, and an upwards movement in the beam are cinematically compatible with global force actions, and area assumed to be the cause of the forces drawn. Black arrows indicate the actions induced by the beam and columns on the joint, whereas red and blue coloured arrows show reactions in the joint and transverse beams. Note that even the model structure was conceived as a 3D specimen, the seismic action was simulated in a 2D fashion. Therefore, there is no equivalent bending moment in the transverse beam, and no torsion reaction in the longitudinal beam, corresponding to the long span in Figure 4.22. Even though torsion effects are described in deeper detail later, the acknowledgment of that reaction for understanding the damage pattern needed. This is because the torsion capacity in the beam will vary depending on the beam acting under positive or negative moment, which corresponds to the slab acting in compression (AC situation) and tension (AT situation), respectively.

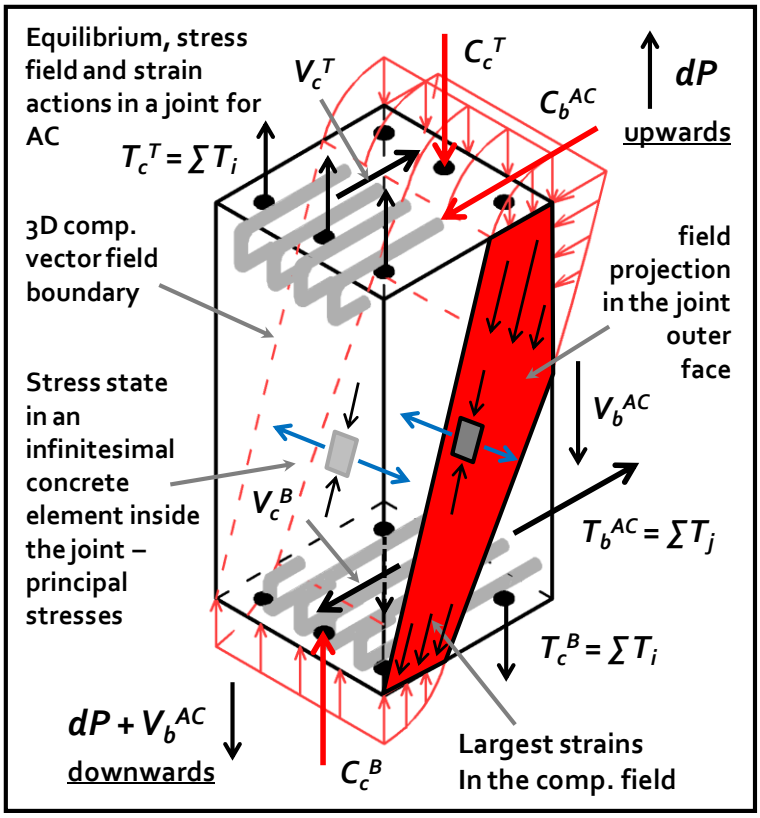

Figure 4.23: Force equilibrium at diagonal compression failure in left corner joint.

In Figure 4.23 a close up of the panel zone of an exterior beam column joint is presented. In Figure 4.23, actions induced by beam and column in the joint are drawn as the compression action induced by the concrete behaving in the almost-linear range. Tension forces from the members opposite face are indicated as individual vectors from every steel bar. Reactions in the joint are represented by a 3D stress vector field named *p(x,y,z)*, with $p \in |R^3$. It is worth noting that with the inclusion of time into the problem, ***p*** becomes a 4D vector ($p(x,y,x,t)$ *with* $p \in |R^4$). As a consequence, the field illustrated in red in Figure 4.23, corresponds to the 'phase state' of the field in the space coordinates. In other words, the 3D field represents a snapshot of the field at a certain time. Given the essence of the approach used in this thesis, which relates to dynamics, fluctuations of the stress field are understood by means of 'phase states' in the joint.

In Figure 4.24 and Figure 4.25 two different phase states of the stress field inside a 2-dimensional exterior joint are presented. The stress field is shown in terms of diagonal lines representing the flow of compression forces inside the joint. The field boundary is delimited by compression strains induced by columns and beams acting in the 'almost linear' range of stress-strains constitutive laws for concrete and limited (almost no) yielding in the steel. Axial strains from induced axial load variation are also drawn in and added to pure bending induced strains. It can be seen that in the most critical state, which corresponds to the AC state. The addition of axial strain modifies the neutral axes locations in the top and bottom columns, changing the boundaries of the compression field. Note in this case strains are used as actions and stresses are used as reactions in the joint.

As the resulting state in the compression field corresponds to a 3-dimensional vector containing two axial and one shear stresses component. In both Figure 4.24 and Figure 4.25, these states are drawn in terms of the principal stresses of an infinitesimal body in the joint, following Mohr's circle approach. In order to avoid congestion in the figures, principal compression stresses have been drawn only (positive principal strain in Mohr's circle). However it is easy to imagine two vectors orthogonal to the vertical faces of the infinitesimal bodies drawn in between compression flow lines, which correspond to tension actions in the concrete. A more detailed explanation of these principles applied to the assessment and retrofit scheme design is presented in the next chapter.

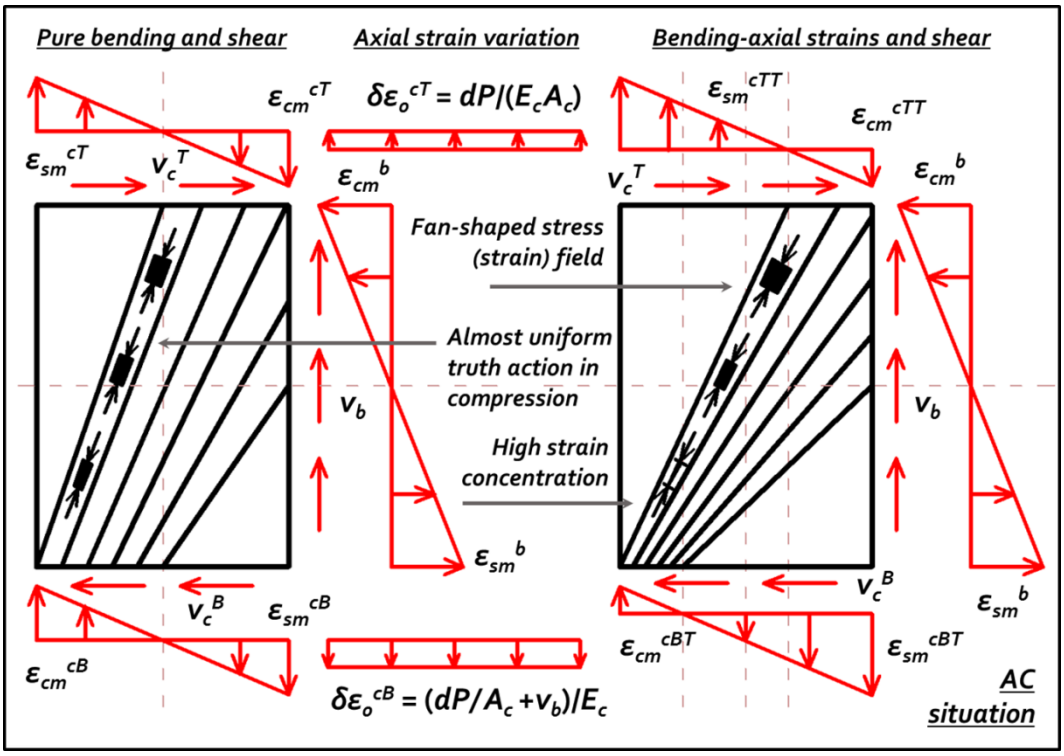

Figure 4.24: Strains in the panel zone when AC – high compression strains in the bottom left.

For now, let us focus on the thickness of the infinitesimal element affected by compression stresses as in Figure 4.24 and Figure 4.25. It can be seen that for AC phase state (or situation) the short sides of the element reduce significantly when approaching to the left bottom part of the joint. As a constant force is transmitted through the field, then it follows that smaller size elements will experience larger stresses that those with a larger cross sectional area perpendicular to the compression flow lines. This theoretical explanation of larger stresses (strains) in the bottom left part of an exterior beam column joint slab element when AC represents an explanation for the observed damage. The influence of the transverse beam providing resistance in torsion has been neglected for now, since it can be ignored when AC as will be discussed in the last part of this chapter. However, this is not the case when AT, which is one critical case for the exterior joints of the internal frame, as shown in the following paragraphs.

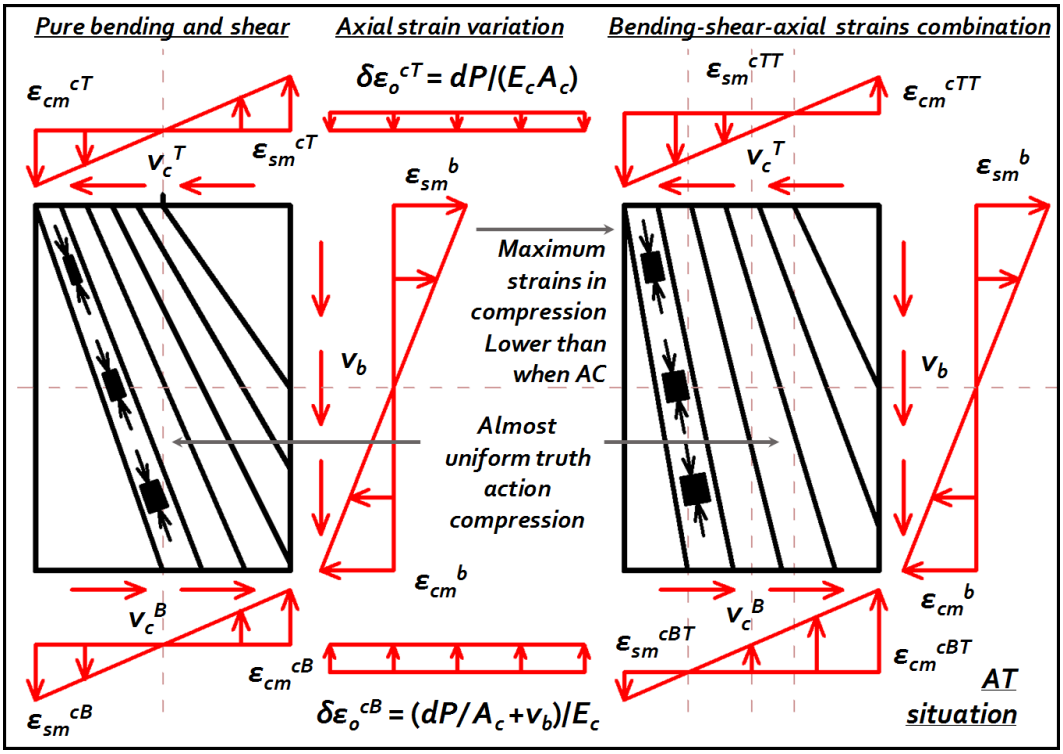

Figure 4.25: Strains in the panel zone when AT – compression strains almost evenly distributed long joint's diagonal strain vector field.

4.6.2 Observed Damage and Failure Mode Mechanics – Internal Frame

The exterior joints of the internal frame suffered considerable damage in a slightly different way to that experienced by the exterior joints of the external frame (corner joints). As the joint is confined in three faces by strong beams, its capacity increases, and the slender columns become the more vulnerable element. Torsional resistance in this case is much larger than for corner joints, since a complete beam, a replica of the longitudinal counterpart, crosses the joint.

In Figure 4.26, pictures of the observed damage in exterior joints of the internal frame are presented. In Figure 4.26 pictures (a), (b) and (c) correspond to the first floor left (long span) corner joint whereas the pictures (d), (e), and (f) to corresponds to the right (short span) counterpart. Inelastic incursions are concentrated in top and bottom columns in both cases, with significant strain penetration. In the left joint though, torsion cracking was developed on the side and bottom faces of the transverse beams. These cracks confirm that torsion resistance contributed to the mechanics of the beam column joint slab element of an internal frame, in line with previous research (Ehsani and Wight 1985, Durrani and Zerbe 1987, Di Franco et al. 1995, Shin et al. 2004, Kam et al. 2010). In Figure 4.26, crushing in the bottom of the second floor columns is large and reveals that inelastic rotations of these elements developed especially during the AT situation, when the beam is much stronger than during AC.

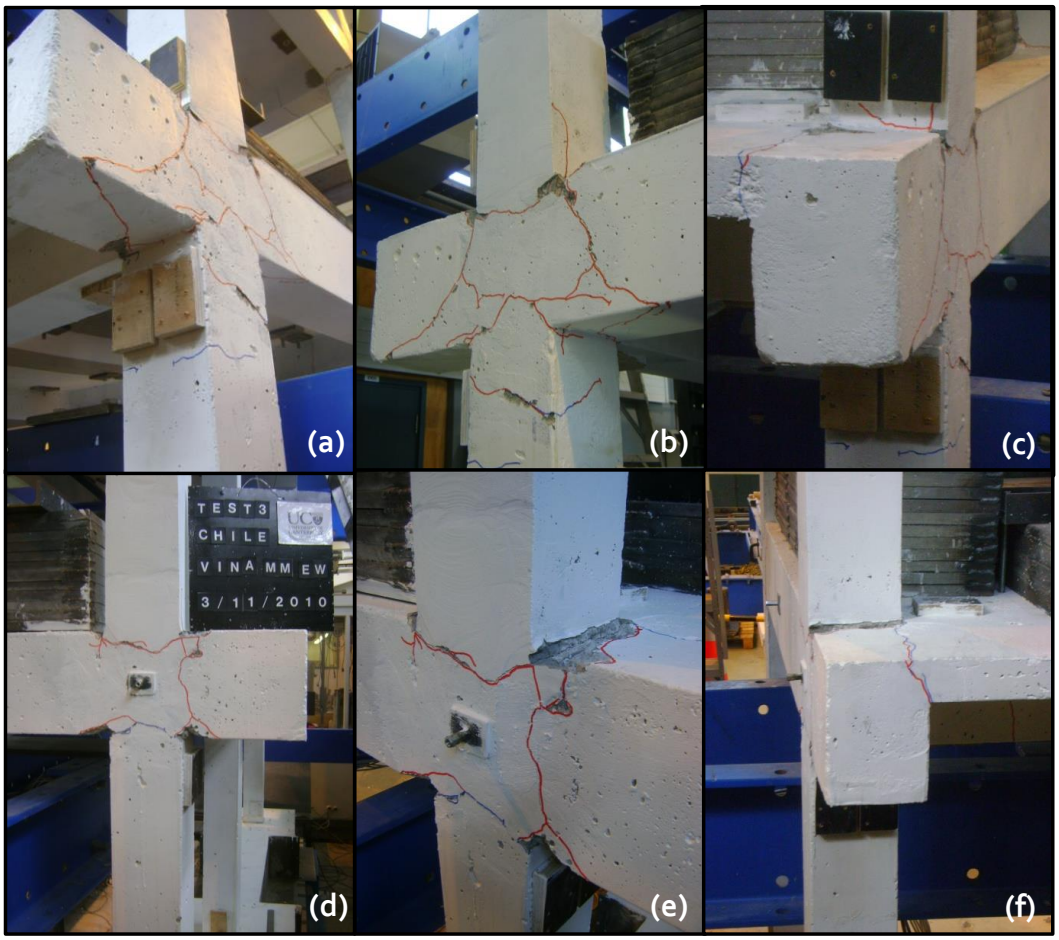

Figure 4.26: Observed damage in first floor exterior joints of the internal frame: (a) long span joint 3D view, (b) long span joint side view, (c) long span joint front view, (d) short span joint side view, (e) short span joint close-up, (f) short span front view.

The joint in this case is confined in three faces, which increases significantly its capacity in shear. As discussed by Ehsani and Wight (1985), in their test of beam column joint subassemblies very similar to that schematically presented in Figure 4.27, even the addition of closed stirrups about the column's longitudinal reinforcement does not significantly upgrade the behaviour of the specimen, since the most relevant parameter for shear strength in the joint was concluded to be the confinement provided by transverse beams.

In Figure 4.27 force and moment equilibrium at AT state is presented. Actions induced by the longitudinal beam and the columns are drawn in black, whereas resisting forces are illustrated in red and blue. Using single vectors in this case, resisting diagonal forces in the joint are drawn as a projection in the transverse beam end for convenience. These forces reacting in the joint have the direction for equilibrating each of the joint's corners (see also Figure 4.22). These arrows indicate a compression and tension resisting path in the concrete, which corresponds to the compression field in Figure 4.25 for the AT state. The resisting torque in the transverse beam is also drawn in on the sides of a stirrup. This torsion reaction in the transverse beam indicates additional shear forces in the joint (for continuity) which have the opposite direction of the reaction torque in the beam. However the sign of those forces corresponds to the opposite of the shear induced by the top and bottom columns. As a consequence, the transverse beam relieves the joint from the total

stresses induces by longitudinal beams and columns in this case, reducing the demands in the joint or taking a part of the actions imposed by the portion of the frame. This is illustrated in the final part of this chapter.

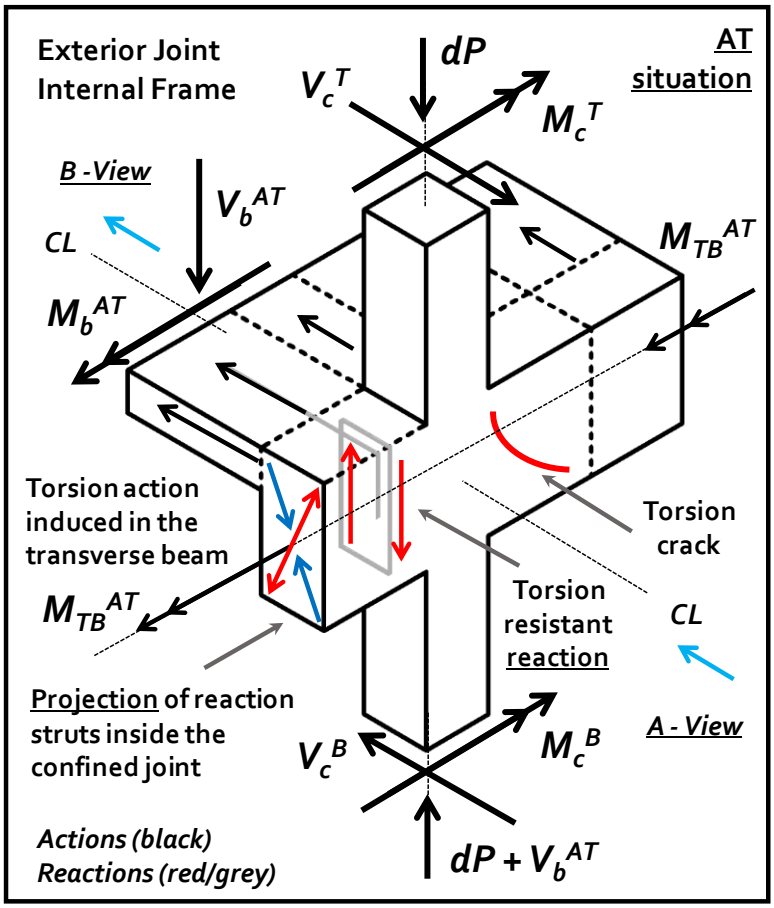

Figure 4.27: External joint of the internal frame inelastic mechanism for AT – torsion activated.

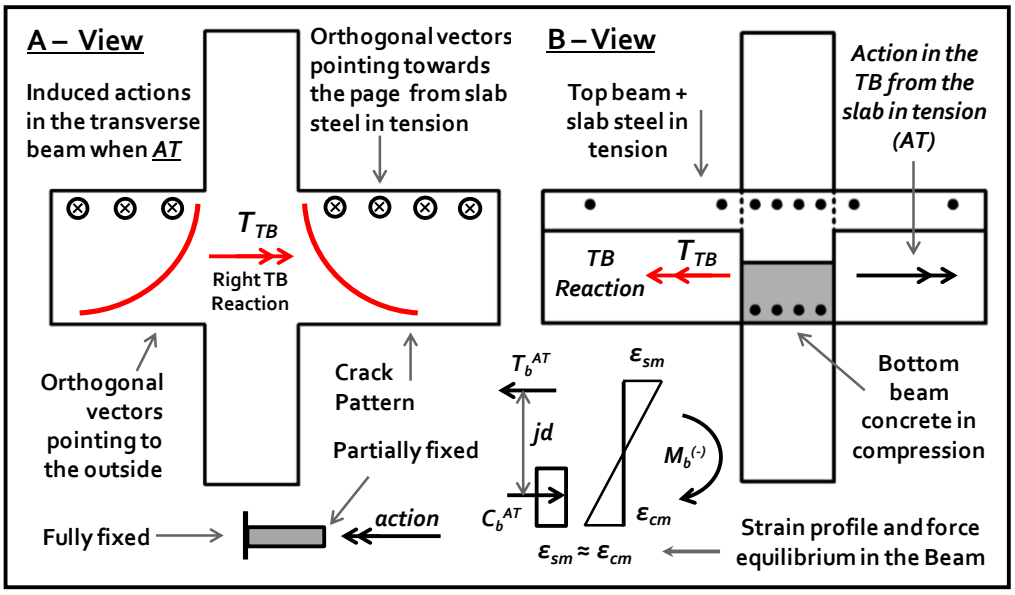

Figure 4.28: Torsion demand in the transverse beam (TB) induced by beam flexural bending in the longitudinal beam – capacity design approach.

In Figure 4.28, two faces of a 3D exterior joint of the internal frame are shown. These drawings correspond to an outside view and from the outside of the specimen, and an inner cross section the joint, respectively. These faces have been called views 'A' and 'B' respectively, from the reference given in Figure 4.27. On the left side of Figure 4.28, the crack pattern in the joint and transverse beam is drawn. Loading in the orthogonal direction to the page represents the induced forces in the top of the transverse beam. A reaction in the joint as a consequence of the torque induced by the transverse beam is shown in red at the centre of the outside face of the cruciform joint. This torque is the result of the eccentricity of the applied load on the top of the transverse beam by the slab reinforcement acting in tension in relation to the centre of twist in the transverse beam (Di Franco et al. 1995).

On the right hand of Figure 4.28, the inside counterpart of the left side hand drawing, the relationship between the bending moment developed in the longitudinal T-shaped beam and the torque induced in the transverse beam is addressed. In Figure 4.28 it is schematically shown that the strains in the section of the beam remain inside or very close to the elastic range. This bending moment is transmitted into the joint, which reacts with a compression strut of field and shear forces. The transverse reinforcement of beams goes though the inside of the joint, forming a completely monolithic body. Per compatibility, the distortion in the joint caused by the beams and columns must be equal to the twist at the interface with the transverse beams. In addition, the equivalent resisting moment of the joint must be equal to the torsion reaction in the transverse beam 'fixed' in the joint.

4.6.3 Influence of the Slab and Transverse Beam in the Joint Resisting Mechanism

As initially discussed by Ehsani and Wight (1985) and Durrani and Zerbe (1987), the addition of transverse beams and a floor slab was not of typical use in the beam column joint sub-assemblies tested since Hanson and Connor (1967), which were used as a benchmark for most of the testing in those days. In Ehsani and Wight (1985) the inclusion of these two elements are discussed in depth. Their conclusions, based on experimental work on cruciform joints, were that the presence of the transverse beams:

1) considerably improves the joint behaviour
2) helps to eliminate the beam bar pull-out
3) increasing the amount of stirrup reinforcement in the joint does not improve the behaviour

At the University of Canterbury, most of the specimens in experimental tests have consisted of specimens without a slab and transverse beams. Only in Kam et al. (2010) specimens similar to those shown in Figure 4.29(b) and Figure 4.29(b) were reported. In Kam (2011), the effect of confinement in the joint is incorporated by increasing the effective width of the joint for calculating the equivalent moment-axial load strength. Nevertheless, torsion is not incorporated. In Akguzel (2011), where the results of tests of 3D corner beam column joints, each longitudinal beam becomes the transverse beam of its counterpart depending on the loading direction. Since specimens did not include a floor slab, the geometrical effect of the slab in terms of specimen boundary conditions, was simulated using rigid braces attached which avoided the ability of the orthogonal beams to separate horizontally one from the other. Torsion in this case was able to

develop in the subassembly, but the absence of the floor slab does not include the asymmetry in the capacity of the beams.

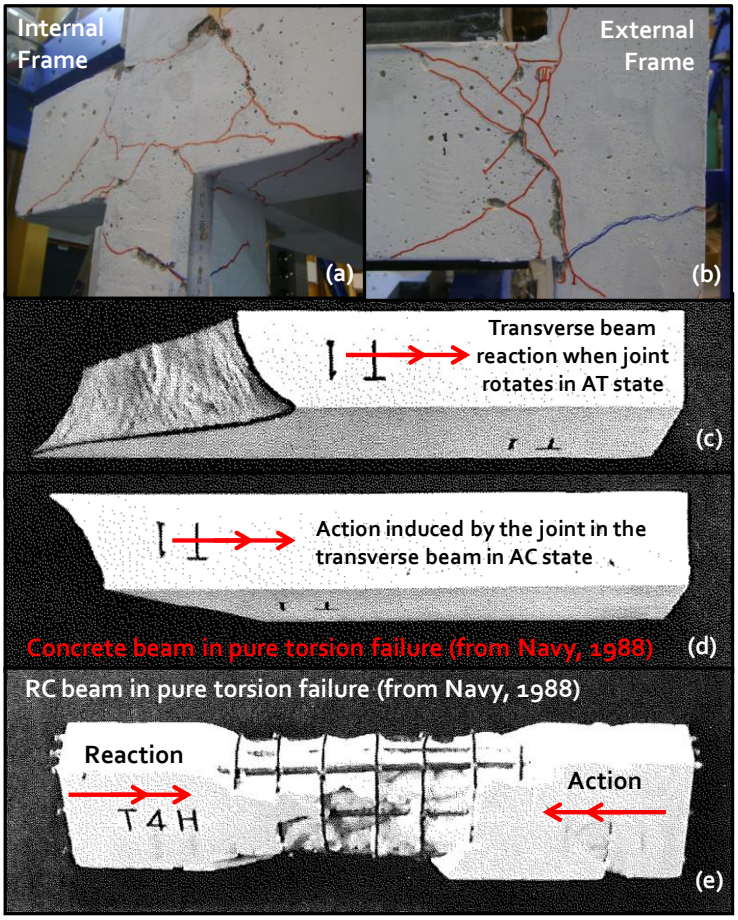

Figure 4.29: Torsion cracking in transverse beams – pure torsion comparison.

In order to understand how the torsion resistance and stiffness of the transverse beams affect the mechanics of non-ductile exterior joints, the crack pattern observed after the tests is compared with that of a concrete and RC beams tested under pure torsion reported by Nawy (1988) (Figure 4.29). It must be emphasised though that any torsion resistance in a beam column joint is enabled by the slab so that if a floor slab is not present, then the role of the transverse beam is almost irrelevant with regards to torsion. In Figure 4.29(a) and Figure 4.29(b) pictures of the exterior joint of the first floor after Test 2.2 are shown. Figure 4.29(c) and (d), both sides of a concrete beam failed in pure torsion are shown, whereas in Figure 4.29(e), an RC beam with a pure torsion failure is presented.

In this case, after Test 2.2, significant torsion cracks developed on the sides of joints where a transverse beam was located. With reference on Figure 4.29(a), cracks in the transverse beams of the cruciform beam column joint developed in a very similar fashion as those in the concrete RC beam under pure torsion. Cracks developed from the top column sides through the larger face of the transverse beam with a parabolic shape ending at about one time the height of the beam in the horizontal direction, creating a square-isosceles triangle as an envelope or boundary.

In the bottom face of the internal frame, short side of the transverse beam, cracks continued to develop, from the intersection of the crack with the beam edge, towards the

joint in an almost straight path till the middle point of the inside face of the bottom column. This is very similar to the boundary of the failure surface in the left hand side of the beam portion shown in Figure 4.29(c). However, crack length measured on the outer face of the transverse beam reflect a 1:1 slope in the horizontal and vertical directions, which is more similar to the RC beam shown in Figure 4.29(e) as would be expected. In this case, the torsion cracks developed correspond to those compatible with the transverse beam resisting in the AT state. In the corner beam column joint, as the one shown in Figure 4.29(b), torsion cracks developed in the transverse beam which are compatible with AT and AC states. Torsion cracking corresponding to the other direction of twist compatible with AC were developed to a larger extent when compare to those compatible with the AT state. This crack pattern is very similar to that of the failure boundary shown in Figure 4.29(d). Cracking developed during the AT state corresponds to the mirror of that highlighted in the left hand side of the top beam shown in Figure 4.29(c).

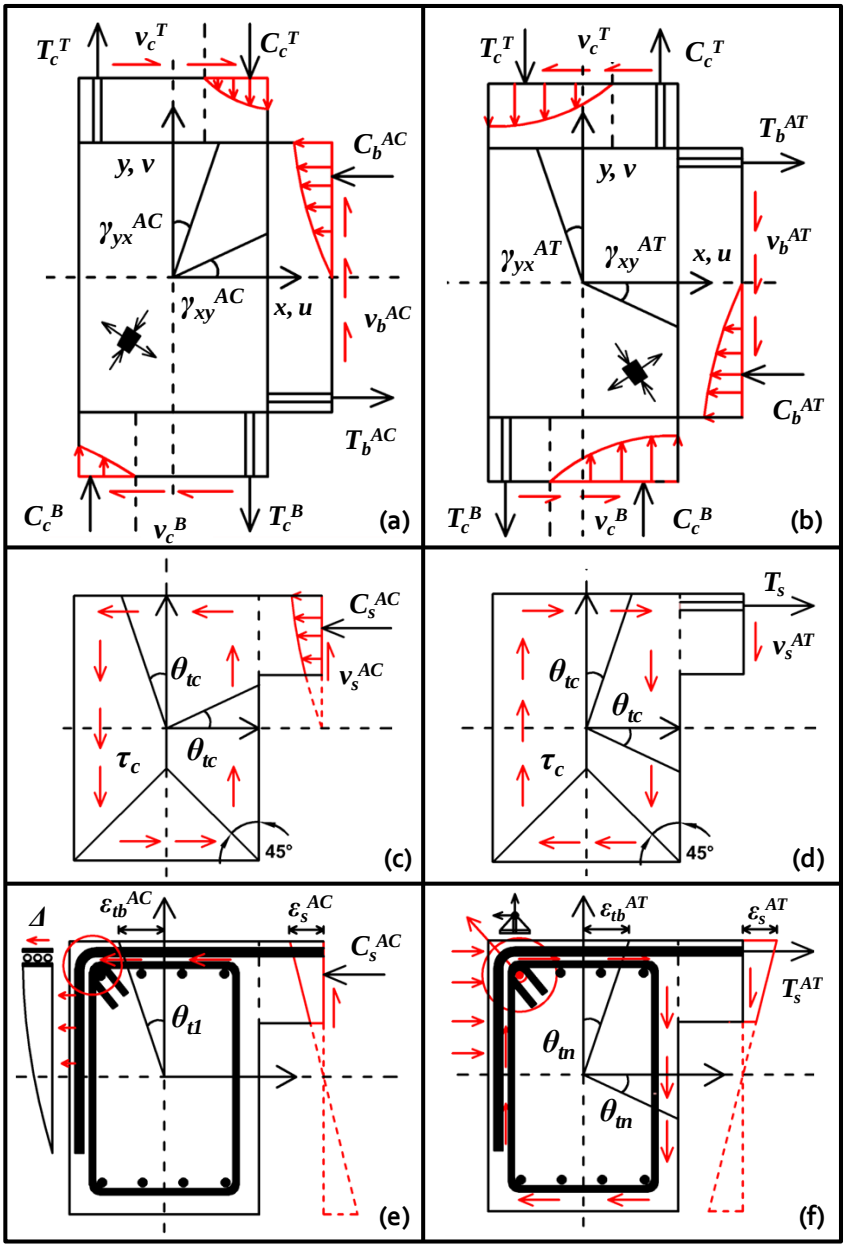

Figure 4.30: Torsion resistance mechanism and stress field interacting with the joint.

In order to explain the reason why the damage in the corner beam-column joints compatible with the AC state was more severe than that consistent with the AT state, and the reason why cruciform joints suffered little damage, firstly torsion stresses acting at both states are presented in Figure 4.30. Torsion resistance is divided into the torsion resisted by the concrete only (T_c), and the torsion resisted by the whole section including stirrups (T_n). As reported by Di Franco (1995), torsional capacity versus angle of twist in the transverse beams of beam column joint slab subassemblies, followed a curve with a stiff initial path which becomes more flexible after cracking occurs. After that, torsion strength remains increasing at a lower rate (stiffness), until failure is reached. As shown in Figure 4.30(e), in the AC situation, the torsion resistance provided by the steel of the slab is not activated because there is a discontinuity in the loading path towards the outside of the transverse beam. However, in the AT situation, as shown in Figure 4.30(f), the spandrel is able to develop the torsional resistance, due to the anchorage of the slab reinforcement into the outside top bar of the transverse beam. That behaviour was the one observed in the experiments on beam column-joint subassemblies tested by Durrani and Zerbe (1985), Ehsani and Wight (1986), Di Franco et al. (1995), and Shin et al. (2004).

4.7 CONCLUDING REMARKS

Considering valuable information gathered during both the Maule and Darfield Earthquakes records from both earthquakes were used in a second stage. The specimen tested under ground motion data recorded at Christchurch Hospital suffered little damage in the form of thin cracks developed in the panel zone, columns and beams, when subjected to Test 2.2 (PGA = 0.20g – as recorded on site), just as observed in RC buildings in the city of Christchurch. Recorded inter-storey drifts remained below 1% in all floors, and were almost identical in shape, indicating a fairly elastic response. Given that result, the specimen was then subjected to a strong ground motion recorded at Marga-Marga station, located in Viña del Mar, during the Chilean Maule Earthquake (Test 3 at PGA = 0.34g – as recorded on site). In this case, severe damage was observed on beam column joints on both exterior and interior frames (for information on the interior frame see Quintana-Gallo et al 2011). Diagonal cracks of considerable width were developed in both corner beam column joints on the first floor with crushing of concrete in the core, as well as crushing in the bottom of columns. In the second floor, lighter damage was observed, mainly in the way of diagonal cracks in the corner beam column joints. On the other hand, almost no damage was developed in the third floor. Inter-storey drift reached a maximum level very close to 4.0% (3.82%) in the first floor, 2.5% in the second, and remained below 1.0% in the top floor, consistent with the observed damage pattern.

The intensity of damage experienced by the specimen after Test 2.2 made it very difficult to repair. In fact, the specimen was repaired for research purposes only, in order to be able to test the retrofit intervention developed. In real life however, the building would have been most likely assessed as non-repairable (in a cost effective manner), and thus demolished.

When comparing all tests, many questions arise about the uncertainly inherent to the response of structures under seismic actions. Firstly, the role of PGA as a seismic hazard parameter appears to be overestimated since it does not seem to provide, by itself, a good correlation with the expected damage that a structure may experience. Frequency content as well as the duration and the Fourier-energy of the input motion are seen to be even or

more important parameters when evaluating the expected performance in terms of damage. Secondly, the records response spectra used in the experiments described herein reveal the importance of considering displacement spectra for the design and assessment of structures within a performance based approach. What can be seen as a severe motion in terms of spectral accelerations, can be relatively less demanding in terms of spectral displacements and vice-versa.

As can be seen in the case of Christchurch Hospital record, spectral displacements are quite low in the short period range, being unable to highly excite structures with fundamental period typical of RC buildings. The Gilroy Array #5 shows extreme spectral acceleration demands, also shifted up by means of increasing PGA levels, but rather moderate corresponding spectral displacement even at peak level. Finally in the case of the Marga-Marga record, even PGA value is not as big as those of the Gilroy Array #5 as well as spectral accelerations (Tests 1.1 and 1.2), observed damage was much larger and drift levels reached are close to those associated to a near collapse limit state. This is attributed to the dominant frequency of the record and the number of cycles of excitation (duration), which was able to reflect the input energy in terms of severe inelastic incursions in brittle elements of the model structure.

4.8 REFERENCES

Akguzel, U. (2011), 'Seismic Performance of FRP Retrofitted Exterior RC Beam-Column Joints under Varying Axial and Bidirectional Loading', *a thesis presented for the degree of Doctor of Philosophy in Civil Engineering*, University of Canterbury, Christchurch, New Zealand.

Aycardi, L. E., Mander, J. B., and Reinhorn, A. M. (1994), 'Seismic Resistance of RC Frame Structures Designed Only for Gravity Loads', *ACI Structural Journal*, Vol. 91(5).

Beres, A., Pessiki, S., White, R, and Gergely, P. (1996), 'Implications of Experiments on the Seismic Behaviour of Gravity Load Designed RC Beam-to-Column Connections', *Earthquake Spectra*, Vol.12 (2), May, pp.185-198.

Boore, D. (2001), 'Effect of baseline corrections on displacement and response spectra for several recordings of the 1999 Chi-Chi, Taiwan, Earthquake', *Bulletin of the Seismological Society of America*, Vol. 91 pp 1199-1211.

Boore, D., and Bommer, J.J. (2005), 'Processing of Strong-Motion Accelerograms: Needs, Options, and Consequences', *Soil Dynamics and Earthquake Engineering*, Vol.25, pp. 93-115.

Di Franco, M. A., Mitchell, D., Paultre, P. (1995), 'Role of Spandrel Beams on Response of Slab-Beam-Column Connections', Journal of Structural Engineering, Vol. 121(3), pp. 408-419.

Durrani, A. and Zerbe, H. (1987), 'Seismic Resistance of R/C Exterior Connections with Floor Slab' *Journal of Structural Engineering*, Vol. 113(8), pp. 1850–1864.

Ehsani, M. R., and Wight, J. K. (1985), 'Exterior Reinforced Concrete Beam-to-Column Connections Subjected to Earthquake-Type Loading', *ACI Journal*, Vol. 84(2), pp. 492-499.

Hakuto, S., Park, R., and Tanaka, H. 2000, Seismic Load Tests on Interior and Exterior Beam-Column Joints with Substandard Reinforcing Details, *ACI Structural Journal*, Vol. 97(1).

Kam, W. (2010), 'Selective Weakening and Post-Tensioning for the Seismic Retrofit of Non-Ductile RC Frames', *a thesis presented for the degree of Doctor of Philosophy in Civil Engineering*, University of Canterbury, Christchurch, New Zealand.

Marriott, D., Pampanin, S., Bull, D.K., Palermo, A. (2007), 'Improving the Seismic Performance of Existing Reinforced Concrete Buildings using Advanced Rocking Wall Solutions', *proceedings of the NZSEE Conference*, Palmerston North, paper 17.

Marriott, D.J. (2009), 'The Development of High-Performance Post-Tensioned Rocking Systems for the Seismic Design of Structures', *a thesis presented for the degree of Doctor of Philosophy in Civil Engineering*, Department of Civil and Natural Resources Engineering, University of Canterbury, Christchurch, New Zealand.

Pampanin, S., Calvi, G.M., Moratti, M. (2002), 'Seismic Behaviour of RC Beam Column Joints Designed for Gravity Loads', *proceedings of the 12th ECEE,* London, England, paper n. 726.

Pampanin, S., Christopoulos, C., Chen, T. (2006) 'Development and Validation of a Metallic Haunch Seismic Retrofit Solution for Existing Under-Designed RC Frame Buildings', *Earthquake Engineering and Structural Dynamics*, Vol. 35, pp. 1739-1766.

Pampanin, S., Kam, W.Y., Tasligedik, A.S., Quintana-Gallo, P., Akguzel, U. (2011) 'Considerations on the seismic performance of pre-1970s RC buildings in the Christchurch CBD during the 10th Sept 2010 Canterbury earthquake: was that really a big one?', *Proceedings of the Pacific Conference on Earthquake Engineering*, Auckland, paper 179.

Park, R. (2002) 'A Summary of Simulated Seismic Load Tests on Reinforced Concrete Beam-Column Joints, Beams and Columns with Substandard Reinforcing Details' *Journal of Earthquake Engineering*, Vol. 6(2), pp. 147-174.

Quintana-Gallo, P., Pampanin, S., Carr, A.J., Bonelli, P. (2010), 'Shake Table Tests of Under-Designed Frames for the Seismic Retrofit of Buildings – Design and Similitude Requirements of the Benchmark Specimen', *Proceedings of the NZSEE Conference*, Wellington, paper 39.

Quintana-Gallo, P., Akguzel, U., Pampanin, S., Carr, A.J. (2011), 'Shake Table Tests of Non-Ductile As-Built and Repaired RC Frames', *Proceedings of the 9th Pacific Conference on Earthquake Engineering*, Auckland, New Zealand.

Shin M and LaFave J. M. (2004), 'Reinforced Concrete Edge Beam-Column-Slab Connections Subjected to Earthquake Loading,' *Magazine of Concrete Research*, Vol.56(5),pp.273-291.

Standards New Zealand (2004), NZS1170.5:2004, *Structural design actions: Part 5, Earthquake actions*, Wellington, New Zealand.

5 SEISMIC ASSESSMENT OF THE REPAIRED SPECIMEN

5.1 INTRODUCTION

After the deficiencies found in experimental Series 1 (as-built specimen-Loma Prieta input motion), the repaired as-built specimen was apparently upgraded after the lap splices problem was mitigated. The repaired specimen was expected to remain apparently elastic in Series 2, when an input motion from the Darfield earthquake was used (see Chapter 4). Nevertheless, the repaired specimen was also proofed to be vulnerable during Test 2.2, when an input motion from the Maule earthquake was used (see Chapter 4). In the last test series the specimen experienced heavy damage in first floor exterior joints and columns as well as interior columns.

In this chapter the assessment of the repaired specimen as explained in Chapter 4 is presented. Using capacity curves of the elements which converge into the panel zone region of exterior beam column joints of the building, the hierarchy of strengths and the expected sequence of events in the bending moment – axial load performance domain is evaluated (Pampanin et al. 2007, Akguzel and Pampanin 2010). Axial load variation with respect to moment in the joint is used as an indicator of the seismic demand. That is, the variation from the initial value corresponding to gravity load when increasing or decreasing the moment capacity from that corresponding to an initial state (t_0 = 0). However, the inclusion of a floor slab and transverse beams had not been incorporated in that performance domain yet. As was explained in Chapter 4, the asymmetric nature of the flanged beam and the torsion resistance of the transverse beam importantly influence the mechanics of beam column joints. As a consequence the method was extended in order to incorporate those effects.

The extension of the M-N performance domain requires the evaluation of two different states in the panel zone: (1) when the slab acts in compression (AC), and (2) when the slab acts in tension. That is equivalent to the states or situations in the panel zone when the resisting moment in the beam is positive and negative, respectively. As a consequence, the M-N diagram becomes a ‘four quadrant’ graph, defined by the axis of zero moment and the vertical line corresponding to the gravity or initial load in the beam column joint. In this graph though, there are only compatible quadrants due to kinematic considerations. Those quadrants correspond to the AC situation, when the moment is positive and the axial load decreases due to the upward shear induced by the beam, and the AT situation, when the moment is negative and the axial load increases due to the downward shear induced by the beam.

In the capacity evaluation of the column, the axial load was varied in order to investigate the effect on the strength and the ductility. That is presented in terms of moment-curvature diagrams. In the evaluation of the flexural capacity of the beam, the main parameter to affect the strength and ductility of the beam was the contribution of the slab. Moment-curvature diagrams for a different number of slab bars activated in tension are presented. That is a variation in the steel ratio that resists in addition to the steel of the beam instead of a specific ‘effective length’ (Di Franco et al. 1995).

The formulation for the capacity of the joint proposed by Akguzel and Pampanin (2010) are derived from equilibrium in the beam column joint and principal stresses in the Mohr's circle. The expressions for the equivalent moment capacity of the joint are re-formulated in terms of a slightly more general case when *jd* (the lever arm of the resisting pair of forces in the beam) is expressly evaluated. That is required because the neutral axis depth is larger in the AT situation than in the AC situation, the latter being similar to that of an equivalent 2D beam. Hence, a value of $jd = 0.9d$ as suggested by Akguzel and Pampanin (2010) was used for the AC situation and $jd = 0.7d$ for the AT state. The result is a smaller resistance of the joint as described in detail in this Chapter.

The calculated capacities are then all evaluated in the extended version of the M-N performance domain introduced in this chapter. There are four (main) cases to be evaluated which are (1) the corner joint AC, (2) corner joint AC, (3) cruciform joint AC, (4) cruciform AT. The results are presented graphically and also using a matrix approach for the visualization of the data obtained with the diagrams. That is in order to establish a familiar environment for practitioner engineers. Finally, the collapse mechanism of the building is formulated, and the base shear capacity estimated based on the capacity of the members calculated before, equilibrium and the virtual work principle applied to plastic analysis.

5.2 THE SYMMETRICAL M-N PERFORMANCE DOMAIN FOR PLANE EXTERIOR BEAM COLUMN JOINTS

4.1.2 Evaluation of Exterior Beam Column Joints as Plane Elements

In Figure 5.1 the actions induced by the beam and columns and the resisting mechanism in the joint are presented for a plane 2D specimen with a rectangular symmetrically reinforced beam. Here no floor slab or transverse beams are present. As a consequence, the states identified in Chapter 4 for the mechanics in the panel zone region - AC and AT - become identical regardless of the sign of the beam moment. However, even if the beam column joint is fully symmetrical the effect of axial load variation imposes an asymmetry in the seismic actions to be resisted, as discussed in Chapter 4.

In Figure 5.1, $M_{by}^{2D(+)}$ and $M_{by}^{2D(-)}$ are the positive and negative yielding moment capacity of the rectangular beam, respectively, and $V_b^{2D(+)}$ and $V_b^{2D(-)}$ their associated shear actions. In the column, M_{cy}^{T} and M_{cy}^{B} represent the yielding moment of the top and bottom column, respectively, while V_c^{T} and V_c^{B} correspond to the shear counterpart actions and $M_j^{2D(+)}$ and $M_j^{2D(-)}$, the equivalent moment capacity of the joint under positive and negative bending, respectively. Seismically induced axial forces in the joints are represented by the vector dP_{2D} which is the variation in the axial load of the top column strictly speaking. That variation will increase when going down through the joint, after shear forces of the beam acting in the same direction are introduced. Both states are named AC-2D and AT-2D, corresponding to the beam experimenting positive and negative bending moments, respectively. As shown in Figure 5.1(a), in the AC-2D situation, when the top fibre (A) of the beam acts in compression, the variation in the axial loads points upwards, which is defined as the negative direction of the axial load (positive corresponds to gravity). In Figure 5.1(b) the AT-2D state is presented. Here, the variation in the axial load as well as the shear developed in the beam point downwards in the positive vertical direction. Therefore, the plane joint will be subjected to two different

states of loading and resisting hierarchies in the elements which converge into the joint, possibly reached at difference instances. This is named the sequence of events predicted by the M-N diagram given a certain seismic demand in terms of the equivalent bending moment in the joint depending on the axial force level achieved.

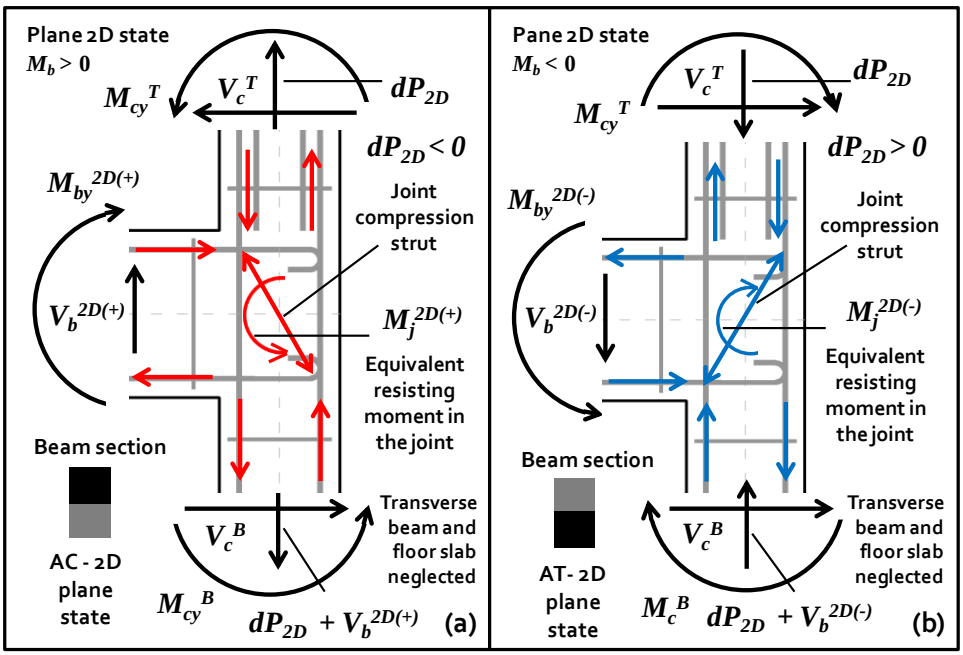

Figure 5.1: acting and resisting forces in a plane 2D beam column joint – slab and transverse beam neglected – symmetry in the beam bending capacity.

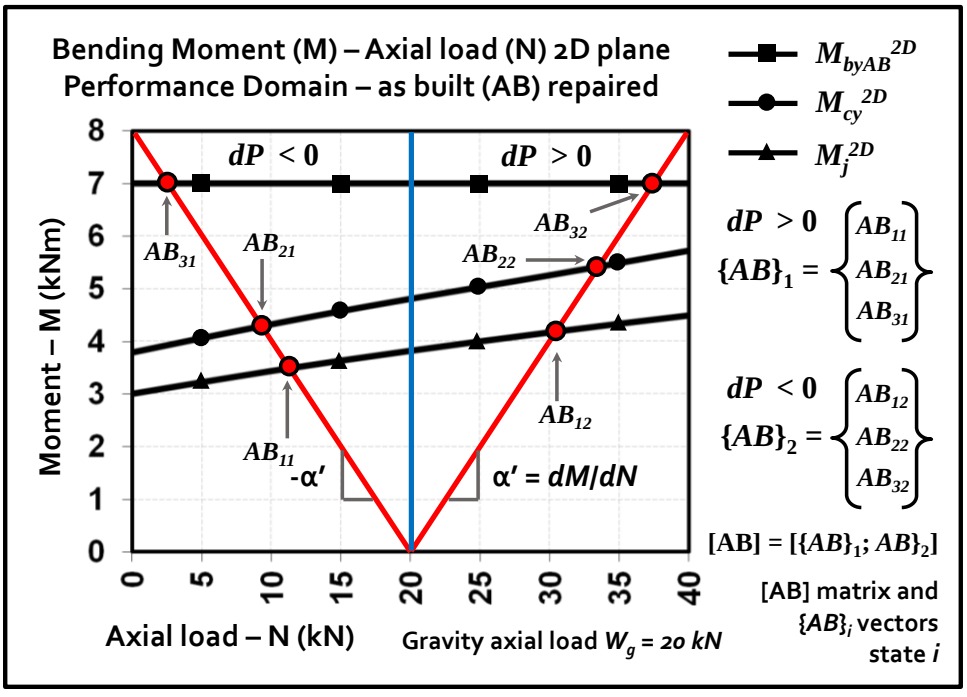

Figure 5.2: Bending moment (M) – axial load (N) performance domain for a 2D plane beam column joint – for specimens without a floor slab and transverse beams.

This is illustrated in Figure 5.2, where the M-N diagrams calculations for an exterior beam column joint of the model building used in this thesis, idealized as 2D plane joints. In this diagram the equivalent M-N capacity curves for the joint were calculated using p_{tD} = 0.3, where p_{tD} is the dimensionless maximum tensile principal stress in the joint when cracking is developed ($p_{tD} = p_t/\sqrt{f_c'}$). Since it has been suggested to use p_{tD} = 0.19 as a limit state for plane beam column joints, which means joints with no confinement at all (Pampanin et al. 2002, Kam 2010, Akguzel and Pampanin 2010), it was recognized that the confinement brought orthogonally by the transverse beam would be a reason for upgrading that stress limit state. Nevertheless, such a small variation in the p_{tD} value does not increase the strength of the joint significantly, so that values for p_{tD} = 0.19 would be very similar to those of Figure 5.2. The capacity of beams and columns were computed using the sectional analysis program BIAX96 (Wallace and Ibrahim 1996). The details of these analyses are presented later in term of moment curvature diagrams and compared with those of the asymmetric beams.

Also in Figure 5.2, the 'events' where the demand intersects the capacity of each member is highlighted and denoted by the position coordinates in the M-N system named AB_{ij}, where AB denotes 'As-Built', i the order in occurrence of the event (capacity-demand intersection), and j the demand curve number j. All these events are grouped into vectors whose rows order corresponds to the order in the sequence of events and whose column order denotes the demand number.

4.1.3 A matrix approach for computing results for different demand scenarios

Grouping these sequential vectors of M-N coordinates into a matrix named [AB] such that each vector corresponds to a column of the matrix, the sequence of events can readily be visualized. In the case of the capacity curves shown in Figure 5.2, there would be two vectors, one corresponding to a decreasing axial load and another one corresponding to an increasing axial load, $\{AB\}_1$ and $\{AB\}_2$. The resulting intersection of the demand curves and the member capacity yield the same sequence of events for all curves in the range of study. That is, both vectors would have different coordinate values for AB_{ij}, but they will correspond to the same element failure sequence. Explicit values for those assessments will be given after extending the M-N performance domain after the slab and transverse beam effects are incorporated in the few next paragraphs. The row vectors AB_{ij} are defined as:

$$AB_{ij} = \langle AB \rangle_{ij} = \langle E_{ij}; N_{ij}; M_{ij} \rangle$$

where $i = event\ number\ 'i'$ for $i = 1, 2, \cdots, n$; n = number of elements evaluated, and $j = demand\ scenario\ 'j'$ for $j = 1, 2, \cdots, m$; m = number of demand scenarios considered; E_{ij}, M_{ij}, and N_{ij} are the elements whose capacity is triggered in the sequence order number 'i' under the demand curve 'j', and the coordinates in the M-N domain in terms of axial and bending moment at that particular point.

If the column vector $\{AB\}_j$ (shown in Figure 5.2) is created as an extended matrix $\in |\mathrm{R}^{n\mathrm{x}3}$ (order nx3) with the AB_{ij} row elements, that matrix can be written as:

$$\{AB\}_j = \begin{Bmatrix} \langle AB \rangle_{1j} \\ \vdots \\ \langle AB \rangle_{ij} \\ \vdots \\ \langle AB \rangle_{nj} \end{Bmatrix} = [AB]_j = \begin{bmatrix} E_{1j} & M_{1j} & N_{1j} \\ \vdots & \vdots & \vdots \\ E_{nj} & M_{nj} & N_{nj} \end{bmatrix}_{nx3}$$

This matrix contains all the data for the assessment of the beam column joints under one demand scenario only, *j* in the case. If the resulting matrixes are grouped into a larger matrix with rank *n*x*m* with *m* different demand scenarios, then that matrix is [AB]:

$$[AB]_{nx3m} = \left[[AB]_1; \dots; [AB]_j; \dots; [AB]_m \right]$$

This would be the assessment matrix which contains the strengths and the sequence of events of *n* structural elements under *m* demand scenarios in the joint. This way of showing the hierarchy of capacities and the sequence in the occurrence of events in the M-N performance domain will be used throughout this chapter. In the 2D case since only the beam, the column and the joint are being considered, then *n* = 3. Also since two different scenarios in terms of seismic demand are being used (increasing and decreasing axial load), then *m* = 2. Elements E_{ij} are defined as B = beam, C = column, J = joint, noting that capital letters are intentionally used instead of numbers are used. The 3x6 matrix is constructed with the intersections of the capacity and demand curves shown in Figure 5.2, leading to the events AB_{ij}.

The resulting matrix for a decreasing (*j*=1) and increasing (*j*=2) axial load is:

$$[AB]_{3x6} = \left[\begin{bmatrix} J & 3.50 & 11.3 \\ C & 4.25 & 9.25 \\ B & 7.00 & 2.10 \end{bmatrix}; \begin{bmatrix} J & 4.10 & 30.5 \\ C & 5.40 & 33.6 \\ B & 7.00 & 37.5 \end{bmatrix} \right]$$

where the axial load (second sub-column) is expressed in kN and the bending moment (third sub-column) in kNm. The position in the first column indicates the sequence of events. In this case, the same sequence is predicted for both scenarios (*j* = 1 and 2). Also note the values of the moment do not vary significantly in between both scenarios as shown in the second column of each sub-matrix inside [*AB*], the complete assessment matrix, though axial load varies considerably. Values range from 37.5 kN to 2.10 kN at a beam failure level, which is located at the end of the sequence of events under both scenarios (see lower row of [*AB*]) However axial load variation for compatible with a joint failure are expected at a lower level of 11.3 to 30.5 kN, which is approximately a 50% decrease and increase from the initial gravity load state, for scenarios 1 and 2, respectively.

So far the assessment has been carried out in the way recently suggested by Pampanin et al. (2007), Akguzel and Pampanin (2010, 2012) as well as other researchers (Kam 2010, Chen 2006), with only a change of the approach for interpreting the results and analyse the capacity curves shown before. However, the problem faced in this thesis deals with 3D elements with the highest possible degree of realism. These are 3D beam column joints with slabs and transverse beams of an external and an internal frame (corner and cruciform). Here the assumption of plane stresses which is assumed in previous work may not be valid anymore. The addition of the slab and transverse beam provides the existence

of a tri-axial stress-strain state in the panel zone. The slab whose bars are anchored into the transverse beam increases importantly the beam negative bending moment capacity (AT) when compared to the 2D counterpart. Nevertheless the positive bending moment capacity of the beam remains very similar to that of the 2D beam. In the next section of this chapter, the changes introduced to the 2D-plane M-N performance domain are presented.

5.3 EXTENDED VERSION OF THE M-N PERFORMANCE DOMAIN ACCOUNTING FOR SLAB AND SPANDREL EFFECTS

As discussed in Chapter 4, the inclusion of floor slabs and transverse beams into the model building introduced a greater degree of realism into the beam column joints that form the building. These are:

1) The existence of an asymmetric cross section in the beam due to the presence of slab and the transverse beam, leading to different magnitudes in the bending moment capacity and stiffness under positive and negative actions (AC and AT).

2) Confinement added in one or two faces of the joint, in addition to the longitudinal beam in the main direction.

3) Torsion resistance provided by the transverse beam-slab action.

The first effect requires the extension of the M-N diagram by explicitly considering negative actions. The second one can be addressed when using larger p_{tD} values in the calculation of the joint capacity. This was done in the previous section, when adopting p_{tD} = 0.3, based on the value p_{tD} = 0.3 suggested by Priestley (1996) and p_{tD} = 0.19 suggested by Pampanin et al. (2002) for plane joints. The torsion resistance and the stiffness provided by the transverse beam, enabled by floor slab, were identified as a relevant part of the resisting mechanism in the panel zone region and are incorporated into the problem, as will be shown in detail in the next section.

The addition of the floor slab introduces asymmetry into the problem, leading to two different states or situations named AC and AT, for the top fibre ‘A’ of the beam acts in compression (positive moment) and in tension (negative moment), respectively. As a consequence the M-N capacities need to be calculated at least for these two states. However, as the states selected are directly related to the bending moment demand, ‘sub-states’ for AC and AT can be studied independently. If the M-N diagram is extended to the negative side of the ordinate axis, for equilibrium of forces and kinematic compatibility, decreasing axial load is only compatible with a positive bending moment in the beam (AC state), and an increasing axial load is only compatible with a negative bending moment in the beam (AT state). In Figure 5.3 a four quadrant domain is shown, named Q-I, Q-II, Q-III, and Q-IV. These quadrants are defined by the positive side of the N axis and the gravitational weight acting initially in the joint projected to the negative side of the M axis, as mentioned before.

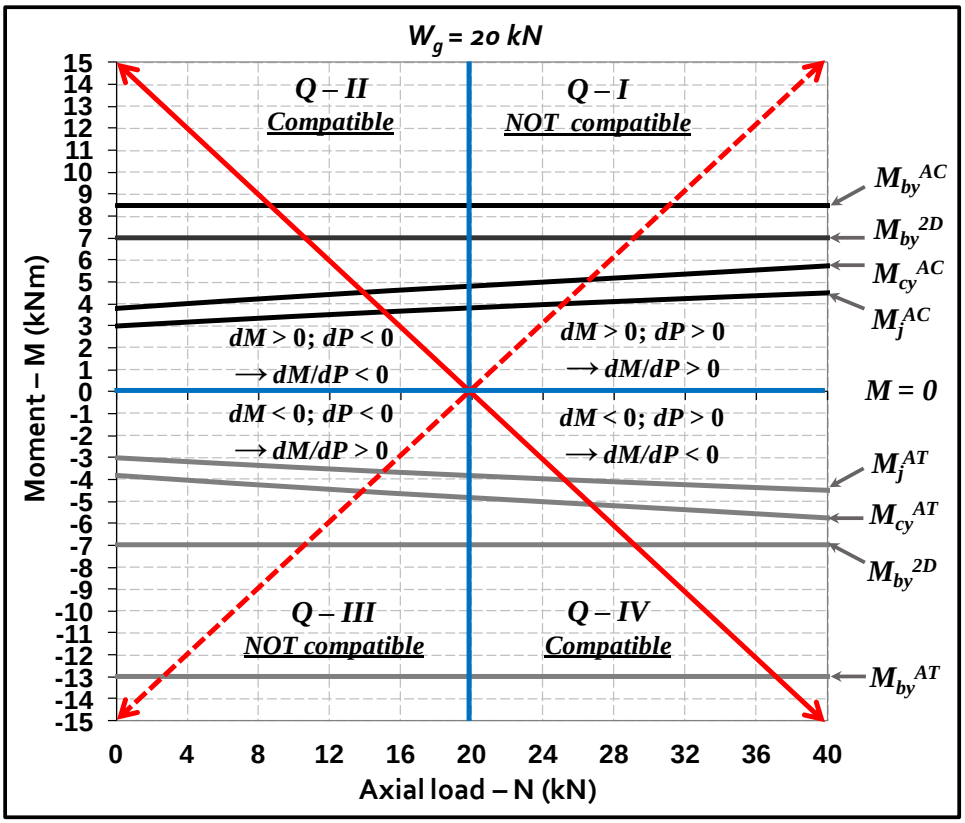

Figure 5.3: Extended asymmetric M-N performance domain.

After introducing the problem of asymmetry in the beam due to the presence of the slab, the M-N performance domain has been extended. It was shown that the M-N diagram presented in Figure 5.2 for the assessment of plane 2D beam column joints is only valid if the bending capacity of the beam is the same under positive and negative bending (symmetrically reinforced rectangular beam). For equilibrium and kinematic compatibility it was shown that certain parts of the extended diagram do not represent compatible scenarios. For a 2D beam column joint as those used in Pampanin et al. (2007), Akguzel and Pampanin (2010), Kam (2010), and Akguzel (2011) amongst others, the evaluation of the hierarchy of strength has been done using an M-N performance in a simplified version.

This method makes use of symmetry in structural elements to create an equivalent projection of the Q-IV (compatible quadrant) when rotating it about the N axis by 90° upwards, if the diagram shown in Figure 5.3 is understood as a dihedral system as used in descriptive geometry, with the origin located in the M = 0 axis. This is possible for columns and joints which are symmetric in this case. However, the difference in the magnitude of the bending capacity of the beam makes that fictitious quadrant not valid anymore. One way of solving this problem would have been to create another fictitious version of the negative side of the M-N diagram, but an explicit way was preferred in order to acknowledge the fact that there exist positive and negative actions in the beam column joint, and they are different in magnitude. Therefore the M-N performance domain used by other researchers to date is a particular case of the extended version of the M-N performance domain introduced in this chapter.

As explained in the next section, the method used for showing the results of the assessment procedure is based on matrices and vectors. It is argued that for possible computational implementations of this method, linear algebra can be very useful, especially for selecting the data one requires. As emphasised in Chapter 4 and throughout this chapter, the effect of the transverse beam in confinement and torsion resistance is very important. The confinement effect has been incorporated by upgrading to p_{tD} = 0.30 the diagonal cracking limit state in the joint when compared to p_{tD} = 0.19 value suggested for 2D plan beam column joints. The importance of the torsion resistance of the transverse beam or spandrel has been addressed theoretically and based on the experimental results of the as-built and repaired specimens.

5.4 MODELLING OF THE CONSTITUTIVE LAWS OF THE MATERIALS

The basic mechanical properties of the materials used for constructing the as-built specimen as well in the repairing process were presented in Chapters 3 and 4, and can also be found in Quintana-Gallo et al. (2011). These properties are used for adjusting stress-strain curves constitutive laws for the concrete and the reinforcement, as required in sectional analysis. In this case, all sectional analyses of beams and columns were done in the program BIAX96 (Wallace and Ibrahim 1996). This program allows the use of stress strain relationships for confined and unconfined concrete, as well as steel or other linear elastic elements like FRP, as presented in this section.

5.4.1 Unconfined and Confined Concrete

For concrete, many stress-strain models have been proposed in the literature. Nevertheless, almost all of them are variations of the original model proposed by Hognestad (1951). Kent and Park (1971), for example adopted the Hognestad model for developing their own formulations of the parameters controlling the shape of the stress-strain law. Park et al. (1982) developed a further refined model, commonly known as 'modified Kent-Park model'. That model includes the effects of confinement when considerably upgrading the slope of the descending line after the peak stress in the concrete has been reached. The maximum compression stress of the confined concrete is increased by *k* times the maximum stress of the unconfined concrete (f_c'), as well as the strain at peak stress (ε_0) by the same factor *k*, which depends on the confinement steel to concrete area ratio (ρ_h). However, this law was developed and calibrated based on experimental data from slow motion tests on rectangular and symmetrically reinforced RC column only. Symmetry of the reinforcement layout is implicit in the way of defining ρ_h, which corresponds to the ratio of the volume of hoop reinforcement to volume of concrete core, measured from the outside of the hoops, equally spaced orthogonally by the distance *s*. The expressions obtained by Park et al. (1982) are presented in Equations 5.1 to 5.6, and reduce to the equations proposed by Kent and Park (1971) for *k* = 1.

$$f_c = kf_c'[2\varepsilon_0/k\varepsilon_0 - (\varepsilon_c/k\varepsilon_0)^2] \qquad \varepsilon_c \leq k\varepsilon_0 \tag{5.1}$$

$$f_c = kf_c'[1 - Z_m(\varepsilon_c/k\varepsilon_0)] \qquad \varepsilon_c > k\varepsilon_0 \tag{5.2}$$

$$k = 1 + \rho_h f_{yt}/f_c' \tag{5.3}$$

$$Z_m = 0.5/(\varepsilon_{50u} + \varepsilon_{50h} - k\varepsilon_0) \geq 0.2\, fc' \tag{5.4}$$

$$\varepsilon_{50u} = (0.025 + \varepsilon_0 f_c')/(f_c' - 0.83) \qquad (f_c' \text{ in MPa}) \tag{5.5}$$

$$\varepsilon_{50h} = 0.75\rho\sqrt{h/s} \tag{5.6}$$

For unconfined concrete, which in this case corresponds to that concrete outside the confinement hooks in beam and columns, as well as the whole slab region, this set of equations was used with k = 1 and ε_{50u} + ε_{50u} = 0.004, and a representative value of f_c' = 25 MPa. For confined concrete, however, this model may not be appropriate since it does not include the effect of the length between lateral restraining hooks and asymmetry in the longitudinal reinforcement layout in plane. Furthermore, this model has not been developed for rectangular sections.

Other models have been proposed for rectangular columns, such as in Mander et al. (1988) and Saatcioglu and Razvi (1992). Both models explicitly include in the calculations of the strains which govern the post peak slope the restrained length of the longitudinal bars in the horizontal and vertical directions. In Equations 5.7 to 5.11 the governing equations which describe the Saatcioglu and Razvi (1992) model are presented. These expressions have been validated using the results of experimental tests done by independent researchers (Sheikh and Uzumeri 1980, Scott et al. 1986, Mander et al. 1988, Salamat and Saatcioglu 1991).

$$f_{cc}' = f_{c0}' + k_1 f_{le} \tag{5.7}$$

$$f_{le} = k_2 f_l \tag{5.8}$$

$$f_l = (\sum A_{st} f_{yt} \sin\alpha)/(s\, b_c) \tag{5.9}$$

$$k_1 = 6.7(f_l)^{-0.17} \tag{5.10}$$

$$k_2 = 0.26\sqrt{\left(\frac{b_c}{s}\right)\left(\frac{b_c}{s_l}\right)\left(\frac{1}{f_l}\right)} \leq 1 \tag{5.11}$$

In the previous equations, f_{cc}' and f_{c0}' = confined and unconfined compression strengths of the concrete, respectively; k_1 = coefficient which depends on the Poisson modulus empirically inferred using regression analyses, as postulated by Richart et al. (1929); f_{le} = equivalent lateral pressure (in MPa); k_2 = coefficient introduced for reducing the average lateral pressure, related to the flexural stiffness of the element restraining longitudinal bars; A_{st} = cross sectional area of horizontal elements restraining in the length b_c, which is the length of the cross section orthogonal to the confining reinforcement direction; f_{yt} = yielding stress of the transverse reinforcement; s = spacing between confinement elements in the longitudinal direction (orthogonal to the section); α = angle between the direction of the transverse bars and the longitudinal direction of the element, s_l = spacing between 'nodes', where stiff lateral restraint is imposed onto the longitudinal rebar.

For rectangular or square sections with different spacing of the longitudinal rebar lateral restrain, Equation 5.12 replaces Equation 5.8 and f_{lX} and f_{lY} are calculated using equations 5.13 and 5.14, together with the factors k_{2X} and k_{2Y} for the X and Y directions of analysis, which are presented in Equation 5.15 and 5.16, respectively.

$$f_{le} = (f_{leX} b_{cX} + f_{leY} b_{cY})/(b_{cX} + b_{cY}) \quad (5.12)$$

$$f_{lX} = (\sum A_{st} f_{yt} \sin\alpha)/(s\, b_{cX}) \quad (5.13)$$

$$f_{lY} = (\sum A_{st} f_{yt} \sin\alpha)/(s\, b_{cY}) \quad (5.14)$$

$$k_{2X} = 0.26\sqrt{\left(\frac{b_{cX}}{s}\right)\left(\frac{b_{cX}}{s_{lX}}\right)\left(\frac{1}{f_{lX}}\right)} \leq 1 \quad (5.15)$$

$$k_{2Y} = 0.26\sqrt{\left(\frac{b_{cY}}{s}\right)\left(\frac{b_{cY}}{s_{lY}}\right)\left(\frac{1}{f_{lY}}\right)} \leq 1 \quad (5.16)$$

In this particular case, when f_c' =25 MPa is used, the increment in the compression strength of the confined core inside the beam corresponds to f_{cc}' = 28 MPa, according to Saatcioglu and Razvi (1992) approach and remains approximately equal to f_{cc}' = 26 MPa according to the modified Kent and Park model. For the column, the enhancement reaches similar values (f_{cc}' = 27 MPa).

All the previous equations are required to find the strength of the confined concrete according to Saatcioglu and Razvi (1992). It has been shown that in this case the increase in the compression capacity of beams and columns is negligible (*k* value is very small). However, the ductility of the confined concrete can be much larger than the ductility of unconfined concrete. In Equations 5.17 to 5.23, the calculations of the parameters that define the ductility of the concrete in terms of the slope of the descending branch of the proposed law by the same authors (Saatcioglu and Razvi 1992).

$$\varepsilon_1 = \varepsilon_{01}(1 + 5K) \quad (5.17)$$

$$K = k_1 f_{le}/f'_{c0} \quad (5.18)$$

$$\rho = \Sigma A_s/s(b_{cX} + b_{cX}) \quad (5.19)$$

$$\varepsilon_{85} = 260\rho\varepsilon_1 + \varepsilon_{085} \quad (5.20)$$

$$Z_m = 0.15/(\varepsilon_{85} - \varepsilon_1) \quad (5.21)$$

$$f_c = f'_{cc}[2(\varepsilon_c/\varepsilon_1) - (\varepsilon_c/\varepsilon_1)^2]^{1/(1+2K)} \qquad \varepsilon_c \leq \varepsilon_1; f_c \leq f'_{cc} \quad (5.22)$$

$$f_c = f'_{cc}(1 - Z_m(\varepsilon_c - \varepsilon_1)) \qquad \varepsilon_c \geq \varepsilon_1; f_c \geq 0.20 f_{cc}' \quad (5.23)$$

In Equations 5.17 to 5.23: ε_1 = strain value corresponding to peak stress (f_{cc}'); ε_{01} = strain corresponding to peak stress for unconfined concrete with the same mechanical characteristics (same f_c'), normally taken equal to 0.002; ε_{85} = strain at 85% of the maximum stress (0.85f_{cc}'); ε_{085} = strain at 85% of the maximum strain ε_{01} of the equivalent unconfined concrete, recommended to be taken as 0.0038; ρ = the reinforcement ratio, ΣA_s = sum of the transverse reinforcement contained in both orthogonal directions (b_{cX} and b_{cY}); s = the spacing between confinement elements; Z_m = the slope of the descending branch after peak stress, f_c = stress at a certain strain ε_c.

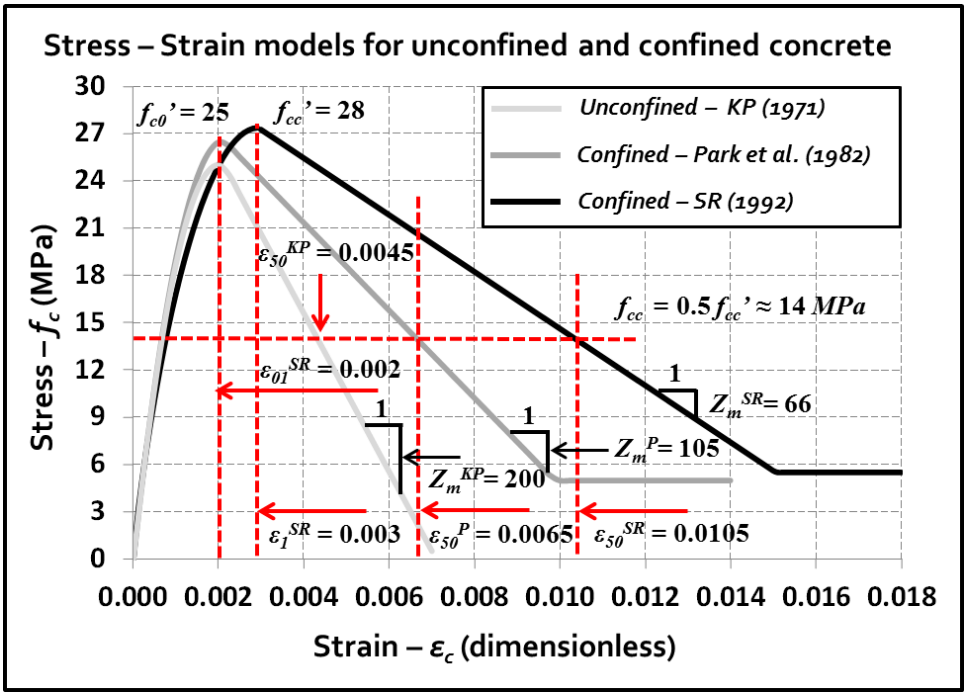

Figure 5.4: Stress-strain constitutive laws models for the concrete in compression.

In Figure 5.4, three stress-strain models for the unconfined and confined concrete in compression are shown. These models correspond to Kent and Park (1971), Modified Kent and Park (Park et al. 1982) and Saatcioglu and Razvi (1992). For this case, as shown in Figure 5.4, a 50% reduction in the compression capacity of the concrete is identified in order to illustrate the strain enhancement in the concrete after maximum stress. In Figure 5.4 the values of the post-peak slope for the three models used are Z^{KP} = 200 for unconfined concrete, Z^{KP} = 105 for modified Kent and Park model, and Z^{SR} = 66 for SR confined concrete model.

5.4.2 Reinforcing Steel

Model for steel reinforcement have widely been studied in the in the past. Those models typically range from simple monotonic models (Saenz 1964; Aktan et al. 1973, Thompson and Park 1978, Mander et al. 1984, Andriono and Park 1986) to more refined models which have been proofed to accurately represent the cyclic behaviour of a rebar under repeated tension-compression cycles (Dodd and Cooke 1992, Restrepo-Posada et al. 1994, Dodd and Restrepo-Posada 1995, Kunnath et al. 2009, Rodriguez et al. 2009, 2013).

In this case, one of the simplest approaches for modelling the complete monotonic curve of the steel under tension is used, in the light of the monotonic nature of the sectional analyses shown in the following paragraphs. A model based on the work presented by Mander et al. (1984) was adopted in BIAX96 (Wallace and Ibrahim 1996). That model is presented in Figure 5.5, where letters A, B, C, and D represent the four main limit states of the material, which delimit the four phases of a steel rebar under monotonic tension. That model was also used for the steel in compression. Even though the maximum compression strain could be reduced due to buckling as explained in Chapter 10 in the light of the high vertical spacing to bar diameter in beams and columns, it was assumed to be the same, just like in well confined RC members (Restrepo-Posada et al. 1994, Dodd

and Restrepo-Posada 1995). That assumption was done in the light of the experimental evidence observed during the tests presented in Chapter 4 and many others reported previously in the literature (Pampanin et al. 2002, Kam 2010, Akguzel 2011), where no buckling of the reinforcement in beams and columns was observed.

The four stages in the stress-strain history of a reinforcing bar are given by (1) the linear range, (2) the yield plateau, (3) the strain hardening region, and (4) the post ultimate or necking region. According to Andriono and Park (1986), for reinforcing steel manufactured in New Zealand, the stress-strain model proposed by Mander et al. (1984) has shown very good agreement with measured strain-stress relationships of steel in tension and compression (if buckling is avoided). This model is described by Equations 5.24 to 5.27.

$$f_s = E_s \varepsilon_s \qquad 0 \le \varepsilon_s \le \varepsilon_y = f_y / E_s \tag{5.24}$$

$$f_s = f_y \qquad \varepsilon_y \le \varepsilon_s \le \varepsilon_{sh} \tag{5.25}$$

$$f_s = f_{su} + \left(f_y - f_{su}\right)\left[\frac{\varepsilon_{su} - \varepsilon_s}{\varepsilon_{su} - \varepsilon_{sh}}\right]^p \qquad \varepsilon_{sh} \le \varepsilon_s \le \varepsilon_{su} \tag{5.26}$$

$$p = E_{sh}\left[\frac{\varepsilon_{su} - \varepsilon_{sh}}{f_{su} - f_y}\right] \tag{5.27}$$

In Equations 5.24 to 5.27, f_s = stress in the steel; ε_s = strain in the steel; E_s = Young modulus of the steel (E_s = 200,000 MPa); f_y = yielding stress of the steel; ε_y = yielding strain; ε_{sh} = strain level at which hardening begins; f_{su} = ultimate stress of the steel; ε_{su} = strain level at which the ultimate stress of the steel is reached (ultimate strain); p = strain hardening power; E_{sh} = strain hardening tangent modulus for steel at ε_{sh}.

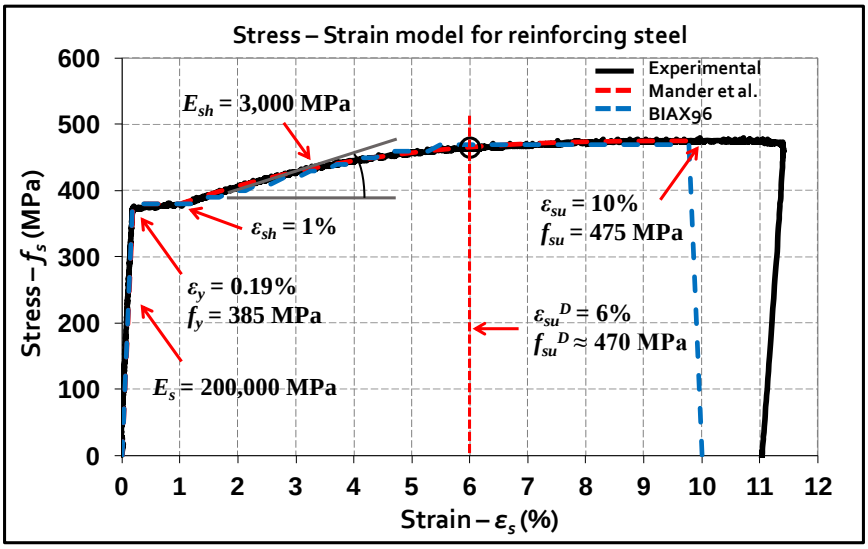

Figure 5.5: Stress-Strain model for ductile reinforcing steel (Grade 300 – NZ standard)

From the parameter required to calibrate the model for a certain steel grade, ε_{sh} and E_{sh} is carefully selected for representing in a proper way the actual steel being used. As was shown in Chapter 3, 6 mm diameter smooth plane round bars grade 300 MPa were used

for all flexural reinforcement in the specimen (beams, columns and slabs). The average characteristics found from a set of 3 samples were f_y = 385 MPa, E_s = 200,000 MPa; ε_y = 0.0019, ε_{sh} = 0.005, f_u = 460 MPa, and ε_{su} = 0.10 to 0.12 (consistent with what is stated in Priestley et al. 2007). In addition, the value ε_{su}^D = 0.6 ε_{su} = 0.06 is considered as a more conservative value for the ultimate strain of the steel to be used in the design and assessment of RC members, as suggested by Priestley et al. (2007). This term is named the 'design' ultimate strain of the steel.

A value for the tangent modulus for strain hardening has not been established. In statistical analysis of measurements corresponding to this parameter (E_{sh}) for Grade 275 MPa and Grade 380 MPa New Zealand steel, mean values of E_s = 5,265 MPa (Grade 275) and E_s = 8,980 MPa (Grade 380) were found, with coefficients of variation of 20% in both cases, approximately (Andronio and Park 1986). It is noted that this parameter is directly proportional to the strength of the steel, which suggests that a 'reasonable' choice value of E_{sh} as a linear interpolation in between the two steel types. The latter yields a value of E_{sh} = 6,150 MPa. Nonetheless, in this case it was found that a value of about half of the latter fits the model more accurately to the measured data, i.e., E_{sh} = 3,000 MPa.

5.5 TRANSVERSE BEAM (SPANDREL) TORSION RESISTANCE

5.5.1 Cracking Limit State

Theories of torsion in linear elastic elements were developed by St.-Venant in 1853 and by Prandtl in 1903. The membrane analogy presented by the latter author provides a simplified approach for pure concrete members under pure torsion. The formulation is presented in Equation 5.28, where T is the torque applied to a rectangular section of sides x and y (x the shorter), G the shear modulus of the concrete given by Equation 5.29, J_E the equivalent polar moment of inertia of the rectangular section given by Equation 5.30, K_t the torsion stiffness of the section in radians per unit of length, and θ_t is the angle of twist.

$$T_c = GJ_E\theta_t = K_t\theta_t \tag{5.28}$$

$$G = E_c/2(1+\nu) = 5700\sqrt{f_c'}/2(1+0.20) \approx 2400\sqrt{f_c'} \tag{5.29}$$

$$J_E = \beta_t x^3 y \tag{5.30}$$

In Equation 5.29, E_c is the Young modulus of the concrete in MPa, and ν the Poisson modulus, taken as 0.2. In Equation 5.30 β_t is a constant which depends on the slenderness ratio of the section x/y, where x and y are the short and long sides of the section, respectively. In this case, for x = 140 and y = 200, then $\beta_t \cong 0.2$ (Park and Paulay 1975). The maximum shear stress associated to the torsion action is expressed in Equation 5.31.

$$\tau_{c,max} = \tau_{cr} = \psi_t T/x^2 y \tag{5.31}$$

In Equation 5.31 ψ_t is a factor which depends on the ratio x/y. Using the graphs presented in Park and Paulay (1975), this factor in this case takes the value of ψ_t = 3.2. According to Hsu (1968) ψ_t can be taken as 3 for all rectangular sections, based on extensive experimental research. In the ACI318-2011 recommendations (ACI Committee 318,

2011), the maximum torsion resisted by the concrete is defined as the cracking torque which yields a maximum shear principal stress in torsion of $\tau_{s,max} = \tau_{cr} = 0.33\sqrt{f_c'}$. Regrouping and combining Equations 5.28 to 5.31, Equation 5.32 can be obtained:

$$T_{cr} = kx^2y \cdot \tau_{cr} \tag{5.32}$$

In Equation 5.32, T_{cr} represents the torque at which torsion cracking is developed in the transverse beam or spandrel, and $k = 1/\psi_t$. The last factor was proposed to be taken as 1/3 for rectangular sections (Hsu, 1968), which is very similar to the 1/3.2 value calculated with graphs (Park and Paulay 1975). Values for τ_{cr} suggested by Hsu correspond to $6\sqrt{f_c'}$ psi ($0.5\sqrt{f_c'}$ Mpa), which is less restrictive than the current ACI318 requirement. However, Hsu also used a safety factor SF = 2.5 for developing a final formulation for T_{cr}, shown in Equation 5.33 for f_c' in MPa, x and y in m and T_{cr} in kNm.

When using the approach explained in Park and Paulay (1975), without using a safety factor and using the stress limit of ACI318-2011 ($0.33\sqrt{f_c'}$, in MPa) calculations lead to the results presented in Equation 5.34. The ACI318-2011 recommendations are based on the maximum shear strain due to torsion in the section. As mentioned before, the maximum shear flow in concrete is associated to that corresponding to cracking limit state ($\tau_{cr} = 0.33\sqrt{f_c'}$).

$$T_{cr} = kx^2y \cdot \tau_{cr} = 1/3 \cdot 0.5\sqrt{f_c'} \cdot x^2y \cdot \frac{10^3}{2.5} \cong 65\sqrt{f_c'}x^2y\ (kNm) \tag{5.33}$$

$$T_{cr} = 0.33 \cdot 10^3/3.2\sqrt{f_c'}x^2y \cong 100\sqrt{f_c'}x^2y\ (kNm) \tag{5.34}$$

Nevertheless, the approach is slightly different to that used for developing the Equations 5.33 to 5.34. As explained in MacGregor and Ghoneim (1995) and the comments of the ACI318 document, this approach is based on the assumption of a thin tube analogy where a continuous shear stress flows through an exterior wall of width t on the sides of the rectangular beam. The thickness of the equivalent wall t is given by Equation 5.35 and the shear flow τ by Equation 5.36 to be $t = 0.75A_{cp}/p_{cp}$, and the stress in the joint $\tau_{cr} = 0.33\sqrt{f_c'}$, as done before.

$$t = \frac{3}{4}\,A_{cp}/p_{cp} \tag{5.35}$$

$$\tau_{cr} = T_{cr}/2A_0t \tag{5.36}$$

$$A_0 = \frac{2}{3}A_{cp} \tag{5.37}$$

$$T_{cr} = 330\sqrt{f_c'}\,A_{cp}^2/p_{cp}\ (kNm) \tag{5.38}$$

$$T_{cr} = 330\sqrt{f_c'}\,x^2y \cdot y/2(x+y) \approx 100\sqrt{f_c'}\,x^2y\ (kNm) \tag{5.39}$$

The resulting cracking torque equation of ACI318 is given by Equation 5.38. In order to compare the values of Equation 5.38 with those obtained with previous approaches, in Equation 5.39 the values of x = 140 and y = 200 corresponding to this case were included numerically in the right hand side. This expression for the torsion strength at cracking limit state has been used in this thesis, acknowledging that values resulting from the

calculations do not vary much. It can be concluded that the expression shown in Park and Paulay (1975) yields exactly the same results as Equation 5.12 derived from current code provisions (ACI Committee 318 2011). The approach developed by Hsu is lightly more conservative than the last ones, but if one multiplies the results by the safety factor SF = 2.5, then the values obtained with Equation 5.10 become 65% greater than those calculated using Equations 5.11 or 5.13. The skew bending theory yields high torsional results and is not considered here.

As in this case x = 0.14 m and y = 0.2 m, and f_c' = 25 MPa, then the cracking torque for the transverse beams of this case using Equations 5.11 or 5.15 corresponds to T_{cr} = 2.0 kNm, whereas when using Equation 5.10, T_{cr} = 1.5 kNm. As the first value is in accordance with the ACI318-2011 torsion provisions, T_{cr} = 2.0 will be used in the calculations presented in the last past of the chapter, even though a lower limit of T_{cr} = 1.5 can be considered as another reference value for parametrical analyses.

5.5.2 Transverse Beam Yielding Limit State

As described in Collins and Mitchell (1992), the space truss analogy theory gives reasonably good estimations for the maximum torque a beam is able to resist after cracking has occurred in the concrete. It is assumed that the concrete beam behaves in torsion in a similar way to a thin-wall box with a constant shear flow. With reference to Figure 5.6(b), the most relevant equations for calculating the nominal torsion resistance provided by the stirrups and the contribution of the longitudinal steel in the corners due to warping effects can be summarized in Equations 5.40 to 5.42.

$$F = A_{sl} f_y = \frac{1}{2} \tau t (x_0 + y_0) \cot \alpha \tag{5.40}$$

$$A_{st} f_y = \tau t s \tan \alpha \tag{5.41}$$

$$T_y = 2 \tau t x_0 y_0 \tag{5.42}$$

In Equations 5.40 and 5.41, F = orthogonal force resisted by the corner longitudinal bars, A_{sl} = area of the corner longitudinal reinforcement bar, f_y = the yielding stress of the reinforcement (same for longitudinal and transverse reinforcement), x_0 = distance measured from the centreline of the perimeter wall of width t in the short side direction, y_0 = distance measured from the centreline of the perimeter wall of width t in the long side direction, t = width of the perimeter wall, τ = shear flow in the width t, and α = angle of direction of concrete cracking in the outside of the beam (normally taken as 45°). In Equation 5.42 T_y is the torque corresponding to the development of yielding in the transverse beam stirrups.

That value also corresponds to the nominal torsion resisting moment of a member under pure torsion in the ACI318-2008 document. In Equation 5.41, A_{st} = area of the transverse stirrup and s = spacing between adjacent stirrups. When combining those equations, Equation 5.43 can be constructed, which is equivalent to Equation 5.44, which takes the form of Equation 5.45 when α = 45°.

$$T_y = 2 x_0 y_0 \sqrt{A_{sl} f_y A_{st} f_y / 2 s (x_0 + y_0)} \tag{5.43}$$

$$T_y = 2x_0 y_0 A_{st} f_y / s \cot \alpha \quad (5.44)$$

$$T_y = 2x_0 y_0 A_{st} f_y / s \quad (5.45)$$

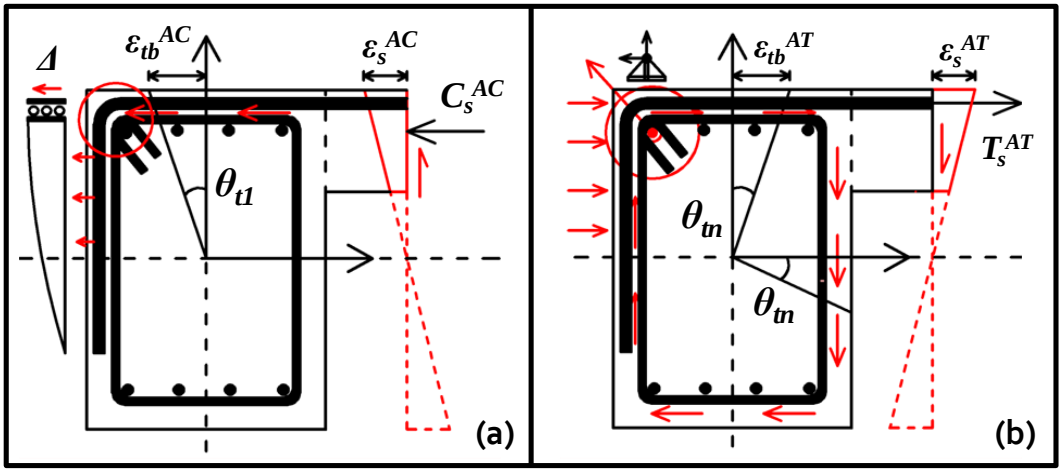

Figure 5.6: Transverse beam (TB) torsion limit states: (a) cracking, (b) yielding or nominal.

In this case, using $\alpha \approx 45°$ as was measured in the specimen after the shake table tests presented in Chapter 4, and for x_0 = 0.12 m, y_0 = 0.18 m, A_{st} = $0.004^2 \cdot \pi/4 = 12.6 \cdot 10^{-5}$ m^2, f_y = 585 MPa, and s = 0.10 m, then T_y = 3.0 kNm. This value has been demonstrated to be very conservative when compared to the results of full-size beam column joint subassemblies with slabs and transverse beams, where the maximum torque capacity was found to be about 1.5 times larger than that calculated with equation 5.45, for the particular case when α = 0 (Di Franco et al. 1995). As a result, an additional limit state corresponding to a 'probable' torsion capacity of the beam is included: T_{pr} = 4.5 kNm.

As described in Chapter 4 the damage pattern developed in exterior joints during the shake table tests of the as-built specimen, revealed that the torsion capacity of the transverse beam is a relevant effect that has influence into that problem. These findings are related to an additional resistance contribution in the direction of rotation of the joint in a beam column slab spandrel subassembly, especially when the slab is in tension (AT). Recalling that the equivalent bending capacity of the as-built joint ranges from 3 to 4.5 kNm, whereas the column bending capacity varies from 4 to 6 kNm, in a 100% axial load variation, values of T_{cr} = 2.0 kNm, T_y = 3.0 kNm and T_{pr} = 4.5 kNm are in the same order of magnitude and can be visualized in the M-N performance domain independently.

The effect of the transverse beam has already been incorporated in terms of confinement and torsion resistance which collaborates with the joint. Nevertheless, the effect of the transverse stiffness of the transverse beam into the longitudinal beam bending capacity has not been addressed yet. It has been argued that the effective width of the slab in tension depends on the stiffness and capacity in torsion of the spandrel or transverse beam, affecting the negative bending capacity of the beam importantly. Strong spandrels similar to the longitudinal beams, like those in the case of this investigation, increase the negative moment capacity up to 1.7 times the positive counterpart (Di Franco et al. 1995).

5.5.3 Transverse Beam Twist Stiffness

The torsion stiffness of the transverse beam for the un-cracked state ($T < T_{cr}$) can be readily calculated using Equations 5.46 and 5.47. Taking β_t = 0.12 (Park and Paulay 1975), the dimensions of beam, and f_c' = 25 MPa. Then the stiffness per unit of orthogonal length unit (twisting curvature stiffness) is calculated as in Equation 5.46.

$$K_t = GJ_E = 2400\sqrt{f_c'}\beta_t x^3 y = 1250\ kNm^2 \tag{5.46}$$

If the torque is assumed to be constant along the transverse beam, and the length of the beam is taken as free to rotate in the mid-span and fixed in the panel zone, then the stiffness for the beam for rotation would be given by Equation 5.47, where L_{eff} is the effective orthogonal length of the transverse beam under torsion.

$$K_{cr} = GJ_E/L_{TB} = 2400\sqrt{f_c'}\beta_t x^3 y/L_{eff} \approx 1250/0.6 \approx 2 \cdot 10^6 kNmm \tag{5.47}$$

The parameter K_{cr} corresponds to the twist stiffness of the transverse beam under pure torsion, for an effective length of half the long span. As it will be demonstrated in the numerical simulations presented in Chapter 8, when this stiffness value is used for modelling joints as rotational springs, the prediction brings reasonably satisfactory results for a blind prediction.

5.6 BEAM MOMENT CAPACITY ACCOUNTING FOR THE SLAB EFFECT

As it has been extensively explained in Chapter 4 and throughout this chapter, the existence of a slab and transverse beams enables the development of different bending capacities in the beam when acting with the slab in compression (AC) and with the slab in tension (AT). As the new beam becomes an L-shaped beam for corner joints and T-shaped for cruciform joints (exterior joints of the internal frame). As it has been previously reported in Kam et al. (2010), Kam (2011), and Quintana-Gallo et al. (2011, 2012), the effect of the effective width of the slab acting in tension for non-ductile RC frames needs to be incorporated into the problem, since it can significantly alter the calculations in the assessment and eventual retrofit procedure. This effective width has also been recognized to be a function of the transverse beam torsion stiffness and strength (Durrani and Zerbe 1987, Di Franco 1995). In this section that problem is addressed.

5.6.1 Slab Effective Width in Tension

For the estimation of the effective slab width (b_{eff}) acting in tension, many formulations have been proposed in the literature. Amongst them, Durrani and Zerbe (1987) proposed to use Equation (5.48), where b_c = width of the column, and h_t the height of the transverse beam, highlighting the finding that b_{eff} strongly depends on the torsion capacity of the transverse beam (spandrel).

$$b_{eff} = b_c + 2h_t \tag{5.48}$$

Many other researchers have focused on inferring formulations with the form of $b_{eff} = k \cdot h_s$, where k is a number larger than zero, and h_s = the slab thickness, like in ACI318-1995 and NZS-1995 'old' code provisions (Di Franco et al. 1995).

In Kam et al. (2010) it was suggested to use $b_{eff} = 2.2h_b$ for non-ductile RC beam column joints. In this equation, it must be emphasised that the parameter h_b can be better understood as the height of the transverse beam. However, in the case of cruciform joint specimen the slab developed important strains in the entire flange (approximately h_b), which means that b_{eff} is potentially larger than the value suggested. If an approach as the one presented in Durrani and Zerbe (1987) is used, then the width of the column should be added, resulting in approximately the same numbers.

Di Franco et al (1995) related b_{eff} to the equivalent section where a certain number of slab reinforcement bars yield in tension, equilibrating the torsion resistance of the transverse beam, also at yield, as shown in Equation 5.49.

$$n = \left(4b_0 A_t f_{yt}\right)/\left(sA_s f_{ys}\right) \tag{5.49}$$

In Equation 5.49, b_0 = effective width of the spandrel for torsion, A_t = area of the transverse hook rebar, f_{yt} = yielding stress of the transverse steel, A_s = area of a single rebar of the slab reinforcement, f_{ys} = yielding stress of the slab steel in tension, and s is the spacing in between stirrups in the spandrel. As this approach is seen to be the most rational of all reviewed, and in the light of the explicit inclusion of the torsion resistance of the transverse beam in the effective slab width, it was selected for this study. In this case:

$$n = \frac{4 \cdot 0.12 \cdot 126 \cdot 10^{-6} \cdot 585 \cdot}{0.10 \cdot 252 \cdot 10^{-6} \cdot 385} = 3.2 \text{ bars}$$

$$b_{eff} = m(n \cdot s_s/N) + b_c \cong 555\ mm \tag{5.50}$$

$$b_{eff}^{es} = (n \cdot s_s/N) \cong 420\ mm \tag{5.51}$$

As this number of bars in the slab is located within 400mm on the side of the beam, b_{eff} is taken as that value plus the column width, as shown in Equation 5.50, where s_s is the separation between the face and the column and the most distant bar considered to be 'active' in tension, N is the actual number of bars inside the distance s_s and n is calculated with Equation 5.49, and m is the number of transverse beam converging to the joint. For a corner beam column joint, m = 2 n = 3.2 for N = 3, s_s = 0.4 and b_c = 0.14, and then b_{eff} = 550mm from the outside of the column. For clarity, the parameter b_{eff}^{es} is defined as the portion the slab on each side of the column effective in tension (Equation 5.51). As a consequence, for exterior joints of the internal frame (cruciform joints) the effective with of the slab would be 2 b_{eff}^{es} +b_c = 970 mm.

In the last paragraphs, the last feature of transverse beam in elements converging in a 3D panel zone has been introduced, when relating directly to it the additional capacity of the longitudinal beam subjected to negative bending moment (AT state). As explained in the few next paragraphs, the bending capacity of the beam increases substantially. In this case it was found that the addition of the slab can increase by a factor close to 2 when

compared to the positive counterpart, the latter being very similar to the capacity of the equivalent rectangular beam calculated for the 2D plane case.

5.6.2 Sectional analysis of L-T-shaped beams

As part of the external frame, the analysis of an L-shaped beam is required for corner joints. That corresponds to the rectangular main beam plus the effective length of the slab on one side only. The resulting RC L-shaped section was implemented in the finite element program BIAX96 (Wallace and Ibrahim 1996), using an appropriate discrimination of the concrete quadrilateral elements, and the concentrated fibres corresponding to steel. The dimensions of the beam are shown in Figure 5.7.

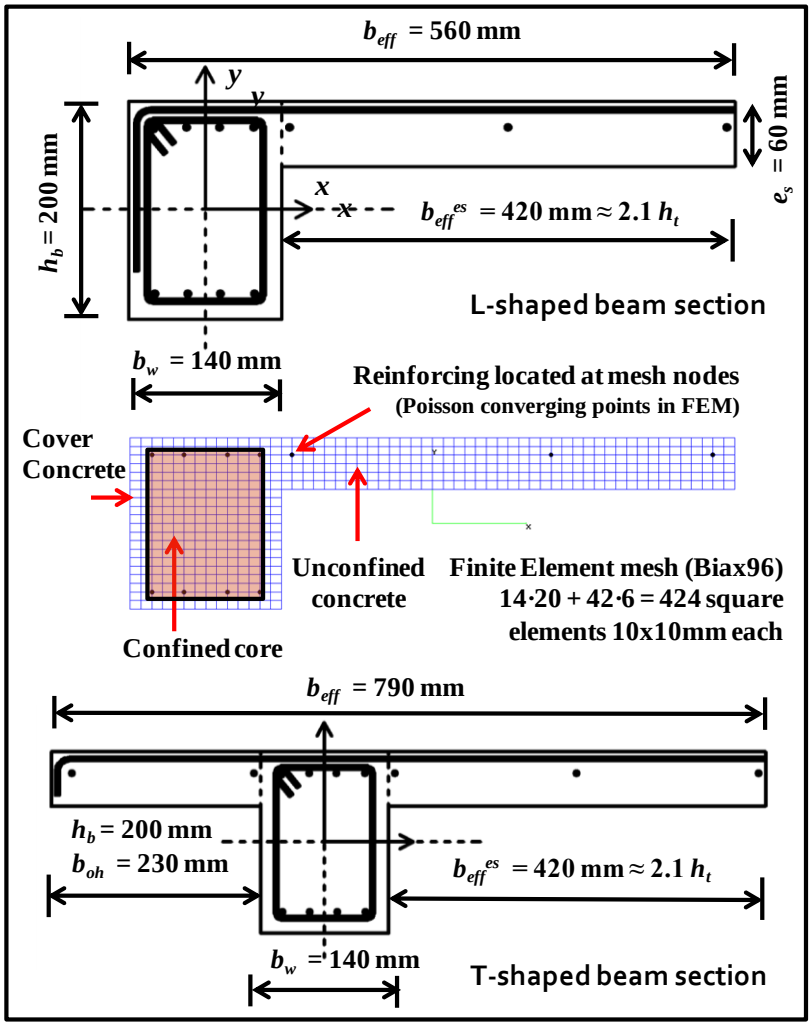

Figure 5.7: L-shaped beam dimensions and finite element mesh generated by BIAX96.

Confined concrete was modelled with the rule of Saatcioglu and Razvi (1992) while cover concrete was modelled with Kent and Park (1971) rule, as explained previously. It was considered that the concrete inside the central core in the web of the beam was confined. All other concrete including the slab was considered unconfined. Steel was modelled using the rule for monotonic tensile behaviour calibrated with the parameters of tensile tests as described previously.

In Figure 5.8 the moment curvature diagrams for an L-shaped beam with an effect slab width of 415 mm on one side of the rectangular core is presented for the AC and AT states (see Chapter 4 for definition of states). In addition, in Figure 5.8 the moment curvature diagram corresponding to an equivalent rectangular beam without a floor slab is presented for comparison.

As can be seen in Figure 5.8 and Figure 5.9, the maximum curvature for both cases is limited by the ultimate strain in the bottom steel (ε_{su} = 6%) being achieved at or below the ultimate unconfined concrete strain (ε_{cu} = 0.003). At a curvature level when $\varepsilon_{su}/2$ = 3% elongation ($\phi \approx 0.16$/m), in both cases (L-shaped and T-shaped beams) the maximum strain in the concrete corresponds to 0.15% and 0.2%, respectively, which indicates that the effect the effective width of the slab being used does not alter the results much. This is also true for higher ductility levels at ε_{su}, where ε_{cu} remains below or equal to 0.3%.

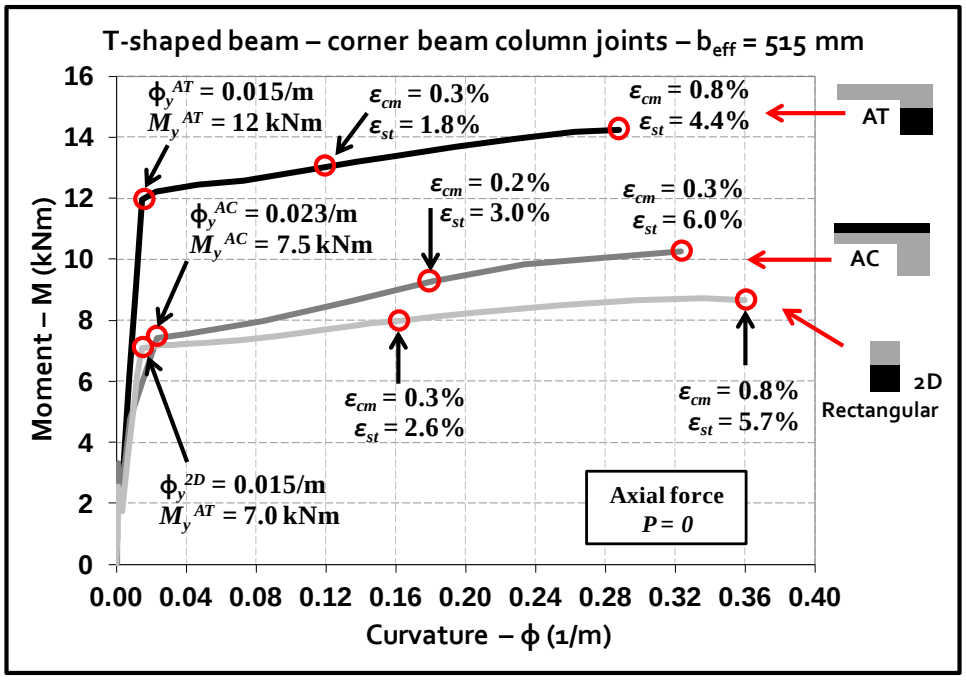

Figure 5.8: Moment curvature diagrams for L-shaped beams (AC and AC) and an equivalent rectangular beam – strain levels and beam yielding moment evaluation; b_{eff} = 515 mm.

When comparing the strain levels at ε_s = 3% of asymmetric beams with those of the rectangular equivalent beam (flange width = 0), then values very close or equal to ε_{cu} = 0.3% where obtained. These values are roughly two times larger than those corresponding to the L-shaped beam and 1.5 times larger for the T-shaped beam counterpart, and correspond to the same curvature level of ϕ = 0.16/m, as shown in Figure 5.8 Figure 5.9. As also indicated in the these figures at higher curvature levels ($\phi \approx 0.32$/m) both asymmetric sections would still experience strains in the concrete smaller than 0.3%, whereas the reference rectangular beam would experience maximum compression levels of ε_{cu} = 0.8%, which has been considered in this study as the ultimate strain in the confined concrete. As a consequence, the addition of the slab on the top part of the beam (section A) significantly reduces compression strain levels in the concrete at ultimate curvature ($\phi^{AC} \approx 0.32$/m; $\phi^{R} \approx 0.36$/m), for maximum tension strains in the bottom steel ε_{su} = 6%.

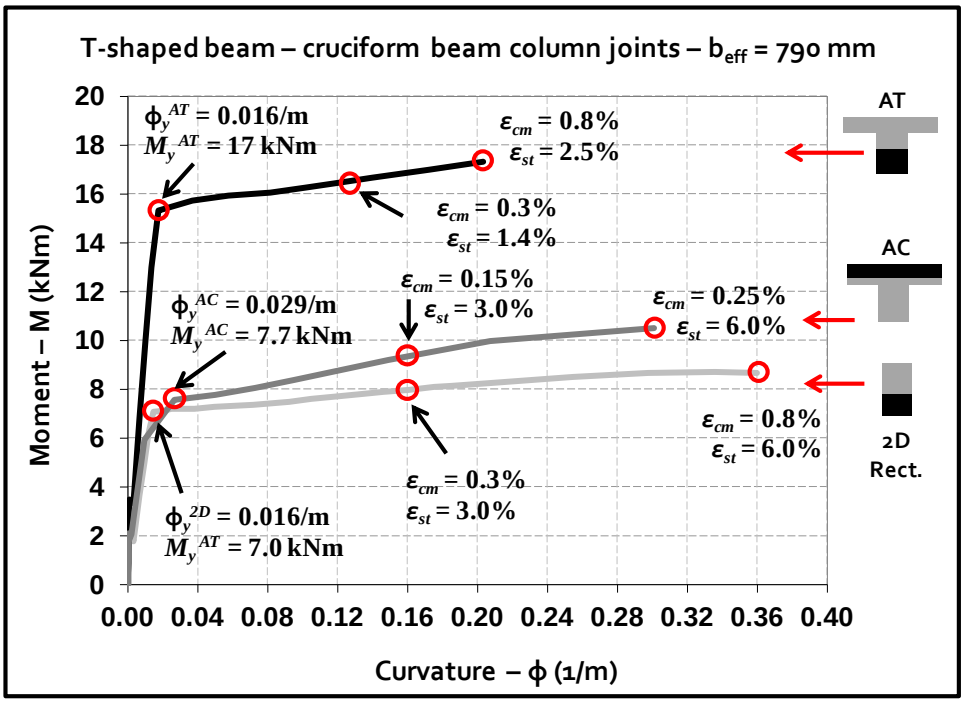

Figure 5.9: Moment curvature diagrams for T-shaped beams (AC and AC) and an equivalent rectangular beam – strain levels and beam yielding moment evaluation; b_{eff} = 960 mm.

On the other hand, when asymmetric sections are being analysed under tension in the top fibre of the beam-slab (AT), an important difference in the bending moment capacity as well as a reduction in the curvature capacity was found, depending on the amount of slab reinforcement being activated, which is also related to the stiffness of the transverse beam (Ehsani and Wight 1985, Durrani and Zerbe 1987, Di Franco 1995, Shin et al 2004).

When comparing those results with the rectangular plane beam, a gain in the bending moment and a loss in curvature ductility capacities are noticed. In Figure 5.8, where the rectangular and L-shaped beam's moment curvature relationships are plotted, the L-shaped beam with 3 bars in the slab reaches 1.6 times that of the plane beam, as well as reduces its ultimate curvature capacity by 1.3 times. Furthermore, when comparing the diagrams of the rectangular beam with the T-shaped counterpart, the increase in the bending moment capacity of the section with N = 5 slab bars is 2 times that of the rectangular beam. The ultimate curvatures associated to each beam section are computed at that stage where $\varepsilon_{cu,c}$ = 0.8% and or ε_{su} = 6%, the lesser. However, in all cases the main restriction in this case is the maximum concrete strain available in the confined central core of the beam's web. The curvature capacity of the flanged beam is almost 1.5 times smaller than the curvature capacity of the rectangular beam.

In Figure 5.10, the effect of the slab in the bending moment magnitude and the ultimate curvature ductility reduction of the section are illustrated. In Figure 5.10, N = the number of active or effective bars of the slab in tension, as a consequence of the evaluation of the transverse beam torsion strength; ρ_{se} = the equivalent transverse reinforcement ratio, (the transverse steel inside a slab portion b_{eff} and of thickness h_s, the slab thickness). In the same figure, the moment is presented in a dimensionless fashion on the right hand side vertical axis. This dimensionless moment m_D is the moment M divided by the compressive strength of the concrete, the width of the beam web b_w, and the square of the

beam height. This way of presenting the moment corresponds to a consistent dimensionless number for this type of analysis as discussed in detail in Chapter 3.

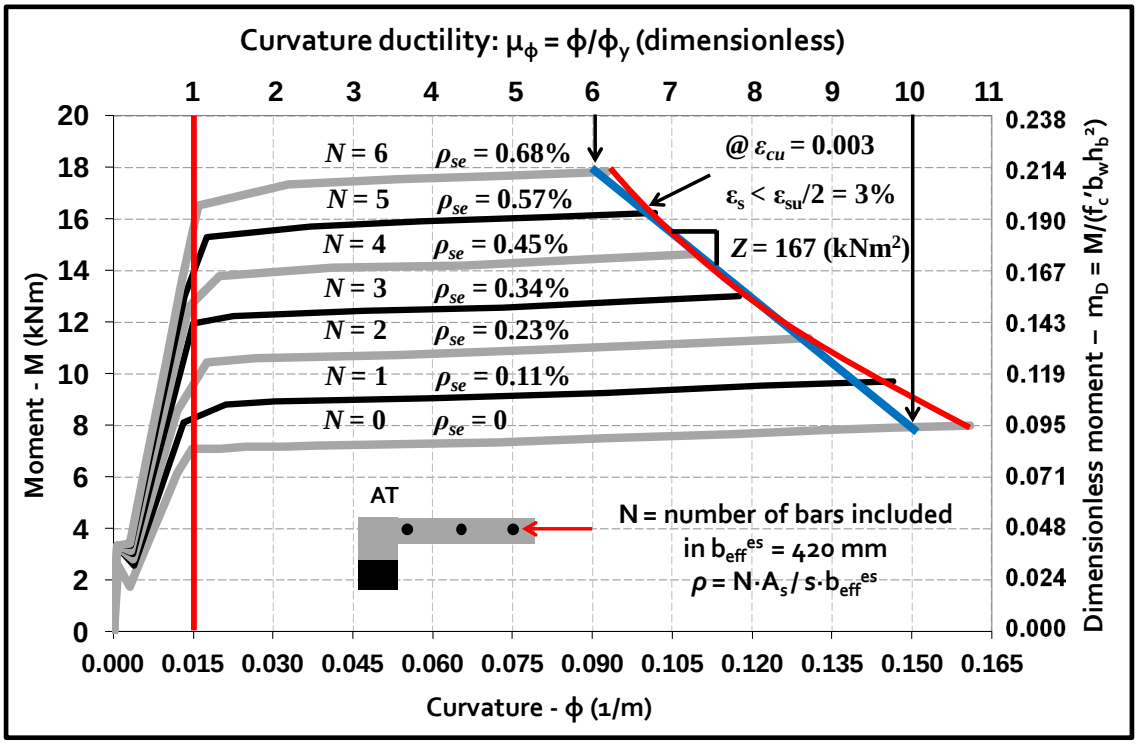

Figure 5.10: Effect of slab effective reinforcement in the ductility of L and T-shaped beams.

In Figure 5.10, a series of moment-curvature analysis are shown for different slab effective reinforcement, referred to multiples of 6mm diameter bars (28mm^2), as it was the reinforcement used in this case. All diagrams are plotted till a 0.003 compression strain is reached at the bottom of the concrete. The yielding curvature of the beam section is estimated as ϕ_y^{AT} = 0.015/m. This curvature is independent of the effective steel in the slab, and sets the starting axis for the calculation of the section curvature ductility capacity. Maximum ductility values range from μ_ϕ = 6 for the maximum amount of effective bars (N = 6) and μ_ϕ = 10 for N = 0. Moment capacities corresponding to those envelope sections correspond to M = 18.0 kNm ($m_D \approx 0.22$) and M = 8.0 kNm ($m_D \approx 0.1$), respectively.

The slope of that line (Z) is presented in Figure 5.10 as well as in Figure 5.11, providing a parameter for the determination of the ductility and the enhancement in the strength of flanged beams when the slab resists in tension (AT) as a function of the slab effective reinforcement (or width). This parameter can be represented in terms units for force times geometric area (kNm^2) or as a dimensionless number in the consistent series of products presented in Chapter 3, which would require the slope to be divided by f_c', b_w, and h_b. This can also be obtained by calculating the slope of the straight line in terms of de variation of m_D and μ_ϕ, which is also dimensionless. As a result, a value of Z_{03D} = 0.030 was estimated for ε_{cu} = 0.003, as presented in Figure 5.10.

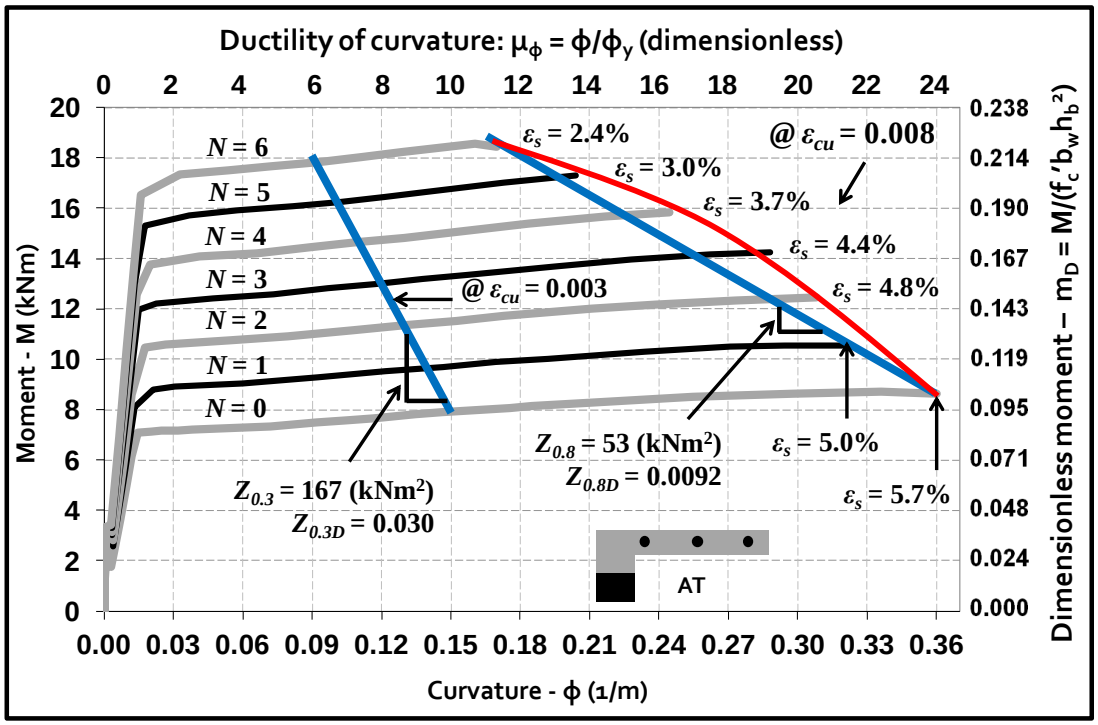

Figure 5.11: Variation of ductility at maximum deformation of confined concrete ε_{cu} = 0.8% for increasing reinforcing ratio in the effective slab; maximum steel strain in at ε_{cu} = 0.8%.

In Figure 5.11, the same diagrams plotted in Figure 5.10 are presented for curvatures where values of ε_c in the most compressed fibre in the concrete goes beyond 0.3%. In this case, diagrams are plotted up to ε_{cu} = 0.8% or ε_{su} = 0.6%, whichever occurs first. As shown in the red line shown in Figure 5.11, a simple arch can be used to represent the envelope of failure points corresponding to different values of slab reinforcement ratios. This arch is conservatively approximated by a straight line from m_D = 0.01 and μ_ϕ = 24 corresponding to the rectangular beam, to m_D = 0.22 and μ_ϕ = 10 corresponding to N = 6. As written in Figure 5.11, the values of the slope which represent the values of the degradation parameters as a function of the effective slab width is estimated as $Z_{0.8D}$ = 0.0092 for ε_{cu} = 0.008. It is highlighted that in none of the cases under study the reinforcement steel maximum strain goes beyond the ultimate strain of ε_{su} = 6%.

5.7 COLUMN MOMENT CAPACITY WITH VARYING AXIAL LOAD

In the sectional analysis of the columns, the same models for representing the behaviour of unconfined and confined concrete, as well as reinforcing steel used in the analysis of the beams were considered (Figure 5.4 and Figure 5.5). The only exception would be the strain at which the 50% of the maximum stress is reached (ε_{50}), since the confinement configurations changes slightly because the height of the cross section is smaller than that of the beam. Therefore, the separation between bottom and top longitudinal bars enable a larger lateral stiffness from stirrup legs providing lateral restraint. However in this case, the increasing in this value is negligible, and was not accounted for in the analyses.

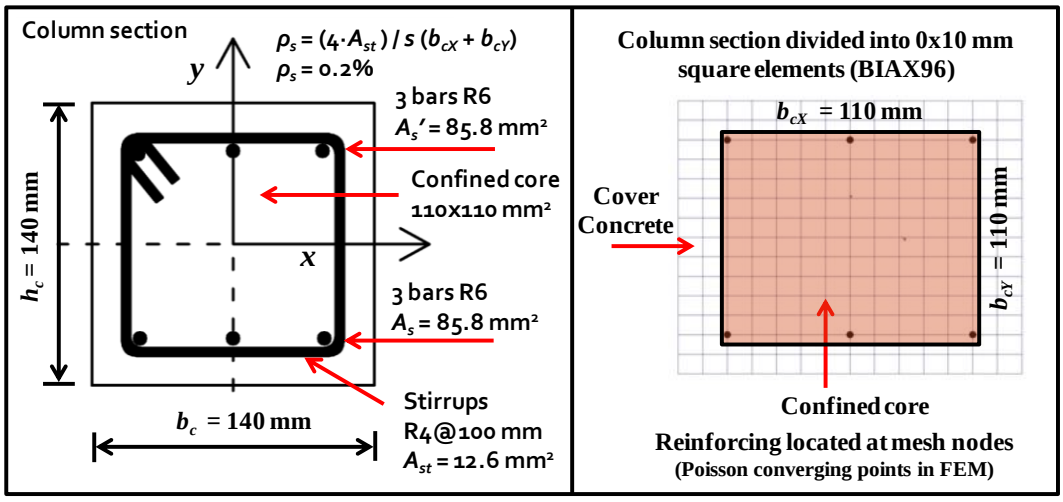

Figure 5.12: Column cross section and FEM implementation in BIAX96 for sectional analysis.

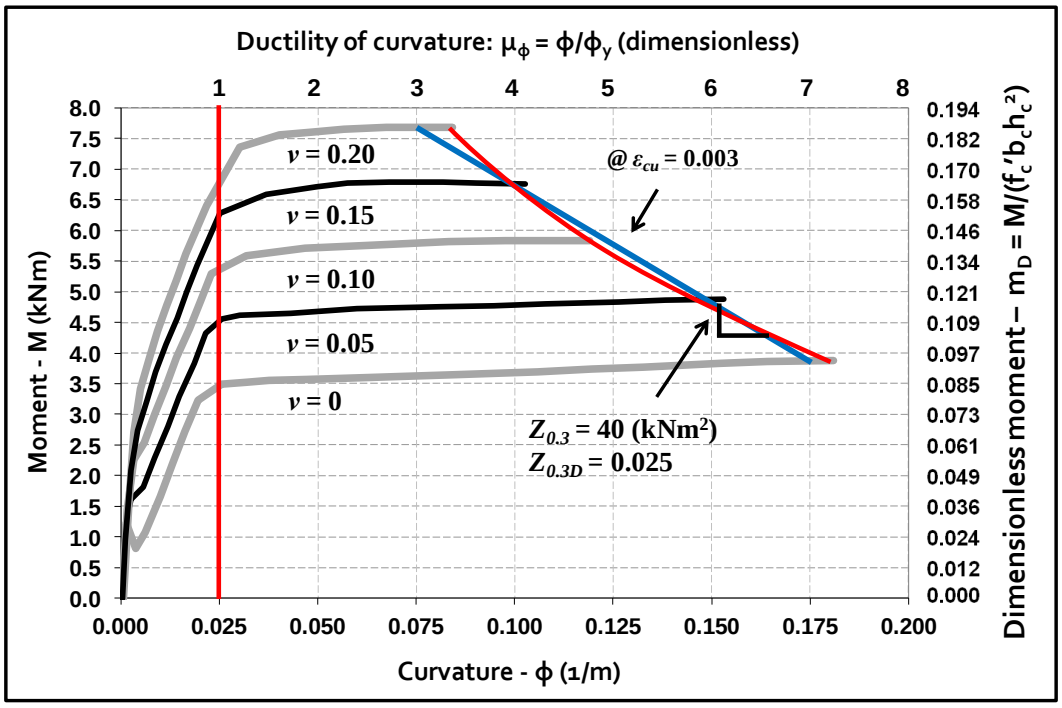

Figure 5.13: Moment curvature relationships for the as-built column under different levels of axial load. Slope of the line constructed at $\varepsilon_{cu} = 0.003$ $Z_{0.3D} = 0.025$.

The cross section of the column as well as the longitudinal rebar and the confinement arrangement are presented in Figure 5.12. On the right hand side of Figure 5.12, the 14x14 square finite element mesh created in BIAX96 is also presented. Results of moment-curvature analyses are shown in Figure 5.13 for increasing values of the axial load from zero, through the gravity load in the reference column (20kN), and up to two times that value (40kN). It is worth noting that the axial load ratio (ν), which is the axial load (P_v) divided by the gross area of the column A_g and f_c' has rather small values. For all columns values of the order of only up to ν = 0.1 were able to be imposed for simulating gravity load (internal columns), due to the shake table weight limitations (exploited to the maximum with this particular specimen). As a consequence, these

columns are much more ductile than equivalent elements subjected to higher initial axial load ratios, of the order of ν = 0.3 to 0.4.

In Figure 5.13, the red arch and a straight line describe with different approximations the ultimate curvature when a maximum value of ε_{cu} = 0.3% is reached in the compressed concrete. The slope of the straight line has been calculated in terms of the normal units used in the analysis as well as the dimensionless slope derived from the dimensionless axial load ratio ν and the curvature ductility. The last number is estimated as Z = 0.025, which is very close to the slope of the line plotted for the ultimate ductility degradation at increasing effective slab widths shown in Figure 5.10. It can be argued that both axial load in a square symmetrically reinforced section and additional tensile reinforcement from the slab, have a similar effects on the degradation of the ultimate ductility of a RC element section. This has been postulated in the absence of ad-hoc experimental research as a theoretical explanation for the particular non-ductile behaviour that some flanged RC walls experienced during the Chilean 2010 Maule earthquake (Chapter 9) and after the New Zealand 2011 Canterbury main earthquake (Chapter 10).

As the axial load acting in the member affects the bending moment capacity, this variation can be readily calculated from Figure 5.13. If one computes the yielding moment of the column for a given axial load level, then the M-N diagram can be approximated easily. With reference in the case corresponding to gravity load only (initial state) then the yielding moment corresponds approximately to 4.5 kNm, decreasing to about 3.5 kNm for pure bending, and increasing to about 5.5 kNm for 2 times the initial axial load in the column. A simple linear interpolation in this case would yield sufficiently accurate results for estimating the M-N curve to be implemented in the extended version of the M-N diagram.

5.8 JOINT EQUIVALENT MOMENT EVALUATION

5.8.1 Equilibrium and Mohr's Circle Stresses Domain

For the estimation of the joint's equivalent resisting moment, the analytical method presented in Akguzel and Pampanin (2010) was used. In this approach, the equivalent resisting moment of the joint is related to principal tensile stresses that produce cracking in the concrete (p_t) (Priestley 1996, Hakuto et al. 2000, Pampanin et al 2002, Pampanin et al. 2007, Akguzel and Pampanin 2010). The equivalent moment in the joint is also related to the geometry of the frame and the dimension of the beam, columns, and joints, as will be shown later. Here, a brief description of the derivation of the joint shear and principal stresses is presented.

In Figure 5.14 a free body of the panel zone in equilibrium is shown for the AC and AT states (left hand and right side in Figure 5.14, respectively). That is needed for the evaluation of the two different parts of the asymmetric version of the M-N performance domain due to the inclusion of the floor slab. From a pure capacity assessment point of view the corresponding shear force transmitted from the beam into the joint in the AC state would be smaller than the shear transmitted at the AT state. Particularly interesting it is to note that the lever arm of the beam moment action is reduced for AT states when compared to those of AC states in experimental and analytical studies on asymmetric

structural RC walls (Thomsen 1995, Thomsen and Wallace 2004, Beyer et al. 2008, Quintana-Gallo 2008).

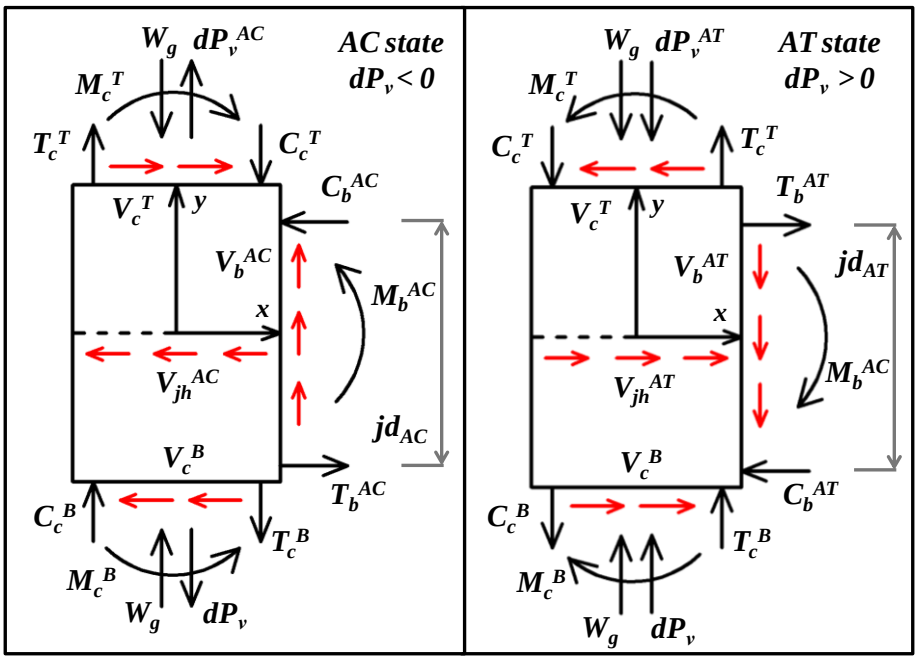

Figure 5.14: Equilibrium in the panel zone region; left: AC state, slab (top fibre A) in compression; right: AT state, slab (top fibre A) in tension.

Equations 5.52 and 5.53 state the definition of the stresses acting in the joint induced by the beams and columns (Hakuto et al. 2000). These equations define the stresses state for constructing the Mohr's circle, required to evaluate the principal stresses acting at a middle of the joint (or geometric centre): $v_{jh} = \tau_{yx}$ = shear stress and $\sigma_v = \sigma_{yy}$ = stress in the direction y, as shown in Figure 5.15.

$$v_{jh} = \frac{V_{jh}}{b_j h_c} = \tau_{yx} = \tau_{xy} \tag{5.52}$$

$$\sigma_v = N_v/(h_c b_c) = \sigma_{yy} \tag{5.53}$$

$$p_{c,t} = \sigma_{c,t} = \sigma_v/2 \pm \sqrt{(\sigma_v/2)^2 + {v_{jh}}^2} \quad for \quad \sigma_{xx} = 0 \tag{5.54}$$

$${v_{jh}}^2 = {p_t}^2(1 + \sigma_v/p_t) \quad for \quad \sigma_{xx} = 0 \tag{5.55}$$

In Equations 5.52 and 5.53, the parameters not defined previously are: b_j = joint effective width, taken in this particular case to the b_c. Note that both axial and shear forces are normalized by the same area in order to obtain stress values. Equations 5.54 and 5.55 have been derived from Mohr's equations assuming a value of $\sigma_{xx} = 0$ for calculating the principal stresses given by Equation 5.54. Since the shear as well as axial stresses are calculated for a deformed state where the shear in the joint develops according to actions induced by the beam and columns, this assumption may not be the most appropriate for cruciform 3-side confined exterior joints. This is also true when composite material such as FRP laminates are being used for confining the joint, as consequently, they will impose a different boundary condition in the joint itself. Equation 5.64 is derived by identifying a

known stresses state in the Mohr's circle domain where principal stresses are found from geometrical considerations. In this case, Mohr's circle has the form of the left hand side of Figure 5.15, where the know states are related to the horizontal shear in the joint and the axial load in the column and joint, and assuming $\sigma_{xx} = 0$ at that state.

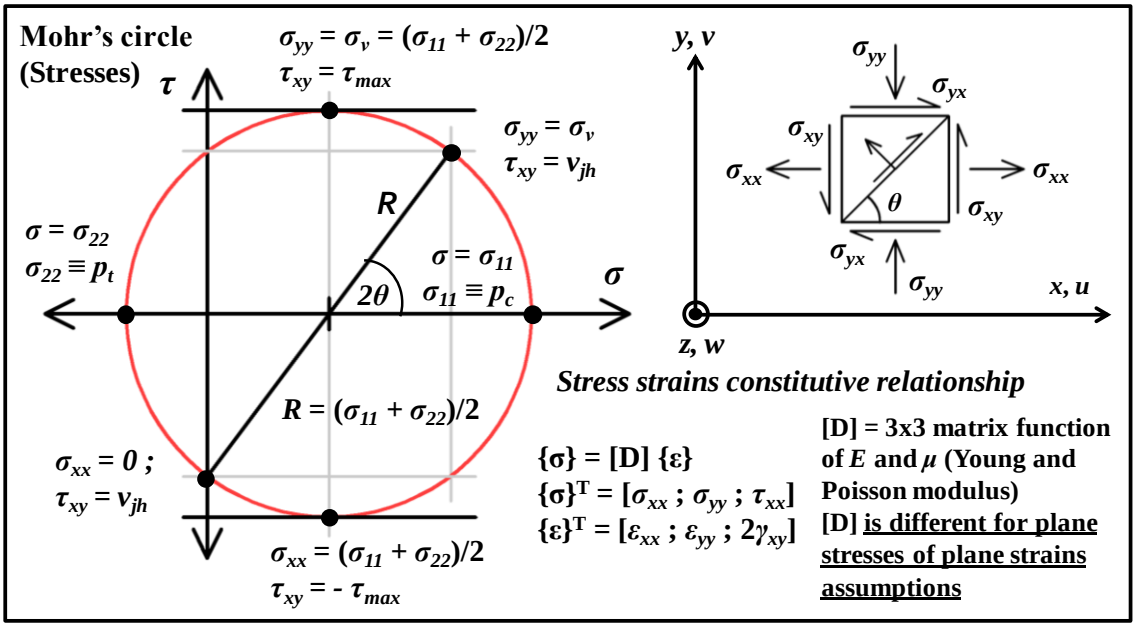

Figure 5.15: Mohr's circle of stresses, stress state at the middle of the joint and stress strain constitutive relationships for a 2D simplified case.

5.8.2 Equivalent Resisting Moment in Exterior Joints

This equivalent resisting moment of the joint depends on the geometry of the frame, the p_t maximum stress, which in turn depends on $\sqrt{f_c'}$, and the lever arm of the resisting moment in the beam (jd). It has been demonstrated using quasi-static tests of plane beam column joints (Akguzel and Pampanin 2010) that when using the appropriate values in the calculations, the analytical prediction of the equivalent resisting moment in the joint yields a good estimation of the joints capacity in the M-N performance domain context. In Equations 5.56 to 5.68 the value of the beam bending moment, the horizontal shear force in the joint, and the moment in the column are presented, respectively.

$$M_b = V_b\left(l_b - \frac{h_c}{2}\right) = Tjd \tag{5.56}$$

$$V_{jh} = V_c\left[\frac{l_c}{l_b jd}\left(l_b - \frac{h_c}{2}\right) - 1\right] \tag{5.57}$$

$$M_c = \frac{V_{jh}}{\left[\frac{l_c}{l_b jd}\left(l_b - \frac{h_c}{2}\right) - 1\right]}\left(\frac{l_c - h_b}{2}\right) \tag{5.58}$$

In Equation 5.56 to 5.58, M_b = beam bending moment; V_b = shear force in the beam at the mid-span; l_b = half of the beam span length, measured from adjacent columns centreline; h_c = column cross section height; T = tension force induced by the steel in the beam when bending; jd = effective lever arm of the force T, measured from the equivalent

compression resulting force in the concrete; d = effective height of the steel in tension; V_{jh} = horizontal shear force in the joint, measured at the mid-height of the joint; V_c = shear force in the columns, measured at the mid-height of two consecutive floors; l_c = column length, measured from the mid-height of two consecutive floors, assumed to me inflection points; M_c = bending moment of the column acting at the face of the joint, conceived as the sum of half of the moment induced by top and bottom columns in the joint. Referring the moment in the joint to the total moment induced by the column (top and bottom), the equivalent resisting moment in the joint (M_j) is given by Equation 5.59 alone, or Equation 5.60 combined with Equation 5.61 (Akguzel and Pampanin 2012).

$$M_j = \frac{p_t b_j h_c \sqrt{1+\sigma_v/p_t}}{\left[\frac{l_c}{l_b jd}\left(l_b - \frac{h_c}{2}\right) - 1\right]} \cdot \left(\frac{l_c - h_b}{2}\right) \tag{5.59}$$

$$M_j = \left(p_t \sqrt{1 + \sigma_v/p_t}\right)/\omega \tag{5.60}$$

$$\omega = \frac{2\left[\frac{l_c}{l_b jd}\left(l_b - \frac{h_c}{2}\right) - 1\right]}{b_j h_c (l_c - h_b)} \tag{5.61}$$

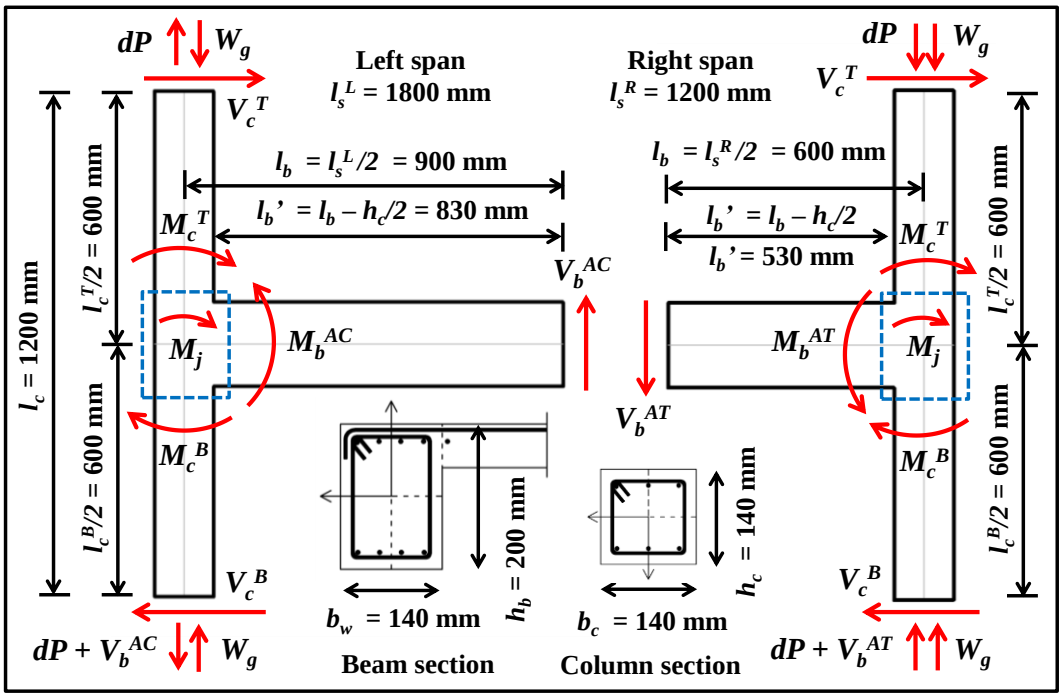

Figure 5.16: Exterior beam column joints equilibrium – left and right hand side spans.

It is worth noting that Equation 5.59 is true only if the top and bottom columns have the same height and cross section geometry. In Figure 5.16 both (left and right) corner joints of the specimen (described in Chapter 3) are isolated from the structure at the centre of each span (long and short, respectively), and the middle height of the first floor. In Figure 5.16 a consistent nomenclature with Equation 5.59 is used. However, the beam length is referred to the span length instead of the beam length, which corresponds in the latter equations to the length of the beam incorporated in the subassembly. In this case, the

value $l_s = 2l_b$ is introduced, where l_s is the length of the beam span, measured between the centre line of the supporting columns.

In the following figures, the equivalent bending moment strength is shown for the left and right hand side exterior joints. These exterior joints correspond to two joints of the external frame (two corners) and two of the internal frame (two cruciform). For the latter, the dimensions shown in Figure 5.16 which correspond to the 'in-plane' dimensions of left and right hand side exterior joints (corner or cruciform) are used. The main difference in the application of this approach in beam column joints with slabs and spandrels relies in the orthogonal direction boundary conditions imposed by the slab and the spandrel. The slab-spandrel combined effect enables the modification of some parameters involved in the equivalent moment calculation, based on what has been previously proposed for plane specimens (Akguzel and Pampanin 2012). These differences can be selected as:

(1) A larger joint effective width ($b_j > b_c$)
(2) A greater confinement of the joint ($p_{tD}^{2D} < p_{tD}^{3D}$)
(3) A smaller effective lever arm of the beam for AT state ($jd^{2D} < jd^{AT}$)

The first effect is related to an increase of the joint effective width due to the presence of the transverse beam. For corner beam column joints, as a transverse beam is located on one orthogonal side only, and assuming that the resisting path is delimited by one time the height of the transverse beam (h_t) (1:1 slope), the average width of the truncated pyramid corresponds to $b_j = b_c + h_t/2$. Analogously, for cruciform joints, the existence of transverse beam at both orthogonal sides yields $b_j = b_c + h_t$.

The second effect deals with the confinement in the joint provided by the transverse beams and the slab. Confinement increases the value of p_{tD} (in absolute value). This value is greater than $p_{tD} = 0.2$ for any other joint typology with the exception of the tee plain joint presented in Akguzel and Pampanin (2010). For joints with some confinement and/or more ductile reinforcement configurations in the beam anchorage, values ranging from $p_{tD} = 0.3$ to 0.5 are suggested as maximum limits for diagonal cracking (Priestley 1996).

Lastly, the lever arm jd for flanged beams can be smaller than that corresponding to a rectangular beam, since in the AT situation (state) there is an increment in the neutral axis depth. In the case of plane joints the assumption made in Akguzel and Pampanin (2010) by taking $jd = 0.9d$ is seen to be approximately correct. This also seems appropriate assumption for flanged beams performing in the AC state, since the neutral axis depth in this case lies in or close to the slab. For the AT state though this assumption may be not entirely correct since a deeper neutral axis is needed to compensate the higher amount of steel acting in tension on the opposite face. In the light of the importance of this parameter in the evaluation of the joint equivalent resisting moment, it is recommended that jd is incorporated explicitly into the problem, in order to evaluate how much M_j varies when using different values. It is recommended to examine at least 3 values of 0.9, 0.8 and 0.7. A more conservative value of $jd = 0.70d$ will be considered as a lower bound for the AT situation, based on the analysis of T-shaped walls done by Quintana-Gallo (2008) and those presented in the second part of this thesis.

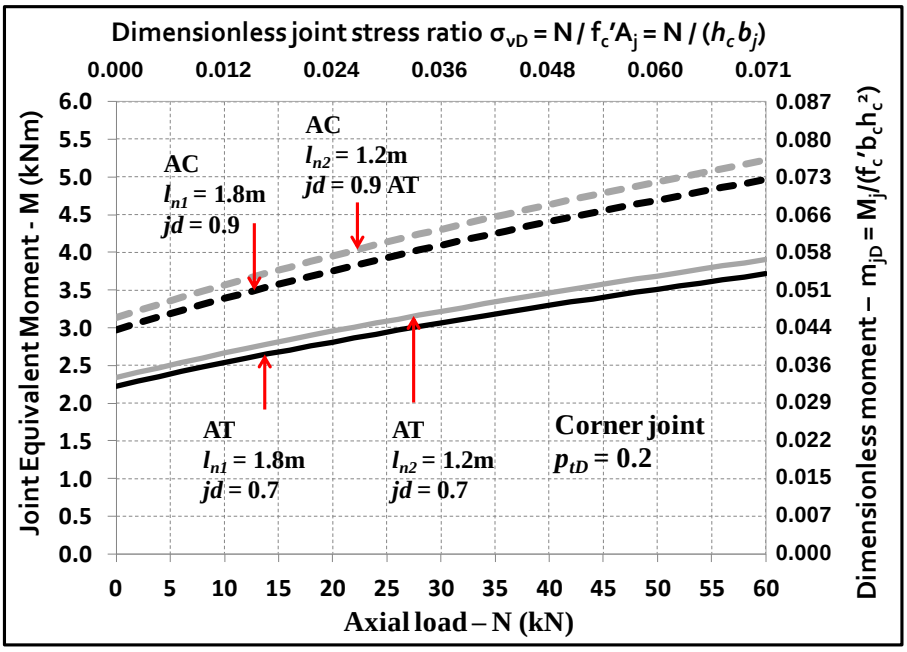

Figure 5.17: Corner beam column joints – long and short span – under AC and AT states (*jd* varies).

In Figure 5.17 the equivalent bending moment capacity is plotted for an appropriate range of axial load. This capacity curves correspond to the corner joints of both long and short span. A conservative value of p_{tD} = 0.20 for the principal stress corresponding to cracking in the joint was used, based on the value p_{tD} = 0.19 suggested by Pampanin et al. (2002). The two states (AC and AT) are also distinguished in Figure 5.17 for it is related to the *jd* factor taken as 0.9*d* for AC and 0.7*d* for AT , as discussed previously. It is observed in Figure 5.17 that the capacity of the joint diminishes considerably when the smaller leaver arm in the beam is being used. Variations in the moment capacity in both cases can be quite high.

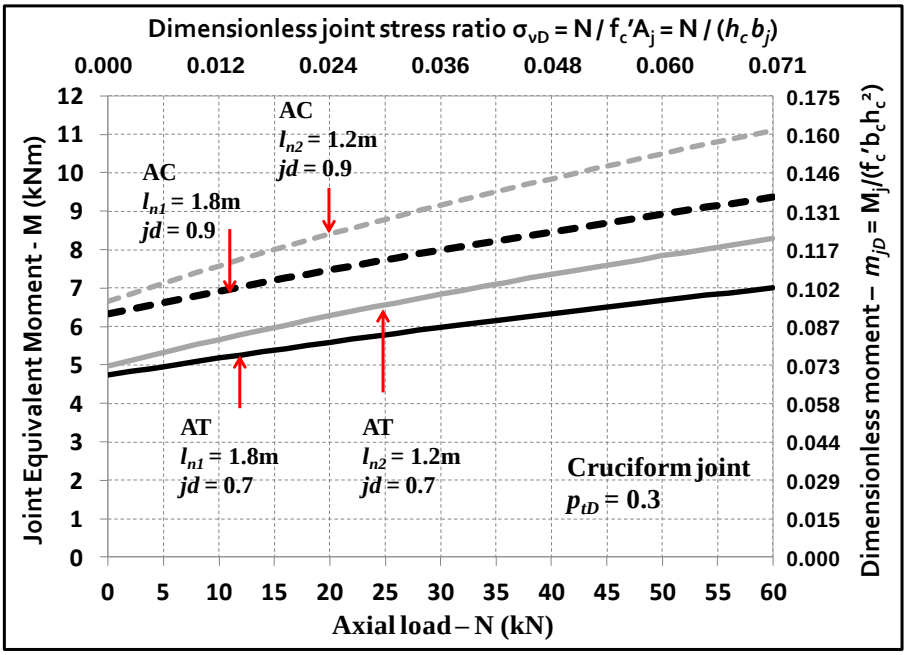

Figure 5.18: Cruciform beam column joints evaluation – long and short spans – AC and AT states.

In Figure 5.18 the capacity curves for cruciform beam column joints are presented. Here, a value of p_{tD} = 0.3 has conservatively been adopted for the principal cracking stress, following what has been suggested by Priestley (1997) for exterior beam column joints with the poorest detailing in the joint. Even if values as high as p_{tD} = 0.58 are proposed by Priestley (1997) for two way 'corner' beam column joints, these specimens were all well detailed (beam bars bent into joint).

As the mechanics involved in the case of 3D cruciform exterior beam column joints includes the slab-spandrel effect, which will significantly differ from that of a plane joint, because of (1) the torsion resistance provided by the spandrel (transverse beam), (2) the larger effective joint width, and (3) the lateral restraint provided by the columns vertical bars. The latter effect is analogous to that of transverse stirrups which provide lateral restraint to longitudinal bars in order to provide resistance to internal pressure caused by orthogonal actions. This is in line with experimental research done in 2/3 scale beam column joint of with the same characteristics and similitude-compatible with the cruciform joint of the model building part of this study (Kam et al 2010). This is also in line with the conclusions of the research done by Ehsani and Wight (1985) and Durrani and Zerbe (1987) for very similar specimens but with a lesser degree of fragility (ductile).

The increase in the equivalent joint moment capacity of cruciform joints when compared to the corner joint case is a sum of two effects in this case: (1) a larger effective with of the joint and (2) a larger p_{tD} value used in the calculations, intended to account for the confinement provided by the transverse beams. In this case an increase of about 2 to 2.5 times is predicted for cruciform joints over corner counterpart.

5.9 HIERARCHY OF STRENGTHS AND EXPECTED SEQUENCE OF EVENTS USING AN ASYMMETRIC VERSION OF THE M-N DOMAIN

As presented in section 5.3 of this chapter, an extended version of the M-N capacity curves for evaluating the strengths and the expected sequence of events in the panel zone region needs to be used in this case where the presence of the slab and the spandrel introduces asymmetry into the problem. This asymmetry is understood by means of the examination of two difference 'states' as was defined in Chapter 4, which corresponds to (1) AC = top fibre of the slab ('A') under compression – positive bending moment in the beam, and (2) AT = top fibre of the slab under tension – negative bending moment in the beam. In addition, due to cinematic compatibility and equilibrium of external actions, it was shown that a positive axial load variation is only compatible with a negative bending in the beam and a negative axial load variation is only compatible with a positive bending in the beam. As a consequence only quadrants QII and QIV presented in Figure 5.3 are permitted. These two quadrants correspond to the AC and AT situations defined before, and will be autonomously be examined in the following sub-sections, where the M-N diagrams for critical corner and cruciform exterior beam column joints are constructed for the most critical span, which is the long one. The torsion resistance of the spandrel at cracking (T_{cr}) and yielding (T_y) limit states for the AC and AT situations, respectively, are also plotted in the M-N diagrams. The four elements are denoted as: B = beam, C = column, J = joint, S = spandrel, so that when using the matrix (linear algebra) approach presented in previous sections of this chapter. In this case, n = 4 elements.

The corresponding evaluation matrix in terms of specific points of the M-N diagram for *m* = 2 'demand scenarios', given by straight lines M = α' N, and so that α' = *d*M/*d*N, the rate of variation of the moment as a function of the axial load. This value can be found by equilibrium in a frame of certain geometry as explained in the next paragraph. In this case though, as shown in Figure 5-5.19, this factor does not alter the results of the imposed mechanism, since the hierarchy of the strengths for all the range of interest is practically the same. Therefore, the 'demand' is somehow irrelevant in this case.

The method for estimating α' is based on equilibrium considerations and the geometry of the frame, as presented in section 5.10. The coefficient α' refers to the rate of variation of moment with axial load and is not the coefficient that relates the shear force to the variation in the axial load of the column, named α (Kam 2010, Akguzel 2011, Akguzel and Pampanin 2012). However, these coefficients are related to each other and both will be shown for illustration. The assumptions involved in the derivation of α and α' are: (1) the shear and the moments are the same in all three columns, (2) the axial load in the central column is neglected, and (3) the inflexion point in the columns is 0.6 times their height (or 0.5 alternatively). Under those assumptions, in this particular case, α can be estimated using Equation 5.62.

$$\alpha = \frac{dP}{V_c} = 4.2\frac{h}{(l_{n1}+l_{n2})} \tag{5.62}$$

In Equation 5.62: h = the inter-storey height, l_{n1} and l_{n2} = the long and short span lengths of the frame, respectively. For h = 1.2m, l_{n1} = 1.8m, and l_{n2} = 1.2m, then α = 1.68. This value is much smaller than that used in the quasi-static tests of beam column joint subassemblies tests by Kam (2010) and Akguzel (2011), where α = 4.63. That is an extreme scenario, derived for a 6-storey, 3-bays building. The relationship between α and α' can be found as follows. For equilibrium, and using assumption (3), the moment in the column is $M_c = 0.6V_c\,h$ and thus α' is given by Equation 5.63.

$$\alpha' = dM/dP = \frac{0.6h}{\alpha} = 0.143(l_{n1} + l_{n2}) = 1/\beta \tag{5.63}$$

In this case, as the total length of the specimen is 3 meters, α = 0.43. The inverse of that number, $\beta = 1/\alpha'$ = 2.33, represents the rate of variation of the axial load as a function of the moment, i.e. $\beta = dP/dM$. In the M-N diagrams, this value is the 'correct' one for the evaluation of the hierarchy of strengths and sequence of events in the panel zone region. Nevertheless, an additional scenario representing half of the rate of variation of the axial load calculated before is also considered. In summary, the coefficients for each demand scenario are:

(1) Scenario 1: α_1' = 0.43; β_1 = 2.33, $\alpha_1 = 0.6h\beta_1$ = 1.68

(2) Scenario 2: α_2' = 0.86; β_2 = 1.16, $\alpha_2 = 0.6h\beta_2$ = 0.84

5.9.1 M-N Diagram Corner Beam Column Joints – Long Span

5.9.1.1 AC State Corner

In the next paragraphs the evaluation of the hierarchy of strengths in terms of the moment-axial load (M-N) interaction diagram is presented for corner beam column joint

of the most vulnerable joint, which is that of the long span of the frame. The AC state, which corresponds to:

(1) compression in the slab,
(2) decreasing axial load due to uplifting seismically induced shear in the beam, and
(3) the resistance of the spandrel in torsion is activated up to cracking only.

Looking back in the first section of this chapter, the right hand side of Equation 5.2, which determines the evaluation matrix for the as-built specimen (AB), is re-written for this particular case as presented in Equation 5.64. In this case, n = 4 elements and m = 2 demand scenarios. In addition the introduction of the upper script AC is required for identifying that the evaluation is being done for the AC state. The latter is used in the next part as well, where an AT upper script was used to denote that the evaluation is being done for the AT state.

$$[AB]_j^{AC} = \begin{bmatrix} E_{1j} & M_{1j} & N_{1j} \\ \vdots & \vdots & \vdots \\ E_{4j} & M_{4j} & N_{4j} \end{bmatrix}_{4x3} \tag{5.64}$$

Based on the $AB_{ij}^{AC} \in |R^{1x3}$ row vectors associated to the event i in the scenario j as found from Figure 5-5.19. The evaluation matrix for the corner joint for scenarios 1 and 2 is summarized in Equation 4.65.

$$[\mathrm{AB}]^{AC} = \left[\begin{bmatrix} S & 2.0 & 15.2 \\ J & 3.4 & 12.1 \\ C & 4.1 & 10.4 \\ B & 7.5 & 2.5 \end{bmatrix}_{j=1} \begin{bmatrix} S & 2.0 & 17.7 \\ J & 3.6 & 15.8 \\ C & 4.3 & 15.0 \\ B & 7.5 & 11.3 \end{bmatrix}_{j=2} \right] \tag{5.65}$$

This is the 'complete' matrix $[\mathrm{AB}]^{AC}$ which incorporates both scenario-matrices as a nx3m dimension matrix. In this case, the sequence matrix is given by Equation 5.66.

$$[SE] = [AB][1,0,0,1,0,0]^T \tag{5.66}$$

In this particular case:

$$[SE]^{AC} = \begin{bmatrix} S & S \\ J & J \\ C & C \\ B & B \end{bmatrix}$$

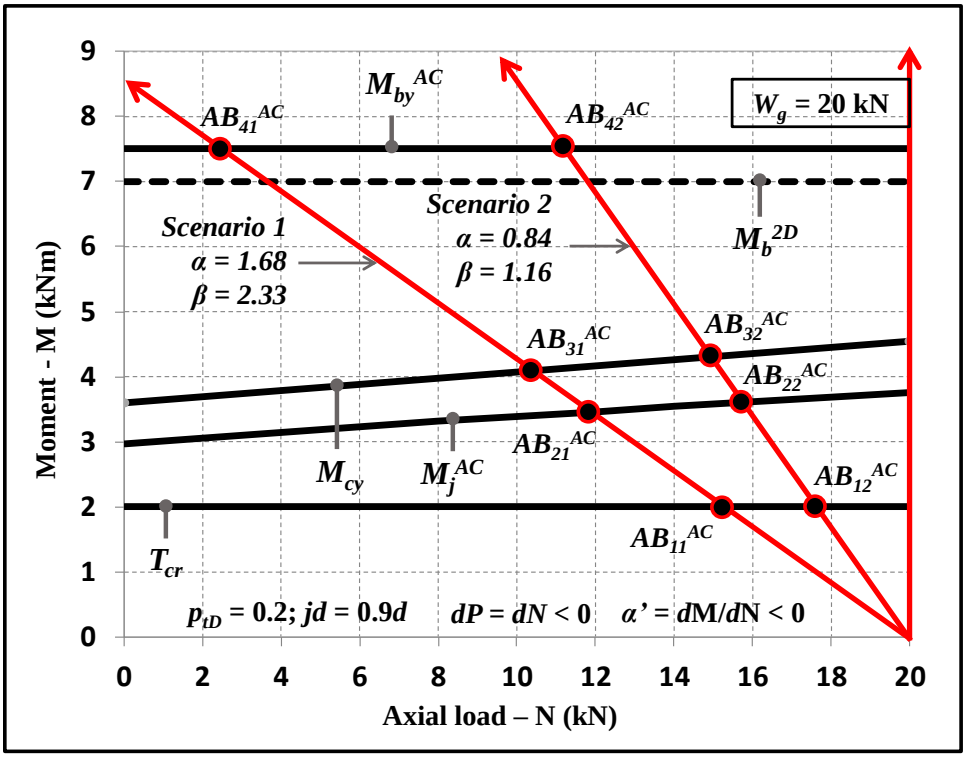

Figure 5-5.19: M-N performance domain in the AC state for corner beam column joints.

The $[SE]^{AC}$ matrix yields that there would be no difference between both scenarios, and that the sequence of events according to the evaluation of the M-N capacities would be:

(1) Cracking in the Spandrel (S)
(2) Cracking in the Joint (J)
(3) Yielding in the column (C)
(4) Yielding in the beam (B)

Note that the difference in the first four events in terms of capacity is rather small when compared to the capacity of the beam, which is about 2 times larger. This evaluation is in line with what was observed in the damage patter of the repaired-modified specimen, where torsion cracks developed significantly even before the joint cracked and failed in compression. It was also observed in that case that the columns and beams in corner joints remained mostly in the elastic range. In addition, it was found that the diagonal damage in corner joint of the long span was larger than in the short span counterpart, which is in accordance to the assumption of the long-span corner joint being the most vulnerable of the two of them.

5.9.1.2 AT State Corner

In this section the evaluation of the hierarchy of strengths in the AT state of the corner joint evaluated before is presented. In this state:

(1) the slab reinforcement is in tension,
(2) the is increasing axial load due to a downward shear in the beam, and
(3) the resistance of the spandrel in torsion is activated until yielding and/or maximum probable values due to over strength are reached (Shin et al. 2004).

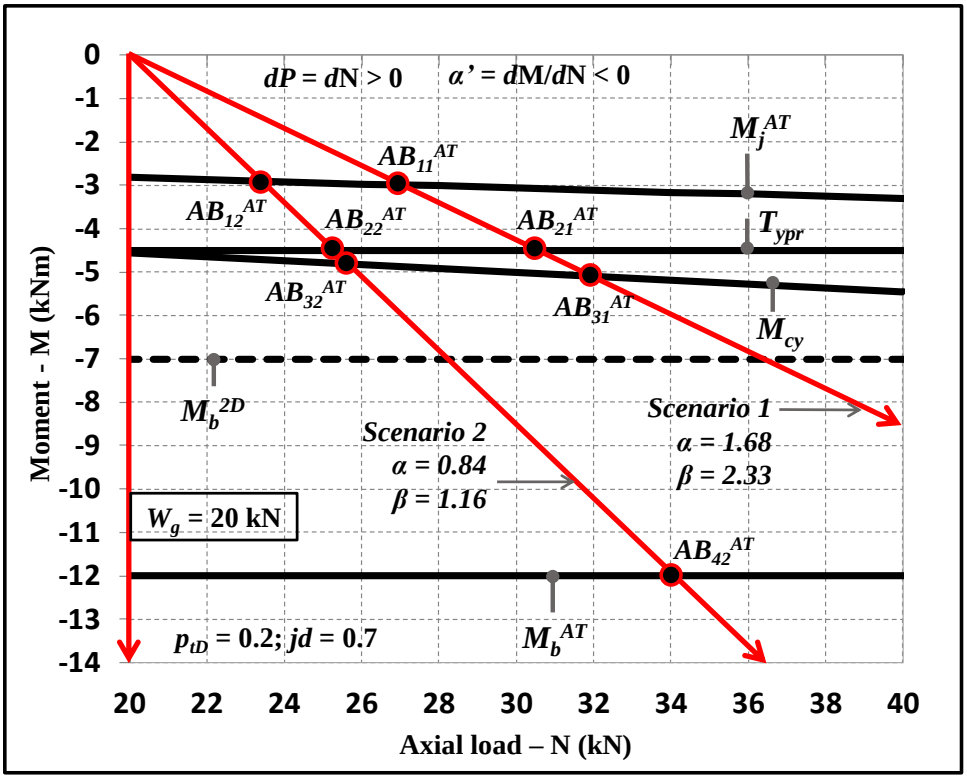

Figure 5-5.20: M-N performance domain in the AT state for corner beam column joints.

In this case, the evaluation matrix is presented in Equation 5.67, where an AT upper script was used to denote that the evaluation is being done for the AT state. In this case the sequence of events is slightly altered due to the greater resistance of the spandrel in the AT state. The over-strength of the beam calculations done for the yielding torque described previously is incorporated, in the light of experimental results done by Shin et al. (2004) on beam column joints with spandrel and slab.

$$[\mathrm{AB}]^{AT} = \left[\begin{bmatrix} J & -3.0 & 27.0 \\ S & -4.5 & 30.5 \\ C & -5.0 & 31.7 \\ B & -12.0 & 48.0 \end{bmatrix}_{j=1} \begin{bmatrix} J & -2.9 & 23.4 \\ S & -4.5 & 25.2 \\ C & -4.8 & 25.6 \\ B & -12 & 33.9 \end{bmatrix}_{j=2} \right] \tag{5.67}$$

The sequence matrix in this case is:

$$[SE]^{AC} = \begin{bmatrix} J & J \\ S & S \\ C & C \\ B & B \end{bmatrix}$$

This matrix reflects that there would be no difference between both scenarios, and that the sequence of events according to the evaluation of the strengths would be:

(1) Cracking in the Joint (J)
(2) Yielding (with over-strength) in the Spandrel (S)
(3) Yielding in the column (C)
(4) Yielding in the beam (B)

It is important to remark that in the as-built repaired specimen after the third series of shake table tests, the spandrel cracked in the AT state, after extensive damage was reached in the opposite direction (AC state) in the joint. Nevertheless it is thought that the full capacity of the spandrel in torsion resisted some of the actions in the panel zone alongside the joint. It is important to recall what was stated in Chapter 4 with regards of a more severe damage developed in the joint in the diagonal direction compatible with the AC state, where this effect was attributed to the a decreasing axial load in the joint, but also to a smaller resistance in torsion of the spandrel for boundary conditions considerations.

5.9.2 M-N Diagram for Cruciform Beam Column Joints (Internal Frame)

5.9.2.1 AC state cruciform

Just as it was done for corner joints, cruciform joints of the long span are evaluated. The same states named as AC and AT are separately studied, due to the asymmetrical nature of the problem due to the presence of the slab and spandrel. In Figure 5.21 the M-N capacity curves of the elements involved in the problem are plotted and the sequence of event evaluated accordingly, for two different scenarios, as it was done for corner joints.

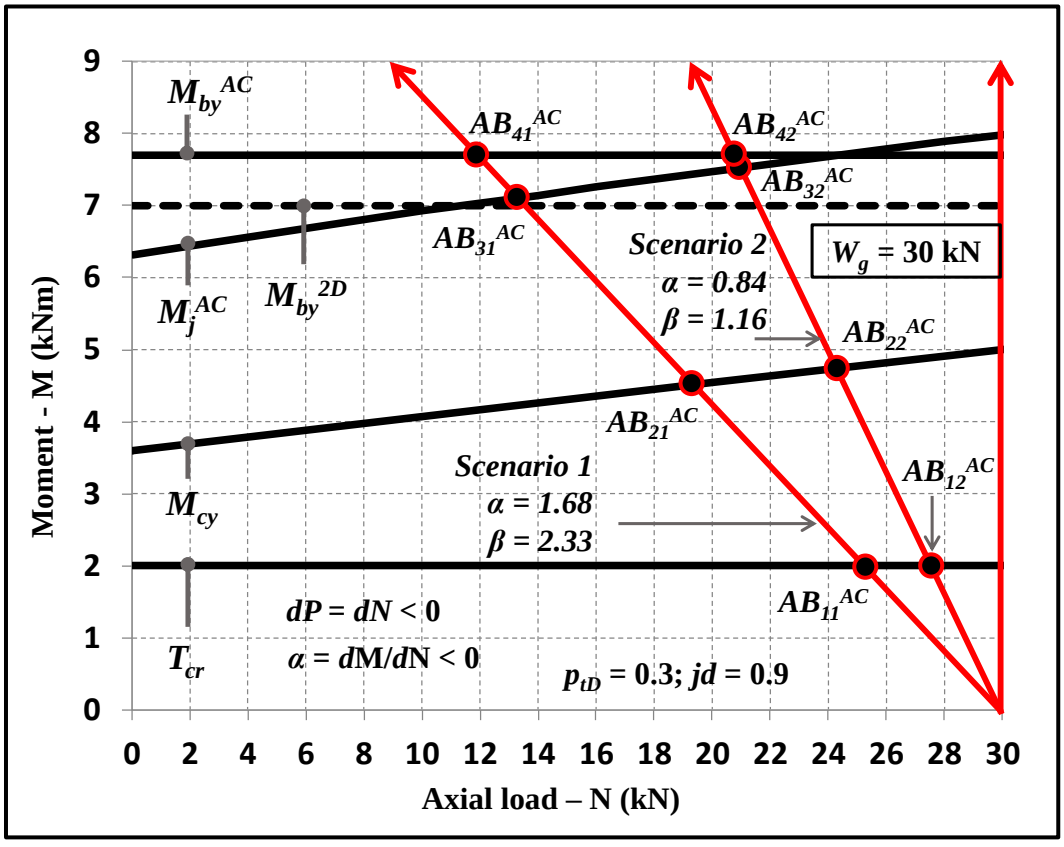

Figure 5.21: M-N domain for cruciform joints under AC state.

Gravitational weight increases in this case due to a larger floor collaborative area supported by internal frame columns when compared to external frames counterparts. The

evaluation matrix in this case is given by Equation 5.68, where the upper script denoted the AC state where the evaluation is being done.

$$[\mathrm{AB}]^{AC} = \left[\begin{bmatrix} S & 2.0 & 25.3 \\ C & 4.5 & 19.5 \\ J & 7.2 & 13.2 \\ B & 7.7 & 12.1 \end{bmatrix}_{j=1} \begin{bmatrix} S & 2.0 & 27.7 \\ C & 4.8 & 24.4 \\ J & 7.2 & 21.3 \\ B & 7.7 & 21.1 \end{bmatrix}_{j=2}\right] \tag{5.68}$$

In this case, the sequence of events matrix is:

$$[SE]^{AC} = \begin{bmatrix} S & S \\ C & C \\ J & J \\ B & B \end{bmatrix}$$

And hence the sequence of events can be summarized as:

(1) Cracking in the Spandrel (S)
(2) Yielding in the Column (C)
(3) Cracking in the Joint (J)
(4) Yielding in the Beam (B)

5.9.2.2 AT State Cruciform

In Figure 5.22 the M-N capacity curves are plotted and the sequence of events evaluated for two different scenarios, at AC and AT states. Gravitational weight is the same as for the previous scenario, meaning W_g = 30 kN. The evaluation matrix in this case is given by Equation 5.68, where the upper script denoted the AC state where the evaluation is being done.

$$[\mathrm{AB}]^{AT} = \left[\begin{bmatrix} S & -4.5 & 38.0 \\ C & -5.3 & 39.5 \\ J & -5.5 & 41.3 \\ B & -17 & 60.0 \end{bmatrix}_{j=1} \begin{bmatrix} S & -4.5 & 35.2 \\ C & -5.2 & 36.0 \\ J & -6.2 & 37.2 \\ B & -17 & 49.7 \end{bmatrix}_{j=2}\right] \tag{5.69}$$

The sequence of events vector in this case is given by:

$$[SE]^{AC} = \begin{bmatrix} S & S \\ C & C \\ J & J \\ B & B \end{bmatrix}$$

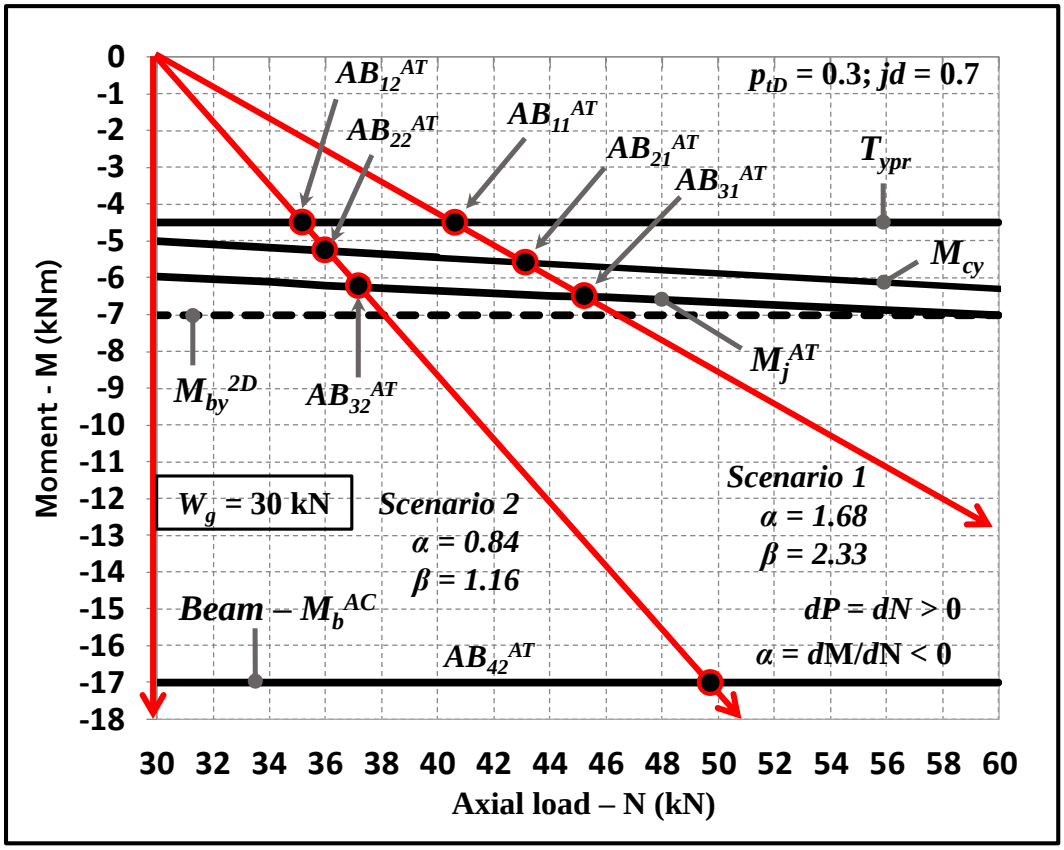

Figure 5.22: M-N domain for cruciform joints under AT state.

The sequence can also be summarized as follows:

(1) Yielding (with over-strength) in the spandrel (S)
(2) Yielding in the column (C)
(3) Cracking in the Joint (J)
(4) Yielding in the beam (B)

5.9.3 Complete Evaluation and Sequence of Events Matrix for all Joints

As was defined in the second section of this chapter, a unique matrix called [AB] which includes all scenarios and both typologies: corner and cruciform beam column joints. In this case, since n=4 and m=2, then [AB] corresponds to the 8x12 dimension matrix defined in Equation 5.70. The sequence of events matrix is given by [SE], an 8x8 dimension matrix, created with the sequence of events vectors for each scenario, state, and joint typology. The evaluation matrix is presented in Equation 5.71 and the sequence of events matrix in Equation 5.72.

In these last equations, the symbol * means that when reaching this event, the resisting moment contribution of the element reduces to zero after its capacity associated to the associated limit state is reached. When values denoted like this are reached in the sequence of events, but the next event in the sequence can still be triggered. The symbol † denotes that once the capacity of that element is reached, then the next ones cannot be developed or triggered, since the inelasticity will keep being cumulated in that element.

Therefore, next episodes in the saga cannot or will not be developed. In Equation 5.70: k = the beam column joint typology: k = 1, 2 refers to corner and cruciform, respectively.

$$[\mathrm{AB}]_{k=1,2} = \begin{bmatrix} [AB]_{j=1}^{AC} & [AB]_{j=2}^{AC} \\ [AB]_{j=1}^{AT} & [AB]_{j=2}^{AT} \end{bmatrix}_{k=1,2} \tag{5.70}$$

$$[\mathrm{AB}]_{k=1} = \begin{bmatrix} S^* & 2.0 & 15.2 & S^* & 2.0 & 17.7 \\ J^\dagger & 3.4 & 12.1 & J^\dagger & 3.6 & 15.8 \\ C & 4.1 & 10.4 & C & 4.3 & 15.0 \\ B & 7.5 & 2.5 & B & 7.5 & 11.3 \\ J^\dagger & -3.0 & 27.0 & J^\dagger & -2.9 & 23.4 \\ S & -4.5 & 30.5 & S & -4.5 & 25.2 \\ C & -5.0 & 31.7 & C & -4.8 & 25.6 \\ B & -12.0 & 48.0 & B & -12 & 33.9 \end{bmatrix} \tag{5.71}$$

$$[\mathrm{AB}]_{k=2} = \begin{bmatrix} S^* & 2.0 & 25.3 & S^* & 2.0 & 27.7 \\ C & 4.5 & 19.5 & C & 4.8 & 24.4 \\ J & 7.2 & 13.2 & J & 7.2 & 21.3 \\ B & 7.7 & 12.1 & B & 7.7 & 21.1 \\ S & -4.5 & 38.0 & S & -4.5 & 35.2 \\ C & -5.3 & 39.5 & C & -5.2 & 36.0 \\ J & -5.5 & 41.3 & J & -6.2 & 37.2 \\ B & -17 & 60.0 & B & -17 & 49.7 \end{bmatrix} \tag{5.72}$$

$$[\mathrm{SE}]_{tot} = \begin{bmatrix} S^* & J^\dagger & S^* & S \\ J^\dagger & S & C & C \\ C & C & J & J \\ B & B & B & B \end{bmatrix} \tag{5.73}$$

Noting that there is no difference in the sequence of events for each case in the two scenarios examined, the complete sequence of events matrix $[\mathrm{SE}]_{tot}$ which contains the four different sequences, each one for every different joint part of the building under study, as presented in Equation 5.73. In the final events matrix, the sequence of occurrence is different in all 4 cases, which is in line with what has been postulated before in terms of the mechanics involved in a beam column joint with slab and spandrel, based on the observations presented in Chapter 4. Note that even rows 3 and 4 seem to be different, they are not, since the symbol * denotes that in the third row the spandrel will lose its resisting capacity after the cracking torsion moment in the AC situation is reached, whereas the yielding (with over-strength) torsion capacity of the spandrel in the AT situation can be maintained after it is reached, just as all other elements in those rows. Therefore, the column would represent the fuse for these two sequences, corresponding to cruciform joints, whereas the joint will be the fuse in the first two rows corresponding to corner ones. The results of the evaluation are also presented in Table 5.1.

Table 5.1: Summary of the M-N performance domain evaluation of beam column joints.

Corner AC						Cruciform AC					
α = 1.68, β = 2.66			α = 0.86, β = 1.16			α = 1.68, β = 2.66			α = 0.86, β = 1.16		
Element	M (kNm)	N (kN)	Element	M (kNm)	N (kN)	Element	M (kNm)	N (kN)	Element	M (kNm)	N (kN)
S	2.0	15.3	S	2	17.7	S	2.0	25.3	S	2	27.7
J	3.4	12.1	J	3.6	15.8	J	4.5	19.5	J	4.8	24.4
C	4.1	10.4	C	4.3	15.0	C	7.2	13.2	C	7.5	21.3
B	7.5	2.5	B	7.5	11.3	B	7.7	12.1	B	7.7	21.1
Corner AT						Cruciform AT					
α = 1.68, β = 2.66			α = 0.86, β = 1.16			α = 1.68, β = 2.66			α = 0.86, β = 1.16		
Element	M (kNm)	N (kN)	Element	M (kNm)	N (kN)	Element	M	N	Element	M (kNm)	N (kN)
S	-3.0	27.0	S	-2.9	23.4	S	-4.5	40.5	S	-4.5	35.2
J	-4.5	30.5	J	-4.5	25.2	C	-5.3	42.3	C	-5.2	36.0
C	-5.0	31.7	C	-4.8	25.6	J	-5.5	42.8	J	-6.2	37.2
B	-12.0	48.0	B	-12	33.9	B	-17.0	69.6	B	-17	49.7

5.10 INELASTIC MECHANISM EQUILIBRIUM AND KINEMATICS

After the evaluation of the capacities at a local level have been evaluated and sequence of events estimated, the inelastic mechanism of the complete structure examined by means of equilibrium and cinematic compatibility. In this case, as was found during the performance of the as-built/repaired specimen, the inelastic dynamic response of the structure was dominated by a concentration of inter-storey drift in the first floor. Following the sequence of events presented in the matrix of Equation 5.73, and acknowledging the finding that some elements lose their resistance once their nominal capacity is reached as well as the tendency of others of absorbing/concentrating inelastic incursions, the inelastic mechanism of a single frame is shown in Figure 5.23.

For equilibrium of forces and moments about column 3, Equations 5.74 to 5.76 must be satisfied, noting that a uniform equivalent lateral set of forces was used as it is consistent with a uniform distribution of displacements along the height of the building.

$$3F = \Sigma V_0 \tag{5.74}$$

$$N_1 = N_3 + N_2 \tag{5.75}$$

$$6Fh = \Sigma M_0 + N_1(l_{n1} + l_{n2}) + N_2 l_{n2} \tag{5.76}$$

In the latter equations: F = the lateral force which produces the inelastic mechanism shown in Figure 5.23 ('collapse' lateral load); ΣV_0 = the sum of the shear forces in the columns at the base of the structure (total base shear); ΣM_0 = the sum of the moments in the columns at the base of the structure; ΣM_T = the sum of the moments at the top of the first storey; h = inter-storey height; N_i = axial force at the base of the column i; l_{n1} and l_{n2} = length of the left and right hand side spans, respectively. Since N_2 is small but not identical to zero due to the difference in the span lengths an assumption of $N_2 = 0$ can be done, still being on the safe side. This assumption is needed since there is a difference in the length of left and right hand side spans. If both span were equal, for symmetry then $N_1 = N_3$ and $N_2 = 0$.

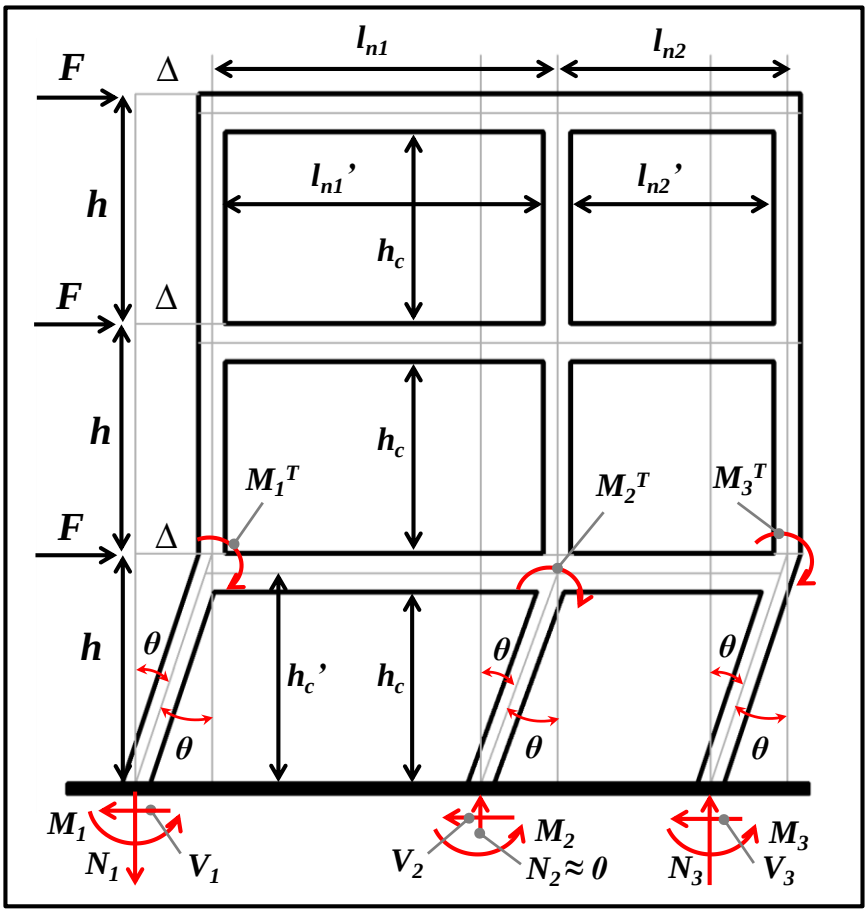

Figure 5.23: Inelastic mechanism – equilibrium of actions and cinematic compatibility.

Assuming that all inelasticity is concentrated in the first floor and using the virtual work theorem – external work applied (W_E) = internal virtual work done (W_I) – Equation 5.79 can be found based on the equality of Equations 5.77 and 5.78. Combining Equations 5.76 and 5.79, Equation 5.80 can be obtained.

$$W_E = 3F\Delta = 3Fh\theta \tag{5.77}$$

$$W_I = \theta(\Sigma M_0 + \Sigma M_T) \tag{5.78}$$

$$F = (\Sigma M_0 + \Sigma M_T)/3h \tag{5.79}$$

$$N_1 = N_3 = \frac{2(\Sigma M_0 + \Sigma M_T) - \Sigma M_0}{(l_{n1} + l_{n2})} \tag{5.80}$$

In the previous equations, new terms are: θ = lateral angle or drift in the first storey; and Δ = the lateral displacement measured at the top of each floor. Equation 5.80 corresponds to the axial load at the base of external columns compatible with the inelastic mechanism and the lateral force F (Figure 5.23). In this case, based on the evaluation of the capacities of critical elements in the building, the resisting moments at the top of exterior columns correspond to the joint equivalent moment capacity, whereas for the central column, its own yielding moment corresponds to the maximum moment capacity at the beam interface. Therefore Equation 5.80 can be re-written as Equation 5.81.

$$N_1 = N_3 = \frac{5M_c+2M_{j1}+2M_{j2}}{(l_{n1}+l_{n2})} \quad (5.81)$$

The solution for the axial load at a collapse level depends on the resisting moment of the element in the first floor which in turn depends on the axial load. Therefore, either analytical expressions are fitted to the capacity curves presented before in this chapter, or an iterative procedure using graphical methods needs to be incorporated. In this case, it can be demonstrated that the axial load which satisfies Equation 5.81 corresponds to N ≈ 11kN and the associated bending moments to M_c = 4.0 kNm, M_{j1} = 3.3kNm, M_{j2} = 3.0 kNm. As a result the lateral force associated to the collapse of the structure (base shear capacity) is estimated as F ≈ 7.3 kN and the base shear $Q_0 = \Sigma V_i$ = 22 kN.

5.11 CONCLUDING REMARKS

In Chapter 5 the assessment of the repaired specimen has been presented. The tools used for that followed sectional analyses of the beams and the columns for varying conditions and the procedure presented in Akguzel and Pampanin (2010) for the evaluation of the joint capacity. The bending moment-axial load M-N diagrams of the elements were compared in an extended version of that presented before in literature, due to the addition of a floor slab and a spandrel (transverse beam) together into the problem. In 3D specimens (Pampanin et al 2007, Akguzel 2011), there is a transverse beam and torsion is introduced by means of slaving the horizontal movement of both beams. However slabs in similar non-ductile specimens are not considered until Kam et al. (2010), Quintana-Gallo et al. (2011, 2012), and Akguzel and Pampanin (2012).

The presence of slab and a transverse beam or spandrel imposes strength asymmetry into the problem. They depend on each other to be activated as a resistant mechanism. With a slab with no spandrel, the steel would hardly yield in tension. It has been found previously (Di Franco 1995) the effective with depends on the strength of the spandrel. On the other hand a spandrel without a slab cannot develop the full yielding torsion resistance, which occurs in the AC case where the full yielding torsion strength cannot be developed. These observations and explanations were useful to explain the observed damage in beam column joints of the repaired specimen, where the diagonal damage in the joint was much more severe in the AC state, as discussed in Chapter 4.

5.12 REFERENCES

ACI Committee 318 (2011), *Building code requirements for structural concrete and commentary (ACI318M-11)*, American Concrete Institute, Farmington Hills, Michigan, USA.

Akguzel, U., and Pampanin, S. (2010), 'Effects of Variation of Axial Load and Bi-Directional Loading on Seismic Performance of GFRP Retrofitted Reinforced Concrete Exterior Beam-Column Joints', *Journal of Composites for Construction*, ASCE, Vol. 14(1), pp. 94–104.

Akguzel, U. (2011), 'Seismic Performance of FRP Retrofitted Exterior RC Beam-Column Joints Under Varying Axial and Bidirectional Loading', *a thesis presented for the degree*

of Doctor of Philosophy in Civil Engineering, University of Canterbury, Christchurch, New Zealand.

Akguzel, U., and Pampanin, S. (2012), 'Assessment and Design Procedure for the Seismic Retrofit of Reinforced Concrete Beam-Column Joints using FRP Composite Materials', *Journal of Composite for Construction*, ASCE, Vol. 16(1), pp. 21-34.

Andriono, T. And Park, R. (1986), 'Seismic Design Considerations of the Properties of New Zealand Manufactured Steel Reinforcing Bars', *Bulletin of the New Zealand Society for Earthquake Engineering*, Vol. 19(3), pp. 213-246.

Beyer, K., Dazio, A., Priestley, M. J. N. (2008), 'Quasi-Static Cyclic Tests of Two U-Shaped Reinforced Concrete Walls', Journal of Earthquake Engineering, Vol. 12(7), pp. 1023-1053

Collins, M. P. and Mitchel, D. (1992), *Prestressed Concrete Structures*, Prentice-Hall, Englewood Cliffs, New Jersey, USA

Chen, T. H. (2006), 'Retrofit Strategy of Non-Seismically Designed Frame Systems Based on a Metallic Haunch System, *a thesis submitted in partial fulfillment of the requirements for the degree of Master in Civil Engineering*, Department of Civil and Natural Resources engineering , University of Canterbury, Christchurch, New Zealand.

Di Franco, M. A., Mitchell, D., Paultre, P. (1995), 'Role of Spandrel Beams on Response of Slab-Beam-Column Connections', Journal of Structural Engineering, Vol. 121(3), pp. 408-419.

Dodd, L. L., and Cooke, N. (1992), 'The Dynamic Behaviour of Reinforced-Concrete Bridge Piers Subjected to New Zealand Seismicity', *Research Report*, 92-04, Department of Civil and Natural Resources Engineering, University of Canterbury, Christchurch, New Zealand.

Dodd, L. L. and Restrepo-Posada, J. I. (1995), 'Model for Predicting Cyclic Behaviour of Reinforcing Steel', *Journal of Structural Engineering*, ASCE, Vol. 121 (3), pp.433-445.

Durrani, A. and Zerbe, H. (1987), 'Seismic Resistance of R/C Exterior Connections with Floor Slab' *Journal of Structural Engineering*, Vol. 113(8), pp. 1850–1864.

Ehsani, M. R., and Wight, J. K. (1985), 'Exterior Reinforced Concrete Beam-to-Column Connections Subjected to Earthquake-Type Loading', *ACI Journal*, Vol. 84(2), pp. 492-499.

Hakuto, S., Park, R., and Tanaka, H. (2000), 'Seismic Load Tests on Interior and Exterior Beam-Column Joints with Substandard Reinforcing Details', *ACI Structural Journal*, Vol. 97(1), pp. 11-25.

Hsu, T. C. (1968), Torsion of Structural Concrete-Behaviour of Reinforced Concrete Rectangular Members', *Torsion of Structural Concrete*, SP-18, American Concrete Institute, pp.261-206.

Hognestad, E., 'A Study of Combined Bending and Axial Load in Reinforced Concrete Members', *University of Illinois Bulletin*, Vol. 49(22).

Kam, W.Y., Quintana-Gallo, P., Akguzel, U., Pampanin, S. (2010) 'Influence of slab on the seismic response of substandard exterior reinforced concrete beam column joints', *Proceedings of the for 9th US and 10th Canadian National Conference on Earthquake Engineering*, Toronto, Canada.

Kam, W.Y. (2010), 'Selective Weakening and Post-Tensioning for the Seismic Retrofit of Non-Ductile RC Frames', *a thesis presented for the degree of Doctor of Philosophy in Civil Engineering*, University of Canterbury, Christchurch, New Zealand.

Kent, D. C, and Park, R. (1971), 'Flexural members with confined concrete', *Journal of the Structural Division*, ASCE, Vol. 97(7), pp. 1969-1990.

Kunnath, S. K., Heo, Y., and Mohle, J. F. (2009), 'Nonlinear Uniaxial Material Model for Reinforcing Steel Bars', *Journal of Structural Engineering*, Vol. 135(4), pp. 335–343.

MacGregor, J.G. and Ghoneim, M. G. (1995), 'Design for Torsion', *ACI Structural Journal*, Vol. 92(2), pp. 211-218.

Mander, J.B., Priestley, M.J.N, and Park, R. (1984), 'Seismic Design of Bridge Piers', *Research Report 84-2*, Department of Civil Engineering, University of Canterbury, Christchurch, New Zealand.

Mander, J.B., Priestley, M.J.N, and Park, R. (1988), 'Theoretical Stress-Strain Model for Confined Concrete', *Journal of Structural Engineering*, ASCE, Vol. 114(8), pp. 1804-1826.

Pampanin, S., Calvi, G.M., Moratti, M. (2002) 'Seismic Behaviour of RC Beam Column Joints Designed for Gravity Loads', *12th ECEE*, London, England

Pampanin, S., Bolognini D., and Pavese, A. (2007) 'Performance-Based Seismic Retrofit Strategy for Existing Reinforced Concrete Frame Systems Using Fiber-Reinforced Polymer Composites', *Journal of Composites for Construction*, ASCE, Vol. 11(2), pp. 211-226.

Park, R. and Paulay, T. (1975) *Reinforced Concrete Structures*, John Wiley and Sons Inc., New York, USA.

Park, R., Priestley, M. J. N., and Gill, W. D. (1982), 'Ductility of Square-Confined Concrete Columns', *Journal of the Structural Division*, ASCE, 108(4), 929-950.

Priestley, M.J.N. (1996) 'Displacement-Based Seismic Assessment of Existing Reinforced Concrete Buildings', *Bulletin of the NZSEE*, Vol. 29(4), pp. 256-267.

Quintana-Gallo, P. (2008), 'Evaluación Analítica del Daño en un Edificio de Hormigón Armado', *thesis submitted in partial fulfilment of the requirements for the degree of Magister en Ciencias de la Ingeniería Civil Área Estructuras*, Departamento de Obras Civiles, Universidad Técnica Federico Santa María, Valparaíso, Chile (*in Spanish*).

Quintana-Gallo, P., Pampanin, S., Carr, A.J., Bonelli, P. (2010), 'Shake Table Tests of Under-Designed Frames for the Seismic Retrofit of Buildings – Design and Similitude Requirements of the Benchmark Specimen', *proceedings of the NZSEE*, Auckland, paper 121.

Quintana-Gallo, P., Akguzel, U., Pampanin, S., and Carr, A.J. (2011), 'Shake Table Tests of Non-Ductile As-Built and Repaired RC Frames', *Proceedings of the Pacific Conference on Earthquake Engineering*, Auckland, paper 201.

Restrepo-Posada, J., Dodd, L., Park, R., and Cooke, N. (1994), 'Variables Affecting Cyclic Behavior of Reinforcing Steel', *Journal of Structural Engineering*, Vol. 120(11), pp. 3178–3196.

Richart, F. E., Brandtzaeg, A., and Brown, R. L. (1929), 'The Failure of Plain and Spirally Reinforced Concrete in Compression', *Bulletin 190*, Univ. of Illinois Engineering Experimental Station, Champaign, 111.

Rodriguez, M. E., Botero, J. C., Villa, J. (1999), 'Cyclic Stress-Strain Behavior of Reinforcing Steel Including Effect of Buckling', *Journal of Structural Engineering*, ASCE, Vol. 125 (6), pp.605-612.

Rodriguez, M. E., Ortiz, A., Torres-Matos, M. A. (2013), 'Diseño Sísmico de Muros de Concreto Reforzado Basado en Desplazamiento', *XIX Congreso Nacional de Ingeniería Sísmica*, Veracruz (*in Spanish*).

Saatcioglu, M. and Razvi, S. R. (1992), 'Strength and Ductility of Confined Concrete', *Journal of Structural Engineering*, ASCE, Vol. 118 (6), pp.1590-1607.

Salamat, A., and Saatcioglu, M. (1991), 'Tests of confined columns under eccentric loading' *Research Report No. 9103*, Department of Civil Engineering, University of Ottawa, Ottawa, Canada.

Shin M and LaFave J. M. (2004), 'Reinforced Concrete Edge Beam-Column-Slab Connections Subjected to Earthquake Loading,' *Magazine of Concrete Research*, Vol. 56(5), pp. 273-291.

Scott, B. D., Park, R., and Priestley, M. J. N. (1982), 'Stress-strain behavior of concrete confined by overlapping hoops at low and high strain rates', *ACI Journal*, Vol. 79(1), pp.13-27.

Sheikh, S. A., and Uzumeri, S. M. (1980), 'Strength and ductility of tied concrete columns', *Journal of the Structural Division*, ASCE, Vol. 106(5), pp.1079-1102.

Thomsen, J.H., (1995), 'Displacement Based Design of Reinforced Concrete Structural Walls: An experimental Investigation of Walls with Rectangular and T-Shaped Cross – Sections', *thesis submitted in partial fulfilment of the requirements for the degree of Doctor of Philosophy*, Clarkson University, Potsdam, New York. USA.

Thomsen, J., Wallace, J. (2004), 'Displacement-Based Design of Slender Reinforced Concrete Structural Walls – Experimental Verification', *Journal of Structural Engineering*, ASCE, Vol. 130, No. 4

Thompson, K.J. and Park, R. (1978), "Stress-Strain Model for Grade 275 Reinforcing Steel with Cyclic Loading", *Bulletin of New Zealand National Society for Earthquake Engineering*, Vol. 11(2), pp.101-109.

Wallace, J. W., Ibrahim, Y. (1996), *Biax-96 for MS Windows – Strength and Analysis of RC Sections*, University of California, Los Angeles, USA.

6 RETROFIT INTERVENTION DESIGN

6.1 INTRODUCTION

After the deficiencies found in experimental Series 1, the repaired as-built specimen, apparently upgraded after the lap splices problem was mitigated, the specimen was found to still be vulnerable, when experiencing heavy damage in first floor exterior joints and columns in Series 2. In order to mitigate the beam column joint problem this time a retrofit intervention consisting in the use of Glass Fibre Reinforced Polymer (GFRP) laminates suitable for the specimen was developed based on previously developed layouts (Pampanin et al. 2007, Akguzel 2011, Akguzel and Pampanin 2012). The concept of selective weakening (Kam 2011) was also incorporated in the intervention, but applied to the floor slab rather than the beam itself as proposed by other researchers.

In this chapter, the layout of the FRP laminates for strengthening the beam column joints as well as the weakening configuration for the floor slab are described. The strategy followed a 'partial retrofit strategy' (Pampanin 2005). That is, interior joints and columns were not modified and left free to rock. Therefore, a pure beam sway mechanism was not targeted in this case, in the light of the high rotation capacity of the as-built columns.

The techniques selected before had been only implemented in beam column joints of plane frames subassemblies, 2-dimensional and/or 3-dimentional subjected to lateral slow motion simulated loading. In the case of GFRP layers, many configurations of FRP layers can be found to date in the literature as shown in Chapter 2. Of the strategies available in the literature, none has the same shape as the one developed and implemented in this work. However, it is directly based on work done by Akguzel (2011) at the University of Canterbury. The design guidelines also available in Akguzel and Pampanin (2012) for corner beam column joints without floor slabs, was used as a basis for designing a suitable GFRP laminates layout suitable for this case where (1) the slab is incorporated, (2) the transverse beam effect is activated, and (3) external joints of internal frames (cruciform joints) are also included.

Weakening of the slab was required to achieve the desired inelastic mechanism, since the contribution of the slab reinforcement acting in tension increases significantly the negative bending capacity of the beam, as shown in Chapter 5. At the University of Canterbury, weakening of beam column joints was part of the work done by Kam (2011). In that case, plain specimens were used for demonstrating the ability of reducing the rectangular beam capacity and increasing confinement in the joint by adding post-tensioned external tendons. Only one specimen was constructed with floor slabs and transverse beam on both sides, which is equivalent to those tested by Ehsani and Wight (1985), but with non-ductile detailing. The conceptual approach of reducing the capacity of critical members in order to upgrade the performance of the complete beam column joint subassembly was used in this thesis as a basic background for the development of the slab weakening. However, beam bars were kept intact, as it is argued that weakening in such a critical part of the structure may be dangerous. Weakening of the floor slab on the other hand, is seen to be a safer intervention, given the ability of floors slabs to redistribute the resisting path due to their high structural redundancy (membrane action).

The intervention developed was evaluated in the extended M-N performance domain presented in Chapter 5. The philosophical approach used in the design process focused on the capacity of the elements, so that the demand was not relevant as a parameter. That philosophy behind is nothing else than capacity design principles for ensuring full ductility until the ultimate state is reached, independently of the demand. In order to achieve the damage relocation during the dynamic response of the upgraded specimen, the inelastic mechanism (statically admissible and kinematical-compatible) of the frame is reviewed. Using the moment diagrams at ultimate state that can be developed in the structure, the length of the laminates was modified. The final retrofit intervention developed was found to be theoretically able to relocate the brittle failure mode observed previously in the joints into ductile inelastic incursions in the beams and some columns.

6.2 RETROFIT STRATEGY

In Figure 5.23, the traditional pushover curve representing the phases that a single degree of freedom structure experiences at increasing lateral displacements is presented. The conceptual framework where this limit states are related to 'intensity' levels was given firstly by SEAOC (1995), in the Vision 2000 document. From there onwards, many other contributions have included Intensity Measures (IM) associated to probability functions.

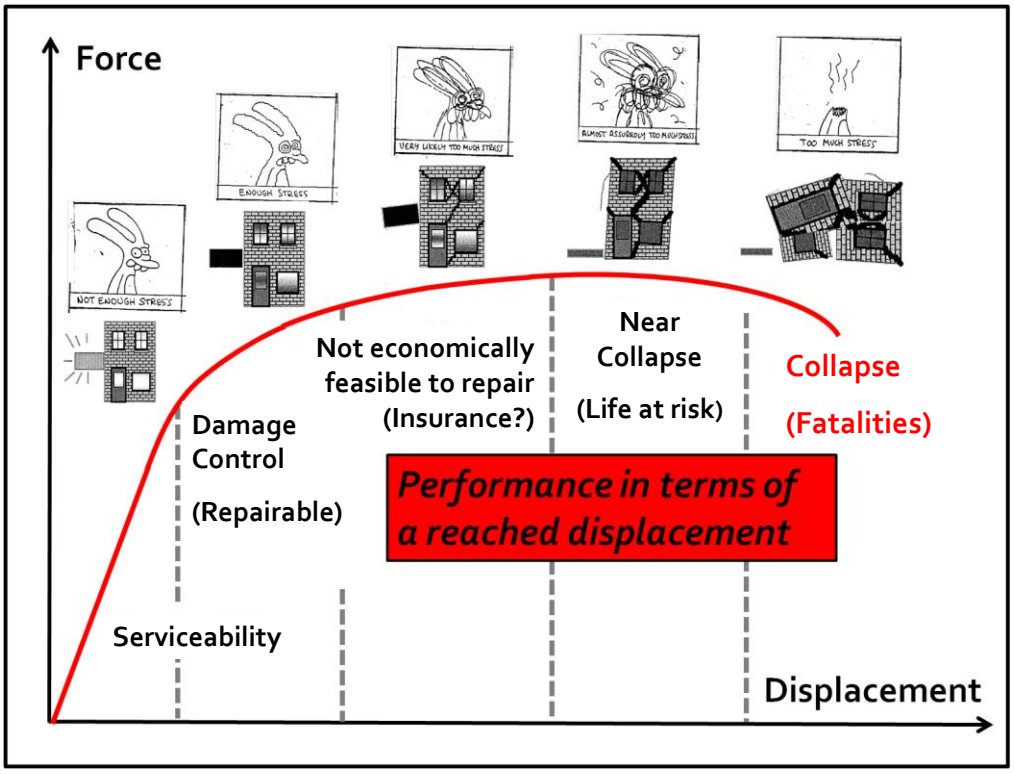

Figure 6.1: Conceptual limit states in terms of capacity and performance.

The demand associated to that limit state is a matter of discussion. In what can be called 'traditional' performance-based design, a certain earthquake should be selected in terms of the level of 'intensity'. The level of the 'intensity' is associated to a certain probability of exceedance of that level of intensity to occur during the design working life of the structure. The demand parameter associated to intensity is typically the amplitude of the

acceleration spectrum. This variation in the amplitude of the acceleration spectra can be associated to a variation of the peak ground acceleration (PGA), which in turn can be described by a probabilistic law (ad-hoc), based on statistical inference of the data recorded to date. There is however, important assumption for this approach randomness of the measured variables, like PGA, for example. The non-periodic nature of damaging earthquakes suggests that the variables associated to damage or seismic intensity may be chaotic in nature (Strogatz 1994, Lorenz 1963, Quintana-Gallo et al. 2013).

In this sense, it can be argued that the 'next' strong event, meaning destructive, can always be larger in terms of intensity as well as in earthquake demand parameters like the response spectrum. Furthermore, as was observed in the shake table tests described in Chapter 4, for similar levels of the spectral acceleration amplitude and PGA, completely different responses were found, the difference being in the frequency content and the duration of the input motion (see Chapter 4). Moreover, the inclusion of time into the problem, which is the main feature of this investigation, the times the inelastic limit state is reached, exceeded or 'nearly reached, is of the most important relevance, and may change the destiny of a building importantly.

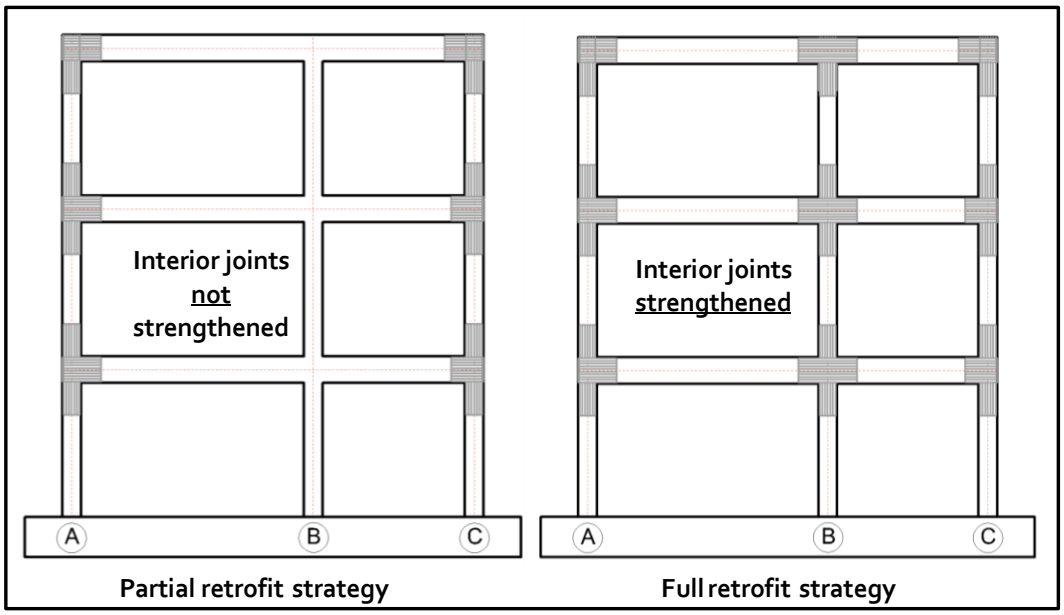

Figure 6.2: Partial and full retrofit strategies as proposed by Pampanin (2005).

Coherently with the ideas stated above, the retrofit intervention was designed to relocate the mechanism and be able to withstand a record motion that could impose large inelastic demands in the building. Therefore the main target in terms of performance is the modification of the inelastic mechanism induced by a very demanding ground motion for the structure. In order to achieve that goal, a partial retrofit intervention was selected as a strategy This partial retrofit strategy consist in the upgrading of exterior beam column joints only (Pampanin 2005), allowing central columns to rock, given that they were predicted to be able to withstand large rotations in a ductile way. A shift of the brittle soft-storey mechanism observed in the shake table tests of the repaired specimen was intended to be achieved. A mixed beam-sway-column mechanism with concentrated inelasticity in the beams of exterior beam column joints and internal and base columns was therefore considered to be enough for withstand large inter-storey displacements in a

ductile and stable way. In Figure 6.2 a partial intervention as well as a full intervention of an individual frames is shown. In this case, FRP laminates have been chosen for strengthening the panel zone region and relocating the damage to the beams.

6.3 MECHANICAL PROPERTIES OF THE FRP

The FRP selected in this case was that made of glass fibres (GFRP). The selection of this material was preferred to carbon fibre sheets (CFRP) because it is cheaper, but mostly because, acknowledging the brittle nature of FRP in general, GFRP has a smaller young modulus than CFRP ('less stiff'), which enables the possibility of experiencing larger strains before reaching the maximum allowable stress and debonding occurs. Therefore, as a composite material, it should be able to undertake the strains induced by seismic actions in structural elements – beam columns and joints in this case.

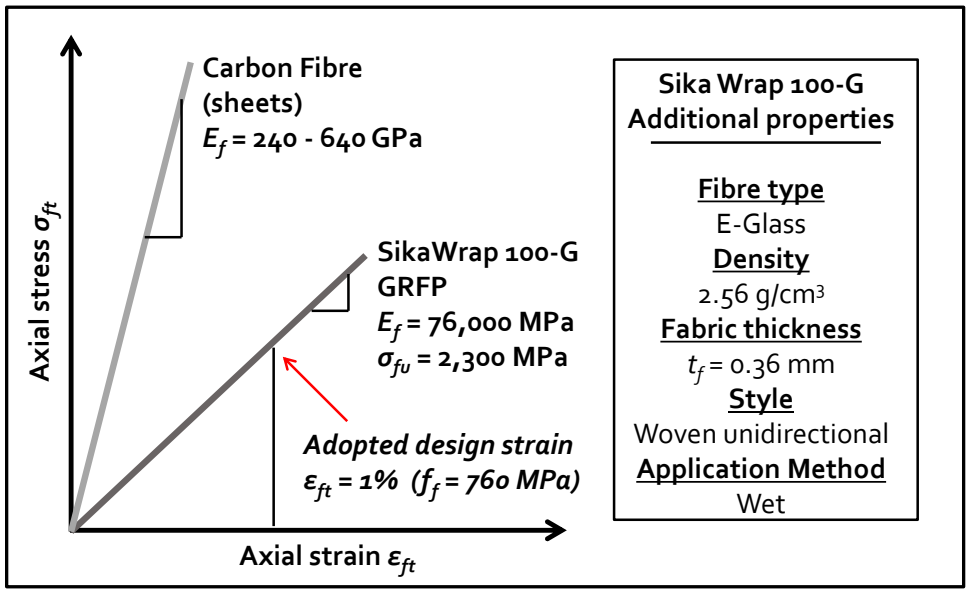

Figure 6.3: GFRP mechanical properties – comparison with carbon fibres in terms of stiffness.

The mechanical characteristic of the GFRP sheets used are presented in Figure 6.3, where the stress-strain curves for both glass and carbon FRP are also shown for comparison. A design maximum strain in GFRP laminates of ε_{ftD} = 1% was selected. This value is lower than that considered in previous research (Akguzel and Pampanin 2012), where a value of ε_{ftD} = 1.8% is used in design. Other references such as design sheets provided by the industry are situated in the range of 2% for glass fibre and 1% for carbon. Debonding effects though, as explained in deep detail in Akguzel (2011), may limit the maximum strain that the layers can take without losing the bond with the adjacent concrete. This value was selected arbitrarily as a conservative value for design during the development of the retrofit intervention.

As shown in Figure 6.3, only a capacity of 760 MPa in tension is being considered as a 'usable' stress of the composite material. This introduces resilience in the capacity of the material, in order to compensate for its brittle nature. With the selection of ε_{ftD} = 1% as limit state in the GFRP layers as well as the mechanical characteristics of steel and

concrete presented in Chapters 3 and 4, the capacity curves of the structural members converging in the panel zone, upgraded with a certain number and layout of GFRP layers are constructed with the aim of reverting the hierarchy of strengths of those members.

The main challenge was to upgrade joints and columns so that their capacity was larger than the beam under negative moment, due to the presence of the floor slab and the consequent greater bending capacity. As will be shown later, weakening of the floor slab around the FRP core in the beam column joint allowed for the retrofit intervention to be feasible as a whole. In the following paragraphs the layout of the FRP sheets used for strengthening corner and cruciform exterior joints is introduced.

6.4 GFRP STRENGTHENING SCHEME DESCRIPTION AND SEQUENCE OF APPLICATION

The GFRP configuration developed in this research was conceived based on the layout used by previous researchers for plane and 3D beam column joints without floor slabs (Akguzel and Pampanin 2010, 2012; Akguzel 2011). The main contribution in that sense, is the improvement of the previously proposed scheme and guidelines to a specimen which has a concrete cast in situ slab, and to develop a similar scheme for exterior joints of internal frames referred here as 'cruciform'.

6.4.1 GFRP scheme overview and features

The design of the retrofit intervention was done following the guidelines proposed by Akguzel and Pampanin (2012) for beam column joint strengthened with GFRP with modifications for the incorporation of the floor slab and transverse beam. The solution was conceived as an extended version of that implemented in beam column joints without floor slabs. The solution has the following features:

1) The FRP sheets for confinement of the orthogonal beam are used for strengthening the beam in flexure as well as lateral sheets.
2) L-shaped sheets where included in the inner side of the column in order increase the flexural capacity under negative moment in the beam (AT situation)
3) The intended place where the inelastic behaviour is intended to be relocated is enhanced by deactivating the slab bars from the rigid FRP core, in a configuration which takes into account the path for inertial forces in the slab (diaphragm).

In Figure 6.4, a 3D view of the retrofitted specimen with all the laminates in place is presented. In Figure 6.4, the four joints which are examined in detailed in the next sections are identified. These are: (1) a corner joint of the long span and an intermediate floor; (2) a corner joint of the long span and the roof level; (3) a cruciform joint of the long span and an intermediate floor, and (4) a cruciform joint of the long span and the roof level.

It is worth noting that all counterpart joints of the short span are almost identical to those explained in this chapter, but differ only on the length of the beam sheets beyond the face of the columns, which is 100 mm instead of 150mm as shown in the next sections. The reason why this length is different is due to the kinematics and capacity considerations

after the collapse mechanism has been developed. That is explained in the last part of this chapter.

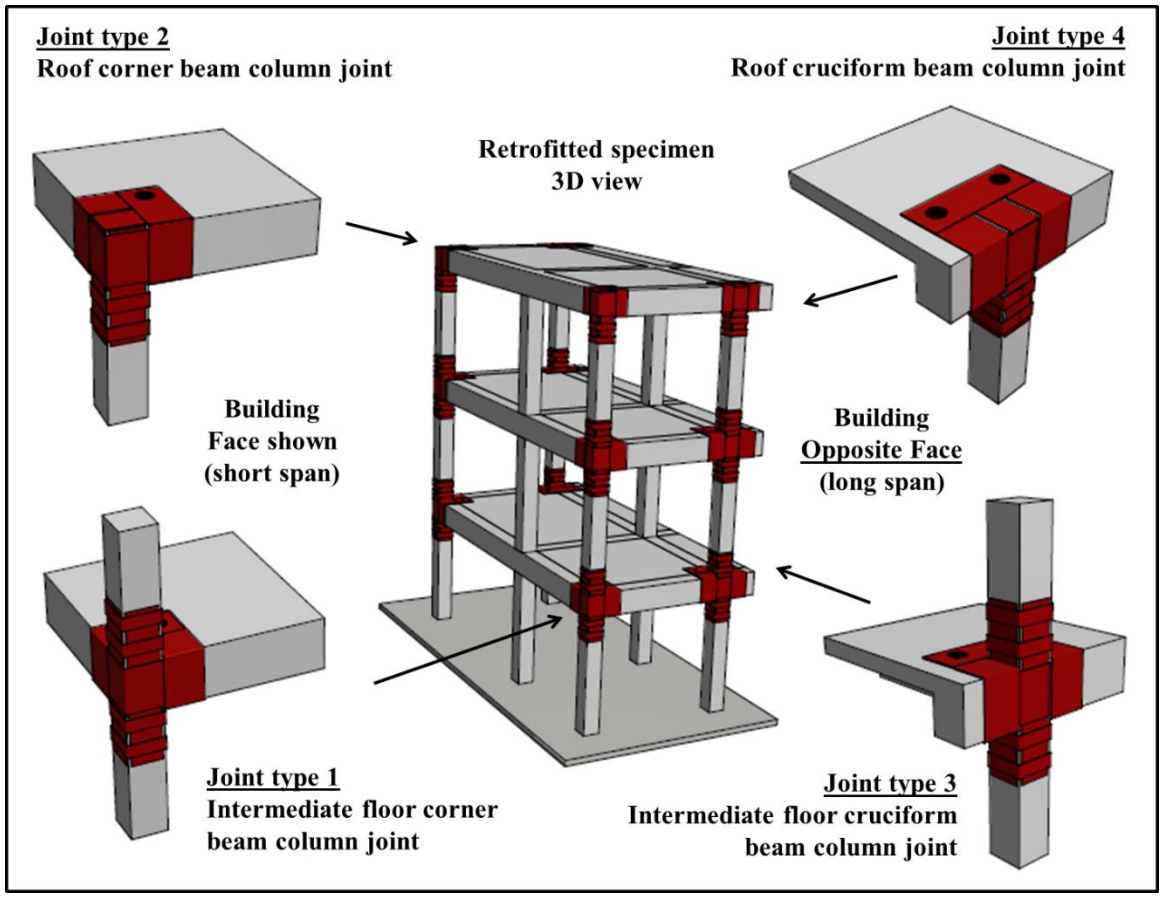

Figure 6.4: Retrofitted specimen 3D view and beam column joint type identification.

The sequence of application of the GFRP layers in the joints identified in Figure 6.4 is shown in the next sections.

6.4.2 GFRP sheets sequence of application for corner beam column joints

The sequence of application of the laminates in corner beam column joints of an intermediate floor (Joint type 1, typical) is presented in Figure 6.5 and Figure 6.6. This joint also corresponds to that of the long span, given the differnce remarked before. In Figure 6.7 and Figure 6.8 the same configuration is shown this time for the top storey (roof) Joint type 2, which has no column at the top part of the panel zone.

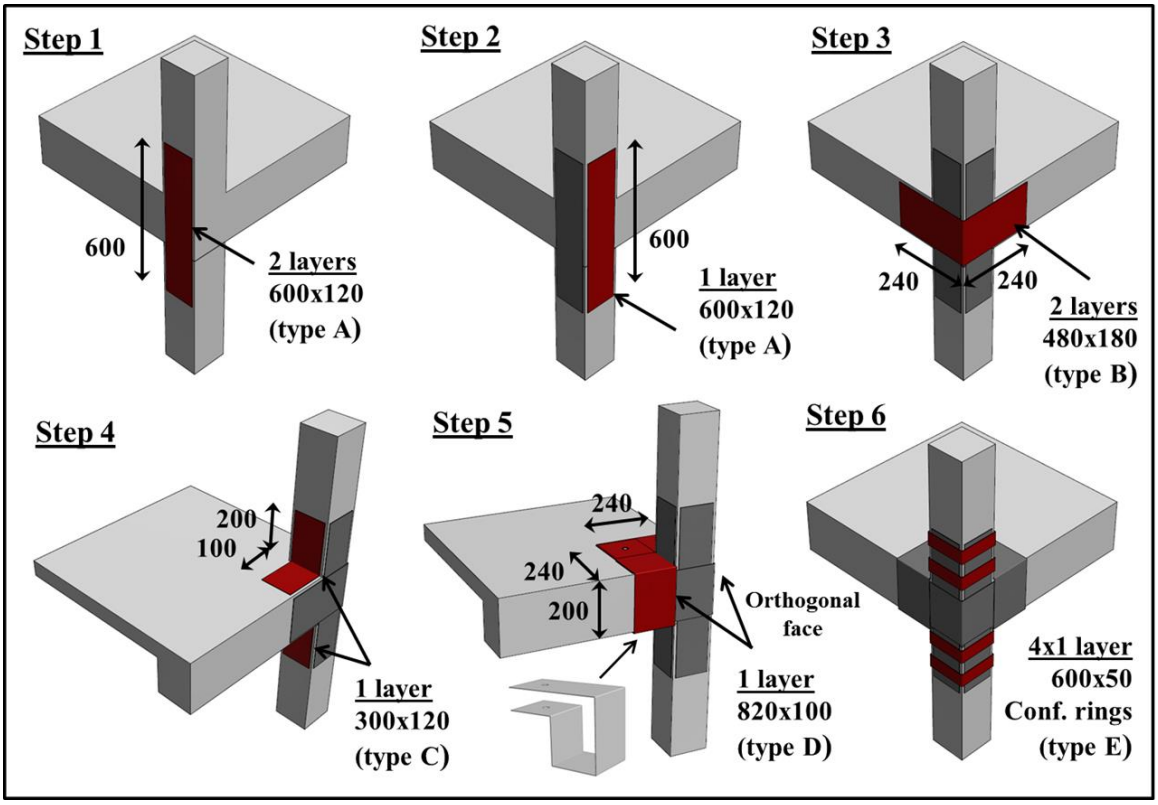

Figure 6.5: GFRP sequence of application for Joint type 1, Steps 1 to 6. Note: for long span joints the length of the sheets in the direction of the beams are 50 mm larger.

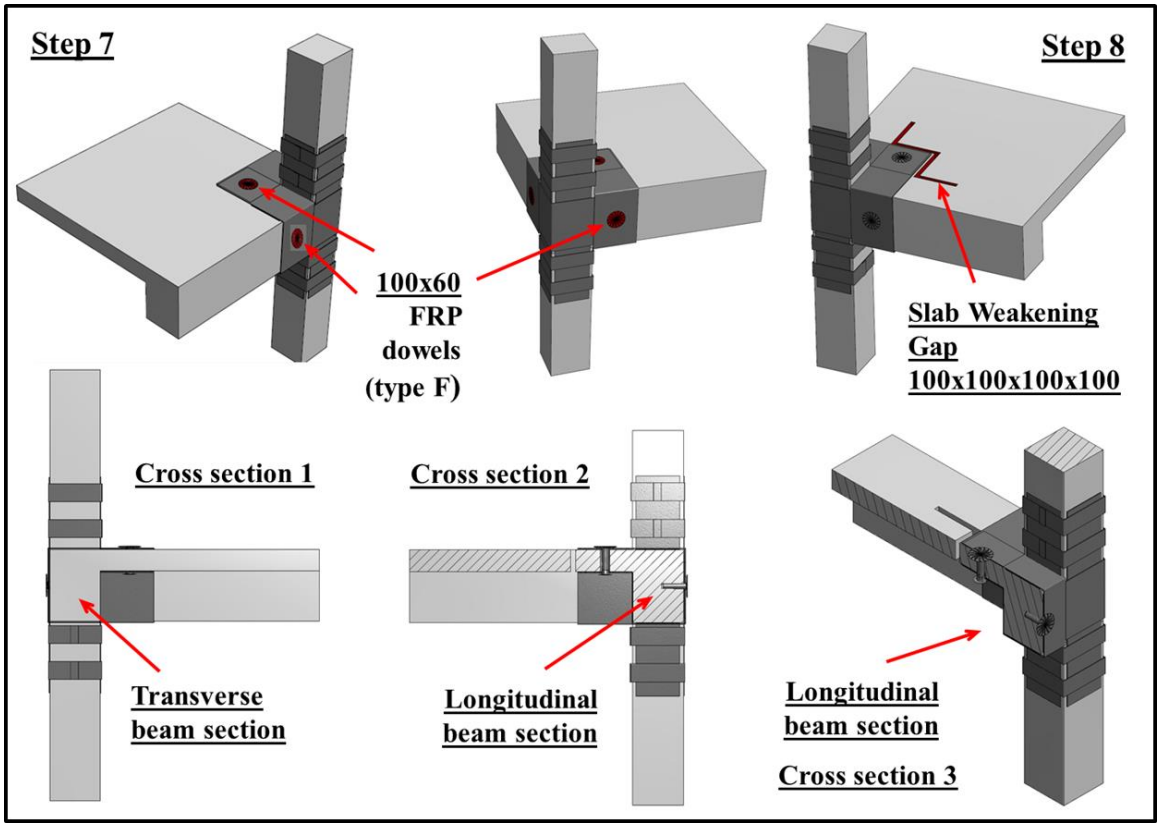

Figure 6.6: GFRP sequence of application Joint type 1, Steps 7 to 8; cross sections showing anchorage.

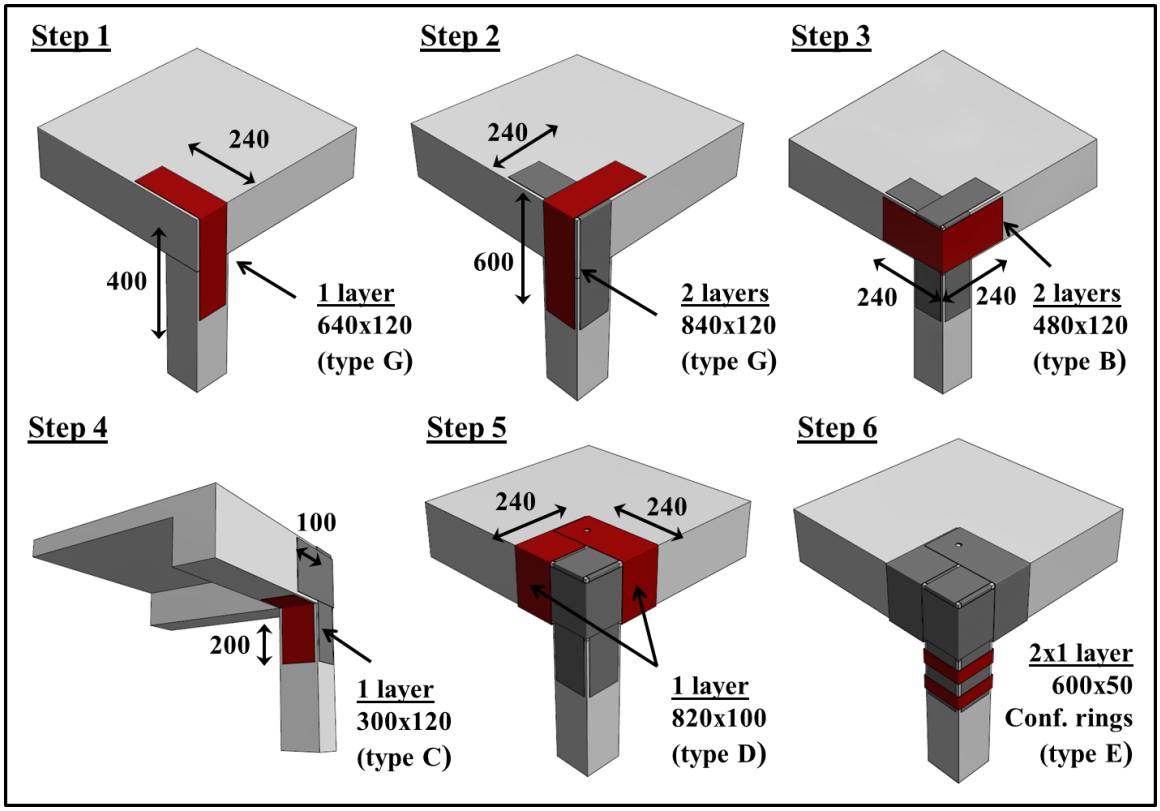

Figure 6.7: GFRP sequence of application for Joint type 2, Steps 1 to 6.

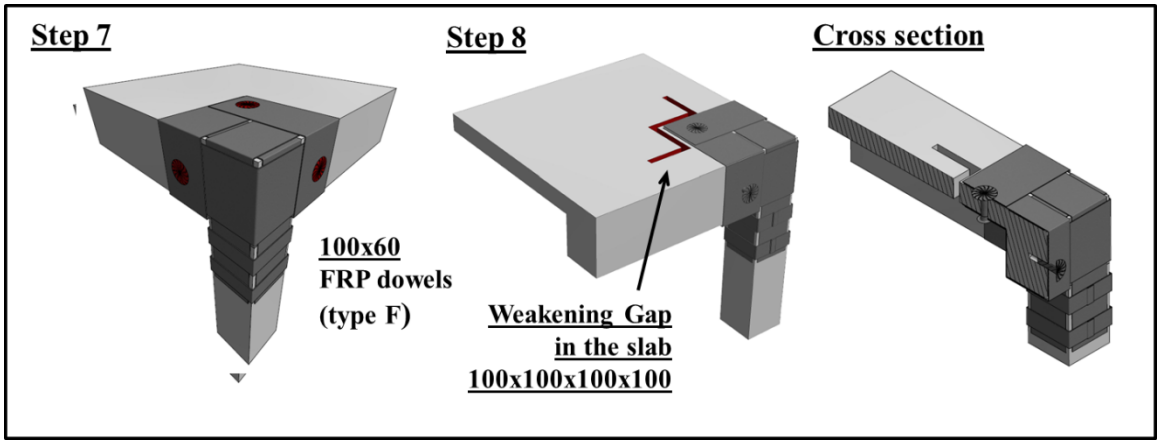

Figure 6.8: GFRP sequence of application Joint type 2, Steps 7 and 8; cross section showing anchorage details.

As will be shown later, weakening of the floor slab around the FRP core in the beam column joint, allowed for the retrofit intervention to be feasible as a whole. In the following paragraphs the layout of the FRP sheets used for strengthening corner and cruciform exterior joints.

6.4.3 GFRP sheets sequence of application for cruciform beam column joints

The sequence of application of the GFRP laminates in cruciform beam column joints corresponds to that described schematically in Figure 6.9 to Figure 6.12. In Figure 6.9 and Figure 6.10 the sequence of application is shown for the cruciform Joint type 3.

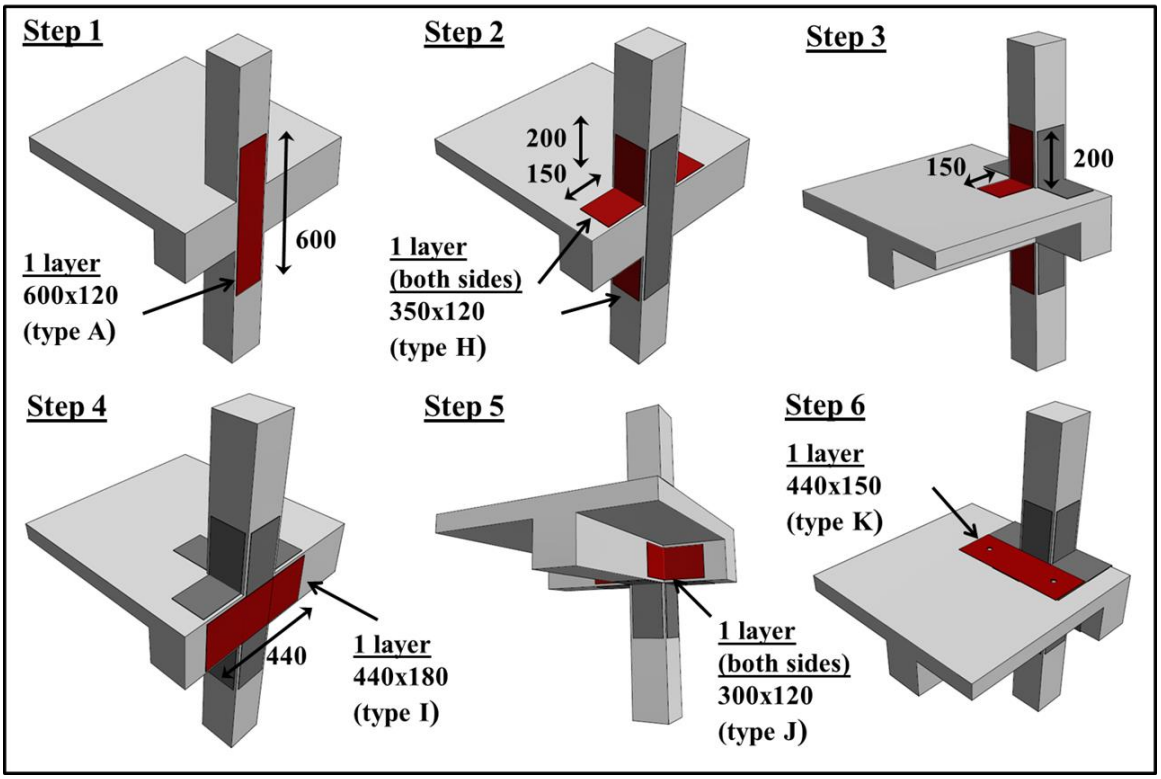

Figure 6.9: GFRP sequence of application Joint type 3, Steps 1 to 6.

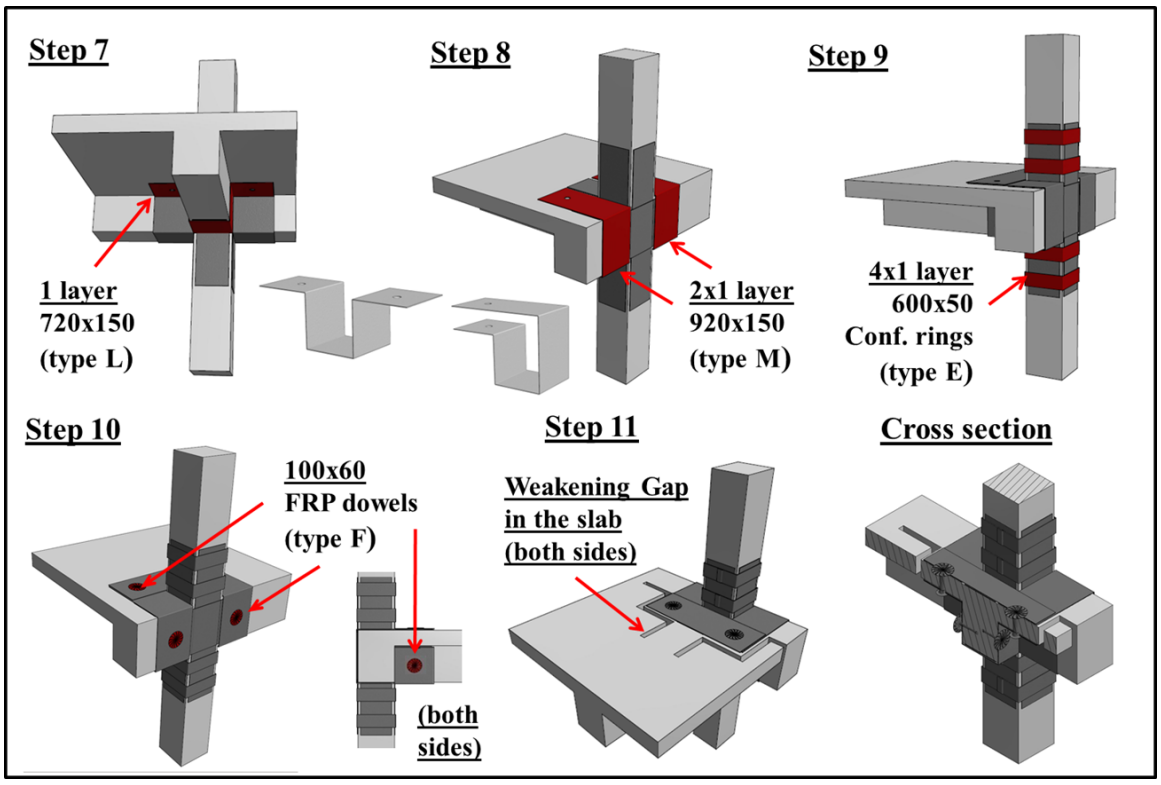

Figure 6.10: GFRP sequence of application Joint type 3, Steps 7 to 11; cross section showing anchorage.

In Figure 6.11 and Figure 6.12 the sequence of applicatio for the top floor Joint type 4 is presented. The layout shown in this figures corresponds to the long span joints, which differ slightly from the short span counterpart as stated before.

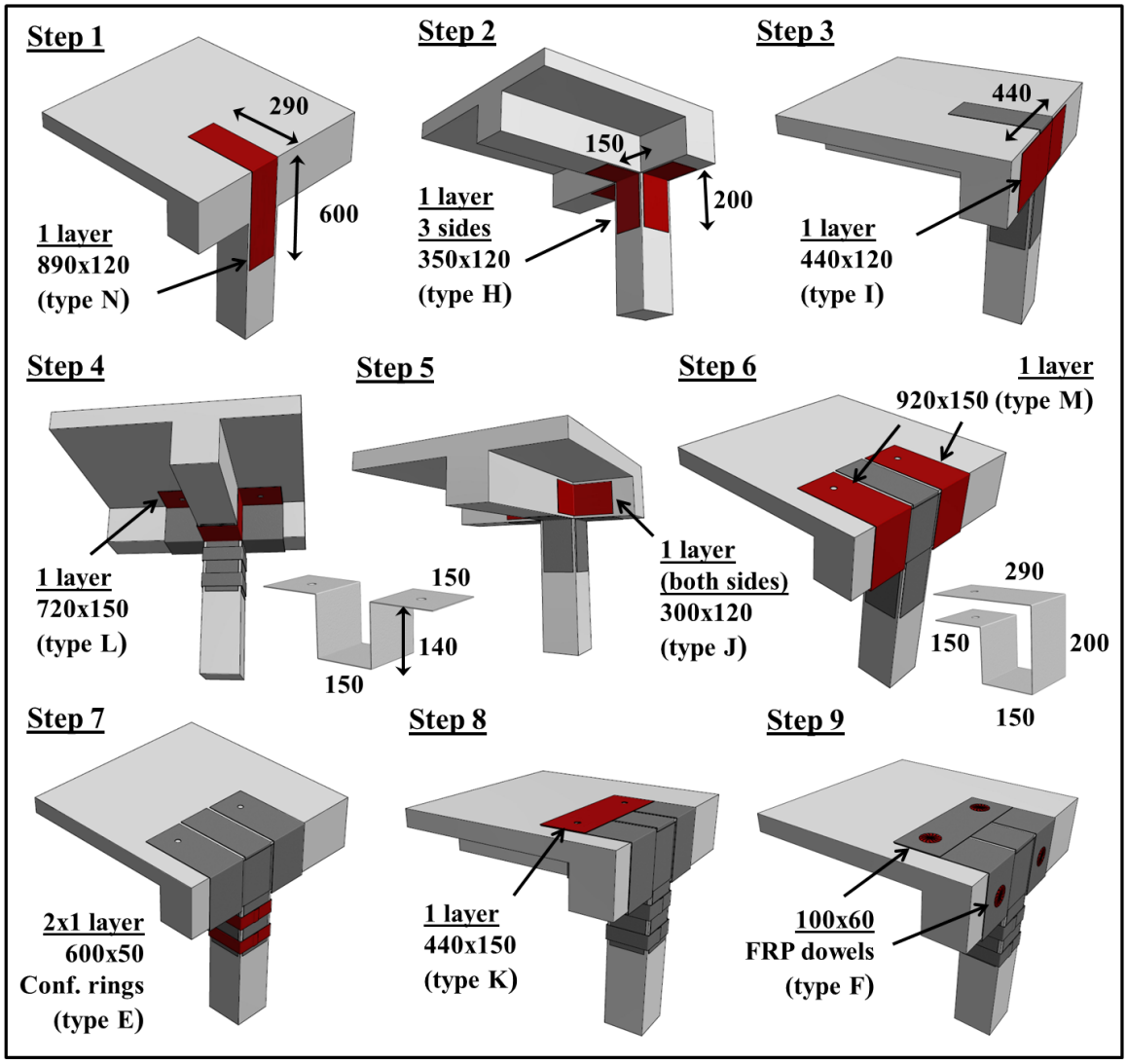

Figure 6.11: GFRP sequence of application Joint type 4, Steps 1 to 9.

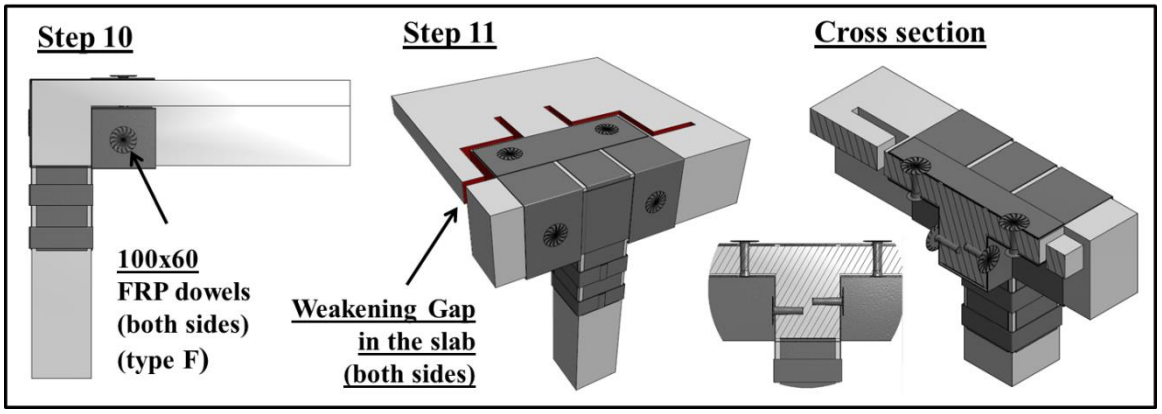

Figure 6.12: GFRP sequence of application Joint type 4, Steps10 and 11; cross section and anchorage details.

6.5 WEAKENING OF THE SLAB: GAP CONFIGURATION

Weakening of the floor slab was carried out in the latest stage of the retrofit intervention. The shape of the length where the slab is saw-cut (gap) was conceived in such a way that it neutralizes the effect of the floor slab on the increase in the beam capacity under negative bending. That is, the steel of the slab in no longer able to take tension in the critical region, where the inelastic behavior is imposed to occur.

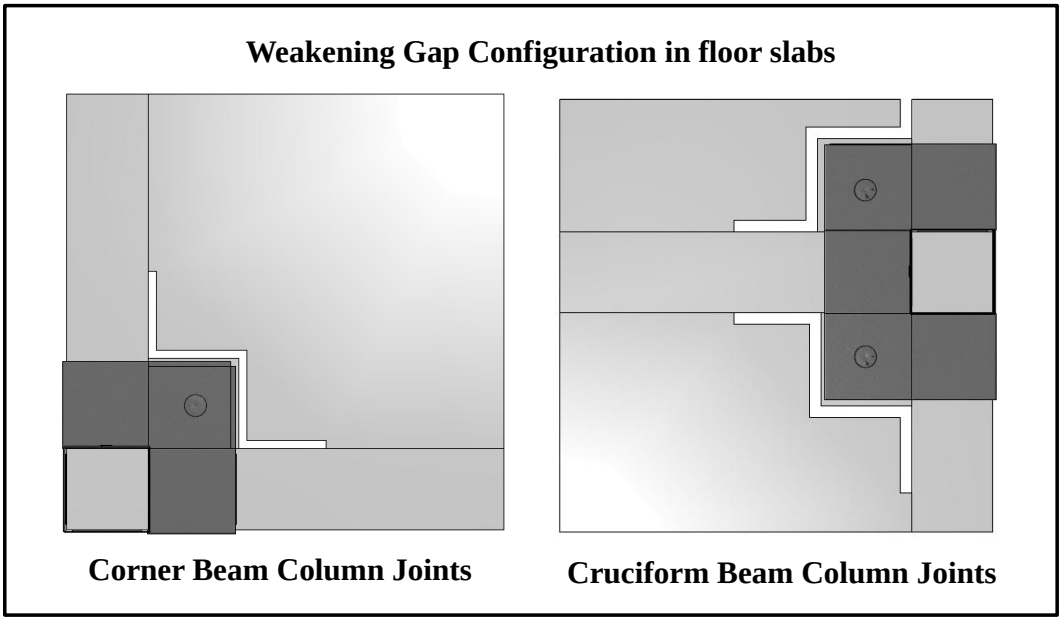

Figure 6.13: Gap configuration in corner and cruciform beam column joints.

In Figure 6.13 the weakening scheme in the floor slab of exterior beam column joints of the external (corner joints) and internal (cruciform joints) frames are presented. The weakest beam section corresponds to the rectangular beam of the longitudinal frames, referred as '2D' beam throughout this thesis. That section is similitude-compatible with the as-built section of the RC beam used in Akguzel (2011), Kam (2010), and Akguzel and Pampanin (2012). Therefore, the resisting moment of the beam of the 2/5 scale beam should be 0.6^3 times that of the 2/3 scale counterpart. Dividing the moment of the 2D beam of this work, M_{by}^{2D} = 7 kNm by 0.6^3, one obtains 32 kNm, very close to the 30kNm reported in Akguzel and Pampanin (2012).

On other important consideration that was taken to account when the weakening geometry was conceived, was the load path followed by the inertial forces in the floor diaphragm. This load path is schematically shown in Figure 6.14 for the most critical situation which is the AT state, slab in tension close to the exterior face of the long span. The seismic actions are indicated as: M_c^T and V_c^T, the bending moment and shear induced by the top column, respectively, M_b^{AT} and V_b^{AT}, the bending moment and shear actions in the beam (AT situation), respectively, M_{slab}^{AT} and V_{slab}^{AT} the moment induced in the slab for compatibility of deformations, M_{by}^{2D}, the resisting moment of the rectangular 2D section of the beam, T_s, the tensile force developed in the top steel of the beam, T_{slab}, the tension force in the slab steel outside the gap region, T_{tb}, the transverse resistance action of the transverse beam outside the gap region. Note that the symbols close to the shear forces indicate that they are pointing downward.

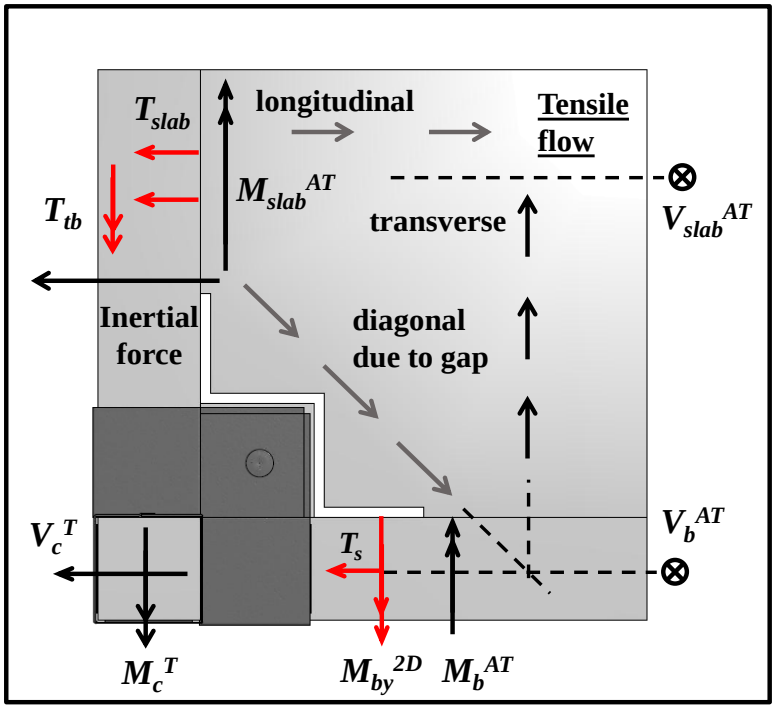

Figure 6.14: Load path in the floor slab: effect of weakening in the distribution of the tensile flow.

The weakening configuration is intended to disable the load paths close to the column and beyond the FRP strengthened region so that no tensile forces of the slab contribute to the flexural resistance of the created fuse in the longitudinal beam. If the slab was weakened just in the longitudinal direction of the beam as thought at an early stage, the contribution of the slab would have been important, and the strengthening of the joint with FRP insufficient. The desired weakening effect could have also been achieved using a square gap close to the column, provided that the slab weakening is extended as shown here. That would have allowed using the complete wrapping of the beam layers similar to those used in Akguzel and Pampanin (2012). However, it is believed that this configuration is less invasive and easier to implement, mostly because the slab needs not to be completely perforated and only from the above.

6.6 RETROFITTED BEAMS FLEXURAL STRENGTH

As has been extensively explained in Chapter 4 and throughout this chapter as well, the existence of a slab and transverse beams enables the development of a larger bending moment capacity in the AT situation (slab in tension). This is also true for the strengthened section of the beam. The FRP layers located in the side of the beam, as done in previous tests (Akguzel and Pampanin 2012), provide extra moment resistance. However, in this case, the layers placed for confinement of the orthogonal beam lateral layers, also provide strength creating a very strong and stiff section, right next to the weakened section of the slab (gap region). In addition, the L-shaped layers introduced in the layout developed in this chapter, also provide resistance to the section, provided that they are well restrained by columns and beam confinement FRP elements. As a result of that modification of the as-built specimen, the composite RC sections of the beams of corner and cruciform beam column joints (L-shaped and T-shaped, respectively), had the dimensions and GFRP active layers described in the next paragraphs. For the estimation

of the moment-curvature relationships, these sections were modelled in BIAX-96 (Wallace and Ibrahim 1996).

In Figure 6.15, the cross section of L-shaped beams of the retrofitted corner beam column joints is presented, and the moment curvature relationships of the beam section in the AC and AT situations are presented in Figure 6.16. The maximum nominal strength and curvature of the sections are defined for a maximum tensile strain in the FRP of ε_{ft} = 1% or a maximum compression strain in the concrete of ε_{cm} = 0.8%, whichever is reached first. This assumes that there are no debonding problems between the concrete and the FRP layers located in the beam, since FRP dowels were used for anchoring those layers into the beams as shown in the sequence of application figures. This assumption was proofed to be correct in this particular case, since no loss of bond (debonding) was observed in any of the FRP layers used in the structure.

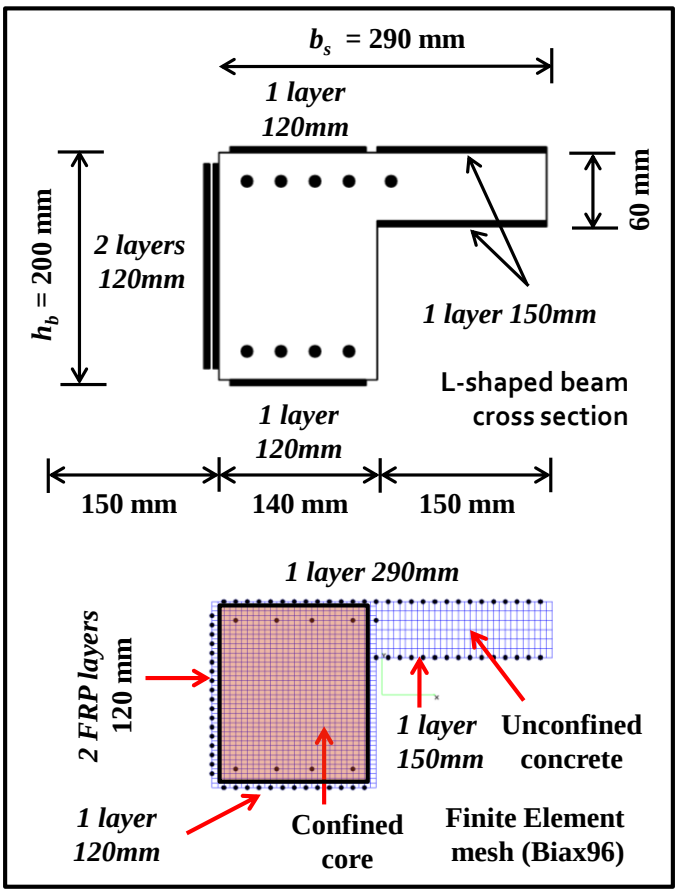

Figure 6.15: L-shaped retrofitted beam cross section and modelling.

The composite section shown in Figure 6.15 corresponds to the part of the beam in between the face of the column and the gap region, where weakened slab is expected to create a fuse for the inelasticity to take place. On the external face of the beam, 2 layers were located, emulating the procedure followed by Akguzel and Pampanin (2012) for plane beam column joints and by Pampanin et al (2007) and Akguzel and Pampanin (2010) for 3D specimens. In this case though, due to the presence of the floor slab, a new configuration was developed for the confinement elements of those layers, as explained previously in this chapter. As a consequence, the top and bottom layers of the confinement elements of the transverse beam provide extra strength, especially in the AT

situation. Moreover the short part of the L-shaped layers located in the internal face of the column (on top and below the beam), provide an additional resisting element.

The sectional analyses of these beams, which certainly assume that plane sections remain plane for all deformation level, provide the moment-curvature diagrams (for $P = 0$) presented in Figure 6.16 for the AC and AT situations. As can be observed in Figure 6.16, the moment capacity of the L-shaped section is larger in the AT situation when compared to the AC counterpart, as expected. The moment resistance of the retrofitted beam section are 30 kNm and 22 kNm in the AT and AC situations respectively. These capacities are associated with a curvature of 0.06 1/m for AT and 0.07 1/m for AC, when the maximum design strain in the GFRP ε_{ft} = 1% is reached, with compression strains in the concrete of ε_{cm} = 0.35% for AT and ε_{cm} = 0.15% for AC, as expected.

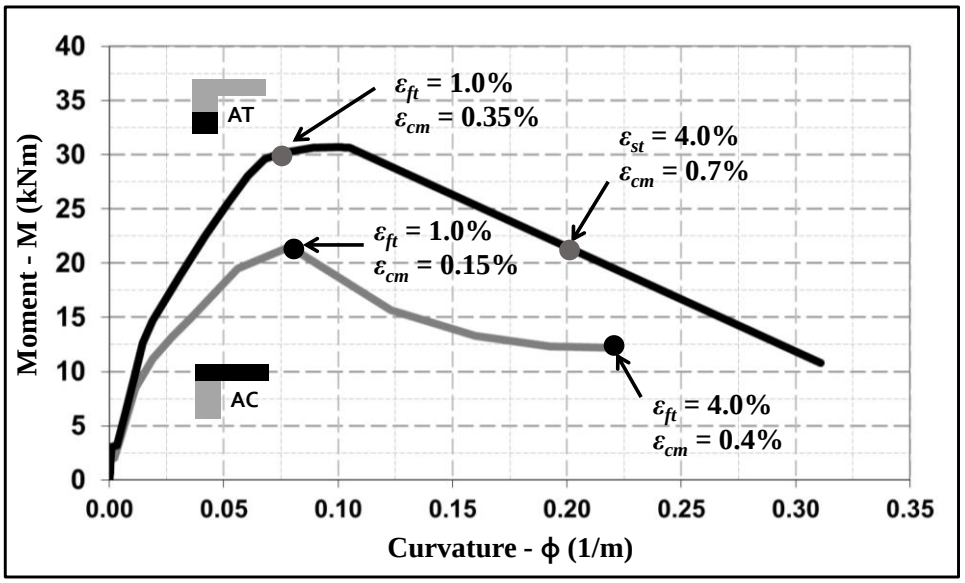

Figure 6.16: Moment-curvature diagram of L-shaped beams.

In Figure 6.17, the cross section of T-shaped beams of the retrofitted cruciform beam column joints is presented, and the moment curvature relationships for the AC and AT situations are presented in Figure 6.18. In this case, since the confinement elements on the transverse beam were located on both sides of the column as described in the sequence of application of the FRP laminates, the contribution of the FRP layers on top and below the floor slab are two times that provided to the L-shaped counterparts. However, due to the presence of the floor slab as well, the FRP layers used on the outer face of the L-shaped beam were not able to be used. In order to cope with this problem, the FRP layers located in T-shaped beams were reduced in width and located in the clear part of the web. Hence the laminates were 60mm smaller than the corner counterparts (120mm and 180mm respectively), as shown in Figure 6.17. As these strips are obviously located at the bottom part of the beam, then the effect of the additional FRP slab reinforcement compensates for the loss of the upper part of these sheets.

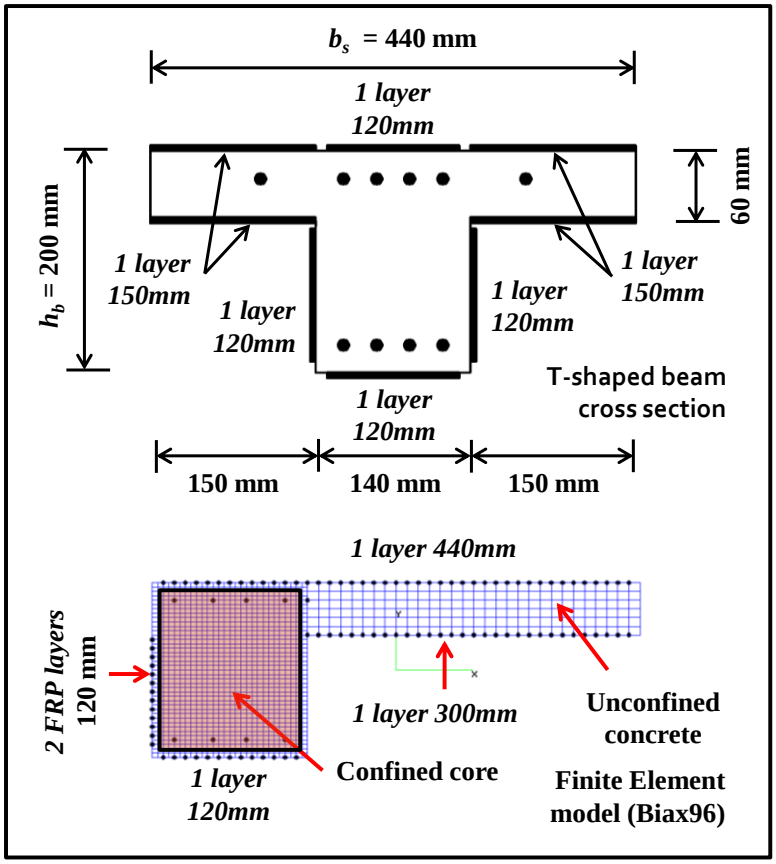

Figure 6.17: Retrofitted T-shaped beam cross section and modelling.

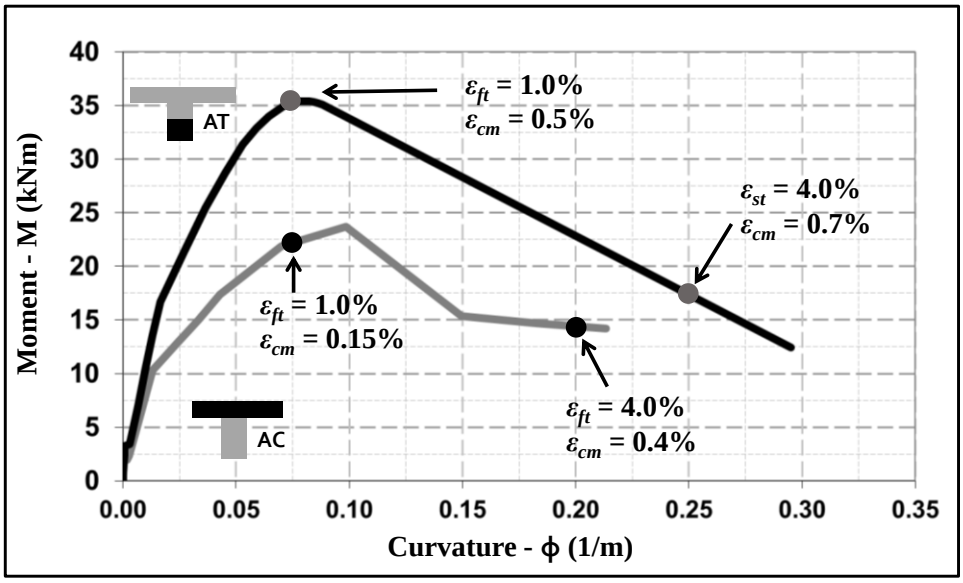

Figure 6.18: Moment-curvature diagram of T-shaped beams.

These speculations or conjectures were thought before the capacities were numerically calculated, so that conceptually the T-shaped had a similar flexural strength than the L-shaped wall. In Figure 6.18, where the moment-curvature of the T-shaped beam for the AC and AT situations is presented, it is shown that the capacity of this beam section is fairly similar to the L-shaped counterpart, but slightly larger. The nominal resisting moment for the design ultimate strain of the FRP in tension ε_{ft} = 1% corresponds to about

35kNm for AT and 23kNm for AC. Therefore, for modelling purposes for example, it would be fair to use one frame only for simulating the response of the complete building if a 2D analysis is being carried out. This is covered in Chapter 8. The curvature associated with both flexural strengths is equal to $\phi = 0.07$ (1/m) approximately, as shown in Figure 6.18.

6.7 RETROFITTED COLUMN FLEXURAL STRENGTH FOR VARYING AXIAL LOAD

The cross sections of the retrofitted columns of the external and internal frames are shown in Figure 6.19. The only difference in the configuration of the layers in these columns relies on the type of sheets used. In the external frame column, as explained before in this chapter, straight layers were used in both exterior faces and an additional L-shaped layer was placed in the interior part of the longitudinal span. In the columns of the internal frame on the other hand, only L-shaped laminates can be used for strengthening the column due to geometry, with the exception of the external face on the short direction of the building.

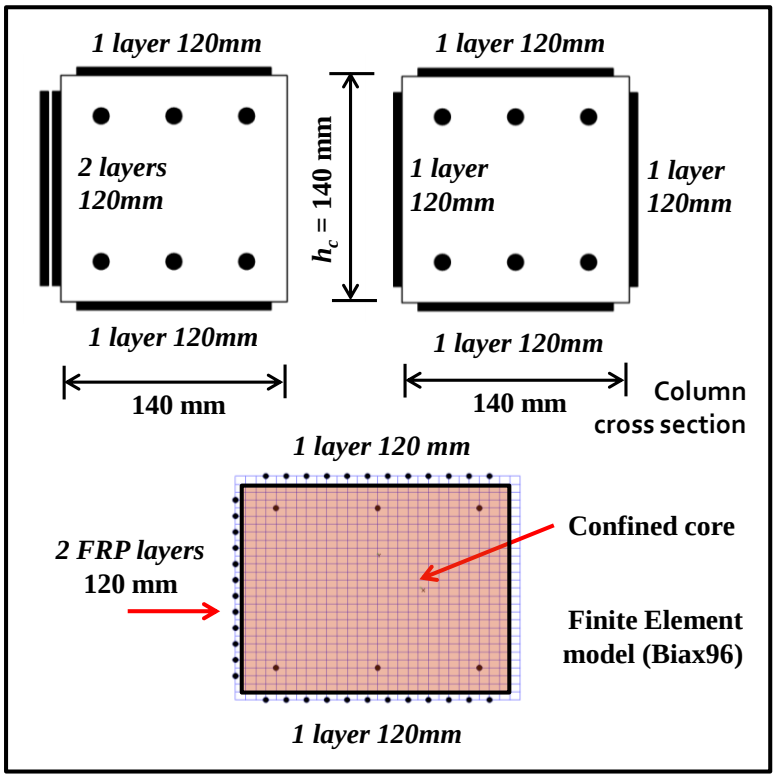

Figure 6.19: Column cross section and F.E. model.

For uni-directional sectional analyses though, both sections are identical and can be modelled in the same way as shown in Figure 6.19. The sectional analyses were constructed using BIAX96 (Wallace and Ibrahim, 1996) for different values of the axial load in the range of interest. In Figure 6.20 it is shown that the flexural strength of the columns ranges from 10 kNm to almost 14 kNm, for $P_v = 0$ to $P_v = 80$. For the columns of the external frame, an axial load P_v = 20 kN was used whereas for the columns of the

internal frame, P_v = 30kN (see Chapter 5). Therefore, the strength would be slightly different at ultimate strain in the FRP, and can be taken as 11kNm for gravity load, being on the conservative side. The curvature associated to the resisting moment for all axial load levels is approximately ϕ = 0.1 (1/m), slightly larger than the nominal ultimate curvature of the beams.

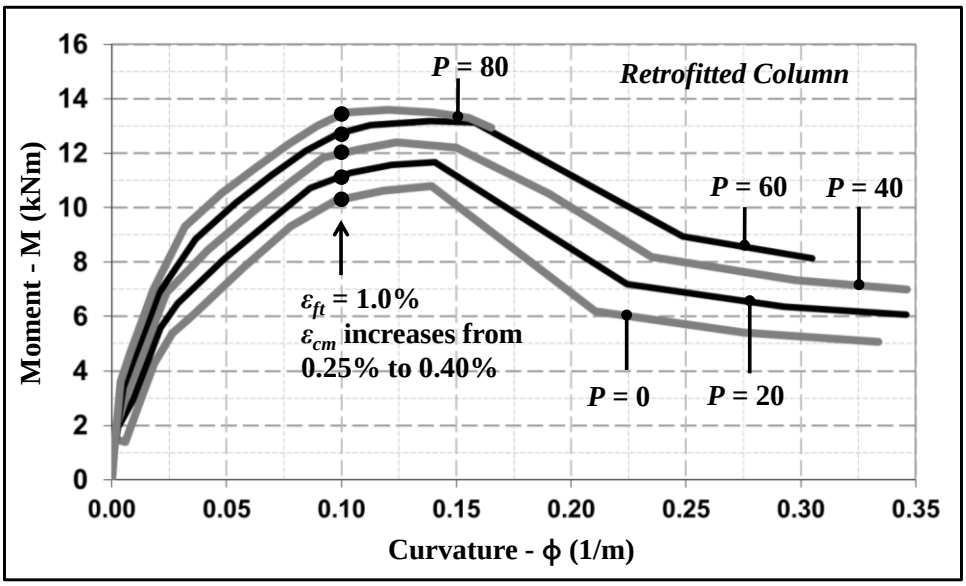

Figure 6.20: Moment-curvature diagram of T-shaped beams.

6.8 RETROFITTED JOINT EQUIVALENT MOMENT CAPACITY

Referring the moment in the joint to the total moment induced by the column (top and bottom), the equivalent resisting moment in the joint is evaluated using the procedure proposed by Akguzel and Pampanin (2012). That procedure is summarized in the following paragraphs. The strength of the joint is divided into two parts: the part resisted by the concrete in the joint itself (as presented in Chapter 5), and the part resisted by the FRP laminates.

After the properties of the materials have been selected, the first step requires the calculation of the horizontal and vertical FRP reinforcement ratios, ρ_{ft} and ρ_{fl}, respectively. These ratios are defined in Equations 6.1 and 6.2 (Akguzel and Pampanin 2012).

$$\rho_{ft} = \left(n_{fb} n_{sf,s} t_f d_{fb}\right)/h_b b_w \tag{6.1}$$

$$\rho_{fl} = \left(n_{fc} n_{sf,s} t_f d_{fb}\right)/h_c b_c \tag{6.2}$$

In Equations 6.1 and 6.2: n_{fb} = number of sheets on the beam face, n_{fc} = number of sheets on the column face, $n_{sf,b}$ = number of beam faces covered with FRP, $n_{sf,c}$ = number of sheets on the column face, t_f = FRP thickness per layer, d_{fb} = depth of the FRP on the beam surface, and d_{fc} = depth of the FRP on the column. In this particular case, only the

strength of corner joints can be evaluated, since in cruciform joints, the implementation of FRP laminates in the joint is not possible due to the geometry of those exterior joints.

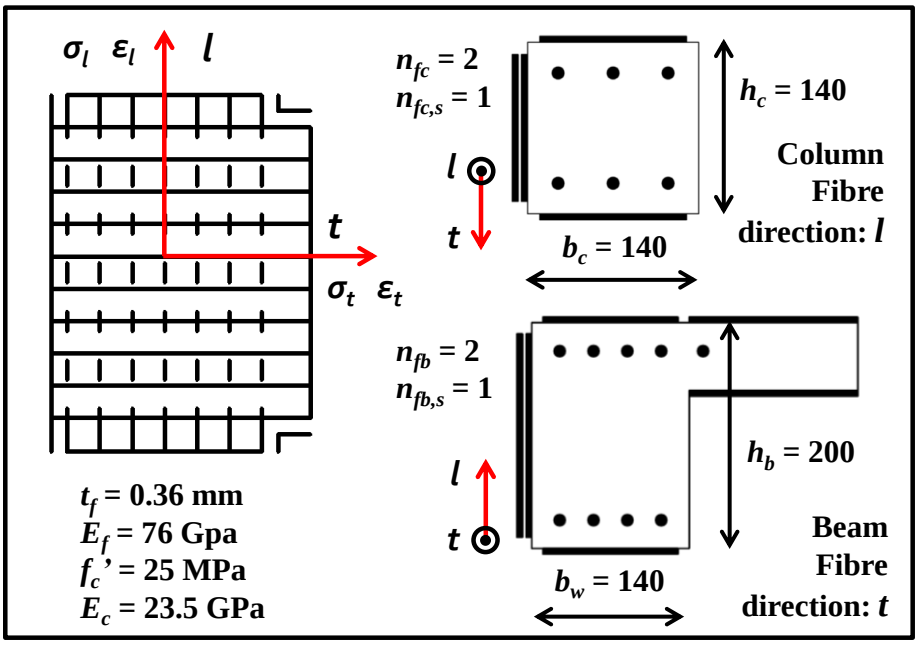

Figure 6.21: Reference axes definition in the panel zone and layers orientation.

For corner joints, the parameters for the calculation of the FRP reinforcement ratios are: n_{fb} = 2, n_{fc} = 2, $n_{sf,b}$ = 1, $n_{sf,c}$ = 1, t_f = 0.36 mm, d_{fb} = 200 mm, d_{fc} = 140 mm, b_w = 140 mm, h_b = 200 mm, h_c = 140 mm, and b_c = 140 mm. The resulting FRP ratios are: ρ_{ft} = 0.00463 and ρ_{fl} = 0.00441. In Figure 6.21 the reference axes orientation is shown, as well as the layers that form the resisting FRP laminates in the joint.

The 'average compressive transverse and longitudinal stresses in the concrete', σ_t and σ_l, respectively, are related to the equivalent strains in the joint ε_t and ε_l, using Hooke's law and the material properties and quantities of the concrete and the FRP as presented in Equations 6.4 and 6.5. In Equation 6.4 it is assumed that all the stress in the transverse direction has the contribution of the FRP only. In Equation 6.5, the stress in the longitudinal direction is calculated as the sum of the stress induced in the FRP and the stress due to axial load in the joint (N_v).

$$\sigma_t = -\rho_{ft} E_f \varepsilon_t \tag{6.4}$$

$$\sigma_l = -\rho_{ft} E_f \varepsilon_l - \frac{N_v}{h_c b_c} \tag{6.5}$$

The stresses and strains developed in the *t* and *l* directions are related to the principal stresses following the Morh's circle theory. The relationship between those stresses (and strains) and the principal stresses (and strains) is presented in Equations 6.6 through Equation 6.11 (Akguzel and Pampanin 2012).

$$\sigma_2 = \sigma_t + \sigma_l \tag{6.6}$$

$$\sigma_t = -v_{jh} \tan\theta \tag{6.7}$$

$$\sigma_l = -v_{jh} / \tan\theta \tag{6.8}$$

$$\tan^2\theta = \frac{\varepsilon_1 - \varepsilon_t}{\varepsilon_1 - \varepsilon_l} \tag{6.9}$$

$$\gamma = \frac{2(\varepsilon_1 - \varepsilon_t)}{\tan\theta} \tag{6.10}$$

In Equations 6.6 to 6.10, the parameters not previously defined are: σ_2 = minimum principal stress in the concrete, v_{jh} = joint nominal shear stress, θ = direction of the principal maximum principal stress σ_1, ε_1 = the maximum principal strain in the panel zone (ε_2 = the minimum principal strain in the panel zone), γ = the average angle of shear distortion in the joint.

In Figure 6.22, the actions in a corner beam column joint when the top fibre of the beam experiences tension (AT) are shown on the left hand side, and the equivalent reaction forces in the joint are presented on the right hand side. In the resisting forces in the joint, the main parameters used in Equations 6.6 to 6.11 (note that $v_{jh} = v_f$) are illustrated.

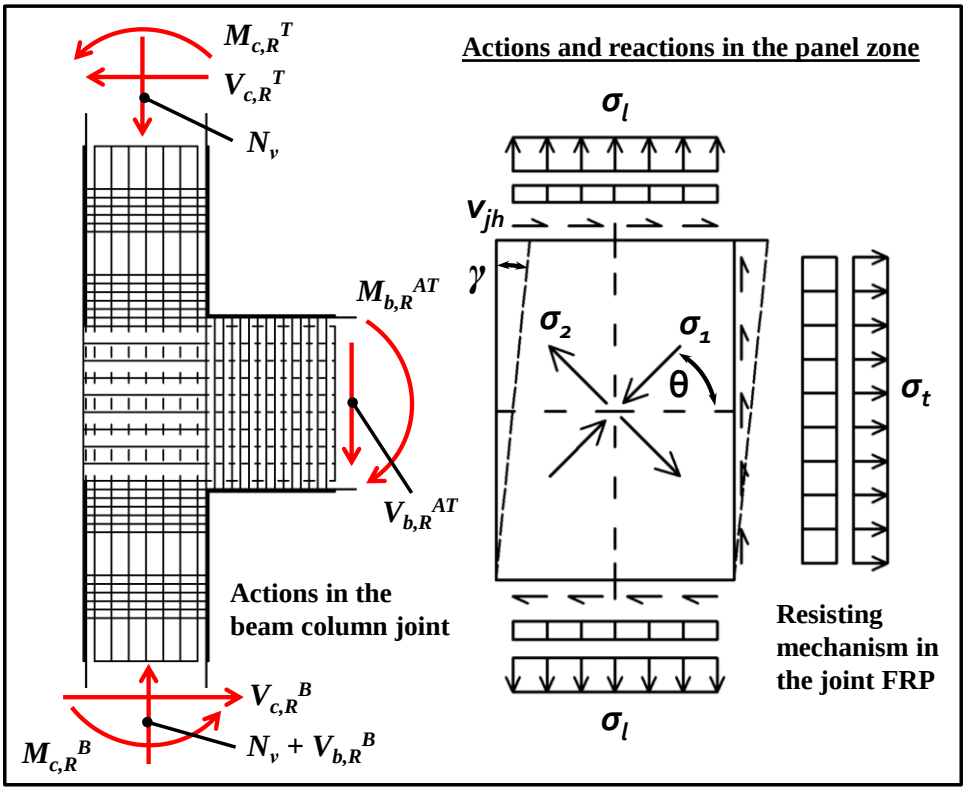

Figure 6.22: Actions in the beam column joint and FRP resisting mechanism in the joint.

The nominal shear stress contribution of the FRP, v_f can be calculated by replacing Equation 6.7 into Equation 6.4, as presented in Equation 6.11.

$$v_f = \frac{\rho_{ft} E_t \varepsilon_t}{\tan\theta} \tag{6.11}$$

In an analogue way as it was done for the as-built joint, Mohr's circle is used for calculating the principal tensile stress in the joint due to the resisting action of the GFRP, p_{tf}. This principal stress is defined in Equation 6.12 (Akguzel and Pampanin 2012), where

$$p_{tf} = -f_v/2 + \sqrt{(f_v/2)^2 + v_f^2} \tag{6.12}$$

In Equation 6.12, f_v is the axial stress in the joint. From the combination and re-arrangement of Equations 6.6 to 6.11, Equation 6.13 can be deduced, which is a quadratic expression for the solution of $\tan^2\theta$ (Akguzel 2011, Akguzel and Pampanin 2012). In Equation 6.13, the parameters not previously defined are: E_c = modulus of elasticity of the concrete, E_f = modulus of elasticity of the GFRP, N_v = axial load.

$$\left(\frac{1}{E_c} + \frac{1}{\rho_{ft} E_f}\right) \tan^4\theta + \left(\frac{N_v}{h_c b_c \rho_{ft} \rho_{fl} E_f^2 \varepsilon_t}\right) \tan^2\theta - \left(\frac{1}{E_c} + \frac{1}{\rho_{fl} E_f}\right) = 0 \tag{6.13}$$

By solving Equation 6.13 with the values of the parameters for this particular case, presented previously, then for a given tensile strain in the transverse direction of the sheets (t), it is possible to calculate $\tan(\theta)$ and hence the shear resisted stress resisted by the FRP can be calculated as well.

For the calculation of the shear resistance of the retrofitted joint, an iterative (or incremental) procedure was postulated by Akguzel and Pampanin (2012). In that procedure, the strain of the joint in the transversal direction is increased at closed intervals until one of three limit states is reached:

1) The ultimate (design) tensile strain of the FRP is reached (ε_{fu})
2) The debonding stress is reached in the FRP ($\varepsilon_{f,deb}$)
3) Diagonal compression failure is reached in the concrete ($p_{c,max}$)

The limit for the ultimate strain in the FRP was taken as 1%, which is a design value, smaller than the ultimate value provided in the technical specifications of the product as mentioned before (see Figure 6.3). One approach for calculating the strain associated to debonding between the concrete and the FRP laminates is found from the expression proposed by Holzenkampfer (1994), presented in Equation 6.14, as suggested to be used in Akguzel and Pampanin (2012). That formula is valid provided that the development length in the beam direction (l_{bt}) is larger than the value $l_{b,max}$ given in Equation 6.15.

$$\varepsilon_{f,deb} = \frac{c_1}{E_f}\sqrt{E_f f_{ct}/t_f n_{fb}} \quad \text{for } l_{bt} > l_{b,max} \tag{6.14}$$

$$l_{b,max} = \sqrt{E_f t_f / c_2 f_{ct}} \tag{6.15}$$

In Equation 6.14: c_1 = an empirical coefficient that can be taken as 0.64 according to Neubauer and Rostasy (1997); and f_{ct} = tensile strength of the concrete. In Equation 6.15: c_2 = an empirical coefficient that can be taken equal to 2 according to Holzenkampfer (1994) (Akguzel and Pampanin 2012).

In other studies on the maximum bond capacity of glass and carbon FRP laminates and concrete (Teng et al. 2003), Equation 6.16 has been proposed. That formulation is part of the current ACI440-2008 requirements for externally bonded FRP laminates (ACI Committee 440, 2008).

$$\varepsilon_{f,deb} = 0.41\sqrt{f_c'/(n_f E_f t_f)} < 0.9\varepsilon_{fu} \tag{6.16}$$

The maximum principal compression stress in the concrete is taken as $0.3f_c'$, as suggested by Priestley et al. (1997) and later confirmed by Prota et al. (2001).

Given the numerical values of the beam column joint geometry, the properties of the materials (concrete and FRP), and the scheme and number of the FRP layers, the procedure for calculating the equivalent resisting moment in the retrofitted joint for a given axial load and the strain limits stated above can be summarized as follows:

1) Select the design maximum tensile strain for the FRP based on the manufacturer information (in this thesis, a value of ε_{fu} = 1% has conservatively been used)

2) Calculate the strain that produces debonding between the FRP and the concrete, $\varepsilon_{f,deb}$ using Equation 6.16.

3) Select the smaller of these two values: $\varepsilon_{f,max} = \min(\varepsilon_{fu}, \varepsilon_{f,deb})$. This value corresponds to maximum tensile strain in the FRP in the transverse direction, ε_{ft}.

4) Solve Equation 6.13 and find the principal directions given by $\tan(\theta)$.

5) Calculate the shear stress resisted by the FRP using Equation 6.11.

6) Calculate the stress due to axial load: $f_v = N_v/(b_j h_c)$

7) Calculate the maximum principal tension stress due to the FRP p_{tf} with Equation 6.12.

8) Calculate the principal tensile strain ε_1 using Equation 6.17:

$$\varepsilon_1 = \frac{E_f\varepsilon_t(\rho_{fl}-\rho_{fl})+f_v\tan^2\theta}{E_f\rho_{fl}(1-\tan^2\theta)} \tag{6.17}$$

9) Calculate the angular distortion γ in the panel zone with Equation 6.10.

10) Using a suitable empirical relationship (see Priestley 1997, Pampanin et al. 2002, Akguzel and Pampanin 2012), find the principal tensile stress in the concrete p_{tc} for the angular distortion γ found in the previous step. The p_{tc}-γ relationship for the as-built joint is assumed to be bi-linear, with the cracking point at $p_{tcD,0}$ = 0.2 and γ_0 = 0.0002 rad for corner beam column joints and $p_{tc,0} = 0.3\sqrt{f_c'}$ and γ_0 = 0.0003 rad for cruciform joints. After that cracking point, p_{tc} reduces to zero at γ = 0.025 rad for both cases. That is, a general beam column joint p_{tc} would depend on γ according to equation (6.18) given that $p_{tcD,0}$ and γ_0 are taken as mentioned before.

$$p_{tc} = p_{tc,0}/\gamma_0 \qquad \text{for } \gamma \leq \gamma_0$$
$$p_{tc} = p_{tc,0}\left(1 - \frac{(\gamma-\gamma_0)}{(0.025-\gamma_0)}\right) \qquad \text{for } \gamma > \gamma_0 \qquad (6.18)$$

11) Calculate the total principal tensile stress in the joint due to the resisting action of the concrete and the FRP, $p_{tt} = p_{tc} + p_{tf}$.

12) Obtain the total shear resisted by the composite section, v_{jt}, using Equation 6.19:

$$v_{jt} = \sqrt{p_{tt}^2 + p_{tt} f_v} \qquad (6.19)$$

13) Calculate the geometric coefficient ω ($1/L^3$ [units]) as described in Chapter 4, explicitly considering the value of the lever arm of the resisting moment in the beam (jd), as it may differ when asymmetric sections are being retrofitted, as in the case of this thesis. The expression for ω is given by Equation 6.20, where l_c = the length of the column, measured from half of the bottom and top storeys, l_b = the length of the mean measured from the centreline of the column to the middle of the span (l_s), h_c = the height of the column cross section, h_b = the height of the beam cross section, and b_j = the effective width of the joint (see Figure 6.23).

$$\omega = \frac{2}{b_j h_c (l_c - h_b)}\left[\frac{l_c}{l_b jd}\left(l_b - \frac{h_c}{2}\right) - 1\right] \qquad (6.20)$$

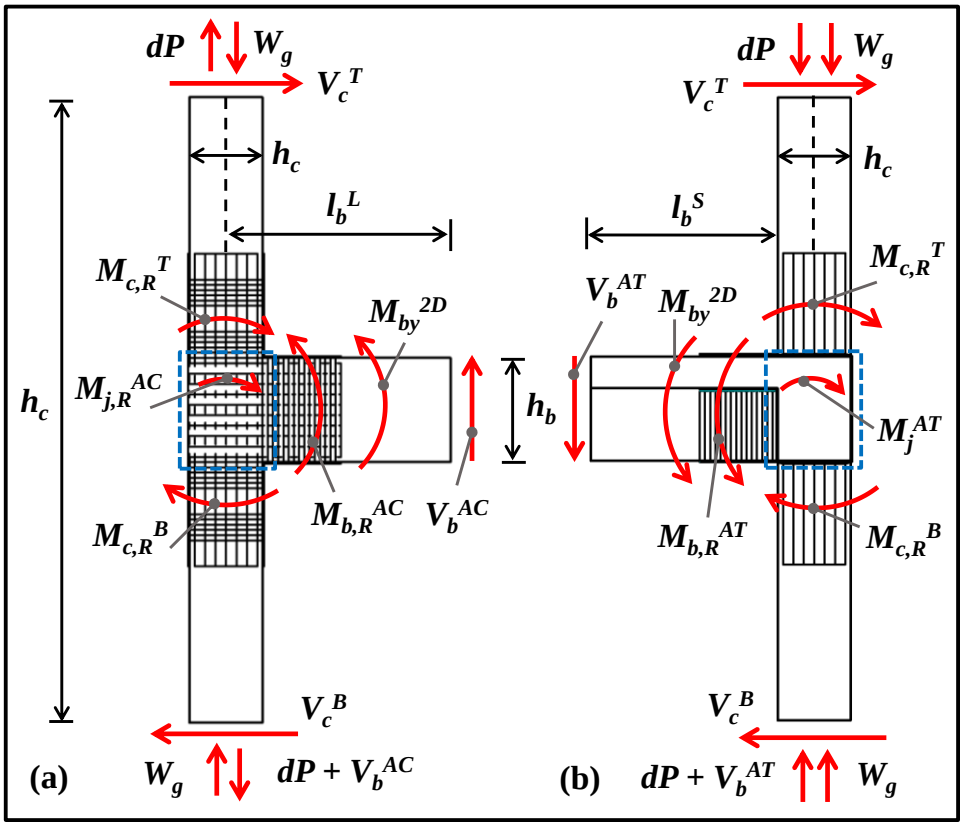

Figure 6.23: Actions and resisting forces in (a) corner long span beam column joint AC situation, and (b) cruciform short span beam column joint AT situation.

14) Calculate the equivalent resisting moment of the retrofitted joint using Equation 6.21. If the units used in the calculations are meters and MPa, then the resulting moment multiplied by 10^3 yields the result in kNm.

$$M_{j,R} = \frac{v_{jt}}{\omega} = \frac{\sqrt{p_{tt}^2 + p_{tt} f_v}}{\omega} \tag{6.21}$$

15) Check that the principal compression stress in the concrete p_{cc}, given by Equation 6.22 is smaller than $p_{cc,max} = 0.3 f_c'$ (Priestley et al. 1996, Prota et al. 2002).

$$p_{cc} = -f_v/2 - \sqrt{(f_v/2)^2 + v_{jh}^2} \tag{6.22}$$

16) If $p_{cc} > p_{cc,max}$, then use a smaller value for $\varepsilon_{ft,max}$ and go to step 4.

The calculation of the equivalent resisting moment of the retrofitted joint is presented in the next section, where it is plotted against the axial load magnitude for the given strain limits defined in this section. As has been mentioned before, a direct strengthening of the joint was only possible in corner beam column joints, as shown in Figure 5.12. As a result, the evaluation of $M_{j,R}$ using the guidelines provided by Akguzel and Pampanin is not valid anymore in that case. However, a tentative value of $p_{tc} = 0.4\sqrt{f_c'}$ was set for the 3-faces confined as well as indirectly retrofitted joint. That is, the presence and disposition of the FRP laminates is being recognized to have an impact in the concrete behaviour of the joint, as explained later in detail.

In addition, the evaluation must be done for the two directions of bending moment in the beam (AC and AT situations), since a sensitivity analysis is being done when the *jd* parameter is considered to be $0.7d$ for the AT state instead of $0.9d$ considered to be appropriate for the AC state only which is similar to the 2D plane case (see Chapter 5). The change in the parameter *jd* changes the value of the geometric actor ω. For the geometry of the long span beam column joint and the values indicated before, the geometric coefficient is ω = 336 1/m^3 for $jd = 0.9d$, and ω = 449 1/m^3 for $jd = 0.7d$, representative of the AC and AT situations, respectively. In the short span these values are ω = 319 1/m^3 and ω = 428 1/m^3, slightly smaller than those of the long span beam column joints.

It seems important to note that the ω factor depends strongly on the effective joint width assumed. In this thesis, as described in Chapter 5, the criteria used for the effective width was based on the experimental evidence presented by Durrani and Zerbe (1987), where the failed surface inside the joint is shown to be mixed with a torsional mechanism. That was also found in this work as presented in Chapter 4 in extension. Also from the findings presented in Kam et al. (2010), where similitude-compatible subassemblies of the beam column joints part of this frame, the torsional cracks and therefore the shear failing surface takes place outside the spandrel forming 45° approximately from the top of the slab towards the bottom. That damage pattern also developed in the beam column joints of the as-built specimen after the shake table tests when the most demanding record was used, as presented in Chapter 4. The effective with is taken then as $b_e = b_c + h_t/2$ at each side of the column if a spandrel exists, where h_t is the height of the transverse beam (spandrel) and b_c the width of the column. A quick (conservative) estimation of the

equivalent resisting moment of the joint, Provided that $p_{cc} < 0.3f_c'$, can be done as follows:

1) $\varepsilon_{ft,max} = 0.009$ (debonding controls)
2) $N_v = 0$ (worst case),
3) $p_{tf} = 2.5$ MPa, $\gamma = 0.023$, $p_{tc} = 0.022\sqrt{f_c'} = 0.11$ MPa yields $p_{tt} = 2.62$ MPa.
4) The total shear stress resisted by the joint is then given by $v_{jt} = 2.51$ MPa
5) The equivalent moment of the retrofitted joint $M_{j,R}^{AC} = v_{jt}/\omega^{AC} = 8.6$ kNm and $M_{j,R}^{AT} = v_{jt}/\omega^{AT} = 6.6$ kNm.

A more refined evaluation of the equivalent moment capacity can be constructed for increasing values of the shear angular distortion in the joint γ, which in turn depends on the value of the tensile strain in the FRP, ε_{ft}. For every value of γ, the principal tensile stress in the concrete and the FRP, p_{tc} and p_{tf}, respectively, can be calculated as described before, and hence the total resisting principal stress of the retrofitted joint, $p_{tt} = p_{tf} + p_{tc}$ (composite action). In Figure 6.24 the graphs with the p_t vs. γ curves are presented.

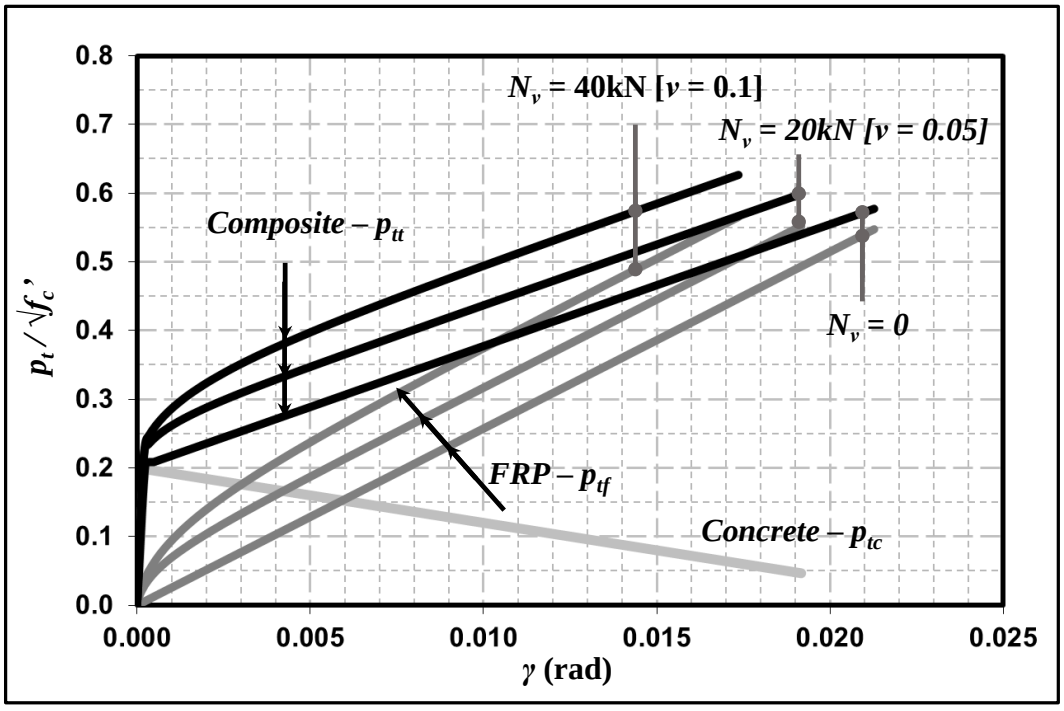

Figure 6.24: Principal tensile stress versus angular distortion – as-built, FRP only and composite joint ($p_{tc} = 0.2\sqrt{f_c'}$ and $f_c' = 25$MPa) for varying axial load (N = 0, 20, and 40kN).

The equivalent resisting moment then is the shear associated to p_{tt} divided by the geometric coefficient ω. As it was discussed previously in this chapter, that coefficient depends importantly in the assumption of the lever arm of the resisting moment in the beam jd. For the AC situation or state, $jd = 0.9d$ was considered, as suggested by Akguzel and Pampanin (2012). However, for the AT situation the lever arm was taken as $jd = 0.7d$. As a result, in this case, the geometric coefficients for both cases are $\omega^{AC} = 336$ 1/m^3 and $\omega^{AT} = 449$ 1/m^3. Using those factors, the equivalent moment in the joint (Mj) for the as-built case (concrete only), the moment contribution of the FRP laminates only, and the equivalent resisting moment of the retrofitted-composite joint are presented in Figure 6.25 for the AC situation and in Figure 6.26 for the AT situation.

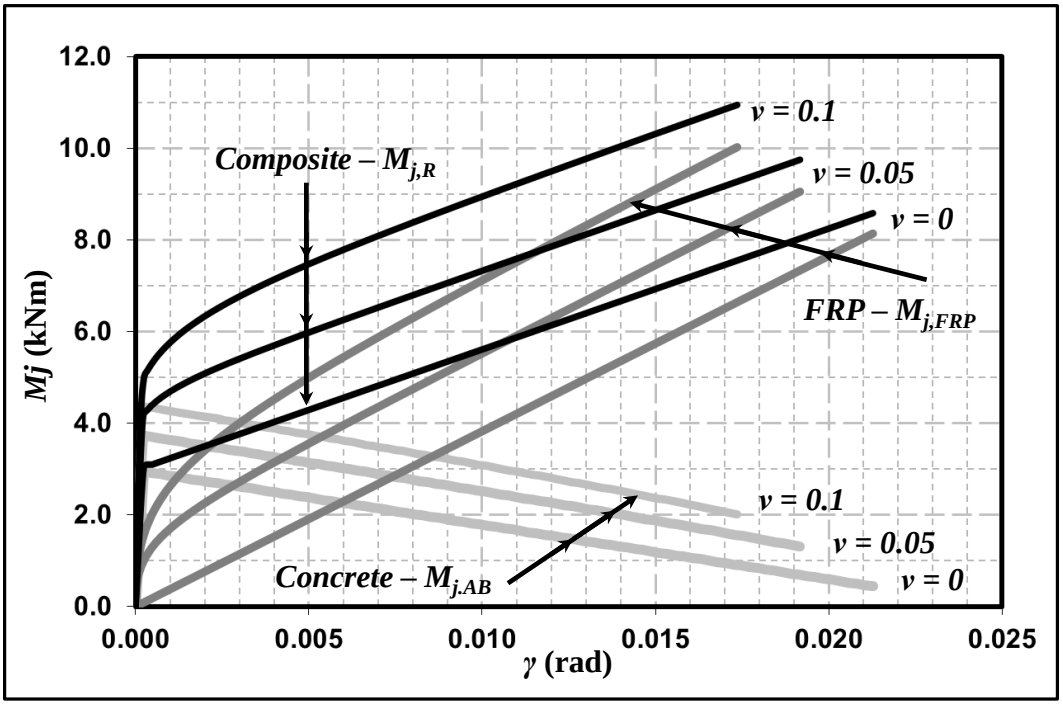

Figure 6.25: Equivalent resisting moment versus angular distortion – as-built, FRP only and composite ($p_{tc} = 0.2\sqrt{f_c'}$) for varying axial load (N = 0, 20, and 40kN); AC state ($jd = 0.9d$).

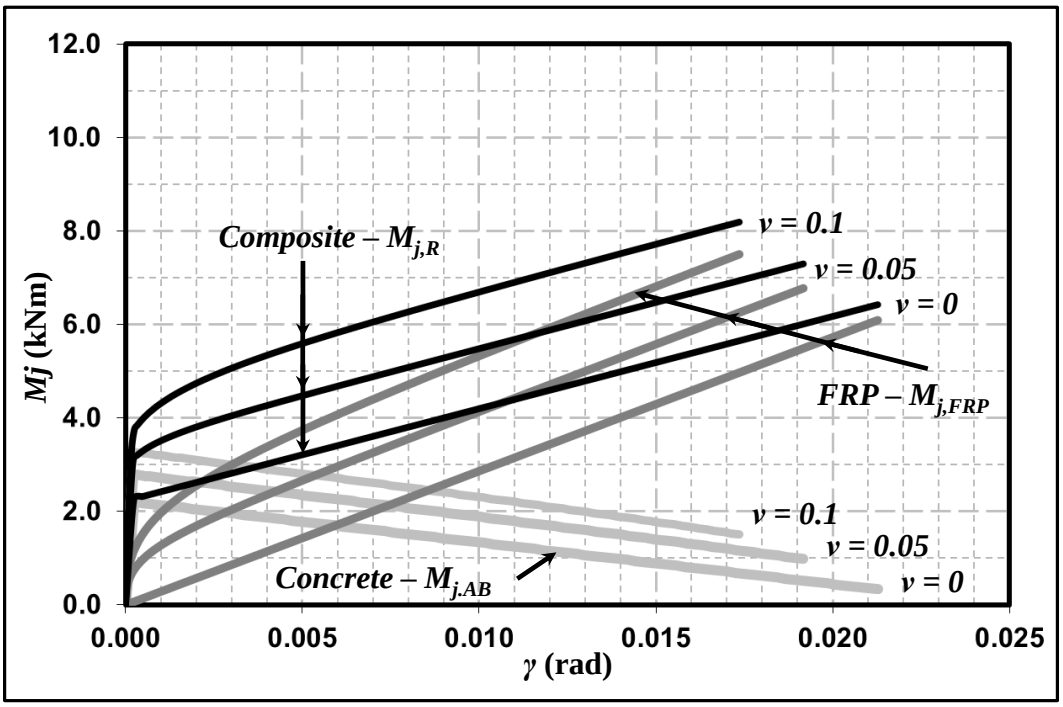

Figure 6.26: Equivalent resisting moment versus angular distortion – as-built, FRP only and composite ($p_{tc} = 0.2\sqrt{f_c'}$) for varying axial load (N = 0, 20, and 40kN); AT state ($jd = 0.7d$).

In Figure 6.25 and Figure 6.26, it can be observed that the FRP action provides an important increase of the joint moment capacity, especially after the principal stress associated to cracking occurs. That is, the $M_{j,AB} - \gamma$ curve is upgraded significantly by the elastic action of the FRP ($M_{j,FRP}$) after cracking of the concrete, so that the resisting moment of the composite retrofitted section ($M_{j,R}$) takes the shape of a classic ductile

behaviour. The ultimate limit state is given in this case by $\varepsilon_{tf,deb}$ = 0.9%, and is consistent with the maximum angular distortion shown in all the graphs of Figure 6.24 to Figure 6.26. It can also be observed that the resisting moment of the as-built and retrofitted joints is larger for the AC than the AT situation as expected, due to the smaller value of *jd* used in the latter in comparison with the former. However, as it is shown later, the axial load level consistent with the AT situation can only be larger than the gravity load, and can only be smaller than that value in the AC situation, as explained in Chapter 5, and hence, they will take similar values for the calculation of the strengths in the M-N diagram as shown in section 6.10 of this chapter.

6.9 TORSION

The effect of the torsional resistance of beam column joints with slabs has been addressed in Chapter 4 based on the findings presented in Chapter 3 and previous research on cuasi-static tests of subassemblies (Ehsani and Wight 1985, Durrani and Zerbe 1987, Di Franco et al 1995, Shin et al. 2004, Kam et al. 2010, Quintana-Gallo et al. 2011).

The torsion resistance of the stiff GFRP region created around the panel zone region, i.e. inside the gap region, is thought to provide an important contribution to the shear resistance of the panel zone. That is, in the joints of cruciform beam column joints where no FRP can be provided to resist shear, torsion can be the main source of resistance against twisting demand, which is equivalent to the rotation demand in the joint. As it was done in Chapter 4, the strength of the spandrel (transverse beam) in torsion is evaluated and incorporated into the M-N diagrams for evaluation the hierarchy of strengths and sequence of events in the panel zone region.

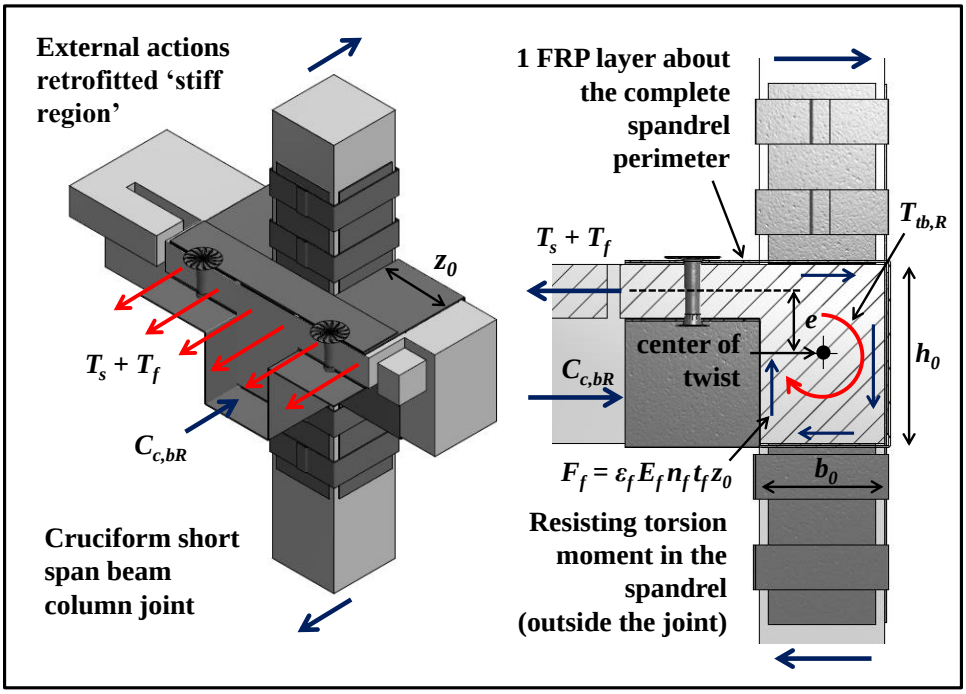

Figure 6.27: Torsion resisting mechanism in the retrofitted spandrel – cruciform joint.

Using an analogy with the methodology for evaluating the torsion resistance of reinforced concrete elements (Collins and Mitchel 1992, MacGregor and Ghoneim 1996), the torsional resistance of the retrofitted spandrel is evaluated as follows. With reference in Figure 6.23, the resisting mechanism in the spandrel is shown. The actions in the beam column joint are referred to the shear in the columns and the tension and compression pair of forces representing the actions in the beam section. The tensile force in the retrofitted slab is $T_{s,ret} = T_s + T_f$, where T_s is the tensile force developed in the top reinforcement of the beam and the active width of the slab, and T_f is the tensile force developed in the FRP laminates on the top of the slab. The compression force in the beam to counteract the effect of this force is $C_{c,bR}$, and the lever arm between them named *jd* as explained in Chapter 5.

On the side of the panel zone, where the spandrel are located, the slab-spandrel mechanism provides the resisting forces trough torsion about the centre of twist of the transverse beam. This torsion resisted by the concrete and in the normal case by the spandrel shear stirrups. In this case, however, the FRP laminates located around the L-shaped section of the spandrel provide an additional resisting force F_f given by Equation 6.23.

$$F_f = \varepsilon_f E_f n_f t_f z_0 \tag{6.23}$$

In Equation 6.23: ε_f = strain developed in the FRP about the spandrel; E_f = Young's modulus of the FRP, n_f = the number of FRP layers used; t_f = FRP laminate thickness; and z_0 = the width of the FRP laminate inside the gap region.

The torsion resisting moment of the cross section of the retrofitted spandrel can be estimated using Equation 6.24, which is an analogy of the torsion yielding moment of a RC beam (see Chapter 5). The only difference is that the effective area of the section is the same as the gross area of the beam and the term $A_{st} f_{yt}$, the axial force at yielding in the spandrel stirrups, is replaced by F_f.

$$T_{tb,R} = 2h_0 b_0 E_f n_f t_f \varepsilon_f \tag{6.24}$$

In Equation 6.21: $T_{tb,R}$ = torsion resisting moment of the retrofitted beam, h_0 = effective height of the spandrel for torsion, taken as h_t, the gross height of the transverse beam, and b_0 the effective width for torsion equal to b_c in this case. In this case: h_0 = 0.2m, b_0 = 0.14m, n_f = 1, t_f = 0.36mm, and E_t = 76,000 MPa, so that for a ultimate strain in the FRP of ε_t = 1%: $T_{tb,R}$ = 13.4 kNm.

Nevertheless, it is important to remind that the strengthened stiff element is inside the weakened region in the slab, and hence, a direct activation of the torsion mechanism shown in Figure 6.27. That is, the external forces can be applied at the beam rectangular section only, for continuity. Also note that in this case the section is expected to resist torsion equally under positive and negative actions in the longitudinal beam, which is not true for the as-built spandrel as discussed in Chapter 5.

6.10 EVALUATION OF THE HIERARCHY OF STRENGTHS AND EXPECTED SEQUENCE OF EVENTS USING THE ASYMMETRIC M-N DOMAIN

As presented in Chapter 5, an extended version of the M-N capacity curves for evaluating the strengths and the expected sequence of events in the panel zone region needs to be used in this case where the presence of the slab and the spandrel introduces asymmetry into the problem. This asymmetry is understood by means of the examination of two difference states as defined in Chapter 4. As it was shown in Chapter 5 the most vulnerable joint is that of the long span, and thus will be the one whose evaluation on the M-N diagram will be carried out.

For the evaluation of the sequence of events, two demand scenarios were considered. These scenarios are determined by straight lines in the M-N diagram, determined by the axial load variation factor as a function of the shear in the column α. As explained in Chapter 5, the variation in the axial load can be expressed in terms of the rate of change of the axial load as a function of the moment in the column, β, the reciprocal being the slope of the curves presented in the M-N diagram (α') (see Chapter 5).

In this case, as the strength of the retrofitted elements are importantly larger than the as-built counterparts, the coefficients α = 1.68 and β = 2.33 (Scenario 1) calculated in Chapter 5 indicate that the strength of the retrofitted elements would only be reached at very high levels of tension in the column, which seems very unlikely to occur in this case. However, a smaller axial load variation scenario, the strength of these elements would be potentially reachable. In this Chapter, an additional scenario with 1/3 of the axial load variation rate corresponding to α = 0.56 and β = 0.78 (Scenario 2) was also considered for illustration.

6.10.1 Corner beam column joints

In the evaluation of the joint equivalent moment, in corner beam column joints the maximum tensile stress in the concrete is taken as $p_{tc,0} = 0.2\sqrt{f_c'}$ at a corresponding angular distortion γ_0 = 0.0002 rad. The maximum tensile strain in the beam direction for the calculation was limited to the a strain equal to $\varepsilon_{f,deb}$ = 0.9%, as obtained with Equation 6.16 (ACI Committee 440 2008). A value of $jd = 0.9d$ was used for the AC state, whereas a value of $jd = 0.7d$ was used for the AT state. For the geometry of the long span beam column joint and the values indicated before, the geometric coefficient is ω = 336 1/m^3 and ω = 449 1/m^3 for the AC and AT situations, respectively.

6.10.1.1 AC State Corner

The AC state defined in Chapter 5 corresponds to:

(1) compression in the slab,
(2) decreasing axial load due to uplifting seismically induced shear in the beam.

Note that in Chapter 5 an additional characteristic of the AC state for the as-built specimen is the existence of torsional resistance in the spandrel until cracking only. In this chapter, the torsion resistance provided by the transverse beam is located inside the weakened region in the slab, and the load path becomes effective in the FRP strengthened

zone only. In addition, the forces are induced by a rectangular section into an L-shaped one (or T-shaped in the case of cruciform joints). This requires the creation of a compression or tension strut in the slab (AC and AT states, respectively) in the strengthened slab in order to activate the torsion resistance of the retrofitted spandrel. As the FRP provides confinement and structural integrity, the resistance of the spandrel may develop with the slab in tension or compression (AT and AC).

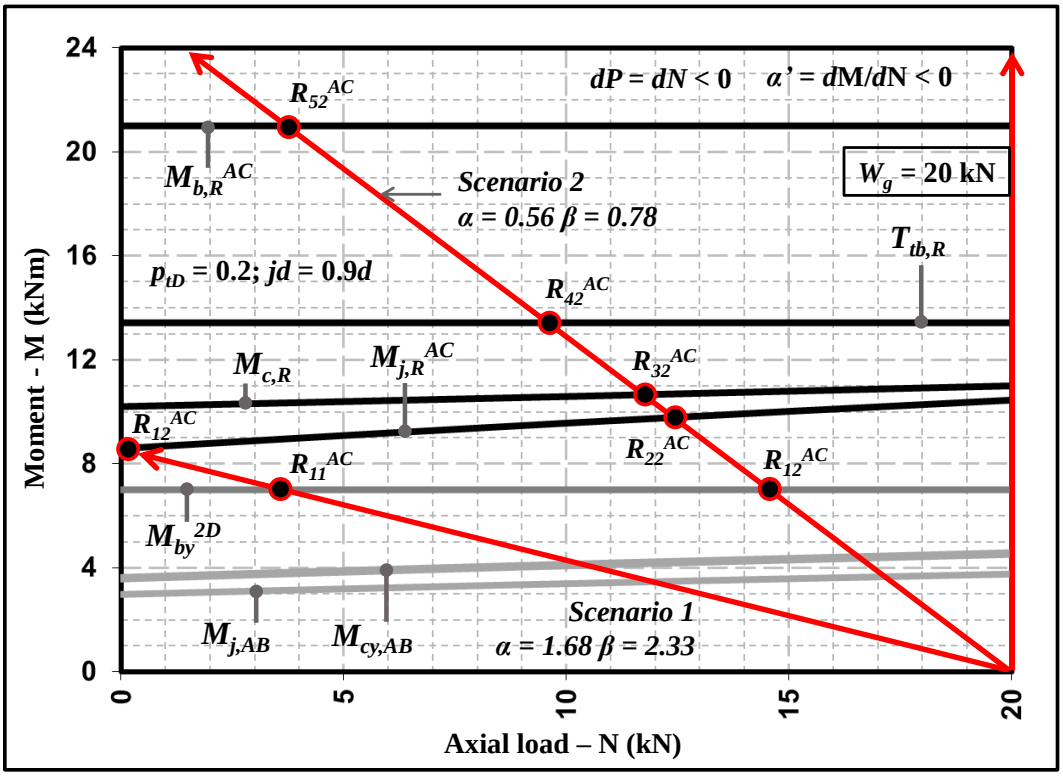

Figure 6.28: M-N performance domain for the retrofitted corner beam column joint of the long span in the AC state; three demand scenarios considered.

In Figure 6.28 the M-N performance domain is presented for the AC situation, where: $M_{j.AB}^{AC}$ = equivalent resisting moment of the as-built joint for cracking limit state (p_t = $0.2\sqrt{f_c'}$), $M_{cy,AB}$ = yielding moment of the as-built column, M_{by}^{2D} = yielding moment capacity of the section of the beam where the slab has been cut (rectangular section), $M_{j,R}^{AC}$ = equivalent moment of the retrofitted corner joint (for debonding limit state in the GFRP in this case), $M_{c,R}$ = retrofitted column moment strength, $T_{tb,R}$ = retrofitted spandrel torsion strength, $M_{b,R}^{AC}$ = bending moment strength of the retrofitted beam for the design strain limit in the FRP (ε_{fu} = 1% in this case). The upper script AC denotes the state corresponds to positive bending moment in the beam (tension in the slab). If that symbol is not present, it means that that value is the same for the AC and AT states (positive and negative bending moment in the beam, respectively).

As can be observed in Figure 6.28, for α_1 (high axial load variation scenario), the strength of the retrofitted column, joint, beam and spandrel would only be reached with tension in the column. The strength of the weakened beam though, would be reached with an 80% reduction in the axial load from the gravity state. In all cases, the sequence of events is the same regardless of the demand or variation of the axial load considered. The results of

the retrofitted matrix are presented in Equation 6.25. This matrix contains the information of the sequence of events with the associated values of the axial load and the bending moment to their eventual occurrence for scenarios 2 and 3. The elements inside the matrix are analogue to the elements defined in Chapter 5 for the assessment matrix. In this case, the previously defined $AB_{ij} \in |R^3$ row vectors are named R_{ij} and defined as follows:

$$R_{ij} = \langle R \rangle_{ij} = \langle E_{ij}; N_{ij}; M_{ij} \rangle$$

Where E_{ij} is the element label in the sequence number i and the demand scenario j, and N_{ij} and M_{ij} the axial load and bending moment corresponding to the intersection of the demand with the capacity curve of the element i in the scenario j. These row vectors are indicated as the points where the demand and the capacity of an element is reached in the M-N diagram, as shown Figure 6.28 to Figure 6.32. In this case, 5 events are incorporated into the matrix since the beam strength is evaluated in the rectangular section in the weakened region of the slab (named *BW*) and the strengthened section (named *BS*), as well as the joint (*J*), the column (*C*) and the spandrel (*S*).

Using that nomenclature and the upper script AC to indicate the state being evaluated, the sequence of events matrix of the beam column joint after the retrofit interventions is presented in Equation 6.63, for scenarios 1 and 2.

$$[\mathrm{R}]^{AC} = \left[\begin{bmatrix} BW & 7.0 & 3.7 \\ J & 8.5 & 0.2 \\ C & 10.0 & -3.3 \\ S & 13.4 & -11.2 \\ BS & 21.0 & -28.9 \end{bmatrix}_{j=1} \begin{bmatrix} BW & 7.0 & 14.5 \\ J & 9.8 & 12.4 \\ C & 10.6 & 11.7 \\ S & 13.4 & 9.5 \\ BS & 21.0 & 3.6 \end{bmatrix}_{j=2} \right] \tag{6.63}$$

The reduced sequence of events matrix is therefore given by (see Chapter 5):

$$[SE]^{AC} = \begin{bmatrix} BW & BW \\ J & J \\ C & C \\ S & S \\ BS & BS \end{bmatrix}$$

Therefore, relocation of the inelastic behaviour has is expected to be achieved, since in this case the weakest link is the rectangular section of the beam.

6.10.1.2 AT State Corner

The AC state defined in Chapter 5 corresponds to:

(1) tension in the slab,
(2) increasing axial load (seismically induced shear in the beam points downward

In this case, the moment in the beam is negative, and hence the evaluation of the strengths of the panel zone elements must be evaluated in the third quadrant as explained in Chapter 5. The M-N diagram the corner joint of the long span (most critical) in presented in Figure 6.29. The same nomenclature used in the evaluation of the corner joint in the

AC state is used in Figure 6.29, with the exception that the upper script indicated the AT situation if that is relevant for the element.

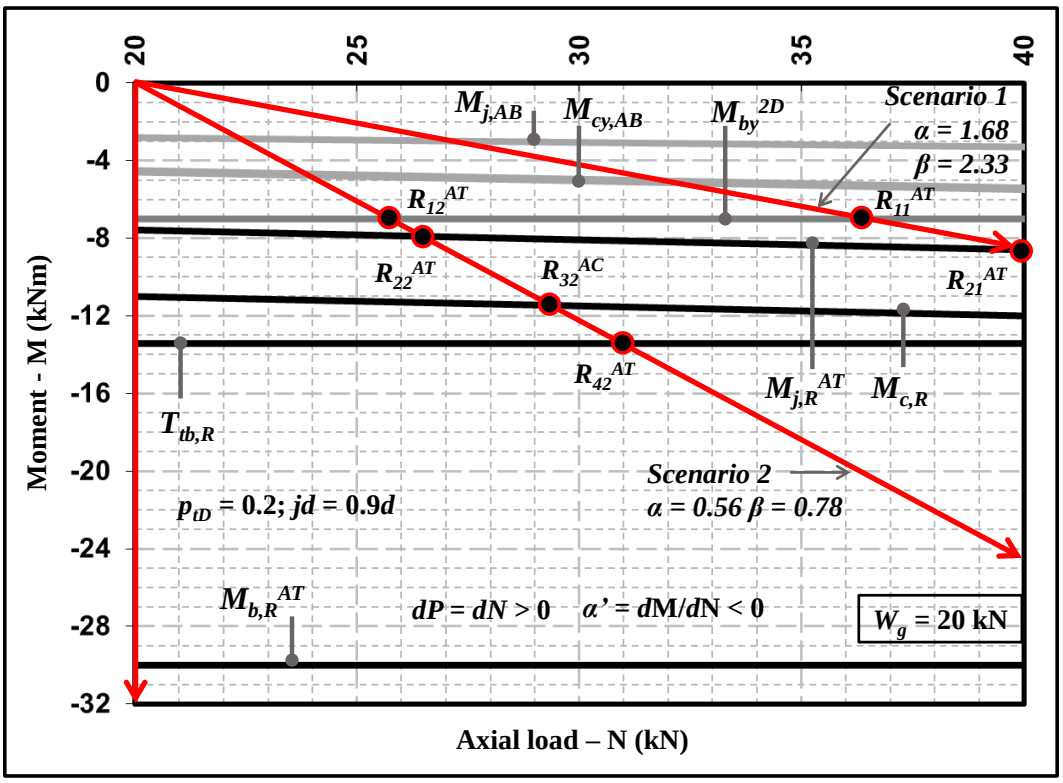

Figure 6.29: M-N performance domain for the retrofitted corner beam column joint of the long span in the AT state; three demand scenarios considered.

Two demand scenarios were also considered as before (j = 1, 2). Again in this case, the demand is irrelevant for the evaluation of the sequence of events, because the hierarchy of the strengths is the same in all the axial load range of interest. The values associated to each events and their order is presented in the evaluation matrix of Equation 6.64.

$$[\mathrm{R}]^{AT} = \left[\begin{bmatrix} BW & -7.0 & 36.3 \\ J & -8.6 & 40.0 \\ C & -12.5 & 49.1 \\ S & -13.4 & 51.1 \\ BS & -30.0 & 89.9 \end{bmatrix}_{j=1} \begin{bmatrix} BW & -7.0 & 25.5 \\ J & -8.0 & 26.2 \\ C & -11.5 & 29.0 \\ S & -13.4 & 30.5 \\ BS & -30.0 & 43.4 \end{bmatrix}_{j=2} \right] \tag{6.64}$$

The sequence of events matrix is therefore given by:

$$[SE]^{AT} = \begin{bmatrix} BW & BW \\ J & J \\ C & C \\ S & S \\ BS & BS \end{bmatrix}$$

6.10.2 M-N Diagram for Cruciform Beam Column Joints (Internal Frame)

In the evaluation of the equivalent moment in the joint, in cruciform beam column joints the maximum tensile stress in the concrete is taken as $p_{tc,0} = 0.3\sqrt{f_c'}$ at a corresponding angular distortion $\gamma_0 = 0.0003$ rad. The same values for jd and ω for AC and AT states apply in this case. However, the effective width of the joint is larger due to the presence of a spandrel on both sides of the joint in the transverse direction. The criterion for the evaluation of the strength of these joints was to increase the p_{tc} value associated to cracking to $0.4\sqrt{f_c'}$, which is the value suggested by Priestley (1997) for well-designed beam column joints of this typology. It is argued that the confinement provided by the FRP laminates to the joint can allow for such an increase in tensile principal stress associated to cracking. It is worth noting that this is not an increase in maximum total pt value that the retrofitted joint can resist, which is $p_{tt} = p_{tc} + p_{tf}$. Nevertheless, more research is required to empirically conform or refute that argument.

6.10.2.1 AC State Cruciform

The evaluation of the cruciform joints of the long span in the M-N performance domain in the AC situation is presented in Figure 6.30. In this case, the gravity load is larger than for corner joints, with a value of 30 kN. In Figure 6.30 the same nomenclature used in the M-N diagram of corner joints was used. The same two demand scenarios described in the previous section are used here.

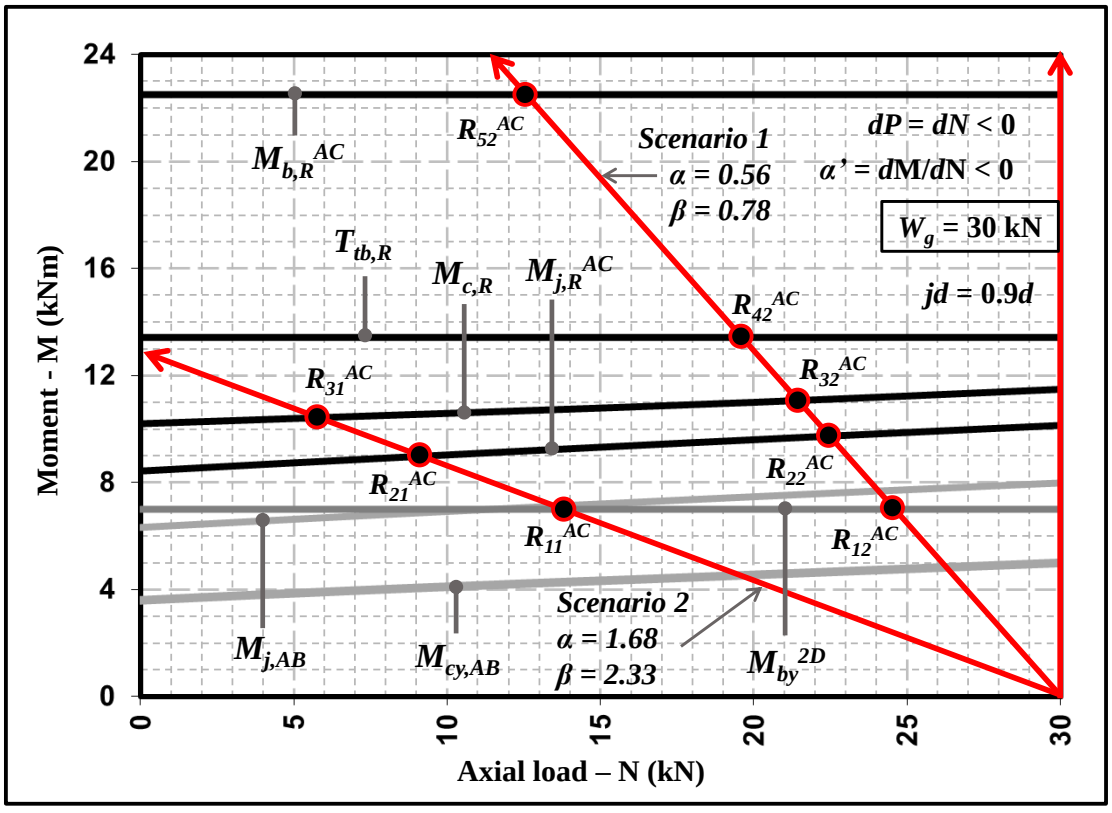

Figure 6.30: M-N performance domain for the retrofitted cruciform beam column joint of the long span in the AC state; three demand scenarios considered.

The results of the sequence of events under these (1 and 2) are summarized in the matrix of Equation 6.65.

$$[\mathrm{R}]^{AC} = \left[\begin{bmatrix} BW & 7.0 & 13.7 \\ J & 9.0 & 9.0 \\ C & 10.5 & 5.5 \\ S & 13.4 & \_1.2 \\ BS & 22.5 & -22.4 \end{bmatrix}_{j=1} \begin{bmatrix} BW & 7.0 & 24.5 \\ J & 9.7 & 22.4 \\ C & 11.0 & 21.4 \\ S & 13.4 & 19.5 \\ BS & 22.5 & 12.5 \end{bmatrix}_{j=2}\right] \tag{6.65}$$

The sequence of events matrix is therefore given by:

$$[SE]^{AC} = \begin{bmatrix} BW & BW \\ J & J \\ C & C \\ S & S \\ BS & BS \end{bmatrix}$$

Hence, the expected sequence of events is the same for the two scenarios examined as well as all the axial load range of interest.

6.10.2.2 AT State Cruciform

In Figure 6.31 the M-N diagrams of the elements of the cruciform beam column joint in the AT situation are presented.

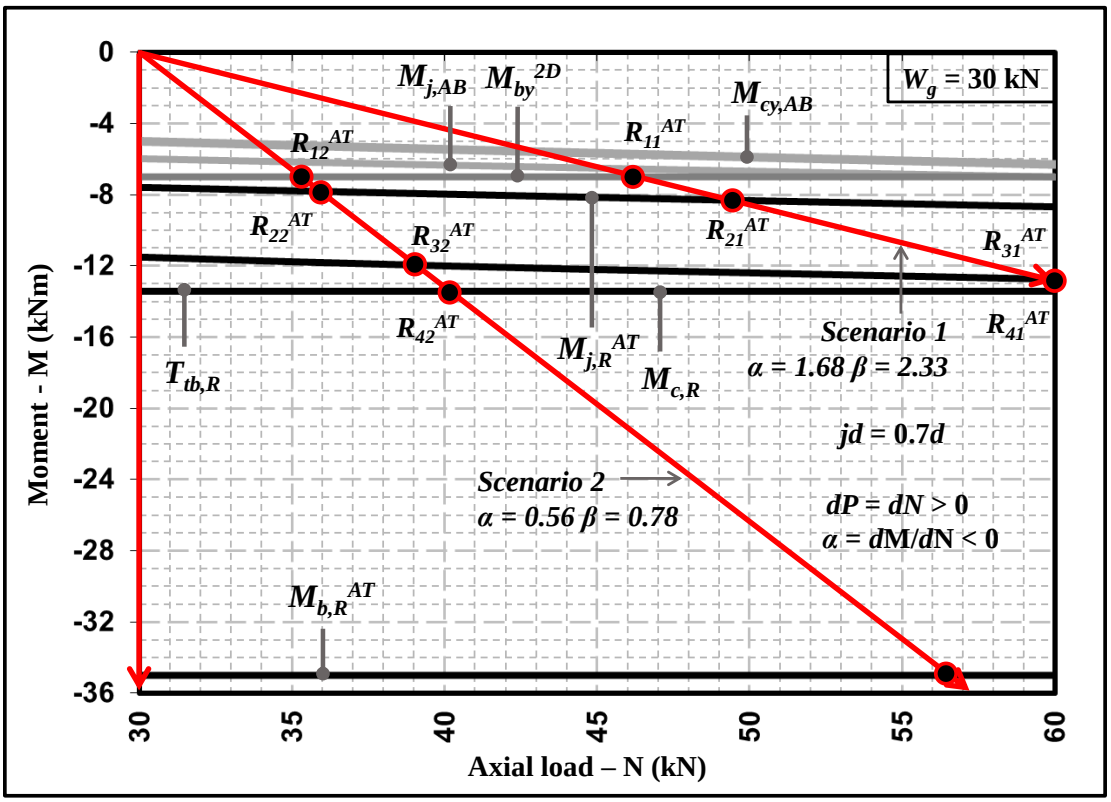

Figure 6.31: M-N performance domain for the retrofitted cruciform beam column joint of the long span in the AT state; three demand scenarios considered.

As can be observed in that Figure, the hierarchy of the strengths remains invariable for the axial load range examined and beyond. In this case, the demand used in scenario 1 intersects four of the five elements under examination. That is, the bending capacity of the strengthened beam section would be reached at very high axial load. The same is true for the demand associated to the scenario 2 (like in the previous cases examined), but the load would not be that great and of the order of 70 kN (2.33 times the gravity load). In the results summarized for the previous evaluations, only scenarios 2 and 3 are shown in the evaluation matrix presented in Equation 6.66.

$$[\mathrm{R}]^{AT} = \left[\begin{bmatrix} BW & -7.0 & 46.3 \\ J & -8.3 & 49.3 \\ C & -12.8 & 59.8 \\ S & -13.4 & 61.2 \\ BS & -35.0 & 112 \end{bmatrix}_{j=1} \begin{bmatrix} BW & -7.0 & 35.5 \\ J & -7.9 & 36.2 \\ C & -12.0 & 39.4 \\ S & -13.4 & 40.5 \\ BS & -35.0 & 57.3 \end{bmatrix}_{j=2} \right] \tag{6.66}$$

The sequence of events matrix is therefore given by:

$$[SE]^{AC} = \begin{bmatrix} BW & BW \\ J & J \\ C & C \\ S & S \\ BS & BS \end{bmatrix}$$

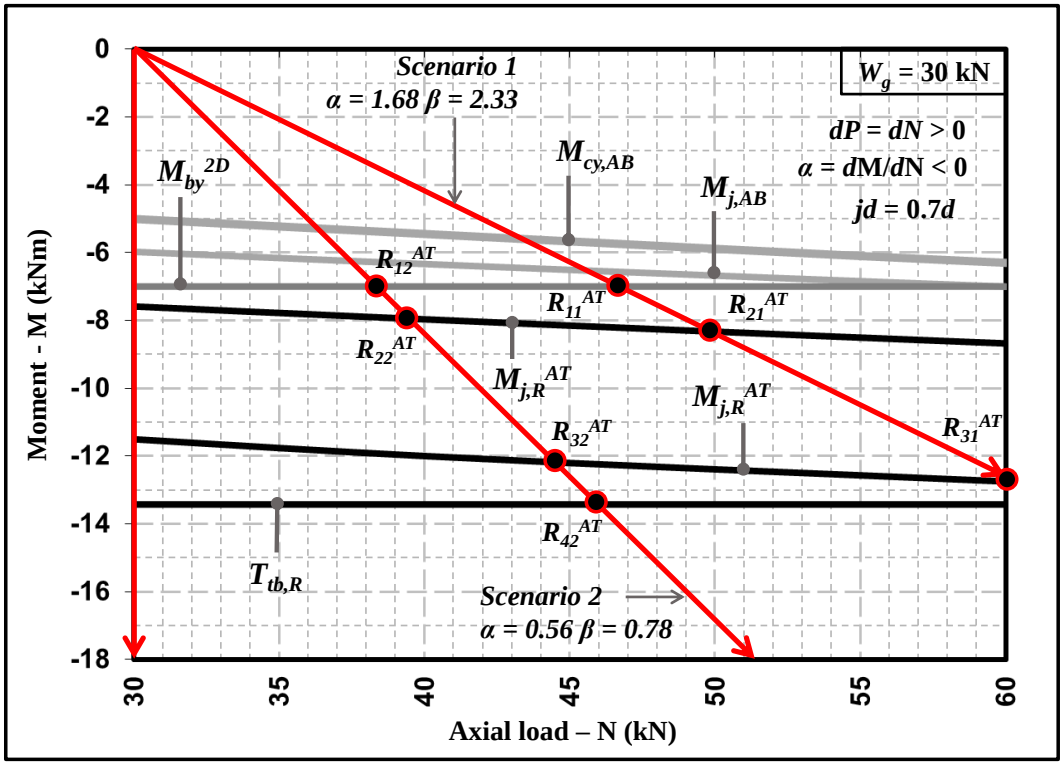

Figure 6.32: M-N performance domain retrofitted cruciform beam column joint long span AT state – close up to half the maximum moment in the graph of Figure 6.31.

As in this case the difference in the bending moment capacity of the strengthened beam section and the strengthened joint and columns as well as the rectangular section of the beam in the gap region, a close up of Figure 6.31 is presented in Figure 6.32. In that

Figure, it can be observed that the difference between the strengthened joint and the weakened beam is rather small, especially for axial load levels close to the gravitational value. This difference can be even less than 1 kNm, which is about 15% of the rectangular beam section moment capacity. Nevertheless, as during the shake table tests of the specimen retrofitted in the way explained in this chapter apparently no damage developed in the well confined cruciform joints, it is argued that the assumption of the maximum tensile principal stress can be even higher that that assumed in this case. However, more research is apparently needed for the estimation of a suitable parameter for this joint typology, the most attractive option being quasi-static tests of subassemblies retrofitted using this retrofit configuration and the extended version of the M-N performance domain developed in this thesis.

6.10.3 Complete Evaluation

As was defined in the second section of Chapter 5, a unique matrix called [AB] can be generated for a complete evaluation of all the cases previously reviewed. In this case, that matrix is renamed [R] for retrofit, with the form of Equation 6.67

$$[\mathrm{R}]_{k=1,2} = \begin{bmatrix} [R]_{j=2}^{AC} & [R]_{j=3}^{AC} \\ [R]_{j=2}^{AT} & [R]_{j=3}^{AT} \end{bmatrix}_{k=1,2} \tag{6.67}$$

In Equation 6.67, the four sub matrices correspond to the matrices generated previously for the AC and AT situations and the demands scenarios j = 2 and j = 3. The subscript k indicates the beam column joint typology so that k = 1 and k = 2 are associated to the corner and cruciform joints, respectively. The complete evaluation of the retrofitted beam column joints is also summarized in Table 6.1.

$$[\mathrm{R}]_{k=1} = \begin{bmatrix} BW & 7.0 & 3.7 & BW & 7.0 & 14.5 \\ J & 8.5 & 0.2 & J & 9.8 & 12.4 \\ C & 10.0 & -3.3 & C & 10.6 & 11.7 \\ S & 13.4 & -11.2 & S & 13.4 & 9.5 \\ BS & 21.0 & -28.9 & BS & 21.0 & 3.6 \\ BW & -7.0 & 36.3 & BW & -7.0 & 25.5 \\ J & -8.6 & 40.0 & J & -8.0 & 26.2 \\ C & -12.5 & 49.1 & C & -11.5 & 29.0 \\ S & -13.4 & 51.1 & S & -13.4 & 30.5 \\ BS & -30.0 & 89.9 & BS & -30.0 & 43.4 \end{bmatrix} \tag{6.68}$$

$$[\mathrm{R}]_{k=2} = \begin{bmatrix} BW & 7.0 & 13.7 & BW & 7.0 & 24.5 \\ J & 9.0 & 9.0 & J & 9.7 & 22.4 \\ C & 10.5 & 5.5 & C & 11.0 & 21.4 \\ S & 13.4 & \_1.2 & S & 13.4 & 19.5 \\ BS & 22.5 & -22.4 & BS & 22.5 & 12.5 \\ BW & -7.0 & 46.3 & BW & -7.0 & 35.5 \\ J & -8.3 & 49.3 & J & -7.9 & 36.2 \\ C & -12.8 & 59.8 & C & -12.0 & 39.4 \\ S & -13.4 & 61.2 & S & -13.4 & 40.5 \\ BS & -35.0 & 112 & BS & -35.0 & 57.3 \end{bmatrix} \tag{6.69}$$

$$[\mathrm{SE}]_{tot} = \begin{bmatrix} BW & BW & BW & BW \\ J & J & J & J \\ C & C & C & C \\ S & S & S & S \\ BS & BS & BS & BS \end{bmatrix} \tag{6.70}$$

Table 6.1: Retrofitted beam column joints evaluation summary.

Corner AC						Cruciform AC					
α = 1.68, β = 2.66			α = 0.56, β = 0.78			α = 1.68, β = 2.66			α = 0.56, β = 0.78		
Element	**M (kNm)**	**N (kN)**	**Element**	**M (kNm)**	**N (kN)**	**Element**	**M (kNm)**	**N (kN)**	**Element**	**M (kNm)**	**N (kN)**
BW	7.0	3.7	**BW**	7.0	14.5	**BW**	7.0	13.7	**BW**	7.0	24.5
J	8.5	0.2	**J**	9.8	12.4	**J**	9.0	9.0	**J**	9.7	22.4
C	10.0	-3.3	**C**	10.6	11.7	**C**	10.5	5.5	**C**	11.0	21.4
S	13.4	-11.2	**S**	13.4	9.5	**S**	13.4	-1.2	**S**	13.4	19.5
BS	21.0	-28.9	**BS**	21.0	3.6	**BS**	22.5	-22.4	**BS**	22.5	12.5
Corner AT						**Cruciform AT**					
α = 1.68, β = 2.66			α = 0.56, β = 0.78			α = 1.68, β = 2.66			α = 0.56, β = 0.78		
Element	**M (kNm)**	**N (kN)**	**Element**	**M (kNm)**	**N (kN)**	**Element**	**M**	**N**	**Element**	**M (kNm)**	**N (kN)**
BW	-7.0	36.3	**S**	-7.0	25.5	**BW**	-7.0	46.3	**BW**	-7	35.5
J	-8.6	40.0	**J**	-8.0	26.2	**J**	-8.3	49.3	**J**	-7.9	36.2
C	-12.5	49.1	**C**	-11.5	29.0	**C**	-12.8	59.8	**C**	-12	39.4
S	-13.4	51.2	**B**	-13.4	30.5	**S**	-13.4	61.2	**S**	-13.4	40.5
BS	-30.0	89.9	**BS**	-30.0	43.4	**BS**	-35.0	112	**BS**	-35	57.3

6.11 INELASTIC MECHANISM AND DAMAGE RELOCATION

Once the desired hierarchy of strengths in the retrofitted beam column joints was achieved, the length of the FRP layers in the beams and the columns must be re-evaluated. This last evaluation must be done in accordance with the imposed (assumed) inelastic mechanism of the frame in order to check that the maximum bending moment in the retrofitted beams and columns is smaller than the nominal moment capacity. If the maximum capacity of the strengthened section is reached, then damage/inelasticity relocation may not occur (see Figure 6.14). For that, the bending moment diagrams (BMD) corresponding to the collapse mechanism of the structure must be constructed. This collapse mechanism must be kinematical-compatible and statically-admissible, following the kinematic and static theorems of plastic analysis, respectively (Massonnet and Save 1966, Neal 1977). The static theorem requires that at ultimate limit state (collapse mechanism) the BMD in all structural elements must be always smaller than or equal to the 'plastic moment' capacity of the element sections. In this case the 'plastic moment' for the beams corresponds to the moment capacity of the rectangular section inside the gap region and outside the strengthened section (M_{by}^{2D}), and for the columns it corresponds to the moment capacity of the as-built section (M_{cy}).

Assuming that both frames, external and internal, can be understood as identical plane frames, the actions imposed the lateral forces are presented in Figure 6.33. It is assumed that the distribution of the inertial forces along the height is uniform. In the case presented in Figure 6.33, seismic actions are represented by forces at floor levels and taken to the right, producing a positive bending moment in the left of the beam of the long span (slab in compression), and negative bending moment in the right hand side of the beam of the short span (slab in traction). In Figure 6.33, the induced actions at the ends of

every structural member are presented as well as the reactions at the bottom of the columns and the shape of the BMD for all members at ultimate state or collapse mechanism. For a collapse mechanism where plastic hinges are formed at the bottom end of all the first floor columns, at the top and bottom ends of the internal columns, and the weakest part of the beams in exterior beam column joints, the magnitude of the associated statically admissible BMD is shown is Figure 6.34 and Figure 6.35.

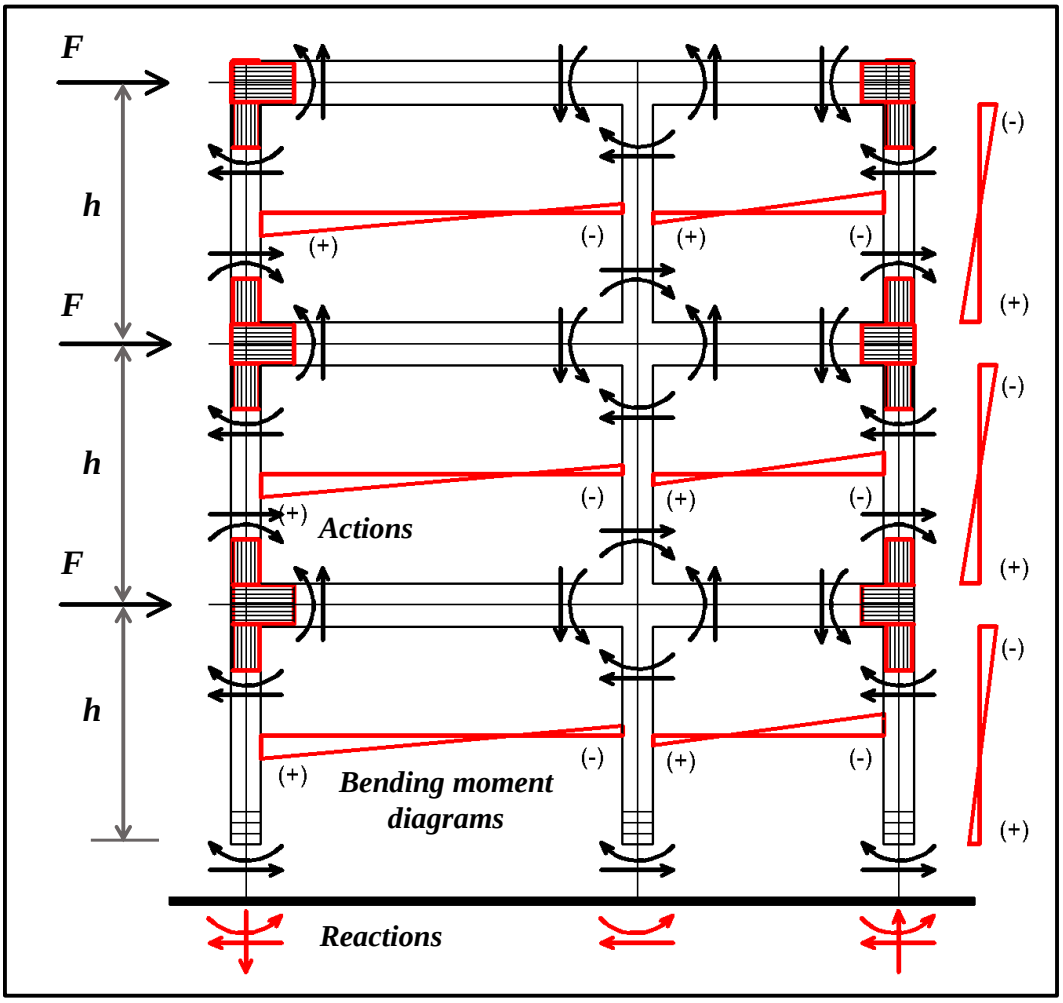

Figure 6.33: Inelastic mechanism, actions in structural elements, and bending moment diagrams.

In Figure 6.34 the BMD in the elements of an isolated exterior beam column joint of the long span is shown. The beam and the columns are shown up to the point in their length where the bending moment becomes zero (inflexion point). Note that the inflexion point in the beam does not correspond to half of the clear span as many times assumed. That is because the moment of the beams at the end close to the interior column is smaller than the moment developed in the other end, due to the existence of a weaker column in that point and no strengthening of the beam or weakening of the slab. Therefore, the maximum bending moment at the internal end of the beam is equal to the yielding moment capacity of the column, taken equal to 4.5kN (moment capacity for N_v = 20kN). In Figure 6.34, the BMD in the beam has been fixed so that the moment in the section outside the strengthened region reaches the yielding capacity of the rectangular beam section, equal to 7kNm. Extending the linear shape of the BMD in the beam to the face

of the column, it can be demonstrated that the maximum bending moment in the strengthened portion of the beam is smaller than the section capacity and thus, that BMD is statically admissible. That bending moment is transmitted to the top and bottom columns in equal parts. The BMD in the columns is then constructed using that moment value at both ends, as it was assumed that at the ultimate limit state the BMD in all upper floors are the same. In Figure 6.34 it is shown that the value developed at the ends of the columns is smaller than the as-built yielding capacity of the section and much smaller than the moment capacity of the strengthened column section. In the bottom floor though, the moment at the base of the columns corresponds to the yielding moment of the as-built columns since no strengthening of those sections was carried out. These sections as well as the created rectangular section of the beam constitute the places where inelasticity is expected to occur given a constant drift in the structure produced by the uniform variation of the later load in the height of the building.

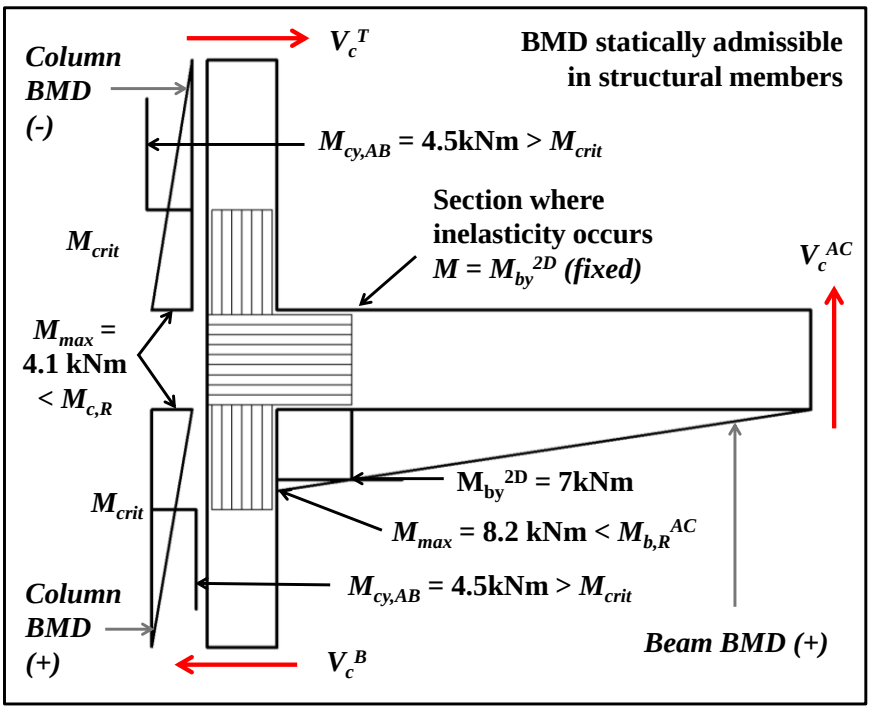

Figure 6.34: Statically admissible BMD of the collapse mechanism, long span beam column joints.

In the corner beam column joint of the short span, the bending moment diagram takes similar values to those shown in Figure 6.34, as presented in Figure 6.34. The only difference is that in this case the slope of the BMD in the beam is larger than the slope of the BMD that develops in the long span corner joint, due to the smaller longitude of the span. The BMD in the beam takes the value of M_{by}^{2D} at the critical section next to the FRP layers, and in the columns has a maximum value very similar to that experienced by the long span beam as shown in Figure 6.34 (approximately 8.2kNm). The BMD in the column compatible with the BMD developed in the beam is smaller than the as-built column capacity in the critical section (M_{crit}), where the FRP laminates end, and much smaller than the capacity of the strengthened column section in the face of the beam.

It is important to note though, that if the capacity of the beam increases significantly due to large inelastic deformations, then the maximum moment in the columns increases as

well as the moment at the critical section where the FRP laminates end. That is, if the model building faces high drift demands during dynamic excitations for example, some damage may also occur in the critical section of the columns. As will be shown in the next chapter where the results of the shake table tests of the retrofitted specimen are presented, the damage developed in the structure revealed that inelasticity concentrated primarily in the beam, but some also occurred in the critical sections of the columns.

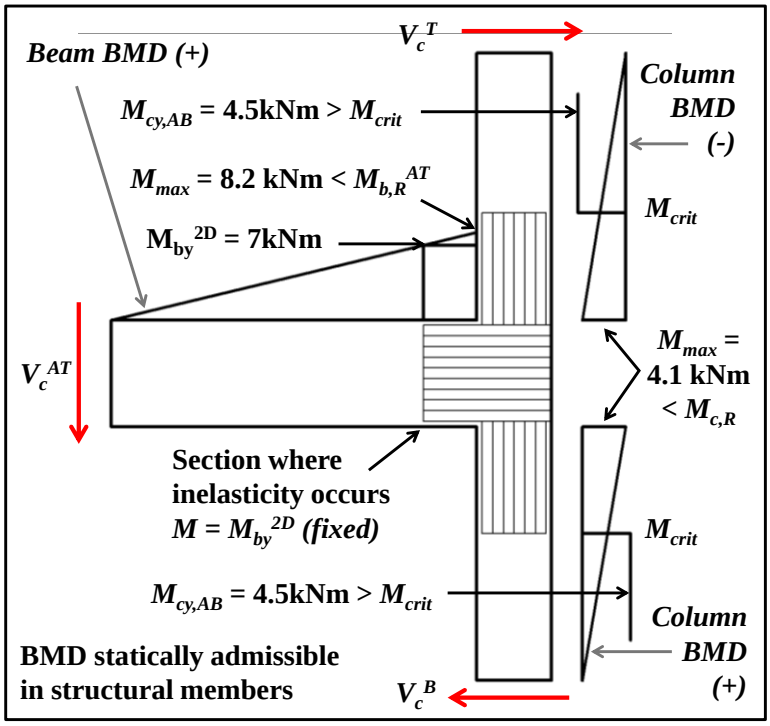

Figure 6.35: Statically admissible BMD of the collapse mechanism, long span beam column joints.

6.12 CONCLUDING REMARKS

In this chapter, the development of the retrofit intervention developed for the model building under investigation has been presented. The retrofit intervention follows a partial retrofit strategy and makes use of FRP laminates for strengthening the joints and the portion of the beams and columns close to the panel zone creating a very stiff region, as well as selective weakening concepts for disabling the effect of the slab and the spandrel in the negative bending moment capacity of the beam. The design was created based on previous research on plane 2D and 3D beam columns joints without a floor slab. Using the extended version of the M-N performance domain, the evaluation of the hierarchy of strengths and the sequence of events in the panel zone was evaluated for corner and cruciform beam column joints, in the AC and AT states. Using this method, it was possible to demonstrate that the developed retrofit intervention (strengthening plus weakening) results in the weakest link being the section of the beam close to the gap region, regardless of the demand scenario given by the variation of the axial load.

The evaluation of the inelastic mechanism and the corresponding statically admissible BMD indicates that extension of the FRP layers in beams and columns is adequate. That means that the inelasticity expected to develop in the weakest section of the beams, the

base of the columns of the bottom floor, and both ends of the internal columns in all floors. Therefore, the expected inelastic mechanism has a hybrid nature, with beam hinging in the exterior ends and hinging of both ends of the internal columns. As it will be shown in Chapter 7, when the specimen retrofitted in the way presented herein was tested on the shake table under a very demanding record, the anticipated inelastic mechanism did develop, but some inelastic incursions were also observed in the critical sections of the column due to an increase in the moment capacity of the rectangular beam section beyond yielding, variations in the capacity of the columns due to fluctuations in the axial load, and the inherent variation between the real and nominal mechanical characteristics of the materials.

The problem thus far has been addressed from an inelastic and pure static or quasi-static perspective. That is, time is not taken into consideration. The dynamical nature of the actual response of structures under earthquake excitations though requires the consideration of time and thus the evolution of the state of a structure when the events described in this chapter (and Chapter 5) occur. The nonlinear dynamics involved in the problem of the examination of the effectiveness of the proposed retrofit interventions are addressed in the next chapter, where the results and findings of the specimen retrofitted as described in this chapter are presented.

6.13 REFERENCES

ACI Committee 440.2 (2002), 'Guide for the Design and Construction of Externally Bonded FRP Systems for Strengthening Concrete Structures', ACI 440.2R-02, Farmington Hills, MI.

Akguzel, U., Pampanin, S. (2010), 'Effects of Variation of Axial Load and Bidirectional Loading on Seismic Performance of GFRP Retrofitted Reinforced Concrete Exterior Beam-Column Joints', *Journal of Composites for Construction*, Vol. (14), pp. 94-104.

Akguzel, U., Quintana Gallo, P., Pampanin, S., Carr, A.J. (2011), 'Seismic Strengthening of a Non-Ductile RC Frame Structure using GFRP Sheets', *Proceedings of the PCEE*, Auckland, paper 197.

Akguzel, U. (2011), 'Seismic Performance of FRP Retrofitted Exterior RC Beam-Column Joints under Varying Axial and Bidirectional Loading', *a thesis presented for the degree of Doctor of Philosophy in Civil Engineering*, University of Canterbury, Christchurch, New Zealand.

Akguzel, U., and Pampanin, S. (2012), 'Assessment and Design Procedure for the Seismic Retrofit of Reinforced Concrete Beam-Column Joints using FRP Composite Materials', *Journal of Composite for Construction*, ASCE, Vol. 16(1), pp. 21-34.

Collins, M. P. and Mitchel, D. (1992), *Prestressed Concrete Structures*, Prentice-Hall, Englewood Cliffs, New Jersey, USA

Di Franco, M. A., Mitchell, D., Paultre, P. (1995), 'Role of Spandrel Beams on Response of Slab-Beam-Column Connections', Journal of Structural Engineering, Vol. 121(3), pp. 408-419.

Durrani, A. and Zerbe, H. (1987), 'Seismic Resistance of R/C Exterior Connections with Floor Slab' *Journal of Structural Engineering*, Vol. 113(8), pp. 1850–1864.

Ehsani, M. R., and Wight, J. K. (1985), 'Exterior Reinforced Concrete Beam-to-Column Connections Subjected to Earthquake-Type Loading', *ACI Journal*, Vol. 84(2), pp. 492-499.

Hakuto, S., Park, R., and Tanaka, H. (2000), 'Seismic Load Tests on Interior and Exterior Beam-Column Joints with Substandard Reinforcing Details', *ACI Structural Journal*, Vol. 97(1), pp.11-25.

Holzenkämpfer, P. (1994), 'Ingenieurmodelle des Verbundes Geklebterbewehrung für Betonbauteile, *Ph.D. dissertation*, TU Braunshwieg (in German).

Kam, W.Y., Quintana-Gallo, P., Akguzel, U., Pampanin, S. (2010) 'Influence of slab on the seismic response of substandard exterior reinforced concrete beam column joints', *Proceedings of the for 9th US and 10th Canadian National Conference on Earthquake Engineering*, Toronto, Canada.

Kam, W. (2010), 'Selective Weakening and Post-Tensioning for the Seismic Retrofit of Non-Ductile RC Frames', *a thesis presented for the degree of Doctor of Philosophy in Civil Engineering*, University of Canterbury, Christchurch, New Zealand.

Lorenz, E. (1963), 'Deterministic Non Periodic Flow', *MIT Press*, Massachusetts, USA.

MacGregor, J.G. and Ghoneim, M. G. (1995), 'Design for Torsion', *ACI Structural Journal*, Vol. 92(2), pp. 211-218.

Massonnet, Ch. and Save, M. (1966), *Cálculo plástico de las construcciones*, Montaner y Simón (in Spanish).

Neubauer, U., Rostasy, F. S. (1997), 'Design Aspects of Concrete Structures Strengthened with Externally Bonded CFRP-plates', Proceedings of the 7th International Conference on Structural Faults and Repair, London, 109–118.

Neal, B.G. (1977), *Plastic Methods of Structural Analysis*, John Wiley and Sons, New York.

Pampanin, S., Calvi, G.M., Moratti, M. (2002), 'Seismic Behavior of RC Beam Column Joints Designed for Gravity Loads', *12th ECEE*, London, England, paper n. 726.

Pampanin, S. (2005), 'Controversial Aspects in Seismic Assessment and Retrofit of Structures in Modern Times: Understanding and Implementing Lessons from Ancient Heritage', *New Zealand Concrete Society Conference*, Auckland, New Zealand.

Pampanin, S., Bolognini D., and Pavese, A. (2007) 'Performance-Based Seismic Retrofit Strategy for Existing Reinforced Concrete Frame Systems Using Fiber-Reinforced Polymer Composites', *Journal of Composites for Construction*, ASCE, Vol. 11(2), pp. 211-226.

Priestley, M.J.N. 1997, Displacement-based Seismic Assessment of Existing Reinforced Concrete Buildings, *Journal of Earthquake Engineering*, Vol. 29, n4, p 356-272.

Prota, A., Nanni, A., Manfredi, G., and Cosenza, E. (2001), 'Selective Upgrade of Beam-Column Joints with Composites', *Proceedings of the International Conference on FRP Composites in Civil Engineering*, Vol. I, Elsevier Science, New York, 919–926.

Quintana-Gallo, P., Pampanin, S., Carr, A.J., Bonelli, P. (2010), 'Shake table tests of under-designed frames for the seismic retrofit of buildings – design and similitude requirements of the benchmark specimen', *Proceedings of the NZSEE Conference*, Wellington, paper 39.

Quintana-Gallo, P., Akguzel, U., Pampanin, S., Carr, A.J. (2011), 'Shake Table Tests of Non-Ductile As-Built and Repaired RC Frames', *Proceedings of the PCEE*, Auckland, paper 201.

Quintana-Gallo, P., Rebolledo, R. and Allan, G. (2013), 'Dealing with Uncertainty in Earthquake Engineering: a Discussion on the Application of the Theory of Open Dynamical Systems, *Obras y Proyectos*, Vol 14(2), pp. 66-77 (*in English*).

SEASOC (1995), *Performance-Based Seismic Engineering*, Structural Engineers Association of California, Sacramento, California, USA.

Shin M and LaFave J. M. (2004), 'Reinforced Concrete Edge Beam-Column-Slab Connections Subjected to Earthquake Loading,' *Magazine of Concrete Research*, Vol. 56(5), pp. 273-291.

Strogatz, S. (1994), *Nonlinear Dynamics and Chaos*, Westview Press, Cambridge, Massachusetts, USA.

Teng, J.G., Smith, S.T., Yao, J., Chen, J.F. (2003), 'Intermediate Crack-Induced Debonding in RC Beams and Slabs', *Construction and Building Materials*, Vol. 17, pp. 447–462.

Wallace, J. W., Ibrahim, Y. (1996), *Biax-96 for MS Windows – Strength and Analysis of RC Sections*, University of California, Los Angeles, USA.

7 SHAKE TABLE TESTS OF THE RETROFITTED SPECIMEN

7.1 INTRODUCTION

After the last test of the building in the as-built/repaired condition was performed, the specimen was standing in a severe damage condition in the Structures Laboratory. The exterior joints of the external frame in the first floor suffered large shear damage with important crushing of the concrete inside the panel zone region. The specimen was repaired by removing the crushed concrete in all exterior beam column joints and some of the base of first floor columns in the first floor, replacing the removed material with more concrete prepared in the laboratory with the same mechanical properties, and by injecting the cracks with epoxy resin. The specimen was then upgraded using the retrofit intervention developed in this thesis and presented in Chapter 6. The implementation of that retrofit intervention was carried out by an external company, BBR Contech New Zealand, and all the retrofit material was provided by SIKA New Zealand. In a first stage, the GFRP laminates with the dimensions and in the sequence described in Chapter 6 were placed. In a second stage, weakening of the floor slabs in the location and configuration presented in Chapter 6 was carried out. The technical procedure required for that implementation is described in the first part of this chapter.

Once the retrofit intervention was implemented, the specimen was tested under simulated earthquake motion excitations in the shake table of the Structures Laboratory of the University of Canterbury. The same experimental protocol and input sequence used in the shake table tests of the as-built/repaired specimen during tests 2.1 and 2.2, described in Chapter 4, was followed. That is, the specimen was firstly tested under a ground motion recorded at the Christchurch Hospital Station (CHH) during the Darfield earthquake that affected the Canterbury region on the 4 of September 2010. After that test, visual inspection as well as non-processed data available in the logging system indicated that the specimen apparently remained in the elastic range of the response, and did not suffer visible damage.

That result enabled the possibility to continue with the experimental sequence, so that in a second experiment, Test 3.2, the undamaged retrofitted specimen was subjected to a ground motion recorded in Viña del Mar Marga-Marga station (VMM) during the 27 of February 2010 Maule earthquake that affected an important part of central Chile (600 km approximately). The response of the retrofitted building in terms of inter-storey drifts and floor accelerations was much larger in magnitude when compared to the previous test. Significant inter-storey drift values were recorded in all floors, especially in the first one, where a maximum (absolute) value of 3.7% was measured. Damage predominantly developed in the beams and internal columns as predicted in Chapter 6 for the case when the inelastic mechanism develops due to large inter-storey drift demands. Second mode effects and torsion were also observed as well as some damage in the as-built part of the external columns close to the GFRP strengthened region.

In this Chapter, the implementation of the retrofit intervention is briefly described, and the applied strengthening scheme and weakening configurations shown. The records used as input ground motions are examined in deeper detail with emphasis on the difference of

the nominal (intended) and the recorded input of the shake table during the experiments. The global results of the experiments are presented in terms of the recorded inter-storey drifts and floor accelerations at every level. Pictures of the damage developed all beam column joint typologies part of the specimen, are also presented as well as a discussion on the results. The effectiveness of the retrofit intervention is discussed in the light of the findings presented throughout the chapter. Finally, conclusions elaborated from the findings are stated.

7.2 RETROFIT IMPLEMENTATION

7.2.1 Concrete surface preparation and GFRP laminates placing

The implementation of the GFRP laminates followed a series of steps from a construction perspective. The replacing concrete in the structure, after curing, was grinded in the surface where the layers were going to be placed, and then saturated with epoxy resin. The FRP layer cut in the specified dimensions to the contractor, where firstly extended over a plane surface covered with plastic and then saturated with epoxy resin. After the concrete and the FRP surfaces were saturated, the laminates were pasted into the concrete using a roller with the aim of eliminating any voids in the interface and ensuring optimum bonding between both materials. The sequence of application of the FRP laminates and dowels described in Chapter 6 was then followed.

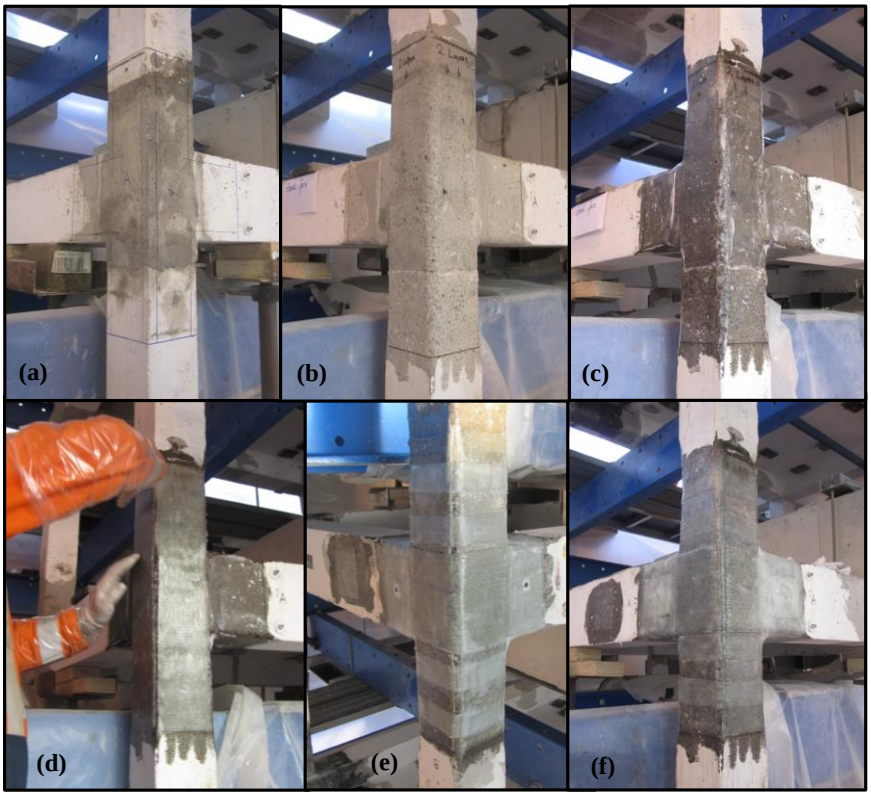

Figure 7.1: Sequence of implementation of the FRP laminates: (a) after replacing the crushed concrete – marking, (b) after grinding the concrete surface, (c) after applying epoxy resin, (d) saturated laminates placing, (e) after all laminates have been placed, and (f) after anchorage.

In Figure 7.1 (a), (b) and (c), pictures of the long span corner beam column joint during the preparation of the concrete for placing the GFRP laminates are shown. In Figure 7.1 (d), (e) and (f) three stages of the laminates sequence of application are presented in the following order: at the start of the process, at the end of the laminates location, and after the dowels were placed, respectively.

In Figure 7.2 the sequence of application of the GFRP dowels is presented in detail. The sequence consists in the following steps: (1) perforation of the beam side layers for inserting the dowels with a depth of 60mm (Figure 7.2(a)); (2) preparation and saturation of the GFRP dowels (Figure 7.2(b)); (3) Insertion of the dowels into the beam, leaving 50mm on the outside (Figure 7.2(c)); and (4) Opening of the glass fibres of the length outside the beam and placing of a 100x100 square epoxy saturated GFRP sheet on top of them in order to provide additional grip of the dowels in the GFRP beam layers (Figure 7.2(d)).

Figure 7.2: Dowels application details.

This type of anchorage was used in every face of the beams (longitudinal and transverse) where FRP layers were placed. In the case of exterior beam column joints FRP sheets were located only on the outer face, whereas in cruciform counterparts, sheets were located in both faces as described in detail in Chapter 6. The dowels used on top of the slab are the same as those shown in Figure 7.2 except that the dowels in that case were inserted all the way through the slab and anchored in both ends, so that they were 50mm longer.

In Figure 7.3 and Figure 7.4 pictures of the strengthened corner and cruciform bam column joins are presented. In the pictures of Figure 7.3(a), (b) and (c), the implemented GFRP laminates in the short span corner beam column joint are show, whereas in Figure 7.3(d), (e) and (f), the strengthening scheme placed in the short span counterpart are illustrated.

Figure 7.3: Strengthened corner beam column joint pictures.

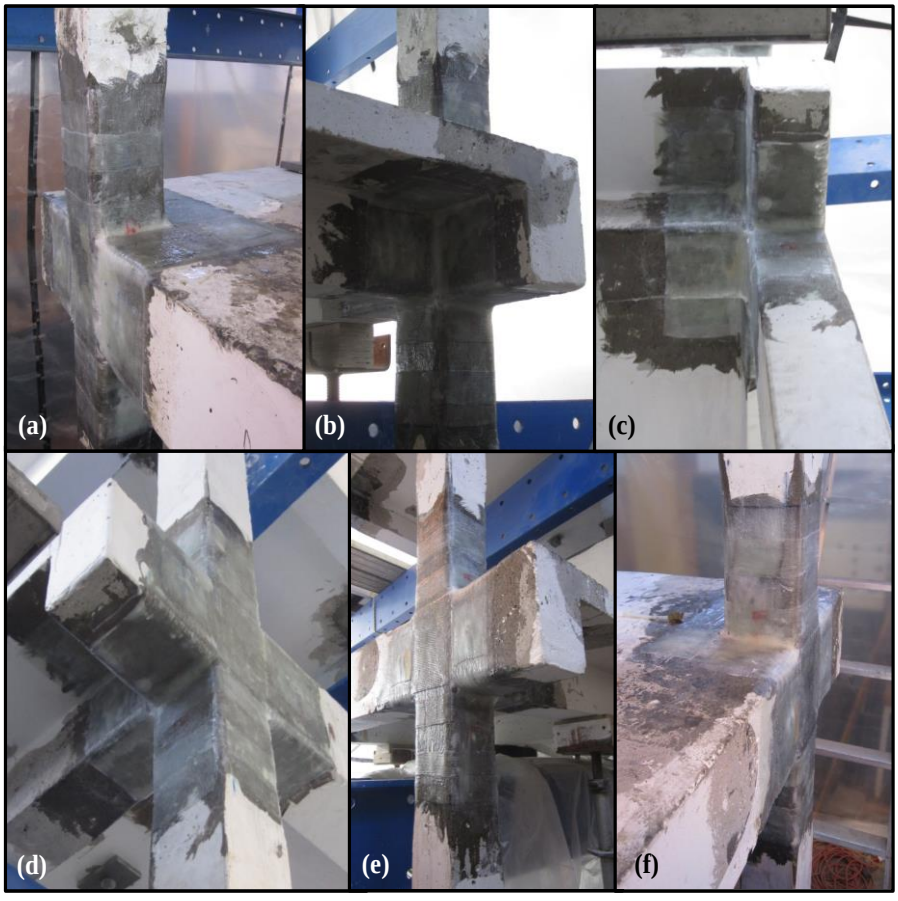

Figure 7.4: Pictures of strengthened corner beam column joints.

In the pictures of Figure 7.4(a), (b) and (c), the GFRP laminates scheme used for strengthening the cruciform beam column joint of the long span are shown, and in the pictures of Figure 7.4(c), (d) and (e), the scheme used in the short span counterpart are presented. The only differences between the dimension of the GFRP laminates of different spans and the same typology is that the length of the laminates placed in the beam direction is larger than that used in the short span. As a consequence, the confining laminates about them have different widths and the rectangular stiff area created on top of the slab is also smaller. Details of those dimensions were presented in Chapter 6.

7.2.2 Weakening of the floor slab and final intervention

Weakening of the floor slab in the configuration described in Chapter 6 was done using a normal concrete cutter. The cutting was done on top of the slab and without a complete penetration through the floor, as the main objective of the weakening strategy is to deactivate the contribution of the slab flexural reinforcement rather than the slab itself. In this case, only one layer of ductile steel mesh was used to reinforce the slab, due to scaling restrictions. In the gap region that reinforcement was located at the top part of the slab only, hence cutting from the top of the floor slab was sufficient.

In real building retrofitting though, it may be possible to cut the required steel in the slab that allows for the hierarchy of strengths and sequence of events to be reverted. That is, the section of the beam outside the strengthened region becomes de weakest link in exterior beam column joints and the fuse where inelastic incursions of the structure are forced to occur. The weakening configuration implemented in the floor slab of a cruciform and corner beam column joints are presented in Figure 7.5(a) and (b), respectively. The configuration follows the shape described in Chapter 6.

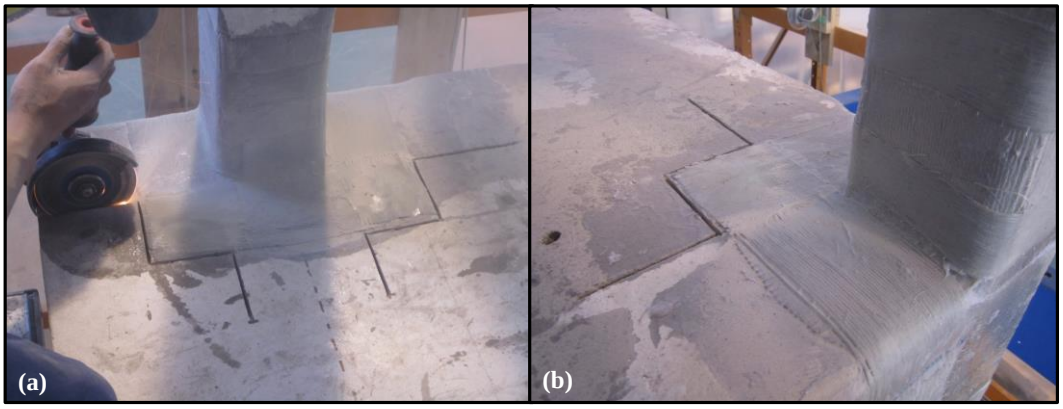

Figure 7.5: Slab weakening in beam column joints (a) cruciform, and (b) corner.

In Figure 7.6 a picture of the specimen after the retrofit intervention was ended is presented. The Fourier amplitude analyses of the response of the specimen under preliminary excitations (and the results of snap-back tests) indicated that the fundamental period of vibration of the specimen was T_1 = 0.32 seconds, approximately. This value is very similar to T_1 = 0.24 sec. and T_1 = 0.27 sec., estimated for the as-built and repaired specimens, respectively (see Appendix C for a description of the procedures).

Figure 7.6: Picture of the retrofitted specimen (University of Canterbury Structures Laboratory September 2011).

7.3 INPUT MOTION AND TEST SEQUENCE

The retrofitted specimen was tested under two ground motions that were meant to represent a low and a very high demanding scenario in terms of the intensity of damage, respectively, based on many factors described later. These two ground motions correspond to one recorded during the 4 of September 2010 Darfield earthquake (New Zealand) and one motion recorded during the 27 February 2010 Maule earthquake (Chile), used in Test 3.1 and Test 3.2, respectively.

Table 7.1: Experimental protocol for the retrofitted specimen.

Test	Earthquake Name	Station Name	Comp.	Record ID	Nominal PGA (g)	Nominal PGD (mm)	Total Duration (s)	Strong Motion (s)
3.1	Darfield	Christchurch Hospital	C1	CHH	0.20	85	40	15
3.2	Maule	Viña - Marga-Marga	EW	VMM	0.33	30	65	30

The characteristics of the input signals as well as their elastic displacement and acceleration spectra and Fourier transform were discussed in detail in Chapter 4, where the main seismological parameters of the earthquakes were presented. In Table 7.1 the experimental protocol is presented. For every test, in Table 7.1 the name of the

earthquake, the station where the ground motion was recorded, the identification name, peak acceleration (PGA), peak displacement (PGD), and duration of the complete motion, and the duration of the strong motion of the earthquake are also presented. In Figure 7.7 and Figure 7.8 the acceleration and displacement time histories of the nominal input records CHH (Test 3.1) and VMM (Test 3.2) are presented, respectively.

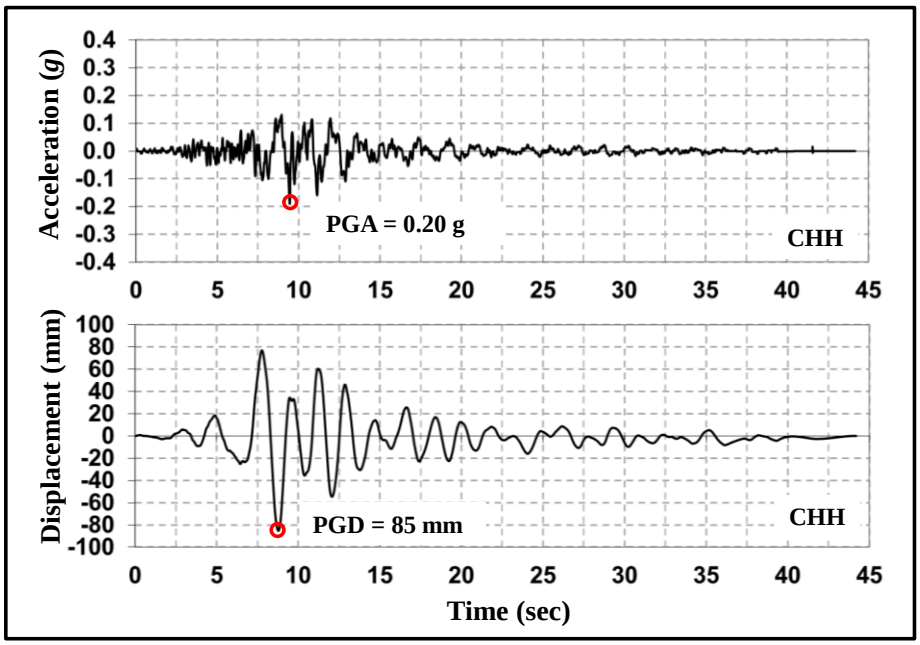

Figure 7.7: Nominal input for Test 3.1: CHH record acceleration and displacements histories.

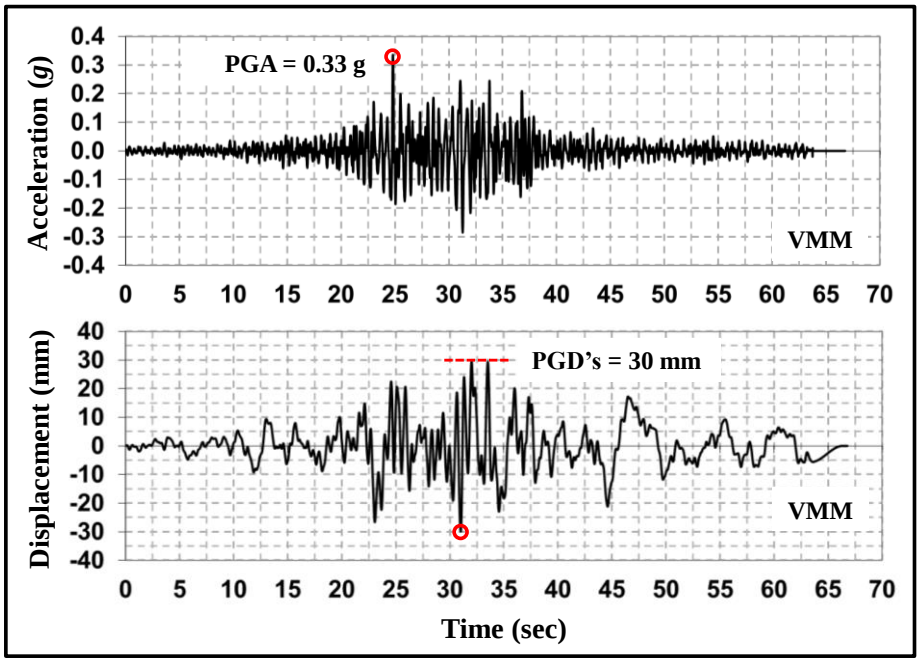

Figure 7.8: Nominal input for Test 3.2: VMM record acceleration and displacements histories.

The response spectra of these records were shown in Chapter 4. They represent the spectra of the nominal input, but not the recorded counterpart. In every test, the motion that the shake table is able to impose in reality is different from that intended to be

imposed. That is the true replication of the nominal input seems like and almost insurmountable task to complete. In the next section, the recorded motion of the shake table during each test is presented and compared with the nominal signals.

7.4 TEST RESULTS: SHAKE TABLE RECORDED MOTION

In Figure 7.9 and Figure 7.10 the motion of the shake table recorded during Tests 3.1 and 3.2 are presented, respectively. The motion is shown in terms of acceleration and displacement (position) of the table in time, recorded with two different instruments. In the graphs of these figures, the corresponding nominal record is also presented for comparison.

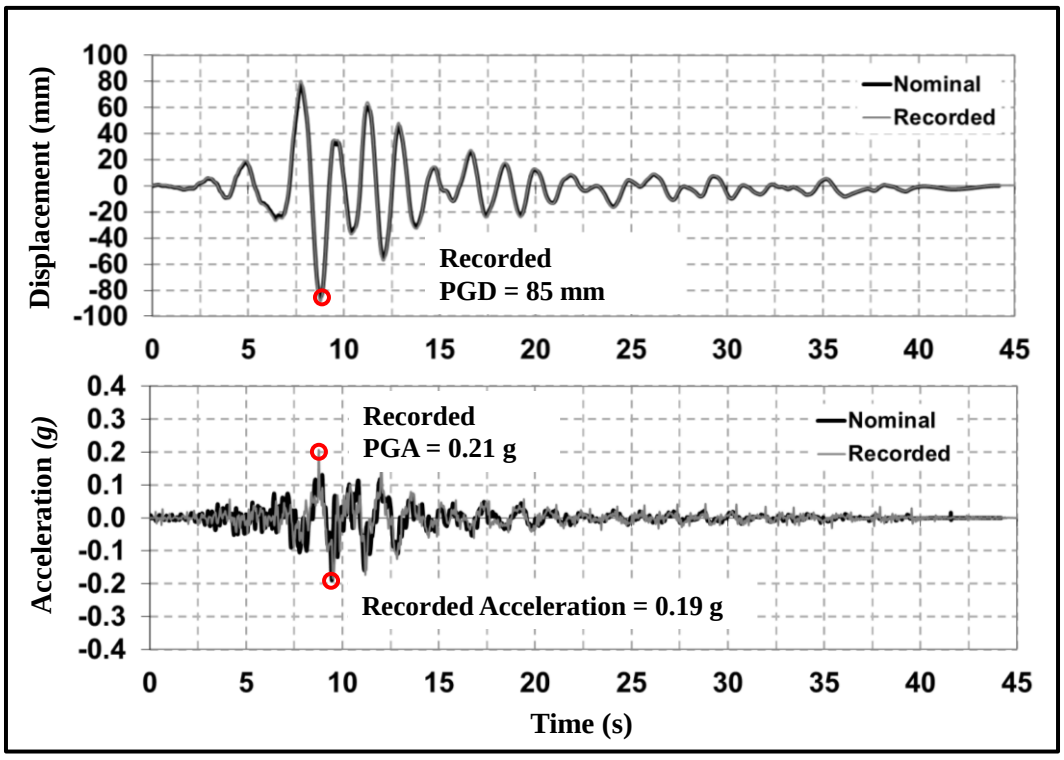

Figure 7.9: Test 3.1 nominal – recorded shake table motion comparison (CHH record).

In Figure 7.9 it can be observed that the recorded shake table displacement matches the input signal very well. However, the recorded acceleration has a slightly different shape, reflecting an important yet not substantial difference. The actual recorded PGA of the simulated ground motion was 0.21g at about 7 seconds. That is a slightly larger value than the nominal PGA = 0.20g. The acceleration peaks of the recorded and nominal signals, however, occurred in different times. In the time where the nominal input is reached (10 seconds app.), the recorded acceleration has a local maximum equal to 0.19g, very close to the intended value. Overall the replication of the nominal record used in Test 3.1 seems satisfactory, considering all the complexity associated to that task.

In Figure 7.10 it can be observed that the recorded and nominal motions of the shake table in terms of displacement (position) match adequately, with some differences between 25 and 35 seconds after the start of the record. The motion in terms of

acceleration matches reasonably well. There are nevertheless differences in the peak value of the recorded and nominal inputs, with the former being 0.33g and the latter 0.28g (both reached in the same instant). When comparing the actual PGA imposed by the shake table to the structure during both tests, the values are fairly similar; 0.21g for Test 3.1 and 0.28g for Test 3.2. The increasing of 0.07g in the PGA of those signals does not seem to match the differences in the magnitude of the response and the intensity of the damage as shown in the next sections.

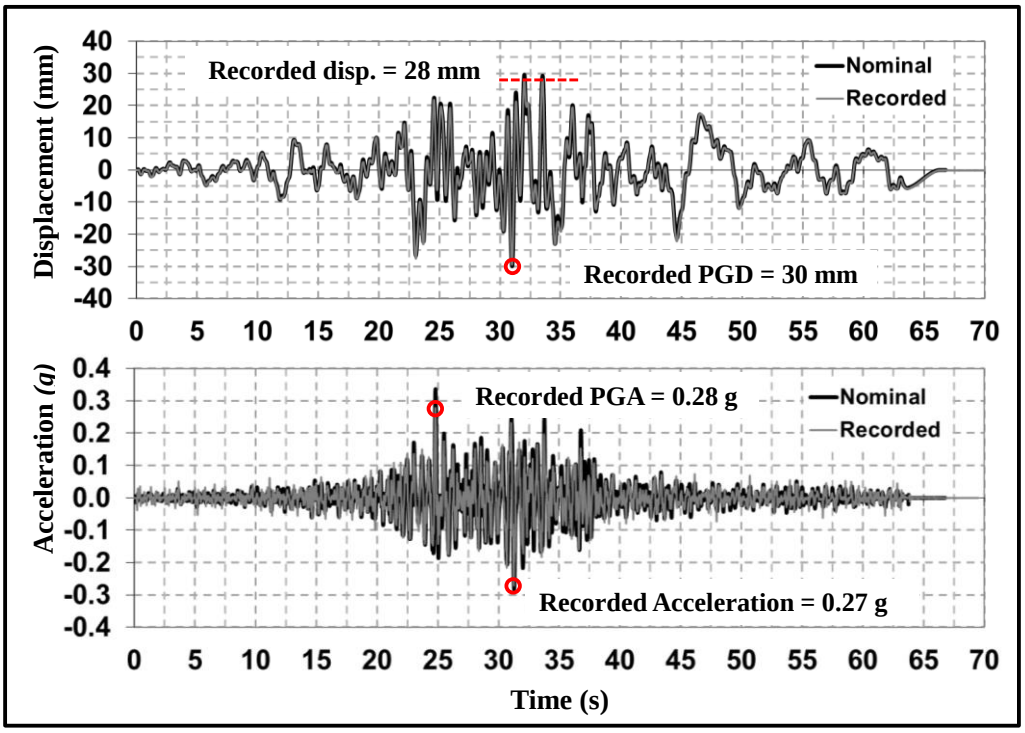

Figure 7.10: Test 3.2 nominal – recorded shake table motion comparison (VMM record).

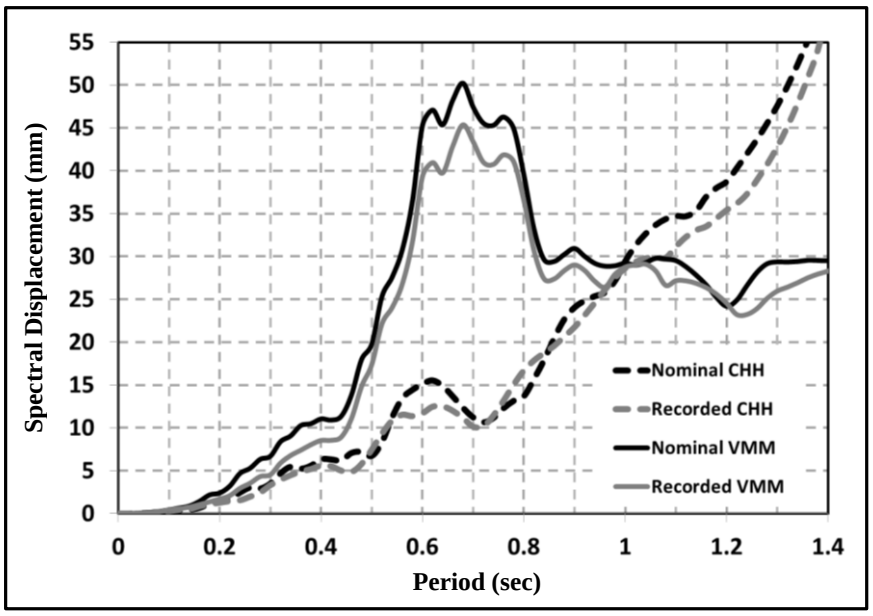

Figure 7.11: Displacement response spectra: nominal/recorded input comparison.

In Figure 7.11 and Figure 7.12, the elastic displacement and acceleration response spectra (for a 5% critical damping) of the nominal and recorded shake table motions of Test 3.1 and Test 3.2 are presented, respectively. In Figure 7.11 it can be observed that the displacement spectrum obtained with the motion recorded during Test 3.1 matches with a reasonable degree of accuracy the spectrum of the corresponding input signal. The displacement spectra obtained with the motion recorded during Test 3.2 and the corresponding nominal input have a very similar shape, even though the former is smaller than the latter for the period range under examination. The difference in the spectral displacements reaches a maximum at about T = 0.6 seconds, two times the measured elastic fundamental mode of vibration of the model building. However, the difference is not substantial enough so that it cannot avoid the very demanding scenario represented by VMM record, as will be discussed later in this chapter and in Chapter 8.

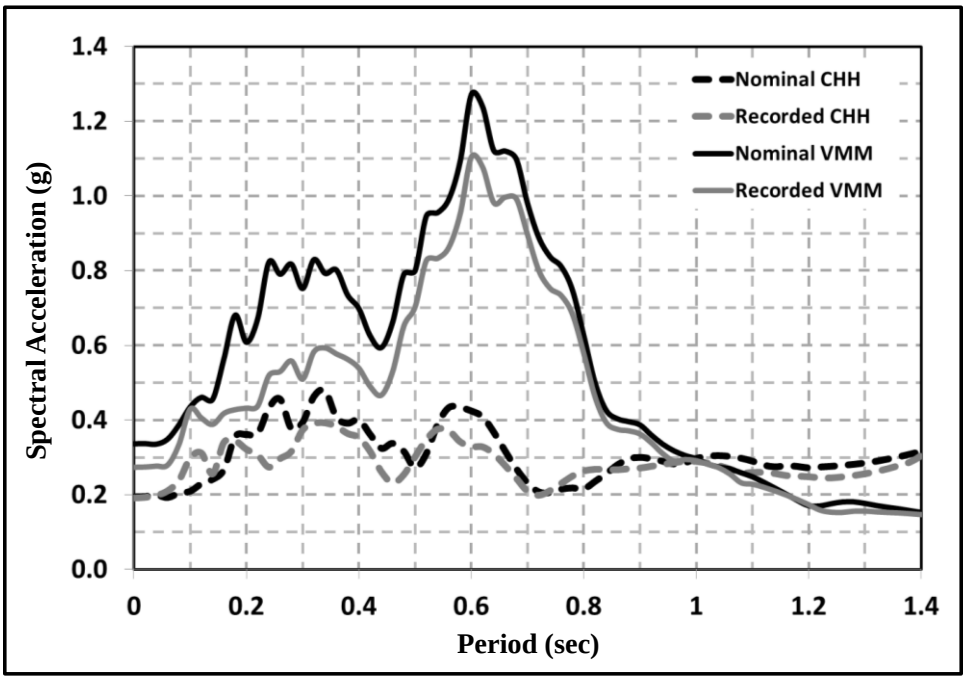

Figure 7.12: Acceleration response spectrum: input/output comparison.

In Figure 7.12 it can be observed that the acceleration spectra of the nominal and recorded input motions differ from each other in magnitude in most of the period range of interest, but have a fairly similar shape. The largest difference belongs to VMM record spectra (Test 3.2), where the spectral displacements of the recorded motion are 25% smaller than those of the nominal input from in the period range of 0.1 to 0.45 seconds. Nevertheless, they become very similar for periods greater than 0.45 seconds. For CHH record (Test 3.1), o the other hand, the spectral acceleration and displacements are very similar in the period range of interest, and given their small magnitude, the difference do not seem important for the scope of this research.

As will be shown later in this chapter, in the particular case of VMM record, the predominance of a particular frequency of the motion in terms of energy, i.e., Fourier amplitude, determined the *hazard* that the ground motion represented to the building in a more representative way than the PGA or the displacement or acceleration spectral demand for the initial elastic fundamental period of vibration by themselves, for example.

That is, if the inelastic dynamically changing fundamental period of the structure reaches a value close to that of the predominant period of the signal due to increasing cracking and the corresponding stiffness degradation, then the building is prone to fall into resonance and be very affected in terms of the intensity of damage.

7.5 TEST RESULTS: GLOBAL RESPONSE

7.5.1 Test 3.1

In Figure 7.13, the recorded response of the retrofitted specimen during Test 3.1 is presented in terms of inter-storey drift time histories of each floor.

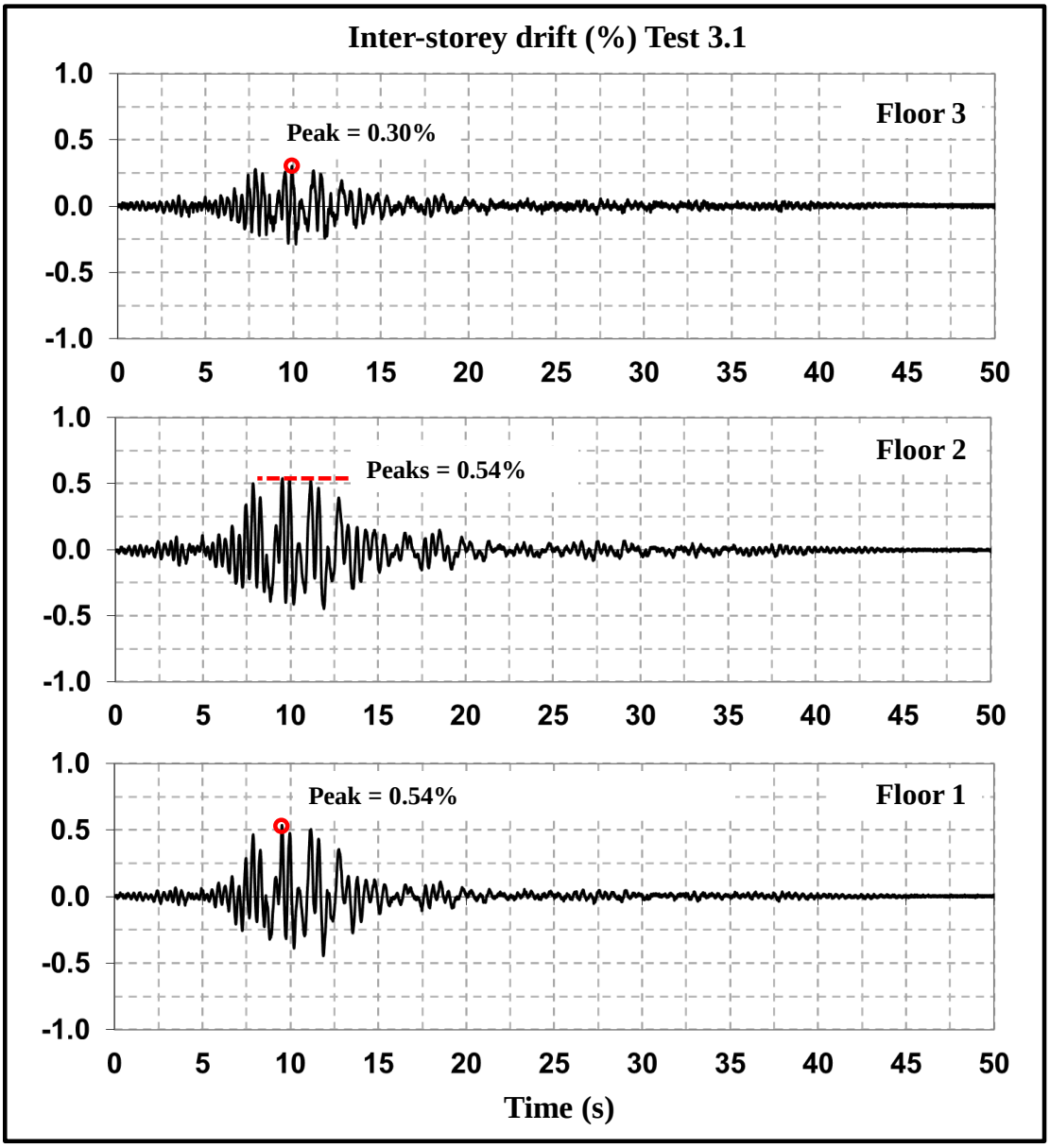

Figure 7.13: Recorded inter-storey drift, Test 3.1, CHH record (Darfield 2010).

In the graphs of Figure 7.13 it is shown that the magnitude of the inter-storey drifts remained below 0.55% in all floors during Test 3.1, with recorded (absolute) maximum values of 0.53%, 0.53% and 0.30% in floors 1, 2 and 3, respectively. The shape of the drift histories of all floors is very similar in shape during the complete duration response. Inter-storey drift values close to 0.5% as those recorded during this tests, are associated to very light cracking in the beam, based on the experimental research on similar beam column joint subassemblies without floor slabs (Akguzel and Pampanin 2010, Akguzel 2011). Hence, the statement of the specimen responding in the elastic range is correct. That is also in line with the observed damage after the tests, which indicated that no inelastic incursions occurred nor visible cracking developed in the beam or other parts of the structure.

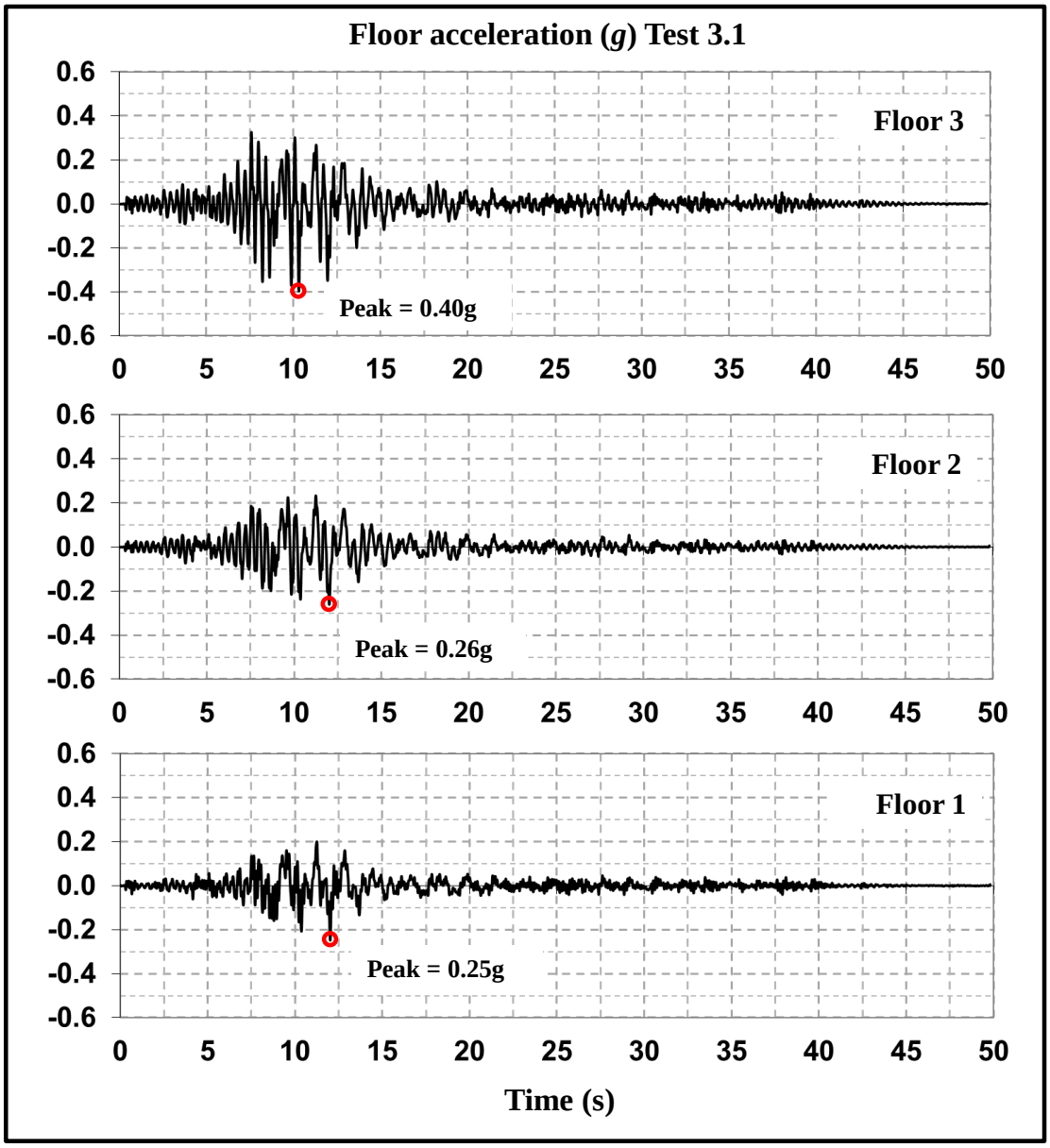

Figure 7.14: Recorded accelerations, Test 3.1, CHH record (Darfield 2010).

In Figure 7.14 the floor accelerations recorded during Test 3.1 are presented. Just as in the case of the inter-storey drift histories, the similarity of the motion of the three storeys is

reflected in those graphs in terms of floor acceleration. The maximum values reached in floors 1, 2, and 3, were 0.25g, 0.26g, and 0.40g, respectively. It is important to note that other local maximum accelerations and inter-storey drifts were reached in the response, which is not relevant in this case because no inelasticity occurred. The maximum values of the response of the building during Test 3.1 are summarized in Table 7.2. In that table, these values are named 'absolute maximum values' with the intention of emphasizing that there are other instants of the response where local maximums are very close in magnitude to the largest value recorded and their quantity and magnitude may be of critical impact in the response of the building. That is especially true in the recorded acceleration in floor 2, where the exact maximum value is reached twice.

Table 7.2: Absolute maximum values of the specimen response – Test 3.1.

Absolute Maximum	Test 3.1 – CHH record	
Floor	Inter-storey drift (%)	Acceleration (g)
3	0.30	0.40
2	0.54	0.26
1	0.54	0.25

7.5.2 Test 3.2

In Figure 7.15 the response of the building during Test 3.2 is presented in terms of inter-storey drifts time histories of each floor. In the graphs of Figure 7.15 it can be observed that the largest drift levels were recorded in the first floor, with an absolute maximum value of 3.7%. In addition to that peak value, in a couple of other instants the specimen experienced inter-storey drifts as high as 3.3%. These values are understood as local maximum values of the response, as they are very similar in magnitude to the absolute maximum. In the second floor a maximum inter-storey drift of 2.2% was recorded, as well as some other local peaks of 2.0% at different instants of the response. In the third floor meanwhile, the inter-storey time-history reached a maximum (absolute) of 1%, value almost reached several other times during the response.

As can be seen in Figure 7.15, the largest inter-storey drifts were recorded in between 20 and 40 seconds from the start of the input motion. As can be particularly observed in the first floor history, the inter-storey drift reached large values at about 25 to 27 seconds, then decreased below 2% until another set of large drifts were recorded at about 32 seconds. This response indicates that the specimen may have fall into resonance during that part of the response, leading to large inelastic incursions in the beams, as it is shown in the next section. The measured values of the inter-storey drifts for the three floors and the observations on the damage they experienced (shown in the next section) are in line the with the findings of experimental research on similitude-compatible beam column joint subassemblies tested under quasi-static loading protocol by previous researchers (Akguzel and Pampanin 2010, Akguzel 2011, Kam et al. 2010). In those tests, important flexural cracks developed in the beam of the retrofitted specimens at drift levels close to 2% and large cracking for drifts equal or larger than 3%, the latter being associated to inelastic rotations in the beam, according to strain gauges readings (Akguzel 2011).

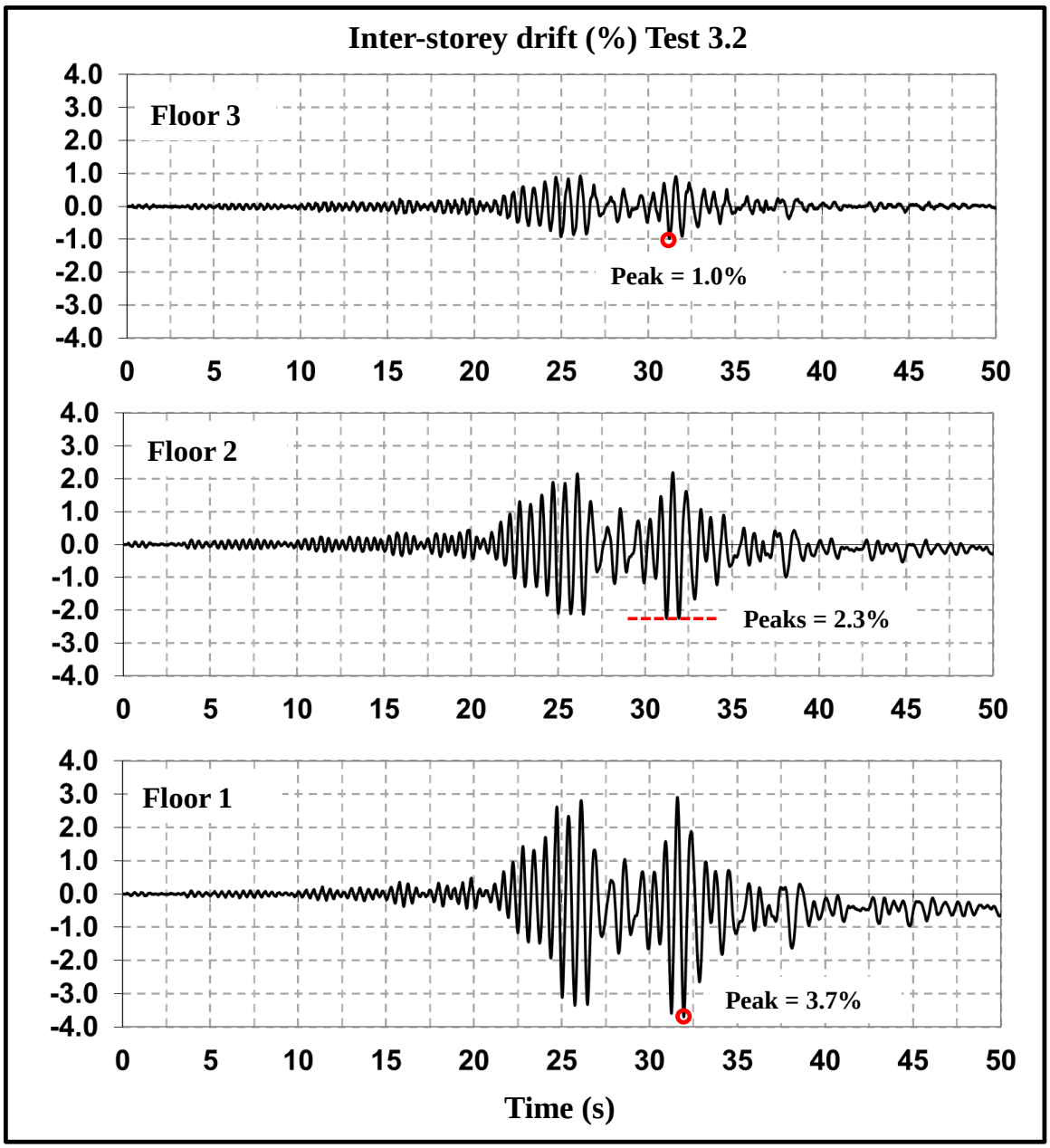

Figure 7.15: Recorded inter-storey drift, Test 3.2 VMM record (Maule 2010).

In Figure 7.16 the recorded floor accelerations in the three levels of the building are shown. The responses had a maximum absolute value of 0.34g, 0.53g, and 0.77g in floors 1, 2, and 3, respectively. The shape of the floor acceleration histories is very similar for all three floors, and has increasing amplitudes for higher levels, as expected. The maximum values recorded coincide in the time of occurrence with the maximum measured inter-storey drifts. In Table 7.3 the maximum absolute recorded values of the inter-storey drift and accelerations in all floors during Test 3.2 are summarized.

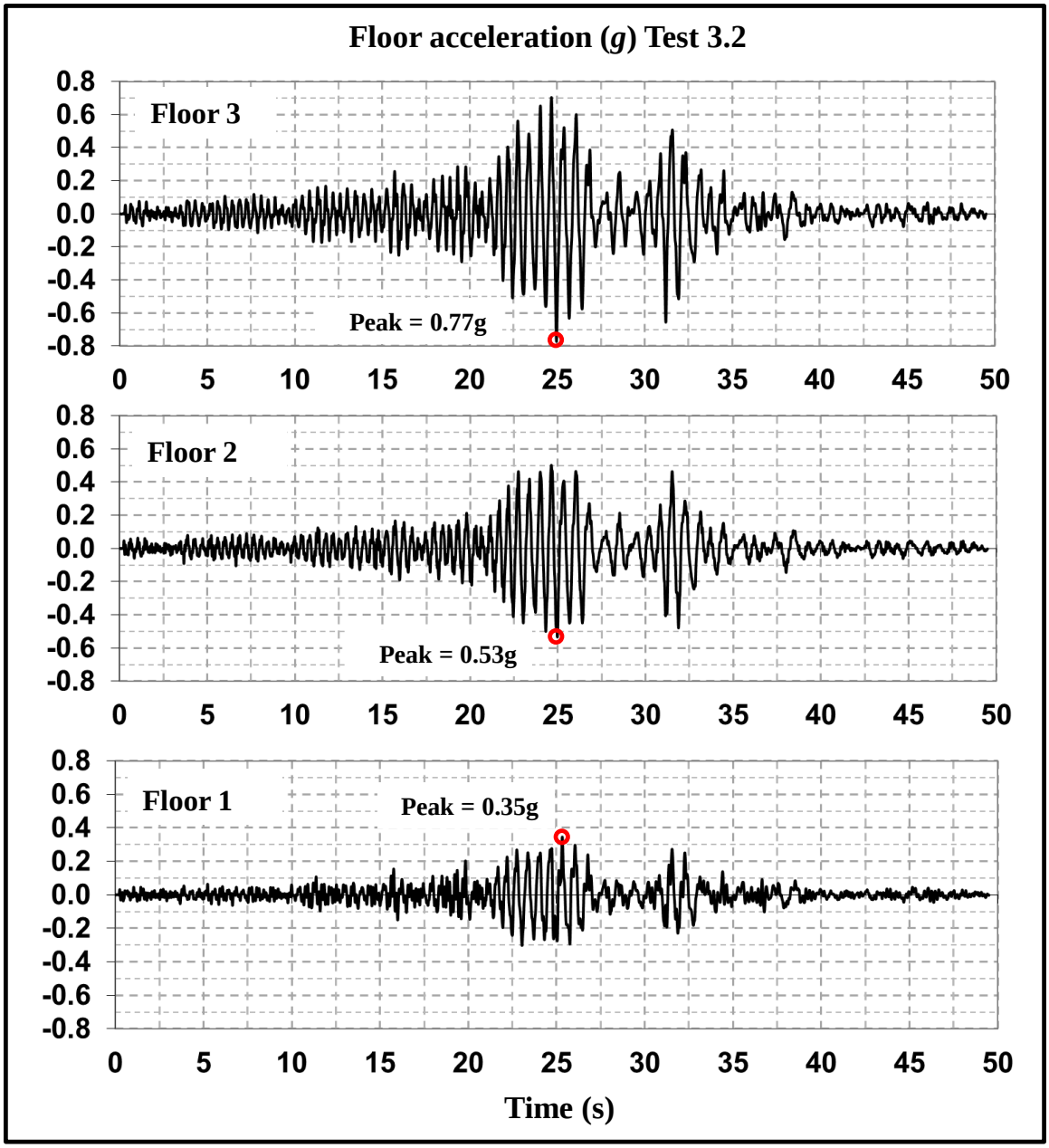

Figure 7.16: Floor accelerations, Test 3.2, VMM record (Maule 2010).

Table 7.3: Absolute maximum values of the specimen response – Test 3.2.

Absolute Maximum	Test 3.2 – VMM record	
Floor	Inter-storey drift (%)	Acceleration (g)
3	1.0	0.77
2	2.3	0.53
1	3.7	0.35

7.6 TEST RESULTS: OBSERVED DAMAGE

During Test 3.1 where CHH record was used, the retrofitted specimen exhibited an elastic stable response, and experienced similar inter-storey drift magnitudes in the three floors, all below 0.55%. The panel zone remained undamaged at all and no visible cracking developed in the intended fuse at the weaker section of the longitudinal beam inside the gap region. During Test 3.2, damage in the form of flexural cracks was developed in the beams, most of them close to the GFRP sheets, showing the ability of the intervention to relocate the brittle shear damage, observed in the as-built specimen after Test 2.2 (VMM record) into ductile inelastic rotations in the beams and the interior columns.

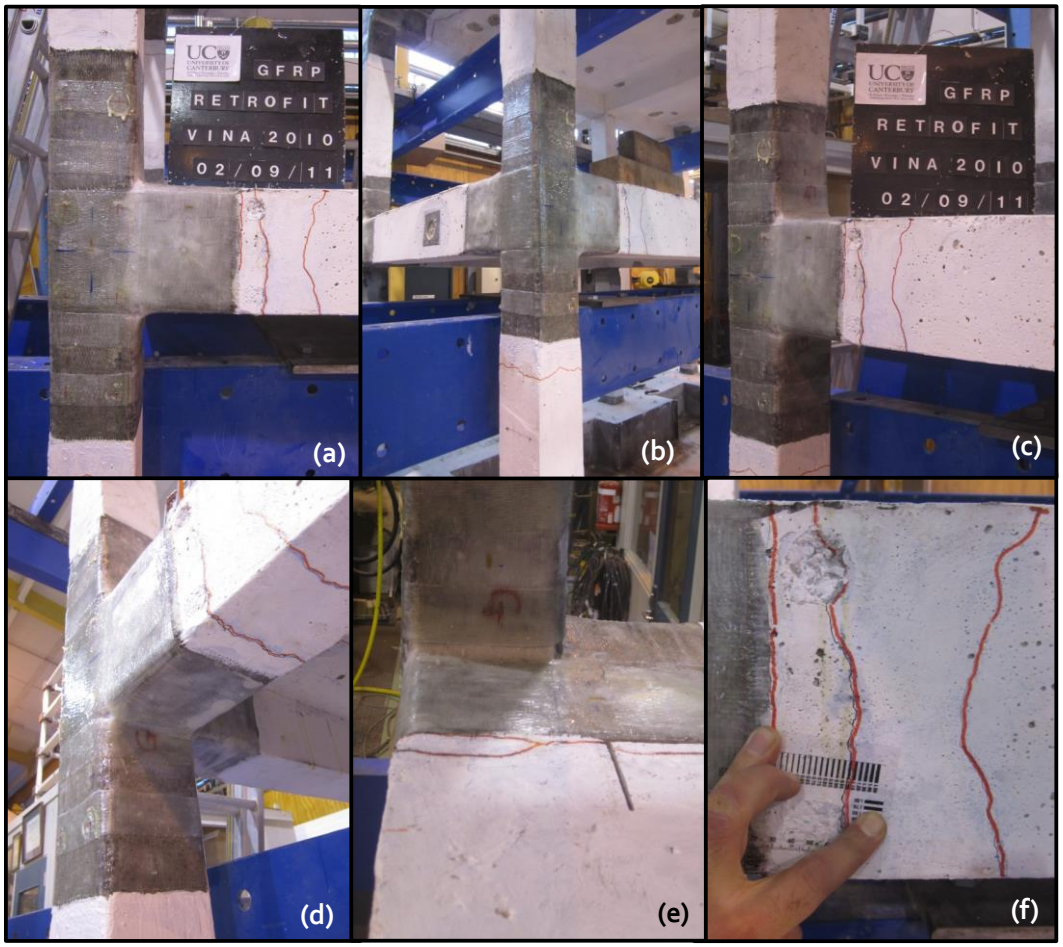

Figure 7.17: Observed damage after Test 3.2: 1st floor long span corner beam column joint.

In Figure 7.17 the damage developed in the corner joint of the long span is illustrated. In the pictures it can be observed that flexural cracking developed in the beam, in the form of one larger crack at approximately 50mm from the GFRP laminate end and some other thinner ones. The maximum crack width was of the order of 1mm (not scaled up and presented for comparison only), as shown in Figure 7.17(f), noting that in the context of a 2/5 scale model this measurement may only be useful as an indicator of relative values of the crack widths within the specimen itself. In the pictures shown in Figure 7.17(d) and (e) it can be observed that the cracks developed in the complete section of the beam in the intended location.

In the pictures of Figure 7.18 the damage developed in the corner beam column joint of the short span is shown. In these pictures, it can be observed that the damage occurred in the beam mostly, where one large flexural crack developed in the intended fuse, very close to the GFRP sheets in the rigid zone. This crack had a maximum width of 1.1mm approximately, and extended along almost the entire beam section. Cracks also developed on the top and bottom of the slab, following the direction of the weakening gap in the intersection with the transverse beam, and 150mm away from the GFRP layers, respectively. In this case, cracks did not develop in the columns.

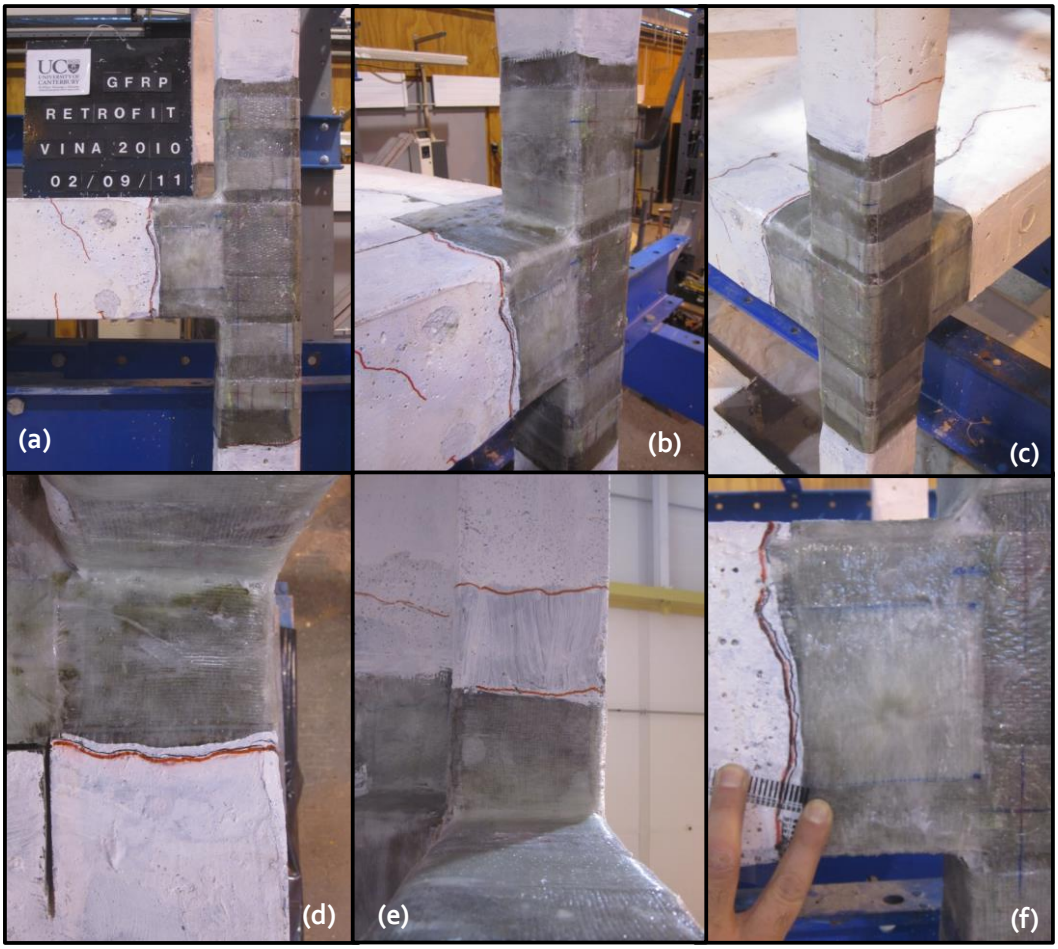

Figure 7.18: Observed damage in the 1st floor short span corner beam column joint; (a) front view, (b) 3D view from the front, (c) 3D view from the top back, (d) top view over the beam, (e) view from below, and (f) view from the side – beam crack close-up.

In Figure 7.19, pictures of the long span exterior beam column joint of the internal frame (cruciform joints) after the tests, are presented. In those pictures, it can be appreciated that cracking developed mostly in the beam, inside the weakened region. Other cracks developed in the slab at the intersection of the slab and the spandrel, following the weakening gap direction. A single crack was observed at the top of the beam as well as the bottom and the sides, as shown in Figure 7.19. That crack continued into the slab beyond the strengthened region towards the external frame, and developed in the complete section of the slab in the stub side. The maximum width of the flexural crack reached about 0.7mm, which is smaller than the width measured in both corner beam column joints of the first floor.

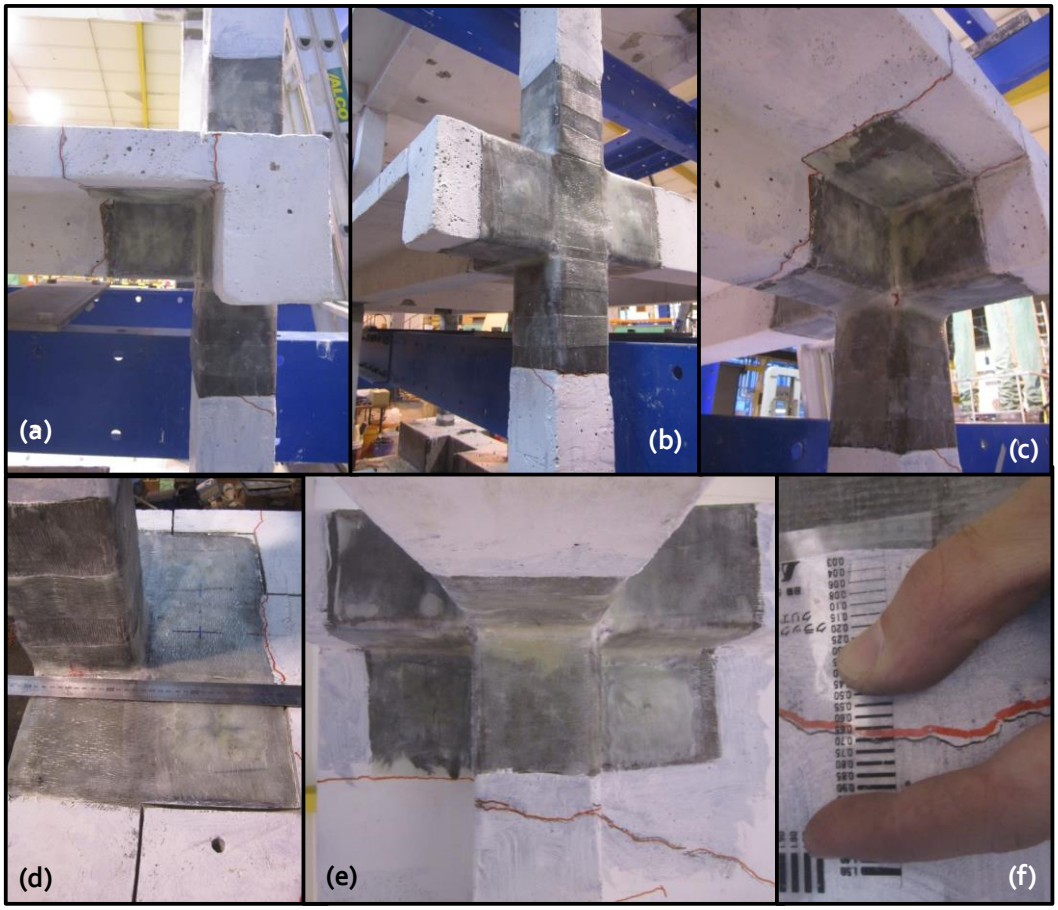

Figure 7.19: Observed damage in the 1st floor long span cruciform beam column joint; (a) front view, (b) 3D view from the front, (c) 3D view from the bottom, (d) top view over the beam-slab, (e) view from below, and (f) view from the bottom – beam crack close-up.

In the pictures of Figure 7.20, the damage developed in the sort span cruciform joint is presented. In this case cracks formed in a very similar way to that observed in the long span beam column joint counterpart. Most of the damage was concentrated in flexural cracking in the beam and the slab close to the strengthened region and along the interface of the slab and the transverse beam. The maximum size of the residual cracks in the beam was smaller than those measured in all other exterior joints. In this beam column joint, cracking also occurred in the non-strengthened part of the column as shown in Figure 7.20(e). The maximum width of these residual cracks in the column was not small, and they indicate that the column may have experienced inelastic rotations in that region as well. This issue will be discussed in depth in the discussion on the effectiveness of the developed retrofit intervention.

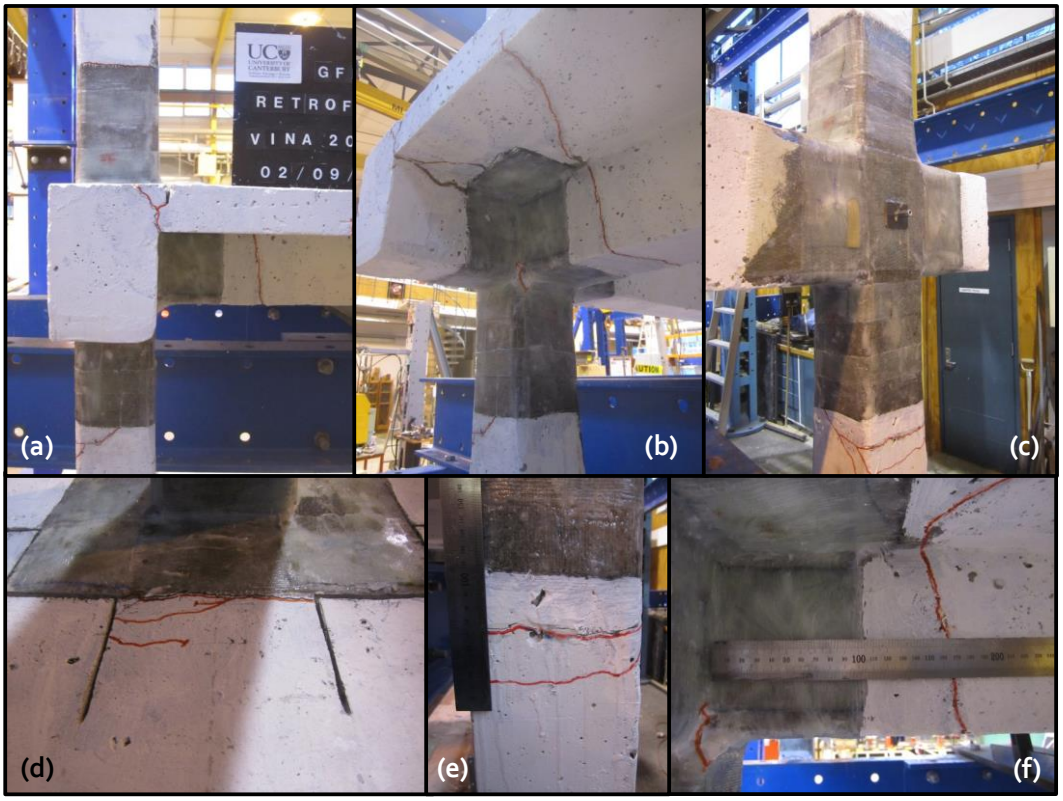

Figure 7.20: Observed damage in the 1st floor short span cruciform beam column joint; (a) front view, (b) 3D view from the front, (c) 3D view from the outside, (d) top view over the beam-slab, (e) bottom column side view, and (f) view from the bottom – beam crack close-up.

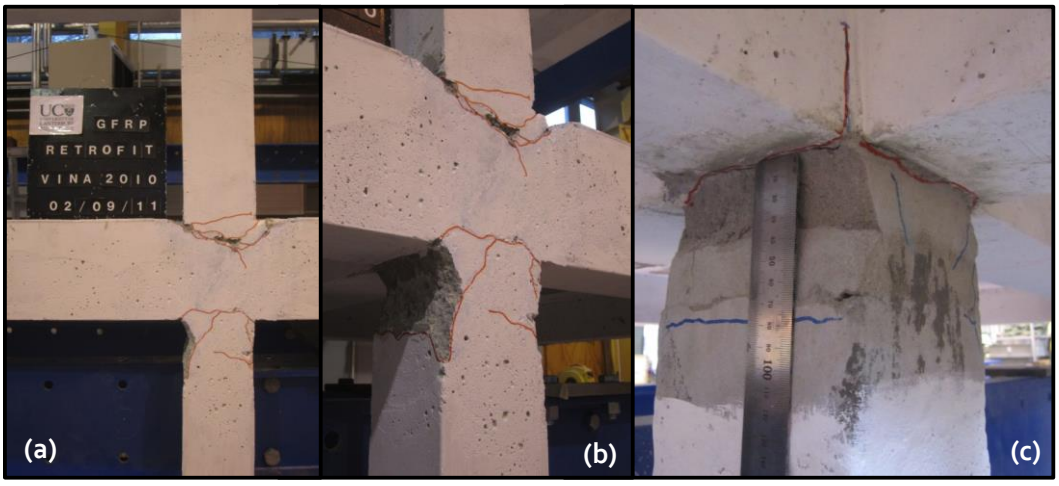

Figure 7.21: Observed damage in columns 1st floor interior beam column joints (a) external frame front view (b) 3D close up of (a), (c) external frame.

In Figure 7.21, pictures with the observed damage in the interior beam column joints of the first floor are shown. In both the external and internal frames, the damage was concentrated in the top and bottom columns, where extensive cracking and crushing of the concrete occurred. The magnitude of that crushing was larger on the top part of the columns as shown in the pictures, whereas at the bottom of the top column a large crack developed with some penetration inside the joint. It is worth noting that the interior

column of the internal frame was repaired after Test 2.2 using structural mortar with the characteristics presented in Chapter 4, due to the excessive damage it experienced.

Finally, in the pictures of Figure 7.22, pictures of the most damaged beam column joints in the second floor are shown. In those pictures it can be observed that the developed damage pattern is the same as that developed in the first floor, shown in detail in the previous figures. In this case however, the residual width of the cracks was much smaller than those measured in the beams of the first floor, which is consistent with the magnitude of the recorded inter-storey drifts and observations of previous researchers on corner and plane beam column joints retrofitted in a similar fashion, as explained before.

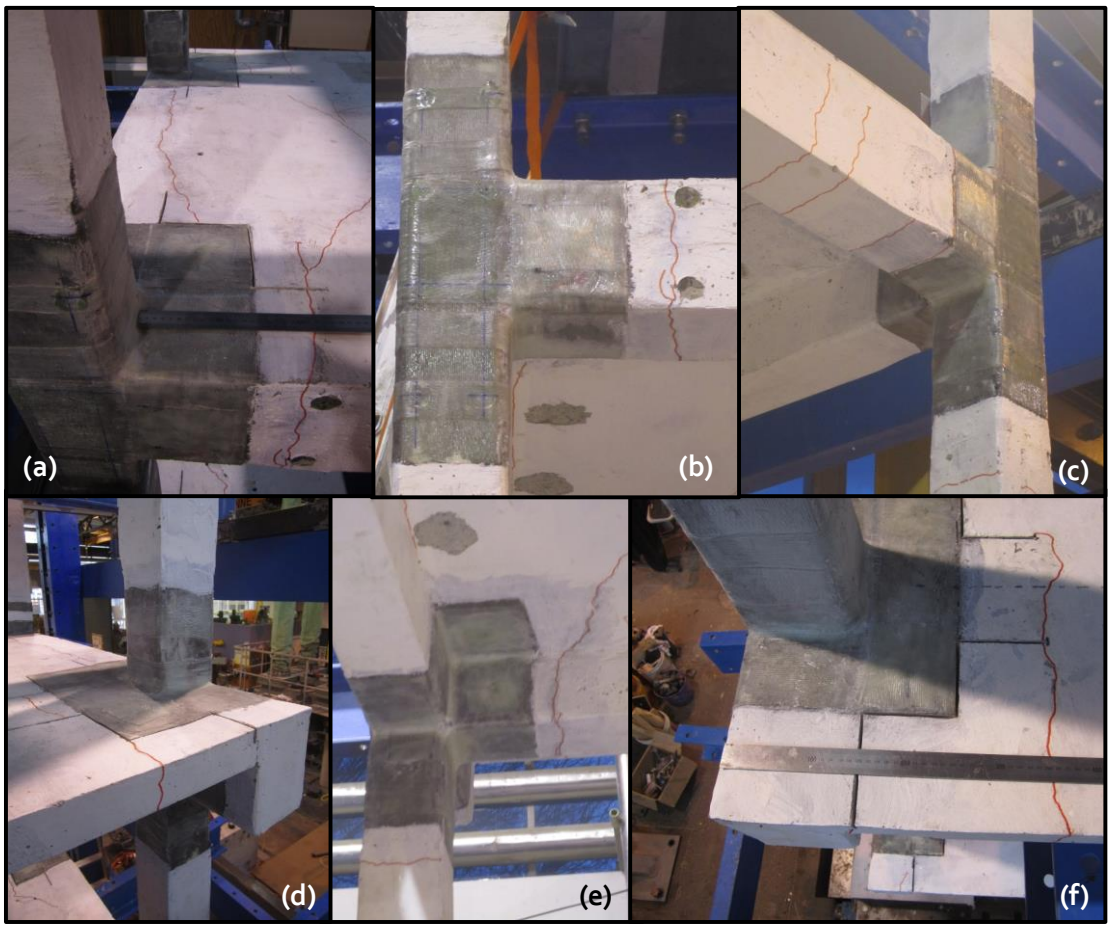

Figure 7.22: Observed damage in 2nd floor beam column joints; (a) long span top view, (b) long span corner, (c) short span corner, (d) long span cruciform top view (e) short span cruciform bottom view, and (f) short span cruciform top view.

7.7 DISCUSSION ON THE RESULTS

The results of Test 3.1 indicate that a fairly elastic response of the specimen was achieved, with low inter-storey drifts in all levels and no visible cracking in the concrete. That result was expected due to the characteristics of the ground motion with very low spectral displacements for periods up to about 0.9 seconds in the model domain (1.26 seconds in the prototype domain), 3 times the estimated elastic fundamental period of

vibration of the building. The duration of the motion was also considered in the sense that the strong part of the input motion does not have a significant length and there were no indications of a hazardous predominant frequency in terms of energy, as can be observed in the Flourier spectra presented in Chapter 4. In addition, the real earthquake that affected the city of Christchurch and the surrounding area did not have destructive consequences upon engineered RC structures, as observed by Pampanin et al. (2012).

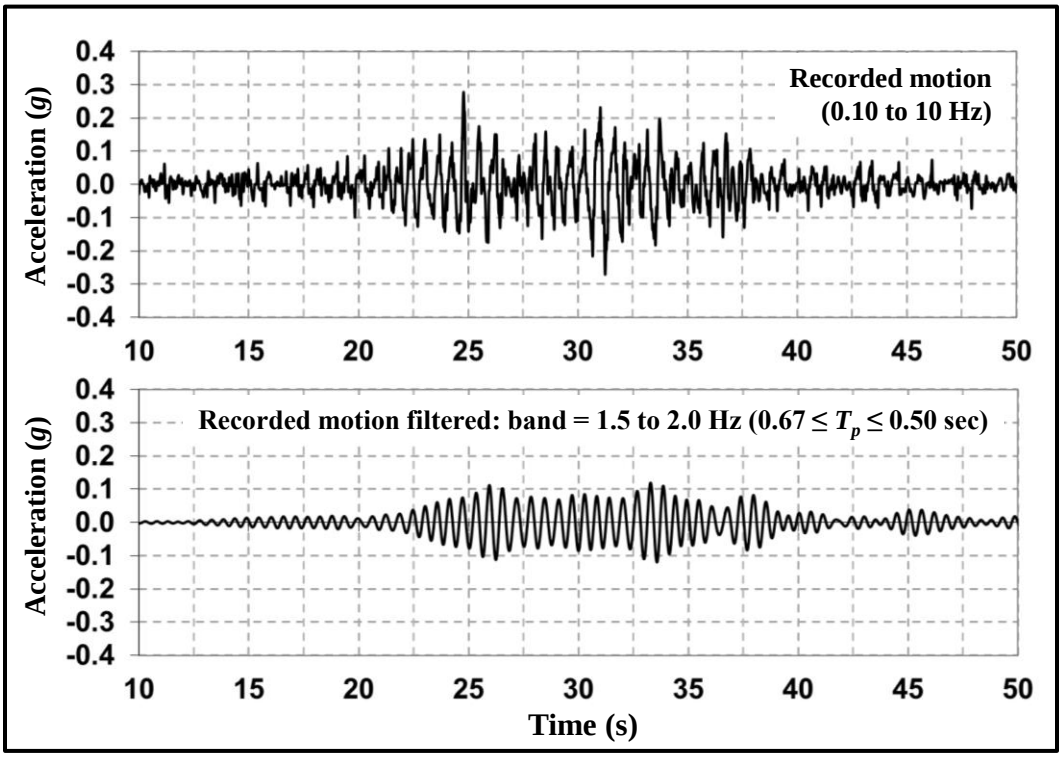

Figure 7.23: Predominant frequency content of the recorded shake table motion, VMM record.

The results of Test 3.2 on the other hand, reflected a high demanding scenario for the structure, meaning that the building was subjected to high inter-storey drifts. In this case, VMM record was selected because it was thought that it could represent probably the worst case scenario for this particular structure due to the dynamical characteristics of the motion. In Figure 7.23 the recorded acceleration of the shake table during Test 3.2 is presented, together with the same signal but filtered using a 4th order Butterworth band pass filter, so that any Fourier-components of the signal outside the frequency range of 1.5 to 2.0 Hz were removed. In the bottom graph of Figure 7.23 it can be appreciated that the filtered shake table acceleration has a very similar shape to a sine function with a predominant frequency of the order of 1.67 Hz (T_p = 0.6 sec.). That signal has very small amplitude at the beginning of the motion, but increases rapidly after 20 seconds, reaching a maximum value of 0.11g at about 26 seconds. From that instant onward, the signal remains with almost-constant amplitude with a magnitude very close to 0.1g until it starts to decrease at about 35 seconds.

In Figure 7.24 the motion of the shake table, as-recorded and filtered as explained previously, are presented in the Fourier spectral domain (fast Fourier transform). In that figure, the elastic displacement response spectra, for a 5% critical damping, obtained with both signals are also shown. In the right hand side of Figure 7.24 it can be observed that

most of the energy of the signal is concentrated in the Fourier components (harmonics) with frequencies in the selected range for filtering the signal, with a clear maximum at T = 0.6 seconds (1.67 Hz). The spectral displacement of the filtered signal is very similar to that of the original recorded motion, but always smaller, as expected. Nevertheless, the maximum spectral displacement reached at T = 0.6 seconds differ by only an 80%, approximately. Therefore, it can be argued that if the signal had only the form of the filtered motion, with maximum amplitude of the acceleration of 0.1g, then similar results may have probably been obtained. That is, with a much smaller PGA = 0.1g, the record may be as *hazardous* as it is with a greater PGA = 0.28g, as recorded in the reality. However, the previous sentence is a conjecture, in the sense that it was not empirically demonstrated in this thesis. From an opposite perspective, the conjecture of the PGA being a parameter that correlates well with the magnitude of the response and the intensity of damage may be refuted. The issue will be addressed in Chapter 8, using nonlinear dynamic analyses.

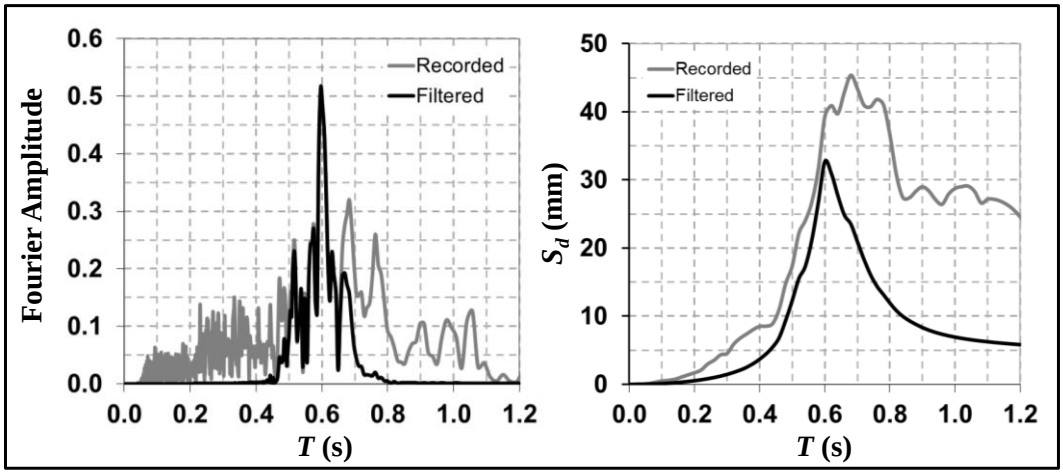

Figure 7.24: Shake table motion; Left: Fourier domain, right: elastic displacement spectra.

In the top part of Figure 7.25 the filtered recorded acceleration of the shake table during Test 3.2 is presented in the time of the response between 20 and 40 seconds from the start of the record. In the bottom part of Figure 7.25, the inter-storey drift history recorded in the first floor is also presented in the same time range. When taking a look at both graphs, it can be clearly observed that during the time that the filtered motion has an increasing in amplitude from very low levels at 20 seconds to 0.1g at 26 seconds approximately, the inter-storey drift magnitude of the first floor also increases from values smaller than 0.25% to values as high as 3%. During this first period of time, the response has a frequency close to the predominant frequency of the record, estimated as 1.67Hz, which is an indication of resonance. From 20 seconds onward, the response decreases in magnitude and in frequency, as the structure must recover from a large amount of strain energy released when achieving large inelastic incursions. After that, the inter-storey drift in the first floor starts to increase in amplitude and frequency, again close to the predominant frequency of the motion, which is an indication that the building after recovering from a large inelastic demand, fell into resonance again. In fact, it was during this second set of large inter-storey drifts when the absolute maximum of the response was reached: 3.7% at about 32 seconds. After that instant the response decreased again in amplitude and became more erratic with maximum values close to 1% drift towards the

negative direction in the position, with indication of some residual drifts. The motion remains with those characteristics until the input signal starts to decrease at about 39 seconds, after preserving practically the same amplitude and frequency during the whole period of time when the building experienced the largest values of the response.

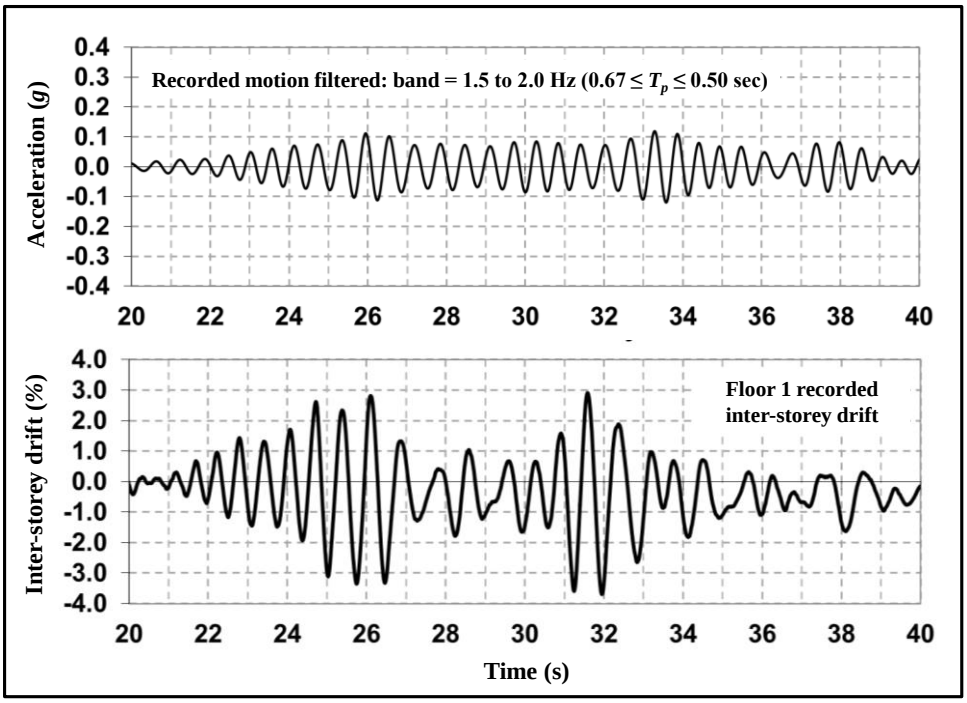

Figure 7.25: Top: filtered VMM record (1.0 to 1.5 Hz) from t = 20 to 40 seconds; Bottom: recorded inter-storey drift in the 1st Floor in the same time range.

One important issue is the accuracy in the estimation of the spectral displacements associated to the period of the fundamental (and other) mode of vibration of the structure (T_1). As it was mentioned before, the measured fundamental period of vibration was estimated as T_1 = 0.3 seconds. With reference in Figure 7.24, for that period the spectral displacement of the spectrum obtained with the recorded shake table motion is S_d = 5mm. If it is assumed that the inter-storey drifts in the first mode of vibration are the same, then the predicted maximum inter-storey drift for the first floor would be $Dr_{1,max}$ = 0.42%. If the fundamental period of vibration increases due to a reduction in the stiffness of the structure them, larger values are expected. If the stiffness is reduces by 4 times, then the period increases by 2 times. If that was the case of this structure, then for a period T_1 = 0.6 seconds, S_d = 40mm, 8 times larger than for the initial measured period. In that case, and under the same assumption of the mode shape, the maximum predicted inter-storey drift would be $Dr_{1,max}$ = 3.33%, much closer the value recorded. The assumption of the drift being the same at every floor though seems to go against the recorded results.

The use of elastic spectrum is not coherent if the inter-storey drift predicted is larger than the yielding drift, after which inelastic capacity compatible spectra should be used, as described later in Chapter 11. Assuming that the elastic spectrum is acceptable, regardless of the inelasticity expected to occur at large inter-storey drifts, then the value obtained with the spectra would be in reasonable agreement with the recorded value. Moreover, if one uses a smaller critical damping ratio, then the prediction may be even more close to the recorded value of 3.7%. Nevertheless, the number of times that the structure can reach

similar values to the estimated maximum is not being taken into consideration, and hence the intensity of the damage under repeated cycles of inelastic incursions not included into that prediction. In the light of the results of this experimental research though, it seems crucial to incorporate the dynamical component into the problem, as it is argued that the damage that the structure would have experienced if it would have reached the maximum inter-storey only, then the results may have been substantially different.

7.8 DISCUSSION ON THE RETROFIT STRATEGY EFFECTIVENESS

During Test 3.2, where the most demanding record was used, inter-storey drifts were slightly reduced when compared to those recorded during Test 2.2, when the as-built specimen was subjected to the same record. In the latter, the maximum inter-storey drifts in the first floor reached a maximum close to 4% and many other local maximum values of 3.5%, whereas in the former, the maximum inter-storey drift reached in the first floor was 3.7% with some other local maximums close to or larger than 3%. This represents an indication that even the retrofit strategy implemented was able to relocate the damage in the desired places locally it was not able to control the response of the structure globally. The latter means that the design presented herein is a necessary condition for upgrading the performance of this building typology, but not a sufficient one. Therefore, it would be recommendable to also include another retrofit technique whose main aim is to bring global stability to the structure as well as provide a stable source of energy dissipation. Some of the techniques that have been developed for those purposes are rocking walls (Marriott 2009), steel buckling restrained braces, hysteretic-dissipating (Uang et al. 2004) or viscous-dissipating (Di Cesare et al. 2012), and Shape Memory Alloys (SMA) braces (Dolce at al. 2000, 2005).

Another aspect is that the relocation of the damage although successful, was not entirely as intended. That is, some important cracking was observed in the as-built part of the column close to the strengthened region in exterior beam column joints, mostly in the internal frame. One explanation for that undesired effect is related to the magnitude and shape of the bending moment diagram (BMD) in the beam column joint when the inelastic mechanism takes place. As was explained in the last section of Chapter 6, if one imposes the plastic hinge in the intended fuse in the beam, and assumes that the inflexion point in the columns occurs at 0.5 times the height of the columns and the length of the beams, then the capacity of the as-built column would not be exceeded. However, it was remarked that variations in the values of the beam capacity due to important strain hardening experienced in inelastic rotations as well as differences in the calculated flexural capacity of the columns due to axial load variation and strain hardening, could lead to some inelastic rotations outside the retrofitted part of external columns. The use of a longer GFRP layers in the column could be plausible, provided that shear does not become a problem.

The nature and intensity of the damage experienced by the retrofitted structure during Test 3.2 though, was smaller than the one experience by the as-built/repaired specimen during Test 2.2. In fact, the specimen could have been repaired after Test 3.2 was conducted. That is another important aspect related to the efficiency of the developed and validated retrofit intervention related to practical applications.

7.9 CONCLUDING REMARKS

In this chapter the most important results of the shake table tests of the retrofitted specimen were presented. The results of the tests were overall satisfactory in the sense that the specimen did not experience damage during Test 3.1, when the Darfield earthquake record was used, as expected. The results of Test 3.2 were also satisfactory but this time in the sense that it was able to impose large deformations upon the structure. Damage relocation, which was the main objective of the retrofit intervention developed in this thesis, was achieved for inter-storey drifts as high as 3.7%. One drawback though in terms of damage, was the existence of cracking in the columns of cruciform beam column joints, indicating that the length of the GFRP layers in the columns could have been larger. One important conclusion then is that the static method used for the estimation of that length might not be conservative enough. Dynamical effects can modify the shape of the bending moment diagrams (demand) even if the capacities at critical sections remain unaltered. Therefore, dynamic amplification factors should be incorporated in such an evaluation. A feasible alternative though, would be the use of GFRP layer in the entire height of the columns, in order to limit the likelihood of shear failure in the central portion.

The retrofit intervention/strategy was able to improve the performance of the structure in a local level, but it was not able to control the global performance, given that the inter-storey drifts in the first floor were not importantly reduced when compared to those experienced by the as-built specimen during Test 2.2. As a consequence, it is suggested that the retrofit interventions developed in this thesis is used together with other retrofit technics that provide stiffness as well as energy dissipaters, such as those mentioned in the previous section.

Nevertheless, it should be pointed out that the structure after suffering the consequences of a very demanding ground motion, was most likely able to be repaired not for research purposes only, but also in the context of real applications.

7.10 REFERENCES

Akguzel, U., Pampanin, S. (2010), 'Effects of Variation of Axial Load and Bidirectional Loading on Seismic Performance of GFRP Retrofitted Reinforced Concrete Exterior Beam-Column Joints', *Journal of Composites for Construction*, Vol. (14), pp. 94-104.

Akguzel, U. (2011), 'Seismic Performance of FRP Retrofitted Exterior RC Beam-Column Joints under Varying Axial and Bidirectional Loading', *a thesis presented for the degree of Doctor of Philosophy in Civil Engineering*, University of Canterbury, Christchurch, New Zealand.

Di Cesare, A., Ponzo, F., Nigro, D., Dolce, M., Moroni, C. (2012), 'Experimental and Numerical Behaviour of Hysteretic and Visco-Recentring Energy Dissipating Bracing Systems, *Bulletin of Earthquake Engineering*, Springer.

Dolce, M., Cardone, D., and Marnetto R. (2000), 'Implementation and Testing of Passive control Devices Based on Shape Memory Alloys', *Earthquake Engineering and Structural Dynamics*, Vol.29(7), pp. 945-968.

Dolce, M., Cardone, D., Ponzo, F., Valente, M. (2005), 'Shaking Table Tests of RC Frames without and with Passive Control Systems', *Earthquake Engineering and Structural Dynamics*, Vol. 34, pp. 1687-1717.

Kam, W.Y., Quintana-Gallo, P., Akguzel, U., Pampanin, S. (2010), 'Influence of Slab on the Seismic Response of Substandard Exterior Reinforced Concrete Beam Column Joints', *Proceedings of the for 9th US and 10th Canadian National Conference on Earthquake Engineering*, Toronto, Canada.

Marriott, D.J. (2009), 'The Development of High-Performance Post-Tensioned Rocking Systems for the Seismic Design of Structures', *a thesis presented for the degree of Doctor of Philosophy in Civil Engineering*, Department of Civil and Natural Resources Engineering, University of Canterbury, Christchurch, New Zealand.

Pampanin, S., Kam, W.Y., Tasligedik, S., Quintana-Gallo, P., Akguzel, U. (2011), 'Considerations on the Seismic Performance of pre-1970's RC Buildings in the Christchurch CBD during the 4th Sept 2010 Canterbury Earthquake: Was that Really a Big One?', *Proceedings of the 9th Pacific Conference on Earthquake Engineering*, Auckland, New Zealand.

Uang, C.M., Nakashima, M., and Tsai, K.C. (2004), 'Research and Application of Buckling-Restrained Braced Frames', *Steel Structures*, Vol. 4, pp. 301-313.

8 NUMERICAL PREDICTION OF THE BUILDING RESPONSE AND COMPARISON WITH EXPERIMENTAL RESULTS

8.1 INTRODUCTION

As it was described in detail in the previous chapters of this thesis, the specimen was tested in three experimental series. In the first shake table experiments, named Tests 1.1, 1.2, and 1.3, the as-built specimen failed due to loss of bond in the lap splices that joined all the columns at every level. That failure mode and the associated damage pattern developed more clearly at the roof level, where very poor quality concrete was used, simulating one of the identified deficiencies of pre-1970's buildings (Hakuto et al. 2000, Pampanin et al. 2002, Pampanin 2005). The mechanics involved in the development of that particular failure mode were explained in Chapter 4, as well as its relationship with the recorded response of the building. In this chapter the numerical blind prediction using the nominal and recorded input motions for Test 1.1 only are shown. As it will be illustrated, the model is not able to capture the behavior of the building with lap-splices because they are not taken into account in the numerical model. Nevertheless, the failure mode is reflected in the differences between the model and the recorded response, especially in terms of inter-storey drifts.

In a second experimental series, the specimen was repaired so that lap-splices were removed as described in Chapter 4, and it was tested using two ground motions recorded during earthquakes that occurred after the first experimental series were performed. Those input motions were one record from Darfield earthquake (10 of September 2010, New Zealand), and one form Maule earthquake (27 of February 2010, Chile). During the first experiment, Test 2.1, the specimen exhibited a predominantly elastic response with very light if no damage, whereas during the second experiment, Test 2.2, the specimen suffered severe damage, especially in corner beam column joints and internal columns as shown in detail in Chapter 4. In the first part of this chapter it is shown that the blind numerical simulation using the nominal input of the shake table was able to capture the response of the specimen with a reasonable accuracy for Test 2.1, but it was not able to represent in a similar way the response of the building during Test 2.2, where great inelastic incursions occurred in the members of the building. That is an indication of the initial model being adequate in the elastic range, but not in the inelastic one.

After those tests were performed, the actual motion imposed by the shake table was recorded and used for running the same analyses that comprised of Tests 1.1, 2.1 and 2.2. The differences in the prediction using the recorded and nominal motions are not substantial for Tests 1.1 and 2.1, as shown later. On the other hand, important differences were found in the numerical simulation of Test 2.2 when using both signals. In that case, when the nominal input is used, the model experiences excessive relative (to the shake table) displacements in the first floor, which is an indication that the small differences found in between the nominal and recorded motions of the shake table, may be critical for making a prediction that includes inelastic behavior, but it may be appropriate enough for making a prediction of an experiment where an elastic behavior is observed. One explanation for that is the high increase in the complexity of the problem when it falls

into the nonlinear or inelastic range, condition that enables the existence of chaotic (or erratic) behaviour (Strogatz 1994). In order to cope with the differences observed in the numerical and experimental response of the as-built/repaired building, the initial model was revisited and modified. These modifications are explained in this chapter, alongside a discussion on what are the most relevant parameters whose values enabled the possibility of capturing with a much greater degree of accuracy the response of the specimen, especially during Test 2.2.

After the second series of tests were carried out, the specimen was again repaired as explained in Chapter 7, and this time it was also retrofitted using the intervention described in Chapter 6 that included strengthening of exterior beam column joints of external and internal frames, as well as weakening of the floor slab with a shape that allows for the fuse to form in the beam, outside the strengthened region. The retrofitted specimen was tested under the same two ground motions used in the experiments of the as-built/repaired specimen, named Test 3.1 and 3.2, respectively. Due to time limitations, it was not possible to have a numerical model of the specimen before the tests. Therefore, no blind prediction of the tests is presented in this chapter. However, considering the modifications done to the initial numerical model used for the blind prediction of Tests 1.1, 2.1, and 2.2, a suitable post-experimental numerical model was constructed in order to capture the response of the retrofitted specimen during Tests 3.1 and 3.2, as described in the last part of this chapter.

A discussion on the accuracy of the numerical model in representing with accuracy the response of the specimen in all the tests mentioned above is also presented, in the light of the comparison with the experimental results. The problem of the differences obtained with the nominal and recorded shake table motions is also addressed, revealing some difficulties in the prediction of a building response before the seismic excitation has occurred indeed. The appropriateness of the model is also discussed, and strong dependences on some key parameters are identified.

8.2 NUMERICAL MODEL DESCRIPTION – AS-BUILT/REPAIRED

The numerical model was implemented in Ruaumoko2D (Carr 2008b). The beams were modelled using ‘Giberson beam’ elements (Sharpe 1974) with concentrated plasticity (or inelasticity) at the ends, and with no interaction between the bending moment capacity and the axial load. The columns were modelled using the same Giberson beam element, but allowing for interaction between bending moment and the axial load. The joints were modelled using a rotational spring element, as suggested by Pampanin et al. (2003). This is schematically presented in Figure 8.1.

In Figure 8.1(a), an image of the graphical interface representing the numerical model generated by Ruaumoko2D is shown. In Figure 8.1(b) a scheme of the panel zone connection is presented. In that scheme the configuration of the springs that represent the joint and their connectivity with the rigid end links of the frame elements are shown. As illustrated in that sketch, there is one node on the top of the master joint, where the top column is attached, and another one below it, where the bottom columns are connected. The beam element is connected to the master joint. As top and bottom nodes are slaved in the rotation, then the springs connected to each of them and the master joint act in parallel. Hence, each of the two rotational springs are modelled with half of the moment

resistance and stiffness of the complete joint, and when results are obtained for the hysteretic behaviour, the actions of both members should be added in time, the rotation being the same.

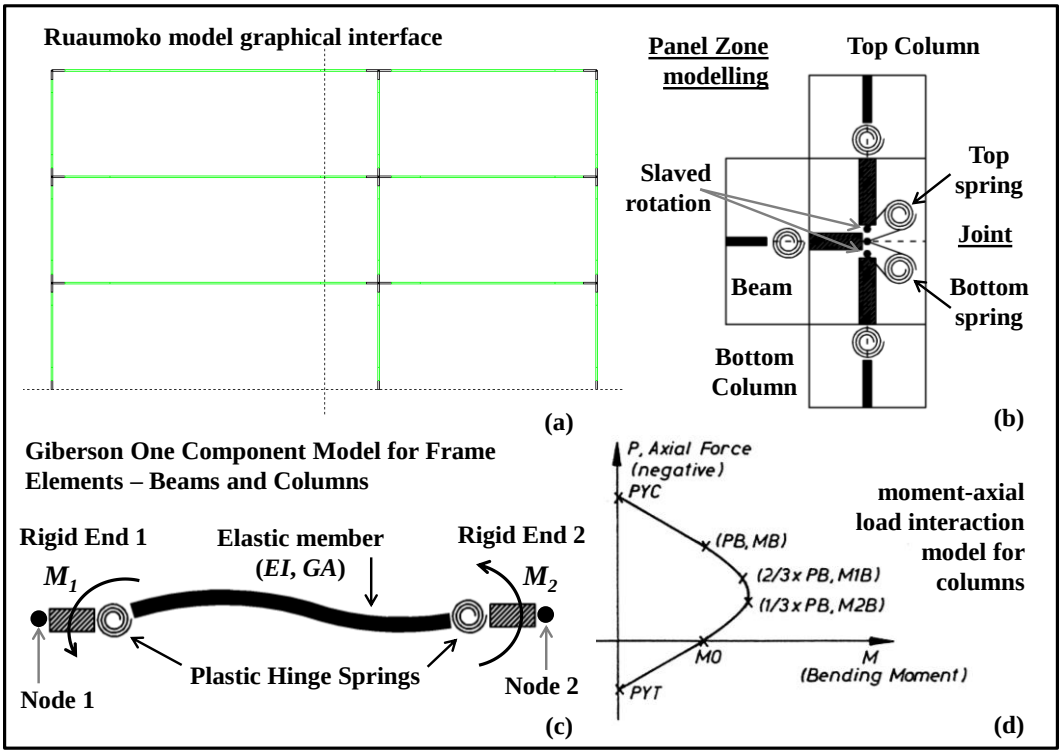

Figure 8.1: Numerical model description; (a) graphical interface of the model constructed in Ruaumoko2D (Carr 2008); (b) panel zone model detail; (c) Giberson beam model for columns and beams; (d) bending moment axial load interaction model for columns (from Ruaumoko2D manual).

In Figure 8.1(c), the model used for beam is schematically presented. The model consists in an elastic central member, with parameters EI and GA_s, with rotational springs at the ends where the inelasticity is concentrated. In those springs the hysteretic behaviour is set using a suitable rule in terms of moment-curvature. That requires the existence of a finite length where the plastic hinge extends, the plastic hinge length, which in this case was taken equal to half of the member cross section height. The bending moment capacity of those springs can be set to be a function of the axial load with the interaction model presented in Figure 8.1(d), used in this case for the columns only.

In columns, the inelastic behaviour at the ends of the elements was modelled with the modified Takeda hysteresis rule (Otani 1974, Carr 2008c). In beams, due to the asymmetry of the cross section and thus the strength and the stiffness, the revisited Takeda hysteresis rule (Saiidi 1979, Carr 2008c) was used. The parameters for the loading and unloading stiffness were set to $\beta = 0.0$ and $\alpha = 0.5$, respectively, representing the most degrading scenario for the stiffness after yielding has occurred (also known as 'thin Takeda'). The initial cracked stiffness of both type of elements, as well as the yielding moment of the beams and the M-N diagrams of the columns (see Figure 8.1(d)) were obtained from the moment-curvature diagrams presented in Chapter 4. The hysteretic behaviour of the joints was modelled in the initial model with the revisited

Takeda rule (Saiidi 1979) with the parameters set to the most degrading form ($\delta = 0.0$, $\gamma = 0.5$).

The two hysteresis models mentioned before are schematically presented in Figure 8.2. In Figure 8.2(a) the Modified Takeda rule (Otani 1974) is shown. That model is bi-linear in the sense that there is only one straight line from zero displacement and force defined by the initial stiffness k_0 and the nominal yielding actions F_y^+ and F_y^- in the positive and negative directions, respectively. The functional then follows another straight line given by the post-yield stiffness rk_0, where r is the bi-linear factor. If a reversal in the displacement occurs when the maximum displacement d_m is reached and the plastic counterpart d_p determined, the force-displacement relationship follows an unloading path determined by the unloading stiffness $k_u = k_0(d_y/d_m)^{\alpha}$, where d_y is the yielding displacement in the corresponding direction, and α is the degrading stiffness power factor. If the displacement continues decreasing after zero force has been achieved, then the force-displacement curve follows a straight line towards the negative yielding point. In the case of this rule there is symmetry in the positive and negative directions, so that $F_y^+ = F_y^-$ must be satisfied, and the same hysteresis path described for the positive direction applies. After the displacement has reached the maximum negative vale and the force has reduced to zero, if the displacement increases, the hysteresis rule follows a straight line from that point towards β times the plastic displacement reached in the previous cycle when yielding occurred, $d_p = d_m - d_y$. As a result, the model is determined by 5 parameters: k_0, $F_y^+ = F_y^-$, r, α, and β.

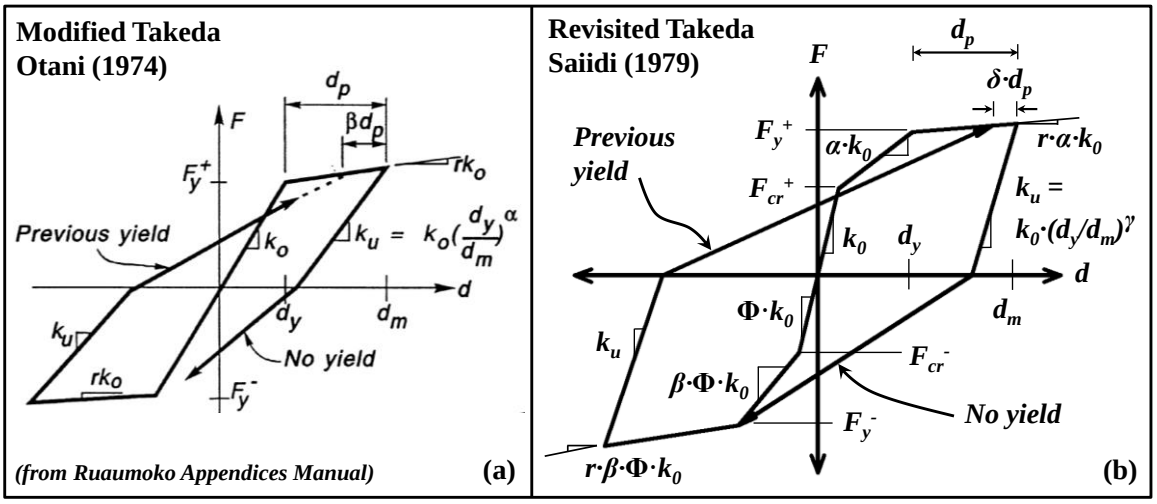

Figure 8.2: Hysteresis rules for beam, columns and joints; (a) Modified Takeda (Otani 1974), (b) revisited Takeda (Saiidi 1979).

In Figure 8.2(b) the revisited Takeda hysteresis rule is schematically shown. That rule follows the same principles of the Modified Takeda rule, described previously, but has an initial tri-linear path and allows for asymmetry in the positive and negative directions. In this model, k_0 is the initial elastic stiffness of the member in the positive direction, the negative counterpart being $\Phi \cdot k_0$. That stiffness is reduced for increasing and decreasing displacements by a factor of α and β after the cracking actions F_{cr}^+ and F_{cr}^- are exceeded in the positive and negative directions, respectively, and they determine the path until yielding is reached. Yielding is determined with F_y^+ and F_y^-, which can be different in magnitude, and should be different unless $\Phi = 1$ and $\alpha = \beta$. The last part of the tri-linear

backbone curve is governed by the post yield stiffness $r \cdot \alpha \cdot k_0$ and $r \cdot \beta \cdot \Phi \cdot k_0$ in the positive and negative directions, respectively. The unloading stiffness after reversal in the displacement is the same as that of the Modified Takeda rule given by $k_u = k_0 (d_m/d_y)^{\gamma}$, where in this case the power parameter is named γ instead of α. The reloading stiffness after yielding has occurred is the same than the one described before for the Modified Takeda rule, with the exception that in this case the parameter β is renamed as δ. Hence, the hysteretic model is determined by 11 parameters: k_0, F_{cr}^+, F_{cr}^-, F_y^+, F_y^-, Φ, α, β, r, γ, and δ.

As was mentioned before, the joints were modelled using springs with symmetrical characteristics (i.e. modified Takeda). That means that the cracking moment in both directions is the same, which is valid as a first approximation, but is not necessarily true in beam column-joints with slabs, as was discussed before in Chapters 5 and 6. The elastic rotational stiffness of the springs was set to $k_0 = 2 \cdot 10^6$ kNmm, as explained in Chapter 4. The initial stiffness used in the spring was not that of the joint alone, but it accounts for torsional effects. As will be shown later, this value has the same order of magnitude of the initial equivalent stiffness of the joint, but is larger than the value used in the Modified SINA Rule (Saiidi 1979) in the model that provides the most accurate numerical prediction of the as-built/repaired building response. A post-yield or (post-crack) stiffness factor $r = 0$ was used in the springs.

The values adopted for the parameters that govern the hysteresis rules of beams, columns and joints of the initial model can be summarized as follows:

As-Built Beams *(Revisited Takeda rule – IHYST = 57 in Ruaumoko2D)*

$k_0 = EI$ = 4,118.4 kNm^2; r = 0.01; F_y^+= 8.0 kNm; F_y^- = -14.0 kNm; α = 0.15; β = 0.25; γ = 0.5; δ = 0.5; Φ = 1.0; $F_{cr}^+ = 0.32F_y^+$; $F_{cr}^- = 0.19F_y^-$.

As-Built Columns *(Modified Takeda rule – IHYST = 4 in Ruaumoko2D)*

$k_0 = EI$ = 157.5 kNm^2; r = 0.01; F_y^+ (@ N = 0) = 4.0 kNm; F_y^- (@ N = 0) = -4.0 kNm; α = 0.5; β = 0.0.

As-Built Joints (*Modified Takeda rule – IHYST = 4 in Ruaumoko2D)*

$k_0 = GJ$ = 2,000 kNm; r = 0; F_y^+ = 3.5 kNm; F_y^- = -3.5 kNm; α = 0.5; β = 0.0.

8.2.1 Damping Model

The damping model used was that of Wilson-Penzien (Wilson and Penzien 1972) with constant damping, extensively described in Ruaumoko's Theory Manual (Carr 2008a), which assigns the same viscous damping to all the modes in the model, in this case 3. The magnitude of that viscous damping was 5% of the critical value. That model was preferred to a Rayleigh model for three reasons:

(1) The Rayleigh damping approach can assign very large damping ratios to higher modes. High levels of damping associated to higher modes may have a strong influence in the inelastic response of the model, especially in the amplitude of the motion (Crisp 1980).

(2) The Wilson-Penzien model was found to provide more stable results in a 2-DOF system based on inelastic dynamic analyses performed in the context of the prediction of shake table tests of fasteners for non-structural elements anchored to RC structural elements (Pampanin et al. 2010).

(3) In the Ruaumoko Theory manual (Carr 2008a) it is recommended that the constant damping approach is used with the same damping value for the two modes that define it.

8.2.2 Pushover Analysis

In Figure 8.3 the numerical pushover curve of the as-built specimen is presented in terms of base shear versus the inter-storey drift in the first floor. The deformed shape is imposed with this method and hence, one can obtain as many pushover curves as desired. In this case a soft storey mechanism in the first floor is expected as discussed in Chapter 5. The initial stiffness of the structure is indicated in the graphs of Figure 8.3, as well as two secant stiffness at 2.5% and 4.0% inter-storey drifts. The initial cracked period of the structure can be estimated from those graphs, provided that an effective mass is assumed for this mode of vibration. If the effective mass (M_e) is taken as the total mass of the structure above the middle height of the first floor columns, i.e. 6,180 kg, then the period is $T_1 = 2\pi\sqrt{(6{,}180 \text{ kg} / 4.2 \cdot 10^6 \text{ N/m})} = 0.24$ seconds. This value is very close to that calculated automatically by the program (0.28 seconds) and the measured value of 0.27 seconds. If the stiffness decreases by 5.53 times so that it becomes equal to $K_2 = 0.76$ kN/mm, then the period increases by a factor of $\sqrt{5.53} = 2.35$ times, so that $T_2 = 0.25 \cdot 2.36 = 0.57$ seconds. This value corresponds to a frequency of 1/0.57 = 1.75 Hz, which inside the band of the 1.5 to 2.0 Hz used to filter the original signal, and where the most powerful Fourier-components of the input motion are concentrated, as extensively explained in Chapter 7.

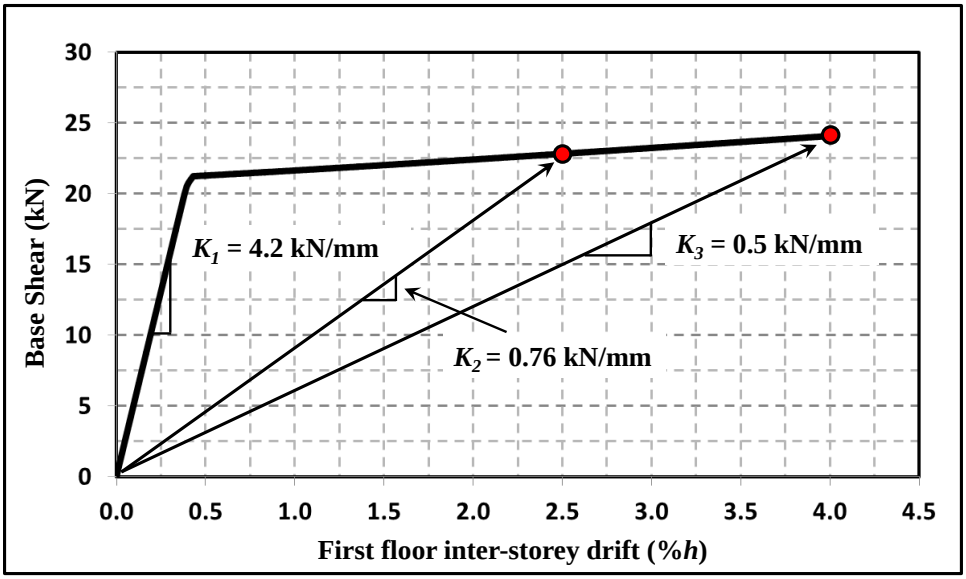

Figure 8.3: Pushover curve of the as-built/repaired specimen numerical model.

Using the second secant stiffness associated to a 4% drift, the degradation from the initial K_1 is 50/6 times, which means that the corresponding period is $T_3 = 0.69$ seconds, or in

terms of frequency 1.44 Hz, which is still very close to the predominant frequencies of the input motion. Using this information, it was thought before Test 2.2 was performed that if during the initial time of the response the structure reached inter-storey drift values of the order of 2.5% in the first floor, then it could fall into resonance and experience large inelastic deformations, as high as 4%.

The simplified approach used in the prediction of the specimen response during Test 2.2 based on the pushover analysis described before, can be very useful. It also yields very similar results to those calculated 'by hand' in Chapter 4. Nevertheless, it is important to note that this approach is quite simplistic but provides information on the lateral capacity of a structure based on the imposition of a given inelastic mode shape, which in this case is a soft-storey mechanism like that shown in Chapter 5. The fact that there are no reversals in the displacement history imposed implies that there is no information about the hysteretic behaviour of the specimen. For a detailed discussion on the pros and cons of a pushover analysis, the interested reader is referred to Krawinkler and Seneviratna (1998).

8.2.3 Cyclic Pushover Analysis

A displacement controlled cyclic pushover was carried out in order to investigate the predicted cyclic response of the structure, as it was pushed back and forth at increasing drift levels. In this case, the soft storey mechanism shown at the end of Chapter 5 is imposed with the displacement histories at each floor, which are the same (Priestley 1997).

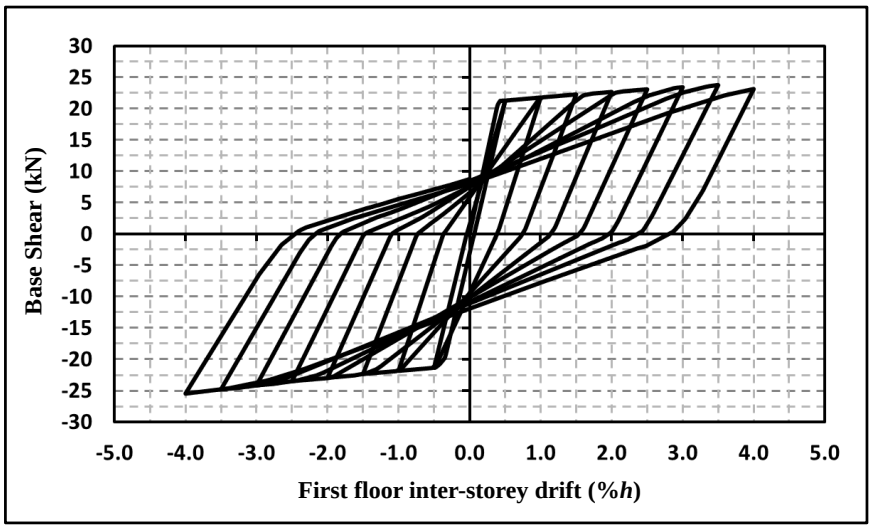

Figure 8.4: Cyclic Pushover curve as-built/repaired model.

In Figure 8.4 the base shear versus first floor inter-storey drift obtained with Ruaumoko2D is presented. In the graphs of that figure, it can be observed that the global hysteretic behaviour of the building reflects the hysteretic shape of a Takeda rule, as expected. Even though no strength degradation is predicted, there is a reduction in the stiffness in the unloading part of the loop, but more remarkably in the reloading part. Hence, after the structure reached 2.5%, for example, the 'unloading' stiffness is 2.4kN/mm, which is 1.75 times smaller than the initial one. In the reloading path from

positive to negative load, the re-loading stiffness of the model has a value of about 0.47kN/mm, very similar to the secant stiffness identified in the pushover curve for a 4% drift.

If the relative magnitude of the imposed floor displacement was changed in order to explore another deformed shape upon the numerical model of the structure, then different results could have been obtained. As this thesis leads with the dynamics involved in the experimental and numerical assessment and retrofit of RC buildings, the aforementioned numerical tool is not relevant. Hence, in the rest of this chapter, only nonlinear dynamic analyses of post-experimental numerical models are performed.

8.3 BLIND PREDICTION OF THE AS-BUILT/REPAIRED SPECIMEN RESPONSE – TESTS 1.1, 2.1 AND 2.2

In this section, the numerical blind prediction of the specimen response during Tests 1.1, 2.1 and 2.2 are presented. The predicted and recorded responses are shown in terms of the relative to the shake table displacement of each floor (absolute displacement minus the shake table displacement) and the inter-storey drifts. The nominal motion used in the controlling system of the shake table is used in this case, as it is obviously impossible to have the true or actual motion imposed by the shake table before the tests are actually performed. In fact, it may also be possible that the real recorded motion of the table depends on the dynamical response of the structure itself, if one understands the structure as an open system in dynamical interaction with the source of movement, in this case the shake table. For an explanation of that theory and possible applications to earthquake engineering, the interested reader in referred to Quintana-Gallo et al. (2013).

8.3.1 Test 1.1: Gilroy Array #5 record (GA5), Loma Prieta

In Figure 8.5, the blind numerical blind prediction of the as-built specimen response during Test 1.1 is presented in terms of relative floor displacements, and in terms of inter-storey drift in Figure 8.6. During that test, as it was mention before, one horizontal component of the ground motion recorded during the Loma Prieta earthquake (California 1989) at Gilroy Array #5 station (GA5 record) was used.

In the graphs of Figure 8.5 it can be observed that the numerical prediction of the relative (to the shake table) floor displacements of the specimen during Test 1.1 is in reasonable agreement with the experimental counterparts. The accuracy of the predictions is larger during the initial part of the response, from 0 to 4 seconds after the start of the test. During that time of the response the prediction of the relative displacement of the first storey is particularly in good agreement with the experimental counterpart. After 4 seconds of the beginning of the test, the prediction of the displacement of all three floors starts to be inaccurate. Both amplitude and phase of the signals become different until about 6 seconds, where the numerical model is able to capture the experimental response again. It seems very important to note that the prediction in the last part of the motion becomes very accurate again, even though there are important differences in previous instants. That is especially true for the third floor, where predicted and measured displacements are remarkably close.

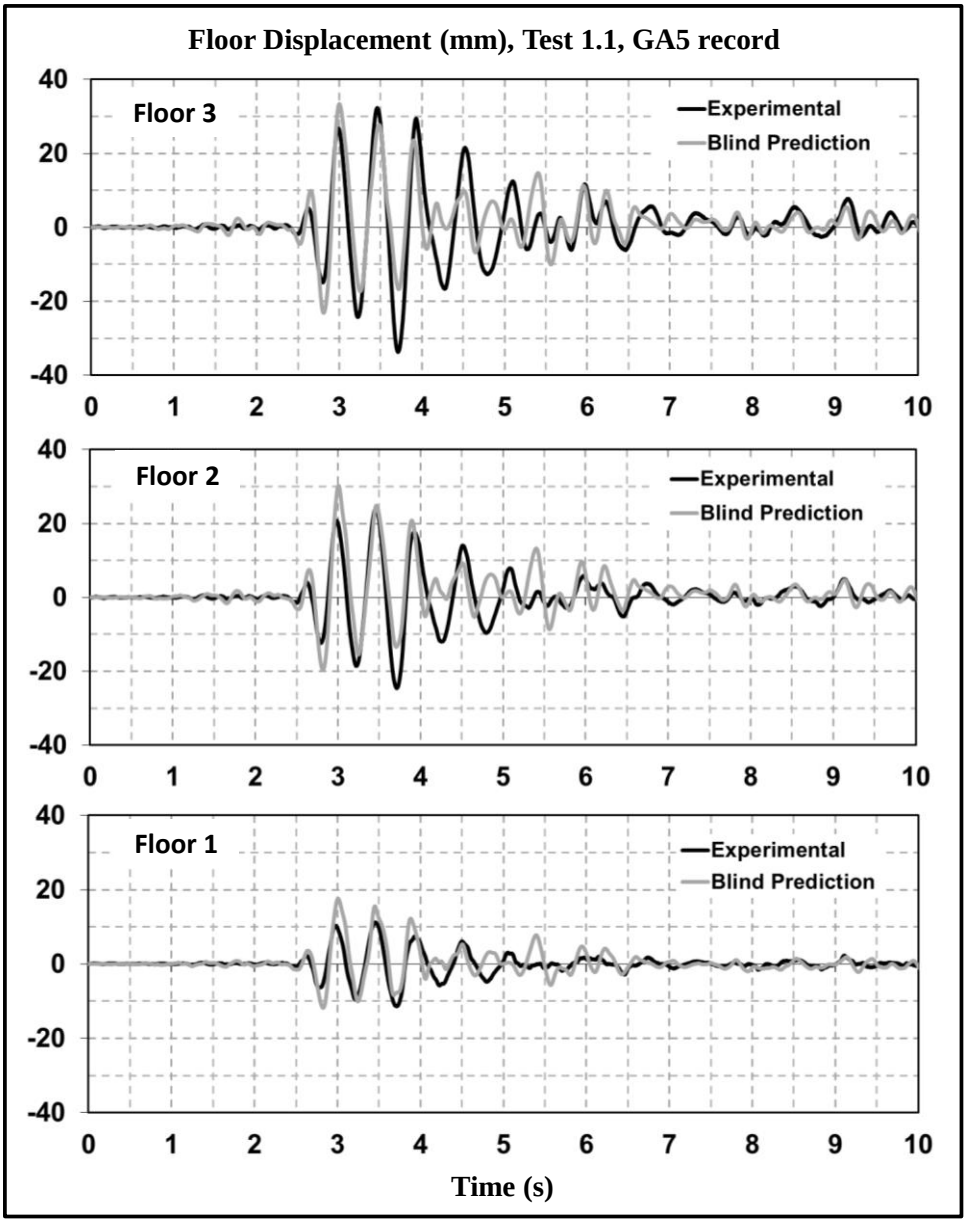

Figure 8.5: Test 1.1 relative floor displacement, GA5 record, blind prediction.

In the graphs of Figure 8.6, it can be observed that the numerical prediction of the inter-storey drifts histories is in reasonable agreement with the experimental data, during the initial part of the motion, from 0 to about 3.5 seconds. The numerical prediction of the inter-storey drift history of the first floor is particularly good during that period, even though it overestimates the amplitude. The accuracy of the prediction of the inter-storey drift histories of the second floor becomes smaller than that of the first floor, and underestimates the response a little. In the third floor, the prediction becomes even less accurate and after 3.5 seconds differs completely from the empirical counterpart. At first, this could be attributed to a lap slice effect in the soft-concrete top floor as well as to a minor extent in the bottom floors. As lap splices were not included in the model, the modelling of that part of the building is proposed to be added in future research, where the recorded motion data can be captured better.

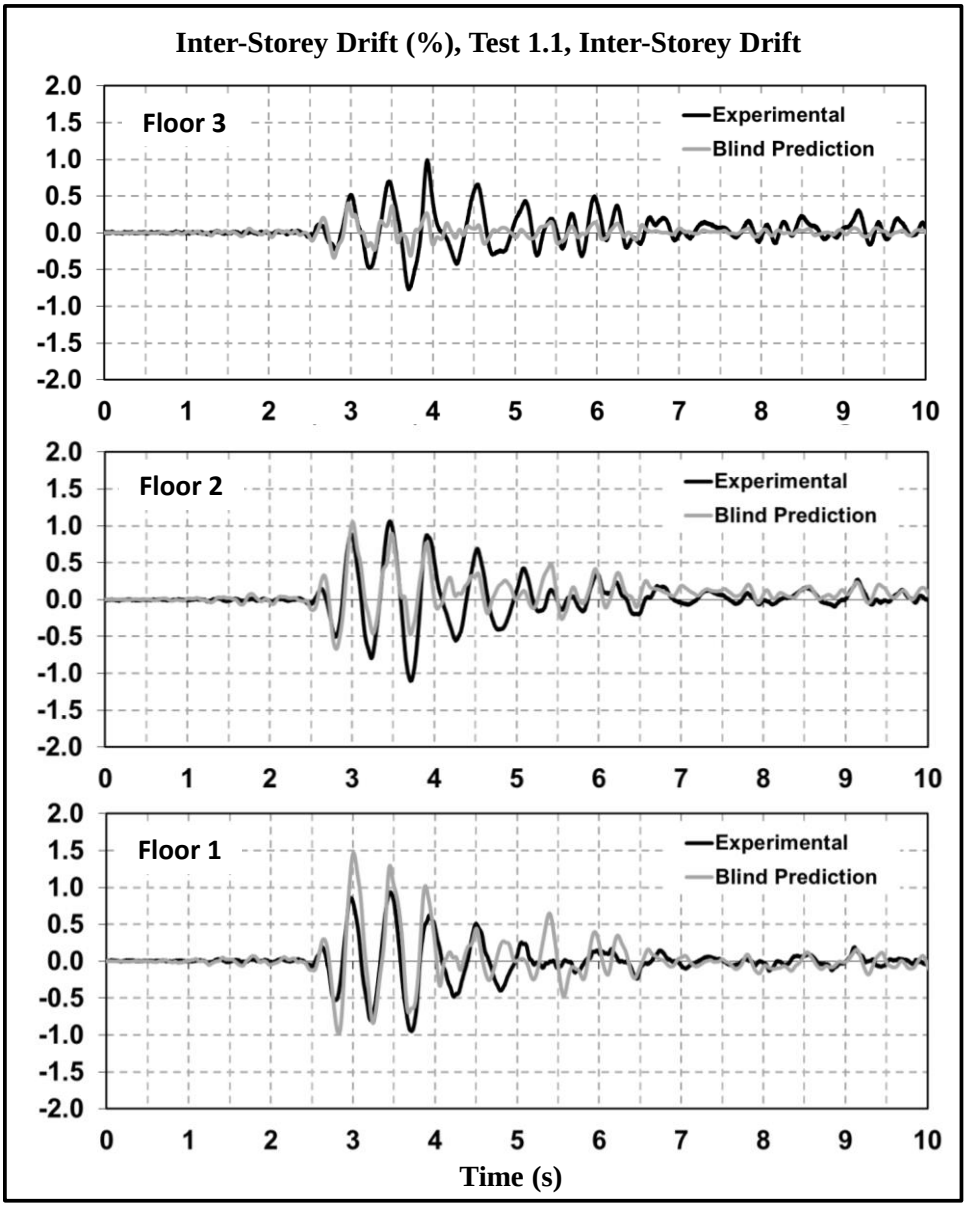

Figure 8.6: Test 1.1 inter-storey drifts, GA5 record, blind prediction.

8.3.2 Test 2.1: Christchurch Hospital record (CHH), Darfield

As mentioned in Chapter 4, during Test 2.1, one horizontal component of a ground motion recorded during the Darfield Earthquake (New Zealand 2010) at the Christchurch Hospital station was used (CHH record). The results of the numerical prediction using that nominal input are presented in Figure 8.7 and Figure 8.8, in terms of relative to the shake table floor displacements and inter-storey drifts, respectively.

In the graphs of Figure 8.7 it can be observed that the prediction of the floor displacements is overall satisfactory, with the most remarkable differences occurring during the strong part of the motion. The numerical and experimental signals match very well during the initial part of the response in all floors, before differences appear at about 6 seconds from the start of the motion. From that instant onward, the numerical and experimental displacements become slightly different, but in a reasonably good

agreement, besides an overestimation of the maximum response in all cases. From about 15 seconds onward, both signals become very similar again in shape, even though small differences exist in the residual displacement they converge to. It seems quite remarkable that even if the numerical model predicts a different path of the response during the strong motion of the record, it becomes accurate again during the last part of the response. That is an indication that both experimental and numerical models responded predominantly in the elastic range. That is true according to the damage observed after the test, which was negligible, and according to the local inelastic behaviour observed in the joints of the numerical model.

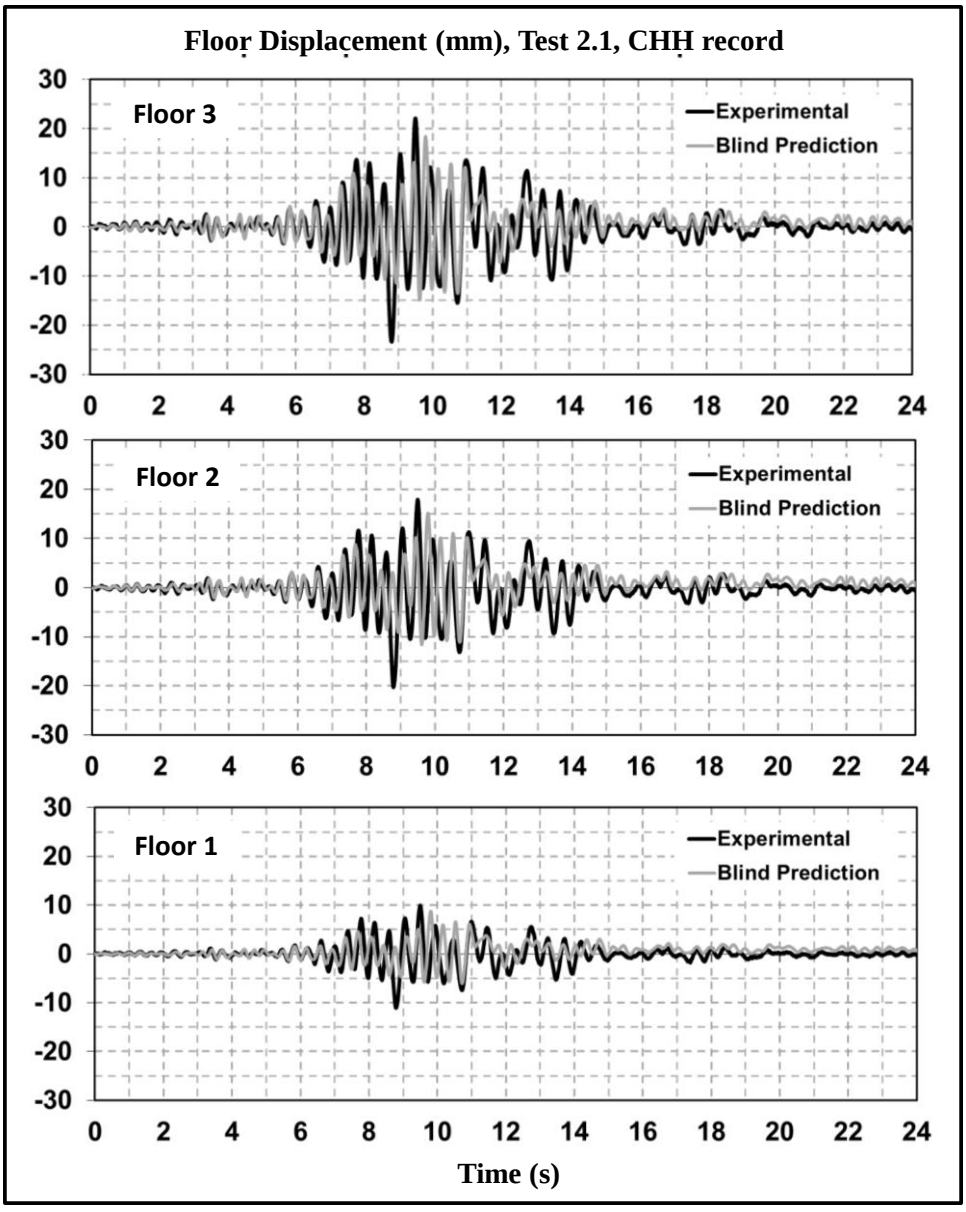

Figure 8.7: Test 2.1 relative floor displacement, CHH record, blind prediction.

The numerical prediction of the inter-storey drifts presented in the graphs of Figure 8.8, are in reasonably good agreement with the experimental counterparts, and basically the same observations discussed before for the building response in terms of floor displacements apply.

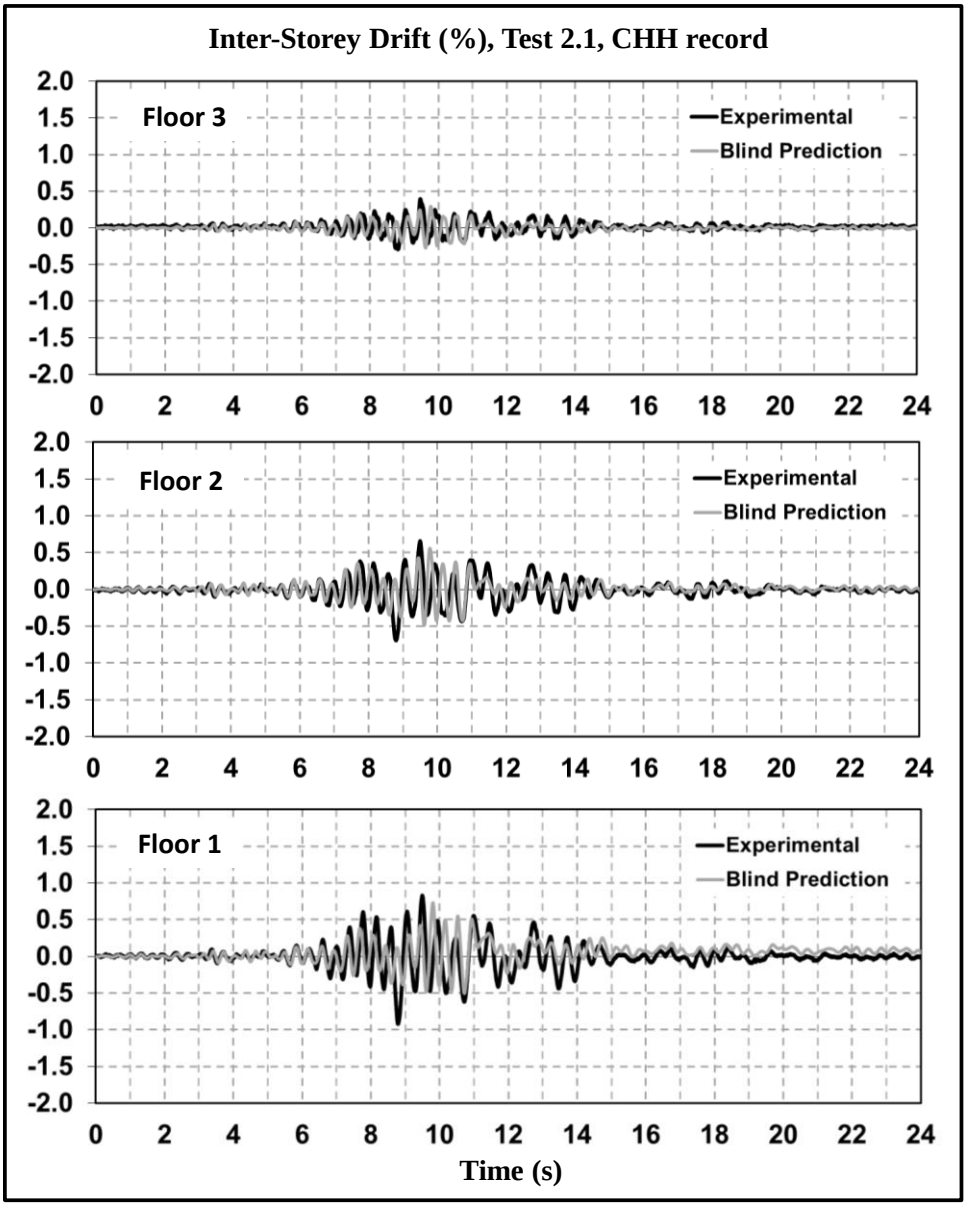

Figure 8.8: Test 2.1 inter-storey drifts, CHH record, blind prediction.

8.3.3 Test 2.2: Viña del Mar – Marga-Marga record (VMM), Maule

In the second experiment of tests of the as-built/repaired specimen, Test 2.2, one ground motion recorded at Viña del Mar (Chile) during the 27 of February 2010 Male earthquake was used (VMM record). The results of the blind prediction of the building response during that test are presented in Figure 8.9 and Figure 8.10, in terms of relative to the shake table floor displacements and inter-storey drifts, respectively. The prediction is plotted with the experimental response for comparison.

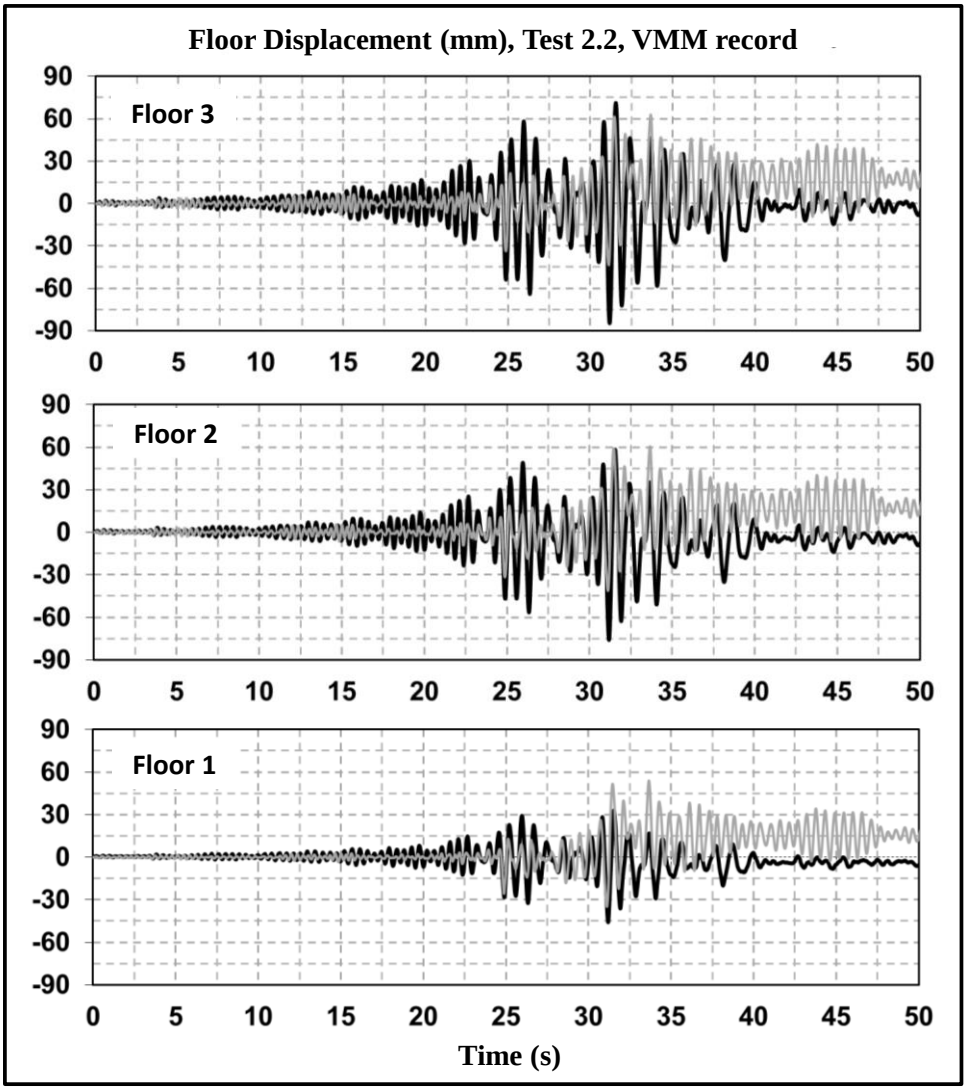

Figure 8.9: Test 2.2 relative floor displacement, VMM record, blind prediction.

In the graphs of Figure 8.9 it can be observed that the predicted floor displacements of the building when subjected to the nominal version of VMM record, do not match entirely well the actual recorded counterparts at every floor. The response is underestimated from the early stages of the motion, but has a very similar frequency. The predicted response is reasonably accurate from about 24 seconds to 30 seconds after the beginning of the test, even though the amplitude of the recorded displacements is underestimated by an important margin. Nevertheless, the frequency and shape of the predicted response is quite similar to that of the recorded counterparts. After 32 seconds of the start of the motion however, the numerical prediction captures the shape of the floor displacements, but it is constantly deviating from the residual or asymptotic recorded displacement. In the context of nonlinear dynamical systems and chaotic behaviour, the numerical and experimental responses have different 'attractors' (Lorenz 1963, 1993, Strogatz 1994).

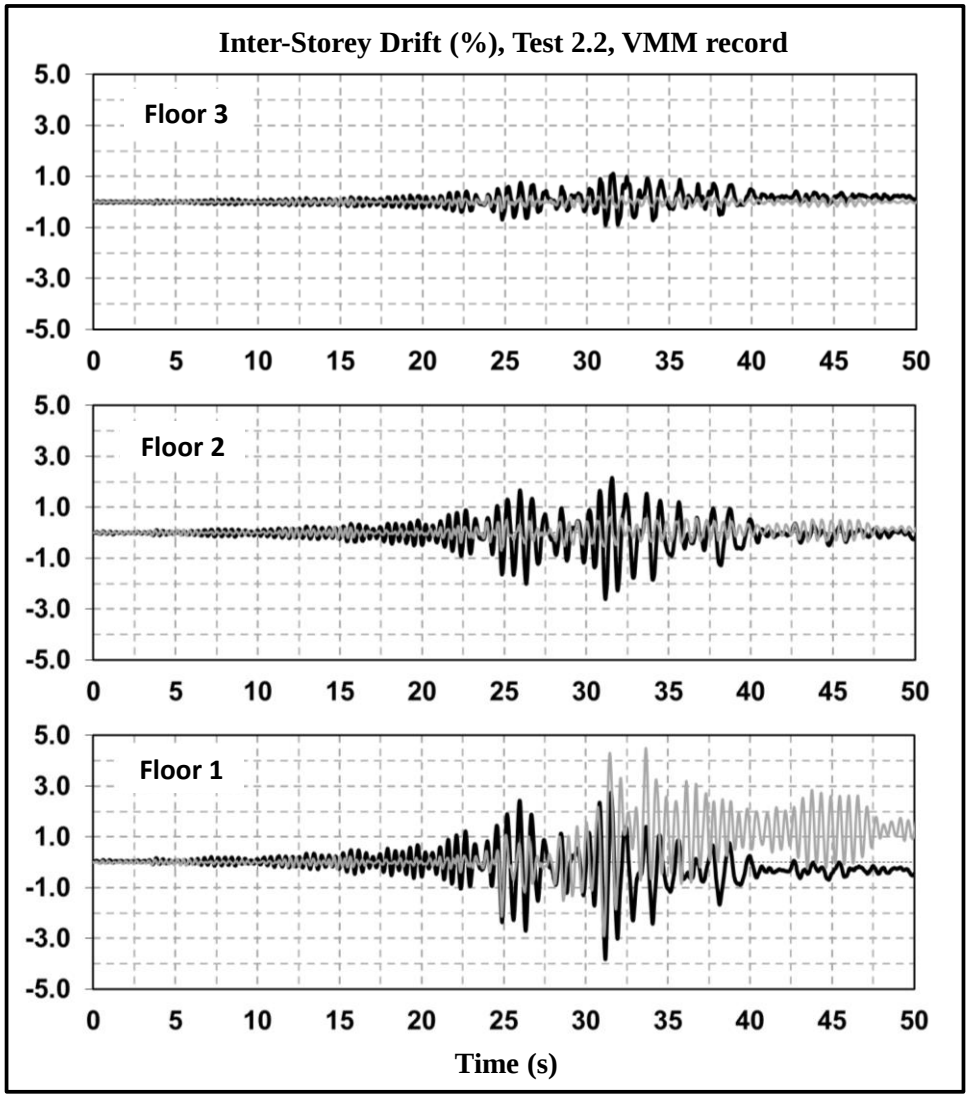

Figure 8.10: Test 2.2 inter-storey drifts, VMM record, blind prediction.

In the graphs of Figure 8.10, it can be observed that the differences in the predicted inter-storey drifts differ importantly in amplitude in floors 2 and 3. Nevertheless, the shape of the experimental and numerical signals is reasonably similar. The prediction of the inter-storey drift of the first floor is more accurate in terms of amplitude from about 23 seconds, and it is able to capture the experimental counterpart with a reasonable accuracy until second 32, approximately. From that instant onward, the predicted inter-store drift history starts to diverge from the recorded response, and begins to oscillate around a value of 1%, as can be observed in the bottom graphs of Figure 8.10. As discussed in the following sections, this bifurcation of the predicted response does not occur when the real recorded motion of the shake table is used, noting that the differences in the nominal and recorded motions are minimal, as shown in Chapter 7. As it is shown later, the use of less degrading parameters in the Modified Takeda rule in the joints also disables the occurrence of that bifurcation (or shift in the attractor of the dynamical response).

In Table 8.1, the maximum experimental and numerical values of the responses in terms of floor displacements and inter-storey drifts are presented. Note that these values are not necessarily reached at the same time of the response, but they provide an indication of the differences in the amplitude overall speaking.

Table 8.1: Maximum response experimental/numerical comparison blind prediction.

		Floor Displacements (mm)			Inter-Storey Drifts (%)		
Test	Floor	Exp.	Num.	Num./Exp.	Exp.	Num.	Num./Exp.
1.1	1	11.3	17.6	1.56	0.93	1.29	1.39
1.1	2	24.5	30.1	1.23	1.10	0.92	0.84
1.1	3	33.7	33.4	0.99	0.99	0.38	0.38
2.1	1	11.0	8.6	0.78	0.92	0.73	0.79
2.1	2	20.2	15.2	0.75	0.69	0.54	0.78
2.1	3	23.2	18.1	0.78	0.40	0.29	0.73
2.2	1	45.3	53.2	1.17	3.82	4.47	1.17
2.2	2	75.9	60.5	0.80	2.60	0.70	0.27
2.2	3	84.8	62.8	0.74	0.90	0.35	0.39

8.4 PREDICTION USING THE INITIAL MODEL AND THE RECORDED SHAKE TABLE MOTION

In this section, the numerical prediction of the same test presented in the previous section is shown. The initial model was not altered, but only the input motion was modified as this time the actual recorded motion of the shake table during each test was used. The differences between both signals were presented in Chapter 7.

8.4.1 Test 1.1 (GA5 record – Loma Prieta Earthquake)

In Figure 8.11and Figure 8.12 the numerical prediction of the as-built specimen (with lap-splices) response during Test 1.1 using the recorded shake table motion is presented in terms of floor displacements and inter-storey drifts, respectively. In those figures, the predicted response is compared with the recorded data as before.

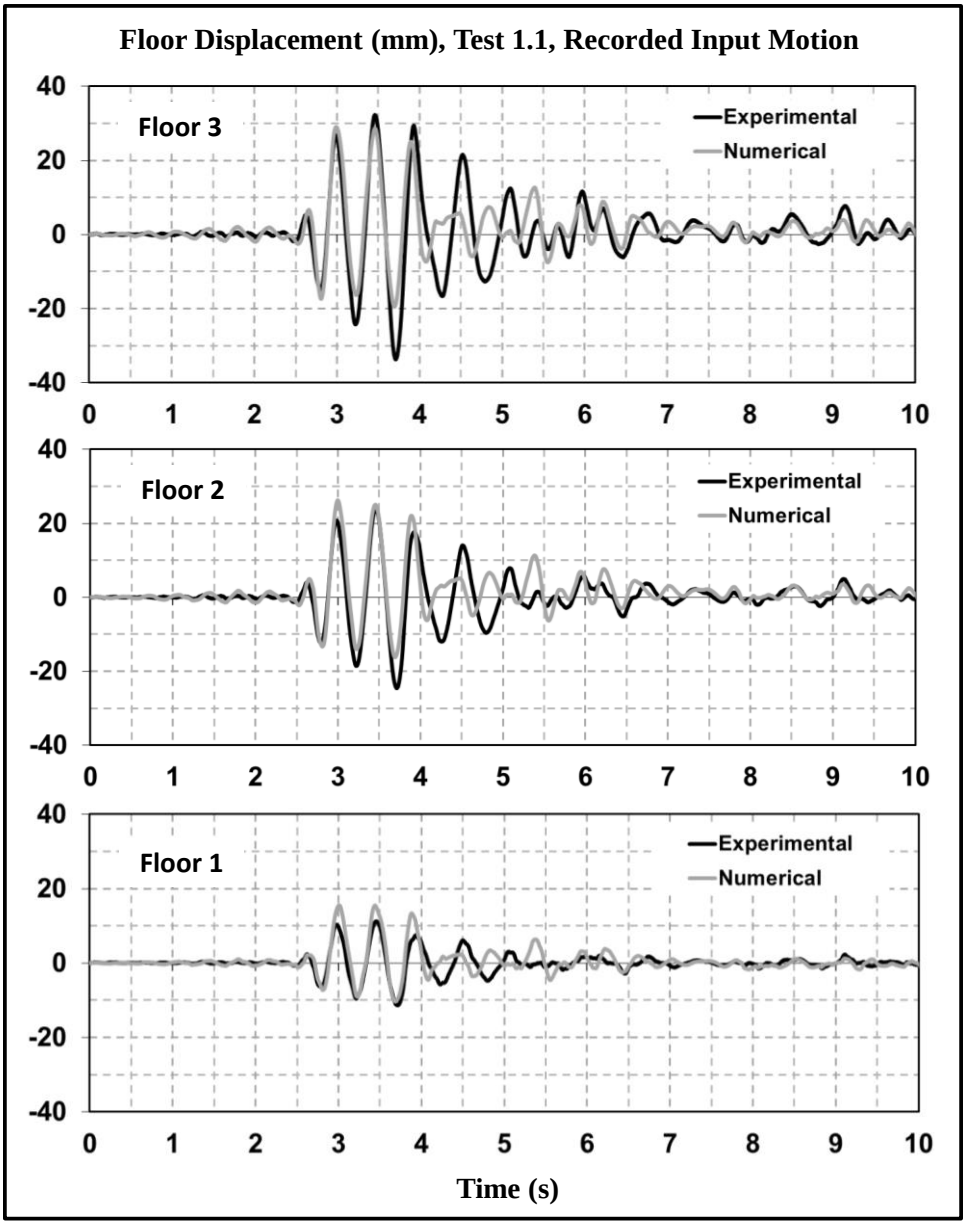

Figure 8.11: Test 1.1 relative floor displacement blind prediction using the recorded input.

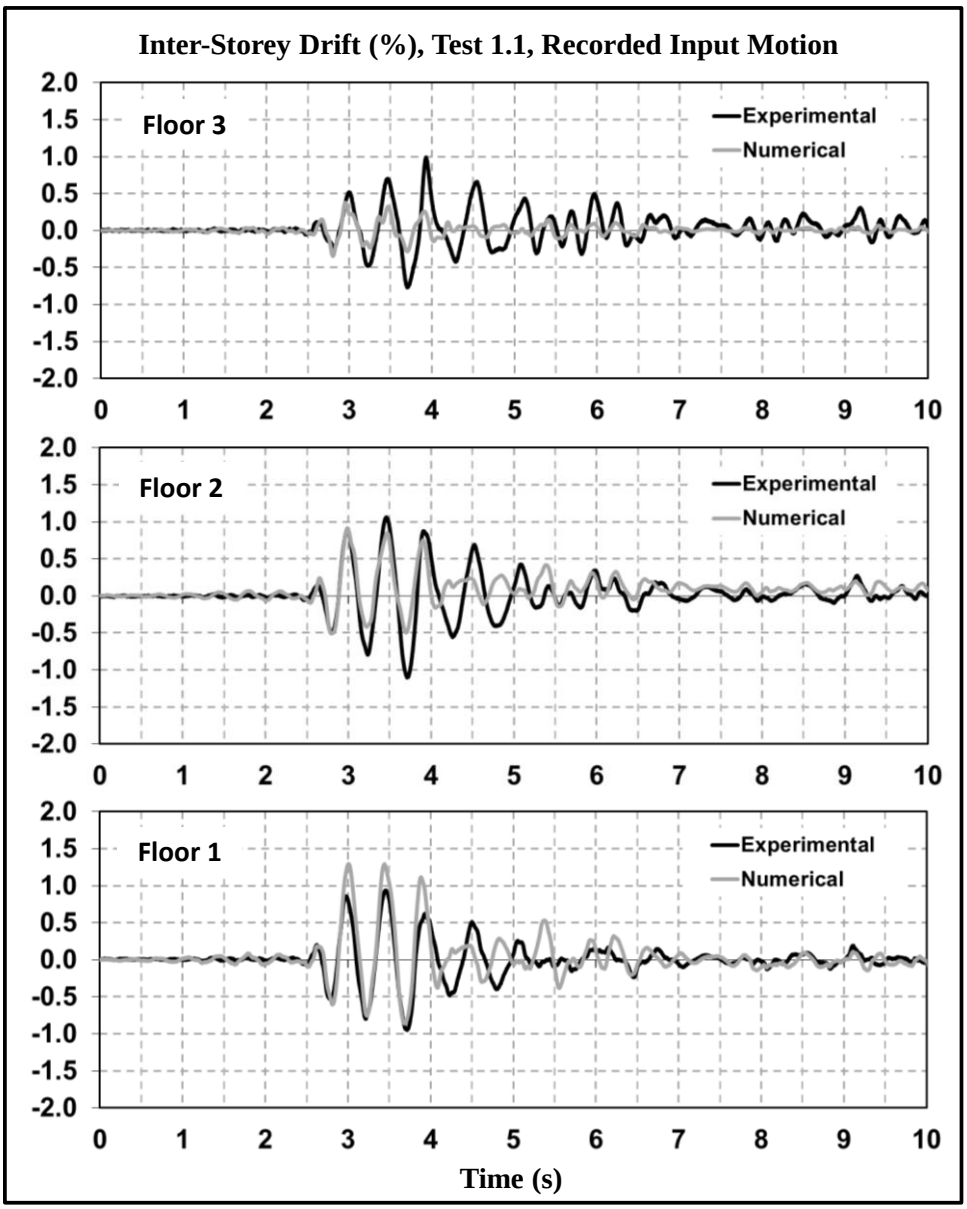

Figure 8.12: Test 1.1 inter-storey drift blind prediction using the recorded input.

Overall speaking the model is able to capture the experimental response, especially during the strong part of the motion. The same observations done for the blind prediction of this test apply.

8.4.2 Test 2.1 (Christchurch Hospital record – Darfield Earthquake)

In the graphs of Figure 8.13 and Figure 8.14 the predicted response of the as-built/repaired specimen (without lap splices) during Test 2.1 using the recorded motion of the shake table is presented in terms of relative floor displacements and inter-storey drifts, respectively. The recorded input motion represents the actual version of the shake table when imposing the nominal CHH record. The predicted response is presented and compared with the experimental results. The prediction captures the experimental response in a similar fashion the blind prediction does, indicating that in this case the

differences in the nominal and recorded motions do not have important consequences in the numerical results.

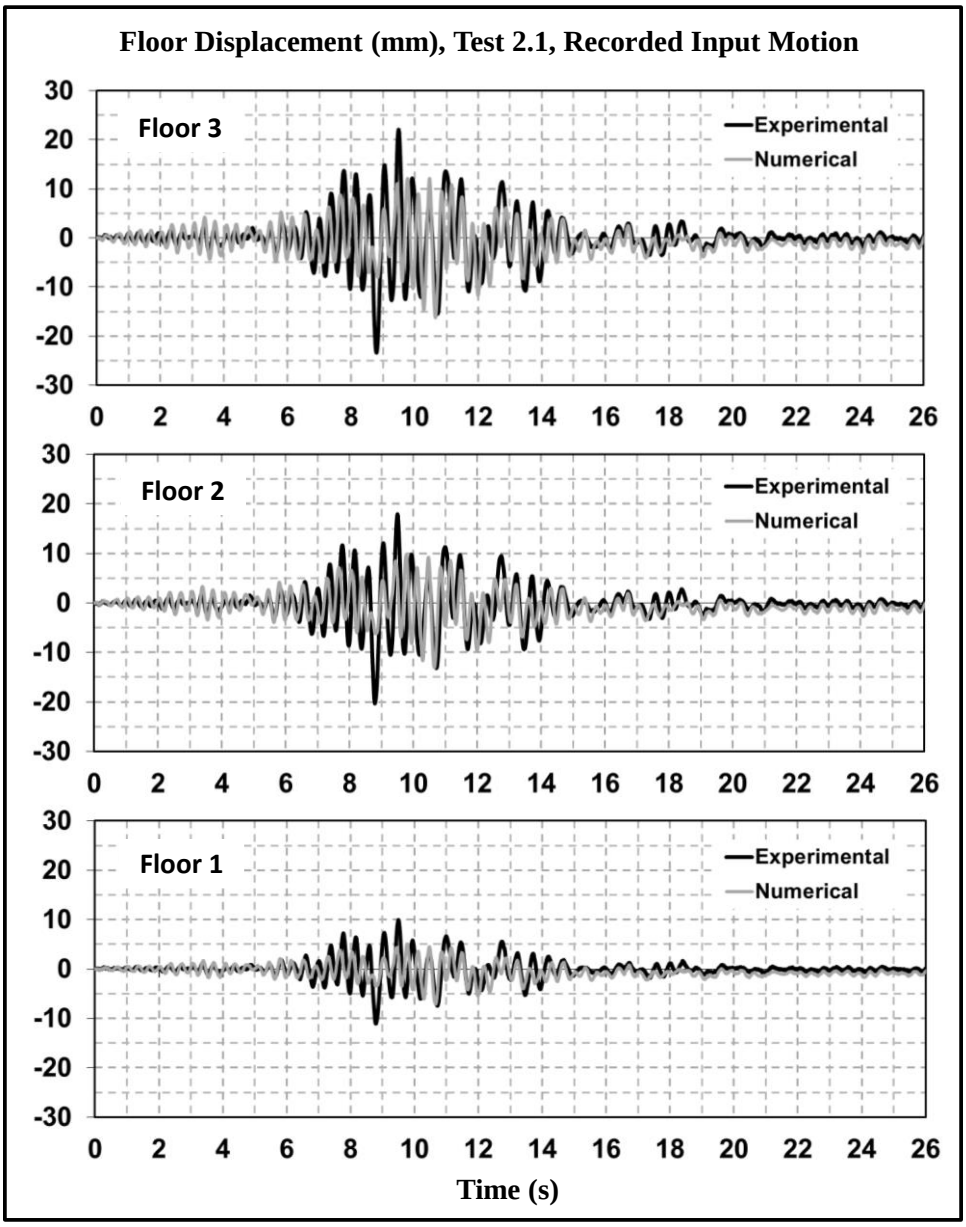

Figure 8.13: Test 2.1 relative floor displacement blind prediction using the recorded input.

In the graphs of Figure 8.13 and Figure 8.14, it can be observed that the numerical model is able to represent with a reasonable degree of accuracy the experimental response in terms of floor displacements and inter-storey drifts during the weak part of the motion at the beginning and end, from 0 to about 6 seconds and then from about 10 to 26 seconds and beyond. In the strongest part of the motion, from 8 seconds onward, the model underestimates the experimental response. As will be discussed in the next section, when the numerical prediction of the tests using the nominal and recorded input motions are compared, there is not much difference in the prediction of the building response during Test 2.2, which is also true for Test 1.1 as mentioned before. The differences in the nominal and recorded-actual motion imposed by the shake table are important though for

the prediction of the most demanding experiment in terms of the response experienced by the building, Test 2.2, as presented in the next subsection.

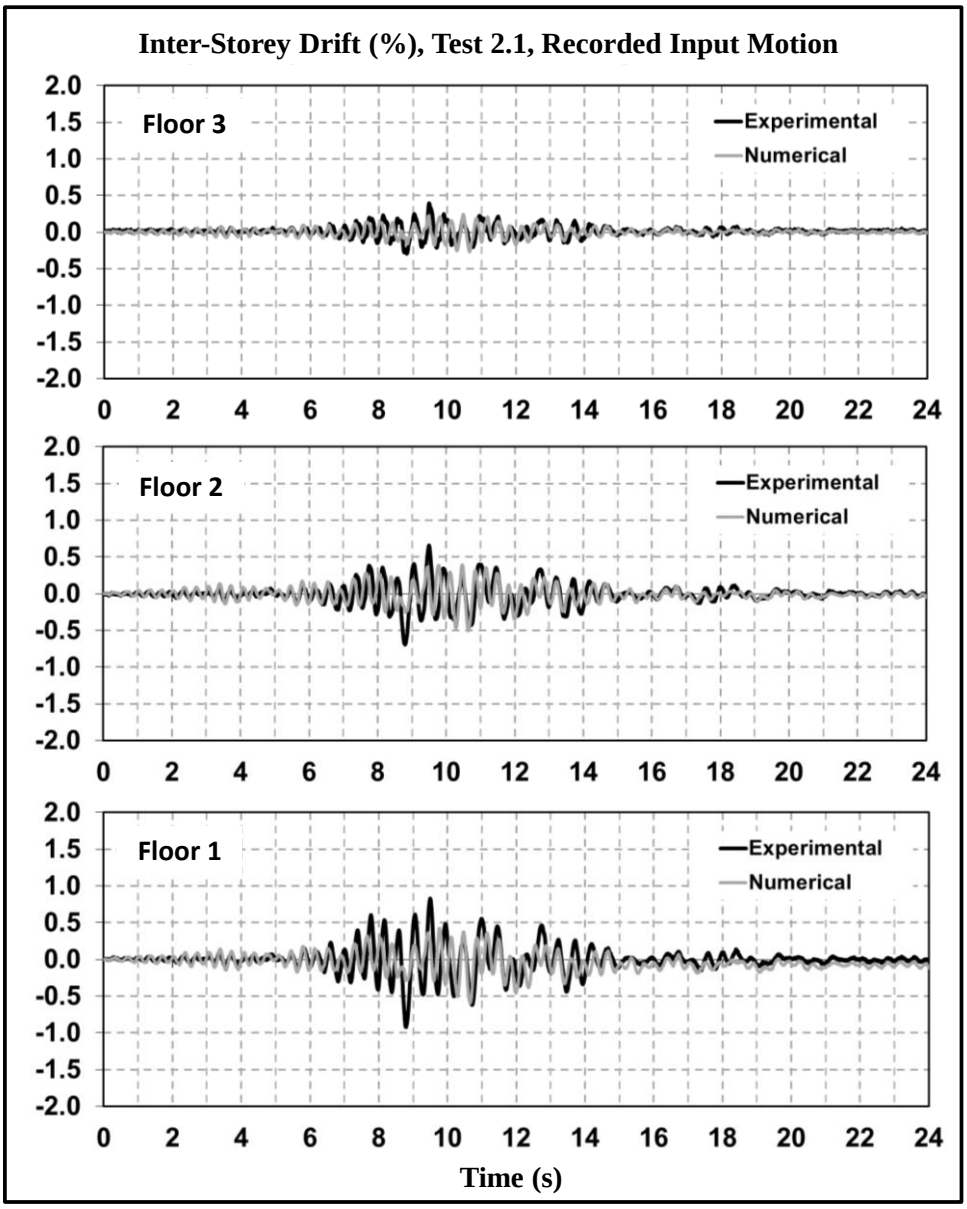

Figure 8.14: Test 2.1 inter-storey drift blind prediction using the recorded input.

8.4.3 Test 2.2 (Viña del Mar – Marga-Marga record – Maule Earthquake)

In Figure 8.15 and Figure 8.16 the predicted response of the as-built/repaired specimen during Test 2.2 using the recorded motion of shake table as input in the numerical model is presented in terms of floor displacements and inter-storey drifts, respectively, and compared with the experimental counterparts.

In the graphs of those figures, it can be seen that the numerical prediction in this case does not 'diverge' from the recorded response as it was the case of the blind prediction using the nominal input. As can be seen in the graphs of Figure 8.15, in all levels, the

floor displacements predicted with the initial model and the recorded motion of the table are similar in shape to the empirical counterparts, but there is a clear underestimation in the amplitude of the signals and some important differences in the frequency after the largest displacements experienced by the structure have occurred.

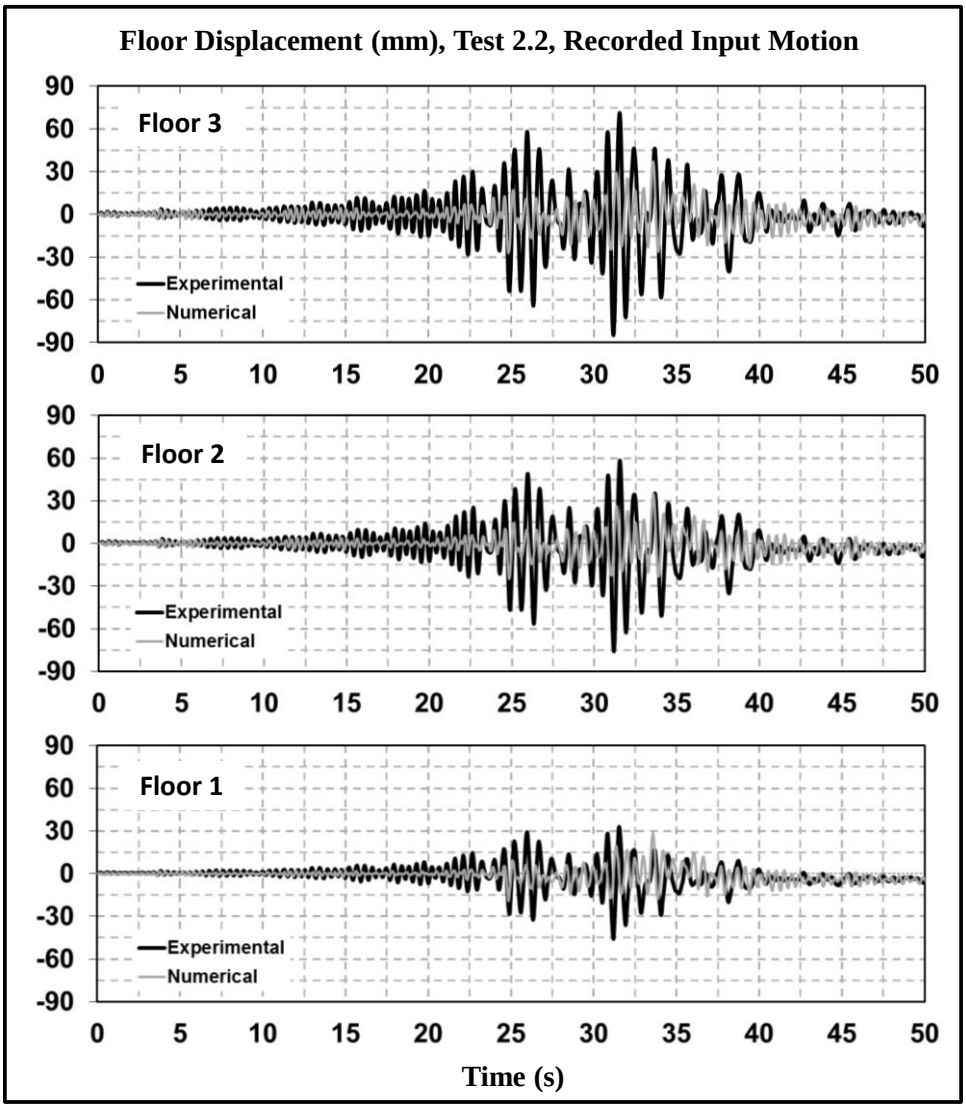

Figure 8.15: Test 2.2 relative floor displacement blind prediction using the recorded input.

In terms of inter-storey drifts, the numerical prediction is also not accurate, as can be observed in the graphs of Figure 8.16. However, with the initial model and using the recorded true motion of the shake table, the theoretical collapse of the structure is not predicted as it was anticipated with the same model and the nominal input as shown in the previous section. This time the selected parameters for the hysteresis rules used in the model of the structural members seem to be adequate so that the response of the building does not diverge from the experimental response. That is, the parameters are such that no bifurcation in the response occurs, which is not true when the nominal input is used. Hence, it can be argued that the stability and suitability of the parameters that control the hysteretic behaviour of the model depend on the input motion and hence it seem hard to state that the use of values such as α = 0.5 and β = 0.0 in the Modified Takeda rule for

joints is a good choice in all of the cases when performing nonlinear dynamic analysis of real structures.

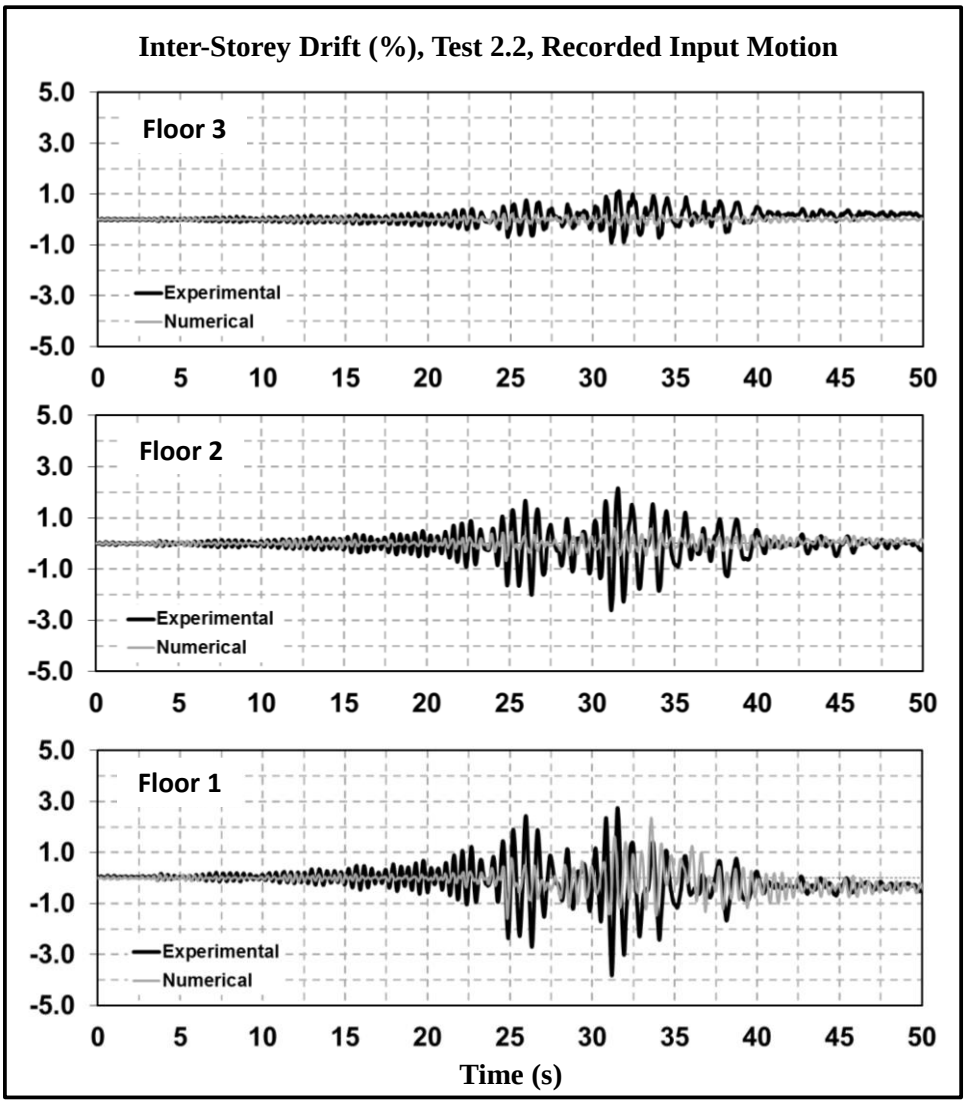

Figure 8.16: Test 2.2 inter-storey drift blind prediction using the recorded input.

In Table 8.2 the peak values of the experimental and predicted responses are summarized. The values do not necessarily coincide in time.

Table 8.2: Maximum response experimental/numerical comparison initial model-recorded motion.

		Floor Displacements (mm)			Inter-Storey Drifts (%)		
Test	Floor	Exp.	Num.	Num./Exp.	Exp.	Num.	Num./Exp.
1.1	1	11.3	15.5	1.37	0.93	1.29	1.39
1.1	2	24.5	26.2	1.07	1.10	0.92	0.84
1.1	3	33.7	29.0	0.86	0.99	0.38	0.38
2.1	1	11.0	7.1	0.65	0.92	0.59	0.64
2.1	2	20.2	13.0	0.64	0.69	0.50	0.72
2.1	3	23.2	16.3	0.70	0.40	0.27	0.68
2.2	1	45.3	27.3	0.60	3.82	2.34	0.61
2.2	2	75.9	33.7	0.44	2.60	0.63	0.24
2.2	3	84.8	36.6	0.43	0.90	0.35	0.39

8.5 COMPARISON OF THE NUMERICAL RESPONSE USING THE NOMINAL AND RECORDED SHAKE TABLE MOTION

In the previous sections, the predicted response of the as-built and repaired specimens have been presented and compared with the experimental data. The numerical simulations have been performed using the nominal and the actual/recorded input motions. In this section, those predictions are compared with each other in order to appreciate the differences and similarities directly.

8.5.1 Test 1.1 (GA5 record)

In Figure 8.17and Figure 8.18 the numerical prediction of the building response during Test 1.1 using the nominal and recorded input motions are presented in terms of floor displacements and inter-storey drifts, respectively.

In the graphs of Figure 8.17 it is shown that there are rather small differences in the predicted response when using the nominal and recorded motions of the shake table. When the recorded input is used, the displacements of every floor predicted with the nominal input are sometimes slightly underestimated and overestimated depending on the time of the response. The shape of the prediction is practically the same in both cases, with the exception of a more important difference between 4.5 and 5 seconds after the start of the test.

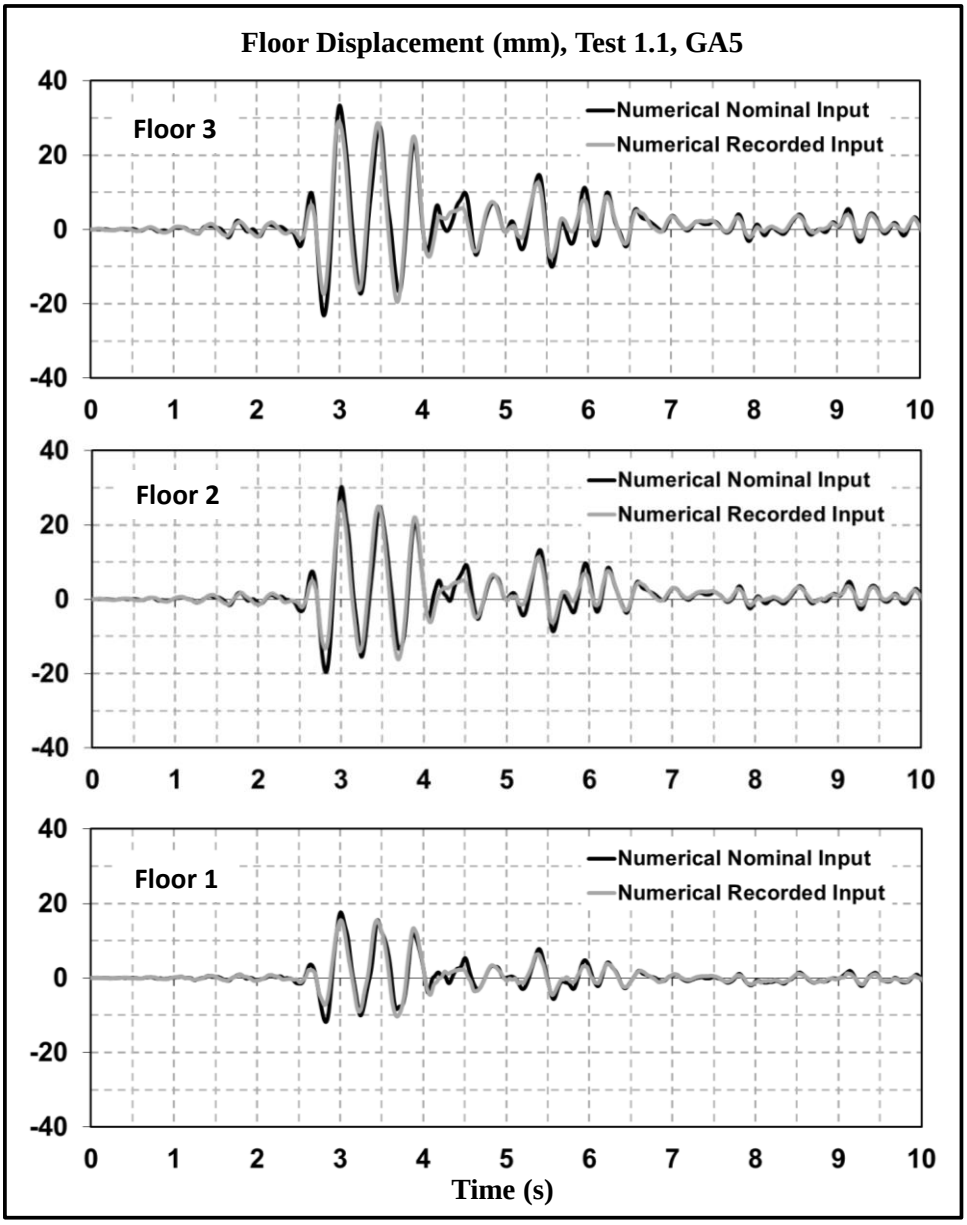

Figure 8.17: Comparison of the numerical prediction using the nominal and recorded input; Test 1.1 relative floor displacement.

In the graphs of Figure 8.18, the inter-storey drift histories predicted with the nominal and recorded motion also reflect that there is little difference between each other. Nevertheless, the difference mentioned before in the prediction of the displacement is observed in the prediction of the inter-storey drifts in between 4 and 4.5 seconds after the start of the test. It is important to note that even if the similarity in the prediction is lost during that period of time, the predictions become close again and almost identical during the last seconds of the motion.

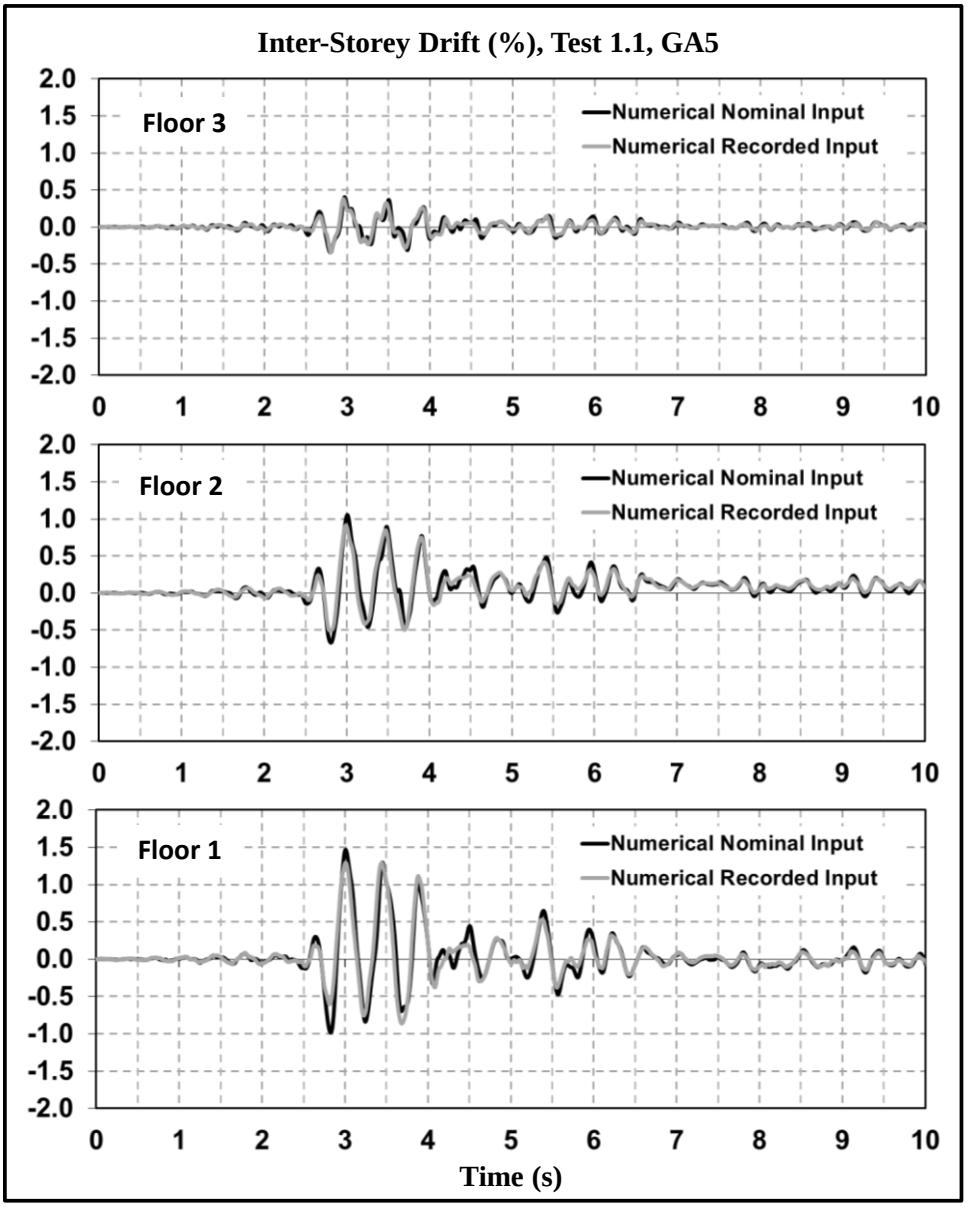

Figure 8.18: Comparison of the numerical prediction using the nominal and recorded input; Test 1.1 inter-storey drift.

8.5.2 Test 2.1 (CHH record)

In Figure 8.19 and Figure 8.20 the predicted response of the as-built/repaired specimen obtained with the nominal and recorded input motions of Test 2.1 are presented in terms of floor displacements and inter-storey drifts, respectively.

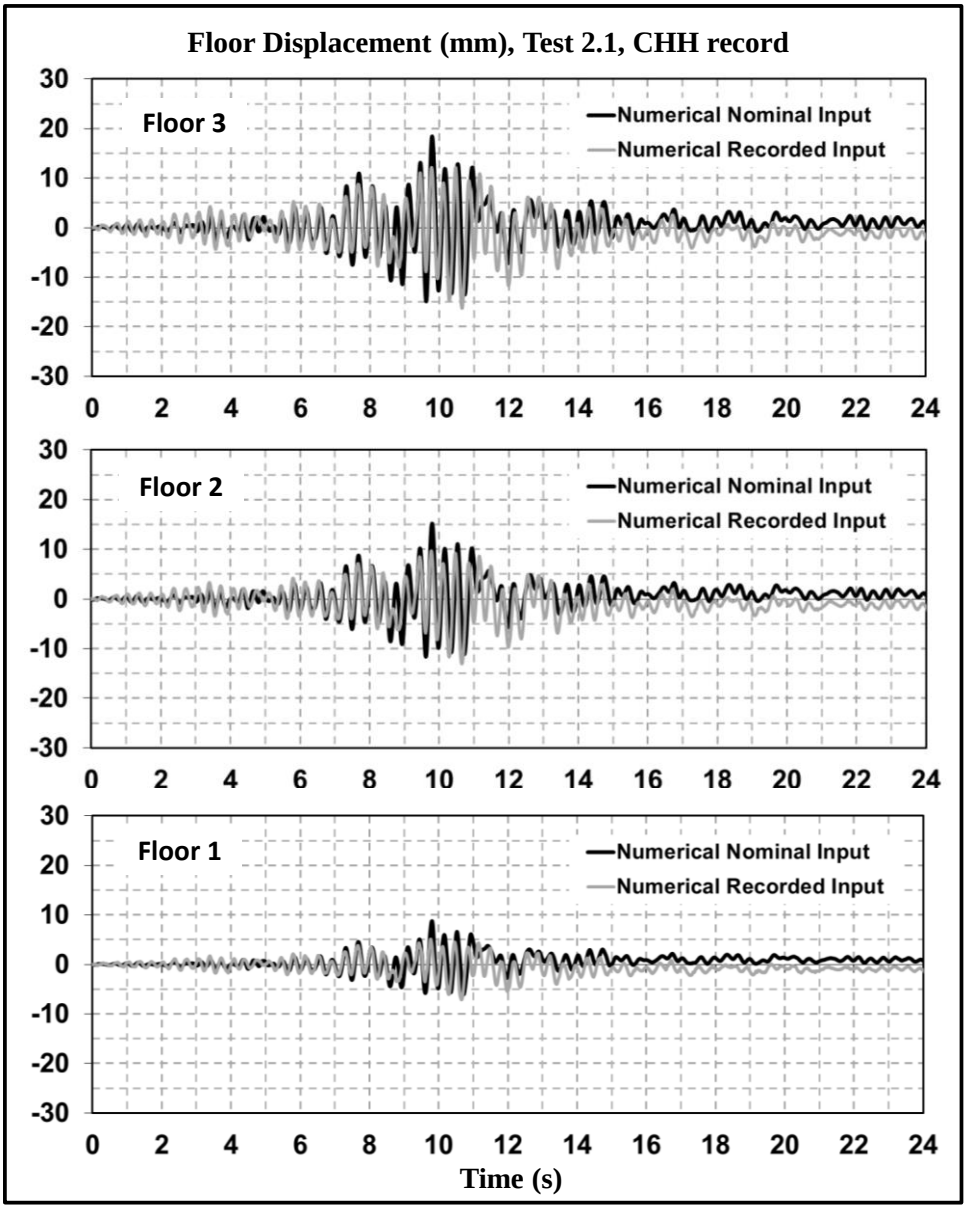

Figure 8.19: Comparison of the numerical prediction using the nominal and recorded input; Test 2.1 relative floor displacement.

In the graphs of Figure 8.19 it can be observed that both predictions differ from each other more importantly than in the case of Test 1.1. The floor displacements predicted with the nominal input are smaller than those predicted with the recorded motion during the first part of the motion, from 0 to about 6 seconds. After that, they become (most of the time) smaller than those predicted with the recorded input, until second 11, when the prediction with the nominal input becomes smaller. From second 11 onward, there is a shift in the residual displacements, or the attractor of the dynamical response, towards the negative direction.

.

In the graphs of Figure 8.20, it can be observed that the main difference in the response of the building in terms of floor displacements is reflected in the inter-storey drift comparison. The difference in the residual displacement or state attractor, mathematically speaking, detected in the predicted floor displacements with the nominal and recorded input motions, is only observed in the first floor, indication of the development or not of

small inelastic incursions in the first floor of a soft-storey prone numerical model. The most relevant finding obtained from the latter observations is that small variations of the input motions such as those shown in Chapter 7 lead to moderate differences in this case, and that this is particularly true if any member of the structure reaches the nonlinear range.

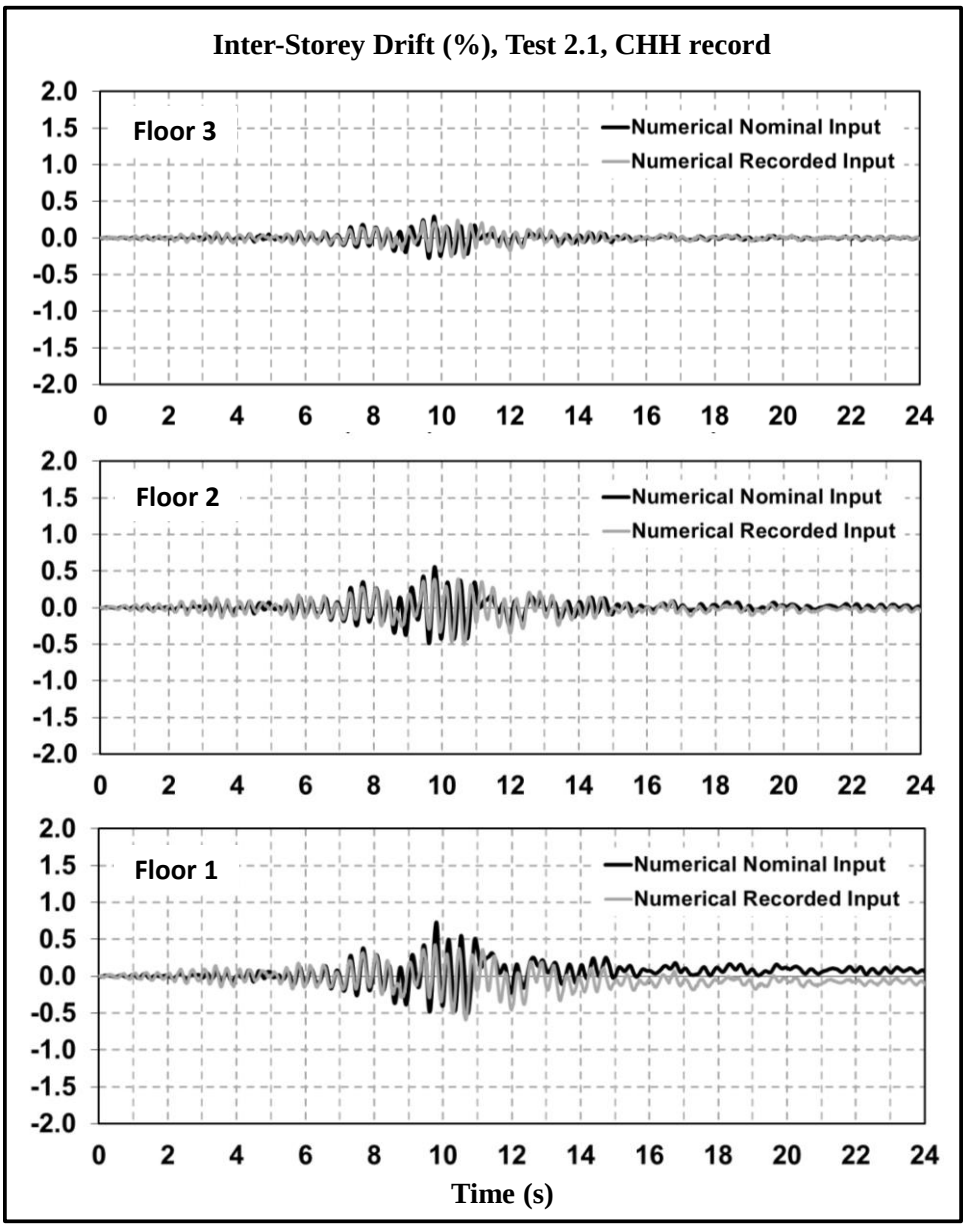

Figure 8.20: Comparison of the numerical prediction using the nominal and recorded input; Test 2.1 inter-storey drift.

8.5.3 Test 2.2 (VMM record)

In Figure 8.21 and Figure 8.22 the predicted response of the as-built/repaired specimen during Test 2.1 obtained with the nominal and recorded shake table motions are presented in terms of relative (to the table) floor displacements and inter-storey drifts.

In the graphs of Figure 8.21, the floor displacements predicted with the nominal and recorded input motions are very similar in the first stages of the tests, from 0 to about 27 seconds, when they start to differ from each other. The predicted response with the nominal input from that instant onward becomes larger in amplitude when compared to the predicted response with the recorded input and begins to diverge from the zero position towards the positive direction in all floors. That is, after the strongest part of the motion starts and the nonlinear part of the hysteretic rule in the structural members, in this case the joints, is activated.

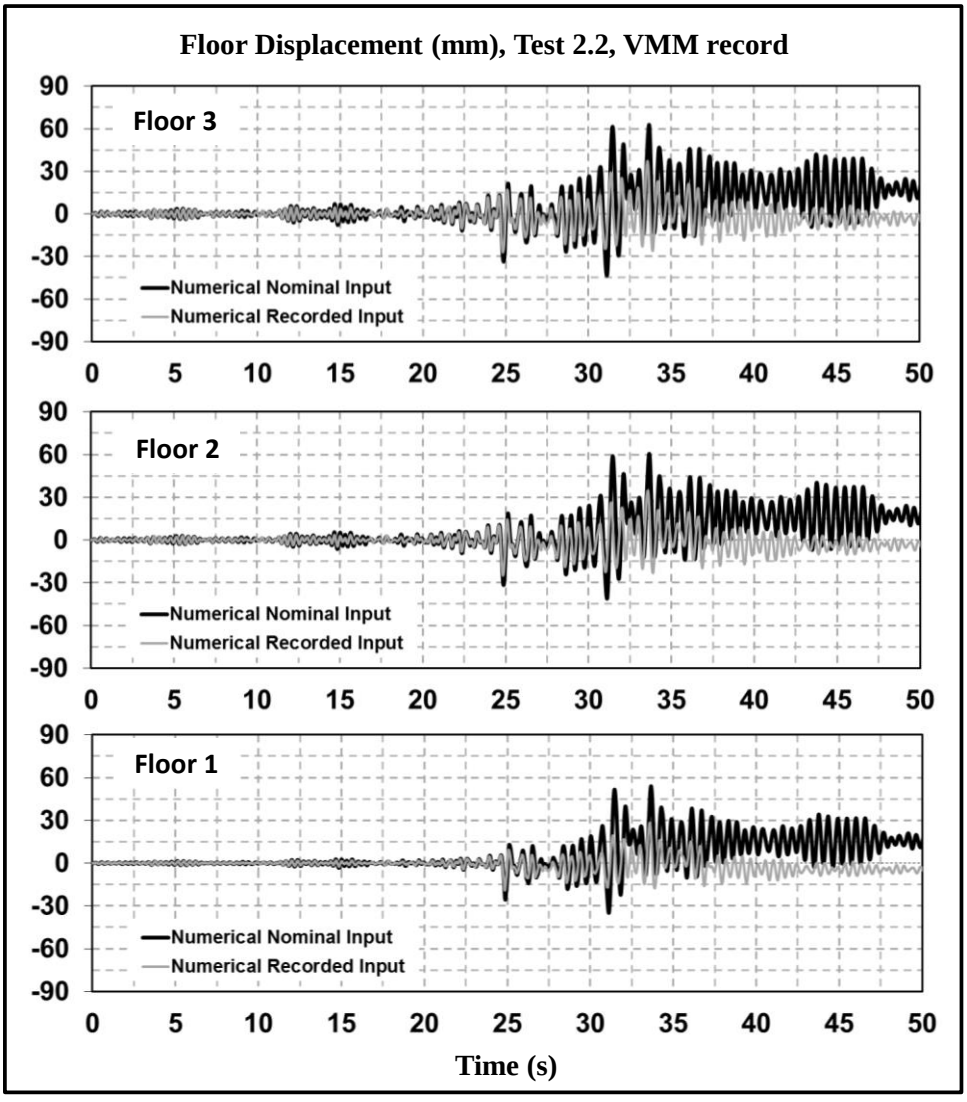

Figure 8.21: Comparison of the numerical prediction using the nominal and recorded input; Test 2.2 relative floor displacement.

In the graphs of Figure 8.22 it can be observed that the main differences of the predicted response in terms of inter-storey drifts using the nominal and recorded input motions are concentrated in the first floor. That is, with the initial model and the nominal input, a soft-storey-like inelastic mechanism of the structure is predicted, whereas with the same model and the recorded motion, a much less demanding scenario is predicted. As will be shown later, the selection of the parameters that govern the hysteretic behaviour of the joints is critical or has an important impact in the predicted response. In this case, where

the most degrading parameters have been used, i.e. α = 0.5 and β = 0.0 in Takeda, it is shown that the prediction becomes very sensitive to relatively small variations of the input motion.

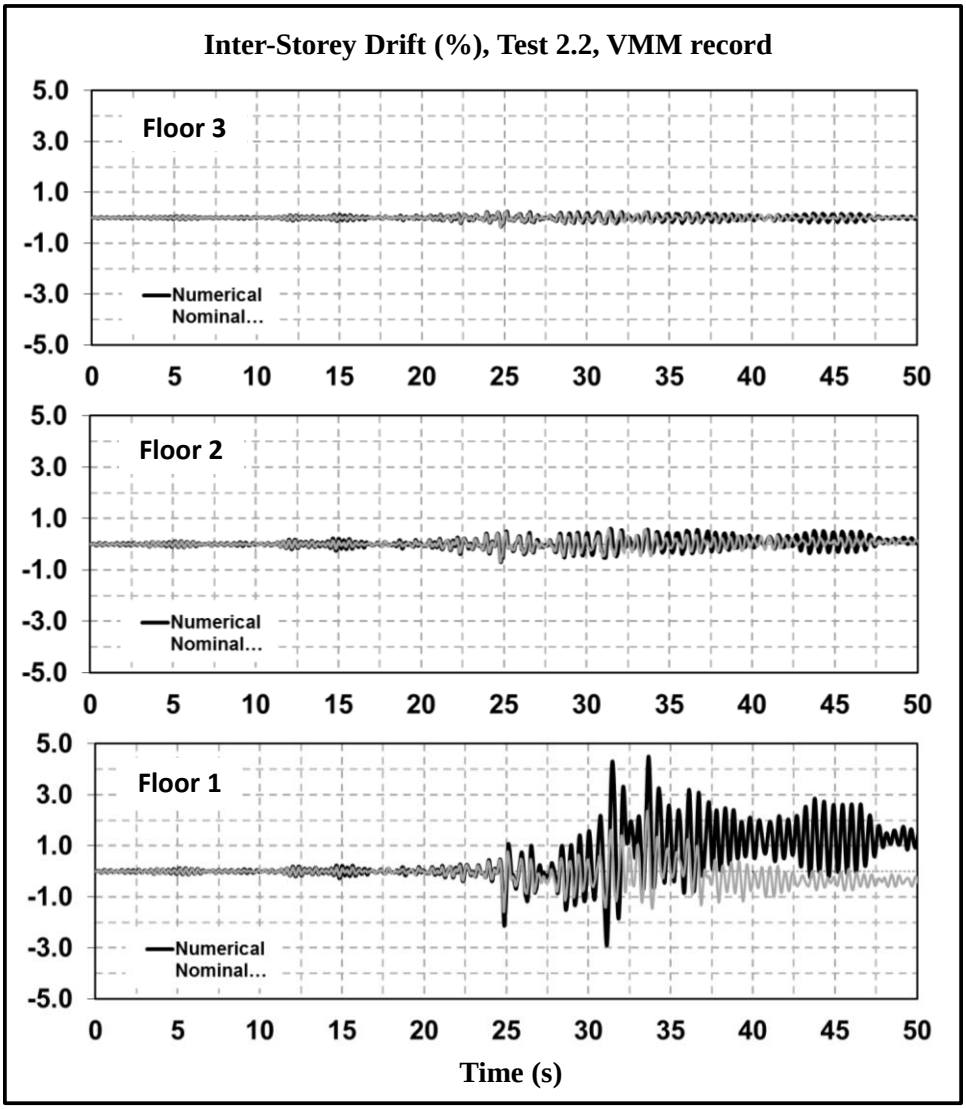

Figure 8.22: Comparison of the numerical prediction using the nominal and recorded input; Test 2.2 inter-storey drift.

8.6 POST-EXPERIEMNTAL PREDICTION – AS-BUILT SPECIMEN

8.6.1 Initial Modifications of the Model – Tuning Takeda Rule

The initial model was modified in order to capture the recorded response of the as-built and repaired specimens with a greater degree of accuracy. After carrying out a series of analyses, the most influential parameters identified to affect the predicted response were those associated to the hysteretic parameters of the joints. Amongst them, the most important one seems to be the initial stiffness of the joints.

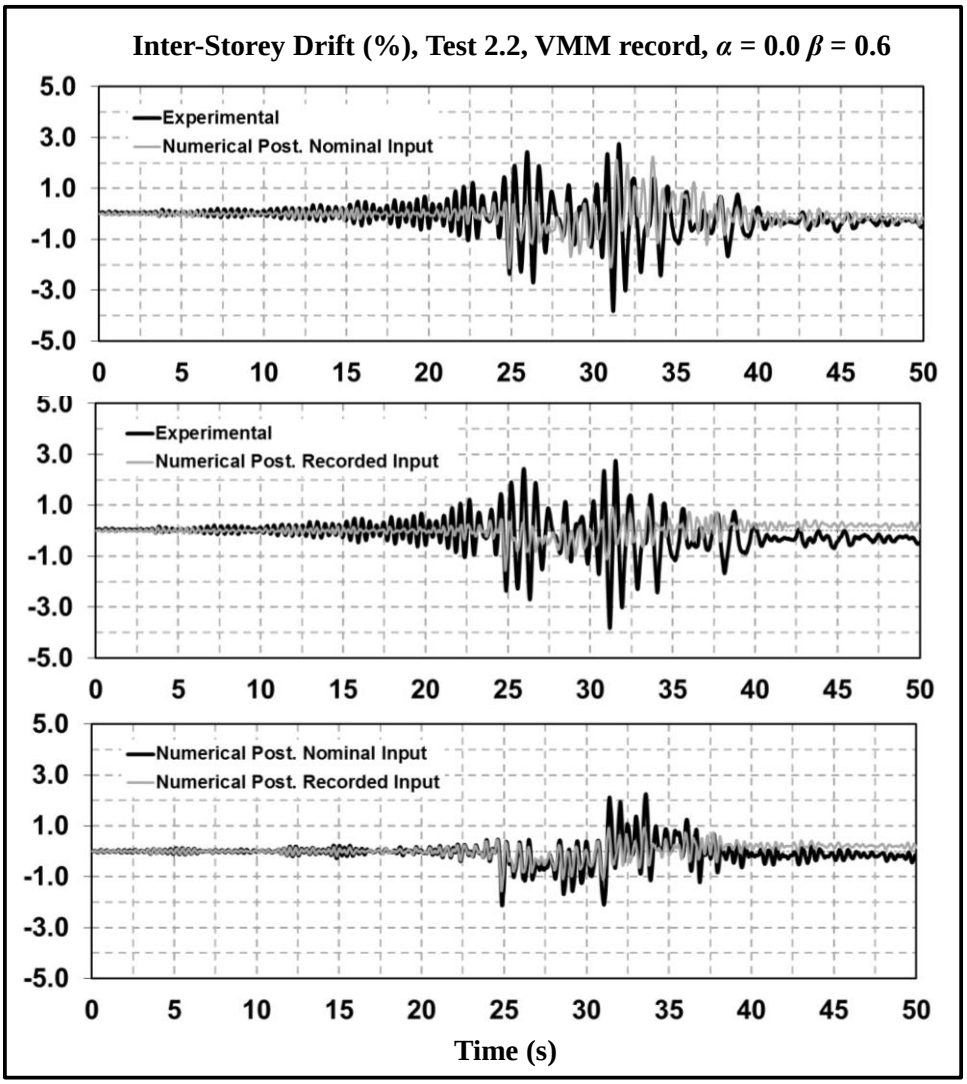

Figure 8.23: First floor inter-storey drift numerical prediction, Test 2.2, Takeda parameters α = 0.0 and β = 0.6 in columns and joints for nominal and recorded input motions.

At first, the modification done to the model focused on the unloading (α) and reloading stiffness parameters (β) of the Takeda hysteresis rule of the joints, in order to make a short investigation on their influence in the accuracy of the prediction.

Using the input motion of Test 2.2, where the most important differences in the numerical and experimental responses were observed the model was tuned initially by changing the Takeda rule parameters of the joint springs and the columns. The parameter α was changed from 0.5 to 0.0, and the parameter β from 0.0 to 0.6, representing the most and less degrading form of that hysteresis rule, respectively. In the beams, the analogous unloading and reloading factors γ and δ, respectively, were kept constant (γ = 0.5 and δ = 0.5). The modification of those factors in both joints and columns was necessary because the response diverged when the degrading parameters were modified only for joints (not shown here). That means that the parameters used in the Takeda rule of columns are also relevant for the accuracy of the prediction. In Figure 8.23 the numerical prediction of the first floor inter-storey drift history during Test 2.2 obtained with the modified model

using the nominal and recorded input motions are presented and compared with the experimental results.

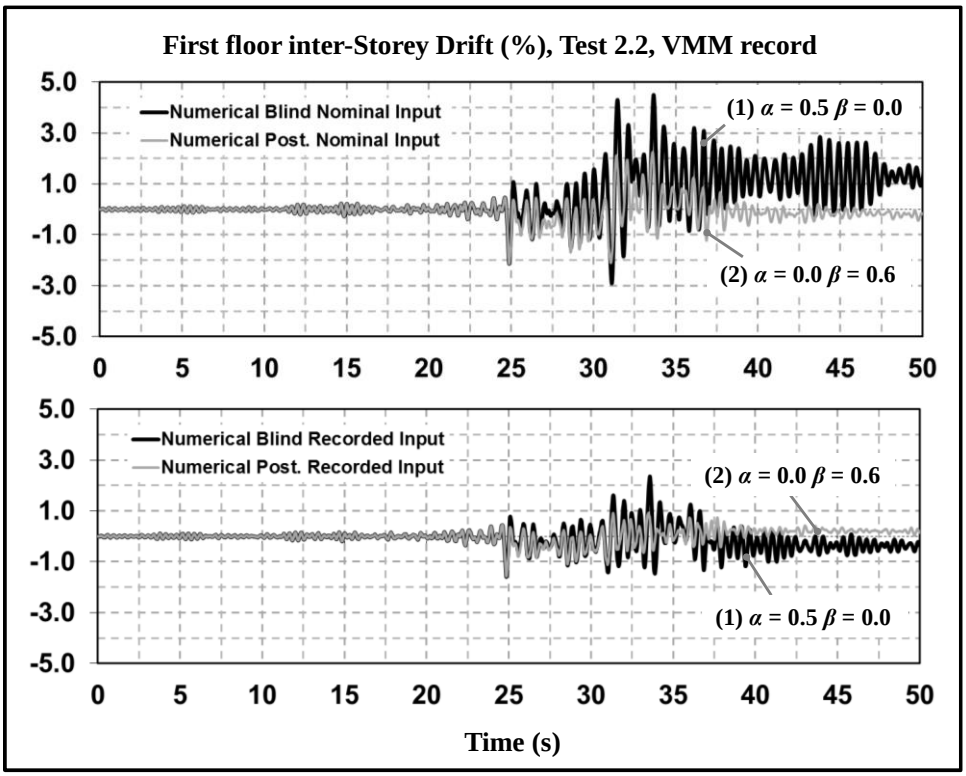

Figure 8.24: First floor inter-storey drift numerical prediction, Test 2.2; comparison of the numerical prediction obtained with α = 0.5 and β = 0.0 and α = 0.0 and β = 0.6 in columns and joints for nominal and recorded input motions.

In Figure 8.24, the numerical prediction obtained with the initial and modified models are compared. The results are shown for the predictions obtained with the nominal and recorded shake table motions. In the top graph of Figure 8.24 it can be observed that when the nominal input is used, the predicted first floor inter-storey drift history using the original and modified models are almost identical in the initial part of the response, where an elastic behaviour is predicted. Nevertheless, they become very different after the vestiges of some yielding in the columns and cracking in the joints occur, at approximately 25 seconds. From 25 seconds of the response onward, the predictions become increasingly different, as the one obtained with the initial model diverges from the recorded counterpart and the inter-storey drift starts to oscillate around a residual drift approximately equal to 1%, towards the positive direction.In the bottom graph of Figure 8.24, the numerical predictions obtained with the initial and modified models using the recorded shake table motion are compared. In that graph it can be observed that there are also differences in the predictions using the actual shake table movement. However, in this case, the predicted responses are closer in magnitude, even though they start to differ after 25 seconds of the beginning of the motion. As was mentioned before, the predicted response with the initial model in this case does not reflect large deviations like in the case when the nominal input is being used. It is worth noting that the response of the building using the initial model is predicted to have a residual drift towards the positive direction and the one predicted with the same model and the recorded motion a residual drift towards the negative direction.

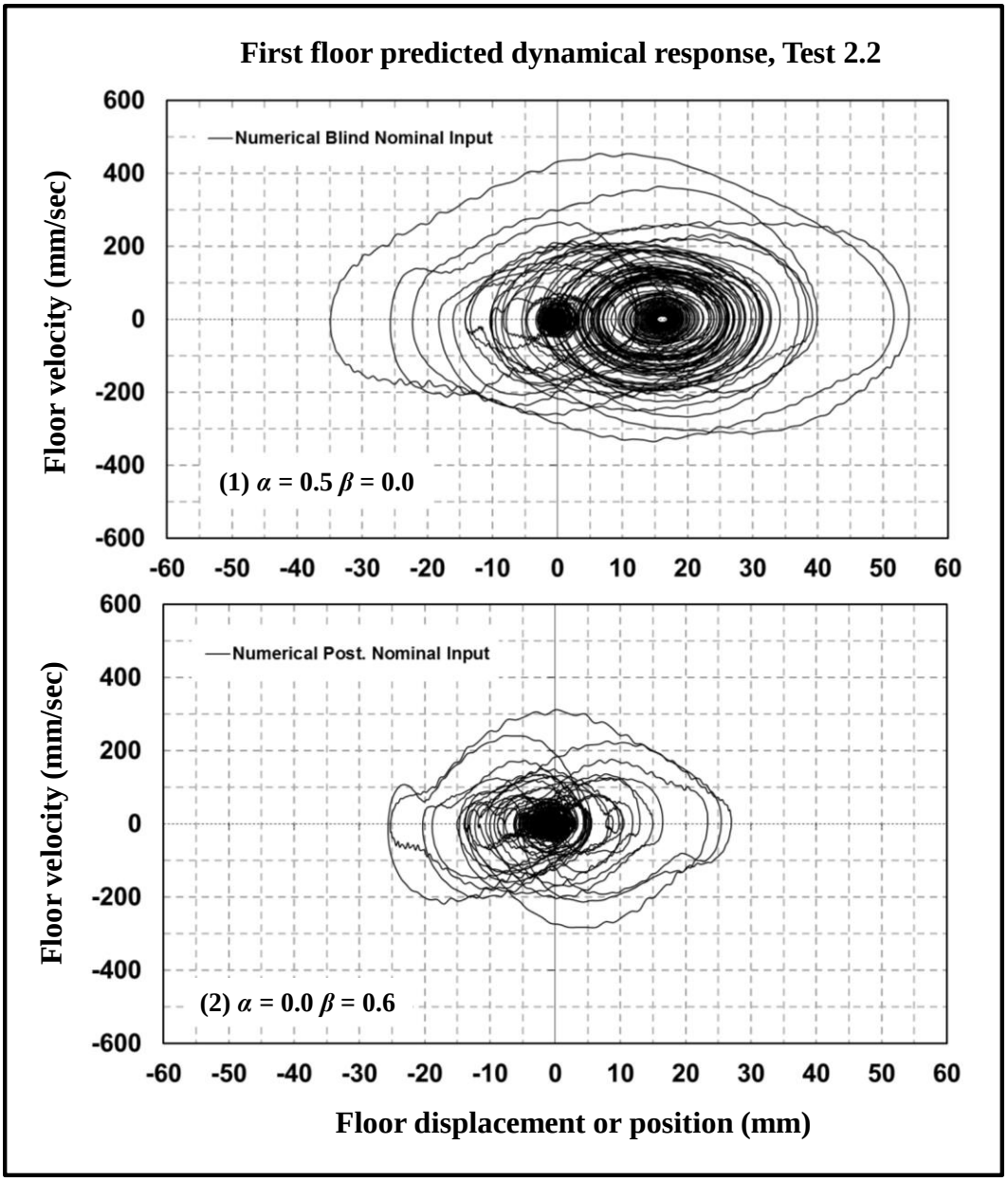

Figure 8.25: Test 2.2 floor 1 displacement (position) versus velocity plots obtained with the nominal input; top: case (1) $\alpha = 0.5$, $\beta = 0.0$; bottom: case (2) $\alpha = 0.0$, $\beta = 0.6$.

If one plots the displacement of the floor versus its momentum or velocity, then the complete dynamical state of the response is represented, as in Figure 8.25. According to these graphs, the numerical prediction of the first floor state obtained with the modified model would converge to a close to zero residual displacement or position, and the state obtained with the initial model would converge to another 'attractor', given by the residual drift. That is a sign of a bifurcation (or a series of bifurcations) taking place at a certain instant(s) of the response, and hence glimpses of chaotic behaviour for certain values of the hysteretic parameters used can be observed (Lorenz 1963, 1993; Strogatz 1994).

In a second stage, the initial model was modified by changing the value of the initial stiffness of the joint springs, identified as critical elements of the system. After a few numerical simulations with $r = 0$ constant, it was found that the prediction became closer

to the experimental results of Test 2.2 in terms of the first floor inter-storey drift for decreasing values of the initial spring stiffness. With an initial stiffness in the joints of k_0 = $5 \cdot 10^5$ kNmm, one fourth of the value used in the initial model, it was found that the model predicted a much better approximation of the experimental response. The Takeda degrading parameters were kept identical to those of the initial model, i.e., α = 0.0 and β = 0.6.

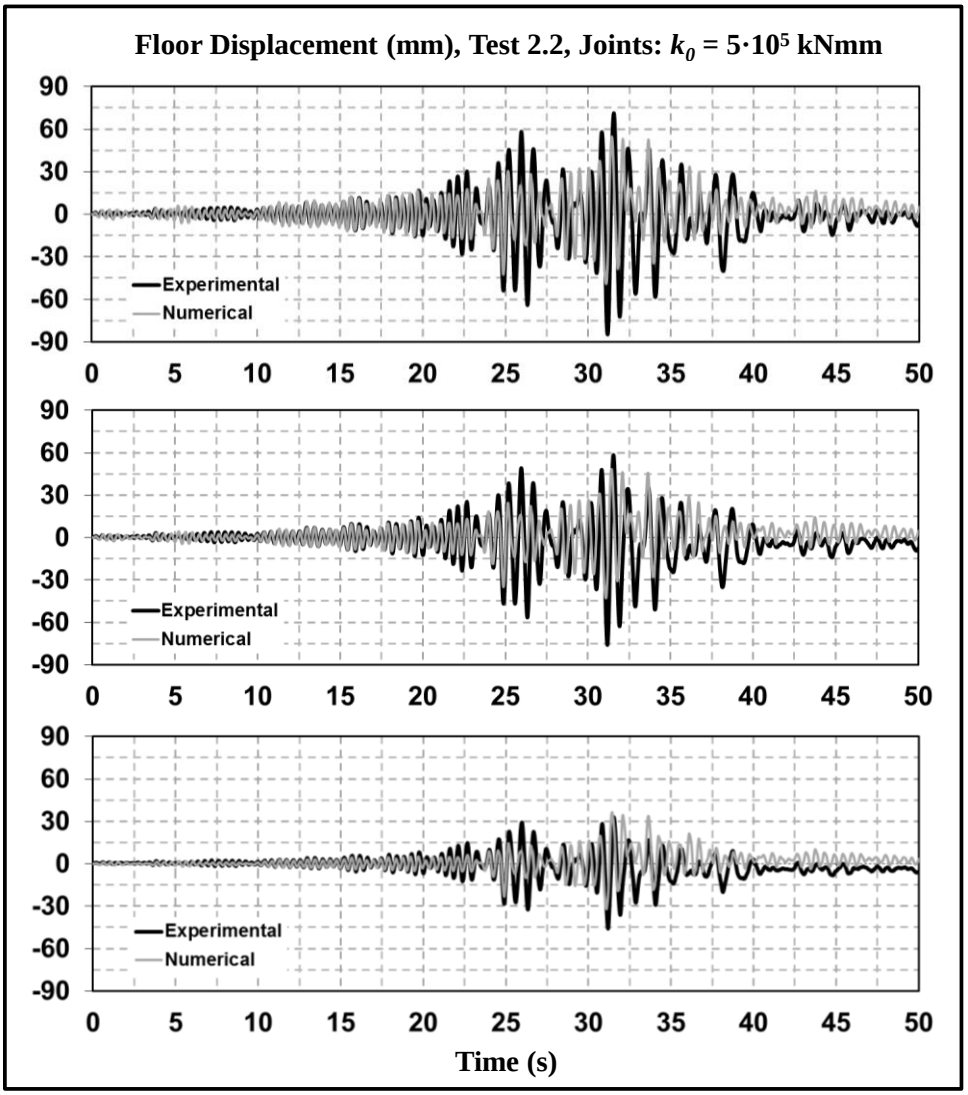

Figure 8.26: Floor displacement post-experimental prediction with α = 0.5, β = 0.0, $k_0 = 5 \cdot 10^5$ kNm and *r* = 0 in joints, Test 2.2, recorded input.

The results of the prediction with the model modified as described above are presented in Figure 8.26 in terms of relative (to the ground) floor displacements and in Figure 8.27 in terms of inter-storey drifts. In these numerical simulations the recorded motion was used.

As it can be observed in Figure 8.26 the predicted response provided by the model with a smaller initial stiffness in the rotational springs that represent the joint provides a much better approximation of the recorded response. A reasonably good degree of accuracy is also reflected in the graphs of Figure 8.27, where the inter-storey drifts are plotted. Nevertheless, the prediction underestimates the recorded inter-storey drifts in floors 1 and

2 during the strong part of the response. The prediction also indicates that the specimen would experience residual drifts in the first floor towards the opposite direction than the recorded response.

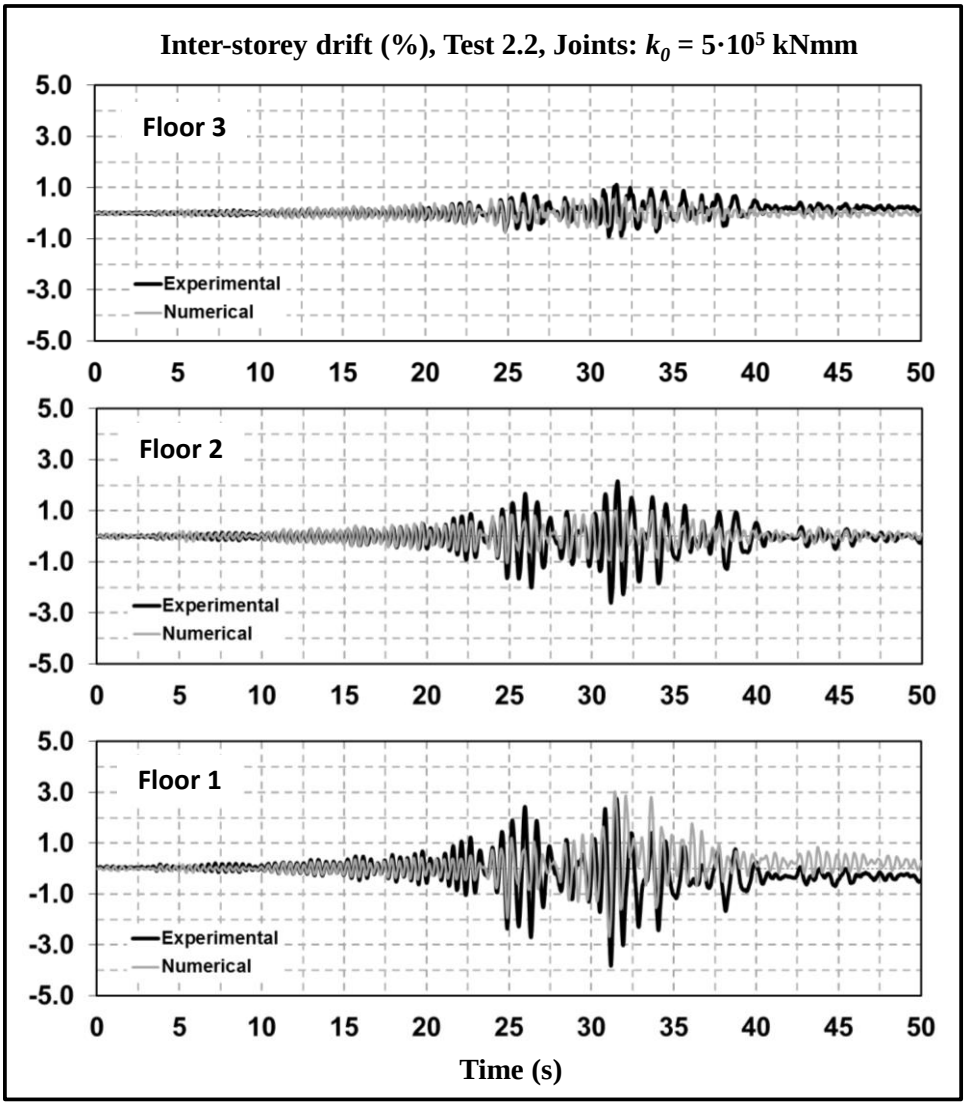

Figure 8.27: Inter-storey drift post-experimental prediction with α = 0.5, β = 0.0, k_0 = 5·10^5 kNm, r = 0 in joints, Test 2.2, recorded input.

The existence of minimal differences in the initial response indicate that the stiffness used in the joints leads to good results, whereas the underestimation of the inter-storey drifts during the strong part of the response, when most of the inelastic energy is dissipated, is thought to be an indication that the pinching effect needs to be incorporated in the hysteresis rule of the joints. Ideally, the Pampanin rule (Pampanin et al. 2003), developed in Pavia for capturing the quasi-static behaviour of beam column joints similar to those part of the building developed in this thesis, would have been used. However, to date when this numerical work was carried out, that rule implemented in Ruaumoko2D, seemed to have some instability problems apparently associated to small cycle modelling. Those instabilities do not occur in a displacement controlled laboratory-like loading protocol such as that used in the cyclic pushover presented earlier in this chapter, but they are of great importance in nonlinear dynamic analyses. In this thesis it is assumed that the

small cycle behaviour is correct, but it is also acknowledged that it constitutes a vast area of investigation that requires attention.

In Table 8.3, the values of the peak experimental response of the model during Test 2.2 are compared with the peak counterpart predicted with the model modified as explained in this section. It is important to note that they may not occur at the same time of the response.

Table 8.3: Maximum response experimental/numerical comparison, model with initial modifications.

		Floor Displacements (mm)			Inter-Storey Drifts (%)		
Test	Floor	Exp.	Num.	Num./Exp.	Exp.	Num.	Num./Exp.
2.2	1	45.3	31.9	0.70	3.82	3.02	0.79
2.2	2	75.9	48.3	0.64	2.60	1.02	0.39
2.2	3	84.8	54.7	0.65	0.90	0.75	0.83

8.6.2 Final modifications to the model – Modified SINA rule in joints

In order to cope with the problem of not being able to use the Pampanin rule (Pampanin et al. 2003) at the moment when this work was done, an alternative pinched model was selected. From the models available in Ruaumoko2D (Carr 2008b), the Modified SINA rule (Saiidi, 1979, Carr 2008c) was selected. That model is presented schematically in Figure 8.28.

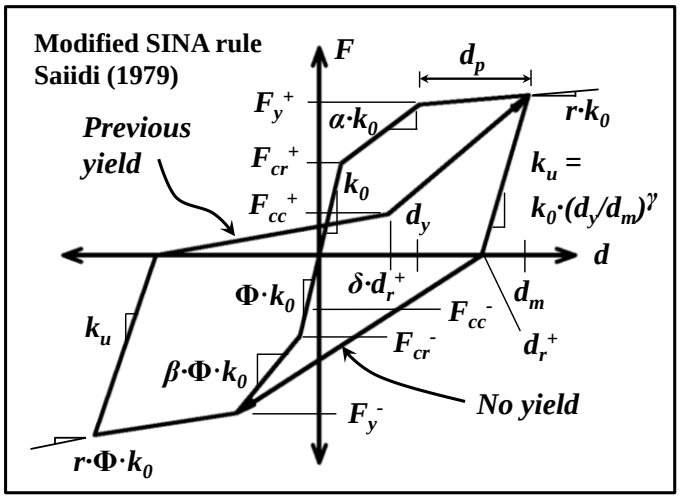

Figure 8.28: Modified SINA hysteresis rule (Saiidi 1979, Carr 2008c).

As can be observed in that figure, the model is almost identical to a Revisited Takeda rule, presented in Figure 8.2 for the particular case when the re-loading factor δ = 0.0. The difference though, relies in the initial part of the reloading path after yielding (or cracking in this case) which has a smaller slope or stiffness extending from the zero force

axis to the point determined by F_{cc} and $\delta \cdot d_r$, the crack closing action and the pinching displacement or rotation, respectively (note that in the SINA rule δ is the pinching factor). Beyond that point, if the displacement continues increasing, the stiffness follows a straight line towards the maximum displacement or rotation reached in the previous cycle, as indicated in Figure 8.28.

As a first approximation and in the light of the results of the preliminary post-experimental prediction, the initial stiffness of each spring representing the joint was taken as $k_0 = 5 \cdot 10^5$ kNmm, which yields a total stiffness of $k_{j,tot} = 1 \cdot 10^6$ kNmm. The bi-linear factor was taken as $r = 0$, the same value adopted in the modified model using the Takeda rule in joints described in the previous section. The positive and negative cracking strengths of each spring, F_y^+ and F_y^-, respectively, were set to half of the strength of the joint with $jd = 0.9d$, for the design gravity load, and taken as equal in absolute value.

The values adopted for the parameters that govern the hysteresis rules of beams and columns were the same as those summarized before. For joints, after an important number of analyses, the set of parameters used for the Modified SINA hysteresis rule can be summarized as follows:

As-Built Joints *(Modified SINA rule – IHYST = 56 in Ruaumoko2D)*

$k_0 = GJ$ = 500 kNm; $r = 0$; F_y^+= 1.85 kNm; F_y^- = -1.85 kNm; $\alpha = 0.9$; $\beta = 0.9$; $\gamma = 0.5$; $\delta = 0.5$; $\Phi = 1.0$; $F_{cr}^+ = 0.5F_y^+$; $F_{cr}^- = 0.5F_y^-$; $F_{cc}^+ = 0.25F_y^+$; $F_{cc}^- = 0.25F_y^-$.

8.6.3 Test 2.2 (VMM record)

In Figure 8.29, the predicted response of the building during Test 2.2 is presented in terms of floor displacements, and it is compared with the experimental counterpart. In the graphs of that figure, it can be observed that the numerical prediction is able to capture with a reasonably good degree of accuracy the recorded displacements that experienced by the building. Note that the results of the prediction and the comparison with the experimental data are presented in the inverse experimental sequence this time, as Test 2.2 was used for tuning the model.

The numerical and experimental floor displacement histories practically coincide during the first part of the test, from 0 to about 22 seconds, time when the numerical model is not able to capture a cycle at low amplitude that stats at about that time of the motion. After that cycle, the experimental and numerical displacements become very similar in amplitude again, and the similarity in the shape of the responses is recovered. That similarity remains during the subsequent small amplitude part of the floor displacements histories in the three floors, and also during the following strong part of the response, from 30 to about 35 seconds after the start of the test. Nevertheless, during that part of the response the numerical prediction loses one large amplitude cycle. From there onward, the numerical and experimental floor displacements tend to lose their prior similitude, and some important differences in between each other arise. At the end of the response though, the predicted and recorded displacements become very similar again, even if they displacement histories shape becomes somehow erratic.

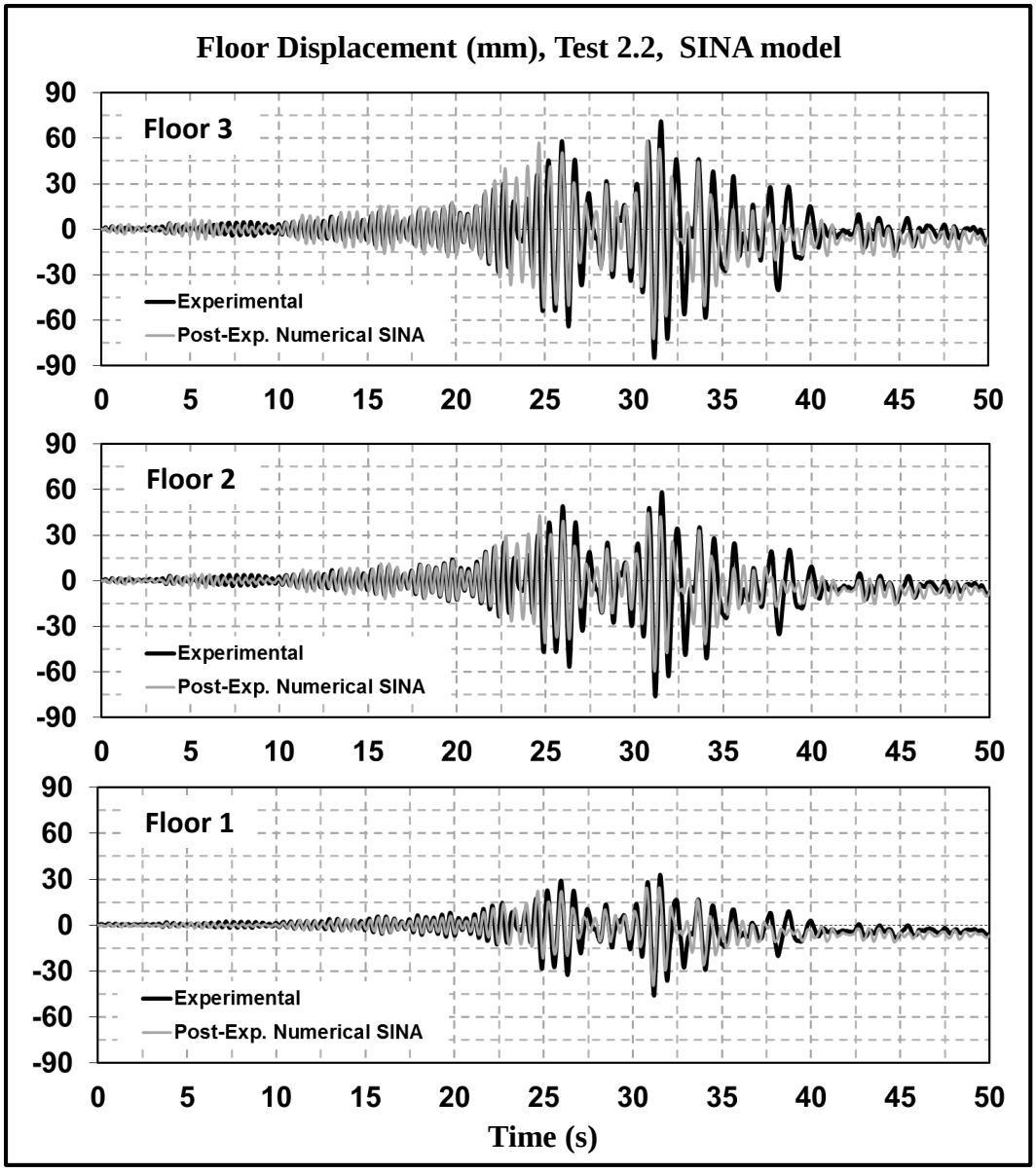

Figure 8.29: Relative floor displacement, post-experimental prediction Test 2.2, SINA rule in joints.

In the graphs of Figure 8.30, the predicted and experimental response of the building during Test 2.2 in terms of inter-storey drift histories is presented. In the first floor, the numerical simulation of the inter-storey drift history is overall in good agreement with the experimental results. During the first part of the motion, both signals are practically the same, until some differences arise in the low amplitude cycle recorded at 23 seconds. During the strong part of the motion, the model is able to predict the response with good accuracy in amplitude and frequency, with some differences close to 32 seconds. The predicted residual drift in the first floor is very close to the experimental one, which means that the final position of the building after the test is being appropriately predicted. In the second floor, the same observations made about the accuracy of the first storey drift prediction are true for the second and third floor counterparts, with the exception that the experimental amplitude is overestimated importantly at the beginning of the strong part of the motion. In the case of the third floor these differences are more remarkable. Besides that disagreement in the numerical and experimental predictions, the shape of the recorded inter-storey drifts histories is well predicted by the numerical model.

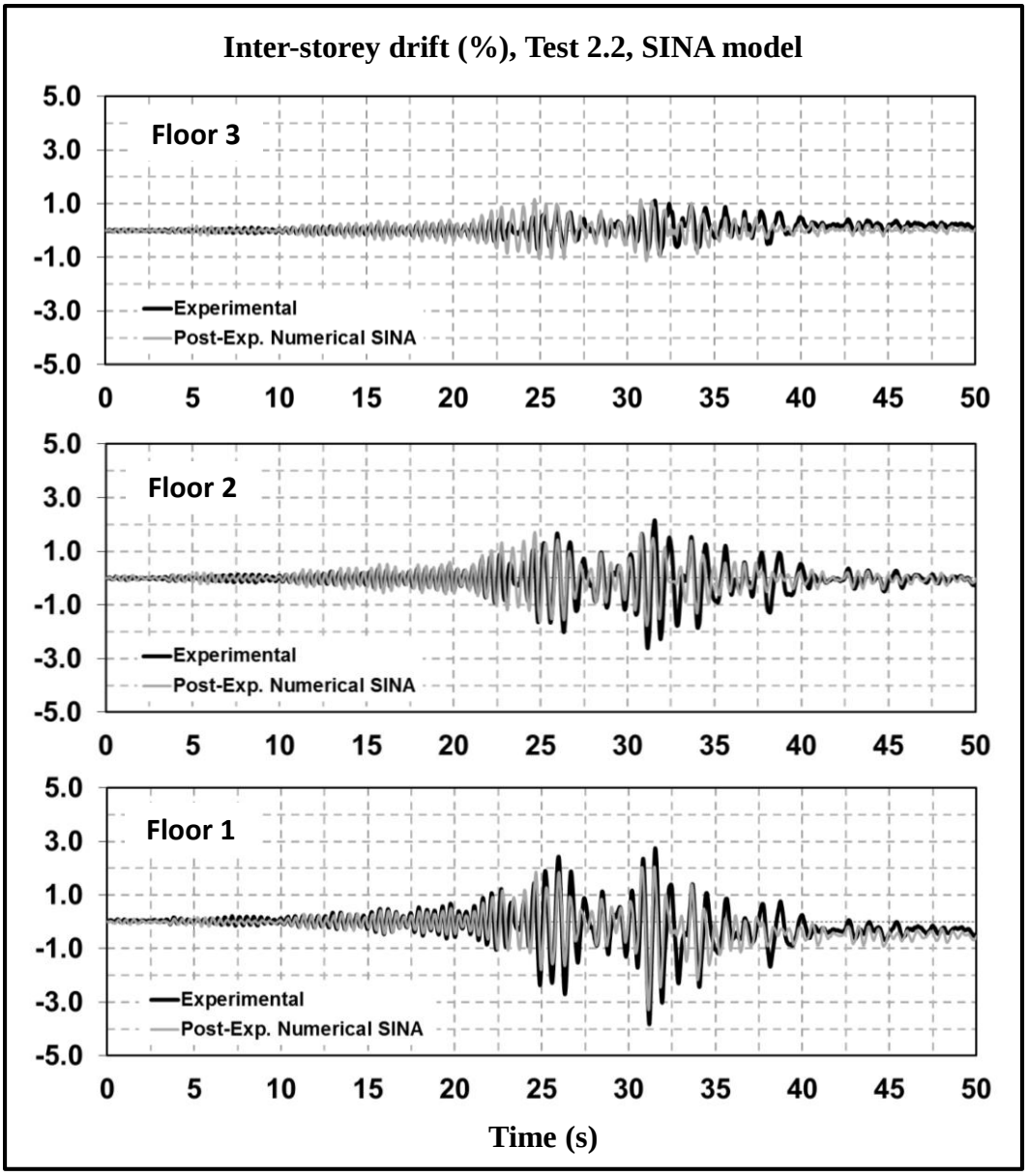

Figure 8.30: Inter-storey drift, post-experimental prediction Test 2.2, SINA rule in joints

8.6.4 Test 1.1 (LP record)

After the hysteretic rule used in the springs was tuned with the experimental results of Test 2.2, the same model was used for the prediction of the response of the building during Tests 1.1 and 2.1.

The numerical prediction of the specimen response during Test 1.1 is presented and compared with the experimental data in Figure 8.31 and Figure 8.32. In the numerical simulation, the actual shake table motion recorded during the test was used. In the graphs of Figure 8.31, it can be observed that the model captures the experimental results in terms of floor displacements with a good degree of accuracy in the three levels. The numerical and experimental displacements are very similar till 4 seconds after the beginning of the test. After that instant, the both signals start to differ from each other, and the model loses the accuracy especially in amplitude and frequency, with a change in

the angle of phase. That difference is larger in the upper floors, especially in the third one, and may be associated to the onset of a lap splices failure, which was the failure mode observed after Test 3.1, as presented in Chapter 4. Even though the numerical and experimental floor displacement histories start to differ from each other at 4 seconds after the beginning of the test, the prediction is able to re-capture the experimental displacements from about 8 seconds onward. The accuracy of the prediction during this period of the response though, has a smaller degree of accuracy when compared to the initial part, from 0 to 4 seconds. Overall speaking the predictions does not seem to improve too much from the blind one.

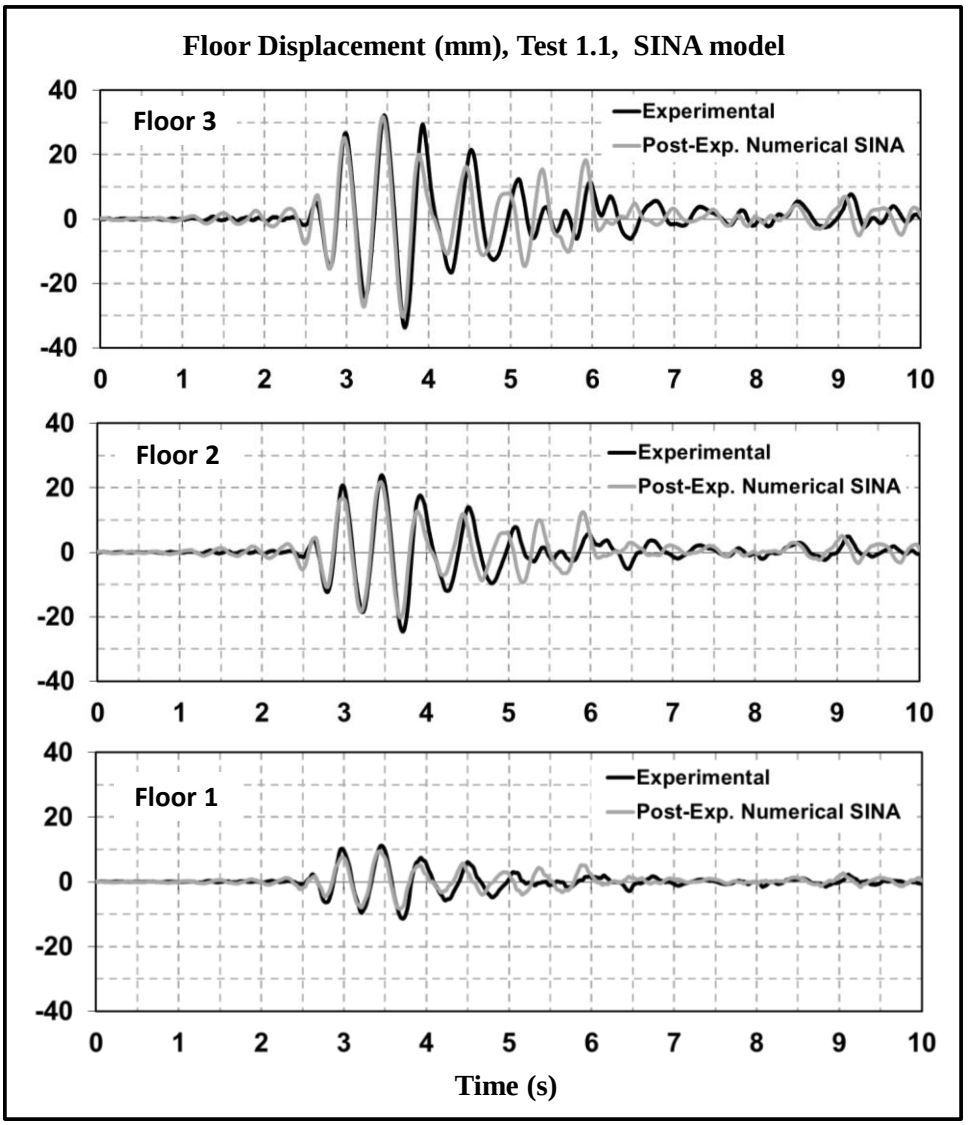

Figure 8.31: Relative floor displacement, post-experimental prediction Test 1.1, SINA rule in joints.

In the graphs of Figure 8.32, the predicted response of the building during Test 1.1 is shown in terms of inter-storey drifts. The predicted histories this time are in a much better agreement with the experimental results that those predicted with the initial model. In this case, the experimental inter-storey drifts history of the first floor is much better represented by the numerical counterpart. The differences described before for the

prediction of the floor displacements are also reflected in the inter-storey drifts histories shown in Figure 8.32.

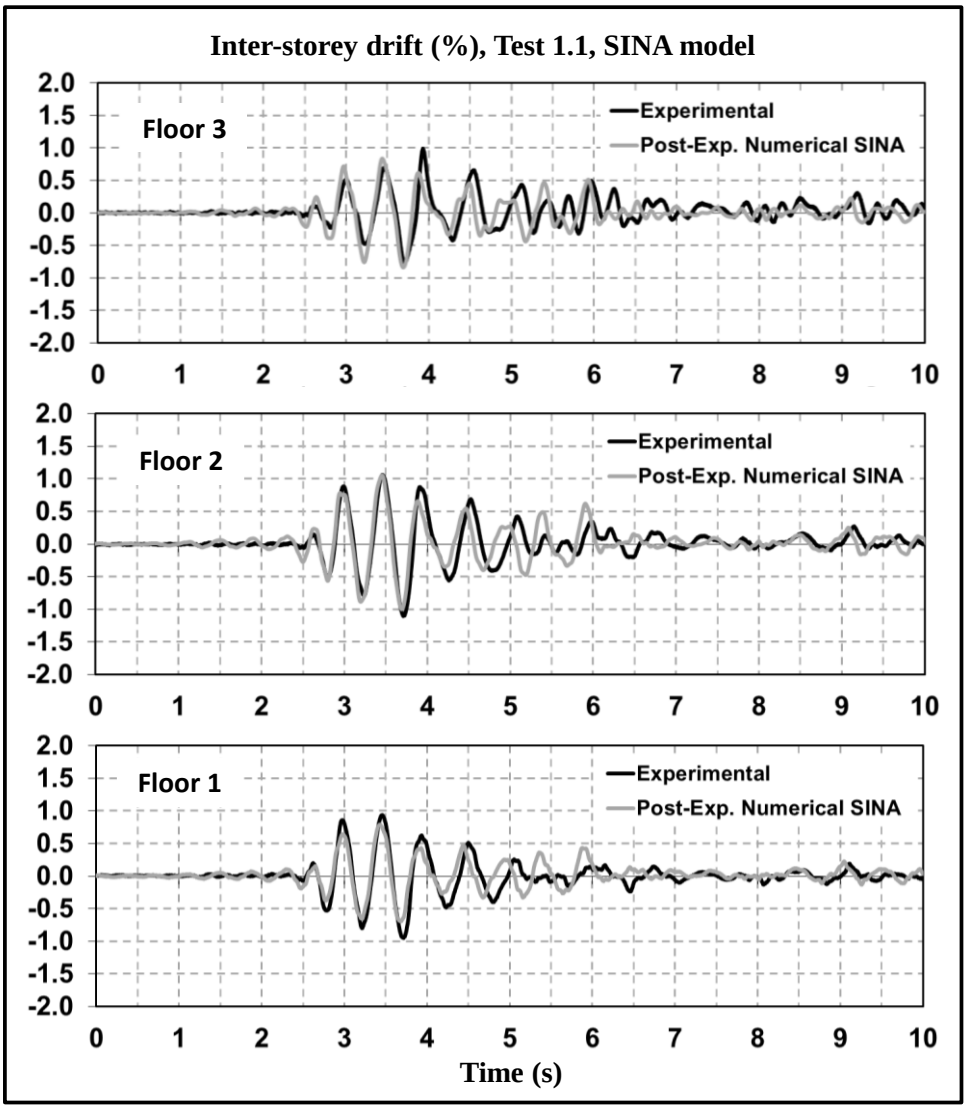

Figure 8.32: Inter-storey drift, post-experimental prediction Test 1.1, SINA rule in joints.

8.6.5 Test 2.1 (CHH record)

The numerical model used for this prediction was identical to that used in the prediction of Test 1.1. The results of the numerical prediction of the building response during Test 2.1 are presented in Figure 8.33 and Figure 8.34 in terms of the floor displacement and inter-storey drift histories, respectively. The predicted histories are compared with the experimental counterparts as before.

In the graphs of Figure 8.33, it can be observed that the numerical prediction is able to capture with a reasonably good degree of accuracy the experimental floor displacement in all three floors. The prediction of the floor displacements is quite accurate during certain periods of the response, but overestimates the amplitude in the weaker part of the response. During the strongest part of the motion, in between 6 and 15 seconds after the

beginning of the test, the prediction in all floors is very similar in frequency as well as in amplitude, especially after 8 seconds. In the first floor the amplitude of the signals during this part of the response is underestimated in most of the cycles, whereas in the upper floors a slight overestimation is observed.

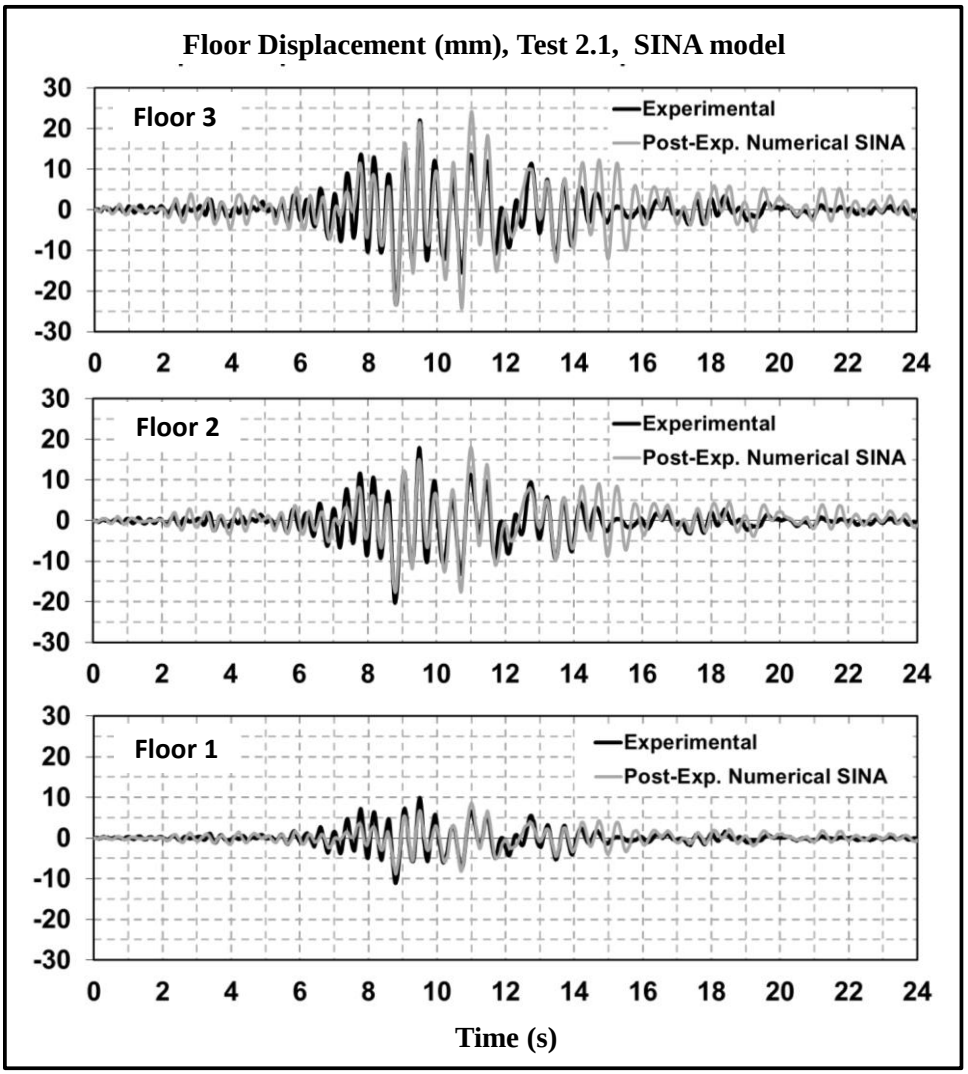

Figure 8.33: Relative floor displacement, post-experimental prediction Test 2.1, SINA rule in joints.

The predicted inter-storey drifts histories shown in Figure 8.34 are in a general good agreement with the experimental counterparts. The same observations written about the accuracy of the prediction in terms of floor displacements are true in this case, confirming the good accuracy of the prediction of the specimen response during Test 2.1. In terms of local behaviour, in the simulation of this test, small inelastic incursions occurred in the springs of the exterior joints, in agreement with the observed damage after the actual test, as presented in Chapter 4, with rotations of the order of 0.5%.

In Table 8.4, the maximum values recorded during the tests presented in this chapter are compared with the numerical results obtained with the numerical model described in the previous section and the recorded shake table input motion. It is worth noting that those values do not necessarily occur at the same time.

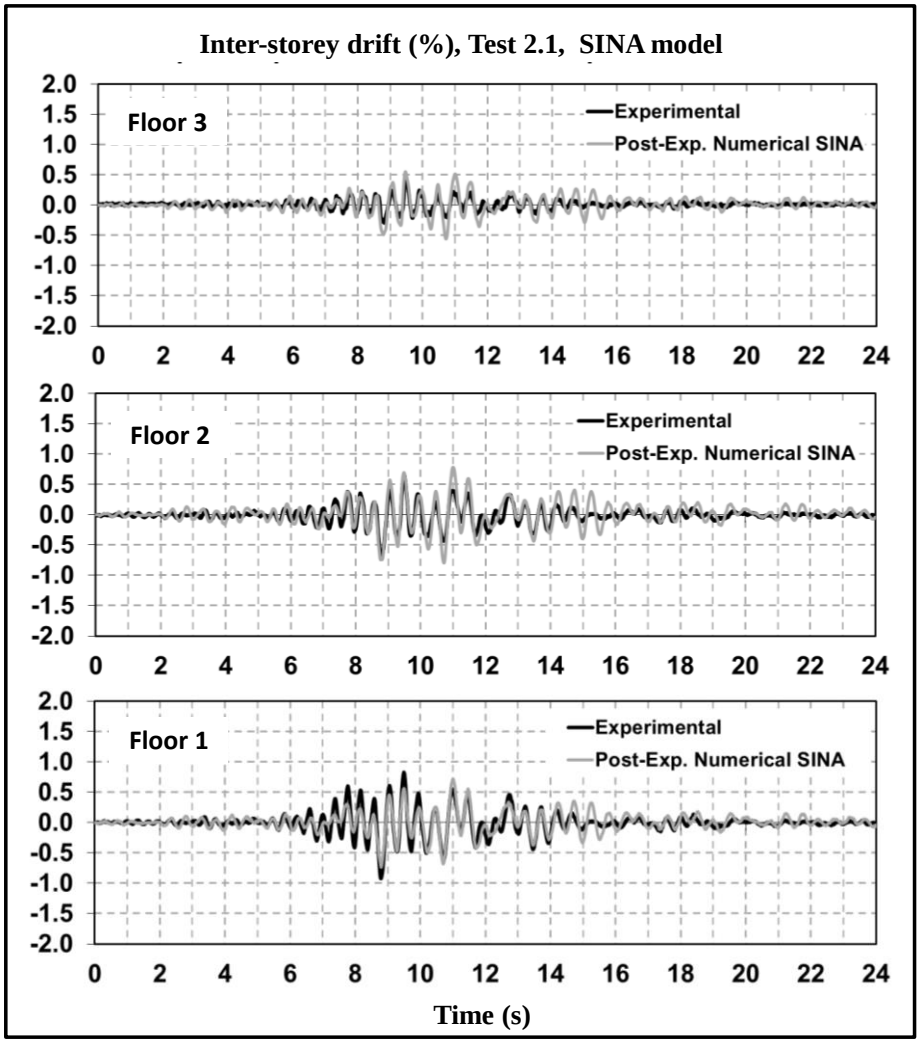

Figure 8.34: Inter-storey drift, post-experimental prediction Test 2.1, SINA rule in joints.

Table 8.4: Maximum Response Experimental/Numerical Comparison Post-Experimental Prediction.

		Floor Displacements (mm)			Inter-Storey Drifts (%)		
Test	Floor	Exp.	Num.	Num./Exp.	Exp.	Num.	Num./Exp.
1.1	1	11.3	15.5	1.37	0.93	1.29	1.39
1.1	2	24.5	26.2	1.07	1.10	0.92	0.84
1.1	3	33.7	29.0	0.86	0.99	0.38	0.38
2.1	1	11.0	7.1	0.65	0.92	0.59	0.64
2.1	2	20.2	13.0	0.64	0.69	0.50	0.72
2.1	3	23.2	16.3	0.70	0.40	0.27	0.68
2.2	1	45.3	27.3	0.60	3.82	2.34	0.61
2.2	2	75.9	33.7	0.44	2.60	0.63	0.24
2.2	3	84.8	36.6	0.43	0.90	0.35	0.39

8.7 RETROFITTED SPECIMEN NUMERICAL MODEL DESCRIPTION

The numerical model of the retrofitted building is described in this section. Basically the model is the same as the one used for the prediction of the as-built/repaired response described at the beginning of this chapter, with the difference that additional elements were introduced. Those elements were frame members that represent the strengthened part of beams and columns with GFRP (glass fibre reinforced polymer) and the rectangular part of the beam, where the slab has been weakened. Those elements had the dimensions and sectional properties described in Chapter 6, and were assembled as schematically presented in Figure 8.35.

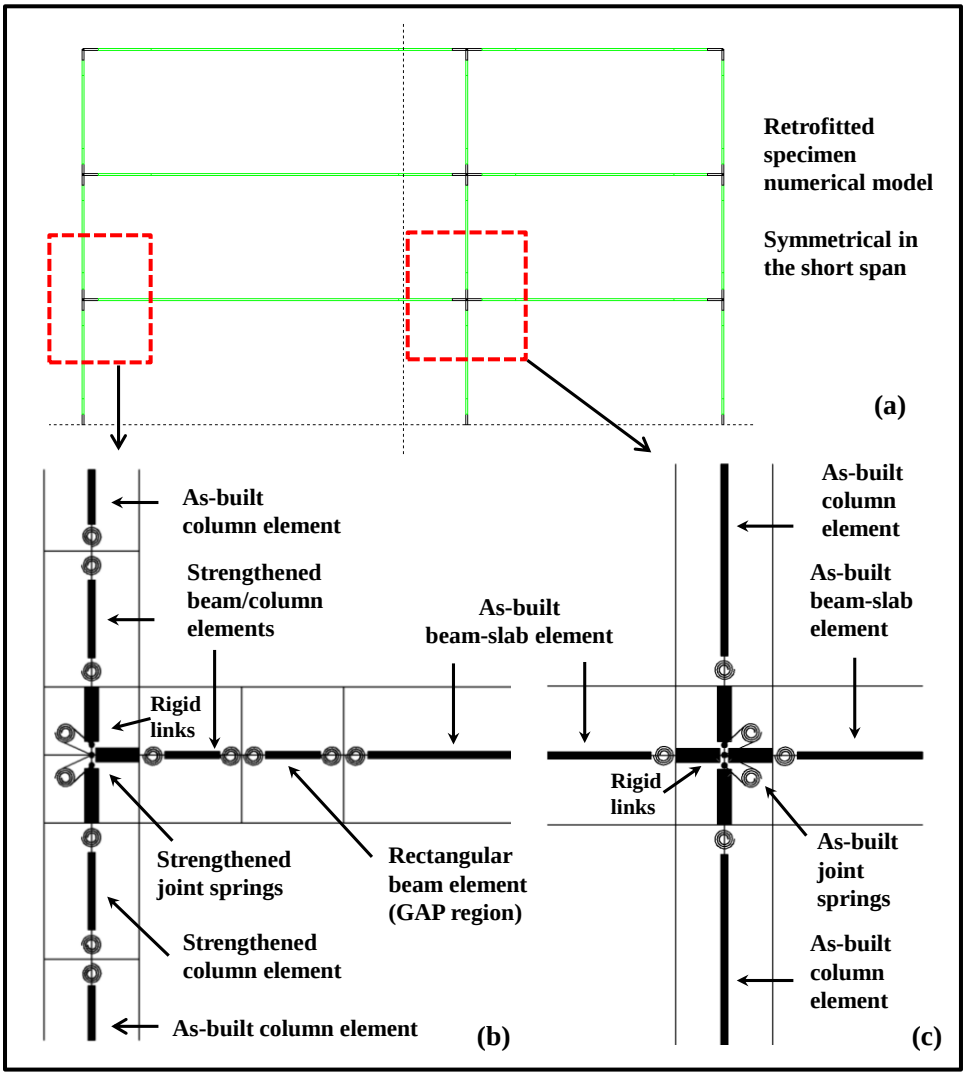

Figure 8.35: Description of the numerical model of the retrofitted specimen; (a) Ruaumoko2D graphical interface model representation; (b) exterior beam column joint modelling, including the GFRP strengthened parts of the beam and columns, and the rectangular section beam; (c) as-built central columns panel zone modelling.

The preliminary model for the retrofitted joints is represented by springs analogous to the as-built counterparts with the only modification being an increased cracking strength in order to account for the contribution of the GFRP. That is, the resistance and stiffness provided by the composite section is conceived as a whole, and this constitutes a macro-

model of a more realistic alternative that would be to model the contribution of the as-built joint and the contribution of the GFRP separately, with springs in parallel. However, in the facts, the most important difference in those modelling approximations would exist in the small cycle part of the response. As the small cycle behaviour of the hysteretic rule used in the spring has not much empirical support for their mathematical formulation, it is understood that in both cases same degree of uncertainty is introduced, and hence both approaches would not be completely accurate in those regards anyway. In the numerical analyses that captured the response of the retrofitted specimen with good accuracy, the springs that represent the strengthened joints remained elastic.

The damping model was the same as the one used in the model of the as-bulit/repaired specimen, i.e. Wilson-Penzien with constant damping equal to 5% of the critical value.

The strengthened-beams and columns elements were added as different frame elements with the capacities obtained with the sectional analyses presented in Chapter 6. Those elements were modelled with Giberson beams with and without interaction with the axial load in beam and columns, respectively. The moment-axial load diagrams of the columns were obtained from the moment-curvature diagrams for varying axial load presented in Chapter 6. The moment capacity of the beams was obtained with the moment-curvature diagrams for the AC and AT situation (positive and negative bending moment) as also presented in Chapter 6. The Revisited Takeda rule was used for modelling lumped inelasticity. In beams a non-symmetrical version of that rule was used, so that there is a difference in the positive and negative bending directions (AC and AT states). The parameters that govern the hysteretic behaviour of those rules were found to be irrelevant in this case, because the demand of curvature or rotations were small enough to keep the structural members in the elastic range.

Special attention required the modelling of the hysteretic behaviour of the rectangular beam, which was the fuse of most of the inelasticity developed in the specimen during the experiments, and also in the predicted response of the model used for obtaining the results shown in the next section. The properties of this member, identified to be critical in the accuracy of the prediction, were tuned so that the empirical response of Test 3.2 was captured. Initially a Revisited Takeda rule like that used for the asymmetric beams was selected. However, it was replaced afterwards by a symmetrical version of the modified SINA rule which allowed the incorporation of the pinching effect normally observed in the hysteretic behaviour of RC members with smooth plain round bars (Pampanin et al. 2002, Pampanin et al. 2007, Kam 2010, Akguzel and Pampanin 2010, Akguzel 2011).

In is important to note that the bending moment capacity of the section was slightly reduced to 6 kN instead of 7 kN which is the nominal yielding value presented in Chapter 6. That modification was done because the results of the prediction were much more accurate and based on the argument that the empirical/actual gross section of the rectangular beam was smaller than the nominal one, due to a reduction caused by the retrofit intervention process. It is also worth recalling that there is uncertainty involved in the quality of the materials and the estimations of the elastic modulus of the concrete as well, which makes the modification in the strength plausible. The associated stiffness decrease is introduced with the parameters α and β.

The values adopted for the parameters that govern the hysteresis rules of beams, columns and joints of the numerical model of the retrofitted specimen can be summarized as follows:

Strengthened Beam *(Revisited Takeda rule – IHYST = 56 in Ruaumoko2D)*

$k_0 = EI$ = 850.0 kNm^2; r = 0.01; F_y^+= 13.0 kNm; F_y^- = -25.0 kNm; $F_{cr}^+ = 0.70F_y^+$; $F_{cr}^- = 0.55F_y^-$; Φ = 1.9; α = 0.20; β = 0.25; γ = 0.5; δ = 0.5.

Weakened Slab Beam *(Modified SINA rule – IHYST = 57 in Ruaumoko2D)*

$k_0 = EI$ = 450.5 kNm^2; r = 0.005; F_y^+= 6.0 kNm; F_y^- = -6.0 kNm; $F_{cr}^+ = 0.70F_y^+$; $F_{cr}^- = 0.70F_y^-$; Φ = 1.0; α = 0.9; β = 0.9; γ = 0.5; δ = 0.5; $F_{cc}^+ = 0.20F_y^+$; $F_{cc}^- = 0.20F_y^-$.

Strengthened Column *(Revisited Takeda rule – IHYST = 56 in Ruaumoko2D)*

$k_0 = EI$ = 308.9 kNm^2; r = 0.01; F_y^+= 10.5 kNm; F_y^- = -10.5 kNm; $F_{cr}^+ = 0.57F_y^+$; $F_{cr}^- = 0.57F_y^-$; Φ = 1.0; α = 0.23; β = 0.23; γ = 0.5; δ = 0.5.

Joints *(Modified SINA rule – IHYST = 56 in Ruaumoko2D)*

$k_0 = GJ$ = 500 kNm; r = 0; F_y^+= 9.5 kNm; F_y^- = -9.5 kNm; $F_{cr}^+ = 0.5F_y^+$; $F_{cr}^- = 0.5F_y^-$; Φ = 1.0; α = 0.9; β = 0.9; γ = 0.5; δ = 0.5; $F_{cc}^+ = 0.25F_y^+$; $F_{cc}^- = 0.25F_y^-$.

8.8 POST-EXPERIMENTAL PREDICTION – RETROFITTED SPECIMEN

As it was described in Chapter 7, the retrofitted specimen was tested twice. In the first experiment the specimen was subjected to CHH record (Darfield earthquake, New Zealand 2010) during Test 3.1, and to VMM record (Maule earthquake, Chile 2010) during Test 3.2. The response of the building during those tests is presented in this section. As it was discussed in the previous sections of this chapter, the correct or 'true' motion of the shake table needs to be used in order to simulate the real recorded response of the building. Hence, in the numerical predictions shown here, only those obtained with the recorded motion of the shake table are presented (see Chapter 7 for a comparison of the nominal and recorded shake table motions). The results are presented in the inverse order of the experimental sequence because the numerical model was tuned using the experimental results of Test 3.2, the one where heavy inelastic incursions were observed in the beams and in some of the columns as described in Chapter 7. The results of the first experiment in the sequence, with the less demanding ground motion, are presented afterwards and somehow constitute a 'blind' prediction using the recorded motion, in the sense that it is the only numerical simulation that was run in Ruaumoko2D. That is, there is no alteration in the parameters used in the model developed to capture the response of the retrofitted building during Test 3.2.

8.8.1 Test 3.2 – VMM record

In Figure 8.36 and Figure 8.37, the post-experimental prediction of the building response during Test 3.1 is presented in terms of floor displacements and inter-storey drifts histories. In the graphs of Figure 8.36 it can be observed that the numerical and

experimental floor displacement histories are in a reasonably good agreement, especially at the beginning of the motion, until about 22 seconds. At that time after the start of the test, the numerical predictions begins to underestimate the recorded floor displacements until the first high amplitude part of the response ends at about 27 seconds. The frequency of the predicted response though, is extremely similar to that of the recorded counterpart.

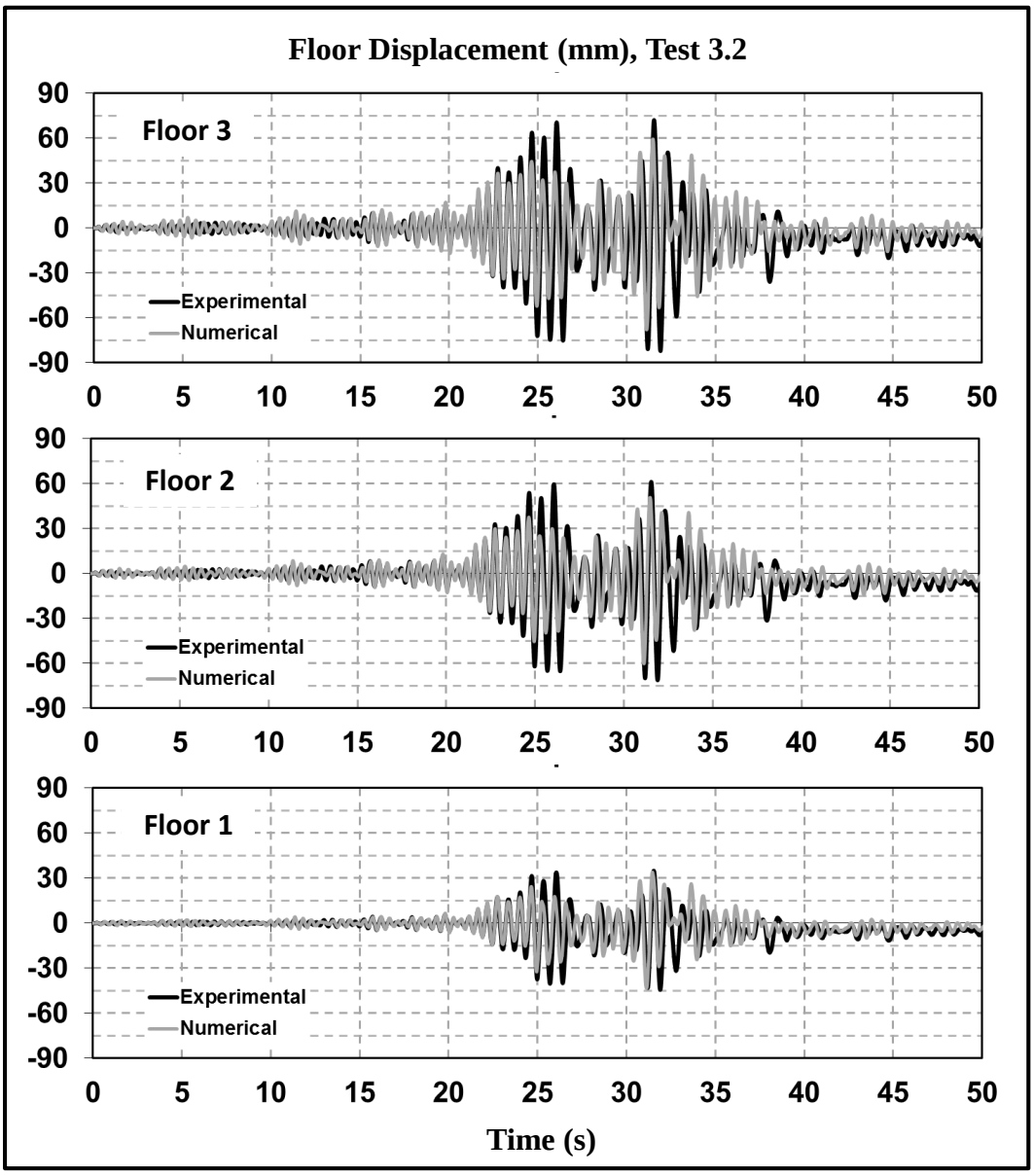

Figure 8.36: Test 3.2 recorded and predicted floor displacements, relative to the shake table, VMM record (Maule earthquake, Chile 2010).

During the low amplitude cycles of the response from about 27 to 31 seconds after the start of the test, the predicted displacement histories lose the phase of the experimental signals at every floor, which can be attributed to the lack of empirical support of the small cycle part of the hysteretic rules. The amplitude of both signals nevertheless, is very similar. During the second high amplitude part of the building response, the numerical model is able to re-capture the experimental displacements. That is from about 31 to 35 seconds after the start of the test. After the new high displacement cycles take place, the

numerical response loses accuracy again, and some not recorded high frequency cycles are predicted. Again, the small cycle behaviour that determines the response of the individual structural members may have played a very important role in the difference of the predicted and experimental floor displacements. However, at the end of the motion, from about 40 seconds after the beginning of the test, the numerical response becomes very close to the experimental counterpart, even after experiencing important differences in the past, which is remarkable.

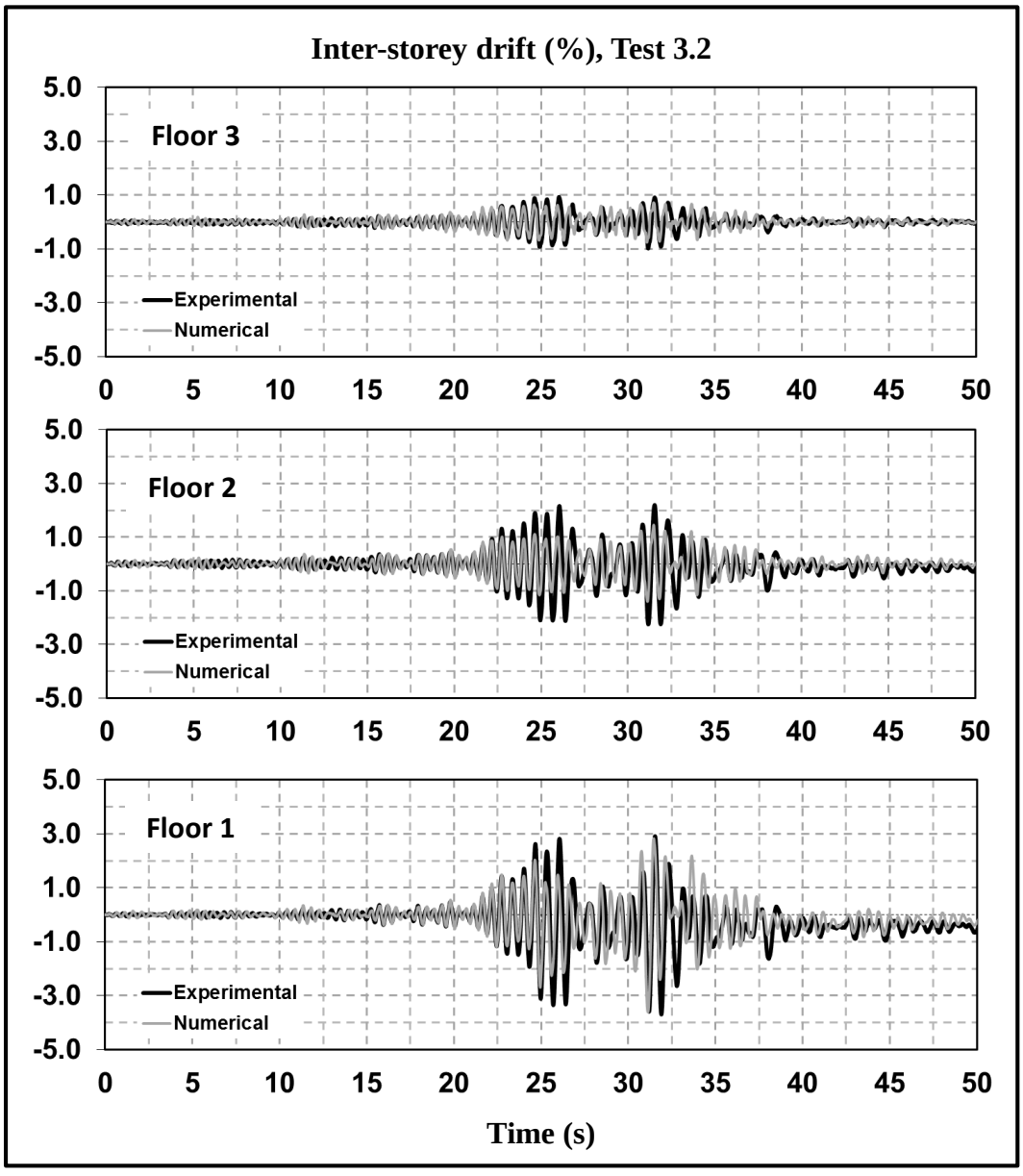

Figure 8.37: Test 3.2 recorded and predicted inter-storey drifts, VMM record (Maule earthquake, Chile 2010).

In Figure 8.37, it is shown that there is an overall good agreement in the predicted and experimental responses, especially those of the first and third floors. The numerical signal of the first floor displacement is very accurate in capturing the experimental data from the beginning of until about 23 seconds after the start of the test, instant when it commences to underestimate the amplitude of the experimental inter-storey drift. From that moment

onward, the numerical prediction maintains a good agreement in terms of frequency with the empirical counterpart, but the amplitude is increasingly underestimated. The differences in amplitude between both signals though are rather small when the complexity of the problem is taken into account. After the first high amplitude part of the response, the prediction is again accurate in amplitude but loses the frequency, as pointed out before that, phenomenon can be attributed to large differences in the true-empirical and numerically-assumed small cycle hysteretic behaviour in structural members.

During the second high amplitude part of the response history, the numerical model is extremely accurate in predicting the experimental response. Local maximum peaks at about 31-31.5 seconds, are predicted exactly, even though the global maximum recorded at about 32 seconds after the beginning of the test is underestimated importantly. At about 32.5 seconds, the prediction of the first floor inter-storey drift loses accuracy again and the agreement in the frequency of the motion is lost, errors in the assumption of the small cycle behaviour being one possible reason. At the aftermath of the motion, the numerical prediction becomes close to the recorded inter-storey drift history and the accuracy increases even after it lost the track during prior instances of the experiment. The predicted inter-storey drift history of the second floor is also in reasonably good agreement with the experimental data. The same observations made for the first floor prediction accuracy are true, with the exception that in this case there is a larger underestimation of the amplitude during the two strong parts of the response. The prediction of the third floor inter-storey drift history is much more accurate than that of the second floor. The frequency and the amplitude of the numerical and experimental signals coincide well, with some exceptions that can be attributed to a small cycle effect.

8.8.2 Test 3.1 – CHH record

After the numerical model was calibrated with the experimental results of Test 3.2, it was used to predict the response of the retrofitted specimen during Test 3.1, with no alteration in any parameter. The input motion used in the numerical simulation was the recorded-actual shake table motion. In Figure 8.38 and Figure 8.39, the numerical prediction of the building response during Test 3.1 is presented in terms of floor displacements and inter-storey drifts histories, respectively. In those figures, the numerical results are compared with the experimental counterparts.

In the graphs of Figure 8.38, it can be observed that overall the prediction of the building response is reasonably good, but can be improved. The numerical prediction overestimates the amplitude of the floor displacements by an important margin at the beginning of the response, from 0 to 5 seconds after the start of the test. However, the frequency characteristics of the experimental and numerical responses are in good agreement. After that time, the predictions start to capture in a much more accurate way the experimental signals, especially after about 8 seconds from the beginning of the test. The accuracy of the prediction is quite high from that instant until about 13 seconds, time when the amplitude of the empirical displacements starts to be overestimated again, this time by an important margin. The prediction becomes closer to the recorded displacements again only from about 37 seconds, very close to the end of the test.

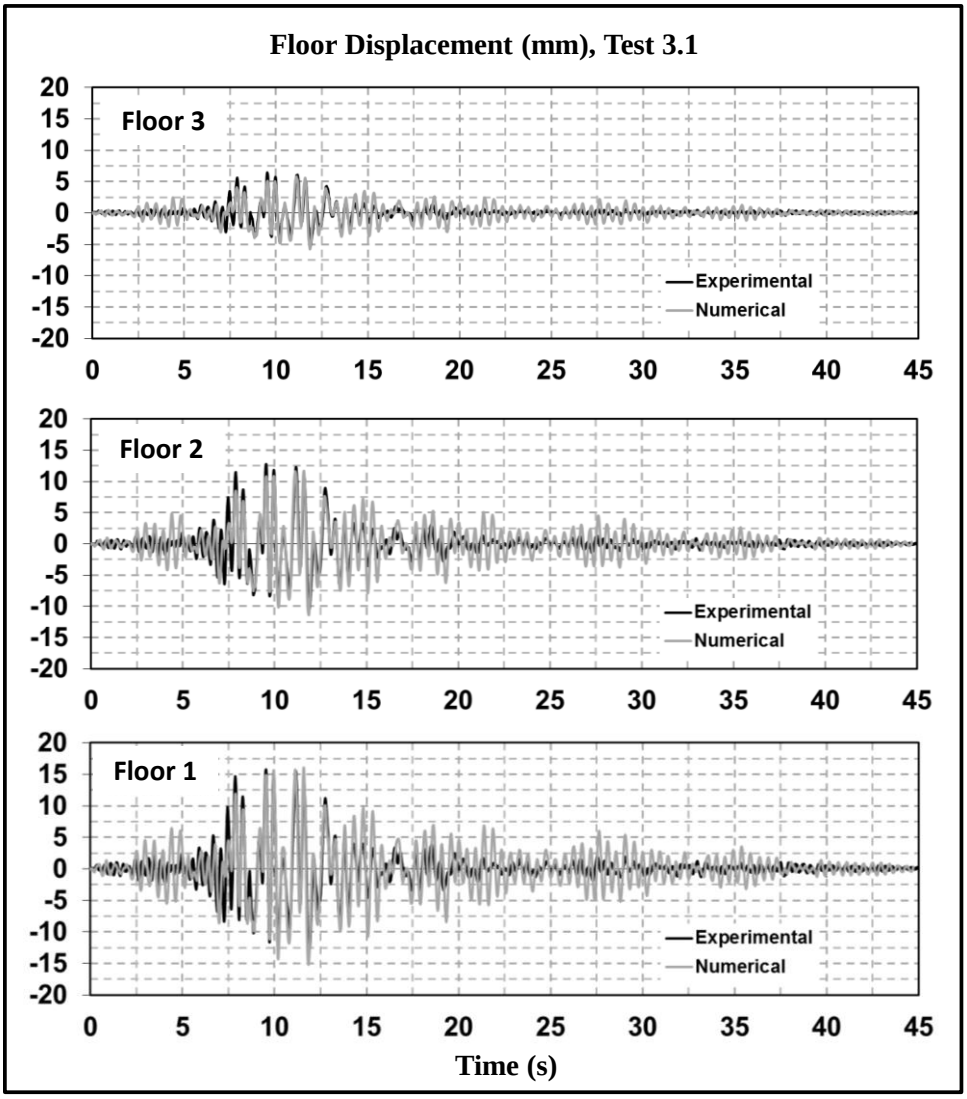

Figure 8.38: Test 3.1 recorded and predicted floor displacements, CHH record.

In the graphs of Figure 8.39, the predicted inter-storey drift histories are compared with the recorded counterparts during Test 3.1. The numerical and experimental signals match reasonably well, overall speaking. The same differences described before in between the empirical and predicted floor displacements exist in the inter-storey drift histories. That is, the experimental signals are overestimated in amplitude during the first stages of the test, but with good agreement in the frequency of the signals, then they are much more accurately predicted until the differences in the amplitude of the numerical histories become large again during the last part of the response, until about 37 seconds of the beginning of the test.

The large differences in the amplitude of the floor displacements and the inter-storey drift histories can be attributed to differences in the values of the viscous damping of the experimental and numerical models. It is important to note that when the damping was measured based on the estimations of the decay in the response during snap-back tests a large scatter was observed. Hence, it is possible that the response can be more accurately predicted if the values as well as the model of the critical damping associated to each mode of vibration are modified.

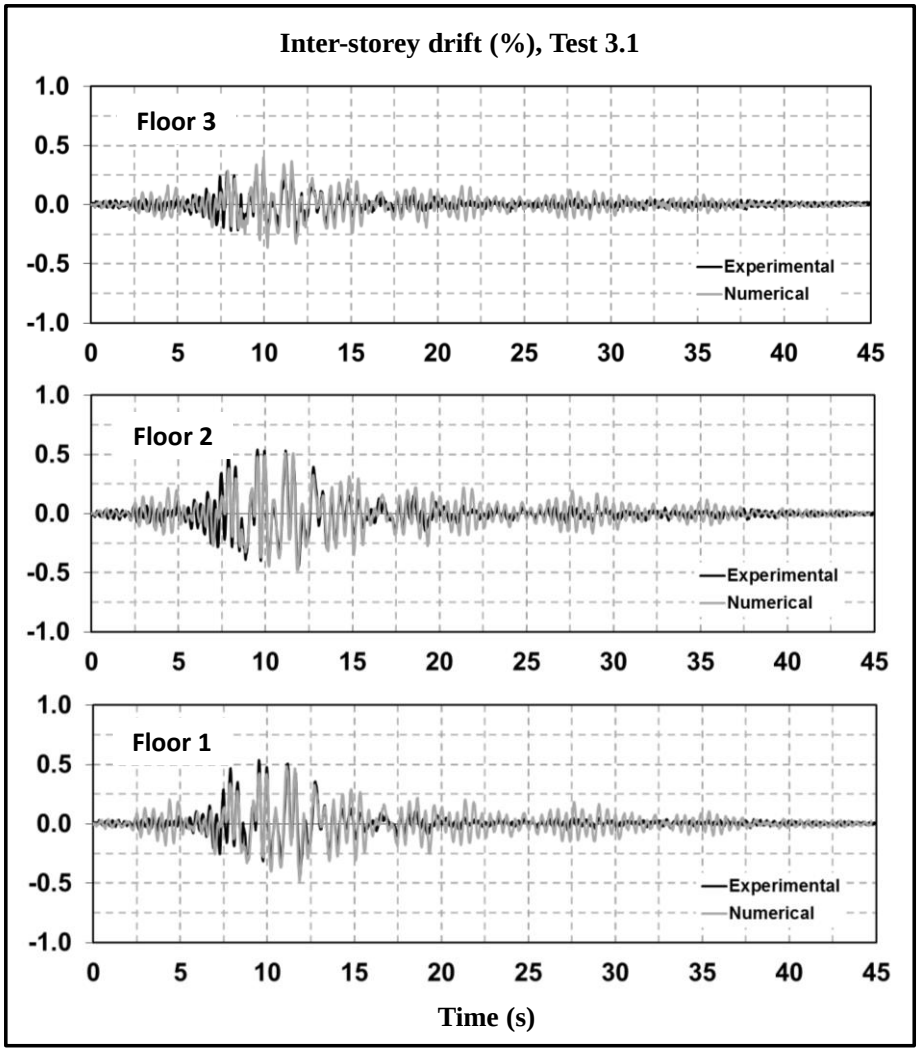

Figure 8.39: Test 3.1 recorded and predicted inter-storey drift, CHH record (Darfield earthquake, New Zealand 2010).

In Table 8.5 the maximum recorded (experimental) and predicted (numerical) responses of tests 3.1 and 3.2 in terms of floor displacements and inter-storey drifts are summarized. It is important to note that these peak values do not necessarily coincide in time.

Table 8.5: Maximum response experimental/numerical comparison post-experimental prediction, retrofitted specimen.

		Floor Displacements (mm)			Inter-Storey Drifts (%)		
Test	Floor	Exp.	Num.	Num./Exp.	Exp.	Num.	Num./Exp.
3.1	1	6.4	5.8	0.91	0.54	0.48	0.89
3.1	2	12.8	11.7	0.91	0.54	0.51	0.94
3.1	3	15.8	16.1	1.02	0.30	0.40	1.33
3.2	1	44.4	43.3	0.98	3.70	3.61	0.98
3.2	2	71.2	60.1	0.84	2.25	1.45	0.64
3.2	3	82.1	73.9	0.90	0.98	0.75	0.77

8.9 DISCUSSION ON THE ACCURACY OF THE PREDICTIONS

There are many factors that have a strong influence on the prediction of the response of structures under seismic events in the context of nonlinear dynamics in general. They can be summarized as:

(1) The selection of the parameters governing the hysteretic behaviour of structural members,
(2) Differences in the nominal and actual/recorded input motion recorded during the experiments,
(3) The adequacy of the assumed small cyclic behaviour of the hysteretic rules, and
(4) The value of the critical damping.

In this particular case, additional factors that constitute a source of differences in the predicted and recorded responses of the building during all tests are the torsional resistance and stiffness of the spandrels, and the existence of in-plane global torsion due to the asymmetry of the structure.

8.9.1 Parameters that Govern the Nonlinear Behaviour of Structural Members

The dependence of the predicted response of the building on the value of the parameters that control the hysteresis rule used in the numerical model of structural members is of extreme importance. As it was shown in section 6, if one uses the most and less degrading parameters in the modified Takeda rule used in as-built columns and joints, a large difference in the prediction of Test 2.2 are predicted. Moreover, the numerical results of the former case diverge from the experimental counterparts, whilst in the latter case a clear underestimation of the recorded response of the building is obtained. That means that the 'correct' value of those parameters may lie somewhere in between those used in the cases presented in section 6, everything else remaining the same (ceteris paribus). Hence, an a priori assumption in the values of α and β in the modified Takeda rule seems very hard to be made without any empirical calibration. As a consequence, if the dynamical response of a building is being predicted, much care should be place on the adequacy of the hysteretic parameters, and at least the two extreme cases in terms of stiffness degradations should be examined.

In some cases though, one may also want to check the results of the numerical prediction using a different hysteresis rule that takes into account pinching or other common effects in large inelastic cycles of structural members. As it was shown in section 6, when the very simple modified Takeda rule was replaced by a degrading modified SINA rule in the springs of the joints, much accurate results were obtained in the prediction of the specimen response. Hence the choice of the hysteretic rule itself in macro-models of key elements of a building may change the prediction importantly.

In the context of Direct Displacement Based seismic design of structures (Priestley et al. 2007), reduction factors used to obtain design spectra from elastic counterparts, are related to the equivalent damping of the elastic equivalent substitute structure (Bommer and Mendis 2005), which in turn depends on the maximum reached ductility ratio. As those relationships are obtained with numerical simulations of single degree of freedom systems at increasing maximum ductility, it strongly depends on the parameters chosen in the hysteretic model as described in Grant el al. (2005) and Dwairi et al. (2007).

However, there is still a question mark related to the influence of the bi-linear factor used in the development of those formulae.

8.9.2 Differences in the Nominal and Recorded Input Motion

As it was shown in Chapter 7, differences in the nominal and recorded input motions of the shake table did exist. Those differences were noted to be almost impossible to avoid from a theoretical perspective, even if the most sensitive apparatus is being used for recording the motion. The differences were found to be larger during the strong part of the motion, which may be an indication that the dynamical interaction of the shake table with the specimen has an influence on them.

In section 5 the predicted responses of the three tests of the as-built and repaired specimens obtained with the nominal and recorded input motions were compared. It was shown that there were little differences in the predictions of Test 1.1, fair differences in the prediction of Test 2.1, and large differences in the prediction of Test 2.2, the most demanding one in terms of the intensity of the damage, when the less degrading Takeda parameters were used in the joints and columns. In the third case, chaotic behaviour was noted to take place at some stage of the numerical simulation, when there is a shift in the phase attractor of the dynamical response in an erratic way. For a detailed explanation on the subject the reader is referred to Strogatz (1994).

8.9.3 Modelling of Small Cycle Nonlinear Behaviour

In the literature, there is an extensive amount of research related to quasi-static push-pull-like tests at increasing amplitudes of the displacement in the ‘loading’ protocol. With few exceptions, all of them have had loading protocols designed to capture the hysteretic behaviour of the structural member represented by the subassembly at increasing displacements amplitudes in a stable and slow motion fashion. Simple numerical models for representing the macro-inelastic behaviour of structural members have been developed since the early 1970’s and have been calibrated with the results of those kinds of tests for a large number of member typologies (Carr 2008c).

In the dynamic range though, the hysteretic path followed by a structural member will be affected by small amplitude fluctuations of the displacement at any instant of the response. However, rigorous studies focused on that kind of behaviour are apparently not available in the literature yet. As a result, in the hysteretic rules developed to date there are assumptions in the path that the loop follows at low amplitude cycles during different parts of the inelastic response that have not been empirically proofed or refuted. The lack of that empirical information introduces some ‘guessing’ in the predictions, which may lead to important differences in the prediction of the response of a structure subjected to ground motions, as has been remarked throughout this chapter.

8.9.4 Damping Model

The way intrinsic damping of the structure is modelled may also have consequences in the response of the structure, as discussed in Carr (2008a), which may be a source of discrepancies in the numerical and experimental signals, like those observed in the floor displacements and inter-storey drifts histories of Test 3.1.

In this investigation, the constant damping Wilson-Penzien model (Wilson and Penzien 1972) was preferred due its simplicity and because it is the model that provides the most stable results, according to preliminary numerical studies on single degree of freedom systems (Pampanin et al. 2010). The choice of the critical damping magnitude though also requires some 'guessing'. The results of the preliminary snap-back tests performed on the specimen for the estimation of the critical damping of the structure had a large scatter, as discussed in Appendix C. Indeed, it was possible to obtain quite different results depending on the instant of the motion where the decay in the amplitude of the response was being measured. Hence, differences in the prediction due to variations in that value could be investigated in the future. In all the predictions presented in this thesis, the value used for the damping was 5% of the critical value for all modes.

8.9.5 Influence of the Transverse Beam and In-Plane Asymmetry

The existence of a spandrel or transverse beam orthogonal to the longitudinal counterpart, as well as a floor slab in the specimen, has an important role in the local performance of the beam column joints part of the specimen under investigation, stressed throughout this thesis. As the mass at each floor is concentrated in the slab, the inertial forces that take place as a result of the movement of the structure imposed by the ground motion are distributed from the slab to the frames. When those forces occur, then the transverse beam at the front and back faces of the building experience twist at the same time that the joints experience angular distortions. Those angular distortions or rotations are not identical, and the resisting mechanism of spandrel and joint occur in series rather than in parallel. That is, the equivalent joint-spandrel resisting mechanism would be more flexible than the joint alone. That conjecture is in line with the value of the initial stiffness in the joints when compared with the stiffness obtained from the equivalent moment-angular distortion curves for plane beam column joints presented in Chapter 6.

Global in-plane torsion of the specimen did exist during the response of the strongest test. The magnitude of the in-plane torsion and the longitudinal associated longitudinal displacements were low during the weak part of the response, and increased when large inelastic deformations took place during the strong part of the motion, especially if they were fragile (as-built/repaired specimen). Even though the relative magnitude of those displacements was low when compared to the recorded displacements shown in this thesis, it is undeniable that they can have some relevance in the differences of the numerical predictions of the building response during the tests under investigation.

8.10 CONCLUDING REMARKS

In this chapter the results of a series of numerical predictions of the experimental response of the most relevant tests performed as part of the empirical work of this thesis have been presented. The numerical predictions were made using a simplified plane-2D finite element model with lumped plasticity elements constructed in Ruaumoko2D (Carr 2008b). It was found that the response of the specimen during Tests 1.1 and 2.1 was captured with a reasonably good accuracy with the initial model and the nominal input motion for the shake table, which constitutes a fair 'blind' prediction. However that prediction did not capture the response of the same specimen (as-built/repaired) during Test 2.1, when the most demanding record was used. From those findings it is concluded that for the same specimen but different ground motions, the model can capture the

response of the specimen during one test, but fails to predict the recorded response during the other.

It was also found that the unsurmountable to avoid differences that exist in the nominal or intended motion and recorded or actual motion of the shake table have consequences on the prediction with the same model. Those differences were much more important in the prediction of the building response during Test 2.2 and were almost negligible in the prediction of the response of the specimen during Test 1.1 and 2.1. It is concluded then, that the use of the nominal input can be adequate in some cases, and not adequate in others, depending most likely in the magnitude of the response of the specimen during the actual experiment, indication that the shake table and the specimen are in 'open' dynamical interaction (Quintana-Gallo et al. 2013).

The initial model was modified in order to capture the results of Test 2.2. Initially, the same hysteresis rules were used in the model and their parameters were tuned. It was found that when the stiffness of the joint was reduced from the initial value used for the blind prediction, the parameters for the unloading and reloading parameters of the modified Takeda rule kept constant, a fair approximation of the building response during that test was obtained.

As a final part of the investigation related to the as-built/repaired specimen, the hysteresis model used in the joints was changed to a modified SINA rule, which incorporated the pinching effect. If was found after a series of numerical simulations that if the same initial and post cracking stiffness values used in the post-experimental prediction with the Takeda rule were also used, the prediction was much more accurate, even if some differences attributed to the assumption of small cycle behaviour as well as the other effects mentioned in the discussion were observed. In that sense it is concluded that the numerical prediction using this model is good. When the same model was run with the record used in Tests 2.1 and 1.1, the model simulated a very good representation of the recorded building response. In the last case, an important improvement in the prediction of the third floor inter-storey drift was found, confirming the adequacy of the model.

Finally, in the numerical simulation of the retrofitted specimen, it was shown that the constructed model after the experiments was able to capture with a good degree of accuracy the experimental results of Tests 3.1 and 3.2. The latter test was used for tuning the model. It was found that there was a strong dependence of the results on small variations of the bi-linear factor and the yielding moment capacity of the as-built beams inside the weakened part of the slab. With that model a pseudo-blind prediction was made, when running the model with the input motion used in Test 2.1 in a second stage. The results showed that the prediction was close to the recorded data. Based on that, it is concluded that the numerical model is suitable for the prediction of the retrofitted specimen tests, but can be improved. For that, modifications to the parameters of the hysteresis rules used in the models described herein constitute an alternative, as well as the addition of a model for the transverse beam, a study on the influence of the critical damping and the use of the Pampanin rule in beam column joints, or the used of more refined fibre model for example, are thought to be plausible efforts for future research.

8.11 REFERENCES

Akguzel, U., Pampanin, S. (2010), 'Effects of Variation of Axial Load and Bidirectional Loading on Seismic Performance of GFRP Retrofitted Reinforced Concrete Exterior Beam-Column Joints', *Journal of Composites for Construction*, Vol. (14), pp. 94-104.

Akguzel, U. (2011), 'Seismic Performance of FRP Retrofitted Exterior RC Beam-Column Joints under Varying Axial and Bidirectional Loading', *a thesis presented for the degree of Doctor of Philosophy in Civil Engineering*, University of Canterbury, Christchurch, New Zealand.

Bommer, J.J., Mendis, R. (2005), 'Scaling of Spectral Displacement Ordinates with Damping Ratios', *Earthquake Engineering and Structural Dynamics*, Vol. 34, pp. 145-165.

Carr, A. J. (2008a), *Ruaumoko – Program for Inelastic Dynamic Analysis*, Volume 1: Theory, Department of Civil and Natural Resources Engineering, University of Canterbury, Christchurch, New Zealand.

Carr, A. J. (2008b), *Ruaumoko – Program for Inelastic Dynamic Analysis*, Volume 2: User Manual for the 2-Dimensional Version, Ruaumoko2D, Department of Civil and Natural Resources Engineering, University of Canterbury, Christchurch, New Zealand.

Carr, A. J. (2008c), *Ruaumoko – Program for Inelastic Dynamic Analysis*, Volume 5: Appendices, Department of Civil and Natural Resources Engineering, University of Canterbury, Christchurch, New Zealand.

Crisp, D. J. (1980), 'Damping Models for Inelastic Structures', *M.E. Report*, Department of Civil and Natural Resources Engineering, University of Canterbury, Christchurch, New Zealand.

Dwairi H. M., Kowalsky, M. J., and Nau, J.M. 'Equivalent Damping in Support of Direct Displacement-Based Design', *Journal of Earthquake Engineering*, Vol. 11(4), pp. 512-530.

Grant, D.N., Blandon, C.A. and Priestley, M.J.N. (2005), 'Modelling Inelastic Response in Direct Displacement-Based Seismic Design', *Report No.2005/03*, European School for Advanced Studies in Reduction of Seismic Risk, Pavia, Italy.

Hakuto, S., Park, R., and Tanaka, H. (2000), 'Seismic Load Tests on Interior and Exterior Beam-Column Joints with Substandard Reinforcing Details', *ACI Structural Journal*, Vol. 97(1).

Kam, W. (2010), 'Selective Weakening and Post-Tensioning for the Seismic Retrofit of Non-Ductile RC Frames', *a thesis presented for the degree of Doctor of Philosophy in Civil Engineering*, University of Canterbury, Christchurch, New Zealand.

Krawinkler, H., and Seneviratna G.D.P.K. (1998), 'Pros and Cons of a Pushover Analysis for Seismic Performance Evaluation', *Journal of Engineering Structures*, Vol. 20, pp. 452-464.

Lorenz, E. (1963), 'Deterministic Non Periodic Flow', *MIT Press*, Massachusetts, USA.

Lorenz, E. (1993), *The Essence of Chaos*, University of Washington Press, Washington State, USA.

Otani, S. (1974), SAKE, *A computer Program for Inelastic Response or R/C Frames to Earthquakes*, University of Illinois, Urbana Champaign, Illinois, USA.

Pampanin, S., Calvi, G.M., Moratti, M. (2002). "Seismic Behavior of RC Beam Column Joints Designed for Gravity Loads", *12th ECEE,* London, England, paper n. 726.

Pampanin, S., Magenes, G., Carr, A. (2003), 'Modelling of shear hinge mechanism in poorly detailed RC beam-column joints', *Proceedings of the fib symposium Concrete Structures in Seismic Regions*, Athens, paper n. 171.

Pampanin, S. (2005), 'Controversial Aspects in Seismic Assessment and Retrofit of Structures in Modern Times: Understanding and Implementing Lessons from Ancient Heritage', *NZ Concrete Society Conference*, Auckland, New Zealand.

Pampanin, S., Moghaddasi, M., Quintana-Gallo, P., Rieder, A. (2010), 'EQ-rod a new generation of earthquake-resistant fasteners', *Report prepared for Fischerwerke Artur Fischer GmbH & Co. KG*, Department of Civil and Natural Resources Engineering, University of Canterbury, Christchurch, New Zealand.

Priestley, M.J.N. (1997), 'Displacement-Based Seismic Assessment of Existing Reinforced Concrete Buildings', *Journal of Earthquake Engineering*, Vol. 29(4), pp.356-272.

Quintana-Gallo, P., Rebolledo, R. and Allan, G. (2013), 'Dealing with Uncertainty in Earthquake Engineering: a Discussion on the Application of the Theory of Open Dynamical Systems, *Obras y Proyectos*, Vol 14(2), pp. 66-77 (*in English*).

Saiidi, M., and Sozen, M.A. (1979), 'Simple and Complex Models for Nonlinear Seismic Response of Reinforced Concrete Structures', *Report UILU-ENG-79-2031*, Department of Civil Engineering, University of Illinois, Urbana Champaign, USA.

Sharpe, R.D. (1974), 'The Seismic Response of Inelastic Structures', *a thesis presented for the degree of Doctor of Philosophy in Civil Engineering*, University of Canterbury, Christchurch, New Zealand.

Strogatz, S. (1994), *Nonlinear Dynamics and Chaos*, Westview Press, Cambridge, Massachusetts, USA.

Wilson, E. L. and Penzien, J. (1972), 'Evaluation of Orthogonal Damping Matrices', *Journal of Numerical Methods in Engineering*, Vol. 4, pp. 5-10.

Part II: RC Walls

9 SEISMIC ASSESSMENT OF RC WALLS AFTER THE 27 FEBRUARY 2010 MAULE CHILE EARTHQUAKE

9.1 INTRODUCTION

On the 27th February 2010 a major earthquake struck central Chile. The seismic event was reported with epicentre offshore close to Constitución, in the Maule Region, about a 100 km away from Concepcion, the closest large city to the fault rupture. The seismic magnitude of the event (M_w = 8.8) is one of the largest established in the recent history of the country, after the Valdivia Earthquake in 1960 (M_w = 9.0). The event affected a large area of the country from Concepcion to Valparaiso on the coast, as well as other cities closer to The Andes, such as Santiago. In these cities, many mid-rise RC buildings were constructed from the 1980's until 2010. Field inspection revealed that most of RC buildings remained apparently elastic – with no apparent structural damage – whereas others suffered brittle failure modes especially in walls. The observed damage was characterized by a wide, inclined or horizontal, spalled/crushed area, as well as buckled vertical reinforcement in the free ends and web of the wall. Longitudinal reinforcement in walls ends was sometimes found fractured, after failing in tension following buckling and cyclic reversals from the ground motions (Bonelli et al. 2010, 2012a,b; EERI 2010, Cowan et al. 2011). The trend of a brittle failure mode indicates that the desired ductile inelastic mechanism was not ensured when the elastic limit was exceeded. Therefore a review of the current normative as well as the state of the practice in design was urgently acknowledged and implemented (INN 2010a,b).

The acceptance in code provisions of not-so-new methods such as direct displacement-based seismic design (Architectural Institute of Japan 1999, Priestley et al. 2007) may well be added to traditional force-based design methods, equally accepting them as valid. In this chapter, focus has been placed in philosophical aspects of the Chilean NCh433 Code (INN 1996) and the ACI318 seismic provisions approach (ACI Committee 318, 2011) for designing RC structures. Chilean design spectra are compared with pre-2010 recorded data, and the data recorded motion during the Michoacán Mexican earthquake (EEFIT, 1986). This was done with the intention of making an evaluation of the scenario after the 27 February 2010 earthquake, regardless of the ground motion recorded during that particular event. This brings back to the basic principles of vulnerability and structural weaknesses of these wall systems being independent from the seismic hazard. The risk of failure would of course depend on the intensity and characteristic of the input motion, but the potential failure modes are inherent characteristics of the systems, dependent only on the design principles and structural details.

The logical approach used for addressing the problem is: (a) description of the design method used, (b) a priori (pre-event) discussion on reinforcement detailing and numerical simulation of an ideal building, (c) empirical evidence from real post-earthquake inspection, and (d) a posteriori discussion on the observed damage pattern and speculative explanations for the inelastic mechanics behind it.

9.2 A REVIEW OF THE PRE-2010 CHILEAN SEISMIC PRIVISIONS APPLIED TO RC BUILDINGS

The seismic code NCh433-1996 (INN 1996) without modifications was mandatory for the seismic design until 2009 in Chile, when minor modifications were introduced after the Nch430-2008 Chilean concrete standard (INN 2008) became the official document for the design of RC structures (Nch433-1996mod2009). The ACI318-95 code was required for design of RC structures in NCh433-1996 appendix B until 2009. In the NCh430-2008 code the ACI318-2005 document was adopted as the basic document to follow, with some differences based on the local experience. Amendments for the seismic design of RC walls were urgently introduced after the 2010 Maule earthquake in the light of the brittle nature damage observed in several RC walls (Bonelli et al. 2012a,b, Massone 2013). That failure mode refuted conjectures about the non-necessity of special confinement elements in structural walls made after the 1985 earthquake which somehow delayed the upgrading in the ACI318 version officially quoted by the seismic standard (Wallace and Mohele 1992, Wood 1991). Those were the supreme decrees DS60 (Decreto Supremo 60, 2011), and DS61 (Decreto Supremo 61, 2011).

The NCh433-1996 code required the use of a traditional elastic equivalent force-based design for buildings up to 6 floors, or a spectral modal analysis for all other structures. In the latter method, a complete quadratic combination method (CQC) is used for combining the actions corresponding to each relevant mode of free-vibration of the structure. The acceleration response spectrum had the shape of Equation 9.1, expression derived as a mean response spectrum from ground motion recorded during the 1985 Valparaíso earthquake and other earthquakes recorded overseas. This spectrum assumed a 5% viscous damping, and could be derived for four soil types, from rock to very soft - not liquefiable soil (Arias 1989, Riddell et al 1989, Hidalgo et al. 1993).

$$\alpha = \left(1 + 4.5\left(\frac{T_n}{T_0}\right)^P\right) \Bigg/ \left(1 + \left(\frac{T_n}{T_0}\right)^3\right) \tag{9.1}$$

$$S_a = \frac{IA_0\alpha}{R^*} \tag{9.2}$$

$$R^* = 1 + \frac{T^*}{0.10 \cdot T_0 + \frac{T^*}{R_0}} \tag{9.3}$$

The basic *elastic* acceleration spectrum α, had the shape of Equation 9.1. It is defined for three different hazard levels by means of different values for the nominal peak ground accelerations (PGA or A_0). This 'basic spectrum' is reduced for design purposes by the reduction factor R^*, obtained for the period T^*, the fundamental period of free-vibration in the direction of the earthquake excitation. The design acceleration spectrum is found from Equation 9.2, where, S_a = spectral acceleration; I = importance factor (1.0 for residential and commercial buildings); A_0 = soil effective acceleration (PGA); T_0, p = soil parameters used to define α (T_0 = 0.3 and p = 1.5 for soil II - typical); T_n = natural period of vibration; and R_0 = modification factor of the structural response.

Given Equation 9.3, the reduction factor *R** factor is related to a value R_0 towards which it asymptotically approaches. In NCh433Of96 it is stated that R_0 'reflects the characteristics of the earthquake resistant structure in absorbing and dissipating energy', as well as 'experience about the seismic performance of different structural typologies and materials' (INN 1996). As a consequence, one may wonder why the same value of R_0 = 11 is assigned to different structural typologies such as RC walls, frames and dual system buildings, as well as for steel buildings.

The resulting forces from the elastic modal analysis after the *CQC* combination are limited in terms of base shear by means of minimum and maximum values (Q_{min} and Q_{max}, respectively), which depend on the weight of the structure (P), soil type, and hazard zone, defined in Equations 9.4 and 9.5.

$$Q_{min} = IA_0P/6g \tag{9.4}$$

$$Q_{max} = 0.35\, I\, S\, A_0/g \quad (for\ RC\ wall\ buildings) \tag{9.5}$$

In Equation 9.4, g is the acceleration of gravity, and all other parameters were defined previously. In Equation 9.5, the additional parameter S is a factor that depends on the soil type. For a soil type II in the NCh433Of.96 defines S = 1.0. For a softer soil type III, for example, S = 1.2. The minimum and maximum base shear requirements lead to very similar seismic equivalent loads to those required by the 1972 Chilean Seismic Standard (INDITECNOR 1972).

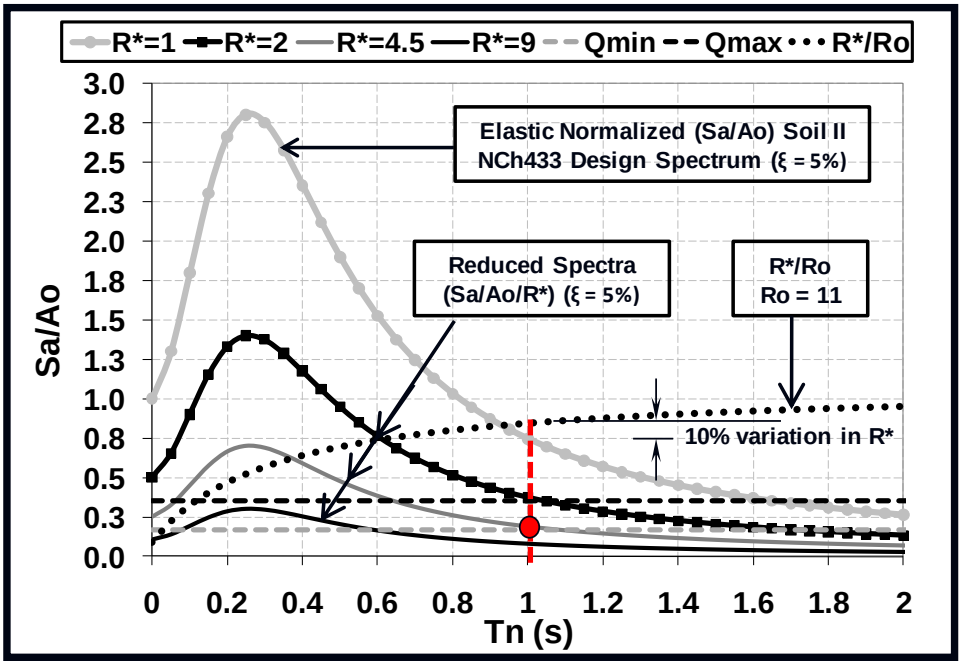

Figure 9.1: NCh433-1996 design spectra and the reduction factor *R*.*

In Figure 9.1, the elastic (not reduced) and reduced spectral accelerations for a SDOF system required by the NCh433Of.96 code, normalized by A_0 (PGA) for a soil type II and a coefficient of importance I = 1.0, are plotted against the natural period of vibration of several oscillators. This is done with the intention of placing focus on the dynamic

amplification factor (DAF) in the system relative to the ground motion. For an oscillator with a period of vibration T_1 = 1 sec, the elastic ordinate is 0.8. For that period, R^*/R_0 = 0.9. For R_0 = 11, the reduction factor required to obtain the design DAF is 9.9. That is, the design DAF is 0.8 times 9.9 equal 0.08.

If Equation 9.4 is rearranged to provide a dimensionless number $Q_{min}\ g/(P\ A_0)$ = 0.167, the corresponding value in the ordinates of the graph shown in Figure 9.1 can be plotted. Now for that value to be achieved in the design value, the compatible spectrum in terms of amplitude corresponds to the elastic one divided by a factor R^* = 4.5. The design DAF would then be 0.167, as well as for all other oscillators with periods lager than 1 sec. An additional factor required for the design of structural members is γ_E = 1.4. Hence the SDOF oscillators would be design with the same seismic force equal to 0.23 the seismic weight of the building. This is representative of a large amount of buildings in Chile constructed before 2010, whose fundamental periods range can be roughly evaluated with the following range of periods: $T_1 = N/15$. For 12-storey buildings $T_1 \approx 0.8$ sec. and for 15-storey building $T_1 \approx 1$ sec, and thus the comments done on the SDOF stand for these wall buildings, acknowledging the simplistic approach for comparing a building with a SDOF system.

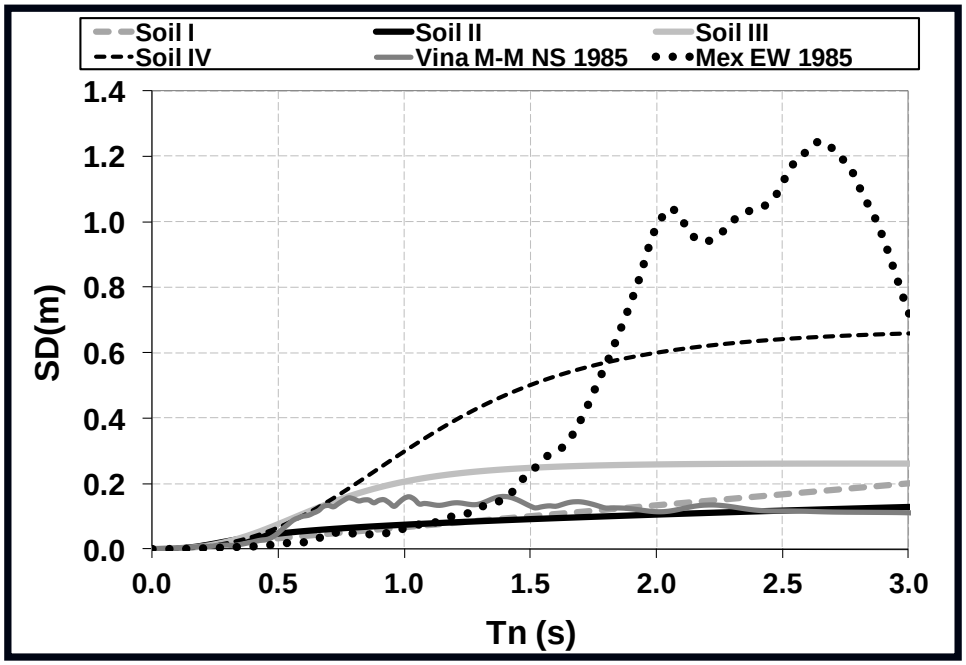

Figure 9.2: NCh433-1996 equivalent displacement design spectra compared with spectra from 1 ground motion recorded in Chile (1985) and 1 recorded in Mexico (1985).

In Figure 9.2 and Figure 9.3, design displacement and acceleration spectra are plotted for different soil types and are compared with spectra derived from pre-2010 ground motions recorded during the Valparaiso (Chile 1985) and Michoacán (Mexico 1985) earthquakes. These ground motions were recorded at stations Marga-Marga and SCT respectively. According to the displacement spectrum for SCT station record, SDOF oscillators would be subjected to significantly larger displacement levels for natural periods of free-vibration in the range of 1 to 2 seconds. On the other hand, less demanding spectral ordinates correspond to data recorded at the Marga-Marga station, being about two times greater than the equivalent - not reduced soil II spectrum, for natural periods in the range

of 0.6 to 1.2 seconds. However, the elastic response spectrum for soil III represents an envelope for the latter. In the case of the SCT ground motions, the soil III design spectrum for natural periods greater than 1.8 seconds is noticeably lower than the derived spectrum. This is also reflected in the comparison of the acceleration spectra (Figure 9.3).

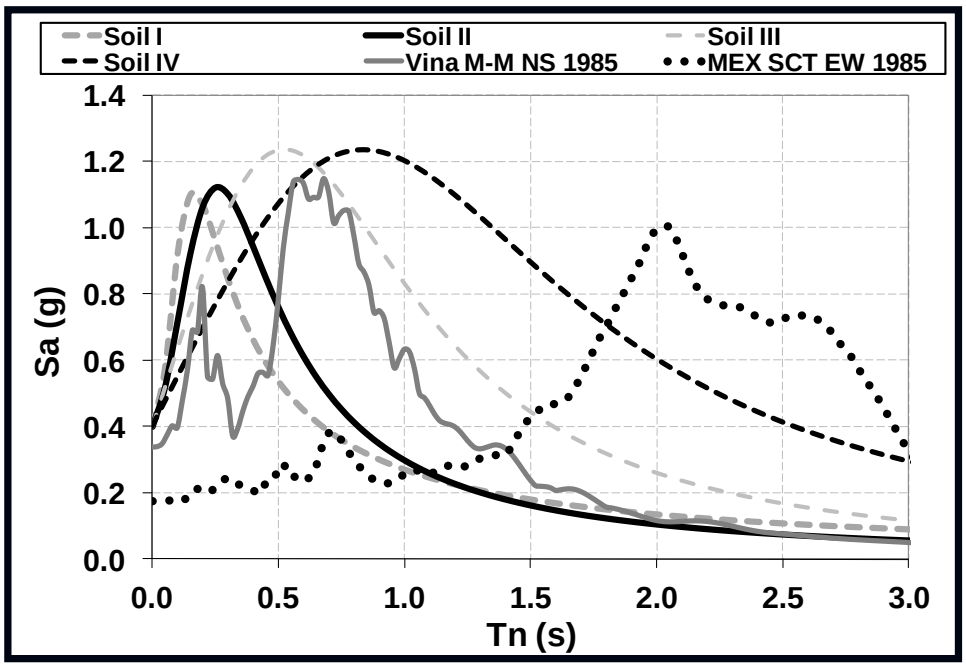

Figure 9.3: NCh433-1996 design spectra compared with spectra from 1 ground motion recorded in Chile (1985) and 1 recorded in Mexico (1985).

Based on the observations of this section, it is postulated that these code requirements (1) underestimate the displacement spectral demand; (2) deals with the serviceability limit state only; and (3) implicitly relies on the material code provisions to ensure the achievement of the desired ultimate ductility capacity.

9.3 THE ACI318-2005/2008 SEISMIC PROVISIONS FOR RC STRUCTURAL WALLS AND ITS USE IN THE CHILEAN PRACTICE

For the seismic design of RC structures, Chile has traditionally used the ACI318 document. In NCh433-1996, the use of the 1995 version of this code was mandatory in the absence of an official RC national code. This is regardless of the fact that substantial modifications were introduced which aimed to improve Chapter 21 seismic provisions in the 1999 version. Only when the Chilean NCh430-2008 code was made official, the use of ACI318-2005 guidelines was incorporated, making it the basis of the new NCh430 official regulations for RC structures with some specific modifications for the seismic design of walls (Bonelli et al 2012b).

In previous work done by Quintana-Gallo (2008), an ideal 12-storey RC dual system building with T-shaped walls was designed using the Nch433-1996 seismic code and ACI318-2005 RC recommendations (see Figure 9.4). However, some additional considerations for the effective flange length were adopted from well-established books

(Paulay and Priestley 1992), and more recent experimental evidence (Thomsen 1995, Thomsen and Wallace 2004). This was done in the absence of clearer guidelines for the design of asymmetric walls in the ACI318-2005 seismic provisions. According to Paulay and Priestley (1992), the effective flange length can be estimated to be about 45% of the wall length in the horizontal-vertical plane of the plastic zone region. Thomsen (1995) found in experimental studies on 1/4 scale T-shaped walls, that the length of the effective flange (based on the strain profile in the flange) depends on the top drift level, being fully effective at a maximum reached top drift of 2.5% when the wall reached failure.

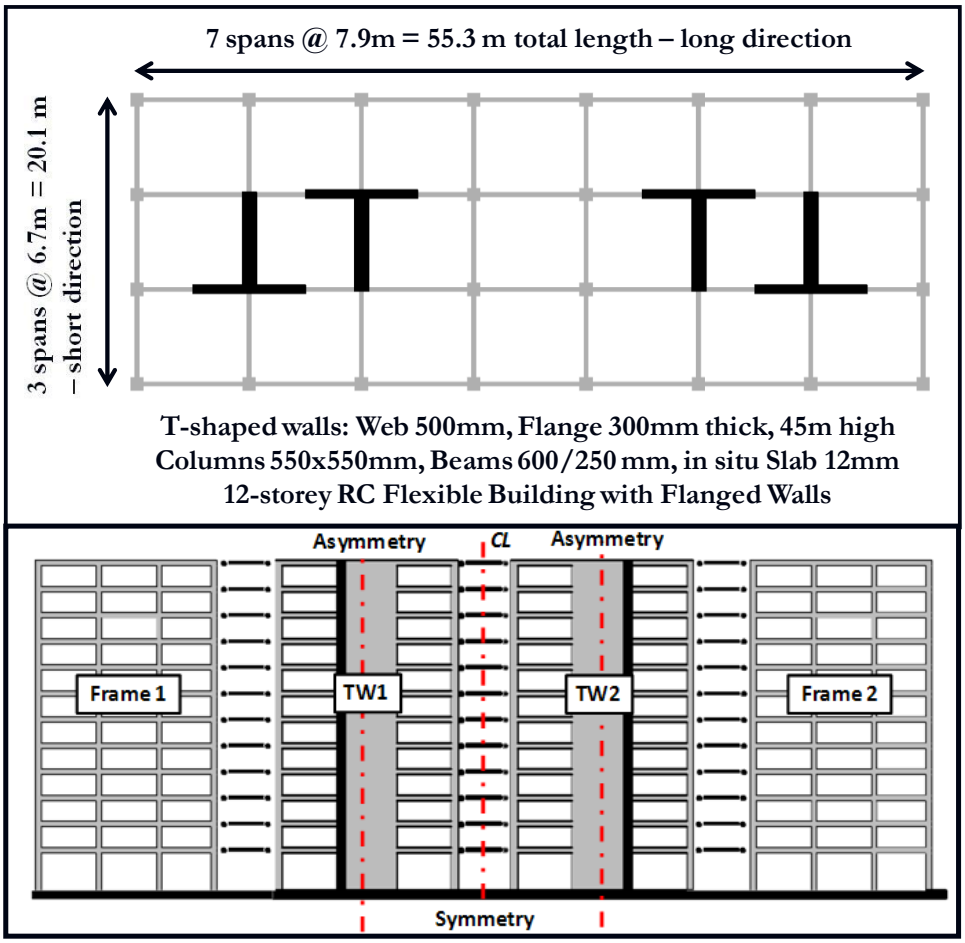

Figure 9.4: Plane view of a 12-storey RC dual system building with T-shaped walls designed with NCh433 seismic code and ACI318-2005 seismic provisions (Quintana-Gallo 2008).

As a consequence, in the calculations for the example shown herein (Quintana-Gallo 2008) T-shaped walls required the use of heavy especial boundary elements in the free end of the web. Whether or not to use these special elements, according to ACI318, is related to the value of the neutral axis (c_u) at the ultimate top displacement level of the wall (δ_u), a value to be the one dictated by the corresponding seismic code of the region where the structure will be constructed, with a minimum of 0.7% times the wall height. If the calculated value of c_u is larger than a critical value c_c, then the use of special boundary elements (SBE) is mandatory. If not, a minimum confinement based on allowable stresses can be used, leading to lightly confined walls in general. Plan dimensions for SBE in this example are shown in Figure 9.5. The height is calculated as the larger value of the wall length (l_w) and a quarter of the height of the shear force resultant from an elastic analysis

at ultimate combinations (M_u/V_u), whereas the length inside the wall cross section is calculated as the larger of $c_u - 0.1 \cdot l_w$ and $c_u/2$.

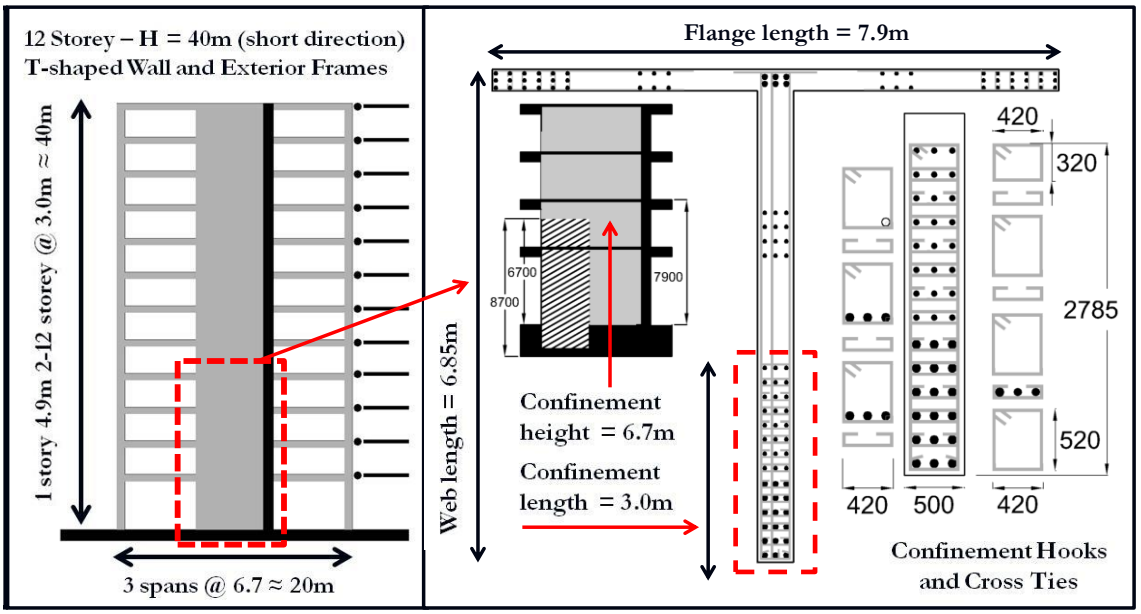

Figure 9.5: T-shaped wall design with NCh433 and ACI318-2005 (from Quintana-Gallo 2008).

In the critical section of the wall, the length of the SBE represents all the compressed area at the ultimate displacement minus 10% of the wall's length. It can be demonstrated that the critical value for the neutral axis at the ultimate state corresponds to a maximum strain in the concrete of $\varepsilon_{cu} = 0.003$, if the plastic hinge length is taken as $l_p = l_w/2$. Therefore, strains greater than the nominal ultimate value in the concrete are tacitly accepted, without the requirement of explicit calculations for the real maximum strain in the confined concrete. For the T-shaped wall used in the example, strains in the concrete as large as 0.01 would be required to be able to develop in the extreme compressed fibre in the web according to sectional analysis, for large displacement (ductility) demands. On the other hand, when the wall acts with the flange in compression, due to the low neutral axis depth required for balancing the tensile force from longitudinal reinforcement in the web, the ultimate nominal strains in the steel will govern the design ($\varepsilon_{su} = 6\%$) (Paulay and Priestley 1992).

Some drawbacks of ACI318 seismic provisions for RC walls can be taken as the lack of:

(1) capacity design for shear;
(2) explicit axial load limitation for ensuring rotation ductility capacity;
(3) a more direct displacement-based procedure for estimating the required confinement in boundaries;
(4) special considerations for asymmetric or flanged walls; and
(5) the use of transverse cross ties and/or hooks all along the web.

From these, the indirect displacement based approach for designing SBE is seen as step forward from the older editions of the same document, which can be further refined by defining a ultimate top displacement related to strain limits in both the concrete and the

steel, which is a special feature of the amended NCh430 code modified in 2010, after the Maule earthquake (Bonelli et al 2012a,b).

9.4 NUMERICAL SIMULATIONS OF THE RESPONSE OF A 12-STOREY PROTOTYPE RC BUILDING WITH A DUAL SYSTEM STRUCTURE

In Quintana-Gallo (2008), a finite element model using lumped inelasticity macro elements was implemented in Ruaumoko2D (Carr, 2008a,b) in order to estimate the building response in the short direction. The SINA hysteresis rule (Saiidi and Sozen 1979) was used for modelling the walls, since it allows for different stiffness and strength depending on the direction of movement, and includes pinching for representing shear interaction as well as Bauschinger effects. In Quintana-Gallo (2008), five different records were used as input for a series of inelastic time history numerical simulations. From those, earthquake ground accelerations recorded at the Marga-Marga station during the 1985 Valparaiso Earthquake (MM1985) and at the SCT station during the 1985 Mexican Earthquake (SCT1985) were selected for the purposes of this chapter. The selected acceleration records, shown in Figure 9.6, are used for illustrating that the difference in the characteristics of the ground motion in terms of predominant frequency and amplitude of the response spectra can alter significantly the expected response, regardless of the PGA.

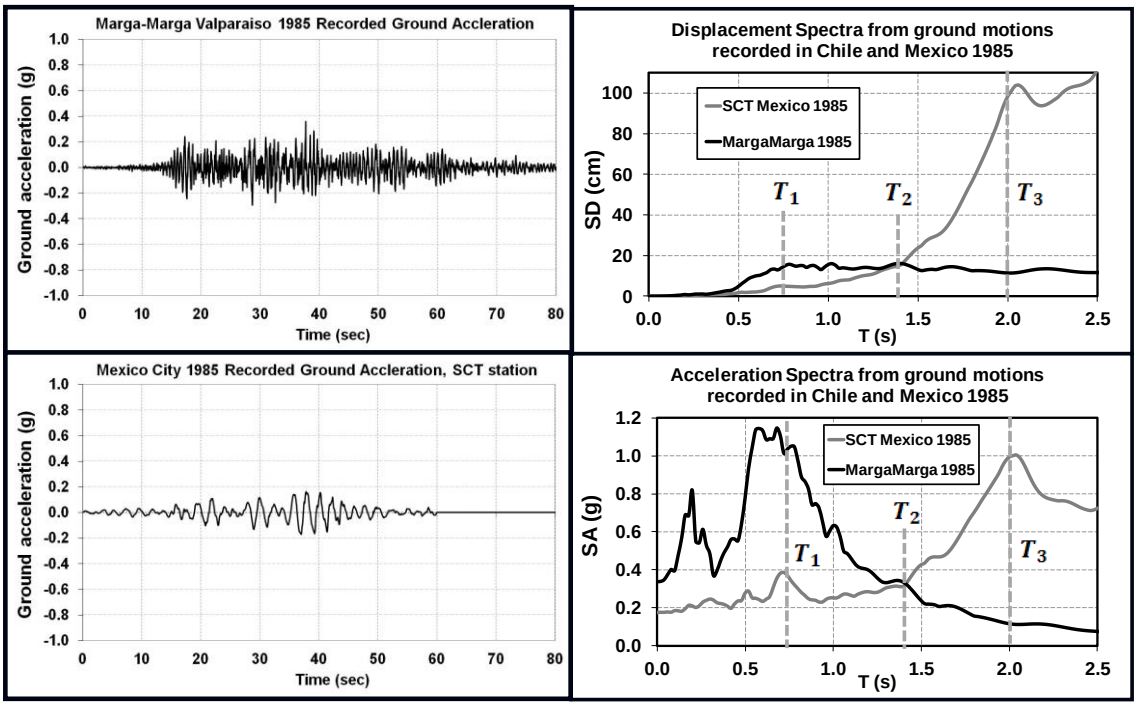

Figure 9.6: Ground motion recorded in MM1985 station (Valparaiso 1985); ground motion recorded in SCT1985 station (Mexico City 1985); displacement and acceleration response spectra.

Global dynamic responses of the model are presented in terms of top drift time-histories, whereas local counterparts at the base of T-shaped walls are shown in terms of moment-curvature diagrams. As shown in the graphs of Figure 9.7, it was predicted that the T-shaped walls would suffered much larger inelastic incursions (damage intensity) under

SCT1985 record. Under the MM1985 record, on the other hand, a fairly elastic behaviour was predicted. This last prediction is in line with inspections after the 1985 Valparaiso earthquake, where only few middle-rise buildings were damaged. When SCT1985 record is used as the input motion, the predicted response at the base of T-shaped walls reached curvature levels of 0.003 1/m in both directions (AT and AC), due to the symmetry of the plan layout of the walls (see Figure 9.4). This curvature corresponds to approximately 1.5% drift at the top of the building following the traditional analytical plastic hinge method for cantilever walls (Paulay and Priestley 1992, Wallace and Mohele 1992). The target curvature is defined as that consistent with a 1.5% top drift in the wall. When running the MM1985 record, curvature levels are predicted to be, in general, below the smallest yielding curvature (AC), corresponding to the flange acting in compression (Priestley et al 2007).

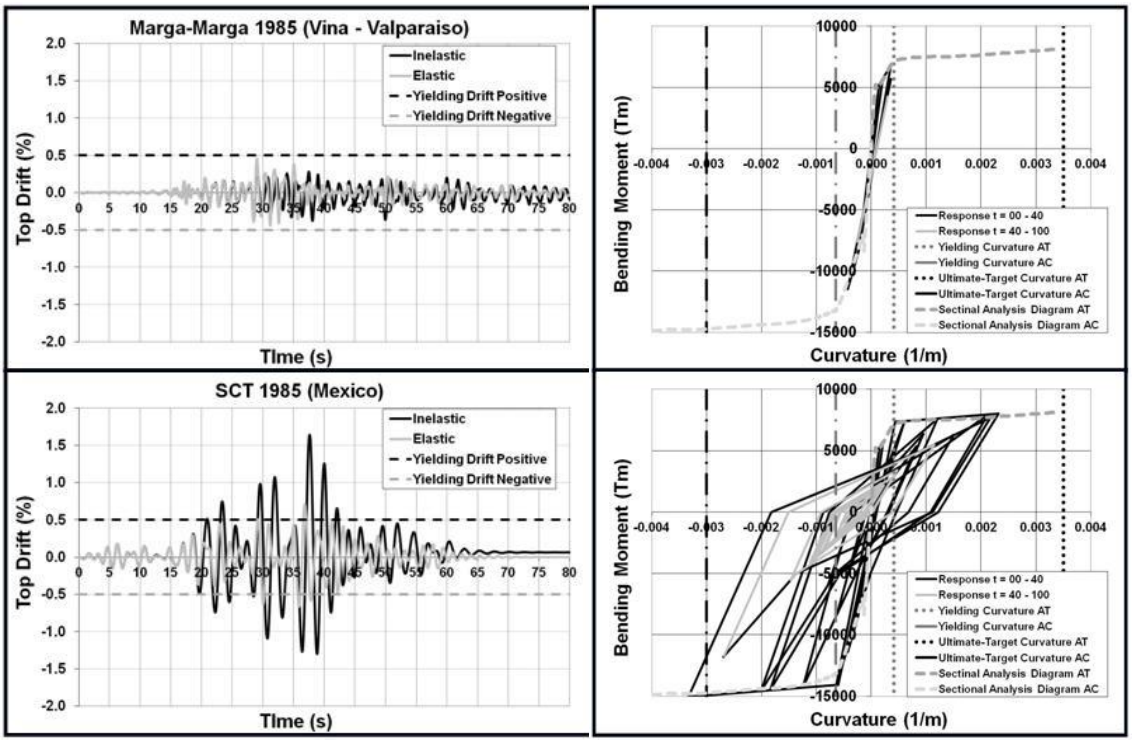

Figure 9.7: Building time-history numerical simulation using MM1985 and SCT1985 records: left: top drift in time (elastic and inelastic); right: moment curvatures in the base of the left side wall.

The predicted global response using elastic properties in the plastic hinge of the wall elements varies significantly from those predicted using inelastic elements. In the elastic case, the response in terms of top drift under SCT1985 ground motion does not exceed 0.5% top drift at all times, significantly smaller than the 1.5% peak value predicted for the inelastic case. Also note that in this last case, the number of cycles at high ductility demand levels and the low energy dissipation capacity due to stiffness degradation is predicted to be quite high. This is equivalent to an increase in the 'transient inelastic period' of the structure, as a consequence of a progressive reduction of the system stiffness. This loss of stiffness is related, at least, to the amount of inelastic cycles experienced, which in turn is related, at least, to the duration of the ground motion with high displacement demands. All these are disregarded when using elastic elements.

The intension of showing the numerically simulated response using ground motions recorded before 2010 is to show that the characteristics of the response of a nonlinear system can differ significantly from earlier observations. After the 1985 Valparaiso earthquake in Chile, where the response of RC buildings was more than satisfactory, little attention was placed in predictions for the eventual response of those buildings (or new ones) under the excitation of ground motions with different frequency characteristics, signal shape, and duration.

Using this numerical example, it was shown that if a ground motion similar to SCT1985 was to occur, then both global and local responses in the building would differ largely from those predicted using ground motions recorded during that earthquake in 1985. Therefore, a fallacy can be identified in the sense of tacitly accepting that in the future the seismic demand in a certain location will be similar enough to those recorded before at the same or nearby location. This was the case of Chile, when fairly similar spectral demands to those corresponding to SCT1985 were seen 25 years after the 1985 Valparaiso earthquake. The observed damage intensity in the earlier Chilean earthquake resulted in excessive confidence in the adequacy of code provisions. This was also the case in New Zealand after the September 2010 Darfield earthquake, which caused little damage intensity in engineered RC buildings. However, in this case, confidence lasted only 6 months, until the 22 February Canterbury with a smaller magnitude severely affected RC buildings.

9.5 OBSERVED DAMAGE IN RC WALLS AFTER THE 27 FEBRUARY 2010 MAULE CHILE EARTHQUAKE

The inspection of damaged RC structures was done immediately after the earthquake occurred. Many walls in RC buildings were damaged by developing a brittle failure mode, illustrated in detail in the following sections using pictures from buildings located in Concepción and Viña del Mar. This suggests that the brittle failure mode constituted a pattern. The failure mode was characterized by a large spall crushed areas with buckled longitudinal reinforcement along the web, and the longitudinal steel, after buckling, was sometimes fractured in the wall ends. In the absence of special boundary confinement in the form of horizontal closed stirrups and crossed ties, as well as 90° end hook anchorage of the shear horizontal reinforcement this can be expected.

Walls developed a continuous horizontal crushed area in the first floor, with buckling of the longitudinal reinforcement all along the web length. This has been thought to be an indication of high axial load due to the observed compression-like damage pattern. Large vertical accelerations may have been also influential, but is out of the scope of this discussion. Under high levels of axial load and the absence of special boundary elements (SBE), the concrete can spall at relatively low top floor displacement levels. Furthermore, the concrete cannot withstand higher strains without crushing at all when experiencing nonlinear dynamic reversals. Buckling is enhanced in vertical reinforcement due to the absence of lateral restraint as well as by initial compression coming from gravitational and additional seismically induced axial strains.

Flanged or *asymmetric* walls experienced a similar, but not identical, damage pattern to that in rectangular walls. The crushed area diminished in size near the flange and was more severe at the free ends. The crushed area (wide-crack) was inclined following an

ideal diagonal compression field or strut which carries the shear component of the seismic action. This may indicate that shear interaction could have been more influential in this case due to the high bending capacity of the asymmetric walls when acting with the flange in tension. At the same time, steel elongation in the web is especially enhanced in free ends of the walls, since, in typical cases, the neutral axis required to balance the tensile forces from in the web is rather small at the ultimate limit state.

Figure 9.8: Building 1 (12-storey, Viña del Mar): (a) west façade; (b) picture of the building south-west corner at ground floor level – indication of damage in the north facade; (c) ground floor plane layout – critical walls identification for other pictures (adapted from Bonelli et al. 2012a).

In Figure 9.8, two pictures and the ground floor plane layout of a 12-storey building constructed in Viña del Mar are presented (Building 1). In Figure 9.8 (a) a picture of the west façade of the building and in Figure 9.8 (b) a picture of the north-west corner of the building at ground level are presented, respectively. In those picture, it can be observed that the building is leaning towards the north (see Figure 9.8 (c) for orientation). The rectangular wall right in the corner shows a significant vertical shortening, as a result of a heavy compression-dominated failure shown in detail later. In Figure 9.8 (3) the structural layout of the building is presented (adapted from Bonelli et al. 2012a). As discussed in Wallace et al. (2012), the wall layout is representative of the typical configuration found

in Chilean buildings, where asymmetric walls are located with their flanges in the centre part of the plane creating a corridor, whereas the web of the walls are used as a separation for the rooms inside apartments or offices. That is a fish-bone like layout.

In Building 1 most of the walls of the north façade developed a continuous horizontal crushed area in the first floor, with buckling of the longitudinal reinforcement all along the web length (see Figure 9.10(a)). This has been thought to be an indication of high axial load due to the observed compression-driven damage pattern. Under high levels of axial load and the absence of special boundary elements (SBE), the concrete can spall at relatively low top floor displacements. Furthermore, the concrete cannot withstand higher strains without crushing at all when experiencing nonlinear dynamic reversals. Buckling is enhanced in vertical reinforcement due to the absence of lateral restraint as well as by initial compression coming from gravitational and additional seismically induced axial strains (coupling effect induced by the slab). That failure mode can be clearly observed in the pictures of Figure 9.9, where the heavy damage developed in walls RW1 and LW1.

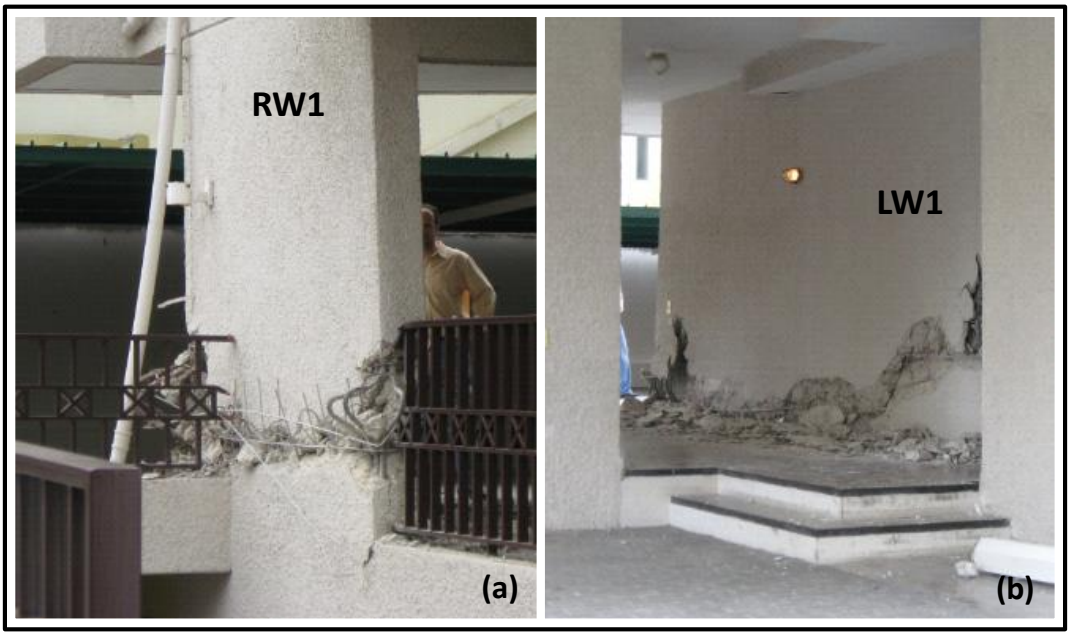

Figure 9.9: Building 1: (a) Rectangular wall (RW1) subject to high gravity load showing a brittle failure mode along the entire web; (b) L-shaped wall located on the east side of RW1 showing a compression governed failure mode in the entire web.

In Building 1, flanged or asymmetric walls experienced a similar, but not identical damage pattern to that observed in rectangular walls. The crushed area diminished in size near the flange and was more severe at the free end(s) of the wall. The crushed area (wide-crack) was inclined following an ideal diagonal compression field or strut which carries the shear component of the seismic action. This may indicate that shear interaction could have been more influential in this case due to the high bending capacity of the asymmetric walls especially when the flange acts in tension. At the same time, tensile strains in the steel of the web can be particularly large in the free end of the walls, since, in typical cases, the neutral axis required to balance the tensile forces associated to those strains is rather small at the ultimate limit state (Thomsen 1995; Thomsen and Wallace 2004; Quintana-Gallo 2008; Wallace et al. 2012; Massone 2013).

Figure 9.10: Building 1: (a) damaged walls in the ground floor north façade; (b) RW3 from the west; (c) RW1 from the north-east – severe buckling and complete crushing along the entire web; (d) TW1 from the north-east; (e) close up of the heavily buckled reinforcing bars at the free end of TW1.

In order to illustrate that fact, in Figure 9.10 pictures of the most damaged part of the building are presented. In the picture of Figure 9.10(a), the damage experienced by the five walls identified in Figure 9.10 (a) is shown. From that picture and the other in the same figure, it is clear that the walls failed to achieve a ductile behaviour. The extensive crushing of the concrete and the severe bucking in the most axially loaded rectangular wall (RW1) can be further appreciated in Figure 9.10(b). In Figure 9.10(c) a picture of the rectangular wall RW3 is shown. The failure mode experienced by that wall is similar to the one developed in RW1, but the intensity of the damage is not as severe. In Figure 9.10(d), a closer view of the damage developed in TW1 is shown. It can be observed that in this case the crushed region in the web of the wall was not horizontal as in the case of rectangular walls, but it was inclined following a diagonal oriented in the direction of the

shear field in that part of the wall. Severe buckling of the longitudinal rebar was observed at the free end of the web and developed in the top part of the ground floor instead of the bottom. That is the opposite of what occurred in the rectangular and L-shaped walls damaged in the same building. In Figure 9.10(e) a closer view of RW1 is shown. The picture reveals that large diameter longitudinal bars were used at the free end of the wall, and that they were restricted laterally by small diameter horizontal rebar only, with poor anchorage and designed to resist the shear action (not confinement). The diagonal orientation of the crushed area in the web of TW1 shows that shear forces and deformations may have been considerable in this particular case and might be an indication of the relevance of that action in the failure mode observed (Thomsen 1995; Thomsen and Wallace 2004; Beyer et al. 2008, 2011; Dazio et al. 2009).

In Figure 9.11, some pictures of the final state of the collapsed Building 2 located in Concepción are shown. The mechanics that led to the collapse of this structure are difficult to explain, due to the big amount of uncertainty involved in the problem, but the same vestiges of the survived damaged buildings (as in Building 1) are depicted in the photographs. Large cracks can be seen in the walls where the boundary was destroyed, showing signs of fracture in some bars, and in other cases elongated as in a monotonic tension test. For example, C-shaped walls failed completely in tension in the strong axis direction.

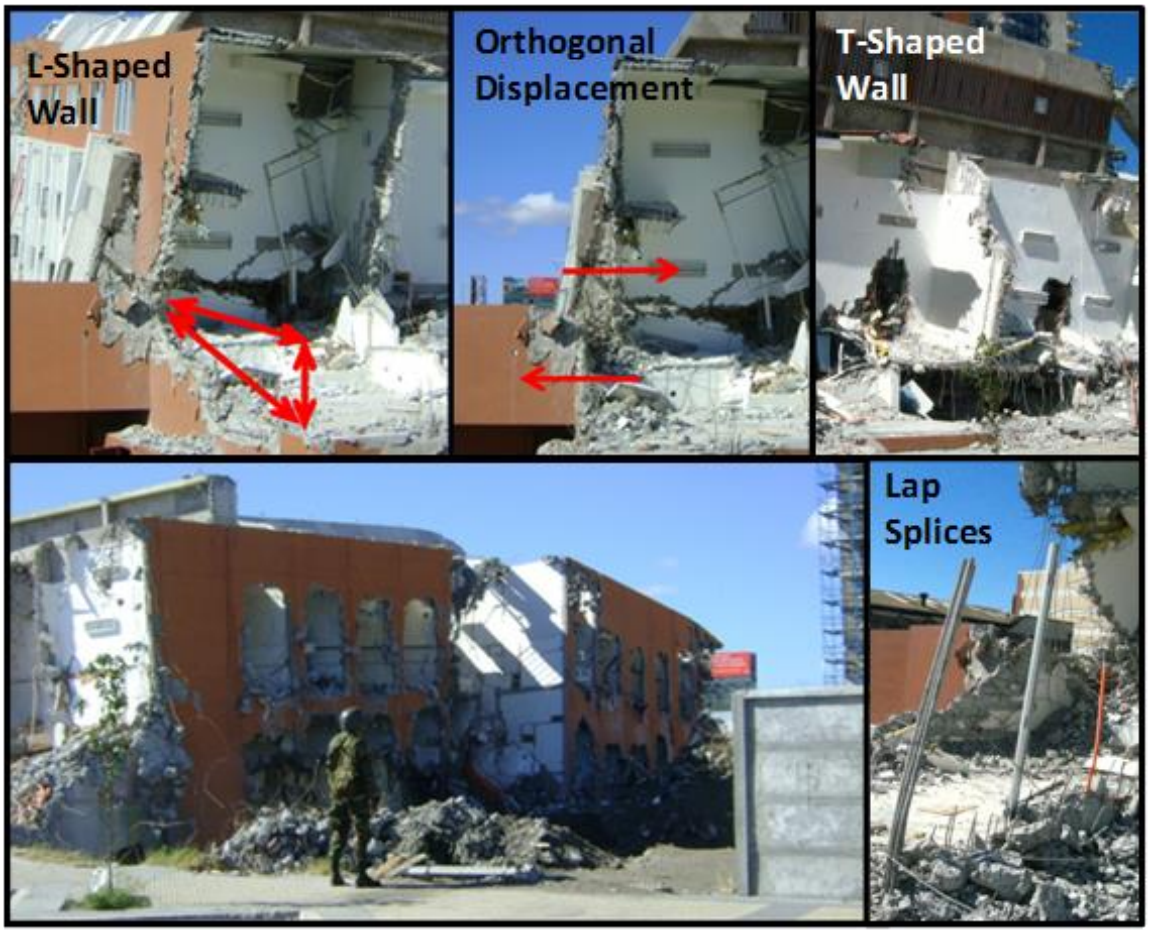

Figure 9.11: Overview of Building 2 (collapsed in Concepcion).

In Figure 9.12, pictures with two damaged walls in Building 3 are presented. Lack of special boundary elements is evident, as well as the inability of the thin horizontal reinforcement provided for shear to avoid buckling of the vertical rebar along the web. The wall shown in the bottom left developed a diagonal crushed area, revealing vestiges of shear interaction with bending-compression actions. Boundary longitudinal steel was found severely buckled and fractured in some cases, as can be seen in the pictures. The wall shown on the bottom right suffered severe buckling along the web as well as an out-of-plane lateral residual distortion.

Figure 9.12: Observed damage in Building 3: 12-storey building in Viña del Mar.

In Figure 9.13, pictures of a 14-storey building which had one of the largest damage intensities in the city of Viña del Mar are shown. This building, which was also damaged during the 1985 Valparaiso Earthquake (EEFIT, 1988), was repaired afterwards with adjacent walls which were not able to work properly during the 2010 seismic event (Cowan et al 2011, Bonelli 2012a). As observed in the pictures taken from the outside, wall ends were heavily damaged. Vertical reinforcement was not confined, and thin bars were used in horizontal mesh layers for shear resistance, which was improperly anchored into the concrete.

Other walls on the inside of the building shown in Figure 9.13 failed in the out-of-plane direction. Severe buckling was observed in the longitudinal bars, but in this case, both

layers were curved towards the same face of the wall. The wall shown in the centre-top of Figure 9.13 had been repaired before, by constructing an adjoining wall on the side. This repairing solution was not efficient in this case, and the new wall simply detached from the previously damaged wall. Moreover, the inner wall severely failed again with crushing and buckling all along the length, just as in the many others described before.

Figure 9.13: Building 4 (Viña del Mar): observed damage in walls of a 14-storey RC building.

Figure 9.14: Heavy SBE and web transverse hooks in the web of structural walls in a building under construction in 2010 in Viña del Mar – Building 5.

Figure 9.14 contains pictures of a new building under construction in Viña del Mar on May 2010. Close spaced horizontal hooks and cross ties were used for confining the wall ends, as well as cross ties along the web for providing a larger lateral restraint to the vertical bars. Also note the horizontal rebar for shear resistance is anchored around the extreme vertical steel bars on the opposite side of the mesh, with 135° end hooks.

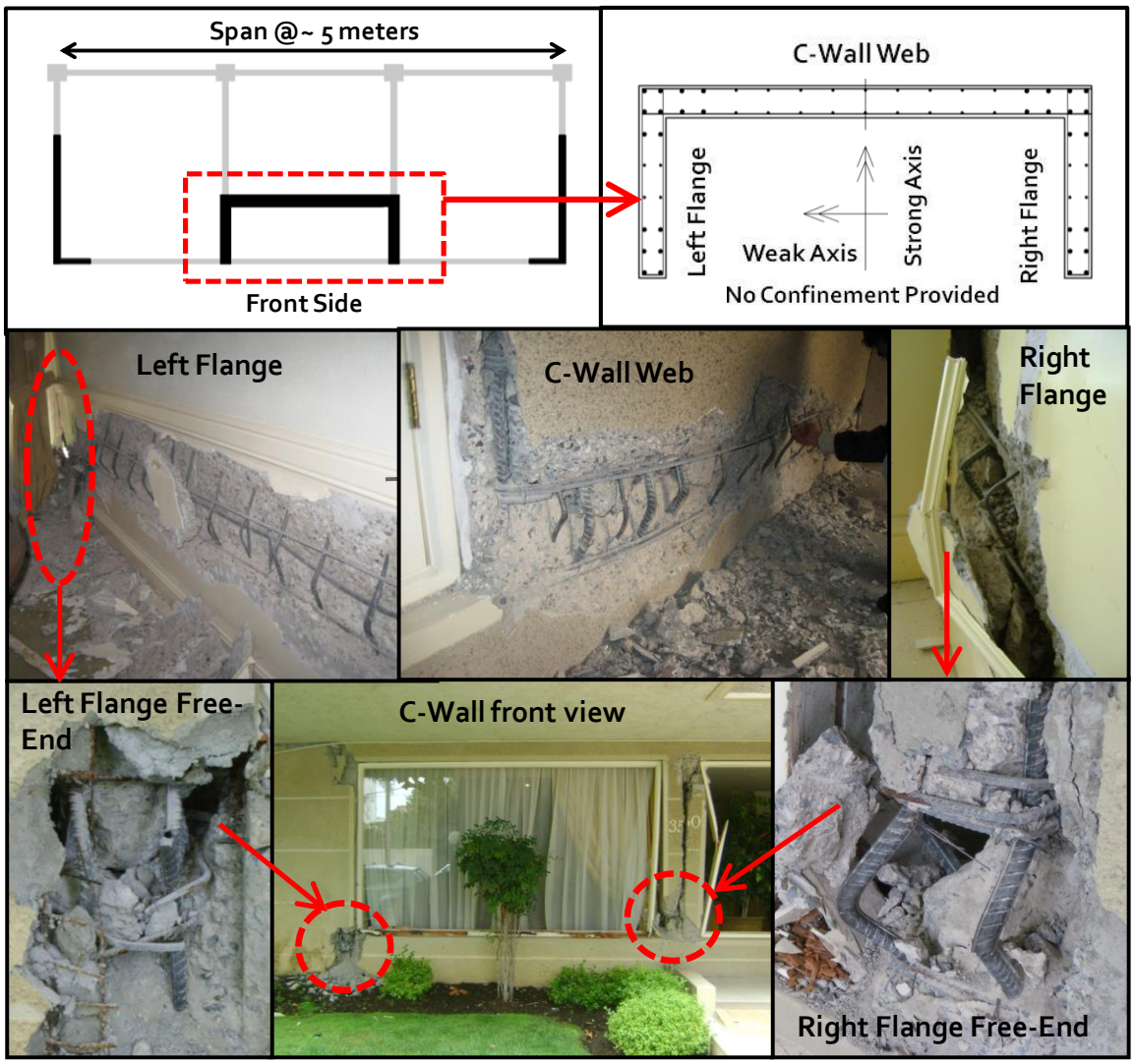

Figure 9.15: C-shaped wall in Building 6, Viña del Mar 12-storey residential building.

In Figure 9.15, a C-shaped wall of a 12-storey RC building in Viña del Mar is shown (Building 6). Crushing of the concrete and buckling in the longitudinal steel bars was observed all along the perimeter of the C. There were also some fractured longitudinal bars in free ends of both flanges. From the perspective of the wall acting about the weak axis, the unrestrained vertical reinforcement all along the C web is an indication that the free ends of the C flanges may have induced important level of compression strains in the flange.

However, for this to happen, the steel in the free ends of the flanges would need to experience significant elongation as a result of strain compatibility in a C section, where the neutral axis will be in or very close to the web at ultimate limit state. In the flanges of

the C-wall, a heavily crushed-buckled area reducing in size when approaching to the flange also indicates that the arms were compressed after some elongation in the steel. In addition, some of the vertical bars were found fractured in free ends of the flanges, indicating that they were most probably subjected to intense elongation-buckling cyclic actions.

From the perspective of wall reacting about the strong direction, due to symmetry, strain compatibility in the section of the wall would be equivalent to that corresponding to a rectangular wall. Therefore, important compressive strains can be generated along the whole compressed flange of the C-wall for equilibrating the high tensile forces developed in the steel of the opposite flange. The web would be expected to experience also important strains by analogy of what was observed in the web of rectangular walls, further enhanced by a relatively thin web withstanding large forces induced by the flanges. Due to the 3D characteristics of the movement, the effects separately described before for weak and strong axes, a combination of both effects should be taken into account. There are also possible vertical acceleration effects which are beyond the scope of this chapter (Bonelli et al 2012b).

9.6 DISCUSSION ON THE MECHANICS BEHIND THE OBSERVED FAILURE MODE IN RC WALLS

The damage pattern corresponding to the brittle failure mode observed in field inspections was characterized by:

(1) a large spalled crushed areas along the webs of the walls,
(2) buckling of the longitudinal reinforcement, in both boundaries and webs,
(3) in some cases fracture of previously buckled boundary bars, and
(4) in some cases, out of plane failure.

This damage patterns are slightly different for rectangular and asymmetric walls. In the rectangular walls inspected, when the brittle mode was observed, the crushed area was almost horizontal, with severe buckling extending along the web length. In the case of most of flanged walls, the damage was strongly concentrated in the free ends, and an inclined crushed area developed towards the orthogonal wall intersection, following the compression strut direction. Pure shear failures were observed in a few asymmetric walls, whereas shear-flexure interaction effects were observed in both wall types.

9.6.1 Asymmetric Walls

The nominal yielding curvature for asymmetric walls acting with the flange in compression (AC) has been recognized to be smaller than the nominal yielding curvature of the same wall acting with the flange in tension (AT), as shown schematically in Figure 9.16 (Priestley et al 2007). As a consequence, in displacement based seismic design, the displacement profile at yield for AT would be greater in magnitude when compared to the yielding displacement profile for AC. In Figure 9.16, yielding and design displacement profiles are plotted for a typical asymmetric wall (T, L, C – shaped) acting in both directions (AC and AT), following procedures well established in literature (Priestley 2003, Priestley et al 2007).

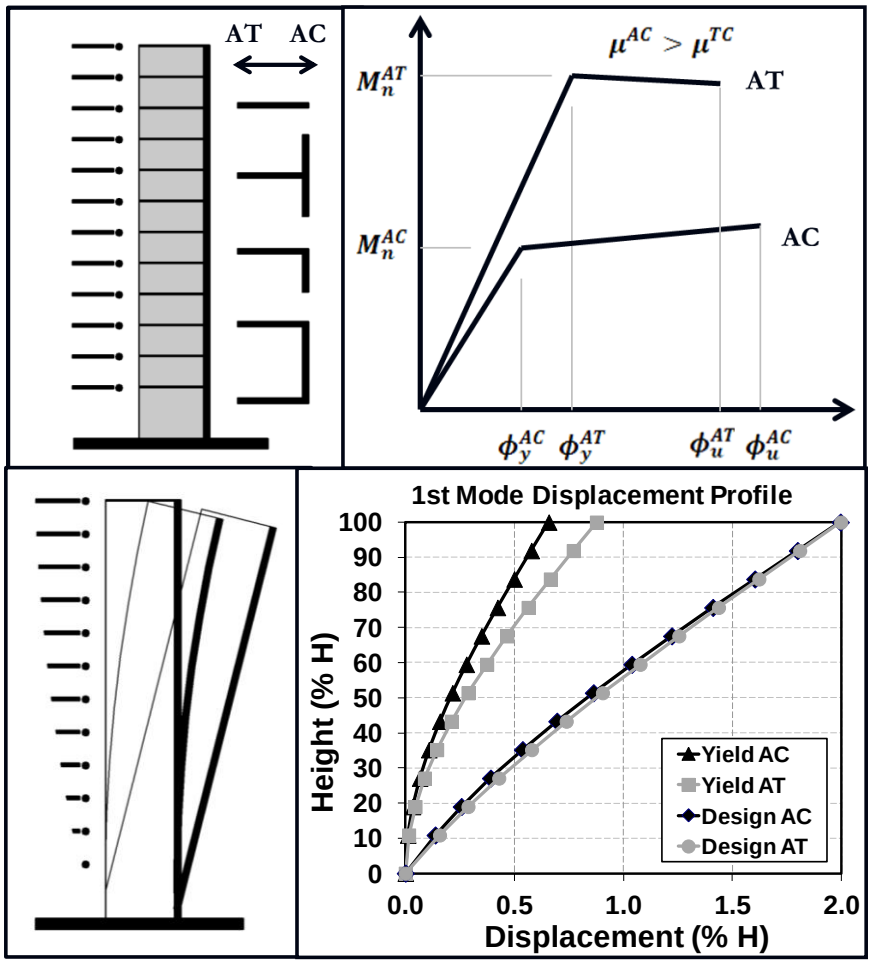

Figure 9.16: Inelastic moment- curvature and displacement profiles for asymmetric walls (following design formulations from Priestley et al. (2007).

As displacements can be larger than nominal yielding values for AC and at the same time smaller than the nominal counterparts for AT, it is theoretically possible that asymmetric walls may experience inelastic incursions in one direction only. In that scenario, the longitudinal reinforcement in the free ends of the walls would be able to yield in tension and subsequently buckle in compression before any inelastic incursion occurred in the opposite end (flange). In addition, for the AT case it would be more difficult to develop high tension strains beyond yield in the steel, considering that the strain profile is not constant along the flange, and that it depends on the displacement level. In repeated cycles then, it would be theoretically possible to keep opening a an opened crack in the free end of the web, stretching more longitudinal bars into yielding towards the flange, until an eventual fracture of the edge rebar is reached, all before any yielding strains are experienced in the flange acting in tension. As a consequence, it would be theoretically valid to expect larger inelastic curvatures when AC than when AT, which implies the development of larger cracks in the free end of the web when compared to cracks forming in the flange, if they develop at all.

In the experimental work carried out by Thomsen (1995) at Clarkson University (Postdam, New York), two 1/4 scale T-shaped RC walls were tested under quasi-static unidirectional loading protocol at increasing top displacements. Specimen geometry, longitudinal reinforcement, and SBE are very similar, in a scaled-down fashion, to those

corresponding to the T-shaped walls used for the numerical example. Experimental results revealed that specimen TW2 (referred to here as 'ductile') reached yielding in the AT direction at about 0.7% top drift (DR_y^{AT}), with tensile strains concentrated in the flange-web intersection. Similarly, in the AC direction, yielding was reached at about 0.5% top drift (DR_y^{AC}), with a large number of reinforcing bars elongated beyond the yielding tension strain along the web.

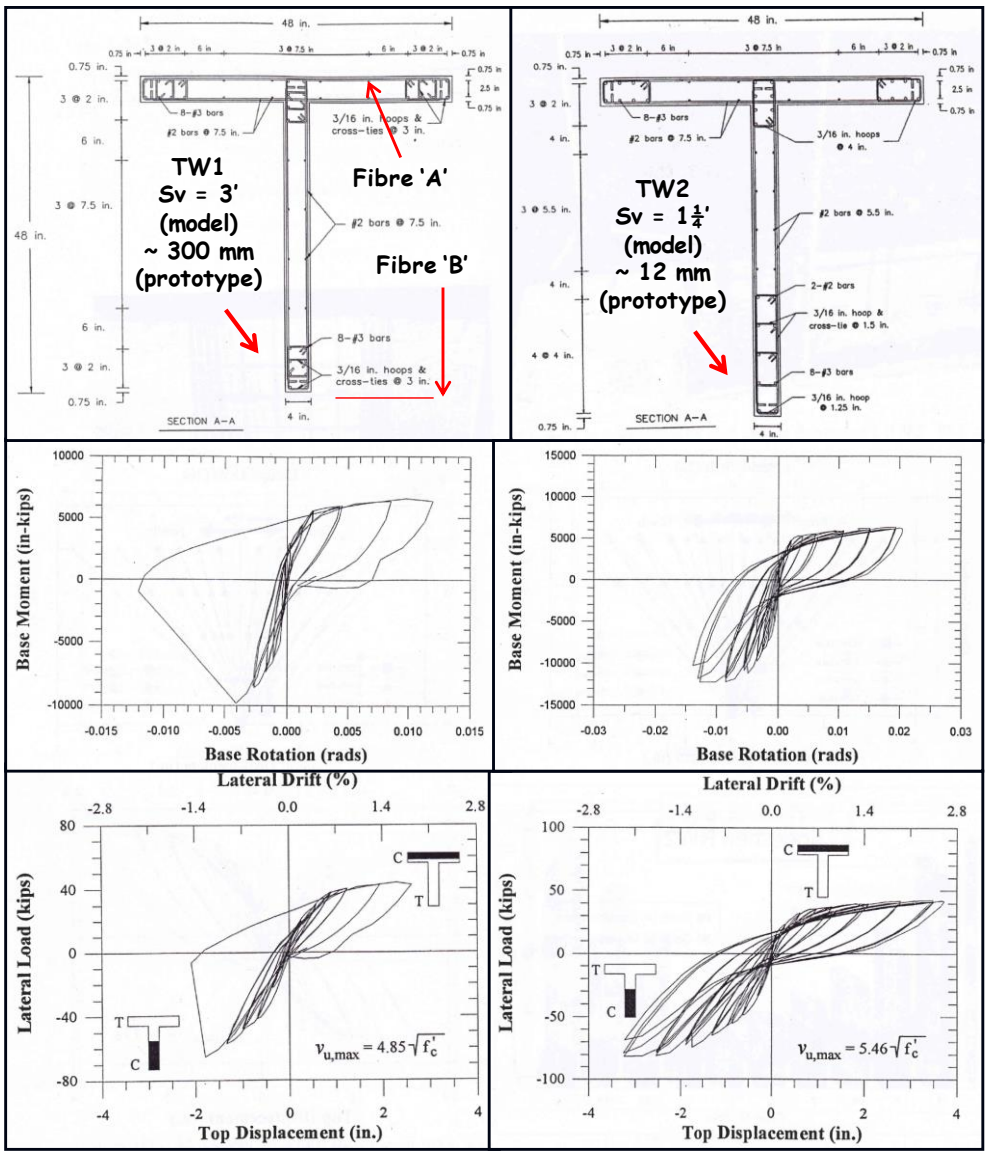

Figure 9.17: Experimental summary from Thomsen (1995); different SBE configuration and tests results in terms of bending moment - base rotation and lateral force - top drift.

This is in line with the fact that yielding curvature is greater for AT when compared to that for AC. Furthermore, as the top yielding displacement for a cantilever wall is proportional to the yielding curvature of the wall section, and the yielding curvature for AC is 3/4 of the one for AT, then theoretically $DR_y^{AC} / DR_y^{AT} = 0.75$, which is very close to the experimental value of $DR_y^{AC} / DR_y^{AT} = 0.5/0.7 = 0.72$.

For AT direction, post-yielding strains increased along the flange with increasing imposed top displacements, until all the steel in the flange yielded at approximately 2.5% top drift, after which failure was reached. When testing specimen TW1 (referred to here as 'non ductile') on the other hand, important strength decay was observed at about 1.25% top drift, forcing the test to be stopped at an early stage when compared with the TW2 test. In Figure 9.17 the experimental hysteretic loops recorded in the experimental tests performed by Thomsen (1995) are shown in terms of top drift (and displacement) as well as in terms of the measured rotation at the base of the walls. The total top drift of the wall can be decomposed into the drift related to pure flexural bending and to shear distortion, which is analogous to what was postulated by Pampanin et al (2005) for frames. Therefore, the difference in the magnitude of the top drift and the rotation (in radians) can be attributed to shear deformation of the wall.

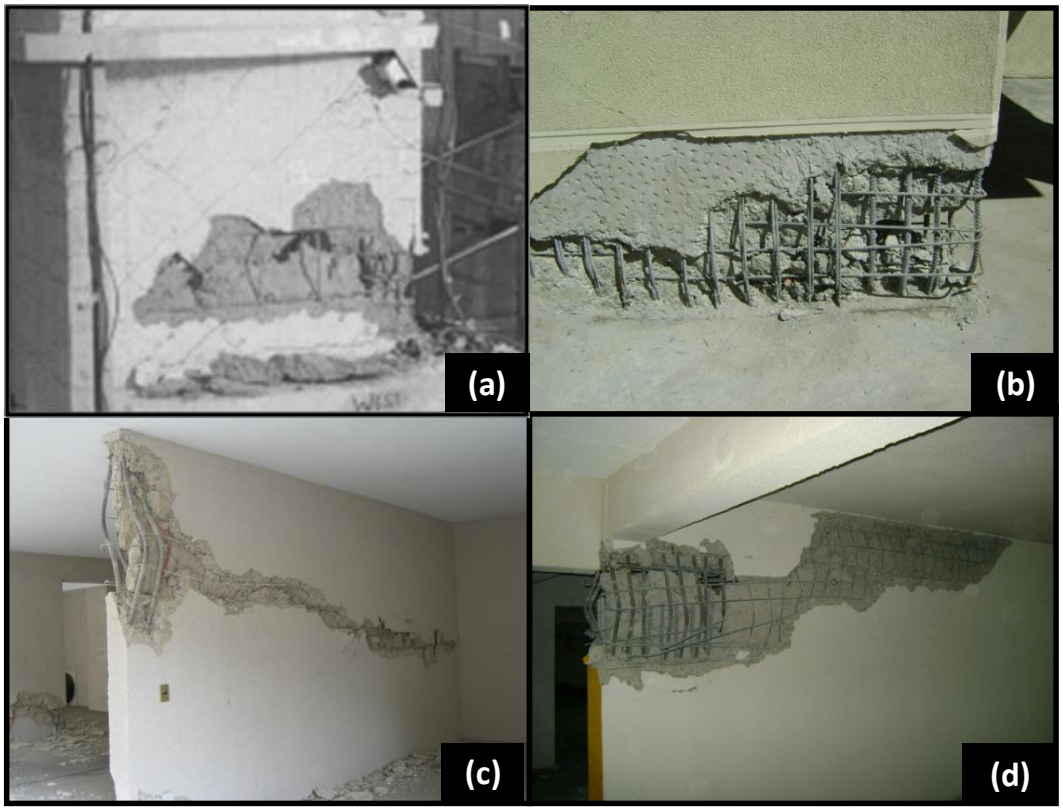

Figure 9.18: Experimental –real-life comparison of non-ductile RC T-shaped walls.

As can be seen in Figure 9.17, for the ductile specimen TW2, a top drift of 2.5% is reached in both directions, AT and AC. However, the rotation measured differs from that value in different magnitudes depending on the direction of the top displacement. In the AC direction a maximum rotation of 2% was reached whereas in the AT direction a rotation of only 1.5% was measured. Therefore, shear distortion for AC would be of about 0.5% and for AT of about 1%, which is 2 times greater. In the non-ductile specimen TW1 for a maximum top drift of about 2%, a rotation of about 1.25% was reached in the AC direction, meanwhile in the opposite direction at a maximum top drift of about 1.25% and a rotation of 0.4% were measured. This means that the shear distortions for this specimen corresponded to about 0.75% and 0.85% respectively, increasing the shear distortion for AT and decreasing for AC. In Figure 9.18(a), the final state of specimen

TW1 is shown and compared with the three asymmetric walls damaged in Viña del Mar after the Maule earthquake (Figure 9.18(b) to (d)).

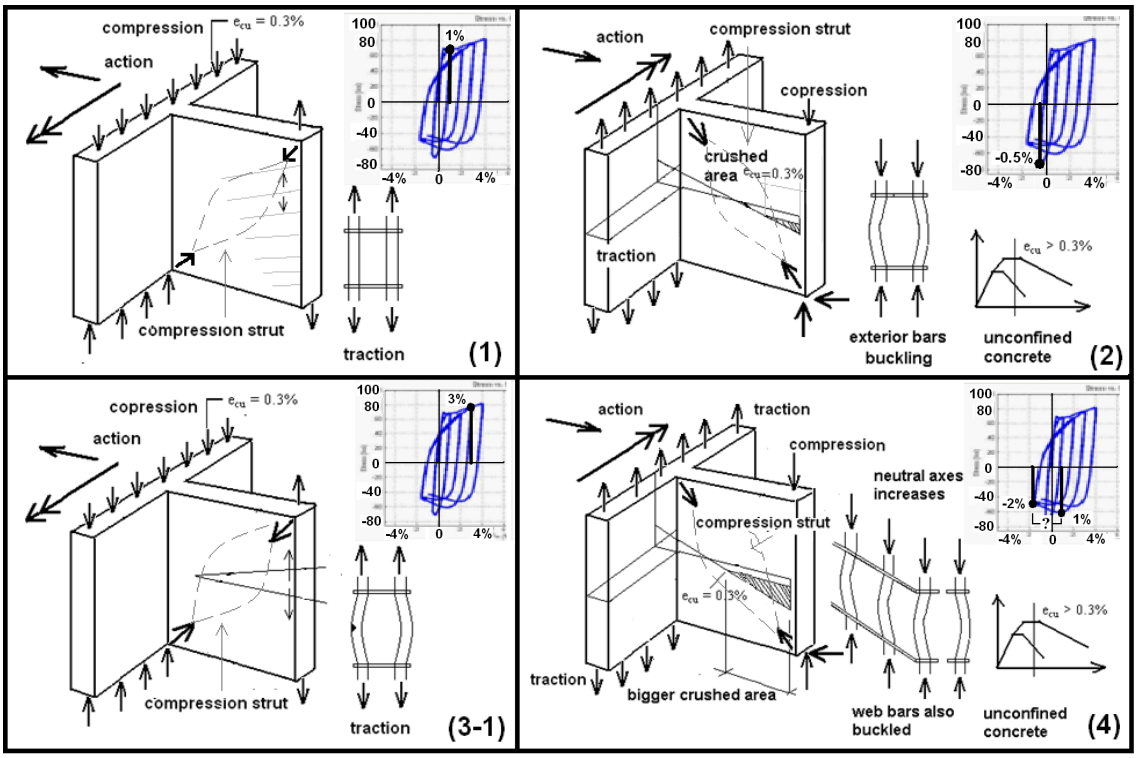

Figure 9.19: Forces acting in the base of a T-shaped wall when subjected to reverse displacements – equilibrium and constitutive law strain compatibility.

In Figure 9.19, the resisting forces acting on the 'plastic hinge' region of a T-shaped wall when subjected to shear and bending moment actions are described. Resisting forces are schematically drawn using a strut-and-tie approach. The sequence of events for *repeated periodic cycles* can be described as follows, starting in the AC direction:

(1) cracking in the free edge of the web for moderate drifts (AC),
(2) crushing of the unconfined concrete and buckling of the reinforcement in the free end of the web (AT),
(3-1) extension of the crack in the web towards the flange and/or fracture of some longitudinal rebar (AC), or
(3-2) opening of the web developed crushed area when AT, extensive fracture in the longitudinal reinforcement at rather extreme top storey drifts leading to collapse, and if (3-1)
(4) further decreasing of the neutral axis depth due to previous damage, creating a large spalled area of crushed concrete and heavy buckling of the vertical reinforcement in a large portion of the web.

In order to support the proposed damage mechanism stated above, in Figure 9.20, the cyclic behaviour of a fixed-fixed reinforcement bar is shown (graphs taken from Restrepo 2002). Further, the pictures of the free ends of two rectangular walls damaged at different stages are shown. Finally, in Figure 9.21, three other failure modes observed in flanged walls are presented. These correspond to:

(1) shear failure when AT,
(2) upper floors flexural-shear damage with a deep/wide crushed area when AC,
(3) out of plane failure in the free end of the web in thin-unstable elements.

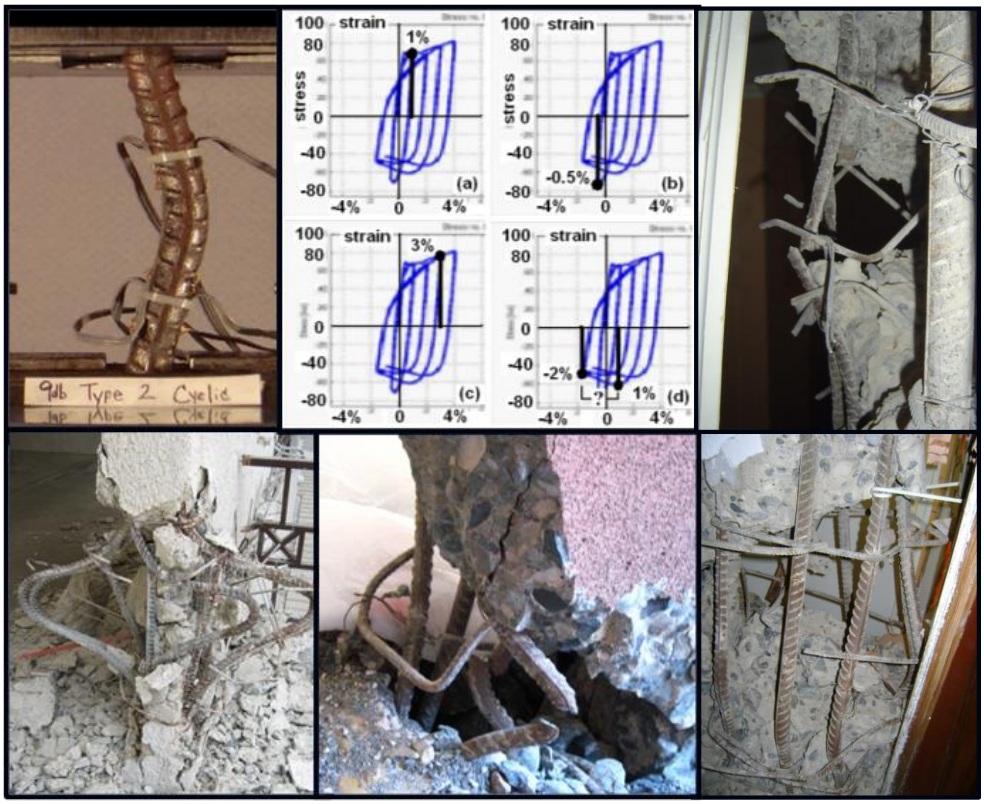

Figure 9.20: Reinforcement bar subjected to repeat cycling loading (courtesy of J. Restrepo); comparison with observed damage in Chile 2010.

Figure 9.21: Shear, higher mode effect, and out of plane failure modes in flanged walls.

4.1.4 Asymmetric Walls

In Figure 9.22 rectangular walls were artificially created by relocating the flanges of T-shaped walls in the layout of the ideal building presented in Figure 9.4 into the facades. As a result, initial gravity axial loads acting on interior walls (short direction), will be

larger in terms of the axial ratio v, since the same axial load is concentrated in a smaller cross section when compared to those corresponding to the T-shaped walls.

The axial load ratio v, is defined as the product $P/A_g f_c'$, where P is the axial force, A_g the gross cross section of the wall and f_c' the nominal compression strength of the concrete. In the ideal T-shaped walls described previously, v = 0.10, whereas in the equivalent rectangular walls v = 0.20, for the same concrete quality (30MPa). Those walls were dimensioned in such a way that the shear stresses due to elastic modal analysis were kept lower than $0.5\sqrt{f_c'}$ (MPa), as suggested by Aktan and Bertero (1985). As a result, relatively thick elements (500 mm webs and 300 mm flange) were used instead of thin unstable walls which would have been allowed by the design codes.

Assume that the thickness of the new rectangular walls is the average of the wall thickness found in the field in Chile for 12-storey buildings: t_w = 200 mm. Also add other short thin walls in the short façades with the intention of keeping the stiffness of the system constant. In such a scenario, central thin walls would have v = 0.43. At the same time, if flanges were brought back to their initial positions in plan, then the thinner web T-shaped wall would have had v = 0.16. Note these values correspond to 30MPa concrete. For a 20MPa concrete for example, in case of the 200mm rectangular wall the initial axial load ratio would be v = 0.50, increasing drastically from the initial value of v = 0.10 for the T-shaped wall and v = 0.20 the equivalent 500mm rectangular wall. Therefore, even if the same stiffness is maintained in the system, together with special detailing for boundary elements, ductility would be reduced due to the excessive axial load.

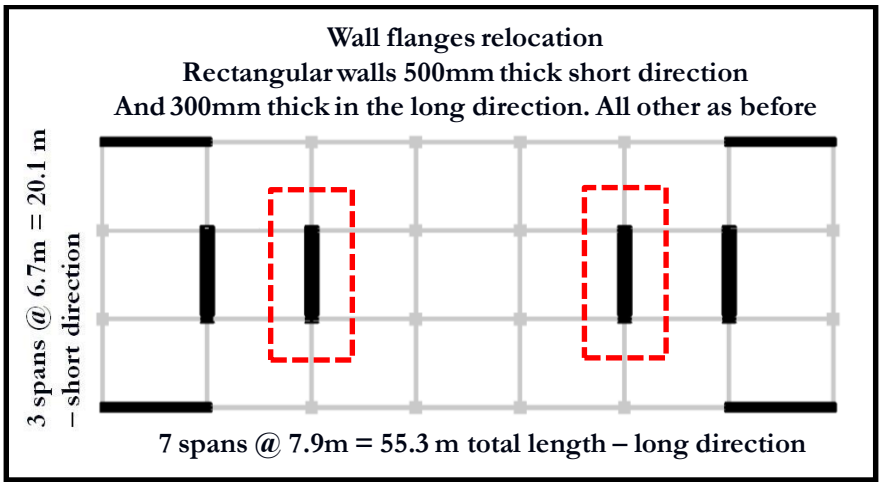

Figure 9.22: Wall relocation in the ideal building of Figure 9.4: rectangular walls with increased initial axial load as a consequence.

In the same experimental sequence previously described for T-shaped walls, Thomsen (1995) also tested two rectangular RC walls. One specimen (RW1) was constructed with light confinement elements in the free ends, whereas the other (RW2) was constructed with heavy SBE, reducing importantly the vertical spacing between transverse hooks and cross ties. The results revealed a relatively good behaviour in both cases in terms of the ability of achieving large and repeated top displacements with no strength degradation, and with high energy dissipation. However, those walls were tested under a low axial level of v =0.10, which does not deteriorate the ductility of the members, as presented in Chapter 10.

Figure 9.23: Top left: artificially created rectangular wall (free end mirror of specimen TW1 from Thomsen (1995); brittle-failure in rectangular walls in Chile 2010.

In the absence of experimental investigations of lightly confined RC walls with high levels of axial load, it is postulated that the effect of the initial axial strains (ε_0) induced by axial loads (v) in rectangular walls, can be understood using an approximation of equivalent actions in a T-shaped wall. These equivalent actions consist in the consideration of laterally induced vertical compression forces developed in the compressed concrete, required to balance the tension force from artificial flanges acting always in tension in both directions, but not resisting in compression at all. Using this approach, equivalent rectangular walls would correspond to the free end of the web of a T-shaped wall subjected to low axial load, with the artificial addition of an additional compression force to balance tensile forces in the fictitious flange always acting in tension. Correspondingly, equilibrium of forces in the wall 'plastic hinge' region requires a larger neutral axis in the concrete for balancing both axial-gravity and seismically induced axial-flexural strains, leading to compression-governed rotations in poorly detailed RC walls. As presented in Figure 9.23, the damage patterns observed on after the earthquake were quite similar to what can be artificially created when using a 'mirror' in the picture of specimen TW1 the end of the test. Different levels of damage are illustrated in the pictures of Figure 9.23, including major crushing and buckling in the web of rectangular walls and shear-flexural-compression interaction vestiges.

9.7 ADDITIONAL NUMERICAL SIMULATIONS USING ONE GROUND MOTION RECORDED DURING THE MAULE EARTHQUAKE

The same numerical model of the 12-storey building described earlier in this chapter was used to simulate the dynamic response of the system under only one additional ground motion recorded during the 2010 Maule earthquake in Concepcion. As shown, this station (Conce2010), a PGA of 0.40g was recorded, which corresponds to the effective design PGA for the location, just as was the case of Viña del Mar station in 1985. In this case, however, the displacement response spectrum is much more similar to that generated with SCT station (Mexico1985), as presented in Figure 9.24. Despite the lower PGA level of 0.15g recorded in Mexico, both spectral responses in terms of displacement are very similar. At the same time, the spectra generated using Viña del Mar (1985) ground motion is quite dissimilar for natural periods greater than 1 second.

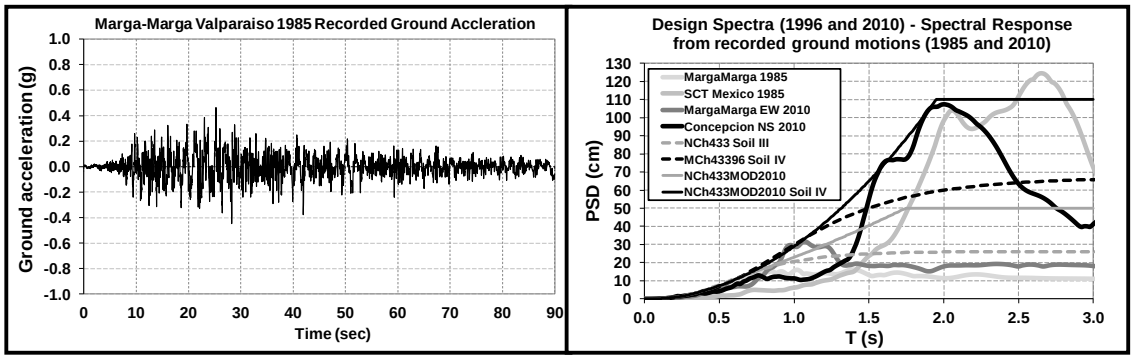

Figure 9.24: Input record and displacement spectra.

The original model for T-shaped walls assumes a ductile inelastic mechanism in the plastic hinge region such as the ductile rotation of well confined walls. As was found in Chile after the 2010 earthquake, this was not the case in the large majority of damaged walls. As a preliminary solution for degrading the sequence of the SINA hysteresis rule (Saiidi, 1979), used on T-shaped walls, the post-yield stiffness (r) at the base of the walls was decreased to r = -5%, in order to account for strength degradation due to the brittle nature of the cyclic reversals. A value of r = 1% was also used as in Quintana-Gallo (2008), in order to compare previous results.

Results of numerical simulations using the model created in Ruaumoko (Carr 2008a,b) are presented in terms top drift global dynamic response and local moment-curvature curves at the base of T-shaped walls, for r = 1% and r = - 5%. Simulations indicate that a fairly similar global response would be achieved in terms of top global drift for both cases, whereas wall local response would be different, since significant deterioration in terms of stiffness and strength in the case of r = -5% are obtained when compared to those obtained when using r = 1%. The residual displacements are only slightly different, being more severe when using r = - 5%, since the symmetric layout of the building compensates for the loss in strength and stiffness in the walls. This is consistent with what has been postulated by Christopoulos et al (2003, 2004), and Pampanin et al (2003) for SDOF systems and multi-storey frames.

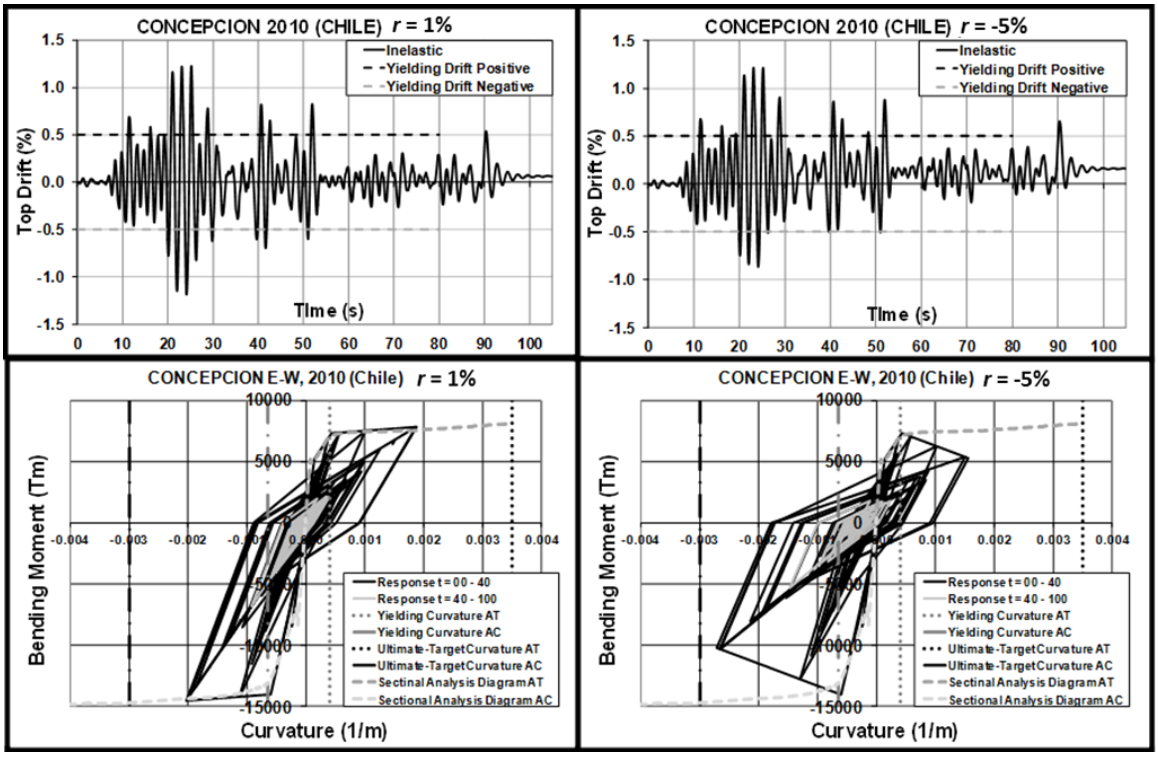

Figure 9.25: Simulated moment- curvature response in the base of T-shaped walls, when located geometrically opposed as shown in Figure 9.4, for r = 1% and r = - 5%.

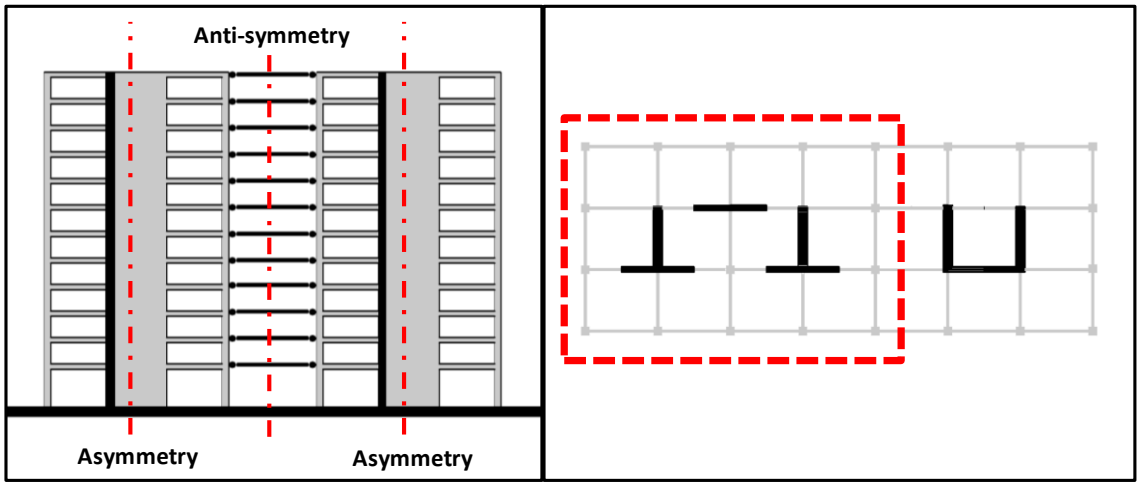

Figure 9.26: Anti-symmetric T-shaped walls location (highlighted in red) – similar layout of a dual system with a central C-shaped core wall (highlighted in red).

In Figure 9.26, symmetry in the building layout has been replaced by anti-symmetry, which was done by relocating the flanges towards the same facade. Using a slightly modified model, for r = 1% and r = -5% and the Conce2010 acceleration record (Chile 2010). In Figure 9.25, results of the numerical simulations in terms of top drift time history global response, and moment-curvature hysteresis loops at the base of the walls are presented. As a result of large repeated inelastic incursions, the walls are predicted to lose a significant amount of stiffness due to the dynamic excitation used and the hysteresis rule used.

Note the similarity on the shape of the moment-curvature loops presented in Figure 9.27 with the empirical hysteresis loops obtained quasi-statically in specimen TW1 shown in Figure 9.17. In this case, when using both values of *r*, the common trend predicted are much larger curvature demands towards the direction where the flanges of T-shaped walls are located. The logical analogy with real walls would be a crack on the free end of the web that, once is developed, would tend to increase in size progressively, forcing the building after repeated cycles towards the façade closer to the flanges of the wall. This is in line with the level of residual deformations / displacements at the final state of the numerical simulations, both globally and locally.

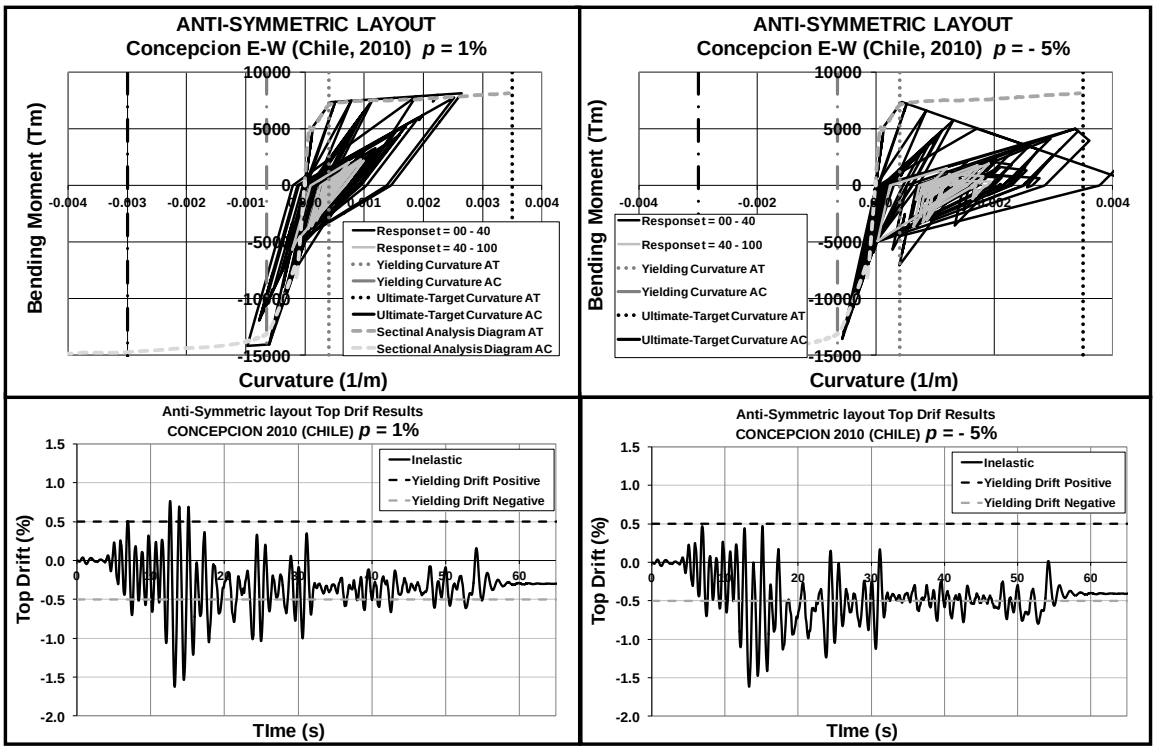

Figure 9.27: Numerical simulation of the hysteretic loop in the base of T-shaped walls similarly aligned in the structural layout, for r = 1% and r = - 5%, respectively.

When using *r* = -5%, the reduction in strength becomes very significant, dropping to below 80% of the nominal strength, which is commonly accepted as the limit for a ductile behaviour. This can be associated theoretically to the presence of the axial load, which would significantly reduce the rotational ductility capacity in walls. However, the addition of a different value of *r* depending on the direction of movement (AC or AT) may also be another parameter to consider, since it may occur, as will be discussed in Chapter 7, that for the same axial load level, strength degradation can be much more severe when the flange acts in tension.

In general, the post-yielding stiffness of asymmetric walls will be different depending on the direction of movement, i.e. in the situations when the flange is in compression (AC) or in tension (AT), as schematically shown in Figure 9.16. Normally, when the wall acts in the AC situation, the post-yielding stiffness will be positive and when it acts in the AT situation it will be negative. In the numerical model used in the simulations presented in this chapter, however, a unique value of the bi-linear factor which controls the post-

yielding stiffness was used. The reason for that is that the frame element used does not allow for different values of that parameter for the positive and negative direction. This issue is seen as a matter of improvement of Ruaumoko2D.

9.8 CONCLUDING REMARKS

Many issues have arisen regarding adequate seismic design of RC wall and wall-frame buildings after the 2010 Chilean earthquake, where undesired brittle inelastic mechanisms were observed in most of the damaged walls. As a consequence, it has been argued that the observed failure modes constituted a pattern (with some variations), revealing a lack of consideration and/or implementation of fundamental concepts of ductile design. Walls with non-ductile detailing, high levels of axial load, small thicknesses and no shear capacity design, remained apparently in the elastic range or were damaged in a brittle fashion. This means, walls which remained undamaged kept intact their vulnerability for future events, if they were designed in the same way as those that failed. However, the problem, from this perspective can still be rectified or mitigated by means of the implementation of an appropriate ad-hoc retrofit intervention.

Our apparent inability for estimating the seismic demand for structural engineering purposes may introduce considerable uncertainty in the design process itself. The importance given to nominal design values in the sense of being reliable can eventually jeopardize the need of using a full ductility design philosophy, when increasing the level of the demand using ad-hoc reduction/amplification factors. Design actions specified in design response spectra and/or time history acceleration records modified to fix them may differ significantly from those recorded in future events.

In the case of Central Chile, where spectral displacements obtained with ground motions recorded in Concepcion (2010), differ significantly and are much more demanding for periods larger than 1 second, when compared to the spectrum corresponding to a ground motion recorded 25 years earlier during the 1985 Valparaiso earthquake in Viña del Mar. In fact, the latest obtained spectrum is closer in shape and magnitude to the one obtained using a record motion from the 1985 Mexican earthquake (SCT station) for the range of natural periods of relevance. This is, after March 1985 and before February 2010, there was an expectation of future seismic demands to be similar, and as low as, those recorded during the Valparaiso earthquake. Demands such as those imposed by ground motions such as those recorded at SCT (Mexico 1985), were thought, prior to 2010, to be far away from what was *expected* to occur. This led to an excessive confidence in the ability of predicting future seismic demands with reasonable accuracy.

9.9 REFERENCES

ACI Committee 318 (1995), *Building Code Requirements for Structural Concrete and Commentary (ACI 318R-95)*, American Concrete Institute, Farmington Hills, Michigan, USA.

ACI Committee 318 (2005), *Building Code Requirements for Structural Concrete and Commentary (ACI318M-05)*, American Concrete Institute, Farmington Hills, Michigan, USA.

AIJ (1999), *Design Guidelines for Earthquake Resistant Reinforce Concrete Buildings on Inelastic Displacement Concept*, Architectural Institute of Japan, Kyoto, Japan (*in Japanese*)

Aktan, A.E., Bertero, V.V. (1985), 'RC Structural Walls: Seismic Design for Shear', *Journal of Structural Engineering*, ASCE, Vol. 111, No.8, pp. 1775-1791.

Arias, A. (1989), 'Proposición de Espectros de Diseño para la Norma Chilena de Diseño Sísmico', *Proceedings of the 5th Chilean Conference on Seismology and Earthquake Engineering*, Santiago, Chile (in Spanish).

Beyer, K., Dazio, A., Priestley, M.J.N. (2008), 'Quasi-Static Cyclic Tests of Two U-Shaped Reinforced Concrete Walls', *J. of Eq. Eng.,* Vol.12, pp. 1023-1053.

Beyer, K., Dazio, A., Priestley, M.J.N. (2011), 'Shear Deformations of Slender Reinforced Concrete Walls under Seismic Loading', ACI Structural Journal, Vol. 18(2), pp.167-177.

Bonelli, P., Restrepo, J., Alarcón, G., (2010), 'Observaciones de Daños en Edificios de Hormigón Armado Producidos por el Terremoto de Chile Central, 27 de Febrero de 2010', *XXXIV Jornadas Sudamericanas de Ing. Estructural*, San Juan, Argentina (*in Spanish*).

Bonelli, P., Boroschek, R., Restrepo, J., Carvallo, J.F. (2012a), The 2010 Great Chile Earthquake - Changes to Design Codes**,** *Proceedings of the International Symposium on Engineering Lessons Learned from the 2011, Great East Japan Earthquake*, March 1-4, Tokyo, Japan.

Bonelli, P., Restrepo, J., Quintana-Gallo, P., Pampanin, S., Carr, A.J. (2012b), 'Improvements for the Seismic Design of Reinforced Concrete Walls in Chile and Suggestions for the Refinement of Other Seismic Code Provisions' Proceedings of the NZSEE Conference, Christchurch, New Zealand, paper 117.

Carr, A. J. (2008a), *Ruaumoko – Program for Inelastic Dynamic Analysis*, Volume 1: Theory, Department of Civil and Natural Resources Engineering, University of Canterbury, Christchurch, New Zealand.

Carr, A. J. (2008b), *Ruaumoko – Program for Inelastic Dynamic Analysis*, Volume 2: User Manual for the 2-Dimensional Version, Ruaumoko2D, Department of Civil and Natural Resources Engineering, University of Canterbury, Christchurch, New Zealand.

Christopoulos, C., Pampanin, S., Priestley, M.J.N. (2003), 'Performance-Based Response of Frame Structures Including Residual Deformations; Part I: Single-Degree of Freedom Systems', *Journal of Earthquake Engineering*, Vo. 7, Issue 1, pp. 97-118

Christopoulos, C., Pampanin, S. (2004), 'Towards a Performance-Based Design of Structures with Explicit Consideration on Residual Displacements', *Journal of Earthquake Technology ISET*, Vo. 41, No. 1, March, pp. 53-73.

Cowan, H., Beattie, G., Hill, K., Evans, N., McGhie, C., Gibson, G., Lawrence, G., Hamilton, J., Allan, P., Bryant, M., Davis, M., Hyland, C., Oyarzo-Vera, C., Quintana-Gallo, P., and Smith, P. C. (2011), 'The M8.8 Maule Chilean Earthquake', *Bulletin of the New Zealand Society for Earthquake Engineering*, Vol.44, No.3, pp. 123-166.

Dazio, A., Beyer, K., Bachmann, H. (2009), 'Quasi-Static Cyclic Tests and Plastic Hinge Analysis of RC Structural Walls', *Engineering Structures*, Vol. 31, pp. 1556-1571.

Decreto Supremo 60 (2011), 'Reglamento que Fija los Requisitos de Diseño y Cálculo para el Hormigón Armado y Deroga Decreto Nº 118, de 2010', Ministerio de Vivienda y Urbanismo, *Diario Oficial de la República de Chile*, Nº 40.133, pp.1-8 (*in Spanish*).

Decreto Supremo 61 (2011), 'Reglamento que Fija el Diseño Sísmico de Edificios y Deroga Decreto nº 117, de 2010', Ministerio de Vivienda y Urbanismo, *Diario Oficial de la República de Chile*, Nº 40.133, pp.8-12 (*in Spanish*).

EERI (1985), 'The Chile Earthquake of March 3, 1985', *Learning from Earthquakes, Special Earthquake Report, Earthquake Spectra*, Vol. 2, No 2, pp. 249-508.

EERI (2010), 'The MW 8.8 Chile Earthquake of February 27, 2010', *Learning from Earthquakes, Special Earthquake Report*, Earthquake Engineering Research Institute, San Francisco, California, USA.

EEFIT (1986), 'The Mexican Earthquake of 19 September 1985', a field report by the Earthquake Engineering Field Investigation Team (EEFIT), Bristol/London, England

EEFIT (1988), 'The Chilean Earthquake of 3 March 1985', a field report by the Earthquake Engineering Field Investigation Team (EEFIT), Bristol/London, England

Hidalgo, P., Arias, A. (1993), 'Fundamentos de las Disposiciones de Diseño y Análisis Sísmico de la Nueva Norma Nch433', *Proceedings of the 6th Chilean Conference on Seismology and Earthquake Engineering*, Santiago, Chile (*in Spanish*).

INDITECNOR (1972), *Earthquake Resistant Design of Buildings*, Instituto Nacional de Investigaciones Tecnológicas y Normalización, Santiago, Chile (*in Spanish*)

INN (1996), *Seismic Design of Buildings*, Norma Chilena Oficial NCh433Of.96, Instituto Nacional de Normalización, Santiago, Chile (*in Spanish*)

INN (2008), *Hormigón armado – Requisitos de diseño y calculo*, Norma Chilena Oficial NCh430Of.2008, Instituto Nacional de Normalización, Santiago, Chile (*in Spanish*)

INN (2010a), *Seismic Design of Buildings*, Norma Chilena Oficial NCh433Of.96 modificada 2010, Instituto Nacional de Normalización, Santiago, Chile (*in Spanish*)

Massone, L. (2013), 'Fundamental Principles of the Reinforced Concrete Design Code Changes in Chile Following the Mw 8.8 Earthquake in 2010', *Engineering Structures*, Vol. 56, pp. 1335-1345.

Pampanin, S., Christopoulos, C., Priestley, M.J.N. (2003), 'Performance-Based Response of Frame Structures Including Residual Deformations; Part II: Multi-Degree of Freedom Systems', *Journal of Earthquake Engineering*, Vo. 7, Issue 1, pp. 119-147.

Pampanin, S., Magenes, G., Carr, A. (2003), 'Modelling of Shear Hinge Mechanism in Poorly Detailed RC Beam-Column Joints', fib 2003 Symposium "Concrete Structures in Seismic Regions", paper n.171, Athens, Greece.

Paulay, T., Priestley, N. (1992), *Seismic Design of Reinforced Concrete and Masonry Structures*, Prentice Hall.

Priestley, M.J.N. (2003), *Myths and Fallacies in Earthquake Engineering Revisited*, ROSE School Report, Pavia, Italy.

Priestley, MJN, Calvi, GM & Kowalsky, MJ (2007), *Displacement-based seismic design of structures*, IUSS Press, Pavia, Italy.

Quintana-Gallo, P. (2008), 'Evaluación Analítica del Daño en un Edificio de Hormigón Armado', *thesis submitted in partial fulfilment of the requirements for the degree of Magister en Ciencias de la Ingeniería Civil*, Departamento de Obras Civiles, Universidad Técnica Federico Santa María, Valparaíso, Chile (*in Spanish*).

Riddell, R., Hidalgo, P., Cruz, E. (1989), 'Response Modification Factors for Earthquake Resistant Design of Short Period Buildings', *Eq. Spectra*, Vol. 5(3), pp. 571 – 590.

Saiidi, M., Sozen, M.A. (1979), *Simple and Complex Models for Nonlinear Seismic Response of Reinforced Concrete Structures*, Report UILU-ENG-79-2031, Department of Civil Engineering, University of Illinois, Urbana-Champaign, Illinois.

Thomsen, J.H., (1995), 'Displacement Based Design of Reinforced Concrete Structural Walls: An Experimental Investigation of Walls with Rectangular and T-Shaped Cross – Sections', *thesis submitted in partial fulfilment of the requirements for the degree of Doctor of Philosophy*, Clarkson University, Potsdam, New York. USA.

Thomsen, J., Wallace, J. (2004), 'Displacement-Based Design of Slender Reinforced Concrete Structural Walls – Experimental Verification', Journal of Structural Engineering, ASCE, Vol. 130, No. 4.

Wallace, J., Moehle, J. (1992), 'Ductility and Detailing Requirements of Bearing Wall Buildings', Journal of Structural Engineering, ASCE, Vol. 118, No 6.

Wallace, J. W., Massone, L., Bonelli, P., Dragovich, J., Lagos, R., Luders, K., Moehle, J. (2012), 'Damage and Implications for Seismic Design of RC Structural Wall Buildings', *Earthquake Spectra*, Vol. 28, pp. S281-S299.

Wood, S. (1991), 'Performance of Reinforced Concrete Buildings During the 1985 Chile Earthquake: Implications for the Design of Structural Walls', Earthquake Spectra, Vol.7 (4), pp.607-638.

10 SEISMIC ASSESSMENT OF RC WALLS AFTER THE 22 FEBRUARY 2011 CANTERBURY NEW ZEALAND EARTHQUAKE

10.1 INTRODUCTION

At 12:51 PM on the 22nd of February 2011an M_w = 6.3 magnitude earthquake affected the Canterbury Region of New Zealand's South Island. The Central Business District (CBD) of the city of Christchurch, located at about 8 km from the nominal fault rupture, had a moderate stock of middle-rise RC buildings. That is 25% of the total stock, the rest being Unreinforced Masonry buildings (EERI 2011, Kam et al. 2011, Elwood et al. 2011, Pampanin et al 2012a,b).

During the field inspection of the RC buildings in Christchurch CBD, it was observed that brittle failure modes developed in some structural walls, following the pattern presented in this chapter. The damage included spalled and crushed concrete at the free ends and along the web of some walls, developing a large crushed area, buckling of longitudinal reinforcement in the boundaries of walls with highly spaced confinement elements or closely spaced stirrups made of small diameter bars, buckling in the web vertical rebar, and out-of-plane buckling or shear failure of the web. Similarly with the pattern observed in Chile after the 2010 Maule earthquake, there is some evidence of fracture of wall reinforcement rebar which can be attributed to the near field characteristics of the shake, e.g. pulse effect, high velocity and short duration of the ground motion, which typically do not impose several reversals at low frequency.

In the first part of this chapter, a detailed description of the damage observed in RC walls in Christchurch CBD is presented, using pictures and drawings of eight selected buildings. The damage pattern is then associated to possible deficiencies in the design of the walls, summarized at the end of the first section. In the second part, in the light of the deficiencies identified with the damage observation, the requirements of the New Zealand Standard NZS3101:2006 (Standards New Zealand 2006) for ductile detailing of RC walls is reviewed as well as those of the ACI318-2011 (ACI committee 318, 2011) and the Eurocode8 ENV1998-2004 document (European Committee for Standardization, 2004). Using a simple example of a 12-storey building with rectangular walls, the detailing requirements for that particular case are investigated.

The evaluation of the ultimate ductility of curvature of the ideal rectangular walls designed in this chapter and the T-shaped wall designed in Quintana-Gallo (2008) and presented in Chapter 9. The ultimate curvature is defined as the curvature when the first of two strain limits is reached: (1) crushing in the concrete (confined and unconfined), (2) maximum elongation in the steel in tension.

The effect of the axial load, the cross section shape (flange effect), and the confinement length are investigated. The results are presented in the form of moment-curvature diagrams as well as figures were the strain profile of the section is shown. The required confinement is also plotted as a function of the axial load. The mechanics behind buckling of vertical rebar is also examined in the light of recent work done by Rodriguez

et al. (1999 and 2013), and the importance of the vertical spacing of confinement elements and the maximum elongation in the steel reached before the compression reversal comes is reviewed. This work though, assumes plane sections remain plane, not strictly true for plane wall cross-sections and does not take into account shear lag in non-planar walls.

Following the evaluation at a cross section level, the maximum top storey drift capacity of the wall is estimated using well established relationships (Wallace and Moehle 1992). This idealized procedure requires the assumption of a certain plastic length where inelastic deformations are concentrated. As variations in the value assumed for that parameter importantly affect the results, three different values were considered for comparison, which are a factor of the length of the wall (l_w). Using that formulation, a series of graphs are constructed for the T-shaped wall acting with the flange in compression (AC) and in tension (AT). Those graphs are also constructed for rectangular slender walls.

The seismic demand is evaluated using elastic and inelastic displacement response spectra. These spectra were obtained with the program INSPECT (Carr 2012) for four ground motions recorded in the CBD during the Canterbury earthquake, and 5 other records from different earthquakes: three from the Maule 2010 Chile earthquake, one from the Valparaíso 1985 Chile earthquake, and one from Michoacán 1985 Mexico earthquake. Using these graphs, as well as all the capacity considerations reviewed along the previous parts of the paper, the concept of a capacity-compatible spectral demand is introduced and used for developing a simplified assessment procedure for RC walls. Conclusions related to the adequacy of some aspects of the current practice for detailing structural wall are presented, in the context of the uncertainty involved in the problem of estimating with accuracy the seismic demand.

The formulations used in this chapter and the suggested simplified assessment procedure assume that the sections of the walls remain plane after deformations take place, and that the shear deformation are much smaller than the flexural counterparts.

10.2 DESCRIPTION OF THE OBSERVED DAMAGE IN RC WALLS OF CHRISTCHURCH CBD

In this section, the observed damage in RC walls in eight of the most affected buildings inspected in the Christchurch CBD after the 22 February Canterbury earthquake is described. For a detailed description of these and other buildings inspected in Christchurch CBD, the reader is referred to Pampanin et al. (2012b).

In Figure 10.1 pictures of Building A damaged walls are shown. In this case, it was observed that many of exterior walls exhibited a brittle failure mode similar to that identified previously in Chile, but to a lesser intensity of damage. In this case, however, spacing of the transverse stirrups as large as 300 mm in the wall ends could not prevent the initiation of buckling in some of the longitudinal bars. Most of the damage was concentrated in the base of the walls, even though some inelastic incursions were also found in upper floors. In some walls, concrete in the bottom of the free ends was crushed. The rather light extent of the crushing in these particular walls is seen to be a

consequence of low levels of gravity axial load, which allowed the wall to withstand larger rotations when compared to their highly axially loaded counterparts.

Cracks in Wall B were developed mostly in one direction on the side closer to that where buckling of the longitudinal reinforcement occurred. This suggests that the steel in that end suffered a considerable elongation when the cracked opened, and then when the cycle reversal came, the steel buckled possibly under tension strains as the vertical spacing of confinement elements was too large. This phenomenon is explained in detail in section 4.6, based on the work done by Rodriguez et al. (1999, 2013).

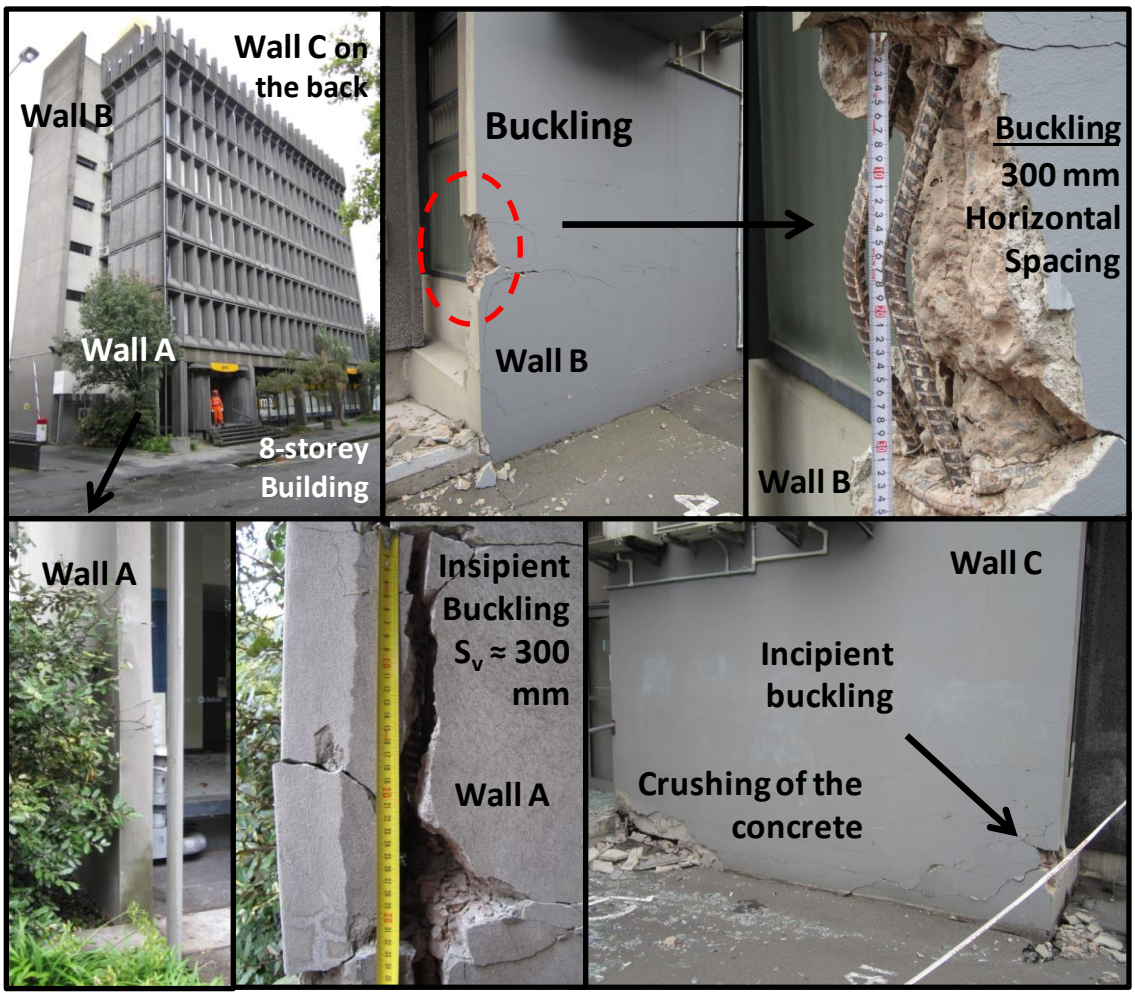

Figure 10.1: Building 'A' (8 storeys): exterior walls damage; incipient buckling in vertical reinforcement due to large spacing of confinement elements.

In Figure 10.2 the damage observed in two of the walls of Building B is presented. This building had RC walls with V-shaped walls on two facades of the rectangular floor plane forming a symmetrical layout. Examples of buildings with this kind of asymmetry were also damaged before in Chile after the Valparaiso 1985 earthquake (EEFIT 1986, EEFIT 1988, Bonelli et al 2010, 2012a). As shown in Figure 10.2, in the highlighted wall longitudinal reinforcing bars buckled in the wall boundary, with the small diameter horizontal confinement stirrups unable to provide lateral restraint to the larger longitudinal bars concentrated in the wall end. Longitudinal reinforcement along the web

of this wall also buckled. In Figure 10.2, pictures of the wall after a repairing process had already started are also shown.

The repairing technique consisted of the addition of an exterior steel cage around the damaged area which was then filled with new concrete. This type of repair would most probably shift the critical section upwards, where the same deficiencies of the as-built portion of the wall would still exist, if confinement is provided at all. A rehabilitation strategy, consisting of upgrading after repairing seems more appropriate in order to ensure a more ductile response during future earthquakes by mitigating the brittle failure mode.

Figure 10.2: Building 'B' (7 storeys): observed wall damage in V-shaped walls.

In Figure 10.3 the observed damage in RC walls in an 8-storey modern building built in 1999 is presented. This building was identified to lack of structural redundancy in terms of the amount of RC walls, even though some reinforced masonry wall panels were used in few resisting axes as an additional resisting system.

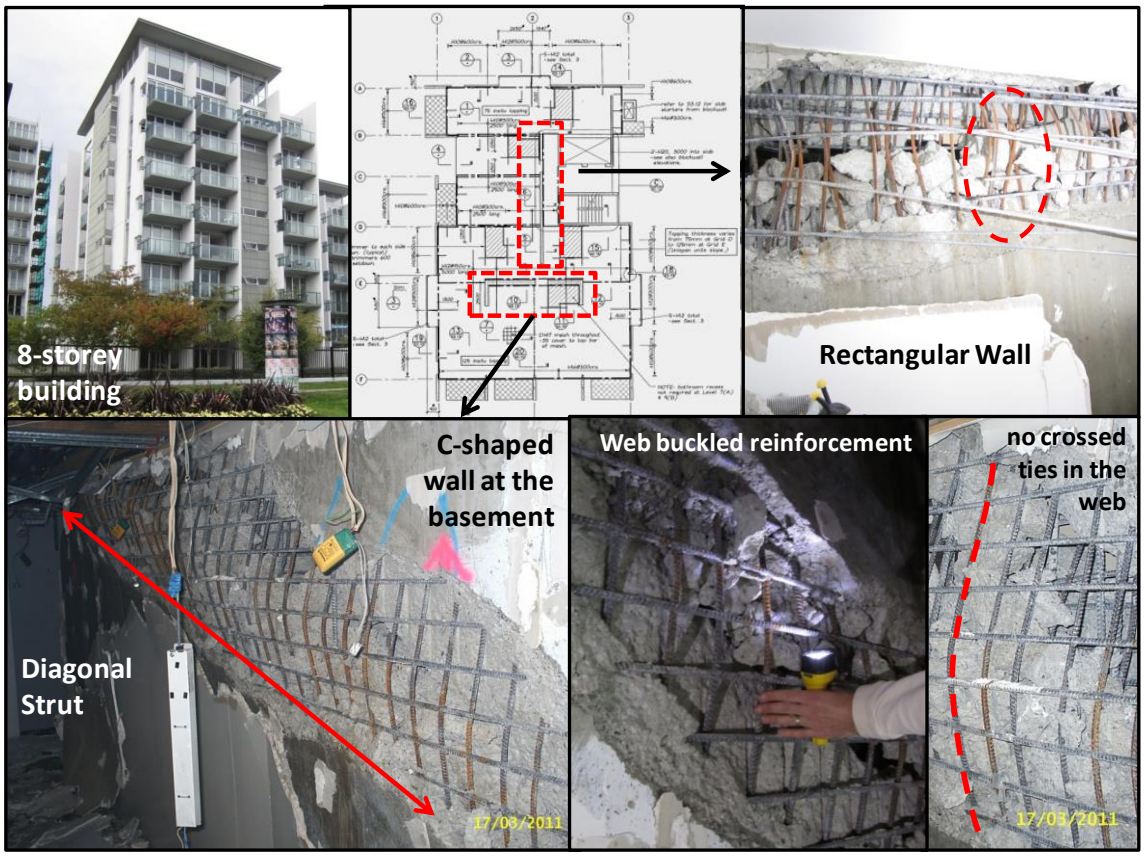

Figure 10.3: Building C (8 storeys): Central RC walls damaged.

The most important damage was observed in a central cantilever rectangular and the C-shaped wall, result of the closed opening at the basement level of two coupled L-shaped walls, both located in the central part of the building. As lustrated in Figure 10.3, these walls suffered significant damage due to a complex mechanism associated to flexural-compression-shear interaction in the asymmetric C-shaped wall and flexural compression failure in the rectangular wall. Shear interaction is a notorious potential issue in C-shaped walls, in the light of the formation of a high stress diagonal compression strut in the web as a result of the high bending moment capacity of the wall when the flange acts in tension. That is, even if opposite flange is able to resist in compression the tensile force developed in the other flange, the web will still be subjected to high shear stresses in the web. Buckling of the web longitudinal reinforcement was observed in both cases, but the rectangular wall was more severely compressed. The observed damage is equivalent to that found in many RC wall buildings in Chile, and their mechanics may be understood in a similar fashion as that presented in Chapter 9.

In Figure 10.4 Building D is presented. This structure, constructed in 1974, was designed using a C-shaped RC wall core on the East façade, with no counterpart on the West side in terms of strength or stiffness. Frames were located on the West, South and North façades. In the central part of the building columns with corbels were used to support a thick cast in situ slab following a very regular pattern. Reinforced masonry infill panels were located close to the open face of the C-shaped wall, in order to enclose the interior space for stairs and elevators. An additional reinforced masonry wall was constructed on the North side, which does not appear in the official drawings shown in Figure 10.4.

The damage observed in the frames was evenly distributed between perimeter beams, columns, and joints. A shear failure was observed in the North face, due to the use of architectural exterior infill panels which led to a shear failure in the first floor columns due to a shortening of the effective height of the column. This shear failure did not develop on the opposite face even though the structural layout is very regular and simple. The C-shaped wall remained appeared to suffer little damage, and was able to control the displacements in the system, surviving the ground motion without collapsing. The cast in-situ slab seemed to have worked as a rigid diaphragm; its connections with the vertical elements were capable of resisting the local horizontal demands maintaining compatibility of displacements in the horizontal plane of the diaphragm.

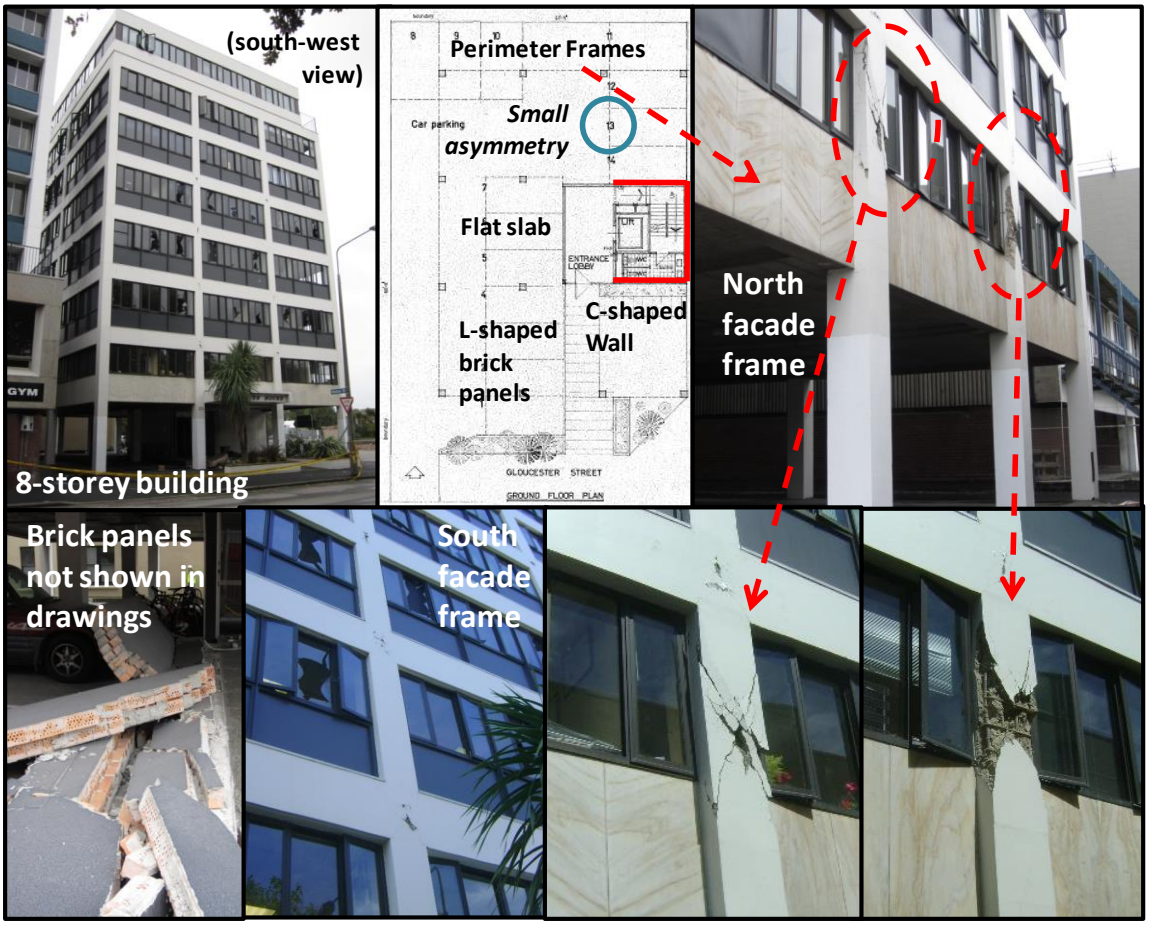

Figure 10.4: Building 'D' (8 storeys): Structural layout and observed damage.

In many older structures frames were designed with no capacity design principles and no limitation of the axial load level to ensure rotation ductility. This resulted in relatively small sized columns when compared to the beams. These columns were, sometimes, spaced very far apart, and not adequately detailed to resist shear. The building shown in Figure 10.5 (Building E) has a very similar structural layout to the one shown in Figure 10.4 (Building D). In this case however, the singly reinforced core wall was not able to resist the earthquake demands in ductile fashion. Once the roof displacement was large enough to induce inelastic behaviour in the wall critical section, it suddenly failed, initiating the collapse of the structure. The rest of the structure, which consisted of frames designed for gravity only, apparently experienced large brittle rotations, being unable to

provide earthquake resistant redundancy to the system and avoid the soft-storey like collapse mechanism experienced by the structure (BECA 2011).

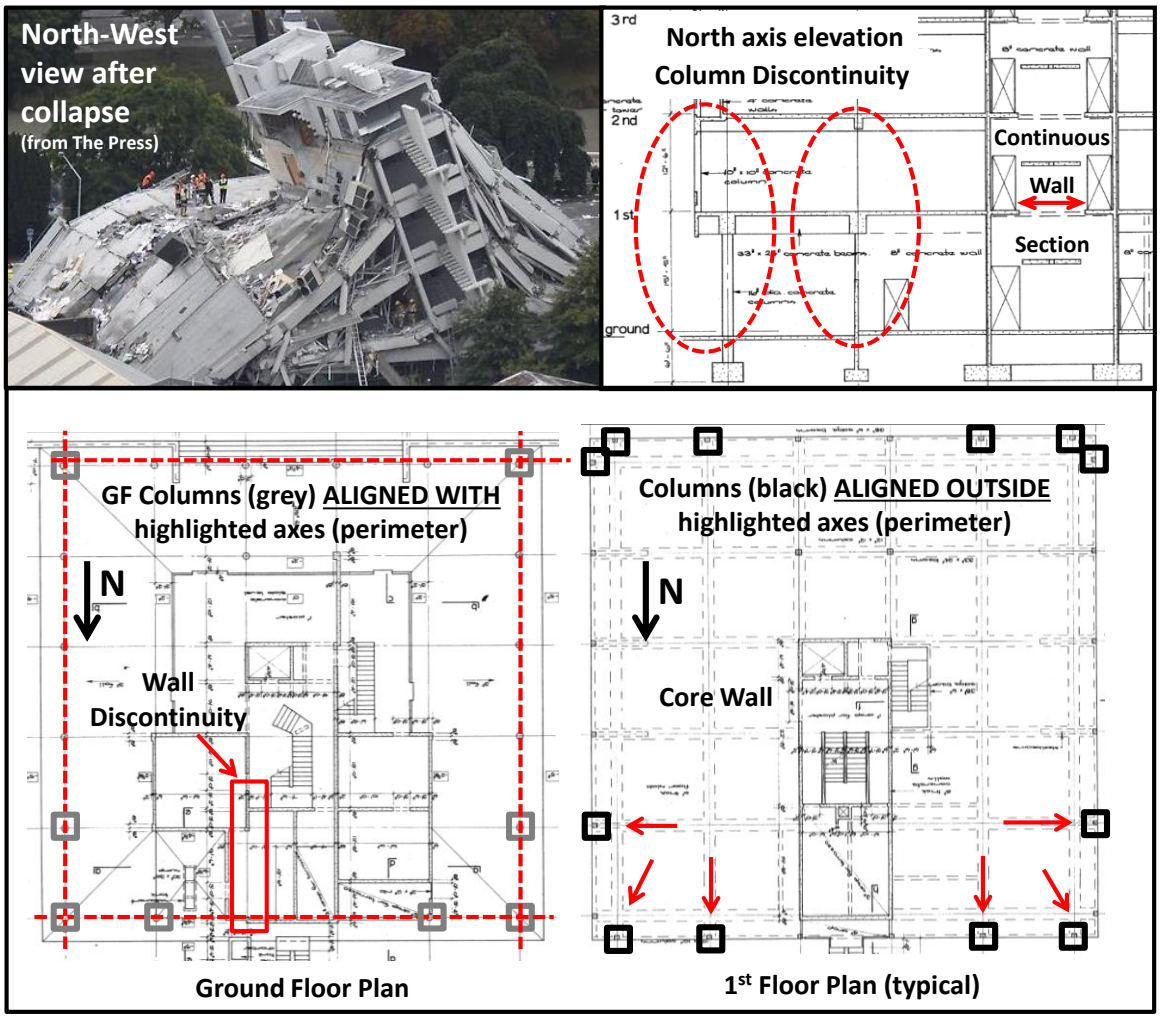

Figure 10.5: Building E: Collapsed 5-storey RC building in Christchurch, during the 22 February Canterbury Earthquake (from The Press), constructed with one core structural wall (singly reinforced) and gravity load (ordinary) frames with a discontinuity in the ground floor level.

In addition, the vertical discontinuity in the perimeter columns as well as in the East part of the core wall in between the ground and first floors (highlighted in Figure 10.5) made the system very unstable under seismically induced displacements, making the task of controlling the inelastic mechanism by the core walls even more difficult. The floor diaphragms, in this case, were able to transmit horizontal strains without failing at the intersections with vertical elements and holding them together rigidly.

In Figure 10.6 some pictures of a 28-storey Building E are presented, together with the critical part of the structural layout. The building had discontinuous systems and was a mixture of frame and wall over differing heights of the structure, the upper part was a frame system with over-hang to the East. The building was conceived as a Hotel with a main tower and a car park appended to it. On a centric part of the city, low rise building surrounded it with modest separation between them. The RC frames had relatively large

spacing between vertical elements to allow for big spaces inside the building. Some heavy cover elements are specified on the tower façade, as shown in the official drawings.

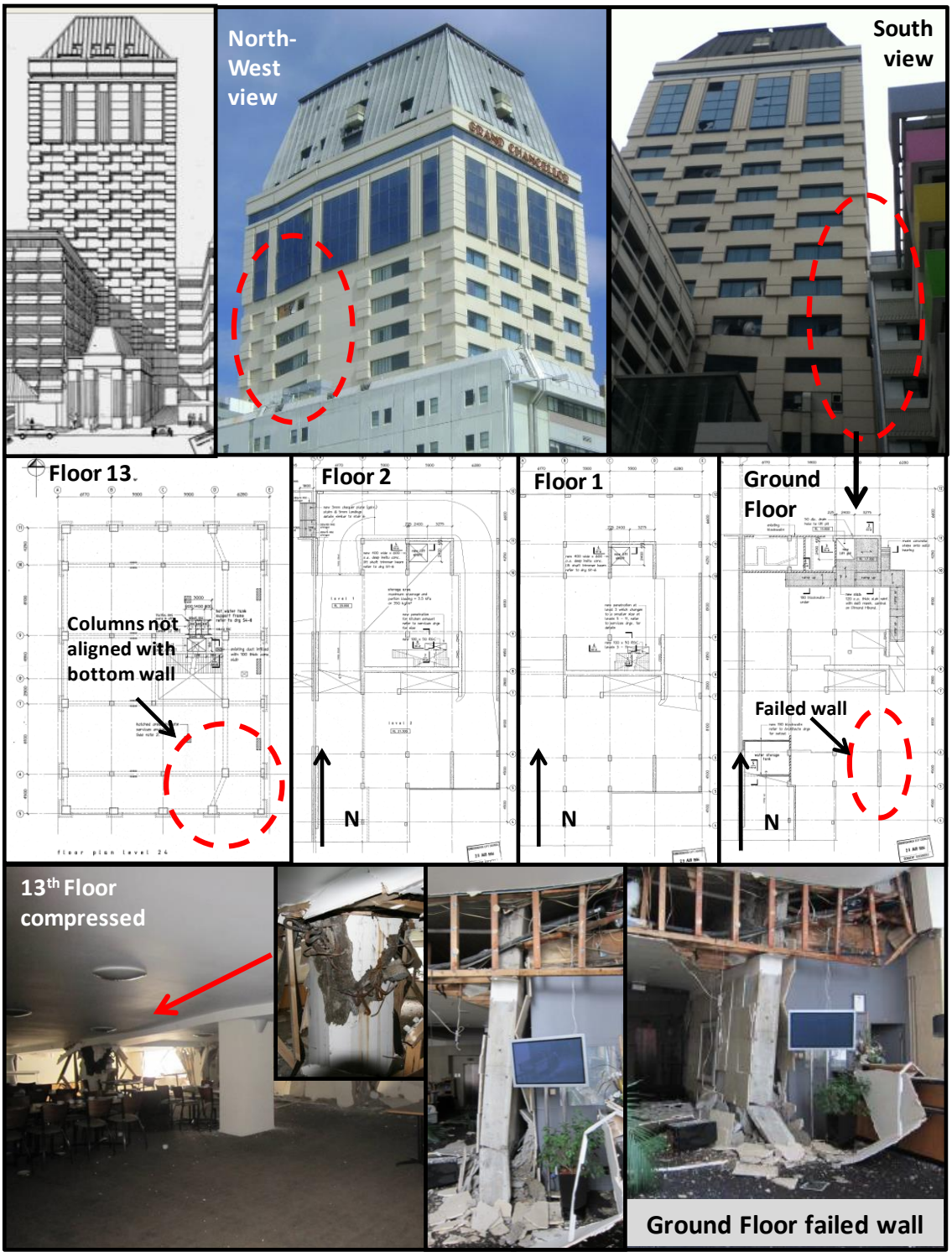

Figure 10.6: Building F (28 storeys): partial collapse due to failure in corner ground level RC wall (bottom pictures courtesy of Professor Nigel Priestley).

Structural earthquake resistant system is conformed primarily by RC precast frames. Some slender RC structural walls are also used on lower floors. Floor system consists in

precast slab units. A reinforced topping is provided to connect precast elements at each level. The main tower is located on the south east part of the main building which also includes a multistory car park as an adjacent structure. In level 3, corner columns on the south – east side of the tower rest on a slender rectangular structural wall, imposing high initial strains on that element, reducing notably the rotation capacity in the plastic region. The structure suffered a partial collapse towards the south-east corner were a slender rectangular wall failed out of the plane at the ground floor. As shown in the bottom right part of Figure 10.6, this rectangular wall was to control high displacement demands resulting from the high flexibility of the system, supporting large initial gravity axial forces, as well as the very hard to estimate axial load due to the bi-directional movement of the ground and the contribution of beam/slab coupling effects.

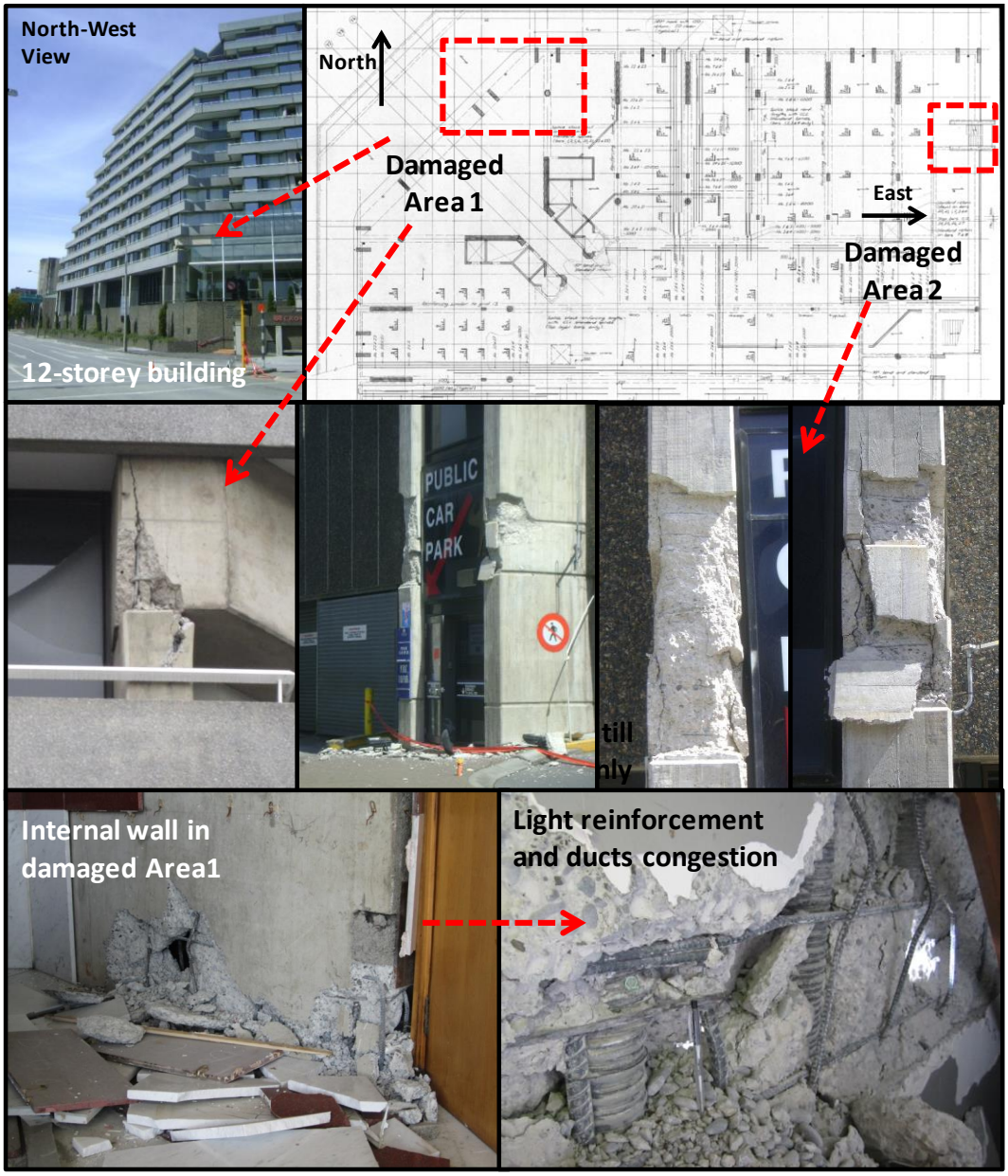

Figure 10.7: Building G (12-storeys) layout and damaged areas. Walls with close spaced boundary elements and internal wall lightly reinforced with ducts congestion.

In Figure 10.7 Building G is presented. In this structure, one of the tallest in Christchurch, only a few RC walls were damaged, as shown in the pictures. Boundary elements on the East walls were able to keep the concrete confined and prevent buckling in the longitudinal bars due to closely spaced transverse reinforcement. Nevertheless, one internal wall at the entrance of the building developed crushing in the concrete. Effects of ducts passing through the wall together with low reinforcement levels were observed. In the short slender walls (rectangular columns) on the North-West façade, damage developed in the form of a brittle out of plane failure in the joint where a 1600 x 600 mm cross section beam was connected. Insufficient anchorage length and lack of continuity in the load path, as well as torsional effects due to the plane asymmetry, may have been important factors contributing to the development of this particular damage mechanism. Liquefaction was also a problem in this structure, as observed on the South-West façade, where differential settlements were evident. However, most the main structural walls did not suffer significant damage; even though the structural layout was quite asymmetric.

Figure 10.8: Building H (4-storeys): Incipient buckling of vertical rebar in precast walls – failed walls repaired with light confinement elements in the boundary and no transverse hooks along the web (courtesy of Matt Shoettler and the UCSD recognisance team).

In Figure 10.8, pictures of a 4-storey hospital, constructed with precast frames and walls are shown. The walls were significantly damaged in some cases, whereas in other cases walls apparently remained in the elastic range though there were some indications of an

incipient, but not developed brittle failure mode. As the pictures were taken after the repair process had started, only pictures of lightly damaged walls are presented in Figure 10.8. Nevertheless, the time of inspection allowed for the evaluation of detailing of replacement walls. As can be seen in Figure 10.8, the walls are lightly confined at their free ends, using large spacing in for the transverse elements. Also note that no additional transverse cross ties and/or hooks along the web of the wall were added, one of the missing details in many RC walls.

The deficiencies in the design of RC walls identified in the light of the observed damage pattern can be summarized as:

(1) The use of large spacing in horizontal confining stirrups or the use of small bar sizes in closely arranged elements,

(2) The absence of horizontal crossed ties or hooks about longitudinal reinforcement in the middle part of the web of the wall – not specified in the NZS3101:2006 and ACI318-2011 codes,

(3) The use of one vertical reinforcement layer in some cases,

(4) High level of initial axial gravity load in some cases,

(5) The use of a small amount of walls in flexible buildings, where the frames are normally designed for gravity only (ordinary frames in ACI318-2011), i.e. the walls are designed to resist all seismic actions in a force-based context.

10.3 DUCTILE DETAILING OF RC WALLS REQUIRED BY THE NEW ZEALAND STANDARD NZS3101:2006 AND OTHER SEISMIC CODES

The New Zealand standard NZS3101 for the design of RC structures follows a traditional Load and Resistance Factor Design (LRFD) method for RC members at the ultimate state, and has significant roots in the ACI318 requirements (Standards New Zealand, 1995). Capacity Design for structural walls was incorporated after the contribution of many researchers during the past decades. Thomas Paulay, for example, improved the seismic provisions for RC walls by critically reviewing the ACI318 code provisions (Paulay 1986), resulting in significant modifications in the 1995 version of NZS3101 standard, which replaced the earlier 1982 edition. The latest approach for confinement requirements is clearer for design than ACI318:2011 recommendations (ACI Committee 318 2011), yet is analogous to the procedure specified in the seismic provisions (ACI318 Chapter 21). This is explicitly quoted in the 2006 version of NZS3101.

Nevertheless, there seems to be some aspects where it can be further improved, in the light of the observed damage and based on the theoretical explanations of the nonlinear mechanics of non-ductile RC walls presented in Chapter 9. Other code provisions for ductile detailing, such as the Eurocode 8 ENV 1998-1:2004 seismic provisions (European Committee for Standardization 2004) are reviewed for identifying ductile detailing that can be incorporated into the New Zealand standard and/or the ACI318 seismic provisions. In particular, it is of extreme interest that in ENV 1998-1:2004 section 5.4.3.4.2 (9) transverse hooks are required to be placed about all longitudinal reinforcement in the web

of the wall outside the confined length, in order to restrain the longitudinal reinforcement preventing it from buckling. The addition of this detailing is thought to be a source of major improvement for the New Zealand and the United States normative for RC elements.

4.1.5 Ideal 12-storey building with rectangular RC walls case study

In Figure 9 the plan view of the typical floor of a modified version of the ideal 12-storey building with T-shaped walls used in the companion paper (unless the companion paper can be read at the same time omit reference to it as it is not helpful) and Quintana-Gallo (2008), is presented. This ideal building has rectangular walls in the interior, 400 mm thick, a value modified from the 500 mm used in the web of the T-shaped wall.

The walls longitudinal reinforcement is designed for seismic actions required by the New Zealand Standard NZS1175.5:2004 (Standards New Zealand 2004) for a structural ductility factor of the building in the direction of analysis of μ = 3. The structure is considered to be of importance 2 ('ordinary'), as defined in the AS/NZS 1170.0:2002 standard (Australian and New Zealand Standards 2002). The structural performance factor is S_p = 0.7, the minimum required by the NZS1175.5 standard.

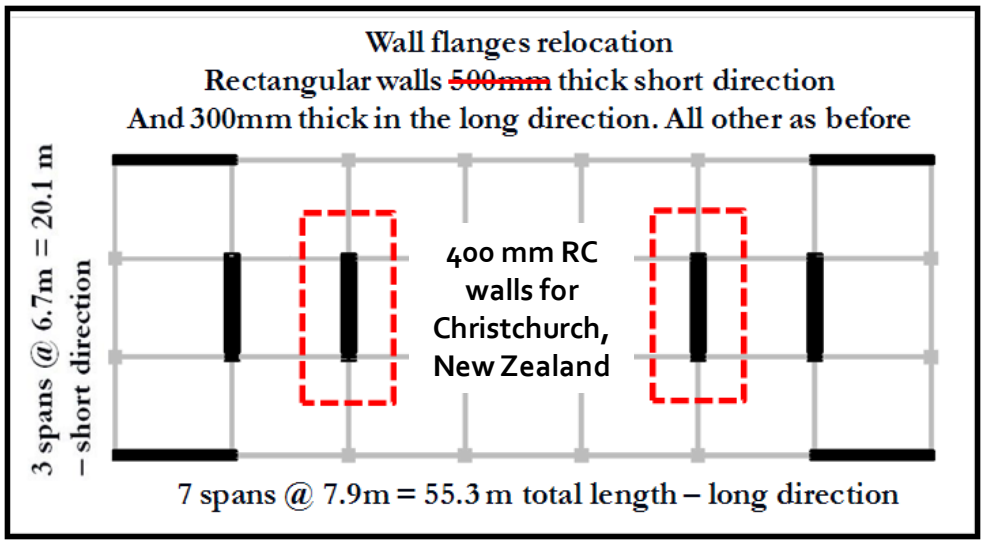

Figure 10.9: Ideal 12-storey building: the flanges of the original T-shaped walls presented in the companion paper have been relocated into de perimeter leading to rectangular crossed section in the highlighted internal walls.

The method selected for obtaining the 'seismic actions' was a traditional elastic modal spectral analysis method with a CQC combination. As required by NZS1175.5:2004, the design spectrum is a scaled down version of the acceleration elastic spectra constructed for a site given and multiplied by parameter which follows a certain probabilistic model (not explicitly described in the standard), named the 'return period factor' (R_u). This factor is associated to a certain probability of exceedance of the seismic actions during the working life of the structure. For an ordinary structure, with an intended working life of 50 years, the probability of exceedance is $|P_{exc}$ = 1/500 (Australian and New Zealand Standards 2002). As a result, R_u = 1. An additional factor which ranges from 1 to 2, named the Near Field factor (N), further multiplies the elastic spectrum. For Christchurch,

this value before the earthquake and to date is set to 1, regardless of the evident near field characteristics of the seismic event which almost destroyed the city.

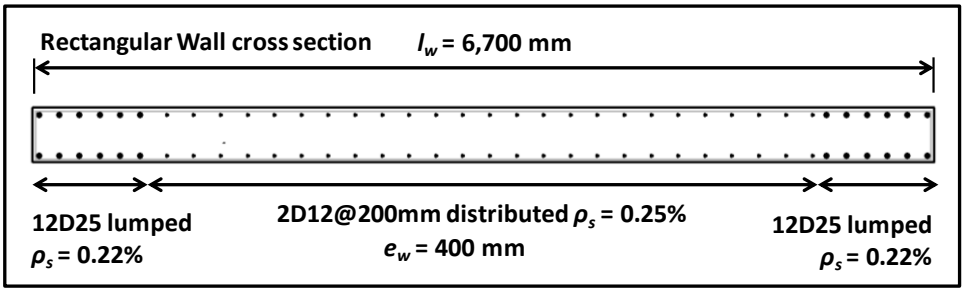

Figure 10.10: Rectangular wall design for resistance, according to NZS1107.5:2004, AS/NZS1170.0:2002 and NZS3101:2006.

The elastic spectra derived in this manner, for a certain PGA (Z = 0.22 in Christchurch before the earthquake, and upgraded to Z = 0.30 in May 2011) is multiplied by a factor equal to S_p/k_μ, where $k_\mu \approx \mu$ (the structural ductility factor) in this case. Therefore, the actual acceleration design spectrum is 0.7/3 = 4.3 times the elastic spectrum of a site, almost the same value used as a reduction factor of the elastic acceleration spectrum used in Quintana-Gallo (2008) for the design of the ideal building with T-shaped walls with the Chilean NCh433-1996 seismic code (INN 1996).

The resulting longitudinal reinforcement in the critical section of the wall (the wall base) consists of the minimum reinforcing ratio required by NZS3101:2006, provided by two layers of 12 mm diameter bars spaced at 120mm in the web, plus additional twelve 25mm diameter bars lumped at the ends of the wall as shown in Figure 10.10.

4.1.5.1 Horizontal confinement length

According to the NZS3101:2006, the required confinement length is calculated by means of the comparison of the neutral axis of the wall at ultimate limit state (c_u) and a critical value given by Equation 10.1 (c_c).

$$c_c = \frac{0.1\varphi_{ow} l_w}{\lambda} \tag{10.1}$$

where c_c = the neutral axis depth in the potential yield regions of a wall, computed for ultimate limit state (ULS); φ_{ow} = ratio of the moment of resistance at over-strength to the moment resulting from specified earthquake actions, where both moments refer to the base section of the wall; l_w = horizontal length of the wall; and λ = 1.0 for limited ductility walls and λ = 2.0 for ductile walls.

In this case, as the structural ductility was taken as μ = 3, then λ = 1. Taking φ_{ow} = 1.25 and since l_w = 6,700 mm, then $\boldsymbol{c_c}$ = 840 mm. For an axial load P_v = 13,000 kN, the value of the neutral axis at ultimate limit state is estimated using a sectional analysis as c_u = 1,900 mm. Thus, the portion of the wall l_c required to be confined, measured from the extreme fibre in compression, is given by Equation 10.2.

$$l_c \geq c_u - 0.7c_c \geq c_u/2 \tag{10.2}$$

In this case, the confinement length required by the New Zealand standard is $l_c^{NZ\text{-}LD}$ = 1,315 mm or $\eta^{NZ\text{-}LD}$ = 0.20, where η is the confinement length ratio ($\eta = l_c/l_w$), and the superscript LD denotes Limited Ductility class. Now if one assumes for the sake of comparison, that the same result in the longitudinal reinforcement of the wall is compatible with the use of a ductility factor of μ = 5, then the wall is classified as 'ductile'. According to Equation 1, the new critical value of the neutral axis is half of that for LD walls, because λ = 2.0 in this case, and hence, using Equation 2, the confinement length would be $l_c^{NZ\text{-}D}$ = 1,605mm ($\eta^{NZ\text{-}D}$ = 0.24). This is an increase in a 20% of the confinement length which is not a great increase from what could be expected to be ductile or have limited ductility. However, as discussed later, there is another critical difference in the assumption of LD or D class wall, which is the vertical spacing of the confinement elements.

The analogue value required by the ACI318-2011 seismic provisions for RC walls (section 21.9), is also obtained using the comparison of the neutral axis at ultimate displacement and a critical value given by Equation 10.3.

$$c_c = \frac{l_w}{600(\delta_u/h_w)} \tag{10.3}$$

where c_c = the largest neutral axis depth calculated for the factored axial force and nominal moment strength consistent with the design displacement δ_u, and the ratio δ_u/h_w shall not be taken smaller than 0.007, with h_w = height of the wall. Note that in typical wall buildings, the nominal top storey yielding drift is normally in the range of 0.5% to 0.7% (Aschheim 2002, Quintana-Gallo 2008). This means that the confinement length must be calculated for a top storey displacement compatible with the occurrence of yielding at the bottom of the wall. In this case, Equation 3 is used with the minimum drift required by the code, and hence c_c = 1,600 mm. The value for the neutral axis is taken as c_u = 1,900 mm, the same value used before in the calculation of the confinement required by the NZS3101:2006, for consistency.

The required horizontal extension of the boundary confinement element from the extreme fibre in compression is then calculated with Equation 10.4. Replacing the values obtained for this simple example, the confinement length required by ACI318-2011 is l_c^{ACI} = 1,230 mm (η^{ACI} = 0.18).

$$l_c = c_u - 0.1 l_w \tag{10.4}$$

Finally, according to Eurocode 8 ENV1998-1:2004 (section 5.4.3.4.2) requirements, the extension of the confinement length is calculated using Equation 10.5, using a much more direct and rational approach.

$$l_c = c_u \left(1 - \frac{\varepsilon_{cu,c}}{\varepsilon_{cu}}\right) \geq c_u/2 \tag{10.5}$$

where c_u = the neutral axis for a given ductility of curvature $\mu_\phi = \phi_u / \phi_y$, $\varepsilon_{cu,c}$ = the maximum compression strain in the confined concrete developed in the extreme fibre in compression compatible with the ultimate curvature assumption, and ε_{cu} = maximum compression strain for spalling of the unconfined concrete, equal to 0.0035. For a maximum strain in the confined concrete of $\varepsilon_{cu,c}$ = 0.008, the resulting confinement length

for a ductility of curvature equal to 5 and a yielding ductility of 0.0006 1/m, is l_c^{EC8} = 1,500 mm (η^{EC8} = 0.22).

In addition, the Eurocode 8 requires the use of transverse hooks about every longitudinal rebar of the wall outside the confined zone, which is not required by neither the New Zealand standard nor the ACI318 seismic provisions for RC. The resulting confinement arrangements obtained with the three seismic codes are shown schematically in Figure 10.11.

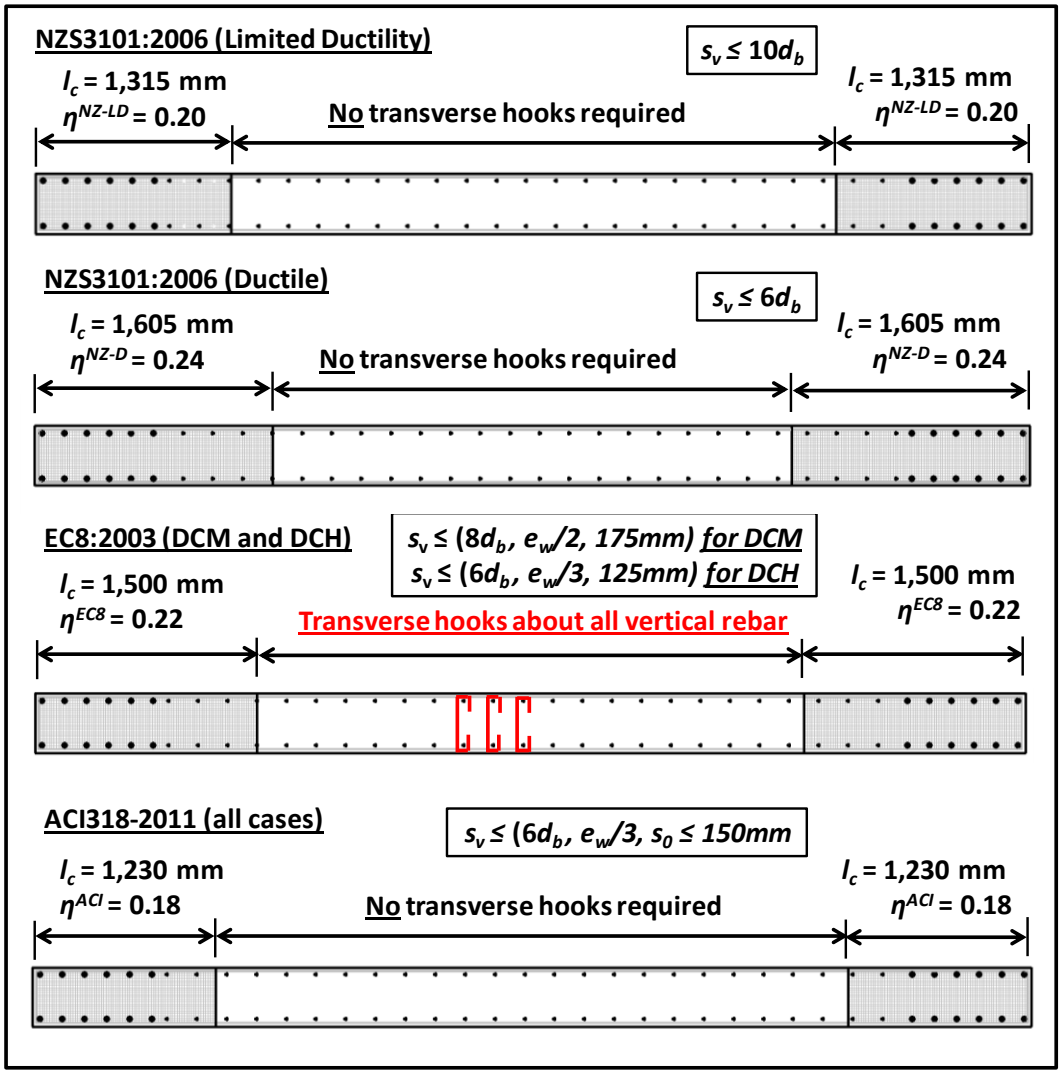

Figure 10.11: Rectangular wall confinement according to NZS3101:2006, ACI318-2011, Eurocode 8 ENV1998-1:2004, for grade 420 MPa reinforcing steel.

4.1.5.2 The importance of vertical spacing of confined elements

In the NZS3101:2006 standard, a maximum vertical spacing of the confinement elements of $6d_b$ and $10d_b$ for ductile and limited ductility elements, because it has been found in extensive experimental and analytical research done in the past that a limit of $6d_b$ is a maximum after which buckling of the reinforcement inevitably occurs before yielding in compression (Mau and El-Mabsout 1989, Mau 1990, Rodriguez et al. 1999, Urmnson and Mander 2011). The relaxation in the vertical spacing of confinement elements to a limit

as large as $10d_b$ can easily jeopardize all previous considerations for ductile behavior and is seen as a matter of concern and urgent improvement.

The problem is analogous to the impossibility of gravity-load-only frames to exist in seismic regions. In this case, since the wall is allowed to be designed for having limited ductility with the argument that larger spectral demands apply for a smaller ductility factor is thought to be a mistake. In the particular case of the example used here, the 25mm diameter bars at the ends of the rectangular wall, it is possible to use a vertical spacing as large as 250mm, a representative value of the spacing found in damaged walls in Christchurch.

According to the ACI318-2011 on the other hand, the vertical spacing of confinement elements should not exceed 1/3 of the wall thickness, $6d_b$, or s_0 which has a maximum value of 15mm. For this case the, the spacing is limited to s_v = 133mm, almost half of the value required by the NZS3101:2006 standard.

The Eurocode 8 ENV1998-1:2003 document requires a maximum spacing of the smallest value of $8d_b$, $b_0/2$, and 175 mm for ductility class medium walls (DCM), and the smallest value of $6d_b$, $b_0/3$, and 125 mm for ductility class high (DCH) elements. This requirement has the same drawback of the New Zealand approach, because there is the possibility of designing a wall to be fully ductile (DCH) or to have 'limited ductility' (DCM). The maximum value of the spacing can be specified to be larger than the experimental limit $6d_b$, critical after which buckling of longitudinal reinforcement in the confined zone is expected to occur before yielding in compression can be reached. For a full comparison of the detailing required by these and other code provisions, the interested reader is referred to fib Bulletin 69 (fib Task Group 7.6, 2013).

4.1.5.3 Vertical extension of confined elements

According to the NZS3101:2006 standard, confinement elements must extend in the vertical direction a length equal to the larger of the wall length (l_w) or 1/6 of the height of the wall (h_w), but does not need to exceed $2l_w$. The ACI318-2011 seismic provisions require a vertical extension of the confinement elements of not less than the larger of l_w and $M_u/4V_u$, where M_u and V_u are the factored bending moment and shear force at the base of the wall obtained with the linear elastic analysis. The Eurocode8 ENV 1998-1:2004 requires the same vertical extension of confinement elements than the New Zealand standard for DCM, with the exception that the value does not need to be taken larger than $2h_s$ for buildings of 7 or more storeys and h_s for 6 or less storeys, where h_s is the clear storey height. In addition, for DCH, the vertical length of confinement elements (h_{cr}) must be taken as $1.5l_w$. Hence, the vertical lengths required by the three documents are fairly similar.

10.4 EVALUATION OF THE ULTIMATE DUCTILITY OF CURVATURE OF THE IDEAL T-SHAPED AND RECTANGULAR WALLS

10.4.1 Introduction

A series of moment-curvature capacity/ductility curves were constructed using the sectional analysis program BIAX96 (Wallace and Ibrahim1996). The RC sections

considered are the rectangular section of the wall designed in the previous section, and the T-shaped wall designed according to the Chilean Seismic code NCh433-1996 (INN, 1996) and the ACI318-2005 seismic provisions (ACI Committee 318, 2005) presented in Chapter 9.

Analyses were made about the strong bending axis of the walls sections. The definition for positive and negative bending actions in illustrated in Figure 10.12, where the positive bending action produces compression in the face 'A' of the wall (AC situation) and a negative bending action produces tension in the same face (AT situation).

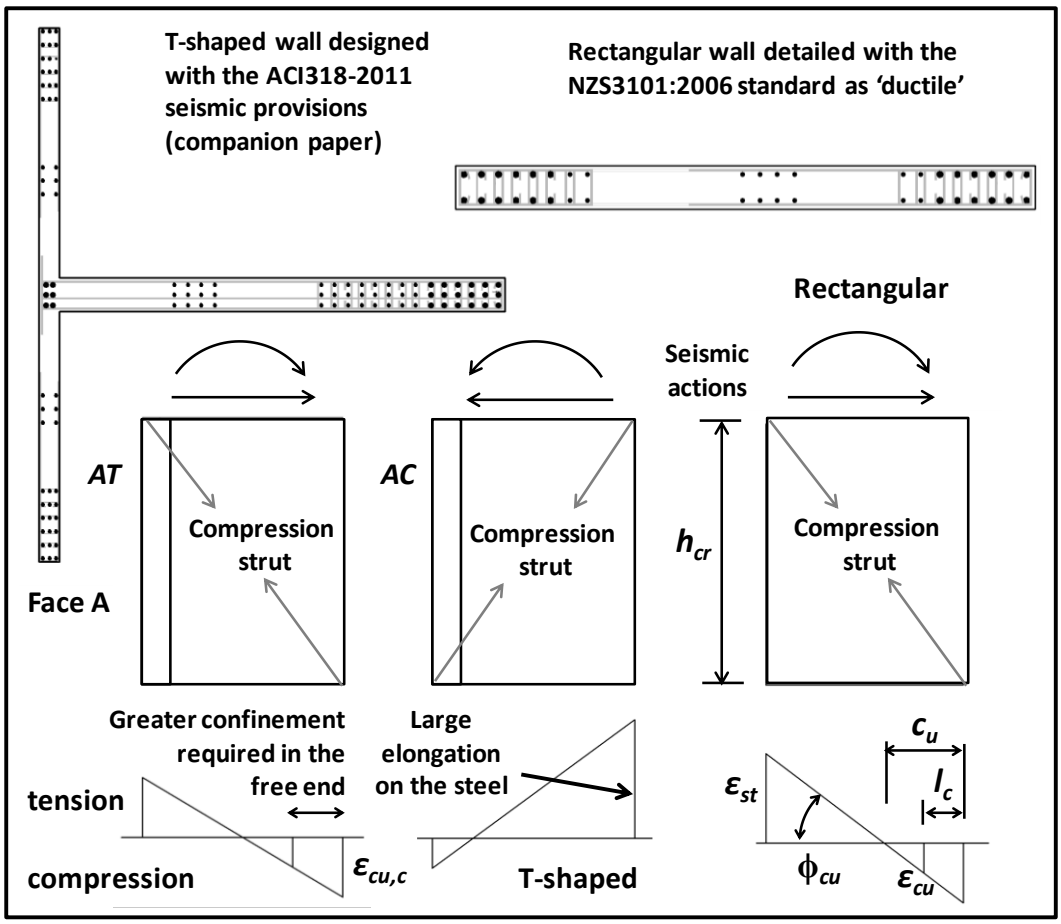

Figure 10.12: Cross section of the wall under study, plus a C-shaped wall for theoretical discussion; definition of positive and negative bending actions in the T-shaped wall.

For the rectangular wall that definition may be irrelevant due to symmetry, but this is very important to consider in a T-shaped section or other asymmetric one (C, L-shaped), where the behaviour of the element differs importantly depending on the bending direction. The variables or physical quantities (Q_i) considered in the problem are presented in Equation 10.6, where the functional f (Q_i) describes the moment in the cross section. In this case, 11 quantities are selected to describe the bending moment of the section, and hence the physical quantities involved in the problem are n =11.

$$M = f\left(\phi, P_v, l_w, l_c, e_w, f_c', \varepsilon_y, \phi_y, A_s, A_f\right) \tag{10.6}$$

In Equation 6: M = bending moment capacity, ϕ = curvature, P_v = axial load, l_w = wall length in the direction of analysis (web length for T-shaped walls), l_c = confined length in the free end of the web, e_w = web thickness, f_c' = nominal compression strength of the concrete, ε_y = yielding strain of the steel, ϕ_y = the nominal yielding curvature, A_s = the area of longitudinal steel concentrated in the wall ends (area of the steel located in the flange for a T-shaped wall), and A_f = the area of the flange of the wall if any.

According to Buckingham's PI-Theorem for dimensional analysis (Buckingham 1914), an equivalent system of $m = (n - k)$ dimensionless numbers which are products (π_j) of the n physical quantities, equally describes the problem. In this case, arbitrarily selecting the length of the wall l_w, the nominal compression strength of the concrete f_c', and the yielding strain in the steel, ε_y, as basic parameters (k = 3), the functional $F(\pi_j)$ of 8 dimensionless quantities presented in Equation 10.7 or Equation 10.8, describes the same phenomenon as does the functional in Equation 10.6.

$$\frac{M}{f_c' e_w l_w^2} = F\left(\frac{\phi l_w}{\varepsilon_y \phi_{yD}}; \frac{P}{(l_w e_w + A_f) f_c'}; \frac{l_c}{l_w}; \frac{e_w}{l_w}; \frac{\phi_y l_w}{\varepsilon_y}; \frac{A_s}{e_w l_w}; \frac{A_f}{e_w l_w}\right) \tag{10.7}$$

$$m_D = F\left(\mu_\phi; \nu; \eta; \lambda; \phi_{yD}; \rho_s; a_f\right) \tag{10.8}$$

In Equation 10.8: m_D = dimensionless bending moment capacity; μ_ϕ = ductility of curvature; η = confinement length ratio; λ = cross section slenderness ratio; ν = cross section axial load ratio; ϕ_{yD} = dimensionless nominal yielding curvature; and ρ_s = the longitudinal reinforcement ratio concentrated at the end of the wall, and a = the flange to web area ratio (if a flange exists). The area of the wall corresponds to $A_g = e_w l_w + A_f$, and is used in the denominator of the axial load ratio shown in the Figures shown later.

Four ultimate strain limits for determining the ultimate ductility sequence in the graphs were considered. These are:

1) Ultimate compression strain in the unconfined concrete: ε_{cu} = 0.003
2) Ultimate compression strain in the confined concrete: $\varepsilon_{cu,c}$ = 0.008
3) Ultimate elongation strain in the steel: $\varepsilon_{su,t}$ = 0.04, and
4) Critical compression strain in the steel at the onset of buckling *after elongation has occurred*: ε_p^*, calculated with the formulation proposed by Rodriguez et al. (1999, 2013), given in Equation 10.9.

These limits are in agreement with common assumption such as: ε_{cu} = 0.003 for unconfined concrete (ACI318 / NZS3101) and $\varepsilon_{cu,c}$ = 0.008 for confined concrete (INN 2011). The strain limit for the elongation of the steel is more arbitrary, but it is seen as a valid assumption based on experimental evidence (Mander et al. 1984, Andriono and Park 1986, Rodriguez el al. 1999). The strain limit for the onset of buckling (ε_p^*) is calculated using the formula proposed by Rodriguez et al. (2013). This applies after at least one reversal has occurred in the element. This strain limit is calculated using Equation 10.9, which is in good correlation with experimental tests (Thomsen 1995, Rodriguez et al. 2009).

$$\varepsilon_p^* = \frac{11 - (5/4)(s_v/d_b)}{100} \tag{10.9}$$

In Equation 10.9 s_v = the vertical spacing of the confinement stirrups and d_b the diameter of the retrained bar. The physical meaning of ε_p^* is discussed in section 10.4.6 using Figure 10.21.

Confinement in both ends of the wall was hypothetically provided by transverse closed stirrups and cross ties arrange in the way presented in Quintana-Gallo (2008), and the parameters for the stress-strain model developed by Saatcioglu and Razvi (1992) were used for modelling that confined concrete. The reader is referred to those publications.

10.4.2 T-shaped wall AC situation: moment-curvature curves for varying axial load, all other parameters constant

In this case, sectional analyses focus on the axial load variation and all other conditions constant. The values of the products which remain constant are given by:

$$[\pi] = [\eta = 0; \lambda = 0.07; \phi_{yD} = 1.5; \rho_s = 0.25\%]$$

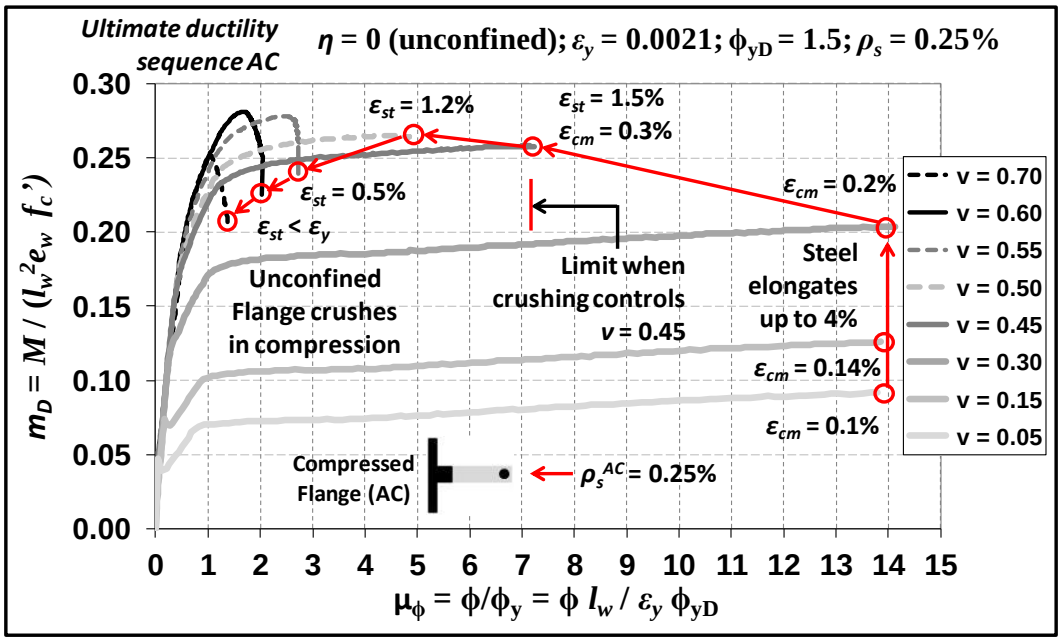

Figure 10.13: T-shaped wall moment v/s curvature AC; *v* varies; all other constant.

As shown in Figure 10.13, the ductility of curvature is expected to be of the order of 14 for axial load ratios ranging from v = 0.05 to v = 0.30. In all these cases the maximum strain limit in the steel (ε_{su} = 0.04) is reached before the maximum strain in the unconfined concrete (ε_{cu} = 0.003) is achieved in the outermost compressions layer in the flange.

For values greater than v = 0.30 though, the curvature capacity reduces considerably to values of $\mu_{\phi u}$ = 7 at v = 0.45 and $\mu_{\phi u}$ = 5 at v = 0.50, and then more drastically to approximately $\mu_{\phi u}$ = 3 at v = 0.55 and $\mu_{\phi u}$ = 2 at v = 0.60, and finally to a complete non-ductile capacity $\mu_{\phi u}$ = 1 (or 1.25) at v = 0.70. From a stability point of view, a bifurcation theory may be a good way of illustrating the mathematical pattern observed (Strogatz 1994). A bifurcation is a relatively sudden change in a stable function when a parameter

involved in the function changes slightly. In this case large changes in ductility capacity occur for slight changes in the value of the axial load at about v = 0.30. For axial loads smaller or equal to this value, the maximum curvature capacity is basically the same ($\mu_{\phi u}$ = 14).

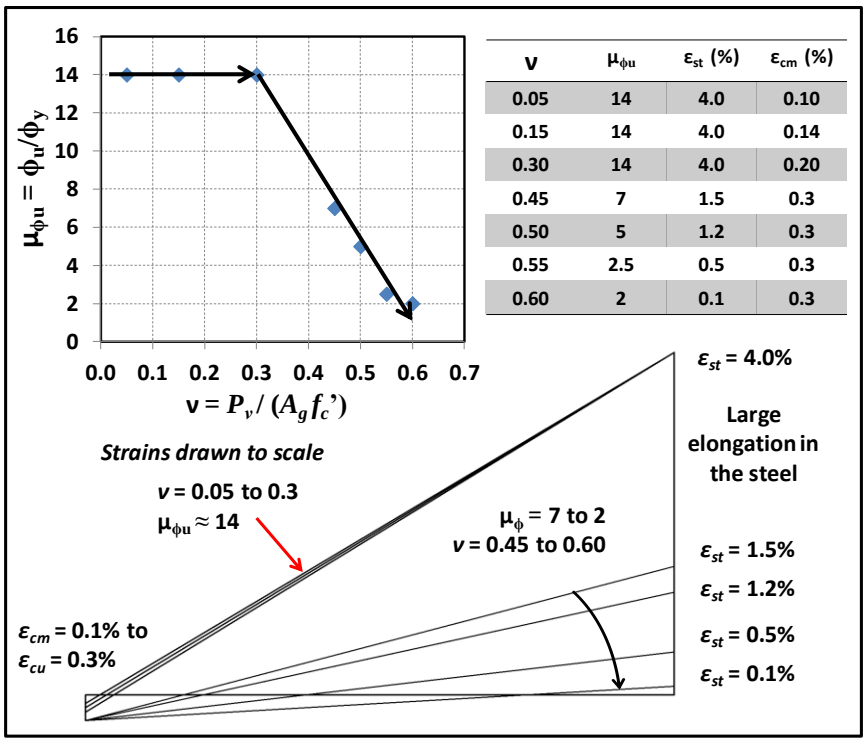

v	$\mu_{\phi u}$	ε_{st} (%)	ε_{cm} (%)
0.05	14	4.0	0.10
0.15	14	4.0	0.14
0.30	14	4.0	0.20
0.45	7	1.5	0.3
0.50	5	1.2	0.3
0.55	2.5	0.5	0.3
0.60	2	0.1	0.3

Figure 10.14: T-shaped wall moment-curvature AC situation; *v* varies; all other constant.

If the axial load increases from v = 0.30 to v = 0.45, the ultimate ductility capacity of the wall reduces to $\mu_{\phi u}$ = 7, half of that obtained for v = 0.30. The reason is that for the former axial load level, the maximum strain in the unconfined concrete is reached before the maximum tension occurs in the steel of the web, leading to the theoretical crushing in the concrete of the whole flange of the T-shaped wall at lower curvature ductility levels, as shown in Figure 10.13. In Figure 10.14, the values of the ultimate curvature and strain levels in the steel in the extreme fiber in tension (ε_{st}) and concrete in the compression (ε_{cm}). The curvature profile is also shown in Figure 10.14 for illustration.

10.4.3 T-shaped wall AT situation: moment-curvature curves for varying axial load, all other parameters constant.

In this case, the fixed parameters are:

$$[\pi] = [\eta = 0.45; \lambda = 0.07; \phi_{yD} = 2.0; \rho_s = 0.70\%]$$

In Figure 10.15 moment – curvature capacity/ductility curves are drawn for the section with the flange acting in tension (AT). Values of v were varied from 0.05 to 0.55, at close intervals. The confinement factor η was taken as 0.45, which corresponds to the value used in Quintana-Gallo (2008). This means that practically half of the web is considered to follow confined concrete laws for the analysis.

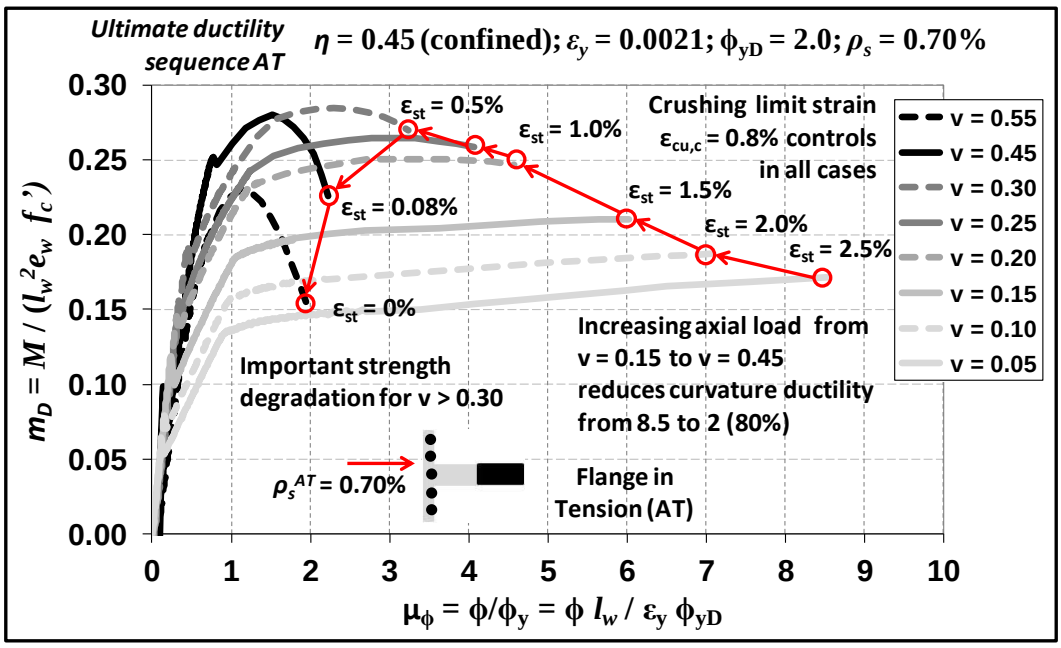

Figure 10.15: T-shaped wall moment-curvature ductility for AT; *v* varies; all other constant.

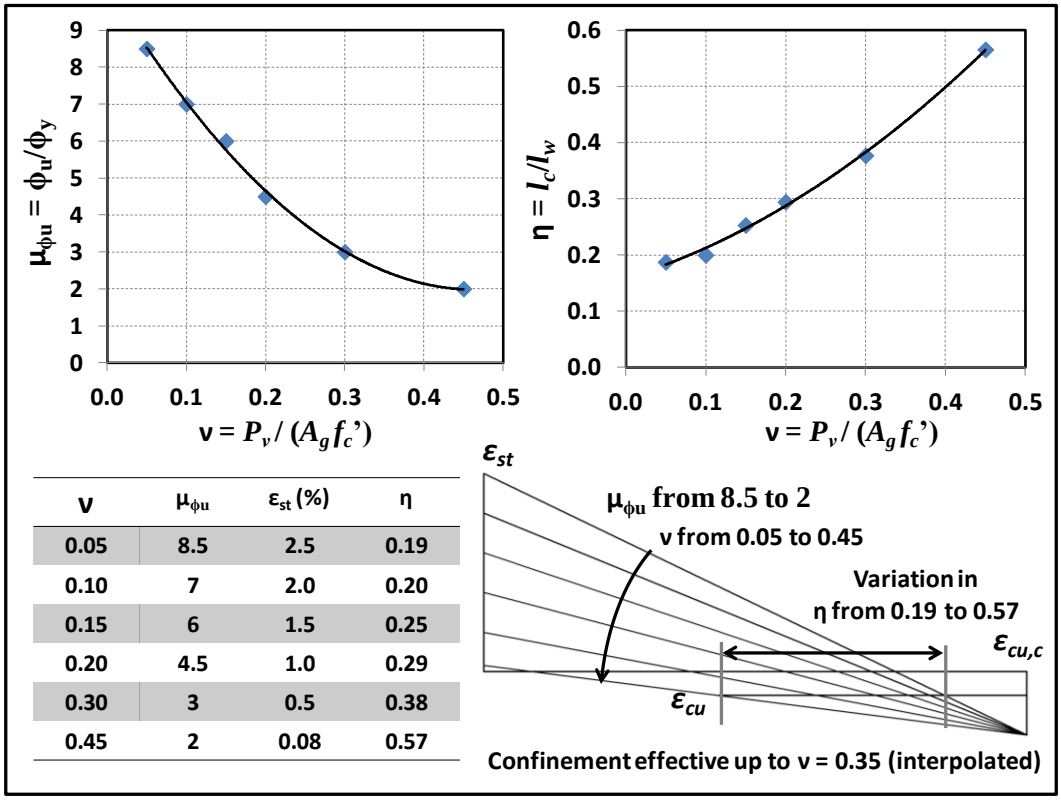

v	$\mu_{\phi u}$	ε_{st} (%)	η
0.05	8.5	2.5	0.19
0.10	7	2.0	0.20
0.15	6	1.5	0.25
0.20	4.5	1.0	0.29
0.30	3	0.5	0.38
0.45	2	0.08	0.57

Figure 10.16 T-shaped wall moment v/s ductility for AT; strain profiles results summary.

As stated before, a maximum compression strain in the confined concrete $\varepsilon_{cu,c}$ = 0.008 was used as a maximum allowed limit. As shown in Figure 10.15, for low axial load ratios the wall acting with the free end in compression, a curvature ductility of 8.5 could be achieved, about half the value obtained with the T-shaped wall acting with the flange in compression. However, for moderate axial load ratios of the order of v = 0.15, the curvature ductility decreases considerably falling to values closer to μ_φ = 4, 3, and 2, for v

= 0.25, 0.30, and 0.45, respectively. Note that there is also a significant degradation in the nominal moment capacity of the section after μ_ϕ = 1 (elastic limit) from v = 0.45. Combining the results obtained for AC and AT, a conservative limit of v = 0.15 seems to be appropriate for achieving a ductile mechanism in T-shaped walls, particularly considering the high compression strains induced in the free end of the web by large tensile forces from the reinforcement in the flange.

The adequacy of the confinement provided can be checked using Equation 10, where the parameter η is related to the maximum tensile strain reached in the steel. In Equation 10.10, the yielding curvature is assumed to be equal $\phi_y = \phi_{yD} \cdot \varepsilon_y / l_w$.

$$\eta = \left(1 - \frac{\varepsilon_{cu}}{\varepsilon_{cu,c}}\right)\left(1 - \frac{\varepsilon_{st}/\varepsilon_y}{\mu_\phi \, \phi_{yD}}\right) \tag{10.10}$$

For ε_y = 0.21%, ε_{cu} = 0.3%, $\varepsilon_{cu,c}$ = 0.8%, and ϕ_{yD} = 2.0 for AT, and using the values obtained from the moment-curvature analyses for the maximum elongation in the steel ε_{st}, the required confinement ratio calculated with Equation 10 and presented as a function of the axial load as well as the ultimate ductility of curvature in Figure 10.16.

10.4.4 Rectangular Wall: moment-curvature curves for varying axial load, all other remains constant

In this part, sectional analyses of the rectangular wall with the confinement length required by the NZS3101:2006 for 'ductile' walls are presented for different axial load levels, keeping all other conditions constant. The values of the products which remain constant are given by:

$$[\pi] = [\eta = 0.25; \lambda = 0.06; \phi_{yD} = 2.0; \rho_s = 0.22\%]$$

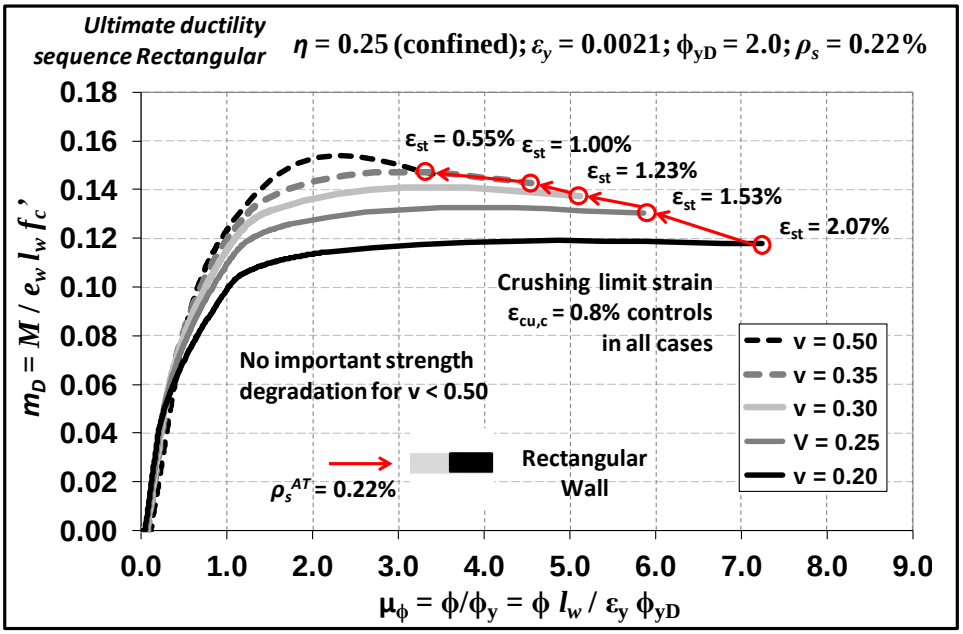

Figure 10.17: Moment-curvature diagrams of the rectangular wall with 'ductile' requirements for confinement according to NZS3101:2006.

In Figure 10.17 the ultimate curvature capacity sequence for the rectangular wall for different values of the axial load is presented. The strain limits selected in this case are the same as those considered for the T-shape wall curves. These are a maximum compression in the confined concrete $\varepsilon_{cu,c}$ = 0.008, and a maximum strain in the steel ε_{su} = 4%. In this case, the ultimate curvature ductility is always associated to the former, due to the absence of a wide compression end (flange). As can be observed in Figure 15 the ductility capacity for v = 0.20 increases to μ_ϕ = 8.5, and decreases almost linearly to approximately μ_ϕ = 3.0 for v = 0.50. For an axial load ratio v = 0.30, the ductility of curvature is reduced to μ_ϕ = 5.0.

A summary with the ultimate ductility of curvature versus the axial load as well as the required confined length due to this variation is presented in Figure 10.27. As noted before, the provided confinement for the rectangular wall required by the NZS3101:2006 standard for 'ductile' wall is adequate till v = 0.3. After this axial load level is exceeded, the wall would experience compression strains in the unconfined zone larger than ε_{cu} = 0.003. If the confinement length used was the one required for 'limited ductility' walls, then that confinement ratio η = 0.20 would be adequate up to v = 0.2 only. Therefore, any increasing in the axial load due to coupling effect of beams and floor slabs would transform into a brittle failure, since in this case the axial load ratio due to gravity loads is v = 0.2.

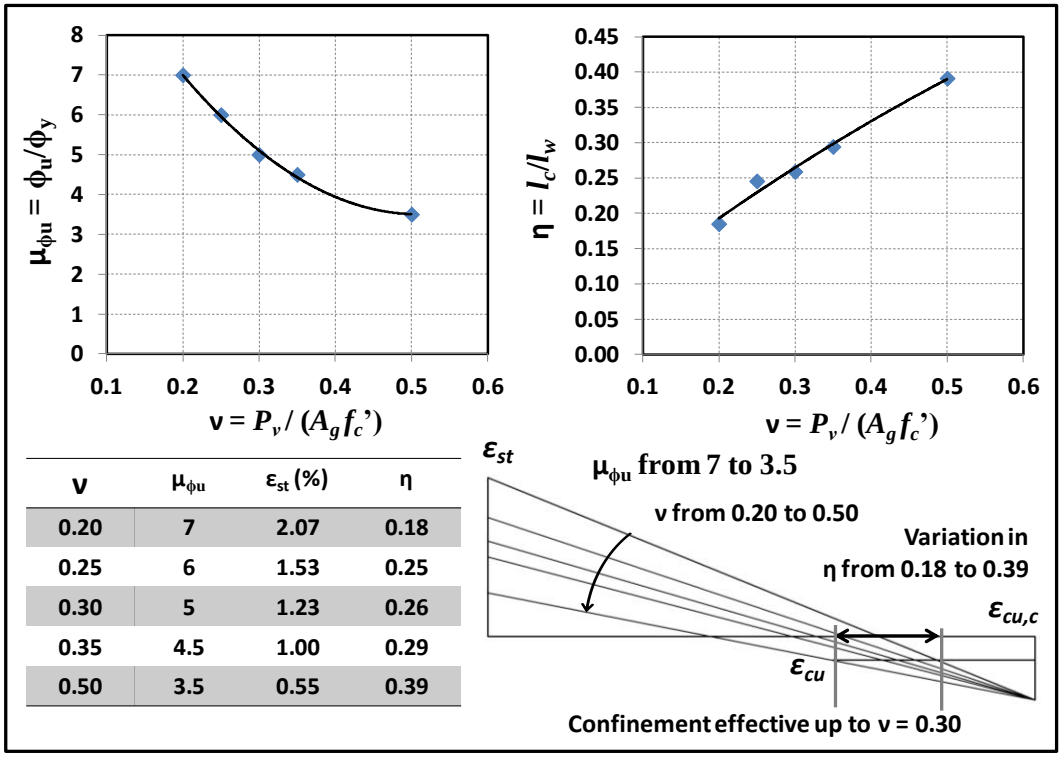

ν	$\mu_{\phi u}$	ε_{st} (%)	η
0.20	7	2.07	0.18
0.25	6	1.53	0.25
0.30	5	1.23	0.26
0.35	4.5	1.00	0.29
0.50	3.5	0.55	0.39

Figure 10.18: Rectangular ductility-axial load ratio, confinement length –axial load ratio, and strain profiles results summary.

10.4.5 Effect of confinement length (η), critical case: T-shaped wall AT situation, all other remains constant

In order to study the influence of the confinement length $\eta = l_c/l_w$ in the ductility of T-shaped walls with the flange acting in compression, two fixed values of the axial load were selected: $v = 0.15$ and $v = 0.3$, as a consequence of the analyses results under the AT and AC situation, respectively, and in line of the $v = 0.33$ limit of the AIJ Guidelines (AIJ 1999). For selecting the values of η, a value of $\eta = 0.45$ is used a comparison basis, since that is the consistent confinement length required by ACI318-2011. The sequence used for analyses is: η = 0.15, 0.30, 0.45, 0.60, and 0.75, which is approximately a ±60% variation from the basic value.

For low axial load: v = 0.15

In Figure 10.19 sectional analyses of the T-shaped wall in the AT situation are shown for $v = 0.15$. The confinement parameter η was reduced to $\eta = 0.15$ as a minimum and increased to $\eta = 0.60$ as a maximum, from the basic value $\eta = 0.45$. According to the curves of Figure 10.19 the effect of the variation in η in the ultimate curvature ductility ratio $\mu_{\phi u}$ is very low for the values of η used here. Values of μ_φ at ultimate are greater than 5 in all cases, reaching a maximum of 6 for $\eta = 0.60$ and $\eta = 0.45$, dropping to $\mu_\varphi = 5$ when $\eta = 0.15$. The curvature ductility becomes almost constant at a value of $\mu_\varphi = 6$, for confinement rations of 0.45 and 0.60, and moreover, it does not fall below $\mu_\varphi = 5$ for the smallest ratio considered of 0.15. It is concluded then, that for AT the effect of a larger confinement length from the free end of the web maintains the bending moment capacity (avoids strength degradation), but does not significantly increase the curvature ductility capacity, for low levels of axial load.

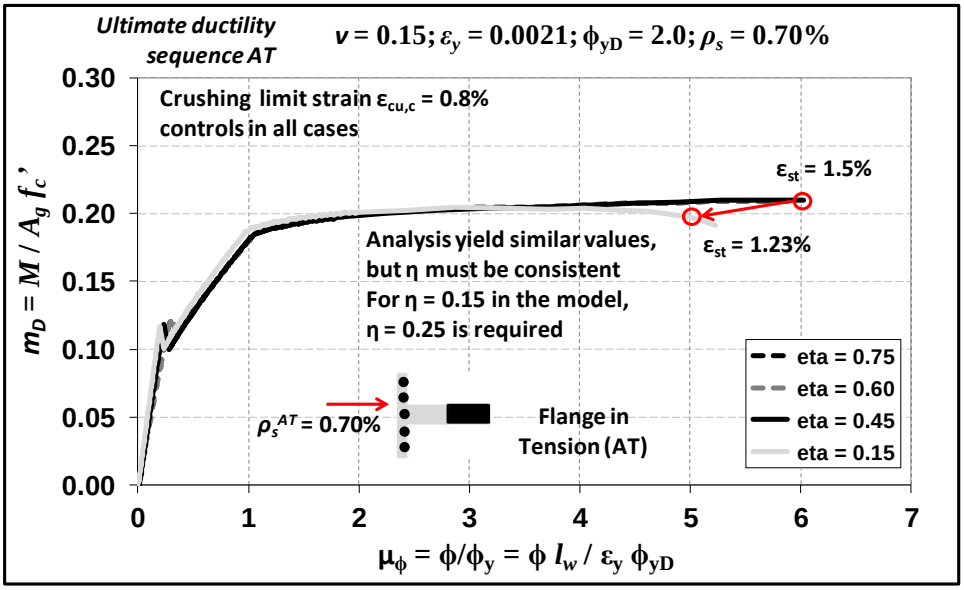

Figure 10.19: Dimensionless moment-ductility of curvature ductility for AT and $v = 0.15$.

In summary, the confinement provided to the wall will not increase the maximum curvature capacity in the critical section of the wall, but it will ensure that the concrete does not reach the maximum unconfined strain $\varepsilon_{cu} = 0.003$ in any part of the wall. As it

has been discussed before it seems reasonable to confine the complete length of the wall in critical regions, disregarding considerations based on demand related principles of allowing limited ductility elements in high or even moderate seismicity locations.

For moderate axial load: v = 0.30

From the curves presented in Figure 10.20, it can be noticed that when the confinement length ratio η increases, a greater curvature ductility capacity is reached, yet the increase is not significant for practical purposes, since μ_ϕ ranges from 2.5 to a 3.25 only. Strength at ultimate curvature is improved with a longer confinement length, so that the moment capacity increases from m_D = 0.18 for η = 0.15 to m_D = 0.28 for η = 0.45 or larger. When η increases from 0.15 to 0.75 at 0.15 intervals, the strength at ultimate is upgraded considerably, yet the curvature ductility is only ensured (strength degradation mitigated) from about η = 0.45 onward. If the free end of wall web is confined in a greater extension (larger η value), a reduction of the bending capacity is avoided and curvature ductility ratio maintained stable up to $\mu_{\phi u}$ = 3 as a maximum.

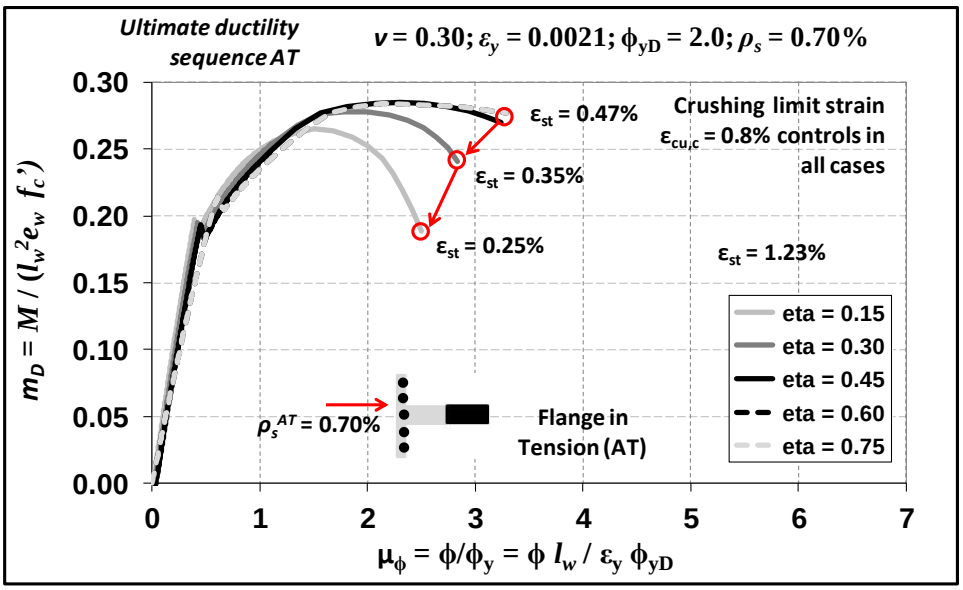

Figure 10.20: Dimensionless moment-ductility of curvature for AT and *v* = 0.30, *η* varies.

In Figure 20, the maximum tensile strains in the steel are shown for every case at ultimate ductility. It can be noted that the magnitude of these strains are very close to the yielding point ε_y = 0.21% for small confinement ratios, and only up to 0.45% for confinement ratios larger than 0.45, value used in the main analyses. This is an indication that even if large confinement lengths are provided, the ultimate ductility of curvature is not increased to a value larger to 3 for a 'moderate' axial load ratio v = 0.3 in a T-shaped wall deforming in the AT situation.

10.4.6 The effect of vertical spacing in buckling limit state

The problem of buckling of reinforcing bars in RC elements requires the understanding of a complex phenomenon where there exists strain distribution in between the crushed concrete and the buckled bar itself (Pantazopoulou 1998, Urmson and Mander 2011). It is also a phenomenon prone to develop after elongation had taken place in the reinforcing

bar. This requires the introduction of the cyclic response of structural members (Dodd and Restrepo 1995, Rodriguez el al. 1999).

In Figure 10.21, the strain profile in the critical section of a T-shaped wall deforming in the AC situation, when large elongations develop, is presented. For a given axial load and confinement length, the maximum tensile strain in the section of the wall is proportional to the curvature demand in the critical section.

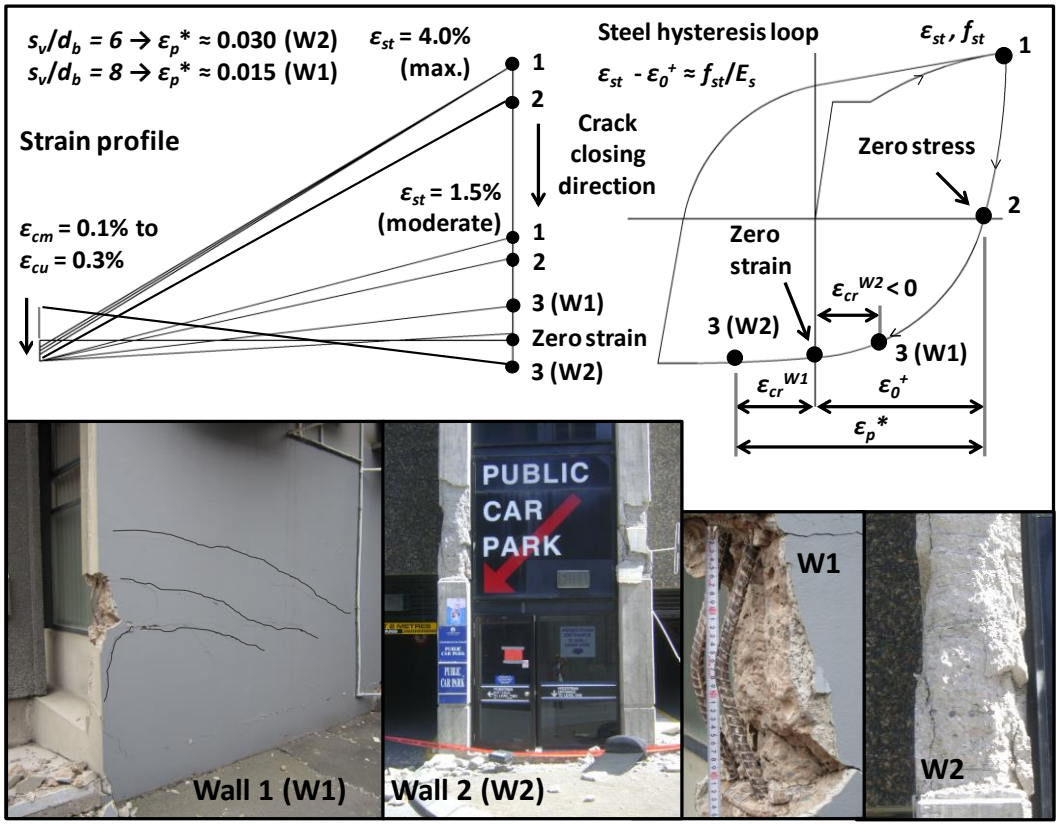

Figure 10.21: Buckling in two RC walls with different vertical spacing of confinement elements.

The achieved tensile strain in the first stretching is identified as point 1 in Figure 10.21. There, two strain levels have been used for the same point, representing large and moderate elongation demand: ε_{st} = 4% (maximum) and ε_{st} = 1.5% (moderate). If failure is not reached at this point, and the steel is able to follow the descending branch of the hysteresis loop from point 1 reaching point 2, the zero stress point. The strain associated to this point, ε_0^+, can be estimated using Equation 10.11.

$$\varepsilon_0^+ = \varepsilon_{st} - f_{st}/E_s \tag{10.11}$$

In Equation 10.11: f_{st} is the stress in the steel at maximum elongation (point 1 in Figure 21). For a 420 MPa (60ksi) grade mild steel assuming a tensile stress $f_{st} = 1.25f_y$ = 525 MPa at peak strain level, then the strain at point 2 is $\varepsilon_0^+ \approx \varepsilon_{st} - 0.25\%$. From point 2 towards point 3, the stress has an increasing compression value, even though the bar remains under tensile strains. If point 3 can be reached, then the bar can experience compression strains which continue to grow until point 4 is reached, which determines the onset of buckling (Rodriguez et al. 1999, 2013).

With Equation 10.9 it is predicted that the value of the strain from point 2 to 4 in Figure 10.21 is ε_p^* = 3.5% for s_v/d_b = 6, and ε_p^* = 1% for s_v/d_b = 8. For values of s_v/d_b greater than 8, Equation 9 is not valid anymore as the onset of buckling may take place at very low strain levels, which is in line the results obtained in most of the research devoted to the topic, such as in Mau (1990), Rodriguez et al. (1999) and Mender et al. (1984). Hence for wall designed to have limited ductility as stated by the NZS3101:2006 standard, where a maximum spacing of only $10d_b$ is required, buckling of the longitudinal rebar is expected to be a source of damage even at moderate ductility demand levels.

Consider as an example the failure mode developed in wall 1, presented in the pictures of Figure 10.21. It can be observed that the spacing is quite large (300mm), and of the order of s_v/d_b = 10. It was also observed in the field inspection that flexural cracks developed in one end of the wall only, as shown schematically in Figure 10.21. This indicates that the end of the wall shown in Figure 10.21 firstly developed tensile strains in the longitudinal rebar and then, when the reversal came, the bar buckled under tension strains, making it impossible for the crack to close, and leading most probably to redistribution of strains towards other structural elements. Consider Wall 2 in Figure 10.21. In this wall, the spacing was much smaller, and as can be seen, even if spalling of the unconfined concrete and some deterioration of the confined core was observed, bars did not buckle or at least the onset of buckling was not notorious. Combining Equations 10.8 and 10.11, with reference to Figure 10.21, the strain at the onset of buckling referred to the zero strain point ε_0^+ is given by Equation 10.12.

$$\varepsilon_{s,cr} = \varepsilon_p^* - \varepsilon_{st} + f_{st}E_s \tag{10.12}$$

Assume for example that a maximum tensile strain in the steel of 1.5% was reached in the first movement of the wall. Then if ε_p^* = 3.5%, the onset of buckling would be $\varepsilon_{s,cr}$ = 1.25% - 3.5% = -2.25%, and then crushing of the confined concrete at $\varepsilon_{cu,c}$ = 0.8% would be reached first. However, if the same elongation is reached in walls detailed as Wall 1 in Figure 21, then ε_{cr} = 1.25% - 1.0% = -0.25% (in compression) and buckling will be the controlling limit state, at very low deformations (lower than ε_{cu}). If larger elongations in the steel are reached before the reversal takes place, then buckling becomes even more critical, and it may occur before flexural cracks close. For example, for ε_{st} = 4% and s_v/d_b = 6 ε_{cr} = 3.75% - 3.0% = 0.75% (in tension). As buckling is associated to the occurrence of previous stretching in the rebar, then the likelihood of its occurrence can only be estimated using cyclic nonlinear (dynamic) analyses.

10.4.7 The effect of wall thickness (λ varies)

The effect of the thickness of the wall is seen as a problem more related to *second order effects*, such as instable out-of-plane failure, which is beyond the scope of a sectional analysis and should be captured with dedicated and more complex member analyses (Paulay and Priestley 1993). The influence of a direct reduction of wall thickness without accounting for second order effects can be evaluated using the results for different values of v and the corresponding values of the axial load (P_v), since a combination of both is included in that dimensionless ratio. A reduction in the thickness would lead to increasing values of v for a given force P, affecting the ductility capacity in an inversely proportional way.

10.5 TOP STOREY DRIFT OF THE WALL AS A FUNCTION OF THE ULTIMATE DUCTILITY OF CURVATURE

The relationship between the top storey displacement (D_t) and the ultimate curvature (ϕ_u) at the critical section of a slender cantilever wall after yielding occurs can be estimated assuming that all inelasticity is concentrated in a critical region at the base of the wall. It is also assumed that this region has a finite length named the plastic hinge length (l_p), and that the wall moves as a rigid body pivoting at half of the plastic hinge length (Wallace and Moehle 1992), as illustrated in Figure 10.22.

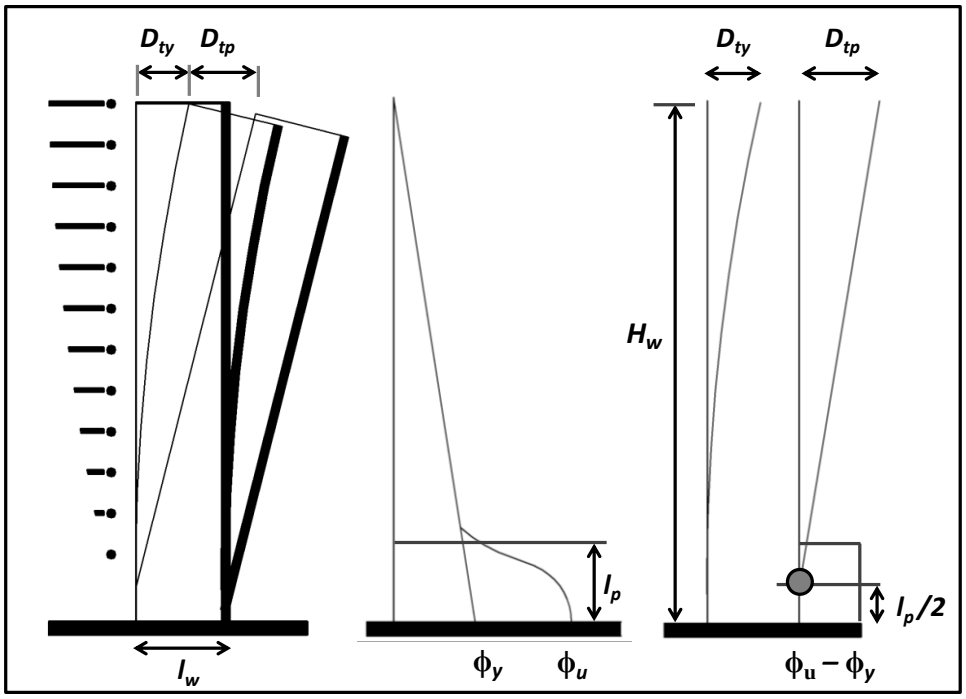

Figure 10.22: Top storey displacement as a function of wall geometry and curvature in the critical region: nominal yield and plastic displacements.

The total displacement at the top the wall can be written in terms of the top storey drift ratio defined as $D_{rt} = D_t / h_w$, where h_w is the height of the wall. For the parameters defined before in this paper, the relationship between the top storey displacement and the ultimate ductility of curvature $\mu_{\phi u}$ can be written as Equation 10.13. Note that the contribution of shear deformations is neglected.

$$D_{tu} = D_{ty} + D_{tp} = \frac{\phi_{yD}\varepsilon_y}{l_w}\left[\frac{11}{40}h_w^2 + l_p(\mu_{\phi u} - 1)\left(h_w - \frac{l_p}{2}\right)\right] \quad (10.13)$$

In Equation 10-12, D_{ty} is the top storey displacement at nominal yielding at the base of the wall, and D_{tp} is the plastic top storey displacement (see Figure 10.22). Note that two additional variables have been incorporated into the problem: the height of the wall and the plastic hinge length. If the wall slenderness ratio is defined as $\psi = h_w/l_w$, and the plastic length is taken as a linear function of the wall length $l_p = \alpha l_w$ for some $\alpha > 0$, then Equation 10-13 can be re-written in a dimensionless fashion as Equation 10.14.

$$D_{rtu} = \phi_{yD}\varepsilon_y\left[\frac{11}{40}\psi + \frac{\alpha}{\psi}(\mu_{\phi u} - 1)\left(\psi - \frac{\alpha}{2}\right)\right] \quad (10.14)$$

Using the tables of the ultimate ductility sequence for the T-shaped (AC and AT situations) and the rectangular walls and Equation 13, the top storey drift at ultimate limit state can be calculated for the appropriate value of the dimensionless yielding curvature, the yielding strain of the steel, and a fixed value of the variables ψ and α. The wall used as example in this contribution has a slenderness ratio of ψ = 45m/6.7m = 6.7. Three values of α were selected: α = 0.25, 0.5 and 0.75, in order to investigate how much do the results change with the assumption in the plastic length. The first term of Equation 10.14 corresponds to the nominal yielding drift ratio D_{rty}, defined formally in Equation 10.15.

$$D_{rty} = \frac{11}{40}\phi_{yD}\varepsilon_y\psi \quad (10.15)$$

Note that once the designer has the geometrical dimensions of the wall, the yielding drift ratio can be readily computed with Equation 10.15, without the need of knowing the reinforcement of the wall. For the case of the T-shaped wall in the AT situation, and for ψ = 6.7, then D_{rty} = 0.77%. For the same T-shaped wall but in the AC situation, the yielding drift values obtained with Equation 10.13 are ¾ of those obtained for the AT situation since ϕ_{yD} = 1.5 instead of 2.0, i.e. D_{rty} = 0.56% (for ψ = 6.7). For the rectangular wall the same values for the T-shaped wall in the AT situation is adequate, given that ϕ_{yD} can also be taken as 2.0 (Priestley et al 2007). If now Equation 10.14 is divided by Equation 10.15, then the top displacement ductility can be calculated directly, as expressed in the form of Equation 10.16.

$$\mu_t = 1 + \frac{40\alpha}{11\psi^2}(\mu_{\phi u} - 1)\left(\psi - \frac{\alpha}{2}\right) \quad (10.16)$$

The computed ultimate drift ratios and top storey displacement ductilities are shown in the tables and figures presented in the following subsections for three cases: (1) T-shaped wall AC situation, (2) T-shaped wall AT situation, and (3) rectangular wall.

10.5.1 Case 1: T-shaped wall AC situation

The ultimate top storey drift ratio sequence for the T-shaped wall in the AC situation is calculated for the ultimate ductility of curvature $\mu_{\phi u}$ associated to increasing values of axial load (up to ν = 0.50), and for ϕ_{yD} = 1.5, ε_y = 0.21%, and η = 0 (unconfined flange). These values are plotted in Figure 10.23, directly as a function of ν for α = 0.25, 0.50 and 0.75. These results are also presented in Table 10.1.

Table 10.1: Ultimate top storey drift ratios T-shaped wall AC for different plastic lengths.

T-shaped AC		D_{rtu} (%)			$\mu_t = D_{rtu} / D_{rty}$; D_{rty} = 0.58%		
ν	$\mu_{\phi u}$	α = 0.25	α = 0.50	α = 0.75	α = 0.25	α = 0.50	α = 0.75
0.05	14	1.6	2.6	3.5	2.7	4.4	6.0
0.15	14	1.6	2.6	3.5	2.7	4.4	6.0
0.30	14	1.6	2.6	3.5	2.7	4.4	6.0
0.45	7.0	1.0	1.5	1.9	1.8	2.6	3.3
0.50	5.0	0.9	1.2	1.5	1.5	2.0	2.5

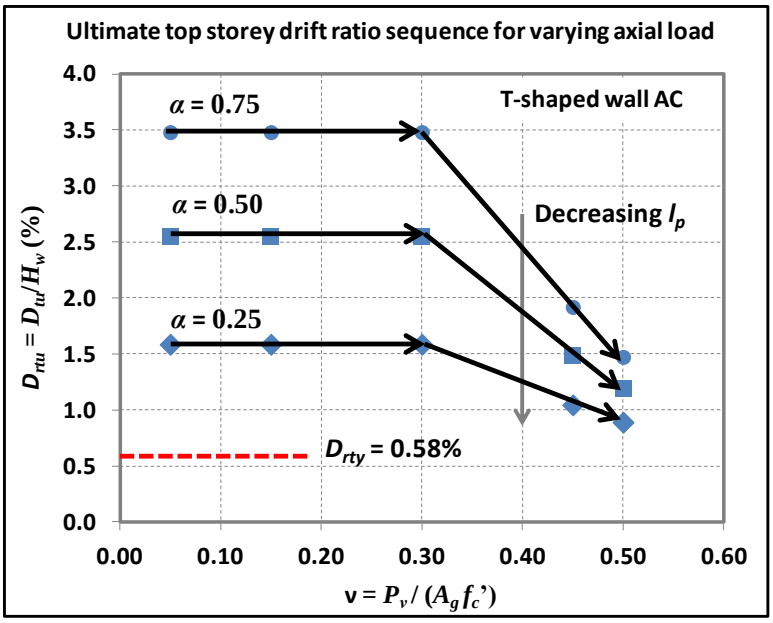

Figure 10.23: Ultimate top storey drift ratio for varying axial load and three values of the plastic hinge length ($l_p = \alpha l_w$), case 1: T-shaped wall AT situation.

10.5.2 Case 2: T-shaped wall AT situation

The ultimate top storey drift ratio sequence for the T-shaped wall under the AT situation is calculated as a function of the ultimate ductility of curvature $\mu_{\phi u}$ associated to increasing values of axial load (up to $\nu = 0.3$), and for $\phi_{yD} = 2.0$, $\varepsilon_y = 0.21\%$, and $\eta = 0.45$. These values are plotted in Figure 24 directly as a function of ν using three different plastic hinge lengths, determined by $\alpha = 0.25$, 0.50 and 0.75. The values plotted in Figure 10.24 are also presented in Table 10.2, where the values of the ductility of curvature and the top displacement ductility are also shown.

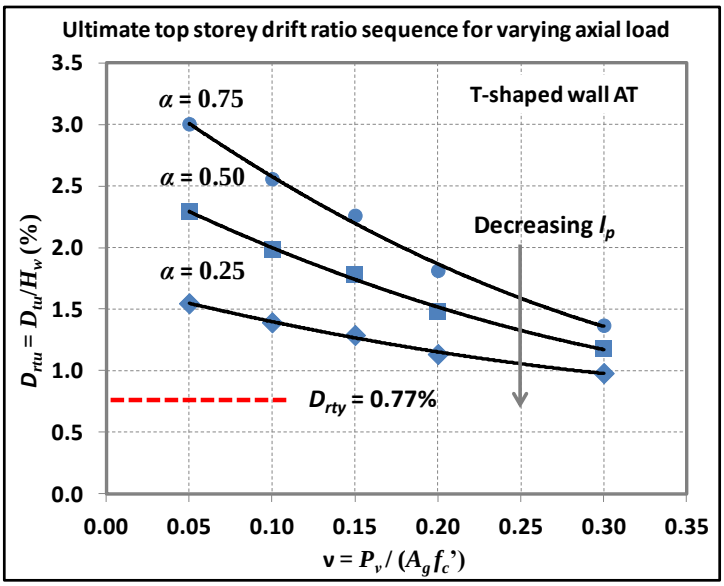

Figure 10.24: Ultimate top storey drift ratio for varying axial load and three values of the plastic hinge length ($l_p = \alpha l_w$), case 1: T-shaped wall AT situation.

Table 10.2: Ultimate top storey drift ratios T-shaped wall AC for different plastic lengths.

T-shaped AT		D_{rtu} (%)			$\mu_t = D_{rtu} / D_{rty}$; D_{rty} = 0.77%		
ν	$\mu_{\phi u}$	α = 0.25	α = 0.50	α = 0.75	α = 0.25	α = 0.50	α = 0.75
0.05	8.5	1.5	2.3	3.0	2.0	3.0	3.9
0.10	7.0	1.4	2.0	2.6	1.8	2.6	3.3
0.15	6.0	1.3	1.8	2.3	1.7	2.3	2.9
0.20	5.5	1.1	1.5	1.8	1.5	1.9	2.3
0.30	3.0	1.0	1.3	1.4	1.3	1.5	1.8

10.5.3 Case 3: Rectangular Wall

The ultimate top storey drift ratio sequence for the rectangular wall is calculated as a function of the ultimate ductility of curvature $\mu_{\phi u}$ associated to increasing values of axial load (up to ν = 0.5), and for ϕ_{yD} = 2.0, ε_y = 0.21%, and η = 0.25. These values are plotted in Figure 25 directly as a function of ν using three different plastic hinge lengths, determined by α = 0.25, 0.50 and 0.75. The values presented in the graphs of Figure 10.25 are also presented in Table 10.3, together with the corresponding ductility of curvature, the top displacement at ultimate limit state, and the corresponding displacement ductility.

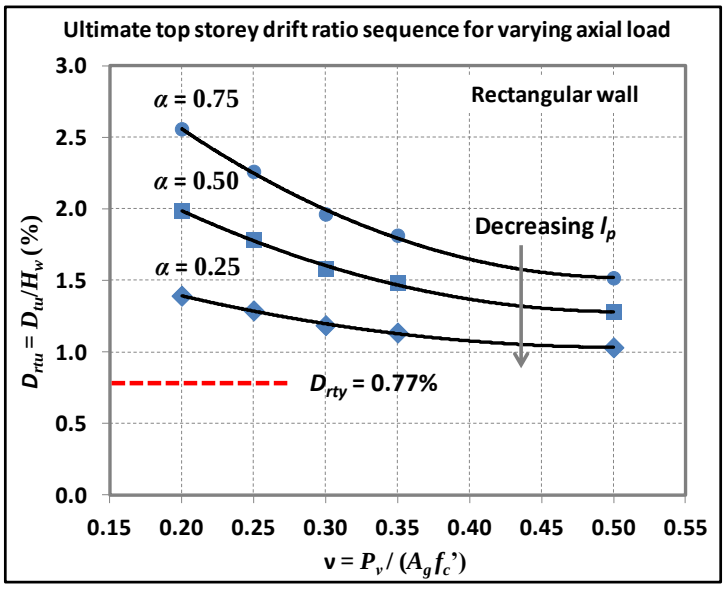

Figure 10.25: Ultimate top storey drift ratio for varying axial load and three values of the plastic hinge length ($l_p = \alpha l_w$), case 3: Rectangular wall.

Table 10.3: Ultimate top storey drift ratios Rectangular wall for different plastic lengths.

Rectangular		D_{rtu} (%)			$\mu_t = D_{rtu} / D_{rty}$; D_{rty} = 0.77%		
ν	$\mu_{\phi u}$	α = 0.25	α = 0.50	α = 0.75	α = 0.25	α = 0.50	α = 0.75
0.20	7.0	1.4	2.0	2.6	1.8	2.6	3.3
0.25	6.0	1.3	1.8	2.3	1.7	2.3	2.9
0.30	5.0	1.2	1.6	2.0	1.5	2.0	2.5
0.35	4.5	1.1	1.5	1.8	1.5	1.9	2.3
0.50	3.5	1.0	1.3	1.5	1.3	1.7	2.0

10.6 EVALUATION OF THE SEISMIC DEMAND USING ELASTIC AND INELASTIC DISPLACEMENT SPECTRA

10.6.1 Ground motion records and elastic response spectra

During the 22 February 2011 seismic event, the ground motion was recorded in some stations located in the most affected area (Kam et al. 2011, Pampanin et al. 2012a,b). In this study, a set of four ground motions consisting in one of the horizontal components recorded at four of those stations was selected. These records are shown in Figure 26 in terms of acceleration.

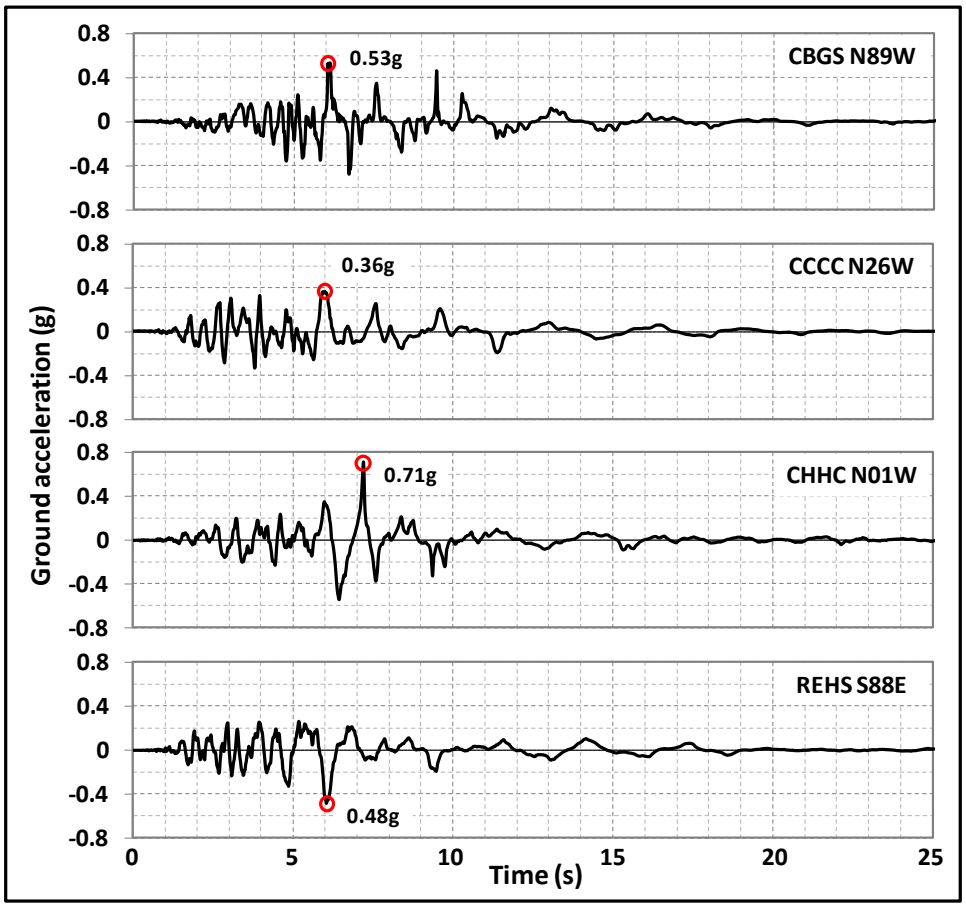

Figure 10.26: Acceleration ground motions recorded at Christchurch CBD during the 22 February 2011 seismic event: GBSG, CCCC, CHHC, REHS stations.

The graphs of Figure 10.26 indicate that the duration of the ground motion is quite small, with a strong motion time of about 10 seconds. The maximum ground accelerations recorded in the four stations are all larger than the nominal PGA (Z factor in NZS1107.5:2004) for Christchurch before May 2011, Z = 0.22g. In May 2011 an amendment to the standard upgraded that value to Z = 0.30. This value is also smaller than those recorded during the 22 February 2011 seismic event in the stations considered herein.

In Figure 10.27, the elastic spectra of those records, obtained with the computer program INSPECT (Carr 2012) for a critical damping ratio of 5% are shown and compared with

the elastic displacement spectra compatible with the design acceleration spectra for the city of Christchurch required by NZS1170.5:2004 for different soil types (note Z = 0.22 as it was prescribed for Christchurch until 2011). These design displacement spectra (S_d) where constructed using Equation 10-17.

$$S_d^{NZS} = (T^2/4\pi^2) C_h \, Z \, R_u \, N \, S_p \tag{10.17}$$

In Equation 10-17, T = the period; C_h = the spectral shape factor; Z = the hazard factor (Z = 0.22 until May 2011); R_u = the return period factor for ultimate limit state; and S_p = the structural performance factor. In this case, R_u was taken as 1.8, which corresponds to a 1/2500 probability of exceedance in 50 years according to AS/NZ1170.0:2002. In order to be consistent with the assumption of elasticity in the response, the structural ductility factor was taken as μ = 1.0, and thus the structural performance factor is S_p = 1.0. However, for an inelastic spectrum developed with a ductility factor $\mu \geq 2.0$, then S_p = 0.7 and this factor decreases linearly from 1.0 to 0.7 from μ = 1.0 to μ = 2.0 and then remains constant, as stated in the NZS1170.5:2004 loading standard section 4.4.2 (Standards New Zealand 2004).

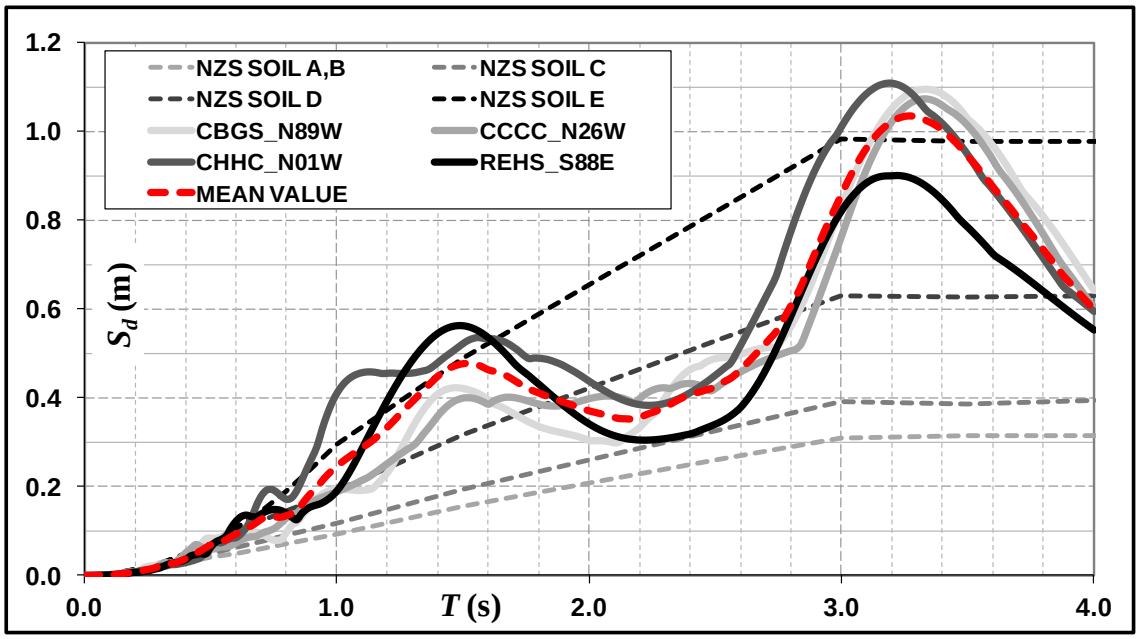

Figure 10.27: Elastic displacement spectra for of the ground motions recorded at Christchurch CBD during the 22 February 2011 seismic event (for Z = 0.22).

In the dynamic analysis accepted by the New Zealand standard NZS1170.5:2004, as well as other seismic codes in the world, the ground motion records used must be scaled up or down to fit the design acceleration spectrum of a given site. As a consequence, both PGA and more importantly the frequency characteristics of the motion are altered. This may lead to substantially different results of the dynamic analyses using the original and the modified records. Hence, if the ground motion produced by the seismic event to come next is such that its spectral response is importantly larger than the design spectrum in the period range corresponding to the predominant period of a structure, then any dynamic analysis performed before that earthquake occurs using the currently accepted

methodology would be proofed to be incorrect, independently of the amount of records used.

This effect can be observed in the graph of Figure 27. For periods of 0.7 to 1.5 seconds, it can be observed that the envelope of the displacement demand of the recordings at stations CBGS and REHS are significantly larger than the design spectra for the worse soil conditions. In the period range between 1 and 1.2 seconds, this envelope has a maximum difference, when S_d = 45cm and S_d^{NZS} = 30cm, for the worse soil conditions (Soil type E). That is a 50% underestimation in the displacement demand. Considering the average value of the spectra obtained with the four records, then the difference is even larger since S_d^{avg} = 25cm, leading to greater underestimations.

This suggest that the use of average values of various spectra calculated with different records are not on the safe side, even if adding the latest information into the pool of historical databases. However, these displacement spectra are limited to the elastic response of a structure. As will be show in the next paragraphs, when deriving inelastic spectra, larger or smaller spectral displacements can be obtained when compared to the elastic counterparts, depending on the period range under examination.

10.6.2 Inelastic displacement response spectra

Displacement spectra of the records presented in the previous section were constructed for the elastic condition (μ = 1), and two inelastic cases with ductilities μ = 2.0 and μ = 3.0, respectively. These spectra were obtained with the computer program INSPECT (Carr 2012), with the following properties of the single degree of freedom (SDOF) system:

- A damping ratio ξ = 2%.
- A hysteretic behaviour that follows the Clough hysteresis rule (Otani 1979), i.e. Modified Takeda hysteresis rule with $\alpha = \beta = 0.0$ (Otani 1974, Carr 2012).
- The post-yield stiffness ratio (bi-linear factor) is r = 0.2.

Note that there is a difference in the spectral ordinates in between the elastic spectra shown in Figure 10.27 and Figure 10.28, due to a larger critical damping ratio used in the former. In addition, the spectra of three ground motions recorded during the Maule Chile earthquake are presented for illustration, as well as one ground motion recorded during the 1985 Valparaíso Chile earthquake and another recorded at SCT station in Mexico City during the 1985 Michoacán Mexico Earthquake are included. Details of the acceleration histories used for the derivation of these spectra can be found in Quintana-Gallo (2008) and Quintana-Gallo et al. (2012).

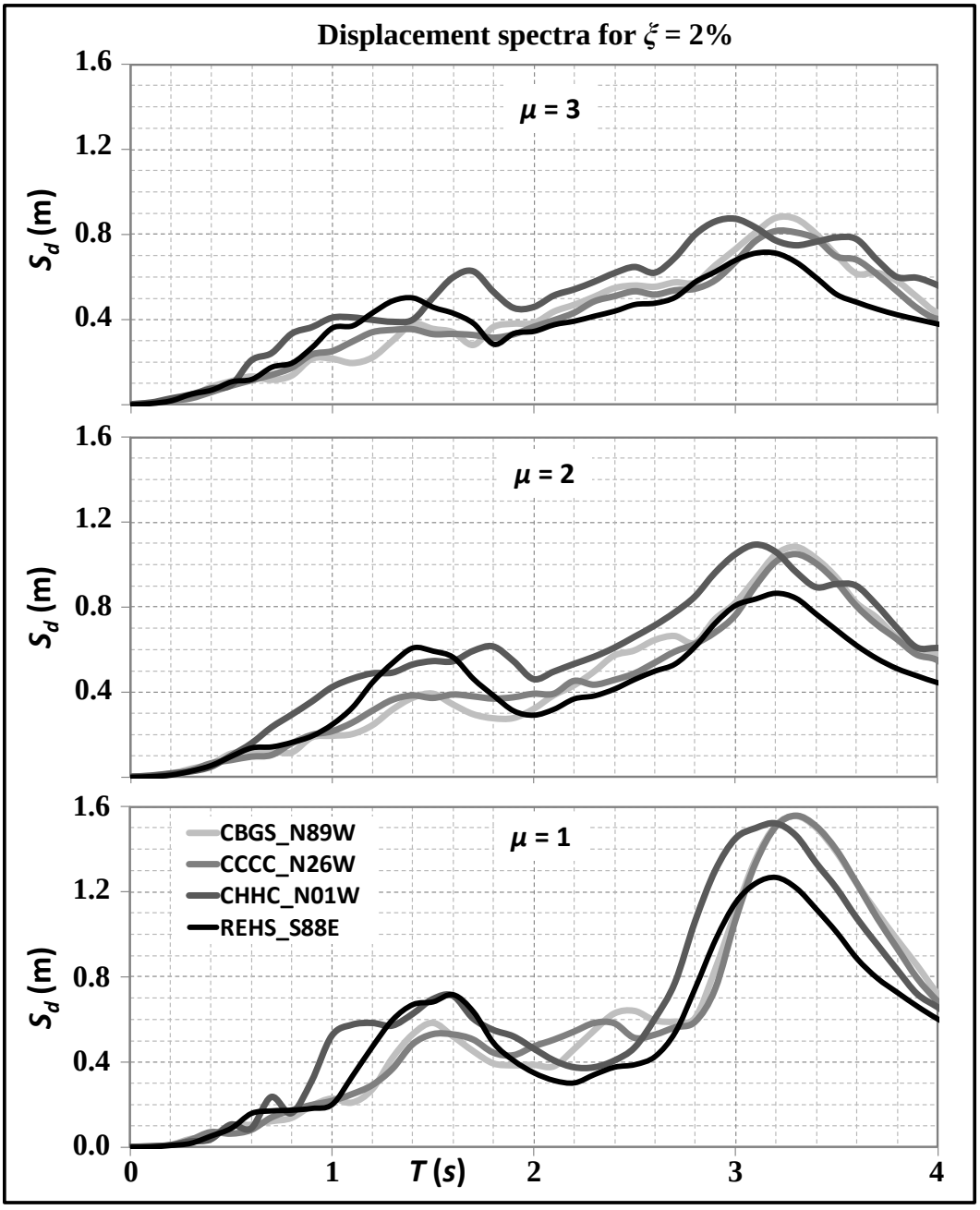

Figure 10.28: Displacement spectra for μ = 1 (elastic) and μ = 2 and 3 (inelastic) – ground motions recorded during the 22 February 2011 Canterbury Earthquake.

In Figure 10.28 the displacement spectra of the selected ground motions recorded during the Canterbury earthquake are presented. In the graphs it can be observed that inelastic spectral displacements sometimes are larger and sometimes are smaller than the elastic counterpart. In the initial ascending branch from T = 0 to 1 sec., there are important differences in the spectral ordinates of the four records. With CHHC record, the larger spectral displacements are obtained in that whole range. The spectral displacements at 1 second for this record are: S_d = 0.55m for μ = 1 and S_d = 0.40m for μ = 2 and 3. The inelastic spectral displacements for periods smaller than 0.9 seconds are larger than the elastic counterpart for the same record (CHHC). This is also true for the spectral displacement obtained with REHS record in the low period range. At 1 second, for example, S_d = 0.20m for μ = 1, S_d = 0.25m for μ = 2, and S_d = 0.35m for μ = 3. However,

with this record, peak spectral larger displacements of S_d = 0.60m for μ = 1 and 2 and S_d = 0.50m for μ = 3 are reached at 1.4 seconds.

These spectral displacements correspond to an envelope of all spectra for the range of 1.25 to 1.4 seconds for μ = 3, and the period range of 1.25 to 1.6 seconds for μ = 1 and 2. From T = 1.6 to 3.1 seconds, larger spectral displacements are obtained with CHHC record for μ = 2 and 3. However, for T = 2.0 to 2.3 seconds and μ = 1, the spectral demands obtained with CCCC record are larger than those of the other three records. The same is true for the spectra obtained with CBGS records for periods in between 2.3 and 2.6 seconds. The largest demands in the first peak of the spectra corresponds to S_d = 0.70m at T = 1.6 seconds for all ductility factors, but the peak at T = 1 second of S_d = 0.40m must also be considered if a straight line is intended to represent an envelope of the displacement spectra.

After 1.6 seconds all spectral demands decrease in general, reaching the lowest value at T = 2 sec. with S_d = 0.50m for all ductilities. From there onward, displacement increase again, forming a second peak at $T \approx 3$ to 3.2 sec. with a maximum spectral displacement S_d = 1.5m for μ = 1, S_d = 1.1m for μ = 2, and S_d = 0.90m for μ = 3. This would have normally been understood as the corner period of the displacement spectra (Faccioli et al 2003). In the four cases, the spectral demands tend to converge to a region oriented as a straight line from peak values at T = 3 sec. to the origin, with some exceptions in the region close to T = 1 sec.

In Figure 10.29, the elastic and inelastic displacement spectra obtained for ductilities μ = 1, 2 and 3 for the additional ground motions are shown. In the graphs shown in Figure 29, it can be observed firstly that the spectral displacements of all records are reduced with increasing ductility factors in a large part of the period range of interest. However, large values are obtained for the smallest ductility factor. The spectra of the Maule earthquake records have an important spectral demand at T = 1.1 sec. That is achieved with VinaMM2010 record, with spectral displacements S_d = 0.4m for μ = 1, S_d =0.3m for μ = 2, and S_d = 0.2m for μ = 3. For that record, the spectral displacements are almost identical in the range of T = 0.9 to 1.2 sec. for μ = 2 and 3.

In the particular case of VinaMM2010 record, the high energy of the Fourier components of the ground motion with a period of 1 second was large, and since the duration of that motion lasted for about 1.5 minutes, then resonance would have been a very important problem for structures with periods close to that value. Note that the effect of the duration of the ground motion enables the possibility of structures with other periods to also experience resonance, if that phenomenon is expected at periods larger than the initial period of the structure, because it elongates during the time that the motion lasts.

This was demonstrated using shake table test of a 3-storey model building at the University of Canterbury in 2010 (Chapter 4). The specimen, with an initial measured period T = 0.5 sec. in the prototype domain, was subjected to that particular record and suffered stiffness degradation in the first cycles which led to an elongation of the predominant period large enough so that resonance was achieved by the specimen.

In Figure 10.29 it can also be observed that after T = 1.4 sec. for μ = 1, the spectrum obtained with the ground motion recorded at Concepción city centre (Conce2010) becomes larger than the other two records from the Maule earthquake for μ = 1. For μ = 2

and 3 though, the spectral displacements become larger at 1.1 and 1 seconds, respectively, where S_d = 0.2m and 0.3m is reached in each case. At T = 1.4, a value of S_d = 0.4m is reached for all μ. Beyond that period, the spectral displacements start to rapidly increase. For T = 1.6, spectral displacements as high as S_d = 1.1m for μ = 1, S_d = 0.8m for μ = 2, and S_d = 0.6m for μ = 3. A maximum value is reached at T = 1.9 sec. where spectral displacements are S_d = 1.6m for μ = 1, S_d = 1.0m for μ = 2, and S_d = 0.8m for μ = 3.

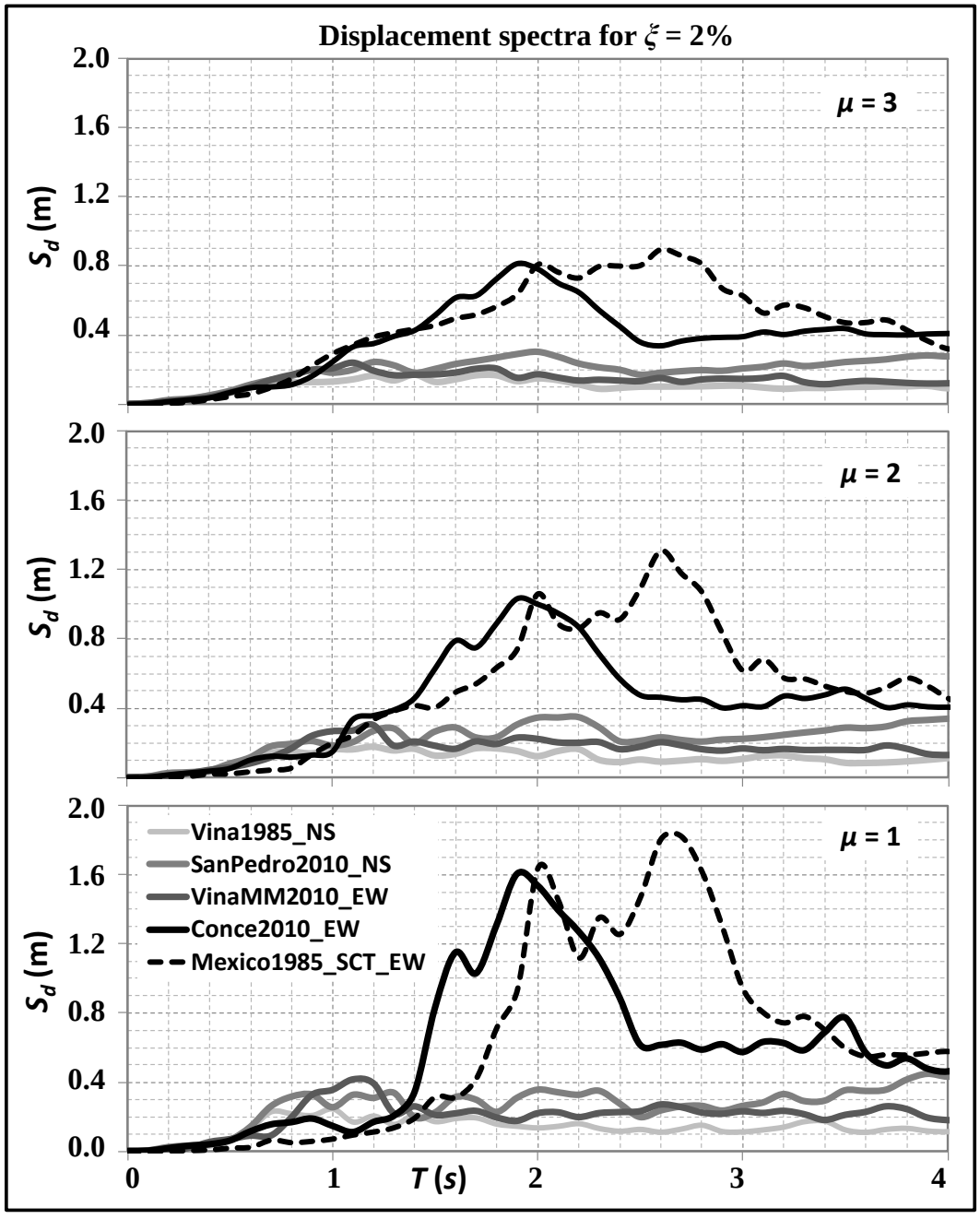

Figure 10.29: Displacement spectra for μ = 1 (elastic) and μ = 2 and 3 (inelastic) – ground motions recorded during the 2010 Maule (Chile), the 1985 Valparaíso (Chile), and the 1985 Michoacán (Mexico) earthquakes.

The displacement spectra obtained with San Pedro record (SanPedro2010) has smaller ordinates when compared to the other two Maule records, with the exception of the period

range between T = 0.6 and 0.9 sec. for μ = 1. However the same order of magnitude is obtained for that record and VinaMM2010 record. The displacement spectra of the record from Valparaíso earthquake, has much smaller ordinates, which is in line with the relatively low damage observed that time (EEFIT 1988).

The Mexico 1985 record is perhaps the most demanding of all the ones reviewed in this contribution. As can be seen in the graphs of Figure 10.29, spectral demands at T = 2.0 seconds reaches values of S_d = 1.6m for μ = 1, S_d = 1.1m for μ = 2, and S_d = 0.8m for μ = 3, with an almost linear reduction when the period decreases from that point to zero for μ = 2 and 3. For μ = 1, the spectral displacements decrease below the values obtained for μ = 2 and 3 for T = 1.8 sec. That is, for T = 1.2 sec, the spectral demand for μ = 1 is S_d = 0.2m, whereas for μ = 2 and 3, S_d = 0.4m, two times the elastic value. These spectra also have high displacement demands in the range of T = 2.0 to 3.0 sec., with an absolute maximum of S_d = 1.85m for μ = 1, S_d = 1.3m for μ = 2, and S_d = 0.9m for μ = 3. The large displacement demand, together with the duration of the ground motion and energy of high demanding Fourier components of the ground motions, led in this case to a very important number of buildings collapsed in Mexico City during the Michoacán earthquake, where an important number of flexible frame buildings had been constructed until 1985 (EEFIT 1986).

In order to compare the capacity of the reinforced walls obtained in terms of the top storey drift ratio, the spectral displacement of the SDOF system elastic or inelastic must be multiplied by a modal participation factor Γ_ϕ and divided by the height of the wall (h_w). Therefore, the top storey drift demand is given by Equation 10.18.

$$D_{rtd} = \Gamma_\Phi S_d / h_w \tag{10.18}$$

The modal participation factor can be taken as Γ_ϕ = 1.45, as suggested in the ASCE-7:2010 document (ASCE, 2010) for wall buildings with more than 8 floors. In other studies, however, a value of Γ_ϕ = 1.3 has been recently adopted in the Chilean normative (INN 2011). This will be illustrated in the next section in the proposed assessment procedure.

10.7 SIMPLIFIED ASSESSMENT PROCEDURE FOR RC WALLS

In this section, an iterative procedure for the seismic assessment of RC walls is presented. The procedure makes use of the top storey drift capacity of the wall based on moment-curvature analysis and the simplified method for relating the top storey displacement to curvature (Wallace and Moehle 1992), suitable for slender walls where shear deformations are negligible. The demand is evaluated in terms of elastic and inelastic displacement spectra, whose ductility level is capacity-compatible, given the invariability of the yielding drift for a given height and wall geometry. The procedure follows the steps presented in the next paragraphs.

Step 1: Given the properties of the steel, the shape of the cross section and the height of the wall, find the value of the parameters ε_y, ϕ_{yD}, and ψ. Calculate D_{rty} using Equation 10.15.

Step 2: Using the graphs shown before, estimate the ultimate top storey drift capacity D_{rtu} for a choice of a plastic hinge length, i.e. a choice of α.

Step 3: Estimate the fundamental period of the building T_1 using the cracked section of the walls and all other structural elements. In the lack of information and for normal inter-storey heights, check with $T_1 = n/10$ and $T_1 = n/15$, were n is the number of storeys (follow Step 4 to Step 9 with each period).

Step 4: Using T_1 enter the elastic spectra generated with one selected record (the most demanding one) and obtain S_d. In the lack of more information, use $\Gamma_\phi = 1.45$ as suggested by the ASCE-7:2010 document (American Society of Civil Engineers 2010) or $\Gamma_\phi = 1.3$ as required by the Chilean seismic code (INN 2011). Calculate the top storey drift demand with Equation 10.18.

Step 5: Compare D_{rtd} for $\mu = 1$ with the yielding drift D_{rty}. Check that $D_{rty} > D_{rtd}$ for $\mu > 1$ (inelastic spectral displacements are sometimes larger than the elastic counterpart). If $D_{rty} > D_{rtd}$ in all cases, then the consistent demand is the elastic one, and the wall is expected to remain elastic under the excitation of *that record*; If $D_{rtd} > D_{rty}$, then the wall is expected to respond in the inelastic range and thus $\mu > 1$ is consistent.

Step 6: For $D_{rtd} > D_{rty}$, calculate S_d with the inelastic spectrum of the same record for $\mu = 2$. If $\mu_{du} = D_{rtd}/D_{rty} \approx 2$, then the spectrum is capacity compatible. If the spectrum is capacity compatible, compare D_{rtd} with D_{rtu}. If $D_{rtu} > D_{rtd}$, the wall is safe with *this record*. If $D_{rtd} > D_{rtu}$, then the wall needs to be retrofitted or replaced. If $D_{rtd}/D_{rty} > 2$, then use the spectrum for the same record with the next ductility factor $\mu = 3$, and recalculate D_{rtd}. If $D_{rtd}/D_{rty} \approx 3$, then the spectrum is capacity compatible as the assumption in the ductility is correct. If $D_{rtd} < D_{rtu}$, then the wall is safe with *this record*. If $D_{rtd} > D_{rtu}$, then the wall needs to be retrofitted or replaced. If D_{rtd}/D_{rty} is 1.5 for example, then use the most demanding value between $\mu = 1$ and $\mu = 2$.

Step 7: After a consistent D_{rtd} has been established, calculate the maximum required ductility of curvature with Equation 10.15. For that curvature, calculate the maximum strain of the steel in tension. Calculate the strain at the onset of buckling ε_p^* with Equation 10.9 (Rodriguez el al. 2013). Calculate the critical buckling strain as a function of the maximum tension strain in the steel reached, using Equation 10-12. Calculate the ductility of curvature associated to this limit state. Calculate the ultimate top storey drift for this curvature using Equation 10.14. This will be the capacity for the cycle reversal. Check that $D_{rtu} > D_{rtd}$, otherwise retrofit for lateral restraining of the vertical reinforcement or replace.

Step 8: With D_{rtd}, check that the confinement length provided η is adequate using Equation 10.10 for the ductility of curvature demand and maximum tensile strain in the steel calculated in Step 7. If η required is larger than the provided length, then retrofit for confinement.

Step 9: Start again from Step 4 with the spectra of *another record*.

10.8 CONCLUDING COMMENTS

This chapter provides a revision of some deficiencies observed in the seismic design practice of RC wall, in the light of the facts observed in field inspection. The most important finding if this chapter is related to the possibility of one key detailing that is might be missing, which is the use of crossed horizontal ties and hooks in the central part of the web, not required by the ACI318-2011 and NZS3101:2006 codes. The failure of well-designed or up-to-standard walls such as those of Building B raises the concern about the importance of that detailing. If that was to be the case, then the eventual retrofit of those structural members may be needed. The factual existence or use of large spacing in horizontal confining elements is also a matter that needs attention. It may be well be possible that many other buildings in different cities of New Zealand with high seismicity can have the same deficiencies of those damaged in Christchurch.

A simple evaluation of the ultimate top storey drift capacity of cantilever RC walls was carried out using the plastic hinge analysis method and moment-curvature diagrams for rectangular and T-shaped walls. The procedure makes use of a certain plastic hinge length (l_p) which in this case is related to the length of the wall by means of a factor α, fraction of the wall length. Three different values of α where used for the selection of l_p, which obviously lead to three different results. There is a question mark about which value of l_p is the most adequate one. Vazquez (2014) did a comparison of several expressions formulated in the literature for the estimation of that parameter. It was concluded that there was a large scatter in the results for a simple case study of a well-designed building. For under-designed walls, which are the subject of this chapter, the uncertainty would even be larger. As a consequence, the designer may wish to use a value that leads to the most conservative predictions of the capacity.

The derivation of inelastic displacement spectra raises the question about the adequacy of the use of reduction factors of an elastic spectrum. It was found that the inelastic spectral displacements were some times larger and others smaller than the elastic counterpart, depending on period range. It is concluded that the revision of that concept in the context of force based design should be revisited.

10.9 REFERENCES

ACI Committee 318 (2005), *Building Code Requirements for Structural Concrete and Commentary (ACI318M-05)*, American Concrete Institute, Farmington Hills, Michigan, USA.

ACI Committee 318 (2011), *Building Code Requirements for Structural Concrete and Commentary (ACI318M-05)*, American Concrete Institute, Farmington Hills, Michigan, USA.

Andriono, T. And Park, R. (1986), 'Seismic Design Considerations of the Properties of New Zealand Manufactured Steel Reinforcing Bars', *Bulletin of the New Zealand Society for Earthquake Engineering*, Vol. 19(3), pp. 213-246.

Architectural Institute of Japan (1999), *Design Guidelines for Earthquake Resistant Reinforce Concrete Buildings on Inelastic Displacement Concept*, Architectural Institute of Japan (AIJ), Kioto, Japan (*in Japanese*).

American Society of Civil Engineers (2010), ASCE-7: *Minimum Design Loads for Buildings and other Structures*, Reston, Virginia.

Aschheim, M. (2002), 'Seismic Design Based on the Yield Displacement', *Earthquake Spectra*, Vol.18(4), pp.581-600.

BECA (2011), 'Investigation Into the Collapse of the Pyne Gould Corporation Building on 22nd February 2011', *Report prepared for the Department of Building and Housing* (DBH), New Zealand.

Bonelli, P., Boroschek, R., Restrepo, J., Carvallo, J.F. (2012a), 'The 2010 Great Chile Earthquake - Changes to Design Codes'**,** *Proceedings of the International Symposium on Engineering Lessons Learned from the 2011, Great East Japan Earthquake*, March 1-4, Tokyo, Japan.

Bonelli, P., R., Restrepo, Quintana-Gallo, P., Pampanin, S., Carr, A. J. (2012b), 'Improvements for the Seismic Design of Reinforced Concrete Walls in Chile and Suggestions for the Refinement of Other Seismic Code Provisions', *Proceedings of the NZSEE Conference*, Christchurch, paper 117.

Buckingham, E. (1914), 'On Physically Similar Systems: Illustration of the Use of Dimensional Equations", *Physical Review*, Vol.4, pp.345–376.

Cowan, H., Beattie, G., Hill, K., Evans, N., McGhie, C., Gibson, G., Lawrence, G., Hamilton, J., Allan, P., Bryant, M., Davis, M., Hyland, C., Oyarzo-Vera, C., Quintana-Gallo, P., and Smith, P. C. (2011), "The M8.8 Maule Chilean Earthquake", *Bulletin of the New Zealand Society for Earthquake Engineering*, Vol.44, No.3, pp. 123-166.

Dodd, L. L. and Restrepo-Posada, J. I. (1995), 'Model for Predicting Cyclic Behaviour of Reinforcing Steel', *Journal of Structural Engineering*, ASCE, Vol. 121 (3), pp.433-445.

EEFIT (1986), 'The Mexican Earthquake of 19 September 1985', *a field report by the Earthquake Engineering Field Investigation Team* (EEFIT), Bristol/London, England.

EEFIT (1988), 'The Chilean Earthquake of 3 March 1985', *a field report by the Earthquake Engineering Field Investigation Team* (EEFIT), Bristol/London, England.

EERI (2010), 'The M 8.8 Chile Earthquake of February 27, 2010', *Learning from Earthquakes Special Earthquake Report*, Earthquake Engineering Research Institute, San Francisco, California, USA.

EERI (2011), 'The M 6.3 Christchurch, New Zealand earthquake of February 22, 2011', *EERI Special Earthquake Report*, Earthquake Engineering Research Institute, San Francisco, California, USA.

European Committee for Standardization (2004), *Eurocode8 – Design Provisions for Earthquake Resistance of Structures, ENV 1998-1 Specific Rules for Various Materials and Elements*, Brussels, Belgium.

fib Task Group 7.6 (2013), Bulletin 69: *Critical Comparison of Major Seismic Codes for Buildings*, International Federation for Structural Concrete, Lausanne, Switzerland.

INN (1996), *Seismic Design of Buildings, Norma Chilena Oficial NCh433Of.9*6, Instituto Nacional de Normalización, Santiago, Chile (*in Spanish*)

Diario Oficial de Chile (2010), Decreto 60 de noviembre de 2011 modificando ACI318S-2008 (*in Spanish*).

Kam, W.Y., Pampanin, S., Elwood, K. (2011), 'Seismic performance of reinforced concrete buildings in the 22 February Christchurch (Lyttleton) earthquake', *Bulletin of the NZSEE,* Vol. 44, No.4, pp. 239-278.

Mander, J.B., Priestley, M.J.N, and Park, R. (1984), 'Seismic Design of Bridge Piers', *Research Report 84-2*, Department of Civil Engineering, University of Canterbury, Christchurch, New Zealand.

Mau, S.T. and El-Mabsout, M. (1989), 'Inelastic Buckling of Reinforcing Bars', *Journal of Engineering Mechanics*, ASCE, Vol. 115 No. 1, pp. 1 – 17.

Mau, S.T. (1990), 'Effect of Tie Spacing on Inelastic Buckling of Reinforcing Bars', *ACI Structural Journal*, Vol. 87(6), pp. 671 – 677.

Pampanin, S., Kam, W. Y., Akguzel, U., Tasligedik, A. S., Quintana-Gallo, P. (2012a), *The Observed Earthquake Damage of Reinforced Concrete Buildings in the Christchurch CBD on the 22 February 2011 Earthquake – Part I: Overview*, Department of Civil and Natural Resources Engineering, University of Canterbury, Christchurch, New Zealand.

Pampanin, S., Kam, W. Y., Akguzel, U., Tasligedik, A. S., Quintana-Gallo, P. (2012b), *The Observed Earthquake Damage of Reinforced Concrete Buildings in the Christchurch CBD on the 22 February 2011 Earthquake – Part II: Damage Observation*, Department of Civil and Natural Resources Engineering, University of Canterbury, Christchurch, New Zealand.

Pantazopoulou, S. J. (1998), 'Detailing for Reinforcement Stability in RC Members', *Journal of Structural Engineering*, ASCE, Vol.124 (6), pp. 263-632.

Paulay, T. (1986), 'A Critique of the Special Provisions for Seismic Design of the Building Code Requirements for Reinforced Concrete (ACI318-83)', *ACI Journal*, Vol. 29, March-April, pp. 274 – 283.

Paulay, T., Priestley, M.J.N. (1993), 'Stability of Ductile Structural Walls', *ACI Structural Journal*, no. 90, pp. 385-392.

Popper, K. (1963), *Conjectures and Refutations*, Routledge, New York, USA

Priestley, M.J.N., Calvi, G.M. & Kowalsky, M.J. (2007), *Displacement-Based Seismic Design of Structures*, IUSS Press, Pavia, Italy.

Quintana-Gallo, P. (2008), 'Evaluación Analítica del Daño en un Edificio de Hormigón Armado', *Thesis submitted in partial fulfilment of the requirements for the degree of Magister en Ciencias de la Ingeniería Civil*, Departamento de Obras Civiles, Universidad Técnica Federico Santa María, Valparaíso, Chile (*in Spanish*).

Quintana-Gallo, P., Akguzel, U., Pampanin, S., Carr, A.J. (2011), 'Shake Table Tests of Non-ductile As-Built and Repaired RC Frames', *Proceedings of the Pacific Conference on Earthquake Engineering*, Auckland, paper 201.

Quintana-Gallo, P., Akguzel, U., Pampanin, S., Carr, A.J., Bonelli, P. (2012), 'Shake Table Tests of Non-Ductile RC Frames Retrofitted with FRP in Beam Column Joints and Selective Weakening in Slabs' *Proceedings of the New Zealand Society for Earthquake Engineering Conference*, Christchurch, New Zealand.

Quintana-Gallo, P., Rebolledo, R. and Allan, G. (2013), 'Dealing with Uncertainty in Earthquake Engineering: a Discussion on the Application of the Theory of Open Dynamical Systems', *Obras y Proyectos*, Vol. 14(2), pp. 66-77 (*in English*).

Rodriguez, M. E., Botero, J. C., Villa, J. (1999), 'Cyclic Stress-Strain Behavior of Reinforcing Steel Including Effect of Buckling', *Journal of Structural Engineering*, ASCE, Vol. 125 (6), pp.605-612.

Rodriguez, M. E. (2012), 'The 2010 Maule and the 2011 great east Japan Earthquakes–lessons learned for the seismic design of structures', *Proceedings of the International Symposium on Engineering Lessons Learned from the 2011, Great East Japan Earthquake*, March 1-4, Tokyo, Japan, pp.1304-1310.

Rodríguez, M. E., Ortiz, A., Torres-Matos, M. A. (2013), 'Diseño Sísmico de Muros de Concreto Reforzado Basado en Desplazamiento', *XIX Congreso Nacional de Ingeniería Sísmica*, Veracruz (*in Spanish*).

Saatcioglu, M., and Razvi, S. R. (1995), 'Strength and Ductility of Confined Concrete', *Journal of Structural Engineering*, ASCE, Vol. 118(6), pp.1590-1607.

Standards New Zealand (2004), NZS1170.5:2004, *Structural design actions: Part 5, Earthquake actions*, Wellington, New Zealand.

Standards Australia and Standards New Zealand (2002), AS/NZS1170.0, *Structural design actions: Part 0, General Principles*, Wellington, New Zealand.

Standards New Zealand (2006), NZS3101:2006, *Concrete structures standard*, Wellington, New Zealand

Standards New Zealand (1995), NZS3101:1995, *Concrete structures standard*, Wellington, New Zealand

Strogatz, S. (1994), *Nonlinear Dynamics and Chaos*, Westview Press, Cambridge Massachusetts, USA

Thomsen, J.H., (1995), 'Displacement Based Design of Reinforced Concrete Structural Walls: An experimental Investigation of Walls with Rectangular and T-Shaped Cross – Sections', *Thesis submitted in partial fulfilment of the requirements for the degree of Doctor of Philosophy*, Clarkson University, Potsdam, New York. USA.

Urmson, C. and Mander, J. (2013), 'Local Buckling Analysis of Longitudinal Reinforcing bars', *Journal of Structural Engineering*, Vol.138 (1), pp.62-71.

Vázquez, V. (2014), 'Evaluación de la Capacidad de Deformación de un Muro T Diseñado de Acuerdo a las Normas Vigentes en Chile desde el año 1996', *Memoria para optar al título de Ingeniero Civil*, Universidad Técnica Federico Santa María, Valparaíso, Chile (*in Spanish*).

Wallace, J. W., Ibrahim, Y. (1996), *Biax-96 for MS Windows – Strength and Analysis of RC Sections*, University of California, Los Angeles, USA.

Wallace, J. W., Moehle, J. P. (1992), 'Ductility and Detailing Requirements of Bearing Wall Buildings', *Journal of Structural Engineering*, ASCE, Vol. 118 (6), pp.1625-1644.

11 PRELIMINARY RECOMMENDATIONS FOR SEISMIC CODE PROVISIONS AND DESIGN GUIDELINES

11.1 INTRODUCTION

In this chapter, suggestions for seismic code provisions related to RC walls are presented, in the light of the empirical evidence of the damage observed in that structural typology the 2010 Chile and 2011 New Zealand earthquakes are formulated. From the inspection of critically damaged RC walls in the Chilean cities of Viña del Mar, Valparaíso, Santiago, and Concepción, as well as Christchurch in New Zealand, deficiencies in the detailing were identified, as presented in Chapter 9 and 10, respectively. These suggestions are presented in the next section.

11.2 RECOMMENDATIONS FOR THE SEISMIC DESIGN OF RC WALLS

Based in the findings and ideas presented in this thesis, it is suggested that the following dispositions are taken into consideration in the design of seismic resistant structural walls:

1) Limit the axial load for rotation capacity deterioration, especially for asymmetrical walls.

2) Incorporate the requirement of providing buckling restraining horizontal cross ties all along the web of the walls in potential plastic hinge regions.

3) Consider introducing the requirement of confining the entire critical section of walls, in order to ensure a robust ductile mechanism, and avoid the dependence on the to-date estimated seismic demand in the calculation of the required confinement length.

4) Reduce the maximum allowable vertical spacing in boundary elements for ‘nominally ductile’ (New Zealand) or ‘ductility class medium’ (Europe) walls in order to mitigate the problem of premature buckling of the longitudinal rebar. Do not accept the use of those walls in moderate or high seismicity regions.

5) Incorporate a minimum value for the ultimate top displacement of the wall associated to a maximum compression strain in the confined concrete $\varepsilon_{cu,c}$ = 0.008, and a maximum tension strain in the steel of the order of 4-6% (research is needed).

6) Use simple configurations in wall geometry and avoid the use of large heavily reinforced flanges.

11.3 RECOMMENDATIONS FOR THE SEISMIC ASSESSMENT OF RC WALLS

In Chapter 10, a simplified procedure for the assessment of RC slender walls was developed. The procedure incorporates checking of the most important issues related to

ductile detailing. The procedure also incorporates the concept of capacity-compatible inelastic displacement spectra for the estimation of the seismic demand. That is, the demand is not obtained using an elastic spectrum reduced by a certain factor to account for inelastic behaviour of the structural members.

It is suggested that the concept of reductions factor and their used in the current design and assessment of RC buildings in general should be revisited, in the light of the findings provided by the inelastic spectra which show that the directly obtained spectral ordinates are some times larger and some others smaller than the elastic counterparts.

11.4 RECOMMENDATIONS FOR THE SEISMIC ANALYSIS OF STRUCTURES

Problem with the mathematical manipulation of ground motions to be used in nonlinear dynamic methods for the analysis of structures in general, have been identified in the light of the shake table test performed on the model buildings presented in Part I of this thesis. Those problems have been corroborated during recent earthquakes that affected Chile and New Zealand in 2010 and 2011, respectively.

Current analysis procedures require that selected ground motions are modified to fit the design spectra 'accepted' for a certain location. However, that requirement makes used of the assumption that all the ground motions that will occur in the future at that location will have the same (or very close) characteristics in the frequency content, the PGA, and obviously the whole spectral shape. That assumption has been refuted after the occurrence of the seismic events mentioned above.

In the case of Chile, in Viña del Mar, the ground motions recorded during the 2010 Maule earthquake exhibited different characteristics than those recorded previously in the same place 25 years earlier (3 March 1985 Valparaíso earthquake) (EERI 1985, EEFITS 1988). Those differences were related to the predominant frequency of the ground, the duration of the motion, and the energy of the predominant frequency in the Fourier domain. As during that particular earthquake the response of RC buildings was overall very good, most of the engineers thought that the worst had already happened and that the undamaged buildings were safe for say another 70 years, from a 'frequentist' conception of the theory of probability. After the 2010 Maule earthquake those conjectures were refuted as explained in this thesis.

In New Zealand, the same problem was observed. As described in the first part of this thesis, on the 10 of September 2010, the Darfield earthquake affected the city of Christchurch. Even though large intensity of damage was observed in lifelines, roads, and houses mainly due to the poor soil conditions, RC structures did not exhibited great damage (Pampanin et al. 2011). Engineers, based on the same assumptions done by their Chilean counterparts 25 years ago, seem to have the conviction that the 'design event', which had a 'return period' of about 500 years, had already occurred, and that they could be safe in the light of the little damage observed in almost all RC structures. That assumption was refuted only 6 months later, when the 22 February 2011 (main) Canterbury earthquake almost entirely destroyed the Central Business District of city of Christchurch, were most of the large buildings were constructed (Pampanin et al. 2012a,b). When the characteristics of the ground motions recorded during both

earthquakes as well as their displacement spectra were reviewed, large differences were found. Moreover, it was found that the displacement spectra obtained with the 2011 Canterbury earthquake did not match the shape of the design counterparts, refuting the adequacy of the modification of those ground motions for the dynamic analysis of structures.

In the light of the findings described above, it is suggested that, considering that in most of the cases future ground motions will most likely not match the specified design spectrum of a place in terms of its shape and magnitude, the use of non-modified ground motions for the nonlinear analysis of structures should be used, in order to estimate the response of those structures under realistically different input motions.

11.5 REFERENCES

Cowan, H., Beattie, G., Hill, K., Evans, N., McGhie, C., Gibson, G., Lawrence, G., Hamilton, J., Allan, P., Bryant, M., Davis, M., Hyland, C., Oyarzo-Vera, C., Quintana-Gallo, P., and Smith, P. C. (2011), 'The M8.8 Maule Chilean Earthquake', *Bulletin of the New Zealand Society for Earthquake Engineering*, Vol.44, No.3, pp. 123-166.

EEFIT (1988), 'The Chilean Earthquake of 3 March 1985', a field report by the Earthquake Engineering Field Investigation Team (EEFIT), Bristol/London, England

EERI (1985), 'The Chile Earthquake of March 3, 1985', *Learning from Earthquakes, Special Earthquake Report, Earthquake Spectra*, Vol. 2, No 2, pp. 249-508.

EERI (2011), 'The M 6.3 Christchurch, New Zealand earthquake of February 22, 2011', *EERI Special Earthquake Report*, Earthquake Engineering Research Institute, San Francisco, California, USA.

Pampanin, S., Kam, W.Y., Tasligedik, A.S., Quintana-Gallo, P., Akguzel, U. (2011) 'Considerations on the seismic performance of pre-1970s RC buildings in the Christchurch CBD during the 4th Sept 2010 Canterbury earthquake: was that really a big one?', *Proceedings of the Pacific Conference on Earthquake Engineering*, Auckland, paper 179.

Pampanin, S., Kam, W. Y., Akguzel, U., Tasligedik, A. S., Quintana-Gallo, P. (2012a), *The Observed Earthquake Damage of Reinforced Concrete Buildings in the Christchurch CBD on the 22 February 2011 Earthquake – Part I: Overview*, Department of Civil and Natural Resources Engineering, University of Canterbury, Christchurch, New Zealand.

Pampanin, S., Kam, W. Y., Akguzel, U., Tasligedik, A. S., Quintana-Gallo, P. (2012b), *The Observed Earthquake Damage of Reinforced Concrete Buildings in the Christchurch CBD on the 22 February 2011 Earthquake – Part II: Damage Observation*, Department of Civil and Natural Resources Engineering, University of Canterbury, Christchurch, New Zealand.

12 CONCLUSIONS AND RECOMMENDATIONS FOR FUTURE RESEARCH

12.1 CONCLUSIONS

The seismic vulnerability of existence RC frame buildings constructed before the 1970's has been widely recognized and investigated. Non-ductile detailing in the beam column joints has been identified as a critical deficiency of those frames, alongside the lack of capacity design considerations and the lack or the improper consideration of seismic actions. In the light of the vulnerability of that building typology, seismic retrofit has become an urgent need, to ensure at least the prevention against the loss of life, final goal the earthquake engineering philosophy. Amongst the many retrofit techniques that have been developed to date, new feasible and non-invasive solutions have been developed and improved at the University of Canterbury. From the solutions investigated, the FRP configuration investigated was of particular interest of the author, mainly because of the increasing popularity of that the material has gained in the industry recently. Equally important, the concept of selective weakening was taken into consideration, as it was found to be required for the FRP retrofit scheme to work properly when a floor slab is incorporated.

This research has provided a valuable investigation related to the dynamic response of a model RC frame building with non-ductile detailing, as-built with lap splices, repaired with the lap-splices connected, and upgraded with an ad-hoc retrofit intervention. The specimen was constructed with a great degree of realism as floor slabs and transverse beams on one or two faces of exterior joints were incorporated. That resulted in the development of a retrofit intervention suitable for practical applications in real structures, an important aspect of the value of this research. Important insight into the problem of predicting the nonlinear dynamic response of the specimens during the shake table experiments was provided with the results obtained with a simple finite element model.

In structural RC walls, after the 2010 Maule Chile earthquake, the vulnerability and fragility of an important stock of buildings constructed in that country was identified, in the light of the observations on the damage pattern developed in RC structural walls, done during and after the inspection of buildings. The inappropriate detailing or the absence of special boundary elements in RC walls is seen as a major source of potential damage or risk, as discussed in this thesis. Concerns about the complete adequacy of the recommendations for the ductile design of RC walls of current codes were raised after the 2011 Canterbury New Zealand earthquake. During the immediate inspection process of the buildings, it was found that some up-to-standard RC walls presented a brittle nature failure.

This research has provided a very important amount of information related to the inspection of damage in RC buildings during two major earthquakes that occurred during the research process complied in this thesis (Chile 2010, New Zealand 2011). The value of that part of this research consists in the identification of a new set of non-ductile RC walls constructed in Chile, as well as the identification of apparent follies in the current practice as a result of the code requirements apparently being unable to ensure ductile behaviour in RC walls, such as in those constructed in New Zealand.

The most important findings of this research are summarized as follows:

Part I

1) Shake table tests of the as-built specimens with lap splices.

- The results of the first experimental series of the as-built specimen indicated that a lap splice failure mode developed at the base of the upper floor columns, especially in the third floor were a very poor concrete was used. It was found that the specimen did not experience large inter-storey drifts even after the input motion was scaled up in amplitude two times after the initial test (Tests 1.1, 1.2 and 1.3). The input motion, a modified version of a ground motion recorded during the Loma Prieta earthquake (CA, 1989) to fit the New Zealand spectrum was found to be unable to impose large inelastic cycles upon the structure.

- After the experiments were done, the specimen experienced the excitation of a real seismic event that affected Christchurch on the 10 of September 2010. It was found that the failure mode previously identified increased in terms of the intensity of the damage, further confirming the experimental findings. Even though the ground motion produced by that earthquake is similitude-incompatible with the model building, observations were found to be useful for understanding the dynamical response of the specimen.

2) Shake table tests of the as-built/repaired specimen without lap splices

- In the first test (Test 2.1), one ground motion recorded during the Darfield earthquake (New Zealand 10 of September 2010) in the Christchurch Hospital station. It was found that the specimen did not suffer important damage and that the response was characterized by low inter-storey drift levels (below 1.5%). It is concluded that in this particular case, that motion did not represent a major source of hazard for the structure.

- During the second test (Test 2.2), where a ground motion recorded during the 27 of February 2010 Maule Chile earthquake was used, the specimen experienced large floor displacements during a significant part of the motion, representatives of a soft-storey mechanism. It was found that both corner joints of the first floor were severely damaged, following the diagonal concrete-wedge cracking pattern. Indications of damage in cruciform joint were also observed. The ends of internal columns were also damaged. Torsional cracks were observed in the spandrels, indicating the activation of that resistance mechanism during the response. It was found that the building experienced inter-storey drifts in the first floor equal or greater than 3% in several instants, with a peak slightly smaller than 4%. The intensity of the damage experienced by the structure after that last test was large enough to evaluate the structure as non-reparable for practical purposes, even though it was repaired in order to be able to implement and validate the retrofit intervention developed in this thesis.

- With these two tests, it was demonstrated that an alternative testing protocol to those typically followed in previous research concerning shake table tests could be

used. The reasoning behind the protocol used was to represent a low and a very high demanding scenario for the same building, proving that a building is still vulnerable if the non-ductile detailing is not eradicated, despite the fact that it was shown to withstand in the elastic range a previous seismic event. The record used in Test 2.2, VMM (see Chapter 4 and 7), was found to be especially destructive for the specimen under investigation, due to the value of the predominant frequency, its energy in the Fourier domain and its duration.

- It was observed that the diagonal cracking developed in corner beam column joints was more severe in the direction compatible with positive bending moments in the beam, i.e. when the slab experienced compression (AC state). It was found that the stress flow inside the panel zone had a narrower path in that situation, due to a smaller neutral axis in the beam and a reduction in the axial load.

3) Evaluation of the hierarchy of strengths and sequence of events in beam column joints with floor slabs and transverse beams.

- The analytical tool for the evaluation of the hierarchy of strengths and sequence of events in beam column joints, named the M-N performance diagram developed for plane specimens, was extended to account for the asymmetry in the beam section as a consequence of the presence of the slab. The M-N diagram was divided into four quadrants, delimited by the zero-moment axis and the vertical line that represents the initial gravity load in the joint. It was also found that only two of those quadrants were kinematic-compatible with the effect of increasing or decreasing axial load. That is, the evaluation for positive moment in the beam is compatible with decreasing axial load (AC state) and the evaluation for negative moment in the beam is compatible with increasing axial load.

- The effect of the torsional resistance provided by the spandrel was incorporated into the problem. The cracking torsion capacity was incorporated as an additional limit state for positive twist, whereas the yielding and probable resistances were incorporated for negative twist, compatible with positive and negative bending moment in the beam, respectively.

4) Development of a practical retrofit intervention using FRP laminates to strengthen the joints and weakening of the slabs.

- An ad-hoc retrofit intervention was developed following a partial retrofit strategy, and based on the previous research on beam column joint subassemblies retrofitted with FRP and the selective weakening concept developed in previous research.

- The configuration of the FRP layers developed previously for 2D plane and 3D corner beam column joints was modified in order to cope with its lack of practicability when considering the existence of a floor slab, resulting in a novel laminates configuration for both corner and cruciform beam column joints. In addition, L-shaped sheets were incorporated in the internal part of the beam-column interface, to provide a symmetrical strengthening for the columns. That was feature was not been used in the 3D subassemblies tested by others, before this retrofit scheme was conceived and numerically evaluated.

- Weakening of the slab was found to be compulsory if the sequence of events of the retrofitted beam column joints in the M-N performance domain was to be altered, and damage relocation ensured. That was found to be especially true for the AT state, when the slab is in tension, due to a very important increasing in the negative bending moment capacity of that element.

- Anchorage of the laminates on the sides of the beams and through the floor slab was also proposed, based on the suggestions done by others. The intention of those anchors, made of FRP, is to postpone or avoid the loss of bond between the FRP laminates and the concrete.

5) Shake table tests of the retrofitted specimen

- The retrofitted specimen was tested twice (September 2011), following the same input motion protocol used in the as-built/repaired specimen experiments. It was observed that the specimen did not experience any apparent damage after the first test (Test 3.1), where the Darfield earthquake (September 2010) ground motion was used. Recorded inter-storey drift histories reflected low demands, with values that did not exceed 1.5% in all floors.

- As could have been expected, in this case, that particular input motion, representative of those recorded during the Darfield earthquake in New Zealand, did not constitute a 'big event' for this building. However, there is a huge difference in the expected performance of this retrofitted building and the as-built/repaired counterpart, due only to capacity considerations. Hence, it is concluded that if only that input motion was used to evaluate the performance of both buildings, and their structural characteristics unknown, they may be categorized as equally non-vulnerable, from a demand-based philosophical perspective.

- During the second shake table test (Test 3.2) it was observed that the specimen experienced large floor displacements forming a hybrid beam sway mechanism with rocking of the internal columns. The largest inter-storey drifts were recorded in the first floor and they exhibited values close to 3% many times during the building motion, reaching a maximum close to 3.7% of the inter-storey height. I was concluded that the particular input motion used in this test was able to bring the specimen to resonance, imposing large inelastic strains in structural members.

- The observed damage after Test 3.2 was mostly concentrated in the portion of the beams where the slab was weakened, as anticipated by the calculations done for the development of the retrofit intervention/scheme. Some damage was also observed in the columns very close to the interface with the FRP layers placed on top of them, but it was relatively minor. The retrofit intervention was proved to be successful in relocating the damage from the joint into de beams, shifting the inelastic mechanism from a brittle-unstable to a ductile-stable one. However, the specimen experienced inter-storey drifts and floor displacements similar to those the as-built/repaired specimen did. It is concluded that the retrofit intervention developed, implemented, and tested in this research constitutes a necessary

condition to upgrade the inelastic mechanism of the typology under investigation, but is not sufficient for reducing the magnitude of the global response.

- Even though the specimen experienced important damage after Test 2.1, the ductile nature of that damage made the specimen qualify as a reparable structure for practical purposes, which was not the case of the as-built/repaired counterpart after Test 2.2. That is an indication of the efficiency of the retrofit intervention in addition to its efficacy to relocate the damage in the intended location.

6) Numerical blind and post-experimental prediction of the most relevant experiments

- Before the shake table tests of the repaired specimen were performed, a finite element numerical model was constructed in Ruaumoko2D, in order to predict the response of the building during the most relevant experiments. In that prediction the nominal input was used, as it was obviously impossible to count with the actual motion that the actual shake table was able to impose in the reality. It was found that the numerical simulations were able to represent with a reasonable degree of accuracy the recorded response of the specimen during Tests 1.1 and Test 2.1. However, it was found that the same model failed to represent accurately the response of the building during Test 2.1, where large inelastic incursions in key structural members. It was found that the parameters that controlled the hysteresis rule in the joints had a major impact on the prediction. It was observed that if the most degrading parameters of a Takeda-like rule were set to the most degrading case, the numerical prediction diverged due to a bifurcation taking place at some stage of the predicted response. On the other hand, if those parameters were set to represent the less degrading case, then the predicted response was found to be stable, but it underestimated the recorded response by far. It is concluded that the choice of those parameter has great influence on the ability of the numerical model to represent the experimental facts.

- The differences between the nominal and recorded motions of the shake table were examined in depth after the tests. It was found that there was a difference in between both versions of the input motion, that they were minor generally speaking, and that they were larger during the strong part of the response, especially when the Chile earthquake record was being used. It was concluded in the light of those findings that the differences between the intended and actual motions of the testing apparatus depends on the dynamical response of the specimen, especially if resonance exists, and thus the prediction of experimental tests in the dynamic range a priori may be very affected by that fact. It was also concluded that the problem of the dynamical interaction of the specimen and the shake table during the experiments could be addressed from the perspective of the theory of open dynamical systems, preliminary applied to structural dynamics by the author and other collaborators recently.

- In the last stage of the numerical simulation of the as-built/repaired specimen, the modified SINA hysteresis rule was used to model the joints. It was found that with this model, the prediction of the critical test (Test 2.2) was more accurate in representing the experimental response of the specimen. That was attributed to the pinching effect that is incorporated in the SINA model. It was also found that this

model was more accurate in predicting the experimental response of the as-built and repaired specimens than the initial model. It was also found that the parameters that define the shape of the hysteresis rule must be carefully selected, and that important differences in the prediction arise when they are changed.

- For the numerical prediction of the retrofitted specimen, was done after the experimental tests were performed. Hence, it constitutes a post-experimental prediction. It was found that the model constructed in Ruaumoko2D with concentrated elasticity elements, was able to predict with reasonably good accuracy the response of the critical test (Test 3.2), when large nonlinear (inelastic) incursions were observed. However, the results obtained with the numerical model were found to be very dependent on the parameters that governed the hysteretic behaviour of the portion of the beam where the slab was weakened, especially on the bi-linear factor and the yielding moment resistance. The numerical prediction of the specimen response during Test 3.1 was found to be overall good, despite a relatively large overestimation of the floor displacements and inter-storey drifts during the initial and final parts of the motion.

- The post-experimental prediction obtained with the simplified model constructed in Ruaumoko2D was found to be quite accurate in all the cases investigated. Nevertheless, differences existed. In some cases it was observed that the predicted response of the specimens was very close to the experimental counterpart from the beginning of the motion, but during a certain period of time the signals were absolutely different. Despite those losses on the accuracy, the numerical prediction recovered, in almost all the cases, the accuracy in the prediction of the experimental response during later stages. The differences are attributed to the assumption of the laws that govern the small cycles in the hysteretic response, which lack of empirical support, and the assumption on the value of the viscous damping. Differences in the real and assumed behaviour during small variation of the response may explain why the numerical model is accurate during some periods of the response, but substantial differences arise in an erratic or non-periodic fashion during others. Also the fact that there is an order that emerges after the non-coincident part of the prediction makes it possible to conclude that there are vestiges of chaotic behaviour in the numerical simulations.

Part II

1) Non-ductile RC walls in Chile

- During the building inspection in some of the Chilean cities affected by the Maule 2010 earthquake where the author was involved, it was observed that most of RC buildings responded apparently in the elastic range or they exhibited brittle-nature damage, mostly in structural walls, not observed previously in the country.

- It was observed that the damage pattern in those structural elements, if it developed, it was characterized by a large crushed region along the entire or most of the web of the wall, with buckled vertical reinforcement, sometimes fractured close to the wall ends. If was found that the brittle damage developed due to the lacked or improper use of special boundary elements, the absence of transverse

hooks or ties all along the web, and the acceptance of high axial gravity load (v = 0.3 to 0.5). It is concluded that the revelation of these follies reveal the existence of a previously not known (to the public) stock of RC walls in large urban areas such as the north part of Chile, a region with high seismicity.

- Chilean RC buildings are designed using the ACI318-2011 requirements. Some follies in that document were identified in the light of the damage observed. Those deal mostly with the non-requirement of crossed ties in the central part of the web of the wall, as prescribed by the ENV1998-1:2004 Eurocode8 document, and the non-requirement of an explicit limit for the initial gravity load that a RC wall can be designed with, to allow for large inelastic rotations to develop, as required by the Architectural Institute of Japan (AIJ) provisions.

- Most of the Chilean buildings responded very well to the demand imposed by the 2010 Maule seismic event. It could be stated that those buildings have proved to be safe because they resisted a 'large' earthquake with no damage, just as it was the case of the repaired model building tested in the shake table with the ground motion recorded during the Darfield earthquake. However, most of the walls of those buildings were constructed most probably with the same reinforcement non-ductile detailing of those walls that failed during the same earthquake, thus, the vulnerability remains. It is concluded that there is an urgent need for the assessment, identification and retrofitting of those RC walls, regardless of the performance exhibited in the past, in the light of the great uncertainty in the estimation of the seismic demand imposed by future events.

2) Non-ductile RC walls in New Zealand

- During the immediate inspection process of the buildings after the 22 February 2011 Canterbury New Zealand earthquake, where the author had the opportunity to participate, it was found that some up-to-standard RC walls presented a brittle nature failure, raising concerns about the complete adequacy of current requirements for the ductile design of RC walls. In some cases large spacing of the horizontal elements located at the ends of some walls was observed. In all cases though, just as in the walls constructed in Chile, there were no horizontal ties or hooks about the longitudinal reinforcement along the web of the walls. It is concluded that those issues worth being included in future revisions of the NZS3101:2006 New Zealand standard.

- It was observed after the revision of the structural drawings of several RC buildings constructed in Christchurch that in most of the cases, walls were used in a small amount and combined with frames, many times not designed to withstand seismic demands (ordinary frames). In a force-based design context, the use of frames not designed to 'take' the seismic actions may be correct, but it may be entirely wrong based on the irrefutable fact that those frames are constructed in seismically active regions, and will very likely need to face earthquake induced demands inevitably. It is concluded that it should only be allowed to construct ductile frames (and walls) in those regions, so that brittle damage is avoided at any 'cost'. The differences in the cost of constructing an ordinary or a ductile frame are negligible when compared to the cost and/or operation of the structure, but most importantly they cannot be compared to the value of human life losses. It

is believed that sophistication in the requirements for reinforcing detailing based on demand considerations should be avoided.

- Observations of the nonlinear (inelastic) and elastic displacement spectra obtained with the ground motions recorded during the 2011 Canterbury earthquake, as well as those of the 2010 Maule earthquake, led to the finding that the inelastic spectral displacement are sometimes larger and others smaller than the elastic counterpart. It is concluded based on that finding that there is no reason why a modification factor of the elastic spectra conceived to match the inelastic counterpart must be smaller than 1. That is, a 'reduction' factor does not seem logical. In is concluded that the use of reduction factors in the context of forced and displacement-based design should be revisited.

- It was observed during this research that the characteristics of the ground motion in terms of predominant frequency, the energy of that frequency in the Fourier domain, and others, will most likely change from one event to the other in the same place. It was also observed that those parameters have important relevance on dynamic response of structures, as it was shown with the shake table tests. In the light of those findings, it is concluded that the procedure for the dynamic analysis of structures that includes the modification of earthquake ground motions to fit a preconceived spectrum should be reformulated.

- Using the inelastic displacement spectra obtained with a ground motion such as those mentioned before, the estimation of the top storey drift by means of the approximations of plastic analysis and the assumption that plane sections remain plain, a simplified method for the assessment of RC walls has been proposed. The feature of that method is that a capacity-compatible displacement spectrum is used for the estimation of the maximum top storey drift of a wall, instead of using an elastic spectra reduced by a certain factor.

12.2 RECOMMENDATIONS FOR FUTURE RESEARCH

As a result of the findings and conclusions obtained in this research, it is believed that the following areas worth being investigated in the future:

- Global stability provided by the retrofit intervention developed

  The main conclusion obtained from the shake table tests was that the retrofit intervention developed was thought to be a necessary but not sufficient condition for upgrading the dynamic response of the model building. That is, damage relocation is ensured, but the inter-storey drifts are not reduced substantially. Hence, experimental investigations on the dynamic response of the building retrofitted as in this thesis with additional rocking walls with external viscous damping such as those tested previously at the University of Canterbury, seem plausible. Similarly, it would be interesting to investigate and compare the response of the as-built specimen retrofitted with external rocking walls only.

- Small cycle behaviour in structural elements.

It was highlighted in the conclusions related to the numerical part of this research that there is a lack of empirical background in the model used to describe the small cycle hysteretic behaviour of structural members. Experimental investigations related to that aspect is suggested to be carried out, because it would provide valuable information to be incorporated in numerical models used to predict the response of structures in the nonlinear dynamic range.

- Numerical prediction of the experimental responses

  In this research a simplified model was used for the prediction of the experimental test results. It is proposed that the model is further modified in order to thoroughly investigate the strong dependence of the prediction on the hysteretic parameters, the viscous damping model, and the inclusion of parallel springs to represent the resisting action of the concrete and the FRP laminates separately. In addition, the development of a more refined model would be very valuable.

- Experimental work on non-ductile RC walls

  Experimental research of RC walls, rectangular and asymmetric, subjected to high axial load (v = 0.3 or larger) with the non-ductile detailing found in Chile, could be tested using quasi-static loading protocol as a first approximation in order to understand how does the damage develops during the cycles. Shake table tests of similar specimens would be worth being performed in order to understand their dynamical response, ideally using records of the 2010 Maule earthquake. Testing of RC walls subjected to moderate and high axial load with the detailing required by the current New Zealand RC standard and with the addition of horizontal ties and hooks about the longitudinal rebar in the portion of the web where no special confinement boundary elements are required. Quasi-static tests would provide insight on the mechanics of both typologies and shake table tests would provide valuable information related to the dynamic response, ideally using ground motions recorded during the 2011 Canterbury earthquake as input. The efficacy of retrofit technics available to date or others developed ad-hoc for upgrading the expected performance of the walls mentioned above is worth being investigated.

- Numerical work on (asymmetric) RC walls

  In this research, the assumption of the plane sections remaining plain whilst deformations in structural walls occur has been used. That assumption may not be entirely appropriate for a deeper understanding and modelling of the behaviour of asymmetric walls in particular. Recent advances in those aspects have led to the development of a fibre model that allows for modelling those aspects (Carr 2012). Studies related to the improvement of that model are recommended to be investigated.

Part III: Appendices

APPENDIX A: TEST 1.2 RESULTS

In this appendix, the results of the shake table experiments during Test 1.2 are presented. As explained in Chapter 4, in the first series of tests, one ground motion recorded during the 1989 Loma Prieta earthquake at Gilroy Array #5 station was used. That record was named GA5 in general and GA-2 in particular for the case of Test 1.2. That record was a scaled-up amplitude version of the nominal record used in the previous Test 1.1, i.e. the peak acceleration of the signal or PGA (and consistently the peak displacement of the signal, PGD) was increased from 0.45g to 0.6g in the nominal input. However, as was mentioned in Chapter 4 and discussed in Chapters 7 and 8, it was found that there were differences in the nominal or intended and the actual recorded motion of the shake table. Those differences are presented in Appendix B, as stated in Chapter 4.

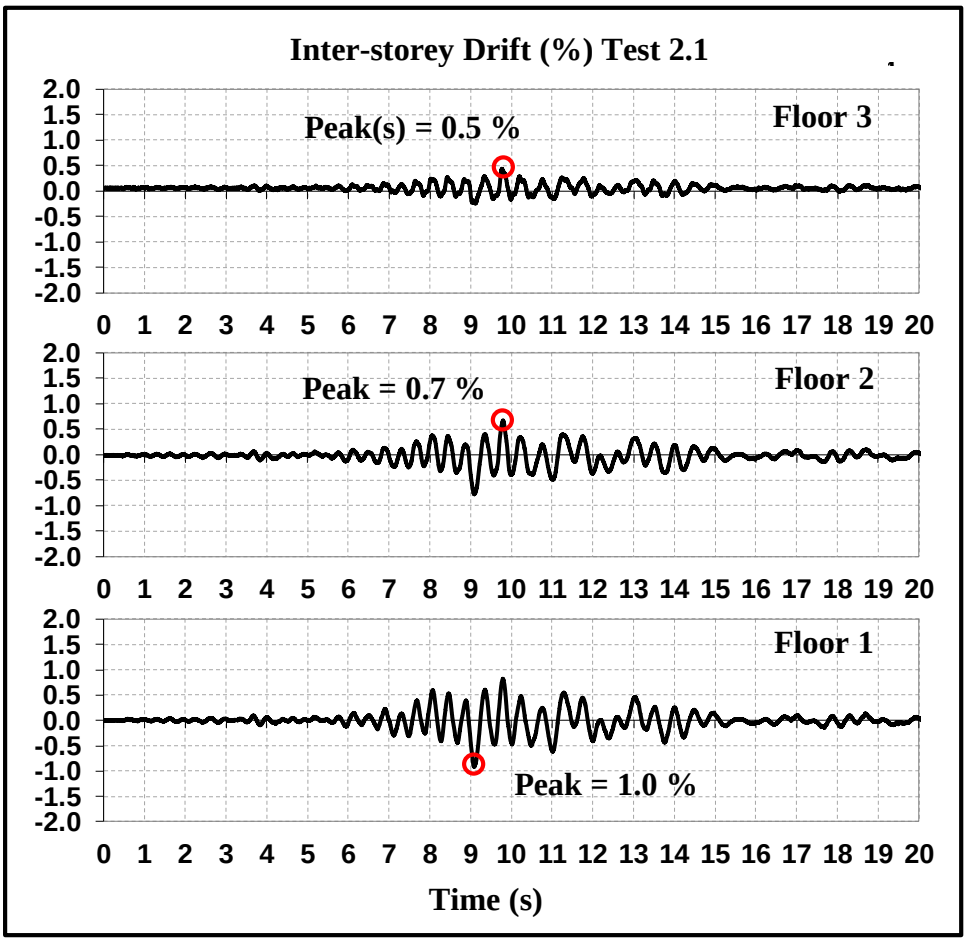

Figure A.1: Test 2.2 recorded inter-storey drifts.

In Figure A.1 the recorded response of the as-built specimen during Test 1.2 are presented in terms of floor displacements and inter-storey drifts histories. In the graphs presented in that picture, it can be observed that the inter-storey drifts of all floors remained below or equal to 1.5%. The maximum recorded inter-storey drifts were smaller in the first floor than in the second one, which in turns were smaller than those recorded in the third floor. Maximum values of the response are 0.9%, 1.2%, and 1.5% for floors 1, 2, and 3, respectively. The inter-storey drift histories denote that the specimen had experiences a

response that does not correspond to an elastic one, as increasing value of the inter-storey drifts with height are not normally expected. As it was shown in the results of Tests 2.1, when the specimen was tested under CHH record (2010 Darfield earthquake), after the lap splices in the columns were connected, the opposite trend was observed.

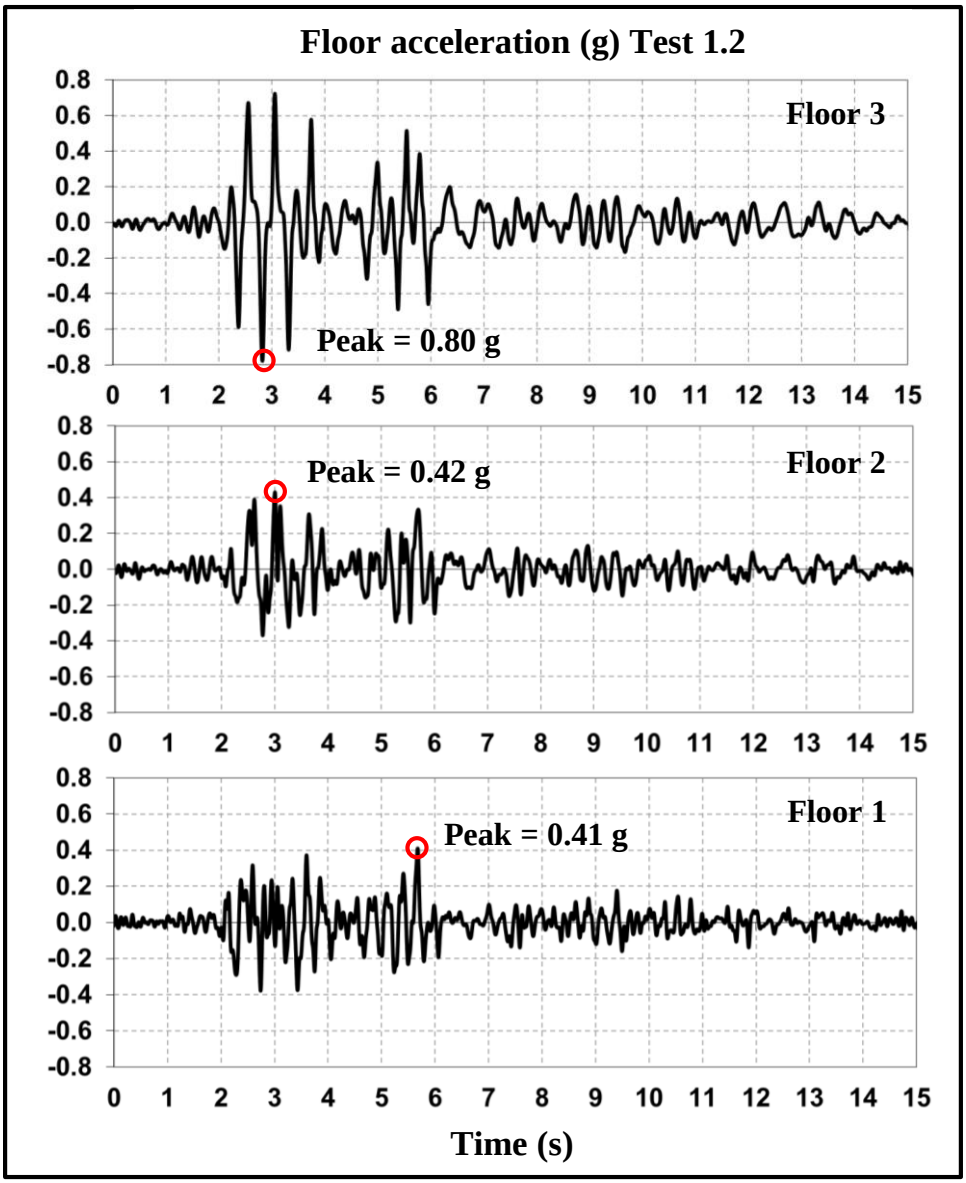

Figure A.2: Test 1.2 recorded floor accelerations.

In Figure A.2 the response of the as-built specimen during Test 1.2 is presented in terms of floor acceleration. In the graphs of that figure it can be observed that remarkably larger accelerations were recorded in the third floor when compared to those of the first and second floors, which in turn were very similar to each other. The maximum recorded values were 0.41g, 0.42g, and 0.80g in floors 1, 2, and 3, respectively. The large difference in the recorded acceleration in the top floor is an indication of the lap-splices mechanism, corroborated with Test 1.3, where the largest amplitude of the input signal was used (PGA), as explained in Chapter 4.

APPENDIX B: NOMINAL-RECORDED INPUT COMPARISON TEST SERIES 1 AND 2

In this appendix, the nominal and recorded input motions of the shake table during the first two experimental series are presented. In Figure B.3, the nominal and recorded motion of the shake table in terms of displacements during Tests 1.1, 1.2, and 1.3 are compared. As it can be observed in the graphs of those figures, there is a good agreements in both signals. However, some differences are notorious during the 'strong' part of the motion, i.e., when the specimen experienced the larges magnitude of the response. That period of time extends between about 2 and 7 seconds. In the bottom graph of Figure B.3, it can be noted that the differences are greater during Test 1.3 than the other two experiments.

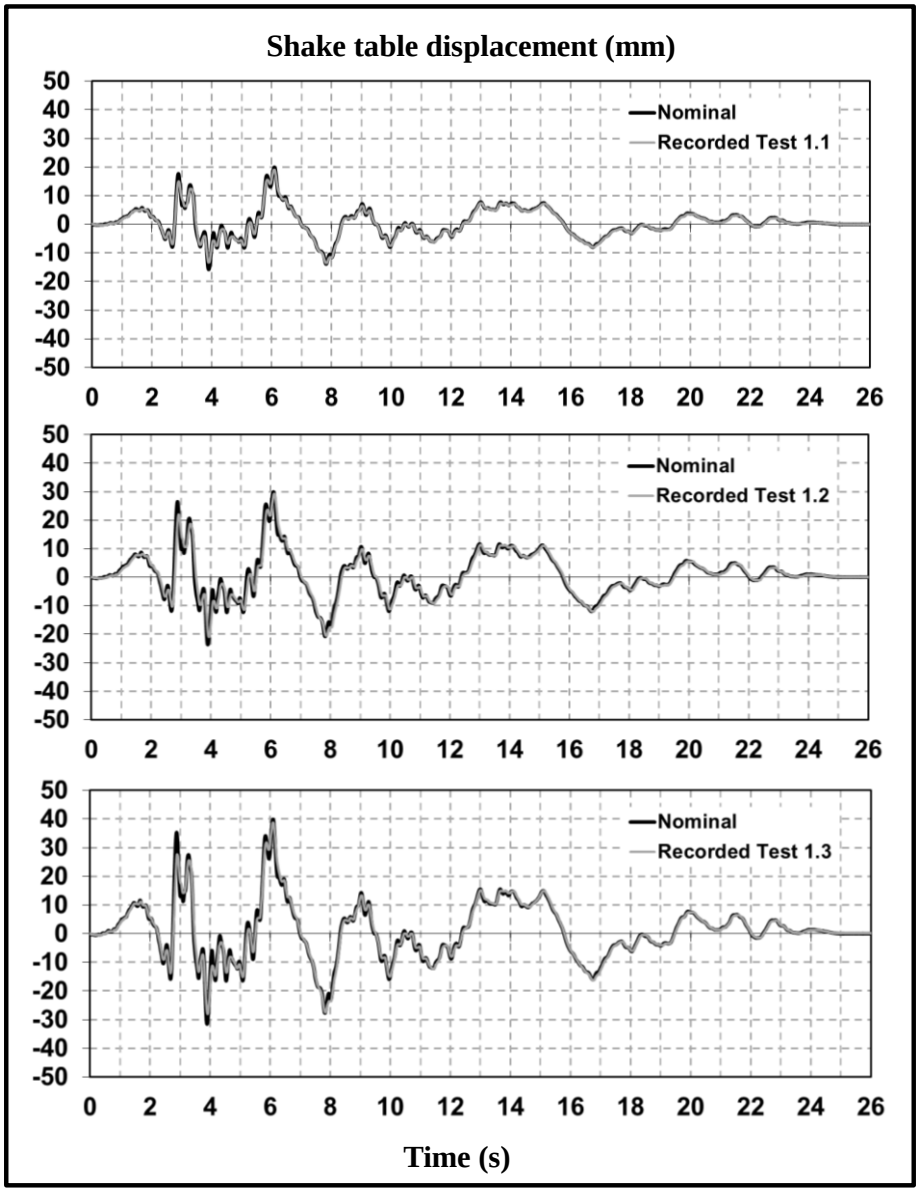

Figure B.3: Nominal and recorded shake table displacement during Tests 1.1, 1.2, and 1.3.

In the top graph of Figure B.4, the nominal and recorded motions of the shake table tests of Tests 2.1 and Test 2.2 are presented in terms of displacement histories. In that graph, it can be observed that there are important differences between the nominal and recorded signals in Test 2.1. It is noted that the recorded displacements of the shake table had a larger magnitude, especially during the period of time when the specimen exhibited the largest response. During the small-amplitude part of the motion, however, the differences are negligible, and the table is able to impose the desired or intended motion with accuracy.

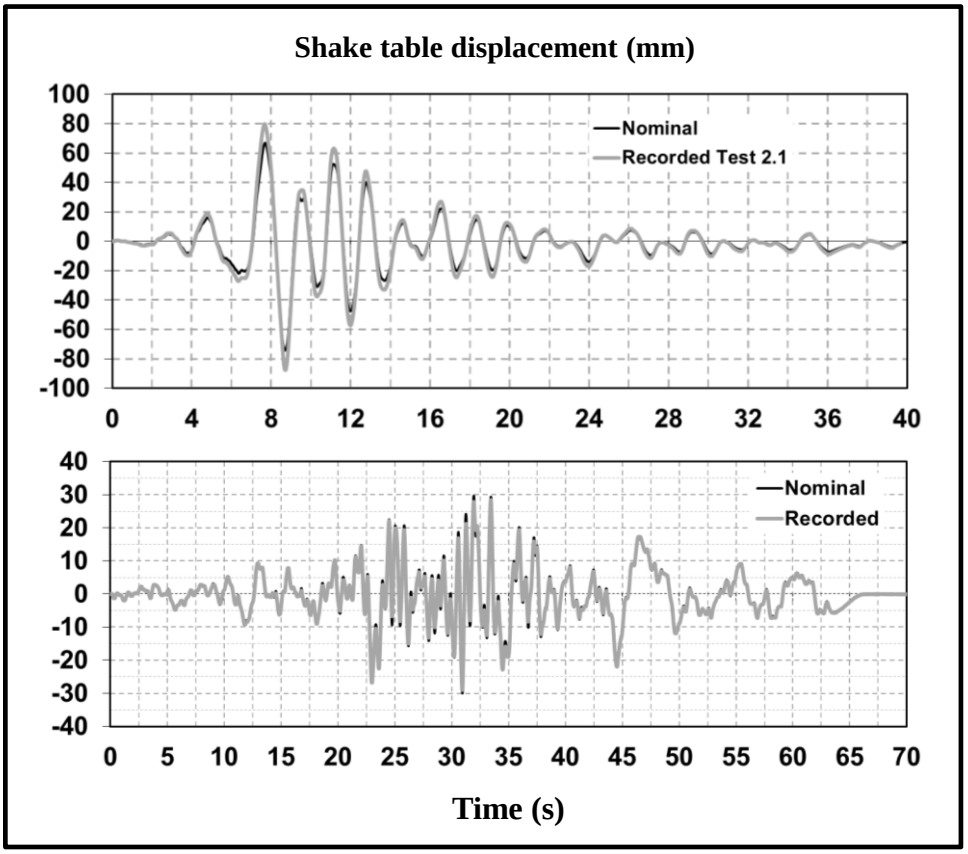

Figure B.4: Nominal and recorded shake table displacement comparison: Tests 2.1 and 2.2.

In the bottom graph of Figure B.4, it can be observed that there is a very good match of the nominal and recorded displacements of the shake table. During the part when the specimen exhibited the largest magnitude in the response, between 20 and 40 seconds of the response, some differences can be observed though.

The fact that the recorded motion differs in a larger magnitude during the large part of the response, is an indication of an unavoidable interaction between the shake table and the specimen being tested. That constitutes a model of an open system in dynamical interaction.

In Figure B.5, the elastic displacement 5% critical damping spectra obtained with the recorded and nominal motions of the shake table are presented and compared. As it can be observed in those figures, there are important differences in the spectra obtained with the nominal and recorded motions, especially for Tests 1.2 and 1.3. Those differences

existed for Test 1.1, but the differences are smaller than in the other tests, and of the order of 2-3 mm. In the spectra obtained for Tests 1.2, the differences increase in magnitude. In all cases, if one divides the amplitude of the recorded motion spectra by that of the nominal counterpart, a ratio of the order of 75% is obtained in the parts of the spectra where the differences were more important.

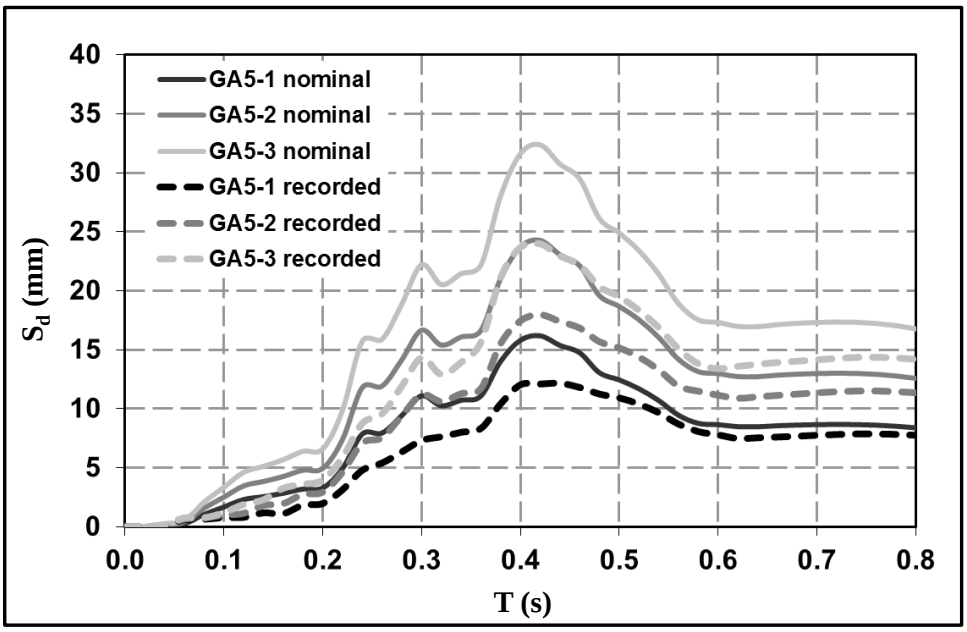

Figure B.5: Elastic displacement spectra (ξ = 5%), obtained with the nominal and recorded motions of the shake table during Test 1.1, 1.2, and 1.3.

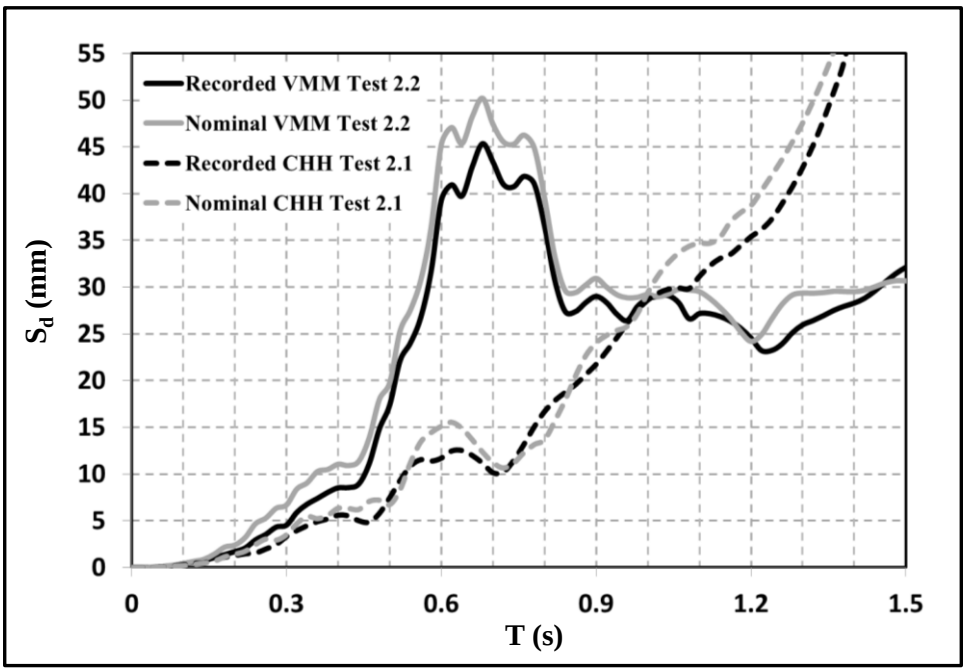

Figure B.6: Elastic displacement spectra (ξ = 5%), obtained with the nominal and recorded motions of the shake table during Test 2.1 and Test 2.2.

In Figure B.6, the displacement spectra obtained with the nominal and recorded motions of the shake table for Tests 2.1 and 2.2 are presented. In the graphs of that figure, it can be observed that the differences in spectra obtained with the recorded and nominal input motions are minimal and much smaller than those found in the spectra of the first experimental series of tests. The differences in the recorded/nominal motions spectra for Test 2.1 are almost negligible, whereas for Test 2.2, some relatively important differences exist. In the latter case, if one divides the spectral displacements obtained with the recorded motion by those obtained with the nominal counterpart, a ratio of the order of 90%, which is a rather small value.

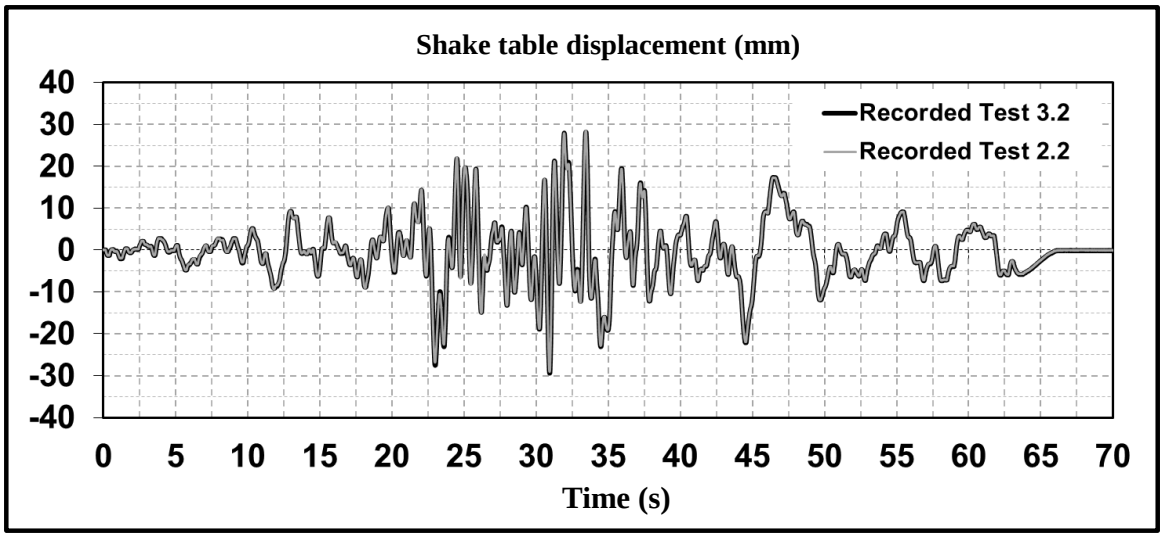

Figure B.7: Comparison of the recorded shake table motion during Tests 2.2 and 2.3.

Finally, in Figure B.7, the recorded shake table motion recorded during Test 2.2 (repaired specimen) and Test 2.3 (retrofitted specimen) are compared. Those motions correspond to the same nominal input (VMM) that represented one ground motion recorded during the 2010 Maule earthquake. In the graph presented in that figure, it can be observed that both recorded motions are almost identical, highlighting the accuracy of the shake table to replicate the same input during different experiments.

APPENDIX C: MEASURED PERIODS OF VIBRATION AND VISCOUS DAMPING

C.1 FUNDAMENTAL PERIOD AND VISCOUS DAMPING MEASURE

In this appendix, measurements of the three modes of vibration and the viscous damping of the specimen before each series of tests were conducted are presented. The procedure used to measure the fundamental period of vibration of the specimen as well as the damping consisted in free vibration tests. The free vibration of the specimen was achieved by imposing a certain displacement in the shake table and then suddenly bringing it back to the zero position. The results presented here correspond to the measured top storey displacement in time.

If one counts the amount of cycles per second that the building experiences, the fundamental period of vibration can readily be estimated. In addition, the viscous damping can be evaluated using a traditional method explained in classical structural dynamics textbooks such as Chopra (1995). That method is summarized herein.

The response of the SDOF oscillator in terms of relative displacement can be described with Equation C.1.

$$x(t) = A \cdot e^{-\xi \omega_n t} \sin\left(\omega_n \sqrt{1-\xi^2} \cdot t + \varphi\right) \tag{C.1}$$

Where, A = amplitude of the displacement, ξ = factor of the critical damping, t = time, ω_n = natural frequency of the oscillator, φ = phase angle; with A and φ depending on the initial conditions. Two different amplitudes of displacement $x_1(t)$ and $x_2(t)$, measured at $t = t_1$ and $t = t_2$, respectively, can be calculated using Equation C.1. Times t_1 and t_2 define the start and end of a given cycle (i.e. they define one period of oscillation). Dividing those amplitudes between each other, Equation C.2 can be obtained, which can be re-written in the form of Equation C.3, with its simplified version presented in the right hand side.

$$\frac{x_1(t_1)}{x_2(t_2)} = exp\left(\frac{2\pi\xi\omega_n}{\omega_n\sqrt{1-\xi^2}}\right) \tag{C.2}$$

$$ln\left(\frac{x_1(t_1)}{x_2(t_2)}\right) = \frac{2\pi\xi}{\sqrt{1-\xi^2}} \approx 2\pi\xi \tag{C.3}$$

Using 10 local peaks of the response where the amplitude of the displacement was evaluated, the viscous damping was estimated for each specimen before the series of tests in each case were performed. The results of the evaluation of the damping at 10 consecutive intervals are summarized in Table C.1. The average values estimated for the as-built, repaired and retrofitted specimens are 2%, 4% and 4%, respectively, with standard deviations of 0.3%, 1.2%, and 0.9% for each case.

Table C.1: Summary with the estimated elastic viscous damping value measured before each series of tests ('Std. Dev.' means Standard Deviation). Note: x_1 and x_2 are in mm.

	As-built specimen			Repaired specimen			Retrofitted specimen		
Interval	x_1	x_2	ξ	x_1	x_2	ξ	x_1	x_2	ξ
1	1.08	0.93	2.4	1.17	0.92	3.8	1.19	0.88	4.8
2	0.93	0.81	2.2	0.92	0.71	4.1	0.88	0.63	5.3
3	0.81	0.73	1.7	0.71	0.57	3.5	0.63	0.49	4.0
4	0.73	0.65	1.8	0.57	0.45	3.8	0.49	0.36	4.9
5	0.65	0.57	2.1	0.45	0.36	3.6	0.36	0.30	2.9
6	0.57	0.51	1.8	0.36	0.27	4.6	0.30	0.22	4.9
7	0.51	0.46	1.6	0.27	0.19	5.6	0.22	0.18	3.2
8	0.46	0.42	1.4	0.19	0.17	1.8	0.18	0.15	2.9
9	0.42	0.38	1.6	0.17	0.13	4.3	0.15	0.11	4.9
10	0.38	0.34	1.8	0.13	0.12	1.3	0.11	0.08	5.1
	Average		2	Average		4	Average		4
	Std. Dev.		0.3	Std. Dev.		1.2	Std. Dev.		0.9

The velocity used for bringing the shake table back to the zero position varied from test to test, and the best result is shown for every series of tests. In the test performed to the specimen before series 1, a velocity approximately equal to 20 mm/s was used, whereas in the tests performed to the repaired specimen, a velocity equal to 10 mm/s was used. As can be observed in the figures with the top storey displacement during the time of free vibration, the velocity in the decay of the motion was different for the three tests. For the as-built specimen, the largest velocity was achieved. Since the calculated value of the damping depends on the velocity of that decay (Crandall 1970, Bert 1973), the differences in the estimated values between the damping of the as-built specimen and the other two can be attributed to that factor.

The results of the recorded free motion of the as-built and repaired specimens in terms of roof displacement versus time are presented in Figure C.8 and Figure C.9, respectively. Based on those measurements, the fundamental period of the as-built and repaired specimens were approximately equal to T_1 = 0.22 sec. and T_1 = 0.27 sec. respectively. The values are very close to each other, indicating that the repairing intervention did not alter the dynamical properties significantly. In Figure C.10, the free vibration of the retrofitted specimen during the initial testing is presented in terms of the top storey displacement in time. This time, the measured period of vibration of the structure is can be estimated as T_1 = 0.34 sec.

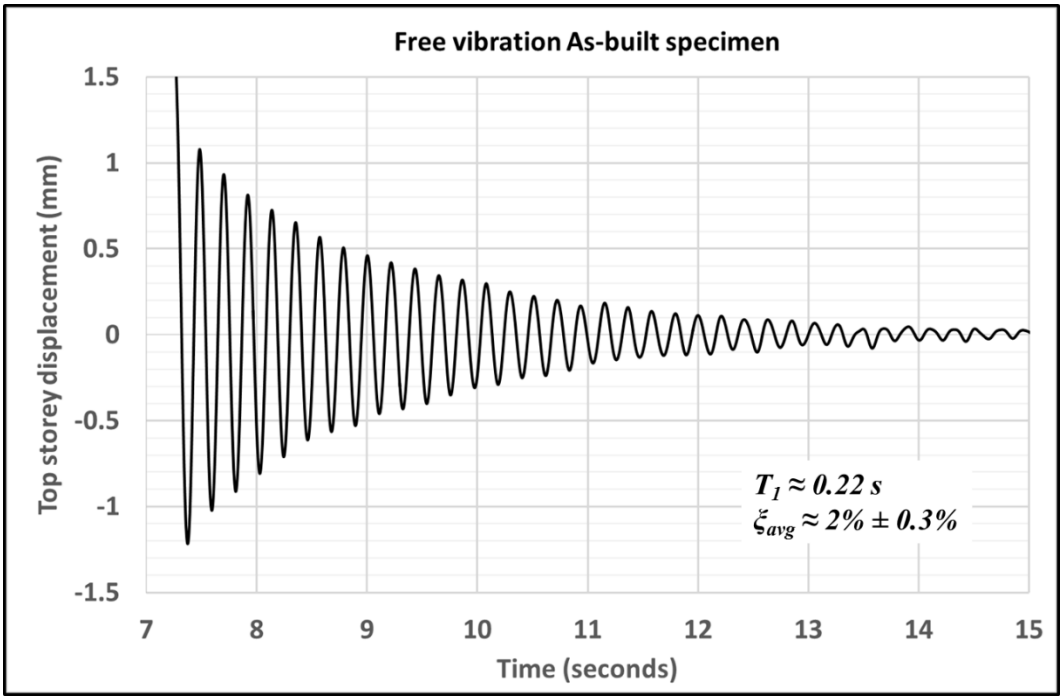

Figure C.8: Free vibration tests, as-built specimen

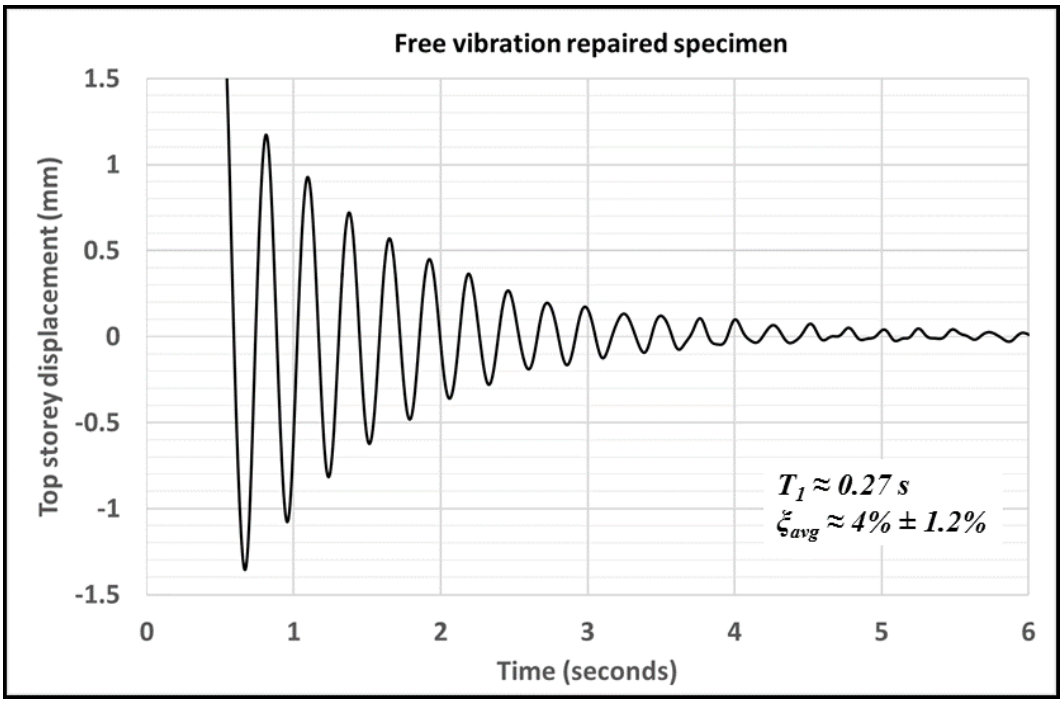

Figure C.9: Free vibration tests, repaired specimen

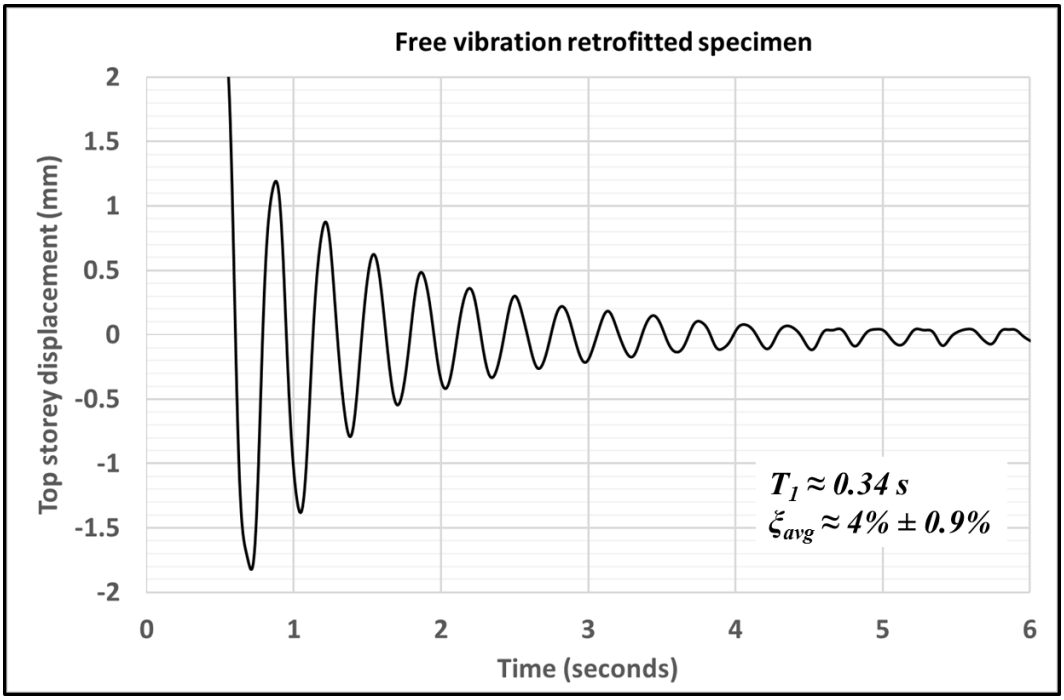

Figure C.10: Free vibration test, retrofitted specimen

C.2 ESTIMATION OF THE INITIAL FUNDAMENTAL PERIODS OF VIBRATION OF THE SPECIMEN IN THE FOURIER SPECTRAL DOMAIN

In the following figures, the three modes of vibration of the specimen before the test series 1, 2, and 3 are evaluated in the Fourier frequency domain. These results were obtained from the acceleration recorded at the top storey of the model building during preliminary tests. In those tests, sinusoidal input motions with different frequencies and small amplitudes were used.

In Figure C.11 the periods of vibration of the repaired specimen are presented. They are T_1 = 0.24 sec., T_2 = 0.13 sec., T_3 = 0.08 sec. In Figure C.12 the periods of vibration of the repaired specimen are shown. They are T_1 = 0.27 sec., T_2 = 0.09 sec., T_3 = 0.06 sec. In Figure C.13 the periods of the retrofitted specimen are presented. They are T_1 = 0.32 sec., T_2 = 0.11 sec., T_3 = 0.08 sec. The values of the fundamental period are very close to that evaluated with using the free vibration methodology.

The periods of the higher modes of vibration are quite similar for the three specimens, considering the distortion involved in the problem inherent to a scale model. The period of the second mode has a value large enough to have played a relevant role in the dynamical response of the building. However, it needs to be reminded that as long as the structure experiences any inelasticity, these values will change.

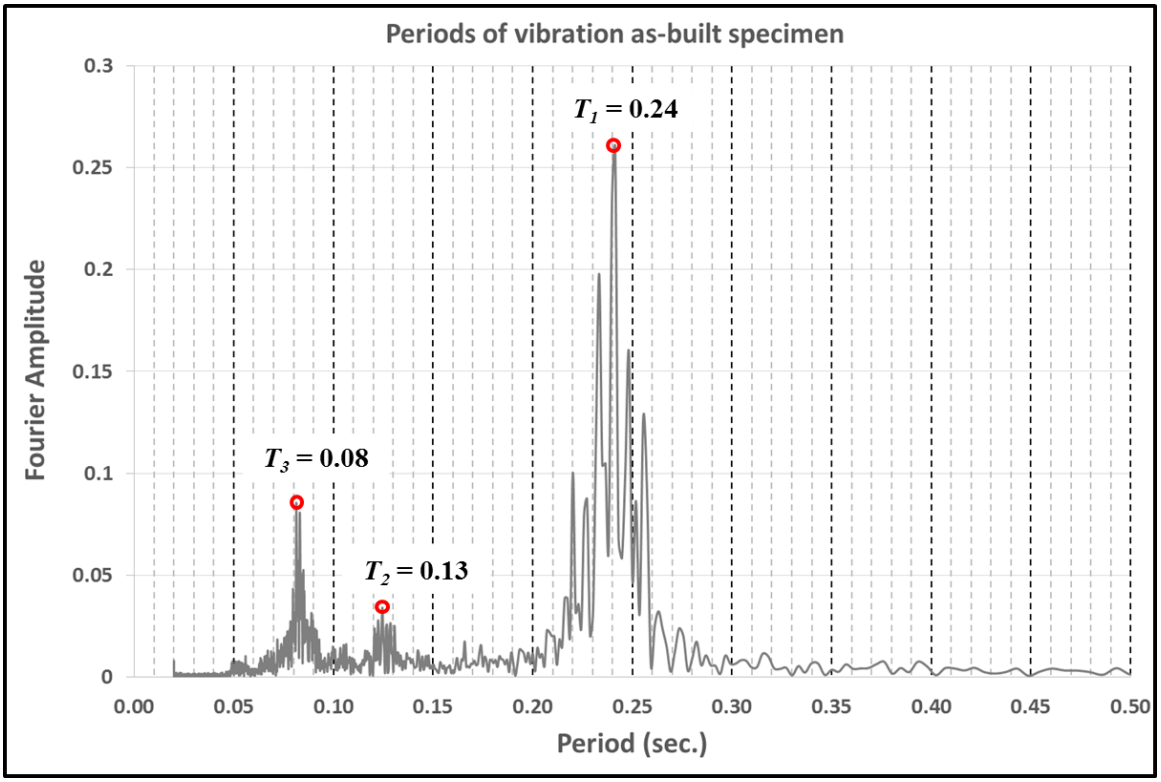

Figure C.11: Periods of vibration, Fourier domain, as-built specimen

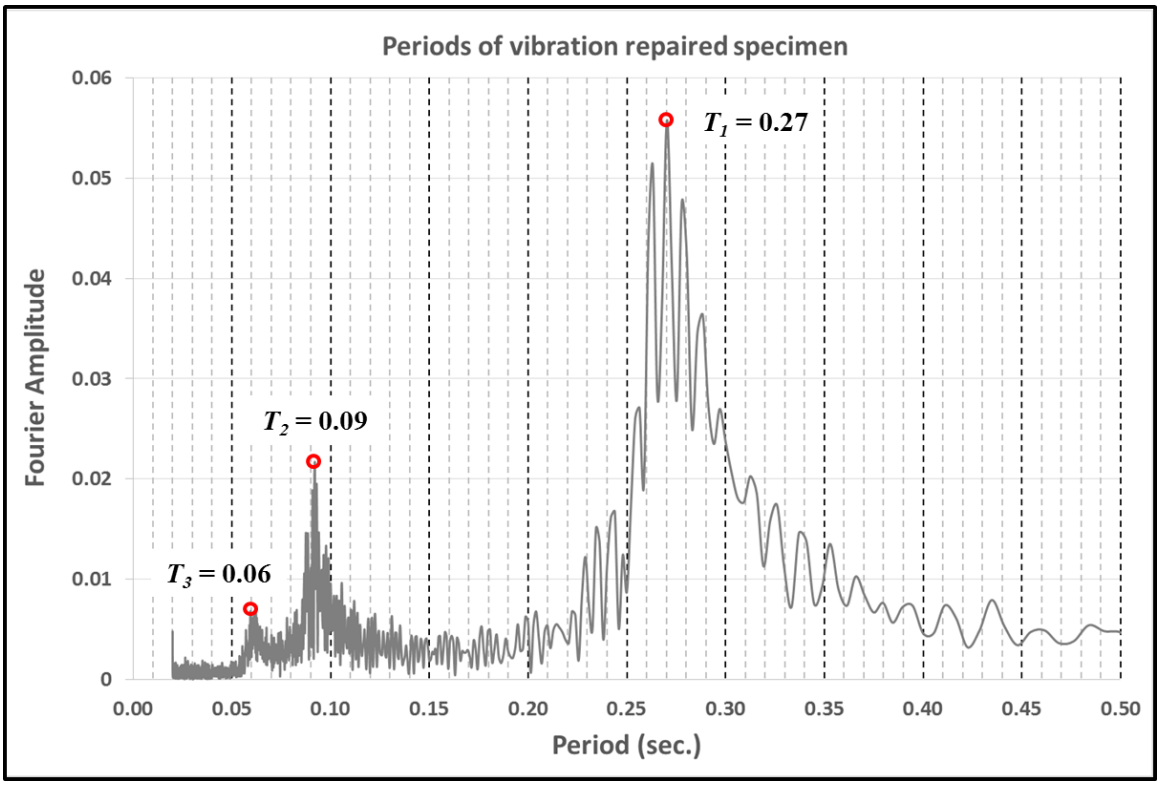

Figure C.12: Periods of vibration, Fourier domain, repaired specimen

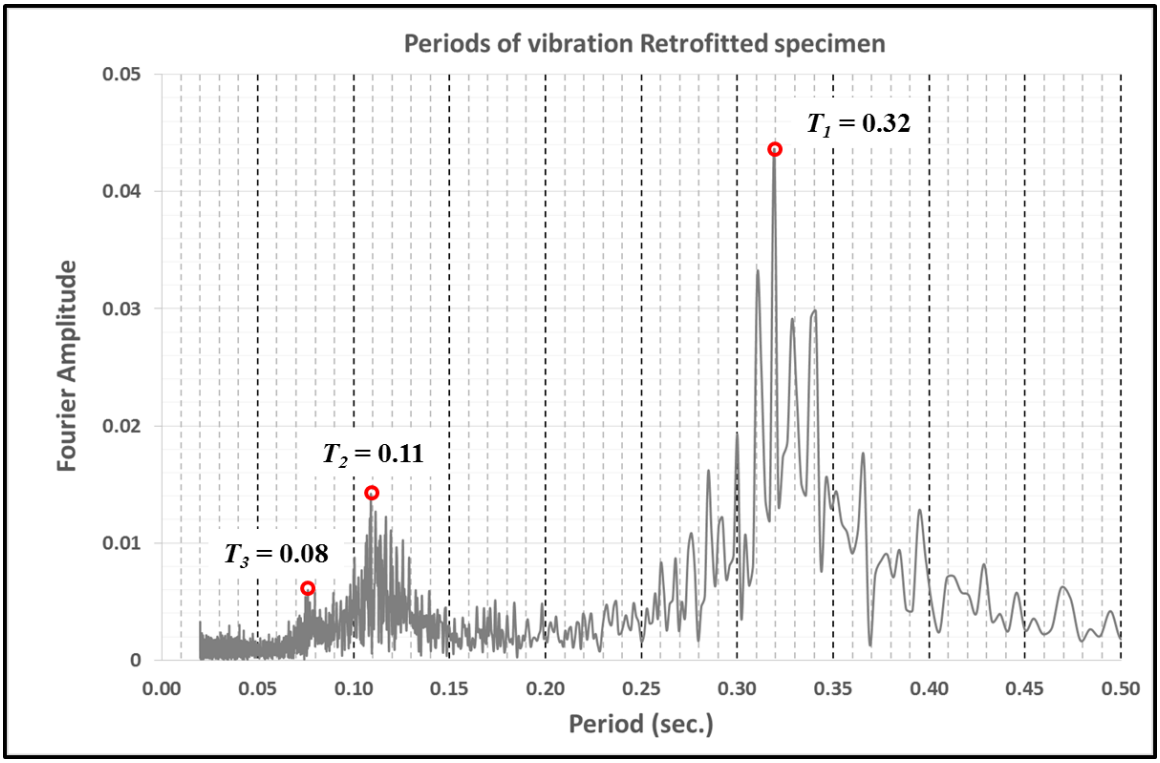

Figure C.13: Periods of vibration, Fourier domain, retrofitted specimen

C.3 ESTIMATION OF THE PERIODS OF VIBRATION AT THE END OF EACH SERIES OF TESTS

In the next few figure, the recorded signal of the top storey of the building at the end of each series of tests, i.e. Test 1.3, Test 2.2 and Test 3.2 are presented in the Fourier frequency domain. In the figures, the periods of the modes of vibration after damage has occurred in the structure can be visualized.

C.4 REFERENCES

Bert, C. W. (1973), 'Material Damping: An Introductory Review of Mathematical Measures and Experimental Techniques', *Journal of Sound and Vibration*, Vol.29(2), pp. 129-153.

Chopra, A. K. (1995), *Dynamics of Structures*, Prentice Hall, New Jersey, USA.

Crandall, S. H. (1970), 'The Role of Damping in Vibration Theory', *Journal of Sound and Vibration*, Vol.11(1), pp. 3-18.

APPENDIX D: ADDITIONAL NUMERICAL WORK

D.1 Capacity Spectrum Method

In this appendix, some additional numerical work is presented. In Figure D.14 the capacity spectrum method proposed by Freeman (1998, 2004) is presented for the as-built specimen and the most demanding record (VMM) as fund from the shake table test results presented in Chapter 4. The method is a simple tool for the evaluation of the so called 'performance point' of a structure, defined as the intersection of the demand in terms of a certain response spectrum and the capacity derived from a pushover analysis. The response spectra is plotted in terms of the spectral acceleration versus the spectral displacements for a certain period range, and for a given viscous damping. The value of that damping though, is not specified in the original method proposed by Freeman (1998) and it is a matter of discussion (fib Task Group 7.2, 2003).

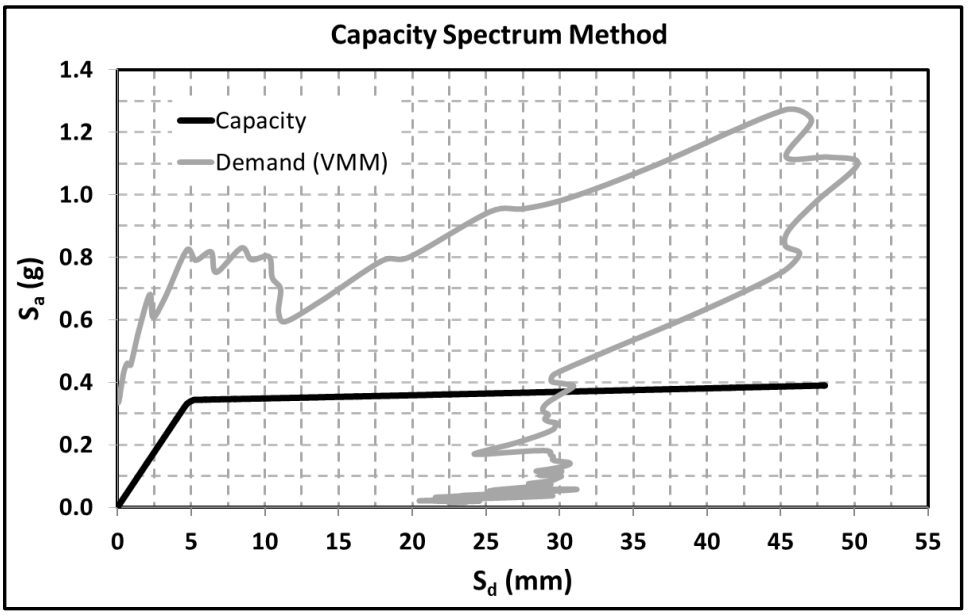

Figure D.14: Capacity spectrum method for the most demanding record according to Chapter 4.

According to the fib Bulletin 25 (fib Task Group 7.2, 2003), the demand could be plotted for different values of equivalent damping to account for 'inelastic behaviour', or alternatively, a reduction factor such as that used in the Eurocode (Priestley 2000) could be used. However, it is noted that the use of a larger equivalent damping or an explicit reduction factor would result in smaller demands upon the structure. According to the intersection of the graphs plotted in Figure D.14, the structure, assumed to experience a soft-storey mechanism as explained in Chapter 8, would experience a maximum displacement of 30 mm at every floor level (rigid body assumption). That is, the structure is anticipated to experience a maximum inter-storey drift approximately equal to 2.5%. Nevertheless, the results of the shake table tests performed to the model building using this record (VMM) showed that the specimen reached much larger inter-storey drift values with a maximum equal to 4%. That is, even if the spectral ordinates are not reduced to account (artificially) for inelastic behaviour, the method yields non-conservative results. As mentioned in Chapter 4, Chapter 7 and the conclusions of this

thesis, as the dynamical component of the problem is neglected, this type of method does not lead to realistic predictions for the response of a building. Furthermore, the term 'performance point' is conceived in a static environment, which is in contradiction with the meaning of the word which deals with the change in the state of a certain structure (or body) in time.

D.2 COMPARISON OF THE PREDICTED AND RECORDED FLOOR ACCELERATION OF SELECTED TESTS

D.2.1 Blind Prediction As-Built/Repaired Specimen (Initial Model, Nominal Input)

In Figure D.15 the blind numerical prediction of the floor accelerations experienced by the as-built specimen during Test 1.1 are presented and compared with the experimental counterparts.

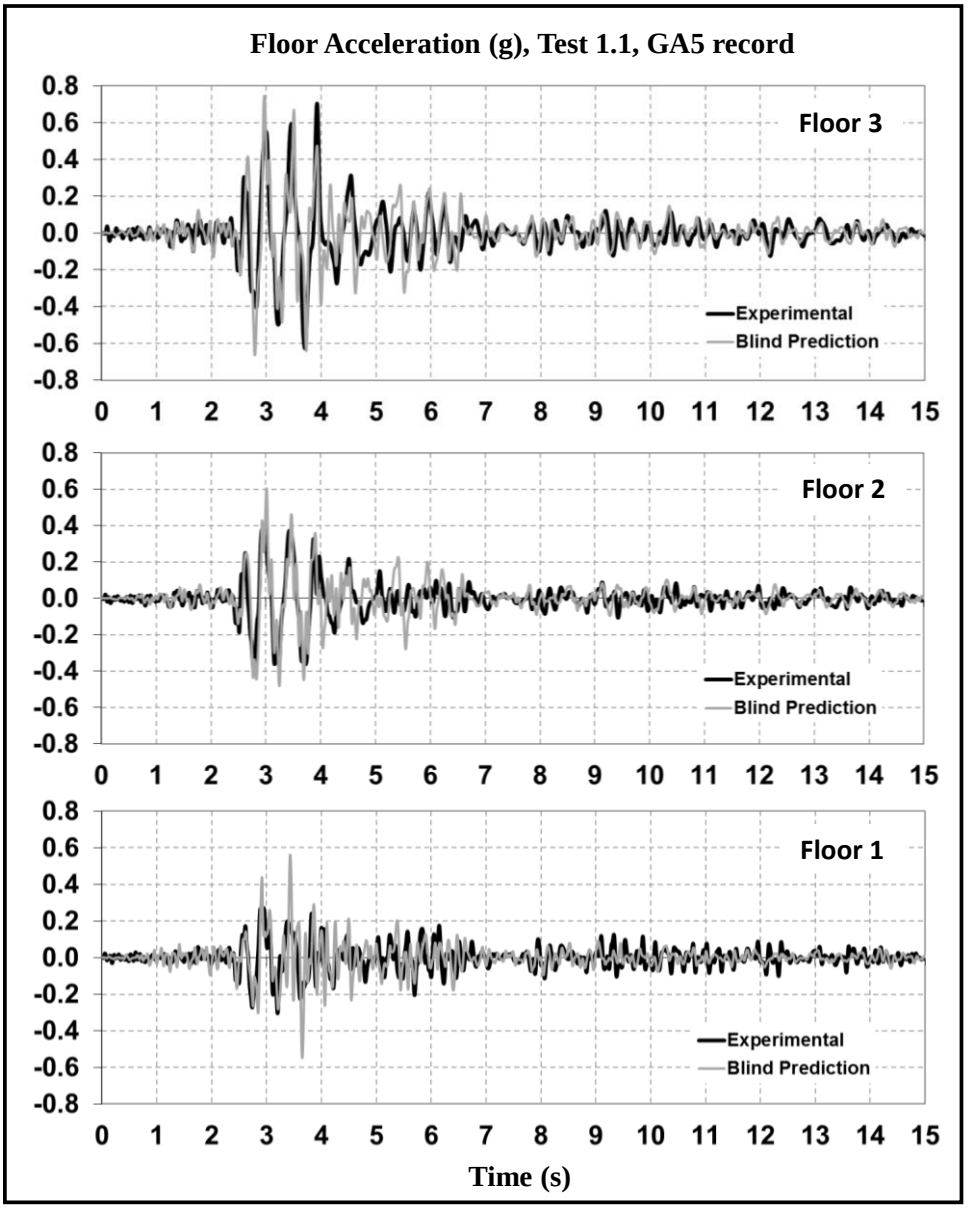

Figure D.15: Test 1.1 floor accelerations, GA5 record, blind prediction.

In those predictions, the nominal input motion was used, which is in agreement with the definition of a 'blind' prediction, when the information of the recorded motion imposed by the shake table is unknown. In Figure D.15 it can be observed that the prediction is in reasonable agreement with the experimental counterpart, even though differences in the shape and particularly in the maximum amplitudes can be clearly appreciated.

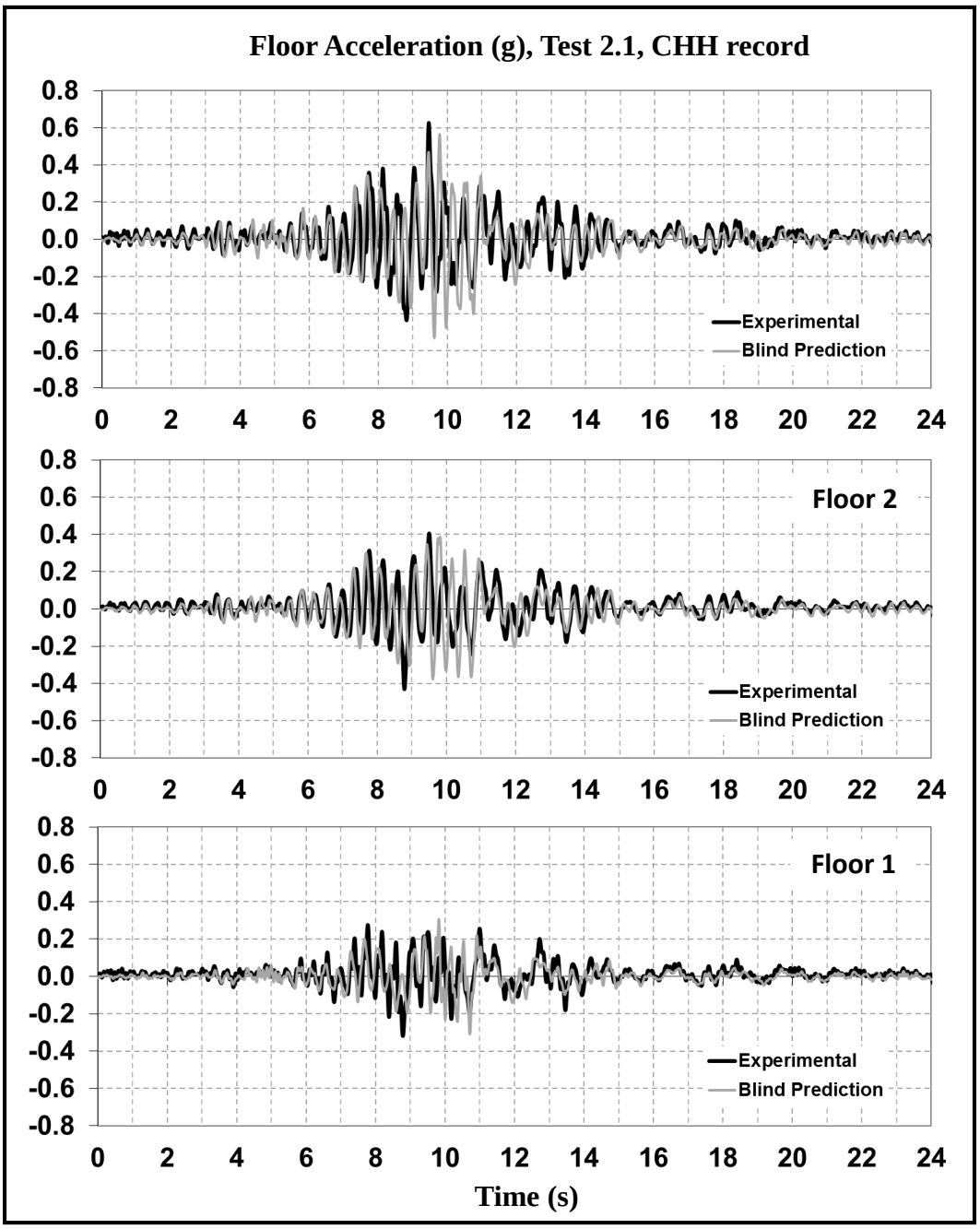

Figure D.16: Test 2.1 floor accelerations, CHH record, blind prediction.

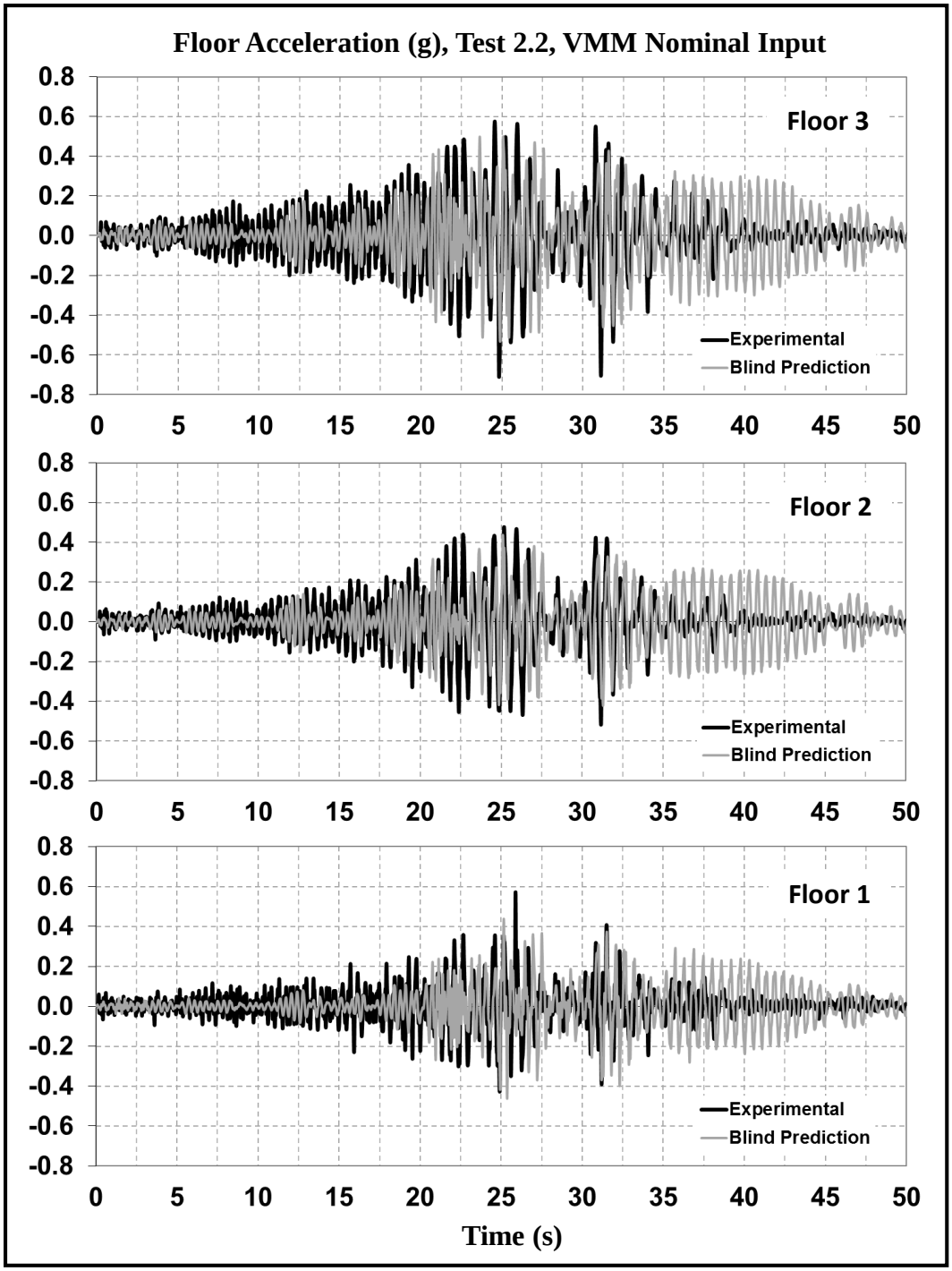

Figure D.17: Test 2.2 floor accelerations, VMM record, blind prediction.

The comparison of the floor accelerations presented in Figure D.17 reveal that the predicted acceleration especially at the end of the specimen response is not the best. It can be clearly appreciated in that figure that the amplitude of the predicted acceleration is much larger than the experimental counterpart. Those are the vestiges of the differences that can be better visualized when comparing the inter-storey drifts and displacements, as presented in Chapter 8.

D.2.2 Pseudo-Blind Prediction As-Built/Repaired (Recorded Input)

In the following figures, the predicted acceleration obtained with the same numerical model used in the blind prediction this time using the recorded motion of the shake table are compared with the experimental results.

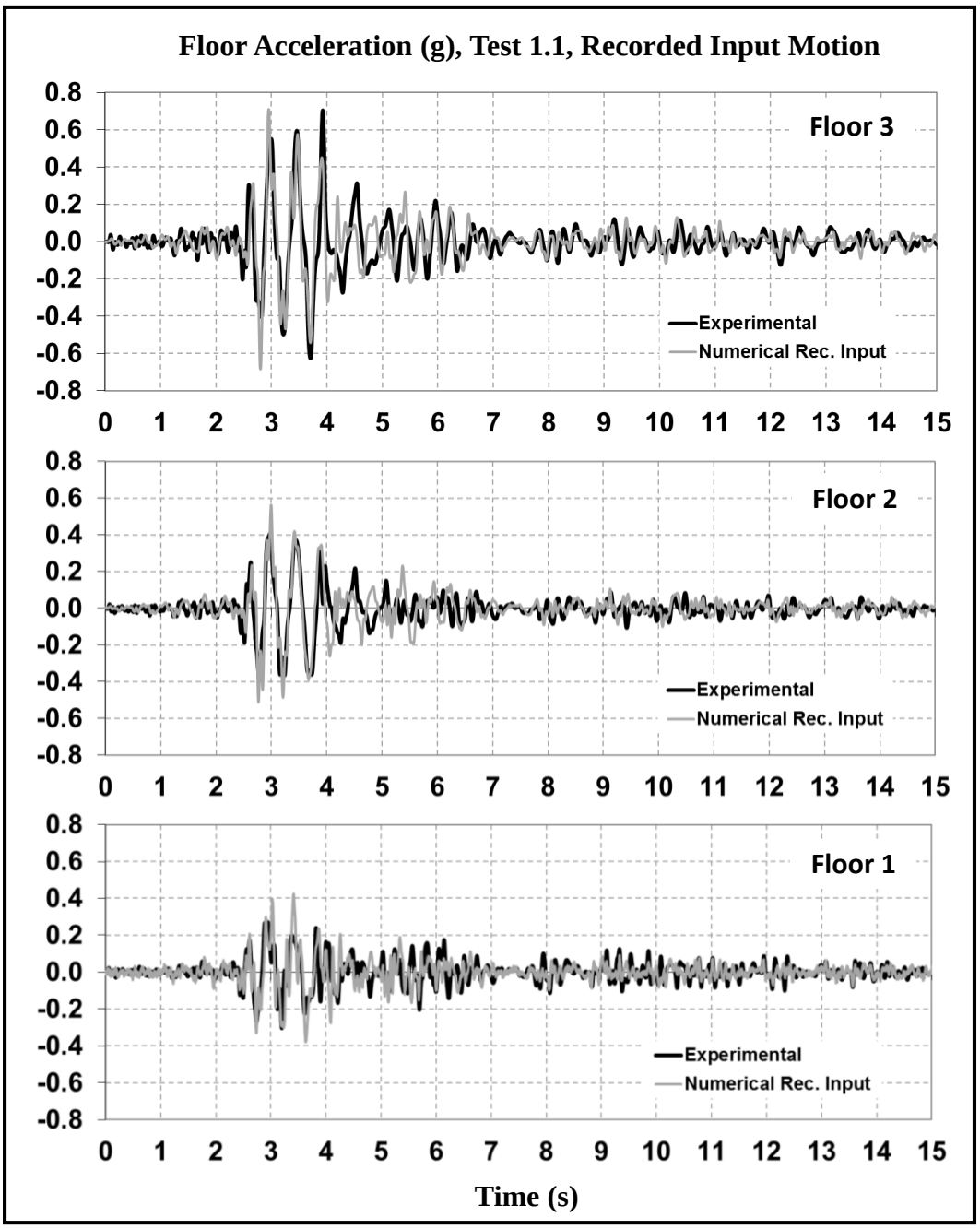

Figure D.18: Test 1.1 floor accelerations, initial model, recorded input motion.

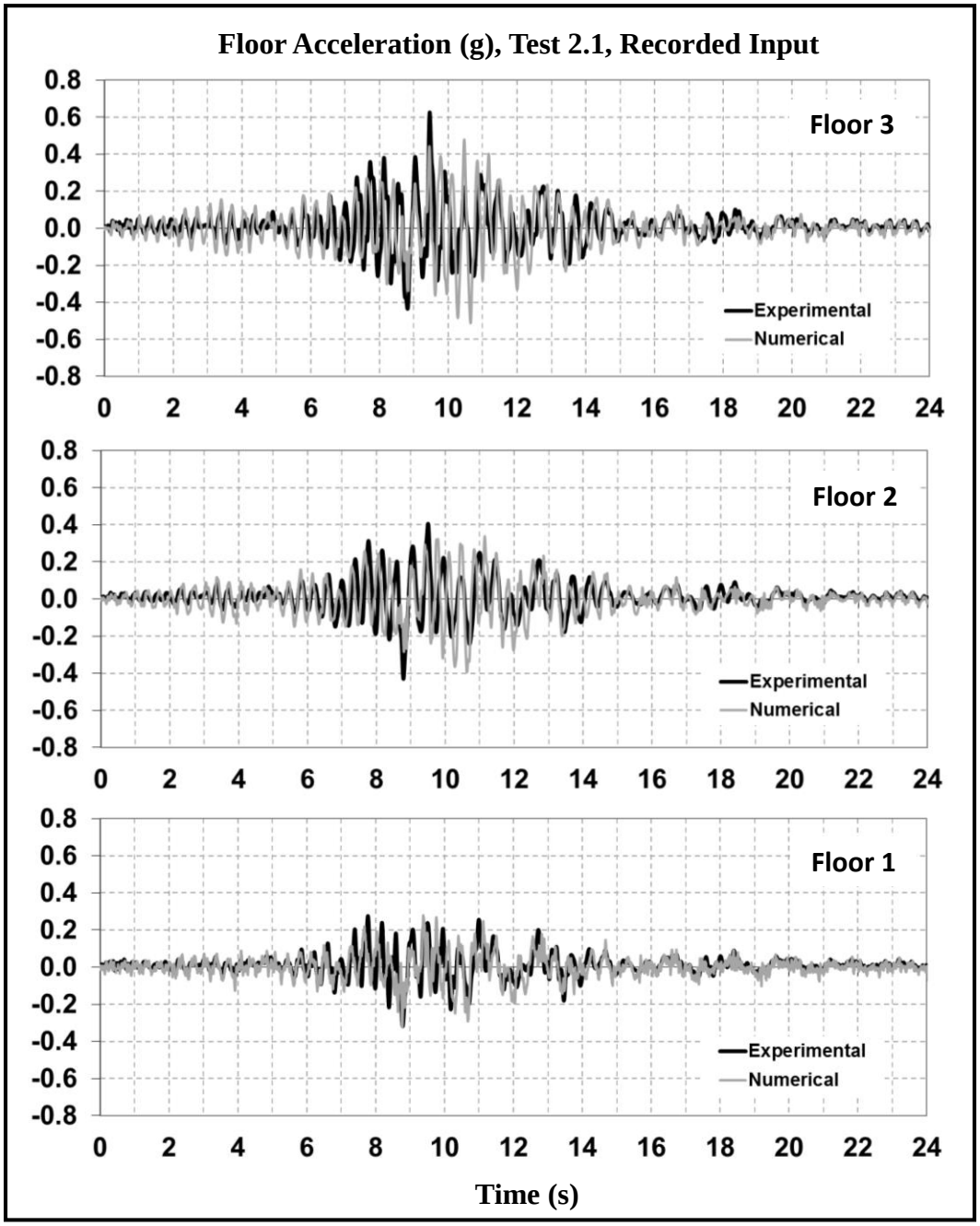

Figure D.19: Test 2.1 floor accelerations, initial model, recorded input motion.

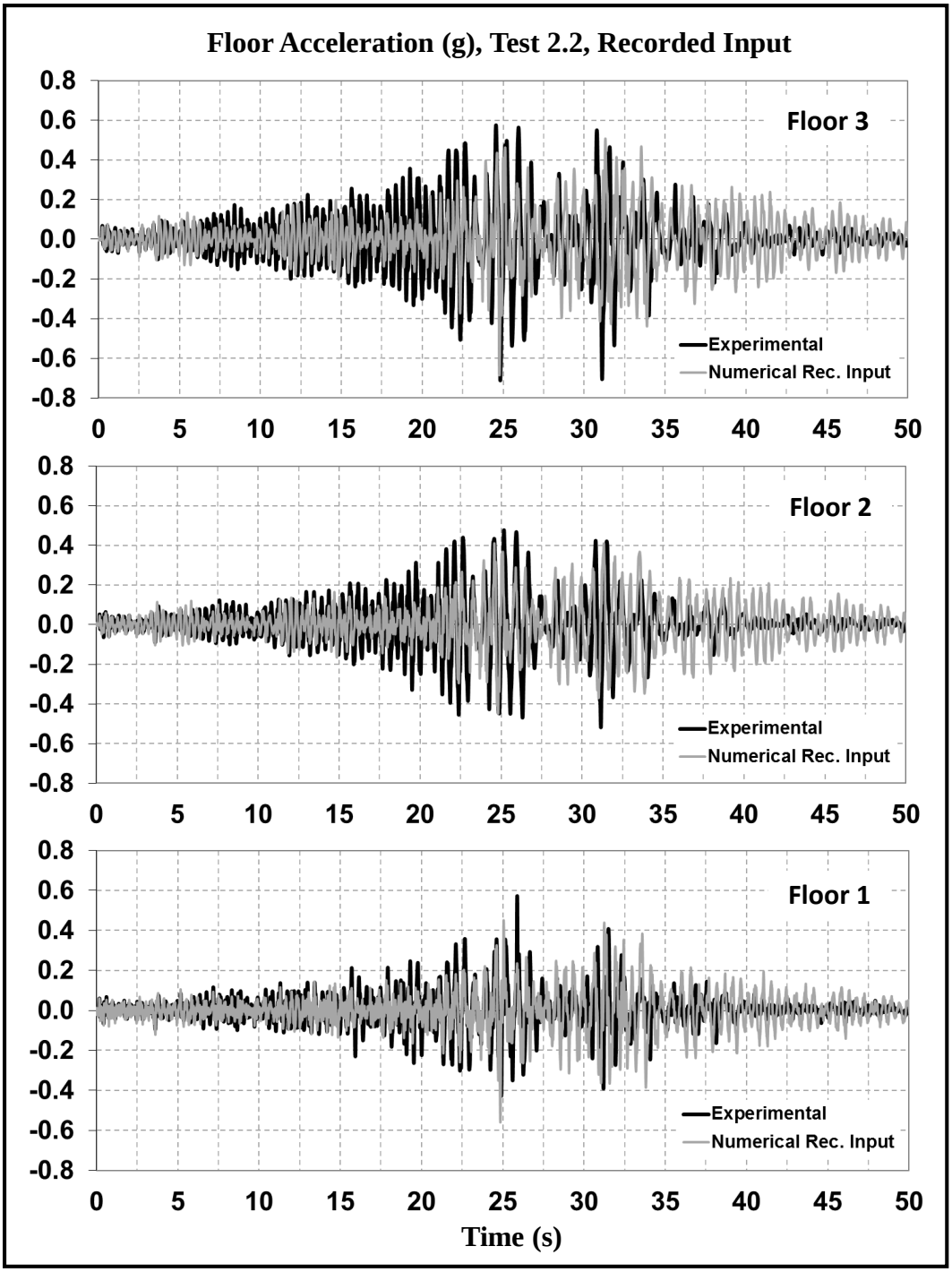

Figure D.20: Test 2.2 floor accelerations, initial model, recorded motion.

Overall speaking, the predicted floor acceleration histories are in a better agreement than those obtained with the blind prediction for all tests (Figure D.18 to Figure D.20). However, the differences that can be visualized with the floor displacement and inter-storey drift counterparts are not evident when comparing the floor accelerations.

D.2.3 Post-Experimental Prediction using the SINA rule in Joints

In the next figures, the numerical post-experimental predictions of the floor accelerations of the as-built and repaired specimens are compared with the experimental results. In the

graphs of those figures (Figure D.21 to Figure D.23), a relatively good agreement in the shape and amplitude of the predicted and recorded signals can be observed.

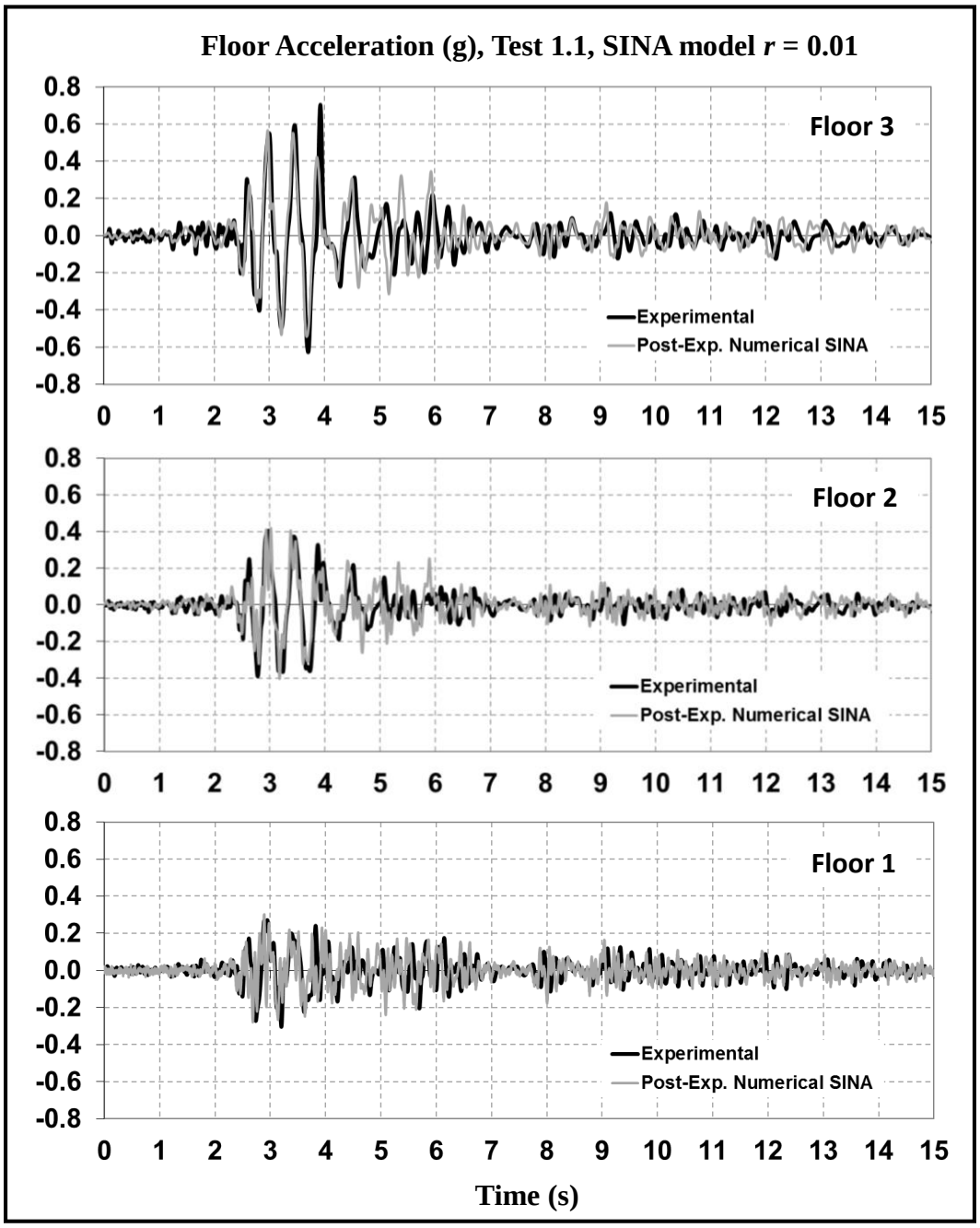

Figure D.21: Test 1.1 floor accelerations, post-experimental prediction.

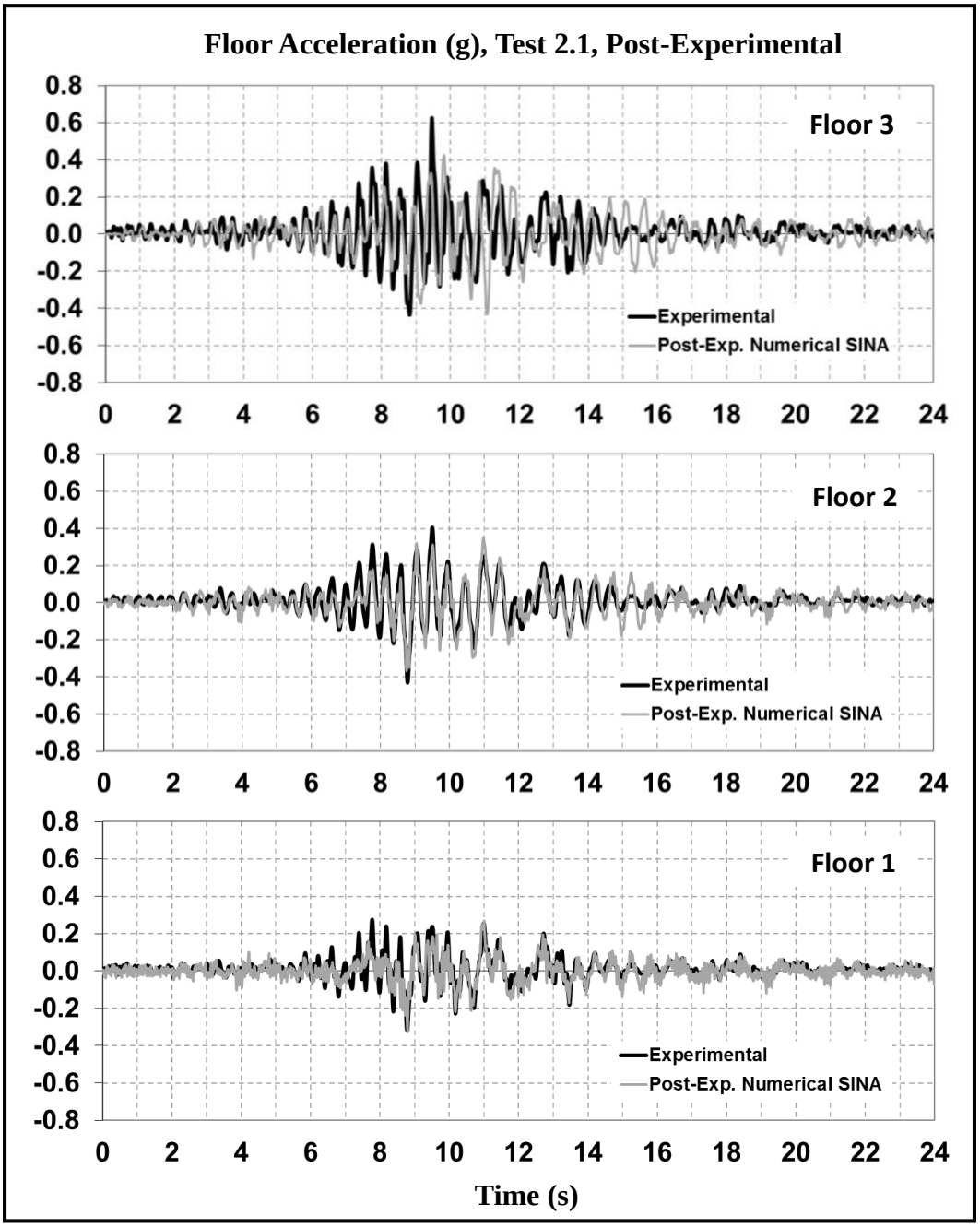

Figure D.22: Test 2.1 floor accelerations, post-experimental prediction.

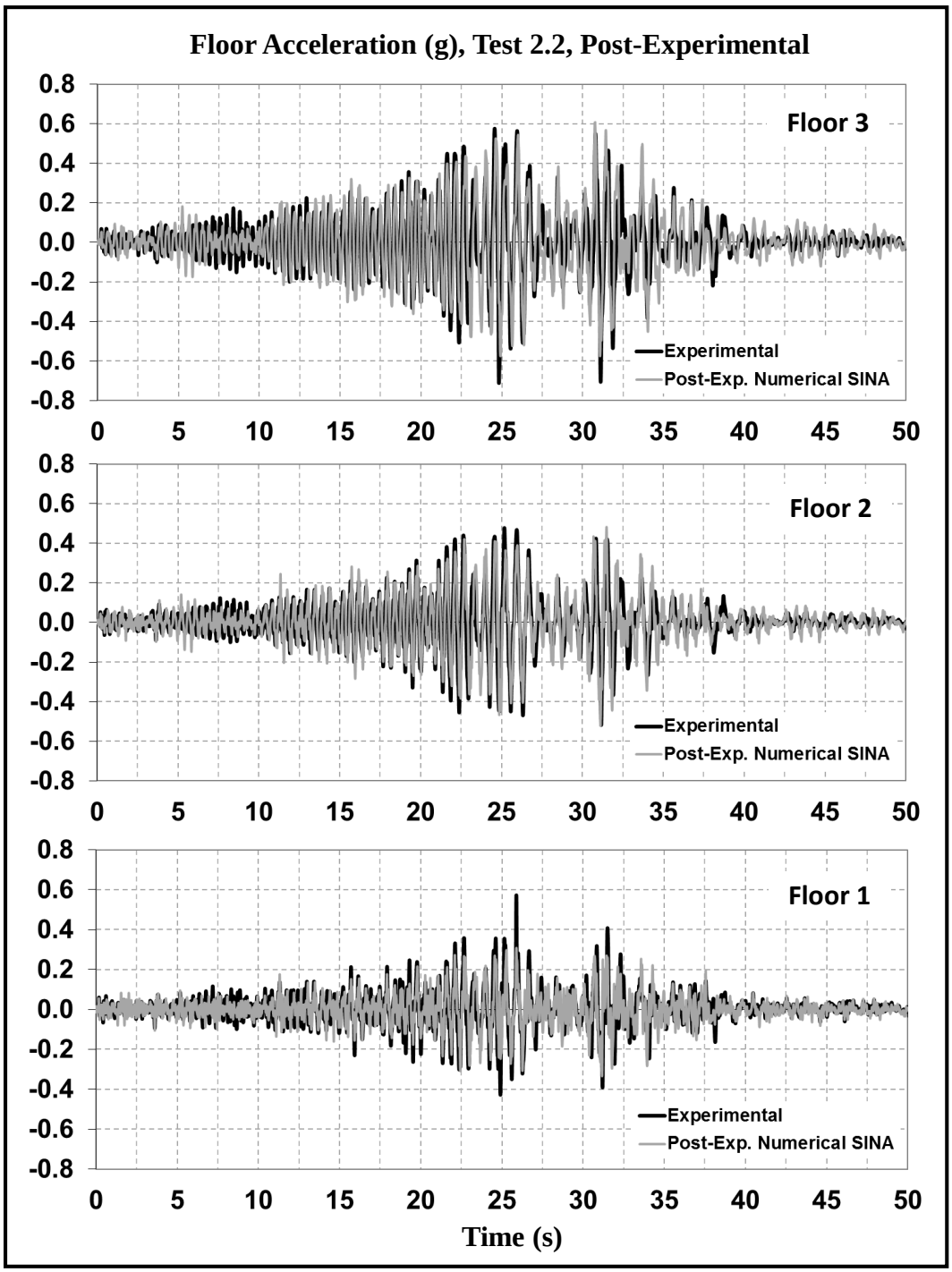

Figure D.23: Test 2.2 floor accelerations, post-experimental prediction.

In Table D.2 the maximum experimental and numerical values of the as-built specimen response in terms of floor acceleration are presented. The table summarizes the results of the three set of predictions as explained in Chapter 8 and this appendix. The peak values do not necessarily occur at the same time after the beginning of the motion, and a numerical/experimental value of 1.00 does not necessarily mean that the prediction is accurate during the rest of the time.

Table D.2: Maximum floor accelerations experimental/numerical comparison as-built/repaired specimens. Note: Initial model rec. input refers to the pseudo-blind experimental prediction.

			Blind prediction		Initial model rec. input		Post-Experimental	
Test	Floor	Exp.	Num.	Num./Exp.	Num.	Num./Exp.	Num.	Num./Exp.
1.1	1	0.30	0.56	1.87	0.42	1.40	0.30	1.00
1.1	2	0.41	0.60	1.46	0.56	1.37	0.42	1.02
1.1	3	0.70	0.75	1.07	0.71	1.01	0.57	0.81
2.1	1	0.32	0.31	0.97	0.32	1.00	0.33	1.03
2.1	2	0.43	0.39	0.91	0.39	0.91	0.37	0.86
2.1	3	0.63	0.57	0.90	0.51	0.81	0.43	0.68
2.2	1	0.57	0.46	0.81	0.56	0.98	0.33	0.58
2.2	2	0.52	0.44	0.85	0.45	0.87	0.52	1.00
2.2	3	0.71	0.53	0.75	0.69	0.97	0.61	0.86

D.2.4 Post-Experimental Prediction Retrofitted Specimen

In the following figures (Figure D.24 and Figure D.25), the predicted floor accelerations experienced by the retrofitted specimen are presented and compared with the recorded counterparts. In Table D.3 the maximum values of the predicted and recorded floor accelerations for Tests 3.1 and 3.2 are summarized and compared. Again, these peak values do not necessarily occur at the same time after the beginning of the motion.

Table D.3: Maximum floor accelerations experimental/numerical comparison retrofitted specimen.

Test	Floor	Exp.	Num.	Num./Exp.
3.1	1	0.25	0.25	1.00
3.1	2	0.26	0.29	1.12
3.1	3	0.40	0.38	0.95
3.2	1	0.35	0.49	1.40
3.2	2	0.53	0.55	1.04
3.2	3	0.77	0.63	0.82

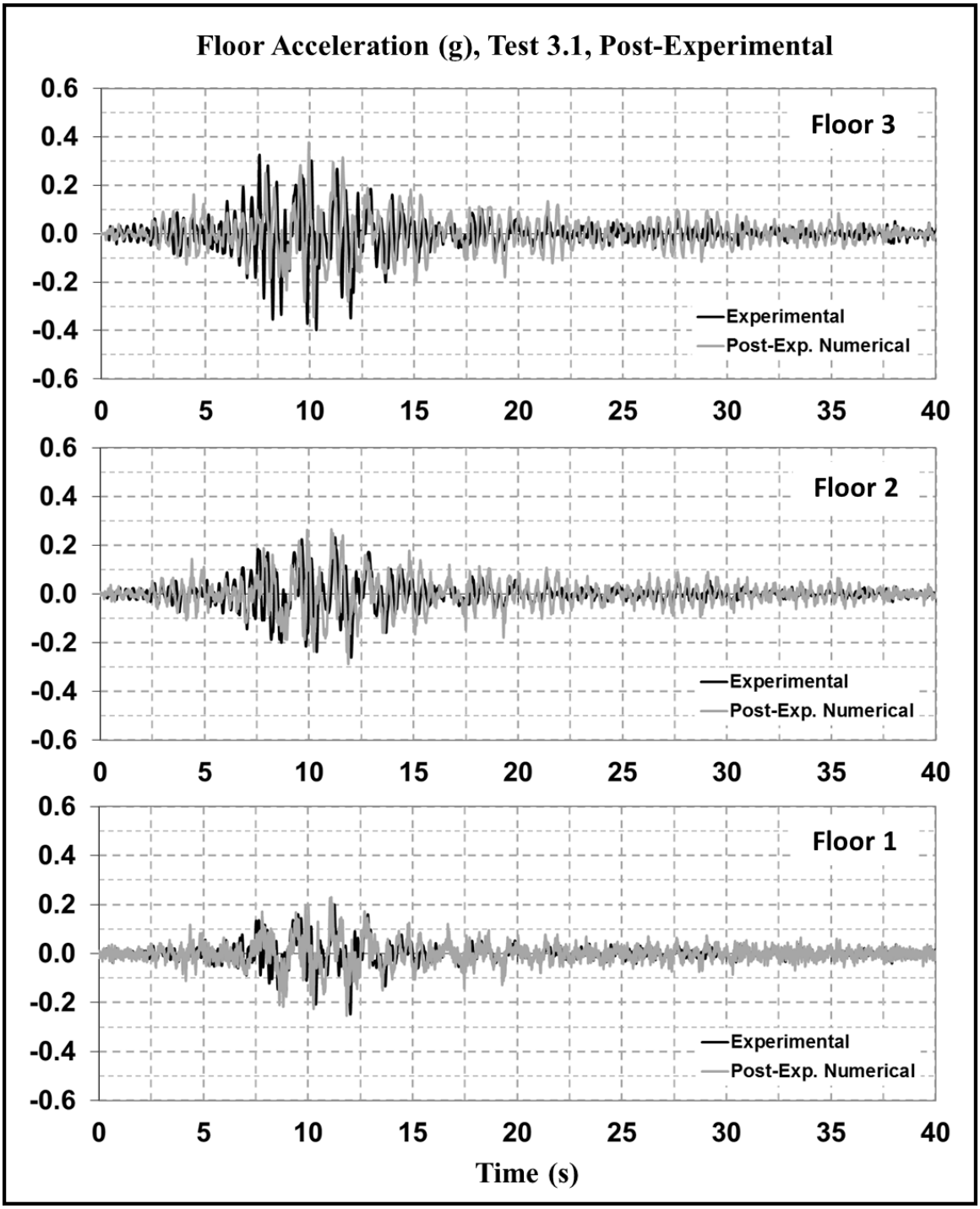

Figure D.24: Test 3.1 floor accelerations, post-experimental prediction.

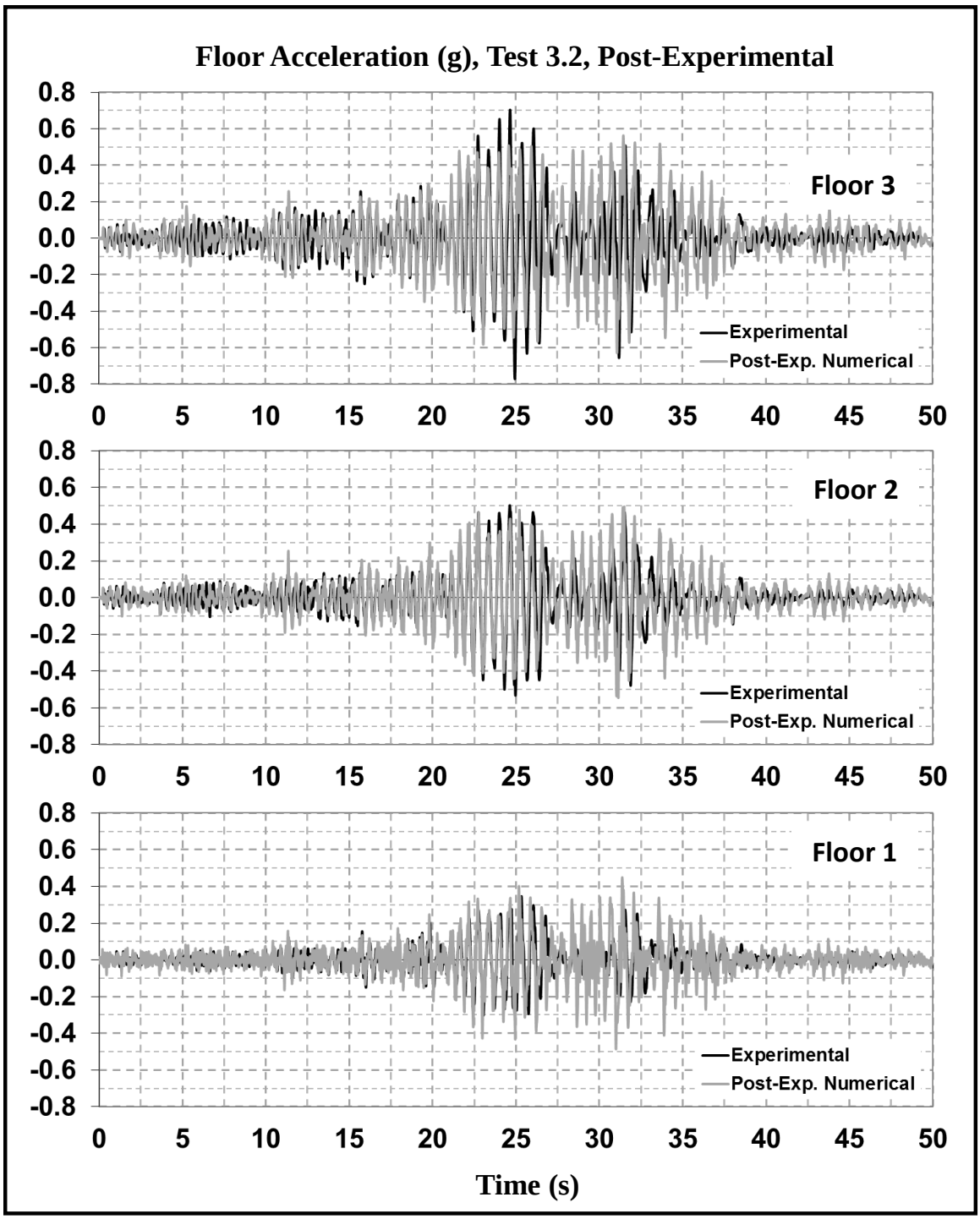

Figure D.25: Test 3.2 floor accelerations, post-experimental prediction.

D.3 MEASURED AND PREDICTED INITIAL PERIODS OF VIBRATION COMPARISON

In Table D.4, the values of the measured periods of the initial modes of vibration of the as-built and repaired specimens using the Fourier domain method are compared with those predicted with the numerical models used for the blind and post-experimental predictions. In Table D.5 the same comparison is made for the retrofitted specimen,

noting that in this case only a post-experimental prediction was done. In those tables, an excellent agreement between the experimental and numerical values of the initial (elastic) periods of the three modes of vibration of the structure can be clearly appreciated.

Table D.4: Measured and predicted periods of vibration as-built and repaired specimens.

	Measured Periods (sec.)		Predicted Periods (sec.)	
Mode	As-built Specimen	Repaired Specimen	Blind Prediction As-built/repaired	Post-Exp. Prediction As-built/repaired
1	0.24	0.27	0.29	0.29
2	0.13	0.09	0.11	0.12
3	0.08	0.06	0.07	0.08

Table D.5: Measured and predicted periods of vibration retrofitted specimen

	Measured Periods (sec.)	Predicted Periods (sec.)
Mode	Retrofitted Specimen	Post-Exp. Prediction Retrofitted
1	0.32	0.32
2	0.11	0.13
3	0.08	0.07

D.4 REFERENCES

fib Task Group 7.2 (2003), Bulletin 25: *Displacement-Based Seismic Design of Reinforced Concrete Buildings*, International Federation for Structural Concrete, Lausanne, Switzerland.

Freeman, S. A. (1998), 'The Capacity Spectrum Method as a Tool for Seismic Design', Proceedings of the 11th European Conference on Earthquake Engineering, Paris, France.

Freeman, S. A. (2003), 'Review of the Development of the Capacity Spectrum Method', *ISET Journal of Earthquake Technology*, Vol. 41, No.1, pp. 1-13.

Priestley, M. J. (2002), 'Direct Displacement-Based Design of Precast/Prestressed Concrete Buildings', *PCI journal*, Vol. 47, No. 6, pp. 66-79.